



International Journal of
Molecular Sciences

Special Issue Reprint

Frontiers in New Drug Discovery

From Molecular Targets to Preclinical Trials

Edited by
Dmitry Aminin

www.mdpi.com/journal/ijms



Frontiers in New Drug Discovery: From Molecular Targets to Preclinical Trials

Frontiers in New Drug Discovery: From Molecular Targets to Preclinical Trials

Editor

Dmitry Aminin

MDPI • Basel • Beijing • Wuhan • Barcelona • Belgrade • Manchester • Tokyo • Cluj • Tianjin



Editor

Dmitry Aminin
Lab of Bioassay
G.B. Elyakov Pacific Institute
of Bioorganic Chemistry
Far Eastern Branch of the
Russian Academy of Sciences
Vladivostok
Russia

Editorial Office

MDPI
St. Alban-Anlage 66
4052 Basel, Switzerland

This is a reprint of articles from the Special Issue published online in the open access journal *International Journal of Molecular Sciences* (ISSN 1422-0067) (available at: www.mdpi.com/journal/ijms/special_issues/Frontiers_New_Drug_Discovery).

For citation purposes, cite each article independently as indicated on the article page online and as indicated below:

LastName, A.A.; LastName, B.B.; LastName, C.C. Article Title. <i>Journal Name</i> Year , Volume Number, Page Range.
--

ISBN 978-3-0365-7683-1 (Hbk)

ISBN 978-3-0365-7682-4 (PDF)

© 2023 by the authors. Articles in this book are Open Access and distributed under the Creative Commons Attribution (CC BY) license, which allows users to download, copy and build upon published articles, as long as the author and publisher are properly credited, which ensures maximum dissemination and a wider impact of our publications.

The book as a whole is distributed by MDPI under the terms and conditions of the Creative Commons license CC BY-NC-ND.

Contents

Dmitry Aminin

Frontiers in New Drug Discovery: From Molecular Targets to Preclinical Trials

Reprinted from: *Int. J. Mol. Sci.* **2023**, *24*, 8321, doi:10.3390/ijms24098321 1

Natalia Smyrska-Wieleba and Tomasz Mroczek

Natural Inhibitors of Cholinesterases: Chemistry, Structure–Activity and Methods of Their Analysis

Reprinted from: *Int. J. Mol. Sci.* **2023**, *24*, 2722, doi:10.3390/ijms24032722 5

Alfonso Annunziata, Paola Imbimbo, Maria Elena Cucciolito, Giarita Ferraro, Vincenzo Langellotti and Alessandra Marano et al.

Impact of Hydrophobic Chains in Five-Coordinate Glucoconjugate Pt(II) Anticancer Agents

Reprinted from: *Int. J. Mol. Sci.* **2023**, *24*, 2369, doi:10.3390/ijms24032369 49

Chrysoula Mikra, Achilleas Mitrakas, Virginia Ghizzani, Katerina R. Katsani, Maria Koffa and Michael Koukourakis et al.

Effect of Arylazo Sulfones on DNA: Binding, Cleavage, Photocleavage, Molecular Docking Studies and Interaction with A375 Melanoma and Non-Cancer Cells

Reprinted from: *Int. J. Mol. Sci.* **2023**, *24*, 1834, doi:10.3390/ijms24031834 67

Jung Moon Kim, Hyewon Kim, Su Hyun Oh, Won Il Jang, Seung Bum Lee and Mineon Park et al.

Combined Administration of Pravastatin and Metformin Attenuates Acute Radiation-Induced Intestinal Injury in Mouse and Minipig Models

Reprinted from: *Int. J. Mol. Sci.* **2022**, *23*, 14827, doi:10.3390/ijms232314827 87

Valeriia V. Sennikova, Alena V. Zalaltdinova, Yulia M. Sadykova, Ayrat R. Khamatgalimov, Almir S. Gazizov and Alexandra D. Voloshina et al.

Diastereoselective Synthesis of Novel Spiro-Phosphacoumarins and Evaluation of Their Anti-Cancer Activity

Reprinted from: *Int. J. Mol. Sci.* **2022**, *23*, 14348, doi:10.3390/ijms232214348 103

Dayana da Costa Salomé, Rosana Helena Coimbra Nogueira de Freitas, Carlos Alberto Manssour Fraga and Patricia Dias Fernandes

Novel Regioisomeric Analogues of Naphthyl-*N*-Acylhydrazone Derivatives and Their Anti-Inflammatory Effects

Reprinted from: *Int. J. Mol. Sci.* **2022**, *23*, 13562, doi:10.3390/ijms232113562 117

David Aebisher, Michał Osuchowski, Dorota Bartusik-Aebisher, Magdalena Krupka-Olek, Klaudia Dynarowicz and Aleksandra Kawczyk-Krupka

An Analysis of the Effects of In Vitro Photodynamic Therapy on Prostate Cancer Tissue by Histopathological Examination and Magnetic Resonance Imaging

Reprinted from: *Int. J. Mol. Sci.* **2022**, *23*, 11354, doi:10.3390/ijms231911354 137

Omar Samir, Naohiro Kobayashi, Teppei Nishino, Mennatullah Siyam, Manoj Kumar Yadav and Yuri Inoue et al.

Transcription Factor MAFB as a Prognostic Biomarker for the Lung Adenocarcinoma

Reprinted from: *Int. J. Mol. Sci.* **2022**, *23*, 9945, doi:10.3390/ijms23179945 153

Shan-Ju Yeh, Tsun-Yung Yeh and Bor-Sen Chen

Systems Drug Discovery for Diffuse Large B Cell Lymphoma Based on Pathogenic Molecular Mechanism via Big Data Mining and Deep Learning Method

Reprinted from: *Int. J. Mol. Sci.* **2022**, *23*, 6732, doi:10.3390/ijms23126732 167

Aleksandra Kvetkina, Evgeny Pislyagin, Ekaterina Menchinskaya, Ekaterina Yurchenko, Rimma Kalina and Sergei Kozlovskiy et al.
Kunitz-Type Peptides from Sea Anemones Protect Neuronal Cells against Parkinson’s Disease Inductors via Inhibition of ROS Production and ATP-Induced P2X7 Receptor Activation
Reprinted from: *Int. J. Mol. Sci.* **2022**, *23*, 5115, doi:10.3390/ijms23095115 **189**

Jiqing Ye, Xiao Yang and Cong Ma
QSAR, Docking, and Molecular Dynamics Simulation Studies of Sigmacidins as Antimicrobials against *Streptococci*
Reprinted from: *Int. J. Mol. Sci.* **2022**, *23*, 4085, doi:10.3390/ijms23084085 **213**



Editorial

Frontiers in New Drug Discovery: From Molecular Targets to Preclinical Trials

Dmitry Aminin

G.B. Elyakov Pacific Institute of Bioorganic Chemistry, Far Eastern Branch of the Russian Academy of Sciences, 690022 Vladivostok, Russia; daminin@piboc.dvo.ru

The intention of this Special Issue is to focus on new aspects of drug discovery, including the search for new molecular targets of various diseases, the creation of new modern methods for diagnosing diseases, the development of new test systems and kits for assessing the selectivity and effectiveness of new drugs, the study of the molecular mechanisms of biologically active compounds, the formulation of new drugs, pharmacokinetic and pharmacodynamic studies and preclinical trials of important molecules.

Most of the articles in this Special Issue are devoted to the creation of new compounds with an antitumor activity and for anticancer therapy and cancer diagnostics. Thus, new platinum (II) cationic five-coordinate complexes and their physicochemical properties were described. Their biological activity was investigated against two pairs of cancer and non-cancer cell lines. The tested drugs were internalized in cancer cells and were able to activate the apoptotic pathway [1]. The regio- and diastereoselective synthesis of novel pyrrolidine-fused spiro-dihydrophosphacoumarins were presented in [2]. This new approach in the synthesis of spiro-dihydrophosphacoumarins is complementary to existing approaches and provides an easy entry to the otherwise inaccessible derivatives, some of which have significantly greater cytotoxic activity against the HuTu 80 cell line than the reference 5-fluorouracil.

Two articles consider the creation of phototoxic compounds and methods of photodynamic cancer therapy. Mikra et al. [3] synthesized a set of arylazo sulfones, known to undergo N-S bond cleavage upon exposure to light, and investigated their activity in the dark and upon the irradiation of DNA. It turned out that exposure to UV light leads to structural rearrangements in some arylazo sulfones, increasing their cytotoxic activity against several cell lines. Thus, the temporal and spatial manipulation of light may enable these new scaffolds to be useful for the creation of phototoxic pharmaceuticals. One study [4] is devoted to the development of a method of minimally invasive focal therapy to reduce the number of prostate tumor cells while maintaining delicate structures in the treatment of prostate cancer. Prostate tissue samples were treated with oxygenated solutions of Rose Bengal or protoporphyrin IX disodium salt and illuminated with visible light. They were then analyzed for changes in morphology using microscopy and assessed for measurements detected using MRI. The parameters recorded indicated a pronounced antitumor effect of the drugs after photodynamic exposure.

In the investigation by Samir et al. [5], the expressions of a number of molecular markers characteristic of tumor-associated macrophages (TAMs) were localized. Immunohistochemical and morphometric analyses of tissue samples from patients with lung adenocarcinoma revealed that higher numbers of a basic leucine zipper transcription factor of macrophage (MAFB+) cells were significantly correlated with increased metastasis, a high recurrence rate, increased lymphatic permeability, higher vascular invasion, and pleural infiltration. It turned out that an increase in the number of MAFB+ cells is accompanied by the poor survival of tobacco-dependent patients, and MAFB can be considered a marker for TAMs and a prognostic biomarker for smokers with lung cancer. Using big data mining and deep learning methods, Yeh et al [6] studied the pathogenesis of two subtypes of

Citation: Aminin, D. Frontiers in New Drug Discovery: From Molecular Targets to Preclinical Trials. *Int. J. Mol. Sci.* **2023**, *24*, 8321. <https://doi.org/10.3390/ijms24098321>

Received: 4 May 2023

Accepted: 4 May 2023

Published: 5 May 2023



Copyright: © 2023 by the author. Licensee MDPI, Basel, Switzerland. This article is an open access article distributed under the terms and conditions of the Creative Commons Attribution (CC BY) license (<https://creativecommons.org/licenses/by/4.0/>).

diffuse large B-cell lymphoma. Applying a modern approach, the authors were able to compare the main signaling pathways and pathogenic mechanisms, making possible to identify pathogenic biomarkers as drug targets for two tumor subtypes. Through the use of a deep-neural-network-based drug-target interaction model that was trained in advance, assessments of the drug regulation ability and drug toxicity were carried out. As a result, the two drug combinations were proposed to alleviate two subtypes of B-cell lymphoma, respectively.

One publication examined the radioprotection activity of two lipid-lowering drugs, Pravastatin and Metformin, that are used to treat type 2 diabetes mellitus [7]. It was found that the combined administration of these two drugs had a therapeutic effect on acute radiation-induced intestinal injury in mouse and mini-pig models and markedly increased animal survival in a radiation-induced intestinal injury model. The effect was accompanied by a significant reduction in radiation-induced biochemical damages.

Several articles concern the study of the anti-inflammatory activities and neuroprotective properties of chemical compounds and their antimicrobial potential and ability to inhibit key enzymes. Three novel regioisomeric analogues of naphthyl-*N*-acylhydrazone derivatives were studied with respect to their anti-inflammatory activity in in vitro and in vivo models of inflammation. The compounds did not have toxic properties. At the same time, they significantly reduced the migration of leukocytes associated with inflammation and the production of nitric oxide and interleukin-1 β ; however, they did not affect the activity of inducible nitric oxide synthase and did not demonstrate an NO scavenger effect. The data show that these substances have promising effects for the development of new drug prototypes [8]. The neuroprotective properties of a series of recombinant sea anemone peptides were studied in [9]. It was established that two selected peptides inhibit the formation of ROS and NO in Neuro-2a neuroblastoma cells induced by paraquat and rotenone to mimic Parkinson disease in vitro. Spectrofluorometry, fluorescence imaging and SPR analysis have shown that the peptide protective mechanism is mediated by the inhibition of the P2X7 receptor's functionality.

Using combined computer simulation methods, the antimicrobial properties of benzoic acid derivatives, sigmacidins, which inhibit the interaction of the bacterial RNA polymerase- σ factor and demonstrate pronounced antimicrobial activity against Streptococci, were studied. The use of the QSAR, docking and molecular dynamics methods made it possible to predict means of further optimizing the chemical structure of sigmacidins in order to enhance their antimicrobial properties and create new drugs against pathogenic *Streptococcus pneumoniae* [10].

Acetylcholinesterase inhibitors are widely used in medical practice. One review [11] collected information on natural inhibitors, the sources of their production, and the relationship of their chemical structures with therapeutic effects and described various methods for determining their biological activity. The review emphasized that further studies of the mechanisms of action and structure–activity correlations are needed to discuss the use of new cholinesterase inhibitors for the treatment of certain diseases.

Conflicts of Interest: The author declares no conflict of interest.

References

1. Annunziata, A.; Imbimbo, P.; Cucciolito, M.E.; Giarita Ferraro, G.; Langellotti, V.; Marano, A.; Melchiorre, M.; Tito, G.; Trifuoggi, M.; Monti, D.M.; et al. Impact of Hydrophobic Chains in Five-Coordinate Glucoconjugate Pt(II) Anticancer Agents. *Int. J. Mol. Sci.* **2023**, *24*, 2369. [CrossRef] [PubMed]
2. Sennikova, V.V.; Zalaltdinova, A.V.; Sadykova, Y.M.; Khamatgalimov, A.R.; Gazizov, A.S.; Voloshina, A.D.; Lyubina, A.P.; Amerhanova, S.K.; Voronina, J.K.; Chugunova, E.A.; et al. Diastereoselective Synthesis of Novel Spiro-Phosphacoumarins and Evaluation of Their Anti-Cancer Activity. *Int. J. Mol. Sci.* **2022**, *23*, 14348. [CrossRef] [PubMed]
3. Mikra, C.; Mitrakas, A.; Ghizzani, V.; Katsani, K.R.; Koffa, M.; Koukourakis, M.; Psomas, G.; Protti, S.; Fagnoni, M.; Fylaktakidou, K.C. Effect of Arylazo Sulfones on DNA: Binding, Cleavage, Photocleavage, Molecular Docking Studies and Interaction with A375 Melanoma and Non-Cancer Cells. *Int. J. Mol. Sci.* **2023**, *24*, 1834. [CrossRef] [PubMed]

4. Aebisher, D.; Osuchowski, M.; Bartusik-Aebisher, D.; Krupka-Olek, M.; Dynarowicz, K.; Kawczyk-Krupka, A. An Analysis of the Effects of In Vitro Photodynamic Therapy on Prostate Cancer Tissue by Histopathological Examination and Magnetic Resonance Imaging. *Int. J. Mol. Sci.* **2022**, *23*, 11354. [CrossRef] [PubMed]
5. Samir, O.; Kobayashi, N.; Nishino, T.; Siyam, M.; Yadav, M.K.; Inoue, Y.; Takahashi, S.; Hamada, M. Transcription Factor MAFB as a Prognostic Biomarker for the Lung Adenocarcinoma. *Int. J. Mol. Sci.* **2022**, *23*, 9945. [CrossRef] [PubMed]
6. Yeh, S.-J.; Yeh, T.-Y.; Chen, B.-S. Systems Drug Discovery for Diffuse Large B Cell Lymphoma Based on Pathogenic Molecular Mechanism via Big Data Mining and Deep Learning Method. *Int. J. Mol. Sci.* **2022**, *23*, 6732. [CrossRef] [PubMed]
7. Kim, J.M.; Kim, H.; Oh, S.H.; Jang, W.I.; Lee, S.B.; Park, M.; Kim, S.; Park, S.; Shim, S.; Jang, H. Combined Administration of Pravastatin and Metformin Attenuates Acute Radiation-Induced Intestinal Injury in Mouse and Minipig Models. *Int. J. Mol. Sci.* **2022**, *23*, 14827. [CrossRef] [PubMed]
8. da Costa Salomé, D.; de Freitas, R.H.C.N.; Fraga, C.A.M.; Fernandes, P.D. Novel Regioisomeric Analogues of Naphthyl-*N*-Acyldiazine Derivatives and Their Anti-Inflammatory Effects. *Int. J. Mol. Sci.* **2022**, *23*, 13562. [CrossRef] [PubMed]
9. Kvetkina, A.; Pisyagin, E.; Menchinskaya, E.; Yurchenko, E.; Kalina, R.; Kozlovskiy, S.; Kaluzhskiy, L.; Menshov, A.; Kim, N.; Peigneur, P.; et al. Kunitz-Type Peptides from Sea Anemones Protect Neuronal Cells against Parkinson's Disease Inductors via Inhibition of ROS Production and ATP-Induced P2X7 Receptor Activation. *Int. J. Mol. Sci.* **2022**, *23*, 5115. [CrossRef] [PubMed]
10. Ye, J.; Yang, X.; Ma, C. QSAR, Docking, and Molecular Dynamics Simulation Studies of Sigmacidins as Antimicrobials against *Streptococci*. *Int. J. Mol. Sci.* **2022**, *23*, 4085. [CrossRef] [PubMed]
11. Smyrska-Wieleba, N.; Mroczek, T. Natural Inhibitors of Cholinesterases: Chemistry, Structure–Activity and Methods of Their Analysis. *Int. J. Mol. Sci.* **2023**, *24*, 2722. [CrossRef] [PubMed]

Disclaimer/Publisher's Note: The statements, opinions and data contained in all publications are solely those of the individual author(s) and contributor(s) and not of MDPI and/or the editor(s). MDPI and/or the editor(s) disclaim responsibility for any injury to people or property resulting from any ideas, methods, instructions or products referred to in the content.



Review

Natural Inhibitors of Cholinesterases: Chemistry, Structure–Activity and Methods of Their Analysis

Natalia Smyrska-Wieleba and Tomasz Mroczek *

Department of Chemistry of Natural Products, Medical University of Lublin, 1 Chodzki Str.,
20-093 Lublin, Poland

* Correspondence: tmroczek@pharmacognosy.org

Abstract: This article aims to provide an updated description and comparison of the data currently available in the literature (from the last 15 years) on the studied natural inhibitors of cholinesterases (IChEs), namely, acetylcholinesterase (AChE) and butyrylcholinesterase (BuChE). These data also apply to the likely impact of the structures of the compounds on the therapeutic effects of available and potential cholinesterase inhibitors. IChEs are hitherto known compounds with various structures, activities and origins. Additionally, multiple different methods of analysis are used to determine the cholinesterase inhibitor potency. This summary indicates that natural sources are still suitable for the discovery of new compounds with prominent pharmacological activity. It also emphasizes that further studies are needed regarding the mechanisms of action or the structure–activity correlation to discuss the issue of cholinesterase inhibitors and their medical application.

Keywords: natural products; acetylcholinesterase inhibitors; butyrylcholinesterase inhibitors; Alzheimer’s disease; central nervous system

1. Introduction

Cholinesterase inhibitors are chemical compounds that impair the activity of cholinesterases: AChE and BuChE. They reduce the hydrolysis of the neurotransmitters acetylcholine (ACh) (acetylcholinesterase inhibitors) and butyrylcholine (butyrylcholinesterase inhibitors), thereby increasing their levels in the body (brain, blood and nerve tissue). Naturally occurring cholinesterase inhibitors affect esterases in a reversible manner [1].

IChE drugs currently used in medicine are synthetically derived. The majority of them originate from natural substances. One of them, tacrine, was approved for treatment, and it has been used similarly to donepezil, galanthamine (1) and rivastigmine. Unfortunately, the first of them causes hepatotoxicity, while the others have side effects including insomnia, diarrhea, nausea and vomiting [2].

IChEs (BuChE and AChE) also show therapeutic activity when applied in treatments for myasthenia gravis, myopathies, disorders associated with peripheral nerve damage, impaired conduction of nervous stimuli, and diseases associated with dementia, such as vascular dementia and Alzheimer’s and Parkinson’s diseases [3–5].

The mechanisms causing Alzheimer’s disease (AD) are not entirely understood. In patients with AD, marked decreases in neurotransmitter levels in the cells are observed. In particular, the concentration of acetylcholine is reduced, together with dopamine, glutamate, serotonin and norepinephrine [6].

Currently, due to the limited knowledge of effective methods of treating the causes of these disorders, therapies, as before, are mainly based on symptomatic treatments (except for Aduhelm® Aducanumab, which underwent accelerated FDA (U.S. Food and Drug Administration) approval [7]). Studies indicate that an increase in the level of cholinergic transmission in patients with AD (increase in ACh) mitigates disease progression. It also has a beneficial effect on cognitive functions and improves the patient’s mood, despite the

Citation: Smyrska-Wieleba, N.; Mroczek, T. Natural Inhibitors of Cholinesterases: Chemistry, Structure–Activity and Methods of Their Analysis. *Int. J. Mol. Sci.* **2023**, *24*, 2722. <https://doi.org/10.3390/ijms24032722>

Academic Editor: Jan Korabecny

Received: 1 December 2022

Revised: 24 January 2023

Accepted: 26 January 2023

Published: 1 February 2023



Copyright: © 2023 by the authors. Licensee MDPI, Basel, Switzerland. This article is an open access article distributed under the terms and conditions of the Creative Commons Attribution (CC BY) license (<https://creativecommons.org/licenses/by/4.0/>).

reduction in cholinergic neurons in the brain [1,5,6]. This can be accomplished by inhibiting the hydrolytic enzyme that decomposes acetylcholine (AChE) after its release from neurons to the synaptic area. There are some studies that suggest that maintaining acetylcholine prevents the formation of senile plaques through its indirect impact on the activation of α -secretase. This is a result of the activation of protein kinase C upon stimulation by the ACh receptor muscarinic M1 [5].

AChE and BuChE can be distinguished in the central nervous system [8]. Both cholinesterases influence the distribution of ACh.

With the level of advancement of AD, the increased function of BuChE with a decrease in AChE was observed [9]. There are reports suggesting that AChE impacts the progression of dementia diseases by increasing the expression of $A\beta$ amyloid precursor, neuronal apoptosis and the aggregation of AChE- $A\beta$ amyloid, which is more toxic than the protein itself [1].

For the mitigation of symptoms such as a decline in cognition, listlessness and mood swings, inhibitors of BuChE may be helpful due to the presence of the enzyme observed in the structures responsible for these functions in the brain (thalamic nucleus and glia). BuChE was also present in pathological structures: senile plaques and neurofibrillary tangles in patients with AD [3,8]. During tests in normal mice, these stimulants showed an increasing tendency of ACh release in the brain. These functions are controlled by the areas of the forebrain. This can lead to the conclusion that decreasing the number of cholinergic neurons in this area can cause a disturbance in attention [10].

Potentially, it can be assumed that drugs that demonstrate the inhibition of both AChE and BuChE are preferable. It is difficult to say which substances prove to be more efficient. Certainly, we know that irreversible AChE inhibitors can cause serious toxicity and may even lead to death; hence, only reversible inhibitors are of therapeutic use [3,5].

There are also opinions in publications suggesting that compounds selectively inhibiting BuChE will be more effective than selective AChE inhibitors. These findings are based on the published results of work relating to the activity of huperzine A and the analysis of the effects of inhibitors presently used in medicine [11]. Galanthamine (1) and donepezil are reversible inhibitors of both cholinesterases (transient bonding), while rivastigmine is pseudo-irreversible (covalent bonding with the enzyme). Hence, a greater focus on selective inhibitors of BuChE is suggested [12].

The purpose of this review is to provide updated information (from the last 15 years) on cholinesterase inhibitors present in plant materials, discuss their structure–activity correlation and describe methods that can be used for their analysis. We hope that such a comprehensive review will serve as a guide for scientists willing to find potentially novel molecules for neurodegenerative disorders, such as AD.

2. Chemistry–Structure Activity

Cholinesterase inhibitors belong to different groups of compounds. It may be noted here that compounds that have shown activity generally are in similar classes and included in the same group of compounds or even the same type in the group.

Compounds of natural origin showing an inhibitory effect on cholinesterase (ChE) can be considered in terms of the potency of their activity, their selectivity for each cholinesterase or their method of binding to the enzyme (reversible, pseudo-irreversible or irreversible inhibitors) [13].

The ability to inhibit cholinesterases is observed in various groups, including alkaloids, anthranoids, bibenzyls, coumarins, chromones, diarylheptanoids, fatty acids, flavonoids, lignans, phenanthrenes, phenylpropanoids, phthalates, phenolic acids, phlorotannins, polyphenols, polyketides, steroids (sterols), terpenes (diterpenes, triterpenoids, lanostane triterpenes and sesquiterpenes (sesquiterpene lactones)), stilbenoids, trilavanones and xanthonoids.

The majority of hitherto known, applied and potent IChEs (e.g., galanthamine (1), rivastigmine and tacrine) are derived from the group of alkaloids. Additionally, flavonoids and coumarins (IBuChE) have become increasingly important as appropriate inhibitors, because they show strong inhibition of ChE and fewer side effects.

Therefore, the focus is on describing the correlation between the activity and structure of selected groups of compounds for which the results of AChE or BuChE inhibition were the most promising (Table 1) [13]. There are reports that suggest a correlation of the activity of a compound on AChE and BuChE with certain components of its structure.

2.1. Alkaloids

These metabolites are characterized by the presence of nitrogen in a negative oxidation state (proton acceptor), in most cases positioned in a heterocycle. This may affect the active site of cholinesterase [13,14].

Because of its use in therapeutics, galanthamine (**1**) may be considered the most important alkaloid inhibiting cholinesterases. It is applied in AD treatment or other neurological disorders. Amaryllidaceae plants are natural sources of galanthamine (**1**). Some species of *Narcissus*, *Leucojum* and *Ungernia* genera are particularly rich in this alkaloid. It can also be obtained synthetically. There were also attempts to obtain it through biosynthesis [15].

Galanthamine (**1**) has a strong inhibitory effect on both AChE and BuChE; however, it is more selective toward AChE. It reveals competitive inhibition; additionally, it has a modulating impact on the nicotinic acetylcholine receptor. Thanks to this effect, it also supports neuromuscular conduction [15–17]. There are many publications describing the inhibition of cholinesterase by galanthamine (**1**). Thus, it is often treated as a reference substance (Table 1). On the basis of research on the interaction between galanthamine (**1**) and AChE from *Torpedo californica*, it was found to bind in the active center of the enzyme. The interaction between the double bond present in the galanthamine (**1**) cyclohexene ring and Trp84 enzyme was observed [18].

Monoterpenoid indole alkaloids from *Nauclea officinalis* exhibit inhibitory activity against BuChE. The inhibitory impact of some of them (Table 1, Figure 1) is greater than that of galanthamine (**1**) [19]. Liew et al. (2015) [19], after performing molecular docking, speculate that the high value of cholinesterase inhibition exhibited by angustidine (**2**) is due to the hydrogen bonding (atom C-19 participates in the hydrogen bond) of the inhibitor with amino acids of the enzyme (Ser 198 and His 438) (Figure 1). On the basis of the structure–activity relationship (SAR), McNulty et al. (2010) [18] indicated that the inhibitory effect of lycorine-type alkaloids on AChE is due to an increase in the involvement of the lipophilic substituent in C-1 and C-2 acting as hydroxyl in galanthamine (**1**) (general structure of lycorine-type alkaloids (**3**)) (Figure 1).

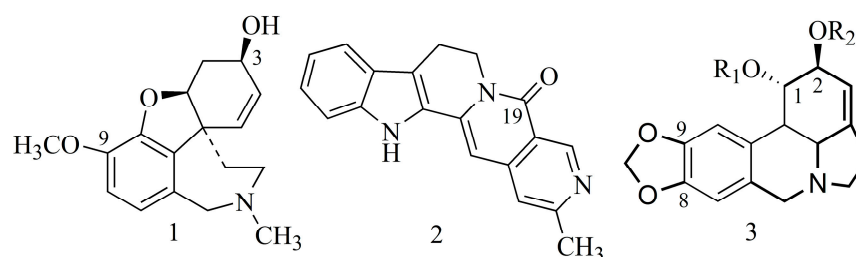


Figure 1. Chemical structures of galanthamine (**1**) and angustidine (**2**) and general structure of lycorine-type alkaloids (**3**).

According to Berkov et al. (2008), the alkaloids *N*-allyl-*nor*-galanthamine (**4**) and *N*-(14-methylallyl)-*nor*-galanthamine (**5**) isolated from the leaves of *Leucojum aestivum* L. demonstrated more potent inhibition of AChE than galanthamine (**1**) (Table 1). It appears that the inhibitory activity of both compounds is due to the substitution of the *N*-methyl derivative (allyl or 14-methylallyl group). The compounds are characterized by the presence of a methoxyl substituent at C-9, and the nitrogen atom also has a substituent alkyl group (Figure 2), which may indicate its greater lipophilicity compared to galanthamine (**1**) [20]. Among the alkaloids belonging to the Amaryllidaceae family (Table 1), sanguinine (**6**)

isolated from *Galanthus woronowii* or *Hieronymiella marginata* [21,22] is the most potent. It is also substituted at the N atom but with a methyl group; however, this is the same moiety as in the case of galantamine. The stronger activity of sanguinine (6) compared to galanthamine (1), *N*-allyl-*nor*-galanthamine (4) and *N*-(14-methylallyl)-*nor*-galanthamine (5) may be explained by the presence of a hydroxyl group at the C-9 carbon and is not due to a methoxy group as in their case. The stronger the directing effect of the hydroxyl substituent (compared to the methoxy group), the stronger the activation of the aromatic ring in the electrophilic substitution reaction (Figure 2).

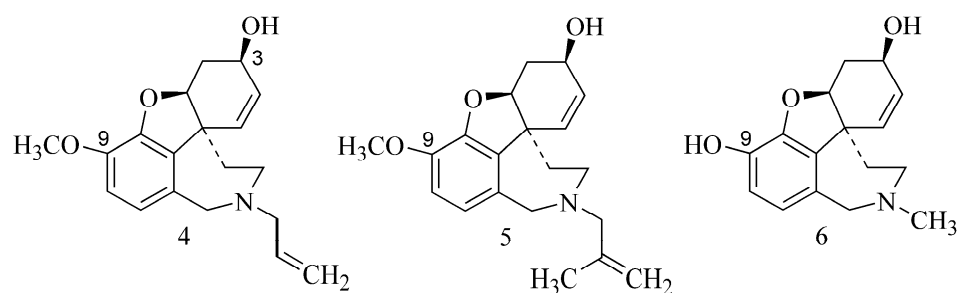


Figure 2. Chemical structures of *N*-allyl-*nor*-galanthamine (4), *N*-(14-methylallyl)-*nor*-galanthamine (5) and sanguinine (6).

The structures of isoquinoline alkaloids of the protoberberine type (Table 1) are similar to the structure of acetylcholine, containing an anionic site—acetoxy—and simultaneously a cationic site (amine). As in the case of acetylcholine, this structure may enable the bonding of the acetoxy group to the serine hydroxyl group at the site of hydrolysis of the substrate located in the esteratic site of AChE. The cationic site may be an isoquinoline nitrogen atom [1]. Protoberberine-type alkaloids (e.g., berberine (7), dihydroberberine (8) and coptisine (9)) such as Amaryllidaceae alkaloids are characterized by the presence of substituent methoxy and hydroxy groups or methylenedioxy groups, but in different positions (at C-2, C-3 and C-9, C-10), as well as a positively charged nitrogen atom [23].

As noted by Song et al. (2021), the presence of a conjugated aromatic system in the B ring is responsible for the strong inhibitory activity (e.g., berberine (7), coptisine (9), epiberberine, jatrorrhizine and palmatine (Table 1)). The hydrogenation of this ring decreases the inhibitory activity of the alkaloid (e.g., dihydroberberine (8)), while the cyclization leading to the methylenedioxy group has no impact on this activity (e.g., coptisine (9)) [23] (Figure 3).

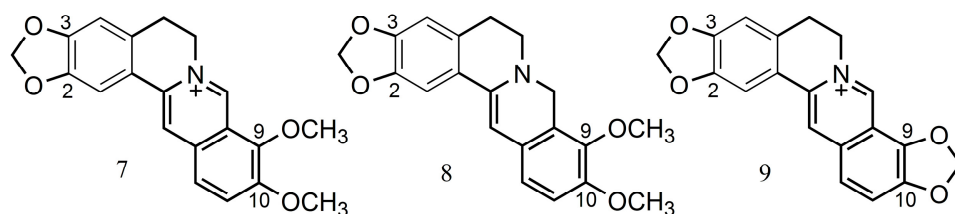


Figure 3. Chemical structures of berberine (7), dihydroberberine (8) and coptisine (9).

In the case of alkaloids extracted from *Lycopodium casuarinoides* (lycoparins A (10), B (11) and C (12)), the structure is also important in the inhibitory activity. Only lycoparin C (12) showed such an ability (Table 1), whereas lycoparins A (10) and B (11) have poor activity ($IC_{50} > 200 \mu M$) as a consequence of the occurrence of carboxylic acid at the C-15 and methyl substituents attached to N (Figure 4) [24].

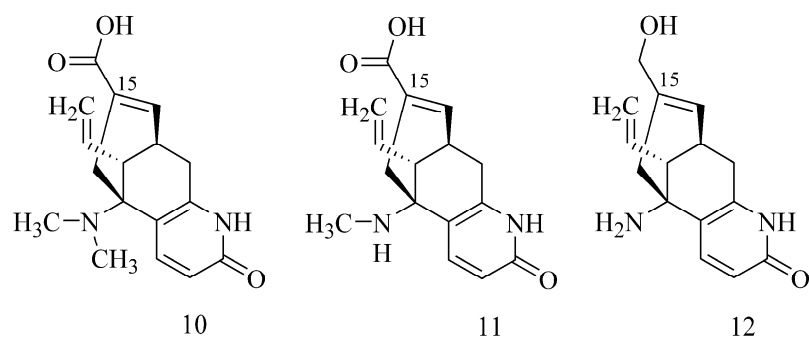


Figure 4. Chemical structures of lycoparin A (**10**), lycoparin B (**11**) and lycoparin C (**12**).

Strong inhibitory activity against AChE comparable to that of galanthamine (**1**) is demonstrated by indole alkaloids from *Ervatamia hainanensis* (coronaridine (**13**) and voacangine (**14**)). Due to the presence of the substituent voacangine (**14**), they have markedly increased AChE inhibition. This is because of the attachment of the methoxyl substituent to the phenyl group, while the substitution of 10-hydroxycoronaridine with a hydroxy group on the phenyl decreases the activity (Table 1) (Figure 5) [25].

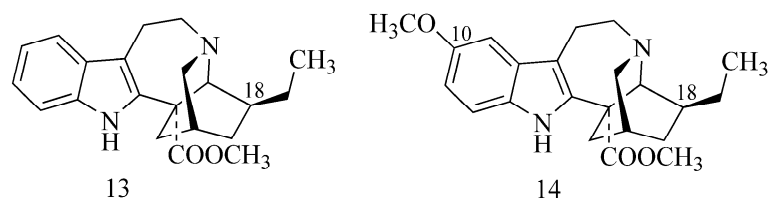


Figure 5. Chemical structures of coronaridine (**13**) and voacangine (**14**).

2.2. Coumarins

Coumarins are derivatives of an α -pyrone ring fused with benzene. Hydroxycoumarin (a hydroxyl group), methoxycoumarin (a methoxy group) (substituted at C-7, C-5 or less so at C-6, C-8), furanocoumarin (a furan ring) and piranocoumarin (a pyran ring) have been distinguished.

Research on the structure and inhibition led to the conclusion that furanocoumarins have more affinity for BuChE than AChE [13,14]. Cholinesterase-inhibiting coumarins are often found in the Apiaceae and Rutaceae families [26].

It is noted that the effect of compounds isolated from an extract of *Citrus hystrix* (6'-hydroxy-7'-methoxybergamottin (**15**) and 6', 7'-dihydroxybergamottin (**16**)) against BuChE depends on the presence of a dioxygenated geranyl chain in their structures (Figure 6) [27].

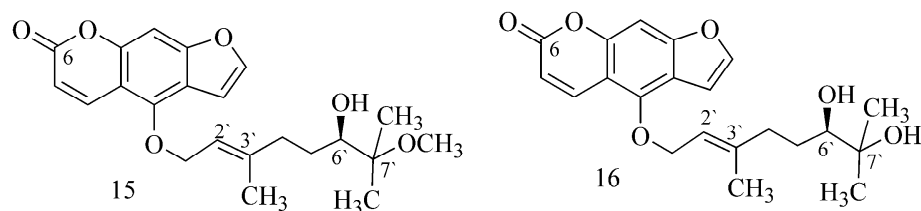


Figure 6. Chemical structures of 6'-hydroxy-7'-methoxybergamottin (**15**) and 6',7'-dihydroxybergamottin (**16**).

In a study of the activity of coumarins from *Angelica archangelica* L., the authors assume that BuChE inhibitory activity occurs only in C-8-substituted furanocoumarins (imperatorin (**17**), heraclenol-2'-O-angelate (**18**) (Table 1)). Simple coumarins (osthole and archangelicin), 5-substituted furanocoumarins (isoimperatorin (**19**), phellopterin, bergapten

and isopimpinellin) and substituted derivatives at both C-5 and C-8 (byakangelicin-2'-O-angelate (**20**) and byakangelicin-2'-O-isovalerate) do not show this effect (Figure 7) [28].

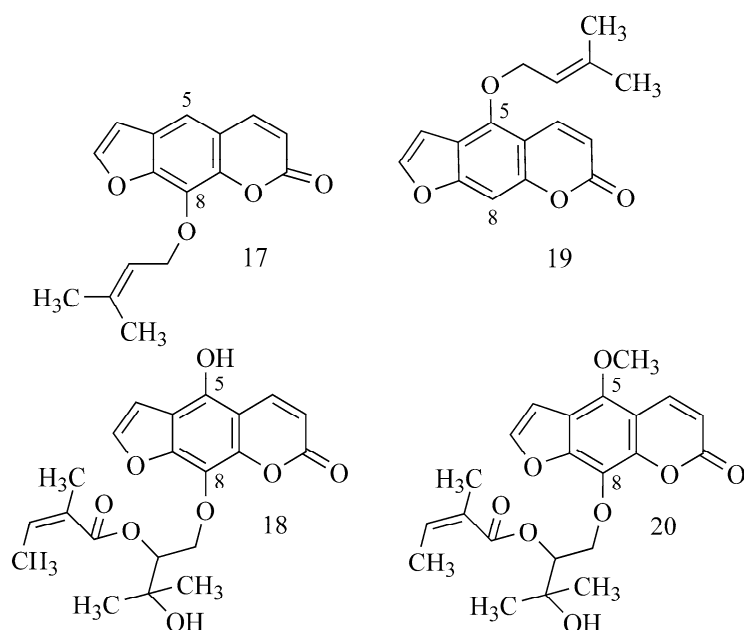


Figure 7. Chemical structures of imperatorin (**17**), heraclenol-2'-O-angelate (**18**), isoperatorin (**19**) and byakangelicin-2'-O-angelate (**20**).

Compounds isolated from *Mesua elegans* such as 4-phenylcoumarins [29] show an explicit impact of inhibiting of AChE, because the activity increases for those which contain a dimethylpyran ring at C-5/C-6 and a prenyl substituent in position C-3 (mesuagenin B (**21**)). For 6-geranylated coumarins (5,7-dihydroxy-8-(3-methylbutanoyl)-6-[(*E*)-3,7-dimethylocta-2,6-dienyl]-4-phenyl-2H-chromen-2-one (**22**)), the activity increases in the case of the presence of a 2-methylbutanoyl group, and it is lower for those with a 2-methylpropanoyl or 3-methylbutanoyl group at C-8 (Figure 8) [29].

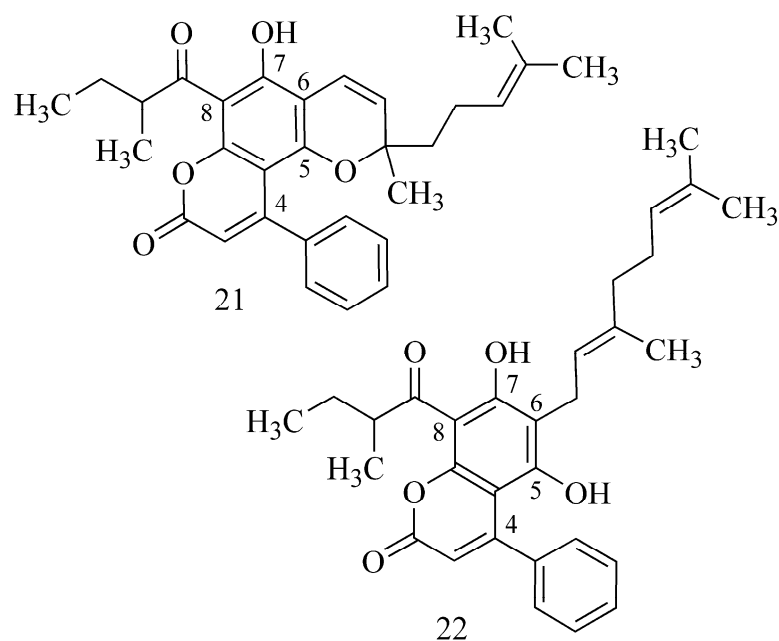


Figure 8. Chemical structures of mesuagenin B (**21**) and 5,7-dihydroxy-8-(3-methylbutanoyl)-6-[(*E*)-3,7-dimethylocta-2,6-dienyl]-4-phenyl-2H-chromen-2-one (**22**). (*Stereochemistry not determined).

2.3. Diarylheptanoids

Diarylheptanoids are a group of natural compounds with structures based on a 1,7-diphenylheptane skeleton [30].

In diarylheptanoids isolated from *Alpinia officinalis* by Lee et al. (2018) [31] (Table 1), it has been observed that the ChE inhibition strength is related to the presence of double bonds in the molecule and is proportional to their number. Thus, (–)-alpininoid B (23) exhibits the strongest AChE and BuChE inhibition, whereas (4E)-1,7-diphenyl 4-hepten-3-one is weaker (24), and dihydroyashsbushiketol is the weakest (25), where additional bonds are absent (Figure 9) [31].

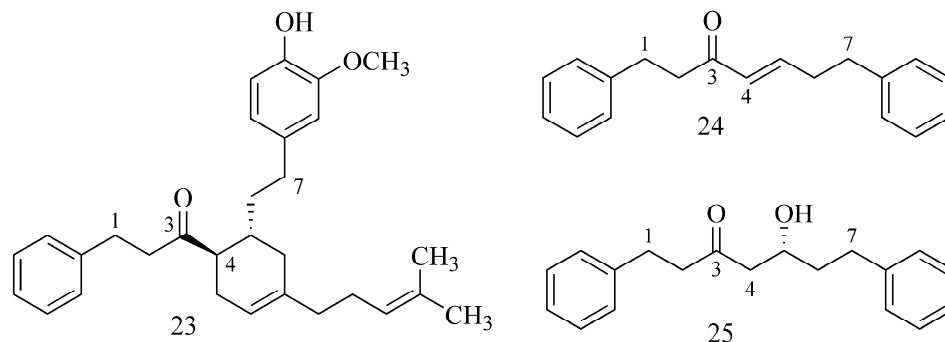


Figure 9. Chemical structures of (–)-alpininoid B (23), (4E)-1,7-diphenyl 4-hepten-3-one (24) and dihydroyashsbushiketol (25).

2.4. Flavonoids

Flavonoids are highly active inhibitors with low toxicity [29]. The flavonoid group consists of flavanones (27), flavonols (28), dihydroflavonols, flavones, isoflavones (29), chalcones, dihydrochalcones and aurones (Figure 10) [14].

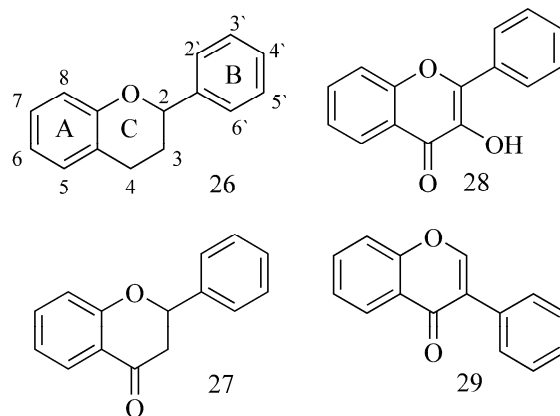


Figure 10. General chemical structures of flavonoid (26), flavanone (27), flavonol (28) and isoflavone (29) rings.

The bond-line formula of flavonoids is made of two aromatic rings linked to diphenylpropane in a C6–C3–C6 system. Most of them have an additional gamma-pyrone system (rings C) divided into types due to the different positions of the B ring, the oxidation number of the C ring and the presence of additional functional groups [13,14,32].

Xie et al. (2014) [32] studied the link between the binding affinities of flavonoids with AChE using a typical measurement—the fluorescence quenching method reported by Ryu et al. (2012) [33]. They checked 20 flavonoids (i.e., baicalin, genistein, chrysin, apigenin, formononetin, 7,8-dihydroflavone, puerarin, luteolin, rutin (36), fisetin, naringenin, daidzein, daidzin, myricetin, myricetrin, quercetin, quercetrin, kaempferol (35), kaempferide and baicalein). According to this research, it can be inferred that inhibitory

flavonoids form a complex with AChE. The presence of a hydroxyl group, especially in the A ring of the flavonoid, as well as the double bond between C-2 and C-3, increases the affinity of the enzyme (hydrogen bonds) and also increases the AChE inhibitory properties of flavonoids. Glycosylation, on the other hand, decreases the activity and affinity of flavonoids toward the enzyme in a manner that depends on the form of the attached sugar moiety (1–5-fold). The presence of a methoxy group affects the activity of a flavonoid differently depending on its type, and no correlation was observed here [32].

Analyzing the impact of the structure of flavonoids from *Paulownia tomentosa* fruits indicated that geranylated flavonoids at C-6 (e.g., diplacone (30)) (Table 1) are pivotal against hAChE and BuChE. The lack of this moiety causes a clear decrease in inhibition (eriodictyol (31) ($IC_{50} = 1663 \mu M$)). It has also been proved that dihydroflavonols (4'-O-methyldiplacol (32)) show stronger inhibition compared to flavones (4'-O-methyldiplacone (33)) (Figure 11) [34].

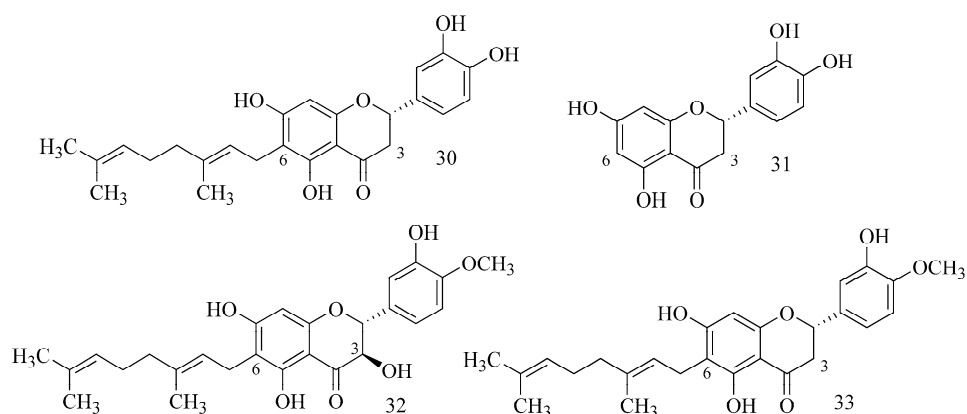


Figure 11. Chemical structures of diplacone (30), eriodictyol (31), 4'-O-methyldiplacol (32) and 4'-O-methyldiplacone (33).

Selected flavonoids have been studied (docking study) (galangin (34), kaempferol (35), quercetin, myricetin, fisetin, apigenin, luteolin and rutin (36)) [35]. The inhibitory potency of flavonoids toward BuChE depends on the presence and the location of OH groups in the structure. A sugar moiety causing steric hindrance reduces these properties. Galangin (34) showed the strongest activity, kaempferol (35) was proved to be weaker, and rutin (36) was the weakest (Figure 12).

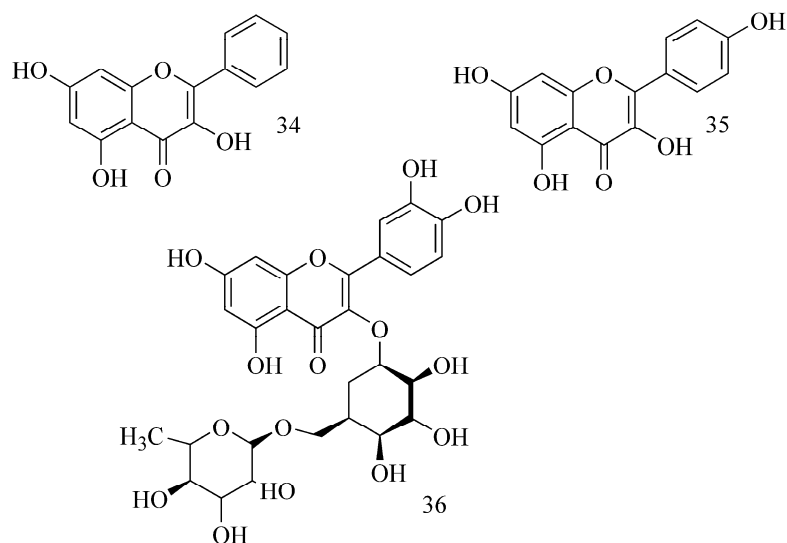


Figure 12. Chemical structures of galangin (34), kaempferol (35) and rutin (36).

2.5. Phenanthrenes

Phenanthrenes are a group of natural compounds with a structure based on the phenanthrene skeleton, occurring in the form of monomeric, dimeric or trimeric derivatives [36].

Phenanthrenes from *Bletilla striata* showed potent and selective inhibitory activity against BuChE [37]. A publication by Liu et al. (2022) described that the presence of substituents at C-2 and C-7 is responsible for the stronger BuChE inhibition of phenanthrenes from *Bletilla striata*. The activity is more potent when the phenanthrene is substituted with a hydroxy group (e.g., 1-[(4-hydroxyphenyl)methyl]-4-methoxy-2,7-phenanthrenediol (**37**)), while substitution with a methoxy group reduces this effect (e.g., 1-(4-hydroxybenzyl)-4,7-dimethoxyphenanthrene-2,8-diol (**38**)). Substituents at C-8 (hydroxy group) and also at C-1 (4-hydroxybenzyl) improve the affinity to the enzyme (Figure 13) [37].

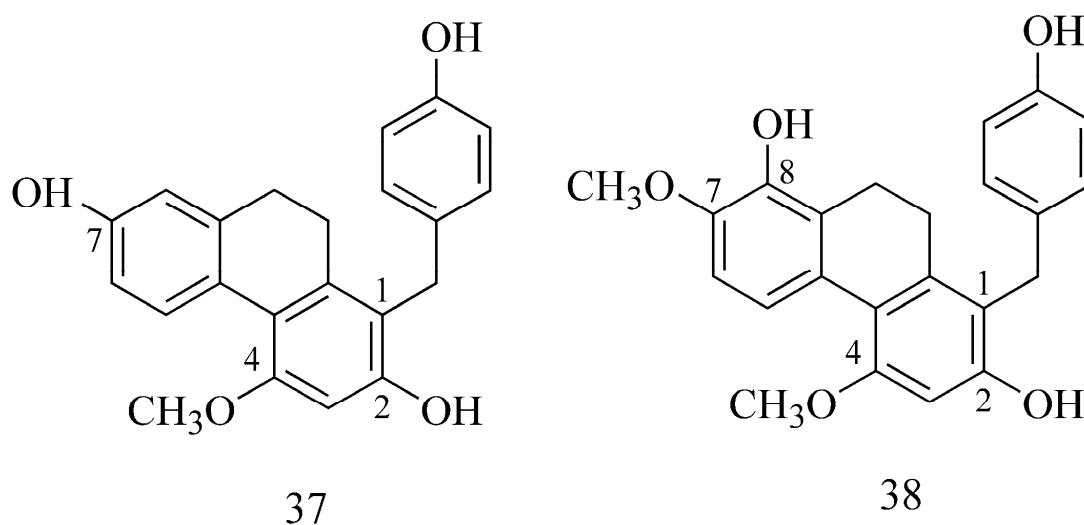


Figure 13. Chemical structures of 1-[(4-hydroxyphenyl)methyl]-4-methoxy-2,7-phenanthrenediol (**37**) and 1-(4-hydroxybenzyl)-4,7-dimethoxyphenanthrene-2,8-diol (**38**).

2.6. Terpenes

These are compounds aggregated from properly bound isoprene subunits. We can distinguish monoterpenes, sesquiterpenes, diterpenes and triterpenes [14].

By testing acetone extracts of the roots of *Salvia miltiorhiza* Bunge, strong inhibitory activity against AChE for the diterpenes dihydrotanshinone I (**39**) ($IC_{50} = 1 \mu M$) and cryptotanshinone (**40**) ($IC_{50} = 7 \mu M$) and weak activity for tanshinone I (**41**) ($IC_{50} > 50 \mu M$) and tanshinone IIA (**42**) ($IC_{50} > 140 \mu M$) [38] (Table 1) were found by Ren et al. (2004). The authors suppose that the activity is probably a result of the existence of a dihydrofuran ring instead of a furan ring present in the compounds indicating weak inhibitory activity. Additionally, compounds containing an aromatic ring in their structures showed much higher activity than those that have a cyclohexane ring at this site [38]. However, the study by Zhou et al. (2011) showed quite different results [39]. Inhibitory activity was not observed in tanshinone IIA (**42**) or cryptotanshinone (**40**), but tanshinone I (**41**) and dihydrotanshinone I (**39**) showed strong activity. Both of these compounds are similar in terms of o-aromatic rings; they only differ in the presence or lack of a double bond in the furan ring. The authors suggest that for the inhibitory effect on AChE, the structure of the aromatic ring may be more important than the furan ring as was thought before (the presence or lack of a double bond) (Figure 14) [39].

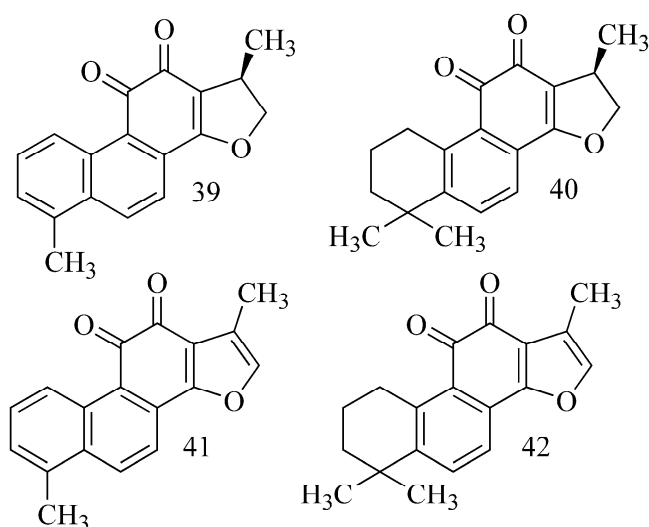


Figure 14. Chemical structures of dihydrotanshinone I (39), cryptotanshinone (40), tanshinone I (41) and tanshinone IIA (42).

2.7. Xanthonoids

Xanthonoids and xanthenes are subgroups of polyphenols with structures based on the tricyclic skeleton dibenzo- γ -pirone [40].

In the study by Urbain et al. (2004), xanthenes isolated from *Gentiana campestris* exhibited inhibitory activity against AChE [41]. Bellidifolin (43) had the best result. It achieved a minimum inhibitory quantity on TLC identical to that of galanthamine (1) (0.03 nM), while weaker results were those of bellidin (44) (0.15 nM) and its bellidifolin glycosides: 8-O- β -glucopyranoside (*nor*-swertianolin) and 8-O- β -glucopyranoside (swertianolin) were even weaker (0.18 and 1.2 nM, respectively) [41]. The weaker inhibition of the enzyme by glycosides can probably be explained by steric hindrance and diverted hydrophobicity. On the other hand, xanthenes containing an additional methoxyl group in the C-3 position showed stronger activity [41].

In a more recent study by Urbain et al. (2008), the activity of xanthenes of *Gentianella amarella* ssp. *acuta* was examined [42]. They exhibited weaker activity (also including bellidin (44) and bellidifolin (43)), and only triptexanthoside C (45) reached significant results for activity against AChE (Table 1) [42]. This compound also has a methoxyl group in its structure, which may influence the higher result of cholinesterase inhibition (Figure 15).

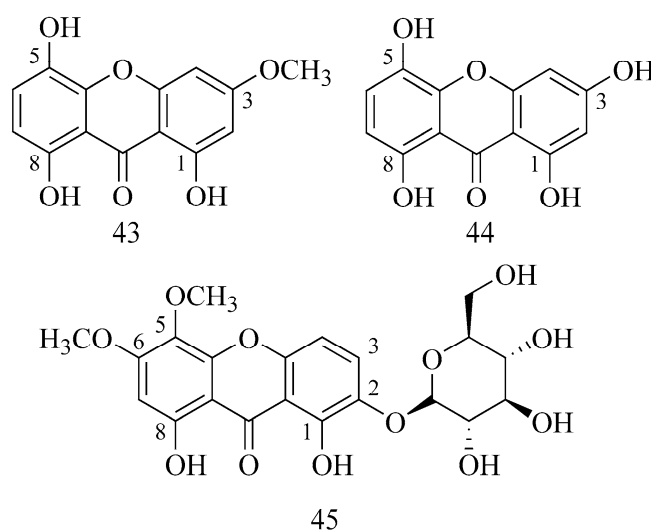


Figure 15. Chemical structures of bellidifolin (43), bellidin (44) and triptexanthoside C (45).

In summary, the potential activity of an acetylcholinesterase inhibitor is influenced by the presence of hydroxyl and methoxyl groups in the molecule and also by the presence of the cationic part of the structure of the compound (e.g., nitrogen in the heterocyclic system). The substrate-like structure of the inhibitor (or acetylcholine) indicates the competitive inhibition of the enzyme, and it is most beneficial in pharmacology. Large molecules, e.g., glycosidic forms of the tested compounds, were characterized by weaker AChE inhibitory activity due to their steric hindrance in the enzyme. The occurrence, different number and localization of double bonds, preferably in conjugated systems (diarylheptanoids and Amaryllidaceae alkaloids), are of utmost importance. With the increase in the number of conjugated double-bond systems, as well as the presence of substituents that polarize the aromatic system, the energy of the cation- π interaction increases, and thus, the binding energy of the inhibitor with the protein residue of the enzyme increases [43]. The presence of these substituents in the compounds was also significant in the inhibition against AChE. This may be related to the ability of BuChE to hydrolyze both butyrylcholine and acetylcholine [1,44]. The structure of the BuChE enzyme molecule enables the catalysis of large acyl groups, which the AChE molecule is not capable of. Hence, in the presented data (Table 1), there are many inhibitors that are inactive against AChE while demonstrating moderate or strong activity toward BuChE [1]. This may be due to the steric hindrance of the AChE enzyme due to the large branched structures of such compounds, as is demonstrated by the weaker activity of glycosides in relation to their aglycones (xanthonoids from *Gentiana campestris*) (Table 1).

The review topic of natural cholinesterase inhibitors has been discussed in other publications, including [45–47]. Most of them are based on the description of results obtained for plant fractions and extracts or, in addition, for compounds isolated from them [45,46]. This article focuses on the comparison of particular isolated natural compounds' activities, considering both plant and animal origins (e.g., alkaloids from scorpions or sponges). Some of the previous reviews did not include this information [45,46]. The current review includes 20 groups (24 subgroups) of compounds; a total of 357 results for cholinesterase inhibition by natural compounds are listed, arranged alphabetically by compound group, species name and compound name. A total of 84 species or their varieties belonging to 44 families were examined. The current review shows, in tabular form, the results of the inhibition of both AChE and BuChE enzymes. The present summary is also characterized by the fact that the type of enzyme and the method used in the study are presented. This review shows that differences are significant and have an impact on the results of enzyme inhibition by the tested compounds. This paper focuses on the review of the results of studies on natural cholinesterase inhibitors tested using *in vitro* methods. The presented overview is also characterized by the description and consideration of the type of method used for the determination of cholinesterase inhibition, which has not been undertaken in other recent reviews, or they were limited to the modifications of colorimetric Ellman's method [46].

The data, mainly from the selected latest publications issued from 2008 to 2022, on cholinesterase inhibitors of natural origin are ordered in the table below (Table 1). The following sources were used to prepare the review article database: Chemical Abstract (SciFinder), Reaxys and Science Direct (partially by authorized access), as well as sources directly obtained from the authors (ResearchGate GmbH).

Table 1. Inhibitors' classification in terms of their affiliation with a group of compounds, their effects on AChE and BuChE, their activity, their origins and the methods of their analysis.

Inhibitors	Source	Activity				Method	Ref.
		Value of Inhibition against AChE	Reference Standard for AChE	Value of Inhibition against BuChE	Reference Standard for BuChE		
ALKALOIDS							
Lindoldhamine isomer	<i>Abuta panuwensis</i> Eichler Menispermaceae (branches)	39.38 ± 0.08 µM ^{a,j}	NEO 3.72 ± 0.03 µM ^{a,j}	nd	nd	MCE	
5-N-Methylmaytenine	<i>Abuta panuwensis</i> Eichler Menispermaceae (branches)	19.55 ± 0.09 µM ^{a,j}	NEO 3.72 ± 0.03 µM ^{a,j}	nd	nd	MCE	
N-trans-Feruloyltyramine	<i>Abuta panuwensis</i> Eichler Menispermaceae (branches)	na	NEO 3.72 ± 0.03 µM ^{a,j}	nd	nd	MCE	[48–50]
Palmatine	<i>Abuta panuwensis</i> Eichler Menispermaceae (branches)	35.25 ± 0.04 µM ^{a,j}	NEO 3.72 ± 0.03 µM ^{a,j}	nd	nd	MCE	
Stepharine	<i>Abuta panuwensis</i> Eichler Menispermaceae (branches)	61.24 ± 0.03 µM ^{a,j}	NEO 3.72 ± 0.03 µM ^{a,j}	nd	nd	MCE	
Aconorine	<i>Aconitum laeve</i> Ranunculaceae (tubers)	2.51 ± 0.037 µM ^{a,e}	GAL 3.26 ± 0.021 µM ^{a,e}	8.72 ± 0.023 µM ^{a,m}	10.13 ± 0.05 µM ^{a,m}	MCE	
Hohenackerine	<i>Aconitum laeve</i> Ranunculaceae (tubers)	4.53 ± 0.062 µM ^{a,e}	GAL 3.26 ± 0.021 µM ^{a,e}	9.94 ± 0.073 µM ^{a,m}	10.13 ± 0.05 µM ^{a,m}	MCE	[51,52]
Lappaconotine	<i>Aconitum laeve</i> Ranunculaceae (tubers)	6.13 ± 0.019 µM ^{a,e}	GAL 3.26 ± 0.021 µM ^{a,e}	11.24 ± 0.12 µM ^{a,m}	10.13 ± 0.05 µM ^{a,m}	MCE	
Swatinine-C	<i>Aconitum laeve</i> Ranunculaceae (tubers)	3.7 ± 0.085 µM ^{a,e}	GAL 3.26 ± 0.021 µM ^{a,e}	12.23 ± 0.014 µM ^{a,m}	10.13 ± 0.05 µM ^{a,m}	MCE	
4-Methoxy-1-methyl-2-quinolone	<i>Atractylis cancellata</i> L. Asteraceae (whole plant)	>50 µg mL ⁻¹ ^{a,k}	GAL 6.27 ± 1.15 µg mL ⁻¹ ^{a,k}	37.49 ± 1.61 µg mL ⁻¹ ^{a,n}	34.75 ± 1.99 µg mL ⁻¹ ^{a,n}	MCE	[53]
Pyrroloquinolone A	<i>Atractylis cancellata</i> L. Asteraceae (whole plant)	18.48 ± 0.33 µg mL ⁻¹ ^{a,k}	GAL 6.27 ± 1.15 µg mL ⁻¹ ^{a,k}	9.66 ± 0.16 µg mL ⁻¹ ^{a,n}	34.75 ± 1.99 µg mL ⁻¹ ^{a,n}	MCE	
Buthutin A	<i>Buthus martensii</i> Karsch Buthidae (whole body of scorpion)	7.83 ± 0.06 µM ^{a,e}	GAL 1.17 ± 0.01 µM ^{a,e} DON 0.049 ± 0.004 µM ^{a,e}	47.44 ± 0.95 µM ^{a,m}	18.78 ± 1.81 µM ^{a,m} DON 5.536 ± 0.018 µM ^{a,m}	MCE	
Buthutin B	<i>Buthus martensii</i> Karsch Buthidae (whole body of scorpion)	61.45 ± 2.34 µM ^{a,e}	GAL 1.17 ± 0.01 µM ^{a,e} DON 0.049 ± 0.004 µM ^{a,e}	122.64 ± 5.21 µM ^{a,m}	18.78 ± 1.81 µM ^{a,m} DON 5.536 ± 0.018 µM ^{a,j}	MCE	[48,54,55]
Trigonelline	<i>Buthus martensii</i> Karsch Buthidae (whole body of scorpion)	97.30 ± 4.18 µM ^{a,e}	GAL 1.17 ± 0.01 µM ^{a,e} DON 0.049 ± 0.004 µM ^{a,e}	441.87 ± 7.99 µM ^{a,m}	18.78 ± 1.81 µM ^{a,m} DON 5.536 ± 0.018 µM ^{a,m}	MCE	
17- <i>oxo</i> -3-Benzoylbuxadine	<i>Buxus hyrcana</i> Pojark. Buxaceae (leaves)	17.6 ± 0.5 µM ^{a,k}	GAL 0.53 ± 0.5 µM ^{a,k} HUP 1.7 ± 0.3 µM ^{a,k}	186.8 ± 1.0 µM ^{a,n}	8.7 ± 1.0 µM ^{a,n} HUP >1000 ± 3.0 µM ^{a,n}	MCE	
31-Demethylclobuxoviridine	<i>Buxus hyrcana</i> Pojark. Buxaceae (leaves)	298.3 ± 1.0 µM ^{a,k}	GAL 0.53 ± 0.5 µM ^{a,k} HUP 1.7 ± 0.3 µM ^{a,k}	15.4 ± 0.5 µM ^{a,n}	8.7 ± 1.0 µM ^{a,n} HUP >1000 ± 3.0 µM ^{a,n}	MCE	
31-Hydroxybuxamine B	<i>Buxus hyrcana</i> Pojark. Buxaceae (leaves)	61.3 ± 2.0 µM ^{a,k}	GAL 0.53 ± 0.5 µM ^{a,k} HUP 1.7 ± 0.3 µM ^{a,k}	112.1 ± 3.0 µM ^{a,n}	8.7 ± 1.0 µM ^{a,n} HUP >1000 ± 3.0 µM ^{a,n}	MCE	
Buxamine A	<i>Buxus hyrcana</i> Pojark. Buxaceae (leaves)	81.4 ± 2.4 µM ^{a,k}	GAL 0.53 ± 0.5 µM ^{a,k} HUP 1.7 ± 0.3 µM ^{a,k}	100.2 ± 1.4 µM ^{a,n}	8.7 ± 1.0 µM ^{a,n} HUP >1000 ± 3.0 µM ^{a,n}	MCE	
Buxamine B	<i>Buxus hyrcana</i> Pojark. Buxaceae (leaves)	79.6 ± 3.0 µM ^{a,k}	GAL 0.53 ± 0.5 µM ^{a,k} HUP 1.7 ± 0.3 µM ^{a,k}	100.5 ± 2.5 µM ^{a,k}	8.7 ± 1.0 µM ^{a,n} HUP >1000 ± 3.0 µM ^{a,n}	MCE	[48,56–58]
Buxhyrcamine	<i>Buxus hyrcana</i> Pojark. Buxaceae (leaves)	18.2 ± 0.3 µM ^{a,k}	GAL 0.53 ± 0.5 µM ^{a,k} HUP 1.7 ± 0.3 µM ^{a,k}	209.0 ± 1.0 µM ^{a,n}	8.7 ± 1.0 µM ^{a,n} HUP >1000 ± 3.0 µM ^{a,n}	MCE	
Buxmicrophylline F	<i>Buxus hyrcana</i> Pojark. Buxaceae (leaves)	22.4 ± 0.7 µM ^{a,k}	GAL 0.53 ± 0.5 µM ^{a,k} HUP 1.7 ± 0.3 µM ^{a,k}	154.2 ± 1.0 µM ^{a,n}	8.7 ± 1.0 µM ^{a,n} HUP >1000 ± 3.0 µM ^{a,n}	MCE	
Buxrugulosamine	<i>Buxus hyrcana</i> Pojark. Buxaceae (leaves)	24.8 ± 1.0 µM ^{a,k}	GAL 0.53 ± 0.5 µM ^{a,k} HUP 1.7 ± 0.3 µM ^{a,k}	160.2 ± 4.0 µM ^{a,n}	8.7 ± 1.0 µM ^{a,n} HUP >1000 ± 3.0 µM ^{a,n}	MCE	
Cyclobuxophylline O	<i>Buxus hyrcana</i> Pojark. Buxaceae (leaves)	35.4 ± 1.0 µM ^{a,k}	GAL 0.53 ± 0.5 µM ^{a,k} HUP 1.7 ± 0.3 µM ^{a,k}	45.0 ± 2.0 µM ^{a,n}	8.7 ± 1.0 µM ^{a,n} HUP >1000 ± 3.0 µM ^{a,n}	MCE	

Table 1. Cont.

Inhibitors	Source	Activity				Method	Ref.
		Value of Inhibition against AChE	Reference Standard for AChE	Value of Inhibition against BuChE	Reference Standard for BuChE		
ALKALOIDS							
Cyclobuxoviridine	<i>Buxus hyrcana</i> Pojark. Buxaceae (leaves)	179.7 ± 0.4 µM ^{a,k}	GAL 0.53 ± 0.5 µM ^{a,k} HUP 1.7 ± 0.3 µM ^{a,k}	304.5 ± 1.0 µM ^{a,n}	GAL 8.7 ± 1.0 µM ^{a,n} HUP >1000 ± 3.0 µM ^{a,n}	MCE	
E-Buxenone	<i>Buxus hyrcana</i> Pojark. Buxaceae (leaves)	71.0 ± 2.5 µM ^{a,k}	GAL 0.53 ± 0.5 µM ^{a,k} HUP 1.7 ± 0.3 µM ^{a,k}	200.7 ± 2.6 µM ^{a,n}	GAL 8.7 ± 1.0 µM ^{a,n} HUP >1000 ± 3.0 µM ^{a,n}	MCE	
Homomoenjodarmine	<i>Buxus hyrcana</i> Pojark. Buxaceae (leaves)	19.5 ± 1.0 µM ^{a,k}	GAL 0.53 ± 0.5 µM ^{a,k} HUP 1.7 ± 0.3 µM ^{a,k}	52.2 ± 3.0 µM ^{a,n}	GAL 8.7 ± 1.0 µM ^{a,n} HUP >1000 ± 3.0 µM ^{a,n}	MCE	
Moenjodaramine	<i>Buxus hyrcana</i> Pojark. Buxaceae (leaves)	25.0 ± 2.9 µM ^{a,k}	GAL 0.53 ± 0.5 µM ^{a,k} HUP 1.7 ± 0.3 µM ^{a,k}	102.4 ± 2.0 µM ^{a,n}	GAL 8.7 ± 1.0 µM ^{a,n} HUP >1000 ± 3.0 µM ^{a,n}	MCE	
N _b -Dimethylcyclobuxoviridine	<i>Buxus hyrcana</i> Pojark. Buxaceae (leaves)	45.5 ± 0.6 µM ^{a,k}	GAL 0.53 ± 0.5 µM ^{a,k} HUP 1.7 ± 0.3 µM ^{a,k}	133.8 ± 3.4 µM ^{a,n}	GAL 8.7 ± 1.0 µM ^{a,n} HUP >1000 ± 3.0 µM ^{a,n}	MCE	
N ₂₀ -Formylbuxaminol E	<i>Buxus hyrcana</i> Pojark. Buxaceae (leaves)	25.5 ± 0.8 µM ^{a,k}	GAL 0.53 ± 0.5 µM ^{a,k} HUP 1.7 ± 0.3 µM ^{a,k}	120.9 ± 2.0 µM ^{a,n}	GAL 8.7 ± 1.0 µM ^{a,n} HUP >1000 ± 3.0 µM ^{a,n}	MCE	
Spiroformabuxine	<i>Buxus hyrcana</i> Pojark. Buxaceae (leaves)	6.3 ± 0.6 µM ^{a,k}	GAL 0.53 ± 0.5 µM ^{a,k} HUP 1.7 ± 0.3 µM ^{a,k}	125.2 ± 1.0 µM ^{a,n}	GAL 8.7 ± 1.0 µM ^{a,n} HUP >1000 ± 3.0 µM ^{a,n}	MCE	
Papillozine C	<i>Buxus hyrcana</i> Pojark. Buxaceae (leaves)	47.8 ± 1.4 µM ^{a,k}	GAL 0.53 ± 0.5 µM ^{a,k} HUP 1.7 ± 0.3 µM ^{a,k}	35.2 ± 2.0 µM ^{a,n}	GAL 8.7 ± 1.0 µM ^{a,n} HUP >1000 ± 3.0 µM ^{a,n}	MCE	
Z-Buxenone	<i>Buxus hyrcana</i> Pojark. Buxaceae (leaves)	87.4 ± 1.7 µM ^{a,k}	GAL 0.53 ± 0.5 µM ^{a,k} HUP 1.7 ± 0.3 µM ^{a,k}	155.8 ± 3.8 µM ^{a,n}	GAL 8.7 ± 1.0 µM ^{a,n} HUP >1000 ± 3.0 µM ^{a,n}	MCE	
Dihydroberberine	<i>Coptis chinensis</i> Ranunculaceae (rhizomes)	1.18 ± 0.03 µM ^{a,e}	BER 1.01 ± 0.01 µM ^{a,e} TAC 0.22 ± 0.004 µM ^{a,e}	38.82 ± 0.52 µM ^{a,m}	TAC 0.014 ± 0.0043 µM ^{a,m}	MCE	[48,59,60]
10-Hydroxy-infractopicrin	<i>Cortinarius infractus</i> Berk Cortinariaceae (toadstool)	12.7 ± 0.16 µM ^{a,d}	GAL 8.70 ± 0.05 µM ^{a,d} PHY 2.58 ± 0.03 µM ^{a,d}	nd < 100 µM ^{a,m}	GAL 24.4 ± 2.84 µM ^{a,m} PHY 1.34 ± 0.279 µM ^{a,m}	MCE	[16,48,61]
Infractopicrin	<i>Cortinarius infractus</i> Berk Cortinariaceae (toadstool)	9.72 ± 0.19 µM ^{a,d}	GAL 8.70 ± 0.05 µM ^{a,d} PHY 2.58 ± 0.03 µM ^{a,d}	nd < 100 µM ^{a,m}	GAL 24.4 ± 2.84 µM ^{a,m} PHY 1.34 ± 0.279 µM ^{a,m}	MCE	
(+)-Adlumine	<i>Corydalis mucronifera</i> Maxim. Papaveraceae (whole plants)	>100 µM ^{a,e}	GAL 1.34 ± 0.11 µM ^{a,e}	>100 µM ^{a,m}	GAL 6.81 ± 0.60 µM ^{a,m}	MCE	
Bicuculline	<i>Corydalis mucronifera</i> Maxim. Papaveraceae (whole plants)	85.89 ± 0.92 µM ^{a,e}	GAL 1.34 ± 0.11 µM ^{a,e}	59.75 ± 2.40 µM ^{a,m}	GAL 6.81 ± 0.60 µM ^{a,m}	MCE	
(-)-Corydalisol	<i>Corydalis mucronifera</i> Maxim. Papaveraceae (whole plants)	51.12 ± 0.27 µM ^{a,e}	GAL 1.34 ± 0.11 µM ^{a,e}	>100 µM ^{a,m}	GAL 6.81 ± 0.60 µM ^{a,m}	MCE	
Demethylcorydalmine	<i>Corydalis mucronifera</i> Maxim. Papaveraceae (whole plants)	71.43 ± 0.55 µM ^{a,e}	GAL 1.34 ± 0.11 µM ^{a,e}	>100 µM ^{a,m}	GAL 6.81 ± 0.60 µM ^{a,m}	MCE	
6,7-Dimethoxy-2-methyl-1,2,3,4-tetrahydroisoquinoline	<i>Corydalis mucronifera</i> Maxim. Papaveraceae (whole plants)	45.70 ± 0.42 µM ^{a,e}	GAL 1.34 ± 0.11 µM ^{a,e}	>100 µM ^{a,m}	GAL 6.81 ± 0.60 µM ^{a,m}	MCE	[16,48,62,63]
1-(1,3-Dioxolo[4,5-g]isoquinolin-5-yl)-ethanone	<i>Corydalis mucronifera</i> Maxim. Papaveraceae (whole plants)	>100 µM ^{a,e}	GAL 1.34 ± 0.11 µM ^{a,e}	>100 µM ^{a,m}	GAL 6.81 ± 0.60 µM ^{a,m}	MCE	
epi-Coryximine	<i>Corydalis mucronifera</i> Maxim. Papaveraceae (whole plants)	92.00 ± 0.19 µM ^{a,e}	GAL 1.34 ± 0.11 µM ^{a,e}	>100 µM ^{a,m}	GAL 6.81 ± 0.60 µM ^{a,m}	MCE	
Hendersine B	<i>Corydalis mucronifera</i> Maxim. Papaveraceae (whole plants)	14.22 ± 0.34 µM ^{a,e}	GAL 1.34 ± 0.11 µM ^{a,e}	>100 µM ^{a,m}	GAL 6.81 ± 0.60 µM ^{a,m}	MCE	
Hydrohydrastinine	<i>Corydalis mucronifera</i> Maxim. Papaveraceae (whole plants)	9.13 ± 0.15 µM ^{a,e}	GAL 1.34 ± 0.11 µM ^{a,e}	>100 µM ^{a,m}	GAL 6.81 ± 0.60 µM ^{a,m}	MCE	

Table 1. Cont.

Inhibitors	Source	Activity				Method	Ref.
		Value of Inhibition against AChE	Reference Standard for AChE	Value of Inhibition against BuChE	Reference Standard for BuChE		
ALKALOIDS							
9-Methyldecumbenine C	<i>Corydalis mucronifera</i> Maxim. Papaveraceae (whole plants)	>100 μM ^{a,e}	GAL 1.34 \pm 0.11 μM ^{a,e}	>100 μM ^{a,m}	GAL 6.81 \pm 0.60 μM ^{a,m}	MCE	
Mucroniferanines H	<i>Corydalis mucronifera</i> Maxim. Papaveraceae (whole plants)	2.31 \pm 0.20 μM ^{a,e}	GAL 1.34 \pm 0.11 μM ^{a,e}	36.71 \pm 1.12 μM ^{a,m}	GAL 6.81 \pm 0.60 μM ^{a,m}	MCE	
Mucroniferanines K	<i>Corydalis mucronifera</i> Maxim. Papaveraceae (whole plants)	>100 μM ^{a,e}	GAL 1.34 \pm 0.11 μM ^{a,e}	>100 μM ^{a,m}	GAL 6.81 \pm 0.60 μM ^{a,m}	MCE	
Mucroniferanines L	<i>Corydalis mucronifera</i> Maxim. Papaveraceae (whole plants)	>100 μM ^{a,e}	GAL 1.34 \pm 0.11 μM ^{a,e}	>100 μM ^{a,m}	GAL 6.81 \pm 0.60 μM ^{a,m}	MCE	
Mucroniferanines M	<i>Corydalis mucronifera</i> Maxim. Papaveraceae (whole plants)	>100 μM ^{a,e}	GAL 1.34 \pm 0.11 μM ^{a,e}	>100 μM ^{a,m}	GAL 6.81 \pm 0.60 μM ^{a,m}	MCE	
(+)-Ochotensine	<i>Corydalis mucronifera</i> Maxim. Papaveraceae (whole plants)	>100 μM ^{a,e}	GAL 1.34 \pm 0.11 μM ^{a,e}	>100 μM ^{a,m}	GAL 6.81 \pm 0.60 μM ^{a,m}	MCE	
(-)-Ochrobrine	<i>Corydalis mucronifera</i> Maxim. Papaveraceae (whole plants)	>100 μM ^{a,e}	GAL 1.34 \pm 0.11 μM ^{a,e}	>100 μM ^{a,m}	GAL 6.81 \pm 0.60 μM ^{a,m}	MCE	
Orientaline	<i>Corydalis mucronifera</i> Maxim. Papaveraceae (whole plants)	83.96 \pm 1.06 μM ^{a,e}	GAL 1.34 \pm 0.11 μM ^{a,e}	>100 μM ^{a,m}	GAL 6.81 \pm 0.60 μM ^{a,m}	MCE	
1R,9S,7'S-Methylegenine	<i>Corydalis mucronifera</i> Maxim. Papaveraceae (whole plants)	>100 μM ^{a,e}	GAL 1.34 \pm 0.11 μM ^{a,e}	>100 μM ^{a,m}	GAL 6.81 \pm 0.60 μM ^{a,m}	MCE	
5,6,7,8-Tetrahydro-1,3-dioxolo [4,5-g]isoquinoline	<i>Corydalis mucronifera</i> Maxim. Papaveraceae (whole plants)	>100 μM ^{a,e}	GAL 1.34 \pm 0.11 μM ^{a,e}	>100 μM ^{a,m}	GAL 6.81 \pm 0.60 μM ^{a,m}	MCE	
Pseudocoptisine	<i>Corydalis turtschaninovii</i> Besser forma <i>yanhusuo</i> Papaveraceae (tuber)	12.8 μM ^{a,i}	TAC 0.175 μM ^{a,i}	nd	nd	MCE	[64]
(-)-Desmethylescantofine	<i>Cryptocarya densiflora</i> Bl. Lauraceae (leaves)	201.52 μM ^{a,e}	PHY 0.16 μM ^{a,e}	166.69 μM ^{a,m}	PHY 0.58 μM ^{a,m}	MCE	
(+)-Laurotetanine	<i>Cryptocarya densiflora</i> Bl. Lauraceae (leaves)	100 $\mu\text{g mL}^{-1}$ —17.51 \pm 0.68% ^{b,e}	nd	100 $\mu\text{g mL}^{-1}$ —22.58 \pm 0.47 μM ^{a,m}	PHY 0.58 μM ^{a,m}	MCE	
(+)-nor-Nanténine	<i>Cryptocarya densiflora</i> Bl. Lauraceae (leaves)	205.55 μM ^{a,e}	PHY 0.16 μM ^{a,e}	94.45 μM ^{a,m}	PHY 0.58 μM ^{a,m}	MCE	
(+)-Oridine	<i>Cryptocarya densiflora</i> Bl. Lauraceae (leaves)	100 $\mu\text{g mL}^{-1}$ —27.89 \pm 0.64% ^{b,e}	nd	288.34 μM ^{a,m}	PHY 0.58 μM ^{a,m}	MCE	
2-Methoxyatherosperminine	<i>Cryptocarya griffithiana</i> Wight. Lauraceae (bark)	100 $\mu\text{g mL}^{-1}$ —31.58 \pm 2.87% ^{b,e}	nd	3.95 μM ^{a,m}	PHY 0.58 μM ^{a,m}	MCE	[48,65,66]
(+)-Reticuline	<i>Cryptocarya griffithiana</i> Wight. Lauraceae (bark)	301.01 μM ^{a,e}	PHY 0.16 μM ^{a,e}	65.04 μM ^{a,m}	PHY 0.58 μM ^{a,m}	MCE	
Atherosperminine	<i>Cryptocarya infectoria</i> Miq. Lauraceae (bark)	100 $\mu\text{g mL}^{-1}$ —2.06 \pm 1.29% ^{b,e}	nd	19.34 μM ^{a,m}	PHY 0.58 μM ^{a,m}	MCE	
(+)-N-Methylisococlaurine	<i>Cryptocarya infectoria</i> Miq. Lauraceae (bark)	100 $\mu\text{g mL}^{-1}$ —14.93 \pm 0.53% ^{b,e}	nd	100 $\mu\text{g mL}^{-1}$ —37.33 \pm 1.56 ^{a,m}	PHY 0.58 μM ^{a,m}	MCE	
(+)-N-Methylaurotetanine	<i>Cryptocarya infectoria</i> Miq. Lauraceae (bark)	100 $\mu\text{g mL}^{-1}$ —38.79 \pm 2.6% ^{b,e}	nd	218.81 μM ^{a,m}	PHY 0.58 μM ^{a,m}	MCE	
Chitralinine A	<i>Delphinium chitralense</i> H. Riedl in Kew Bull. Ranunculaceae (aerial parts)	13.86 \pm 0.35 μM ^{a,e}	GAL 10.12 \pm 0.06 μM ^{a,e} ALA 8.23 \pm 0.01 μM ^{a,e}	28.17 \pm 0.92 μM ^{a,m}	GAL 20.62 \pm 0.08 μM ^{a,m} ALA 18 \pm 0.06 μM ^{a,m}	MCE	[48,67]
Chitralinine B	<i>Delphinium chitralense</i> H. Riedl in Kew Bull. Ranunculaceae (aerial parts)	11.64 \pm 0.08 μM ^{a,e}	GAL 10.12 \pm 0.06 μM ^{a,e} ALA 8.23 \pm 0.01 μM ^{a,e}	24.31 \pm 0.33 μM ^{a,m}	GAL 20.62 \pm 0.08 μM ^{a,m} ALA 18 \pm 0.06 μM ^{a,m}	MCE	

Table 1. Cont.

Inhibitors	Source	Activity				Method	Ref.
		Value of Inhibition against AChE	Reference Standard for AChE	Value of Inhibition against BuChE	Reference Standard for BuChE		
Chitralinine C	<i>Delphinium chitralense</i> H. Riedl in Kew Bull. Ranunculaceae (aerial parts)	12.11 ± 0.82 μM ^{a,e}	GAL 10.12 ± 0.06 μM ^{a,e} ALA 8.23 ± 0.01 μM ^{a,e}	26.35 ± 0.06 μM ^{a,m}	GAL 20.62 ± 0.08 μM ^{a,m} ALA 18 ± 0.06 μM ^{a,m}	MCE	
Dihydropentagynine	<i>Delphinium denudatum</i> Ranunculaceae (aerial parts)	11.2 ± 0.23 μM ^{a,e}	GAL 10.1 ± 0.06 μM ^{a,e}	22.2 ± 0.33 μM ^{a,m}	GAL 20.6 ± 0.08 μM ^{a,m}	MCE	
Isotalatizidine hydrate	<i>Delphinium denudatum</i> Ranunculaceae (aerial parts)	12.1 ± 0.43 μM ^{a,e}	GAL 10.1 ± 0.06 μM ^{a,e}	21.4 ± 0.23 μM ^{a,m}	GAL 20.6 ± 0.08 μM ^{a,m}	MCE	[51,68]
Jadwarine-A	<i>Delphinium denudatum</i> Ranunculaceae (aerial parts)	9.2 ± 0.12 μM ^{a,e}	GAL 10.1 ± 0.06 μM ^{a,e}	19.6 ± 0.72 μM ^{a,m}	GAL 20.6 ± 0.08 μM ^{a,m}	MCE	
Coronaridine	<i>Ervatamia hainanensis</i> Tsiang Apocynaceae (stems)	8.6 μM ^{a,e}	GAL 3.2 μM ^{a,e}	nd	nd	CE	[25,48]
Voacangine	<i>Ervatamia hainanensis</i> Tsiang Apocynaceae (stems)	4.4 μM ^{a,e}	GAL 3.2 μM ^{a,e}	nd	nd	CE	
1-O-Acetyl-9-O-methylpseudolycorine	<i>Galanthus woronowii</i> Losinsk Amaryllidaceae (aerial parts and bulbs)	78.7 μM ^{a,f}	GAL 0.15 μM ^{a,f}	nd	nd	MCE	
Galanthine	<i>Galanthus woronowii</i> Losinsk Amaryllidaceae (aerial parts and bulbs)	7.75 μM ^{a,f}	GAL 0.15 μM ^{a,f}	nd	nd	MCE	
Lycorine	<i>Galanthus woronowii</i> Losinsk Amaryllidaceae (aerial parts and bulbs)	na	GAL 0.15 μM ^{a,f}	nd	nd	MCE	
Narwedine	<i>Galanthus woronowii</i> Losinsk Amaryllidaceae (aerial parts and bulbs)	11,79 μM ^{a,f}	GAL 0.15 μM ^{a,f}	nd	nd	MCE	[21,48,69]
O-Methylleucotamine	<i>Galanthus woronowii</i> Losinsk Amaryllidaceae (aerial parts and bulbs)	16.42 μM ^{a,f}	GAL 0.15 μM ^{a,f}	nd	nd	MCE	
Salsoline	<i>Galanthus woronowii</i> Losinsk Amaryllidaceae (aerial parts and bulbs)	na	GAL 0.15 μM ^{a,f}	nd	nd	MCE	
Sanguinine	<i>Galanthus woronowii</i> Losinsk Amaryllidaceae (aerial parts and bulbs)	0.007 μM ^{a,f}	GAL 0.15 μM ^{a,f}	nd	nd	MCE	
Sternbergine	<i>Galanthus woronowii</i> Losinsk Amaryllidaceae (aerial parts and bulbs)	0.99 μM ^{a,f}	GAL 0.15 μM ^{a,f}	nd	nd	MCE	
Chlidanthine	<i>Hieronimiella marginata</i> Hunz Amaryllidaceae (bulbs)	23.50 ± 0.65 μM ^{a,e}	GAL 1 ± 0.05 μM ^{a,e}	196.79 ± 2.67 μM ^{a,m}	GAL 14 ± 0.03 μM ^{a,m}	MCE	
Lycorine	<i>Hieronimiella marginata</i> Hunz Amaryllidaceae (bulbs)	>200 μM ^{a,e}	GAL 1 ± 0.05 μM ^{a,e}	>200 μM ^{a,m}	GAL 14 ± 0.03 μM ^{a,m}	MCE	[22,48,70]
Sanguinine	<i>Hieronimiella marginata</i> Hunz Amaryllidaceae (bulbs)	0.10 ± 0.03 μM ^{a,e}	GAL 1 ± 0.05 μM ^{a,e}	21.50 ± 0.04 μM ^{a,m}	GAL 14 ± 0.03 μM ^{a,m}	MCE	
Tazettine	<i>Hieronimiella marginata</i> Hunz Amaryllidaceae (bulbs)	>200 μM ^{a,e}	GAL 1 ± 0.05 μM ^{a,e}	>200 μM ^{a,m}	GAL 14 ± 0.03 μM ^{a,m}	MCE	
Hamayne	<i>Hippeastrum argentinum</i> Pax Amaryllidaceae (bulbs)	>200 μM ^{a,e}	GAL 0.48 ± 0.03 μM ^{a,e}	>200 μM ^{a,m}	GAL 22.39 ± 0.09 μM ^{a,m}	MCE	
7-Hydroxycyclivonine	<i>Hippeastrum argentinum</i> Pax Amaryllidaceae (bulbs)	114.07 ± 0.08 μM ^{a,e}	GAL 0.48 ± 0.03 μM ^{a,e}	67.3 ± 0.09 μM ^{a,m}	GAL 22.39 ± 0.09 μM ^{a,m}	MCE	[48,69,70]
Lycorine	<i>Hippeastrum argentinum</i> Pax Amaryllidaceae (bulbs)	>200 μM ^{a,e}	GAL 0.48 ± 0.03 μM ^{a,e}	>200 μM ^{a,m}	GAL 22.39 ± 0.09 μM ^{a,m}	MCE	

Table 1. Cont.

Inhibitors	Source	Activity				Method	Ref.
		Value of Inhibition against AChE	Reference Standard for AChE	Value of Inhibition against BuChE	Reference Standard for BuChE		
4-O-Methylningustine	<i>Hippeastrum argentinum</i> Pax Amaryllidaceae (bulbs)	>200 μM ^{a,e}	GAL 0.48 \pm 0.03 μM ^{a,e}	>200 μM ^{a,m}	GAL 22.39 \pm 0.09 μM ^{a,m}	MCE	
Montanine	<i>Hippeastrum argentinum</i> Pax Amaryllidaceae (bulbs)	>200 μM ^{a,e}	GAL 0.48 \pm 0.03 μM ^{a,e}	>200 μM ^{a,m}	GAL 22.39 \pm 0.09 μM ^{a,m}	MCE	
Panacracine	<i>Hippeastrum argentinum</i> Pax Amaryllidaceae (bulbs)	>200 μM ^{a,e}	GAL 0.48 \pm 0.03 μM ^{a,e}	>200 μM ^{a,m}	GAL 22.39 \pm 0.09 μM ^{a,m}	MCE	
Discorhabdin C	<i>Latrunculia bififormis</i> Latrunculiidae (sponge)	14.5 \pm 1.5 μM ^{a,e} 152 \pm 12 μM ^{a,f}	PHY 3.0 \pm 0.3 μM ^{a,e} PHY 14.5 \pm 2.0 μM ^{a,f}	15.8 \pm 3.5 μM ^{a,m}	PHY 28.5 \pm 3.0 μM ^{a,m}	MCE	
Discorhabdin G	<i>Latrunculia bififormis</i> Latrunculiidae (sponge)	1.3 \pm 0.2 μM ^{a,e} 116 \pm 9 μM ^{a,f}	PHY 3.0 \pm 0.3 μM ^{a,e} PHY 14.5 \pm 2.0 μM ^{a,f}	7.0 \pm 1.0 μM ^{a,m}	PHY 28.5 \pm 3.0 μM ^{a,m}	MCE	
Discorhabdin B	<i>Latrunculia bocagei</i> Latrunculiidae (sponge)	5.7 \pm 0.8 μM ^{a,e} 49.4 \pm 7.5 μM ^{a,f}	PHY 3.0 \pm 0.3 μM ^{a,e} PHY 14.5 \pm 2.0 μM ^{a,f}	137 \pm 14.5 μM ^{a,m}	PHY 28.5 \pm 3.0 μM ^{a,m}	MCE	[48,71]
Discorhabdin L	<i>Latrunculia bocagei</i> Latrunculiidae (sponge)	25.7 \pm 3.0 μM ^{a,e} 158 \pm 15 μM ^{a,f}	PHY 3.0 \pm 0.3 μM ^{a,e} PHY 14.5 \pm 2.0 μM ^{a,f}	531 \pm 45.0 μM ^{a,m}	PHY 28.5 \pm 3.0 μM ^{a,m}	MCE	
Lupanine	<i>Leontice leontopetalum</i> L. subsp. <i>ewersmannii</i> . Berberidaceae (tubers)	200 $\mu\text{g}/\mu\text{L}$ −35.41 \pm 3.55% ^{b,k}	GAL 200 $\mu\text{g}/\mu\text{L}$ −89.98 \pm 0.61% ^{b,k}	200 $\mu\text{g}/\mu\text{L}$ −81.77 \pm 2.41% ^{b,n}	GAL 200 $\mu\text{g}/\mu\text{L}$ −92.47 \pm 0.63% ^{b,n}	CE	[48,72]
N-(14-Methylallyl)-nor-galanthamine	<i>Leucojum aestivum</i> L. Amaryllidaceae (aerial parts)	0.16 \pm 0.01 μM ^{a,e}	GAL 1.82 \pm 0.40 μM ^{a,e}	nd	nd	MCE	
N-Allyl-nor-galanthamine	<i>Leucojum aestivum</i> L. Amaryllidaceae (aerial parts)	0.18 \pm 0.01 μM ^{a,e}	GAL 1.82 \pm 0.40 μM ^{a,e}	nd	nd	MCE	[20,69]
Casuarinine C	<i>Lycopodiastrium casuarinoides</i> Spring Lycopodiaceae (whole plant)	20.9 μM ^{a,i}	HUP 0.125 μM ^{a,i}	nd	nd	MCE	
Casuarinine I	<i>Lycopodiastrium casuarinoides</i> Spring Lycopodiaceae (whole plant)	12.1 μM ^{a,i}	HUP 0.125 μM ^{a,i}	nd	nd	MCE	
N-Demethylhuperzine	<i>Lycopodiastrium casuarinoides</i> Spring Lycopodiaceae (whole plant)	15.0 μM ^{a,i}	HUP 0.125 μM ^{a,i}	nd	nd	MCE	[48,73]
Huperzine C	<i>Lycopodiastrium casuarinoides</i> Spring Lycopodiaceae (whole plant)	0.489 μM ^{a,i}	HUP 0.125 μM ^{a,i}	nd	nd	MCE	
Lycoparin C	<i>Lycopodium casuarinoides</i> Spring Lycopodiaceae (whole plant)	25 μM ^{a,k}	nd	nd	nd	CE	[24,48]
Serratezomine D	<i>Lycopodium serratum</i> Thunb. var. <i>serratum</i> Lycopodiaceae (whole plant)	0.6 mM ^{a,e}	GAL 6.4 μM ^{a,e}	nd	nd	CE	[48,74]
Berberine	<i>Mahonia bealei</i> Carrière, <i>Mahonia fortunei</i> Fedde Berberidaceae (root, stem, leaf)	0.52 \pm 0.06 μM ^{a,k}	GAL 0.81 \pm 0.08 μM ^{a,k}	nd	nd	MCE	
Coptisine	<i>Mahonia bealei</i> Carrière, <i>Mahonia fortunei</i> Fedde Berberidaceae (root, stem, leaf)	0.53 \pm 0.04 μM ^{a,k}	GAL 0.81 \pm 0.08 μM ^{a,k}	nd	nd	MCE	[23,48,75]
Corypalmine	<i>Mahonia bealei</i> Carrière, <i>Mahonia fortunei</i> Fedde Berberidaceae (root, stem, leaf)	130.10 \pm 9.81 μM ^{a,k}	GAL 0.81 \pm 0.08 μM ^{a,k}	nd	nd	MCE	
Dihydroberberine	<i>Mahonia bealei</i> Carrière, <i>Mahonia fortunei</i> Fedde Berberidaceae (root, stem, leaf)	7.33 \pm 0.47 μM ^{a,k}	GAL 0.81 \pm 0.08 μM ^{a,k}	nd	nd	MCE	
Epiberberine	<i>Mahonia bealei</i> Carrière, <i>Mahonia fortunei</i> Fedde Berberidaceae (root, stem, leaf)	0.80 \pm 0.15 μM ^{a,k}	GAL 0.81 \pm 0.08 μM ^{a,k}	nd	nd	MCE	[23,48,75]

Table 1. Cont.

Inhibitors	Source	Activity				Method	Ref.
		Value of Inhibition against AChE	Reference Standard for AChE	Value of Inhibition against BuChE	Reference Standard for BuChE		
Jatrorrhizine	<i>Mahonia bealei</i> Carrière, <i>Mahonia fortunei</i> Fedde Berberidaceae (root, stem, leaf)	0.51 ± 0.04 µM ^{a,k}	GAL 0.81 ± 0.08 µM ^{a,k}	nd	nd	MCE	
Palmatine	<i>Mahonia bealei</i> Carrière, <i>Mahonia fortunei</i> Fedde Berberidaceae (root, stem, leaf)	0.74 ± 0.13 µM ^{a,k}	GAL 0.81 ± 0.08 µM ^{a,k}	nd	nd	MCE	
Stylopine	<i>Mahonia bealei</i> Carrière, <i>Mahonia fortunei</i> Fedde Berberidaceae (root, stem, leaf)	5.07 ± 0.16 µM ^{a,k}	GAL 0.81 ± 0.08 µM ^{a,k}	nd	nd	MCE	
Tetrahydroberberine	<i>Mahonia bealei</i> Carrière, <i>Mahonia fortunei</i> Fedde Berberidaceae (root, stem, leaf)	13.13 ± 0.4 µM ^{a,k}	GAL 0.81 ± 0.08 µM ^{a,k}	nd	nd	MCE	
Tetrahydropalmatine	<i>Mahonia bealei</i> Carrière, <i>Mahonia fortunei</i> Fedde Berberidaceae (root, stem, leaf)	47.56 ± 1.46 µM ^{a,k}	GAL 0.81 ± 0.08 µM ^{a,k}	nd	nd	MCE	
Mahanimbine	<i>Murraya koenigii</i> L. Rutaceae (leaves)	0.03 ± 0.09 mg mL ^{-1 a,d}	GAL 0.006 ± 0.001 mg mL ^{-1 a,d}	nd	nd	MCE	[48,76]
1,2-Dihydrogalanthamine	<i>Narcissus jonquilla</i> 'Pipit' Amaryllidaceae (bulbs)	0.19 µM ^{a,e}	GAL 0.27 µM ^{a,e}	nd	nd	BTLC by Mroczek	[77]
Haemanthamine	<i>Narcissus poeticus</i> 'Pink Parasol' Amaryllidaceae (bulbs)	>500 µM ^{a,f}	GAL 1.7 ± 0.1 µM ^{a,f} HUP 0.033 ± 0.001 µM ^{a,f}	>500 µM ^{a,l}	GAL 42.3 ± 1.3 µM ^{a,l} HUP >500 µM ^{a,l}	MCE	
Hippeastrine	<i>Narcissus poeticus</i> 'Pink Parasol' Amaryllidaceae (bulbs)	>500 µM ^{a,f}	GAL 1.7 ± 0.1 µM ^{a,f} HUP 0.033 ± 0.001 µM ^{a,f}	>500 µM ^{a,l}	GAL 42.3 ± 1.3 µM ^{a,l} HUP >500 µM ^{a,l}	MCE	
Homolycorine	<i>Narcissus poeticus</i> 'Pink Parasol' Amaryllidaceae (bulbs)	64 ± 4 µM ^{a,f}	GAL 1.7 ± 0.1 µM ^{a,f} HUP 0.033 ± 0.001 µM ^{a,f}	151 ± 19 µM ^{a,l}	GAL 42.3 ± 1.3 µM ^{a,l} HUP >500 µM ^{a,l}	MCE	
Incartine	<i>Narcissus poeticus</i> 'Pink Parasol' Amaryllidaceae (bulbs)	208 ± 14 µM ^{a,f}	GAL 1.7 ± 0.1 µM ^{a,f} HUP 0.033 ± 0.001 µM ^{a,f}	>500 µM ^{a,l}	GAL 42.3 ± 1.3 µM ^{a,l} HUP >500 µM ^{a,l}	MCE	
Lycoramine	<i>Narcissus poeticus</i> 'Pink Parasol' Amaryllidaceae (bulbs)	456 ± 57 µM ^{a,f}	GAL 1.7 ± 0.1 µM ^{a,f} HUP 0.033 ± 0.001 µM ^{a,f}	>500 µM ^{a,l}	GAL 42.3 ± 1.3 µM ^{a,l} HUP >500 µM ^{a,l}	MCE	
Masonine	<i>Narcissus poeticus</i> 'Pink Parasol' Amaryllidaceae (bulbs)	304 ± 34 µM ^{a,f}	GAL 1.7 ± 0.1 µM ^{a,f} HUP 0.033 ± 0.001 µM ^{a,f}	229 ± 24 µM ^{a,l}	GAL 42.3 ± 1.3 µM ^{a,l} HUP >500 µM ^{a,l}	MCE	[48,78]
Narcipavline	<i>Narcissus poeticus</i> 'Pink Parasol' Amaryllidaceae (bulbs)	208 ± 37 µM ^{a,f}	GAL 1.7 ± 0.1 µM ^{a,f} HUP 0.033 ± 0.001 µM ^{a,f}	24.4 ± 1.2 µM ^{a,l}	GAL 42.3 ± 1.3 µM ^{a,l} HUP >500 µM ^{a,l}	MCE	
Narwedine	<i>Narcissus poeticus</i> 'Pink Parasol' Amaryllidaceae (bulbs)	281 ± 33 µM ^{a,f}	GAL 1.7 ± 0.1 µM ^{a,f} HUP 0.033 ± 0.001 µM ^{a,f}	>500 µM ^{a,l}	GAL 42.3 ± 1.3 µM ^{a,l} HUP >500 µM ^{a,l}	MCE	
nor-Lycoramine	<i>Narcissus poeticus</i> 'Pink Parasol' Amaryllidaceae (bulbs)	>500 µM ^{a,f}	GAL 1.7 ± 0.1 µM ^{a,f} HUP 0.033 ± 0.001 µM ^{a,f}	>500 µM ^{a,l}	GAL 42.3 ± 1.3 µM ^{a,l} HUP >500 µM ^{a,l}	MCE	
Oduline	<i>Narcissus poeticus</i> 'Pink Parasol' Amaryllidaceae (bulbs)	>500 µM ^{a,f}	GAL 1.7 ± 0.1 µM ^{a,f} HUP 0.033 ± 0.001 µM ^{a,f}	>500 µM ^{a,l}	GAL 42.3 ± 1.3 µM ^{a,l} HUP >500 µM ^{a,l}	MCE	
seco- Isopowellaminone	<i>Narcissus poeticus</i> 'Pink Parasol' Amaryllidaceae (bulbs)	293 ± 33 µM ^{a,f}	GAL 1.7 ± 0.1 µM ^{a,f} HUP 0.033 ± 0.001 µM ^{a,f}	>500 µM ^{a,l}	GAL 42.3 ± 1.3 µM ^{a,l} HUP >500 µM ^{a,l}	MCE	
Incartine	<i>Narcissus jonquilla</i> var. <i>henriquesii</i> Samp. Amaryllidaceae (bulbs)	208.2 ± 14.3 µM ^{a,f}	GAL 1.7 ± 0.06 µM ^{a,f} HUP 0.03 ± 0.0 µM ^{a,f} PHY 0.06 ± 0.0 µM ^{a,f}	943.4 ± 140.7 µM ^{a,l}	GAL 42.3 ± 1.3 µM ^{a,l} HUP >1000 µM ^{a,l} PHY 0.13 ± 0.0 µM ^{a,l}	MCE	[48,79]
Narwedine	<i>Narcissus poeticus</i> 'Brackenhurst' Amaryllidaceae (bulbs)	281.2 ± 33.9 µM ^{a,f}	GAL 1.7 ± 0.06 µM ^{a,f} HUP 0.03 ± 0.0 µM ^{a,f} PHY 0.06 ± 0.0 µM ^{a,f}	911.3 ± 68.7 µM ^{a,l}	GAL 42.3 ± 1.3 µM ^{a,l} HUP >1000 µM ^{a,l} PHY 0.13 ± 0.0 µM ^{a,l}	MCE	

Table 1. Cont.

Inhibitors	Source	Activity				Method	Ref.
		Value of Inhibition against AChE	Reference Standard for AChE	Value of Inhibition against BuChE	Reference Standard for BuChE		
11-Hydroxygalanthine	<i>Narcissus tazetta</i> subsp. <i>tazetta</i> L Amaryllidaceae (bulbs and leaves)	0.67 μM ^{a,e}	GAL 0.15 μM ^{a,e}	18.17 μM ^{a,m}	GAL 2.47 μM ^{a,m}	MCE	
9-O-Demetil-2- α -hydroxyhomolycorine	<i>Narcissus tazetta</i> subsp. <i>tazetta</i> L Amaryllidaceae (bulbs and leaves)	19.84 μM ^{a,e}	GAL 0.15 μM ^{a,e}	na	GAL 2.47 μM ^{a,m}	MCE	
Narcissidine	<i>Narcissus tazetta</i> subsp. <i>tazetta</i> L Amaryllidaceae (bulbs and leaves)	1.85 μM ^{a,e}	GAL 0.15 μM ^{a,e}	na	GAL 2.47 μM ^{a,m}	MCE	[48,80]
Pancreatine-C	<i>Narcissus tazetta</i> subsp. <i>tazetta</i> L Amaryllidaceae (bulbs and leaves)	na	GAL 0.15 μM ^{a,e}	32.04 μM ^{a,m}	GAL 2.47 μM ^{a,m}	MCE	
Pseudolycorine	<i>Narcissus tazetta</i> subsp. <i>tazetta</i> L Amaryllidaceae (bulbs and leaves)	32.51 μM ^{a,e}	GAL 0.15 μM ^{a,e}	21.64 μM ^{a,m}	GAL 2.47 μM ^{a,m}	MCE	
Angustidine	<i>Nauclea officinalis</i> Merr. & Chun. Rubiaceae (bark)	21.72 μM ^{a,e}	GAL 0.94 μM ^{a,e}	1.03 μM ^{a,m}	GAL 28.29 μM ^{a,m}	CE	
Angustine	<i>Nauclea officinalis</i> Merr. & Chun. Rubiaceae (bark)	100 $\mu\text{g mL}^{-1}$ —40.19 \pm 0.65% ^{b,e}	GAL 0.94 μM ^{a,e}	4.98 μM ^{a,m}	GAL 28.29 μM ^{a,m}	CE	
Angustoline	<i>Nauclea officinalis</i> Merr. & Chun. Rubiaceae (bark)	261.89 μM ^{a,e}	GAL 0.94 μM ^{a,e}	25.10 μM ^{a,m}	GAL 28.29 μM ^{a,m}	CE	[19,48,81]
Harmene	<i>Nauclea officinalis</i> Merr. & Chun. Rubiaceae (bark)	300.68 μM ^{a,e}	GAL 0.94 μM ^{a,e}	13.18 μM ^{a,m}	GAL 28.29 μM ^{a,m}	CE	
Nauclefine	<i>Nauclea officinalis</i> Merr. & Chun. Rubiaceae (bark)	100 $\mu\text{g mL}^{-1}$ —34.61 \pm 4.84% ^{b,e}	GAL 0.94 μM ^{a,e}	7.70 μM ^{a,m}	GAL 28.29 μM ^{a,m}	CE	
7,8,13,14-Dehydroorientalidine	<i>Papaver setiferum</i> Goldblatt Papaveraceae (capsules)	nd	NEO 6.0 \pm 1.1 μM ^{a,e}	nd	NEO 92.7 \pm 2.2 μM ^{a,m}	MCE	
7,8-Didehydromecambridine TFA salt	<i>Papaver setiferum</i> Goldblatt Papaveraceae (capsules)	10.3 \pm 1.1 μM ^{a,e}	NEO 6.0 \pm 1.1 μM ^{a,e}	100 \pm 5 μM ^{a,m}	NEO 92.7 \pm 2.2 μM ^{a,m}	MCE	
7,8-Didehydroorientalidine TFA salt	<i>Papaver setiferum</i> Goldblatt Papaveraceae (capsules)	3.4 \pm 4.7 μM ^{a,e}	NEO 6.0 \pm 1.1 μM ^{a,e}	98.5 \pm 0.6 μM ^{a,m}	NEO 92.7 \pm 2.2 μM ^{a,m}	MCE	
Alborine	<i>Papaver setiferum</i> Goldblatt Papaveraceae (capsules)	6.8 \pm 4.5 μM ^{a,e}	NEO 6.0 \pm 1.1 μM ^{a,e}	63.1 \pm 0.5 μM ^{a,m}	NEO 92.7 \pm 2.2 μM ^{a,m}	MCE	
Isothebaine	<i>Papaver setiferum</i> Goldblatt Papaveraceae (capsules)	260 \pm 1 μM ^{a,e}	NEO 6.0 \pm 1.1 μM ^{a,e}	2.8 \pm 3.0 μM ^{a,m}	NEO 92.7 \pm 2.2 μM ^{a,m}	MCE	[48,82,83]
N-Methylcodamine	<i>Papaver setiferum</i> Goldblatt Papaveraceae (capsules)	nd	NEO 6.0 \pm 1.1 μM ^{a,e}	221 \pm 1 μM ^{a,m}	NEO 92.7 \pm 2.2 μM ^{a,m}	MCE	
N-Methylisothobainium	<i>Papaver setiferum</i> Goldblatt Papaveraceae (capsules)	nd	NEO 6.0 \pm 1.1 μM ^{a,e}	7.1 \pm 2.7 μM ^{a,m}	NEO 92.7 \pm 2.2 μM ^{a,m}	MCE	
N-Methylorientaline	<i>Papaver setiferum</i> Goldblatt Papaveraceae (capsules)	nd	NEO 6.0 \pm 1.1 μM ^{a,e}	342 \pm 3 μM ^{a,m}	NEO 92.7 \pm 2.2 μM ^{a,m}	MCE	
Orientalidine	<i>Papaver setiferum</i> Goldblatt Papaveraceae (capsules)	5.0 \pm 1.0 μM ^{a,e}	NEO 6.0 \pm 1.1 μM ^{a,e}	104 \pm 4 μM ^{a,m}	NEO 92.7 \pm 2.2 μM ^{a,m}	MCE	
Salutaridine	<i>Papaver setiferum</i> Goldblatt Papaveraceae (capsules)	nd	NEO 6.0 \pm 1.1 μM ^{a,e}	335 \pm 4 μM ^{a,m}	NEO 92.7 \pm 2.2 μM ^{a,m}	MCE	

Table 1. Cont.

Inhibitors	Source	Activity				Method	Ref.
		Value of Inhibition against AChE	Reference Standard for AChE	Value of Inhibition against BuChE	Reference Standard for BuChE		
19(S)-Hydroxybogamine	<i>Tabernaemontana bufalina</i> Lour. (Apocynaceae)	nd	nd	20.1 μM ^{a,m}	TAC 0.025 μM ^{a,m}	MCE	[48,84,85]
3 α -Dihydrocadambine	<i>Uncaria rhynchophylla</i> Miq. ex Havil Rubiaceae (stems)	37.01 \pm 1.57 μM ^{a,e}	TAC 4.39 \pm 0.80 μM ^{a,e}	33.34 \pm 0.51 μM ^{a,m}	TAC 3.25 \pm 1.86 μM ^{a,m}	MCE	
7- <i>epi</i> -Javaniside	<i>Uncaria rhynchophylla</i> Miq. ex Havil Rubiaceae (stems)	2.85 \pm 0.50 μM ^{a,e}	TAC 4.39 \pm 0.80 μM ^{a,e}	2.13 \pm 0.10 μM ^{a,m}	TAC 3.25 \pm 1.86 μM ^{a,m}	MCE	
Cadambine	<i>Uncaria rhynchophylla</i> Miq. ex Havil Rubiaceae (stems)	26.12 \pm 2.12 μM ^{a,e}	TAC 4.39 \pm 0.80 μM ^{a,e}	30.69 \pm 0.69 μM ^{a,m}	TAC 3.25 \pm 1.86 μM ^{a,m}	MCE	[48,86]
Strictosamide	<i>Uncaria rhynchophylla</i> Miq. ex Havil Rubiaceae (stems)	46.57 \pm 0.58 μM ^{a,e}	TAC 4.39 \pm 0.80 μM ^{a,e}	6.47 \pm 0.72 μM ^{a,m}	TAC 3.25 \pm 1.86 μM ^{a,m}	MCE	
Vincosamide	<i>Uncaria rhynchophylla</i> Miq. ex Havil Rubiaceae (stems)	12.4 \pm 0.86 μM ^{a,e}	TAC 4.39 \pm 0.80 μM ^{a,e}	23.18 \pm 0.14 μM ^{a,m}	TAC 3.25 \pm 1.86 μM ^{a,m}	MCE	
Deoxyvobtusine lactone	<i>Voacanga globosa</i> Merr. Apocynaceae (leaves)	10 ^{-4.3} M—91% ^{b,e}	GAL 0.64 μM ^{a,e}	20.2 μM ^{a,m}	GAL 8.40 μM ^{a,m}	MCE	
Deoxyvobtusine	<i>Voacanga globosa</i> Merr. Apocynaceae (leaves)	10 ^{-4.3} M—87% ^{b,e}	GAL 0.64 μM ^{a,e}	6.2 μM ^{a,m}	GAL 8.40 μM ^{a,m}	MCE	[87–89]
Globospiramine	<i>Voacanga globosa</i> Merr. Apocynaceae (leaves)	10 ^{-4.3} M—94% ^{b,e}	GAL 0.64 μM ^{a,e}	16.4 μM ^{a,m}	GAL 8.40 μM ^{a,m}	MCE	
Vobtusine lactone	<i>Voacanga globosa</i> Merr. Apocynaceae (leaves)	10 ^{-4.3} M—90% ^{b,e}	GAL 0.64 μM ^{a,e}	18.0 μM ^{a,m}	GAL 8.40 μM ^{a,m}	MCE	
ANTHRANOIDS							
2-Geranylmodin	<i>Psorospermum glaberrimum</i> Hochr. Hypericaceae (stem bark)	0.1 mM—12.9% ^{b,e}	GAL 0.50 \pm 0.001 μM ^{a,e}	11.30 \pm 0.23 μM ^{a,m}	GAL 8.50 \pm 0.001 μM ^{a,m}	MCE	
3-Prenyloxyemodin	<i>Psorospermum glaberrimum</i> Hochr. Hypericaceae (stem bark)	0.1 mM—35.0% ^{b,e}	GAL 0.50 \pm 0.001 μM ^{a,e}	13.3 \pm 1.10 μM ^{a,m}	GAL 8.50 \pm 0.001 μM ^{a,m}	MCE	
Acetylvismione D	<i>Psorospermum glaberrimum</i> Hochr. Hypericaceae (stem bark)	0.1 mM—45.70% ^{b,e}	GAL 0.50 \pm 0.001 μM ^{a,e,e}	10.1 \pm 0.20 μM ^{a,m}	GAL 8.50 \pm 0.001 μM ^{a,m}	MCE	[48,90]
Bianthrone 1a	<i>Psorospermum glaberrimum</i> Hochr. Hypericaceae (stem bark)	63.0 \pm 0.46 μM ^{a,e}	GAL 0.50 \pm 0.001 μM ^{a,e,a,e}	9.25 \pm 0.25 μM ^{a,m}	GAL 8.50 \pm 0.001 μM ^{a,m}	MCE	
3-Geranyloxyemodin anthrone	<i>Psorospermum glaberrimum</i> Hochr. Hypericaceae (stem bark)	100 μM —5.4% ^{b,e}	GAL 0.50 \pm 0.001 μM ^{a,e,e}	11.60 \pm 0.20 μM ^{a,m}	GAL 8.50 \pm 0.001 μM ^{a,m}	MCE	
3-Prenyloxyemodin anthrone	<i>Psorospermum glaberrimum</i> Hochr. Hypericaceae (stem bark)	100 μM —13.8% ^{b,e}	GAL 0.50 \pm 0.001 μM ^{a,e}	10.1 \pm 0.5 μM ^{a,m}	GAL 8.50 \pm 0.001 μM ^{a,m}	MCE	
Emodin	<i>Talaromyces aurantiacus</i> FL 15 (strain from leave <i>Huperzia serrata</i>)	>100 μM ^{a,e}	RIV 1.82 \pm 0.13 μM ^{a,e} HUP 0.045 \pm 0.01 μM ^{a,e}	>100 μM ^{a,m}	nd	MCE	
Physcion	<i>Talaromyces aurantiacus</i> FL 15 (strain from leave <i>Huperzia serrata</i>)	>100 μM ^{a,e}	RIV 1.82 \pm 0.13 μM ^{a,e} HUP 0.045 \pm 0.01 μM ^{a,e}	>100 μM ^{a,m}	nd	MCE	[48,91,92]
Chrysophanol	<i>Talaromyces aurantiacus</i> FL 15 (strain from leave <i>Huperzia serrata</i>)	>100 μM ^{a,e}	RIV 1.82 \pm 0.13 μM ^{a,e} HUP 0.045 \pm 0.01 μM ^{a,e}	>100 μM ^{a,m}	nd	MCE	
BIBENZYL							
3,3'-Dihydroxy-4-(4-hydroxybenzyl)-5-methoxybibenzyl	<i>Bletilla striata</i> Reichb. f. Orchidaceae (tuber)	25 $\mu\text{g mL}^{-1}$ —2.6 \pm 2.8% ^{b,e}	GAL 25 $\mu\text{g mL}^{-1}$ —94.8 \pm 0.9% ^{b,e}	25 $\mu\text{g mL}^{-1}$ —22.6 \pm 2.1% ^{b,m}	GAL 25 $\mu\text{g mL}^{-1}$ —64.2 \pm 0.6% ^{b,m} 46.3 \pm 5.8 μM ^{a,m} TAC 0.0101 \pm 0.0005 μM ^{a,m}	MCE	[37,48]
3',5-Dihydroxy-2-(4-hydroxybenzyl)-3-methoxybibenzyl	<i>Bletilla striata</i> Reichb. f. Orchidaceae (tuber)	25 $\mu\text{g mL}^{-1}$ —5.0 \pm 1.5% ^{b,e}	GAL 25 $\mu\text{g mL}^{-1}$ —94.8 \pm 0.9% ^{b,e}	25 $\mu\text{g mL}^{-1}$ —51.3 \pm 2.0% ^{b,m} 80.3 \pm 5.2 μM ^{a,m}	GAL 25 $\mu\text{g mL}^{-1}$ —64.2 \pm 0.6% ^{b,m} 46.3 \pm 5.8 μM ^{a,m} TAC 0.0101 \pm 0.0005 μM ^{a,m}	MCE	

Table 1. Cont.

Inhibitors	Source	Activity				Method	Ref.
		Value of Inhibition against AChE	Reference Standard for AChE	Value of Inhibition against BuChE	Reference Standard for BuChE		
Bulbocol	<i>Bletilla striata</i> Reichb. f. Orchidaceae (tuber)	25 µg mL ⁻¹ −16.3 ± 3.8% b,e	GAL 25 µg mL ⁻¹ −94.8 ± 0.9% b,e	25 µg mL ⁻¹ −67.7 ± 0.3% b,m 33.5 ± 3.7 µM a,m	GAL 25 µg mL ⁻¹ −64.2 ± 0.6% b,m 46.3 ± 5.8 µM a,m TAC 0.0101 ± 0.0005 µM a,m	MCE	
Gymconopin D	<i>Bletilla striata</i> Reichb. f. Orchidaceae (tuber)	25 µg mL ⁻¹ −48.1 ± 6.3% b,e	GAL 25 µg mL ⁻¹ −94.8 ± 0.9% b,e	25 µg mL ⁻¹ −66.2 ± 3.4% b,m 40.5 ± 5.6 µM a,m	GAL 25 µg mL ⁻¹ −64.2 ± 0.6% b,m 46.3 ± 5.8 µM a,m TAC 0.0101 ± 0.0005 µM a,m	MCE	
COUMARINS							
Scopoletin	<i>Scopolia carniolica</i> Jaqc. Solanaceae (roots)	168.6 µM a,e	GAL 3.2 µM a,e	nd	nd	MCE	[16,48,93–95]
Decursinol	<i>Angelica gigas</i> Nakai Apiaceae (underground parts)	28 µM a,k	nd	nd	nd	MCE	
Isoimperatorin	<i>Angelica gigas</i> Nakai Apiaceae (underground parts)	69 µM a,k	nd	nd	nd	MCE	
Marmesin	<i>Angelica gigas</i> Nakai Apiaceae (underground parts)	67 µM a,k	nd	nd	nd	MCE	[48,96–98]
Nodakenin	<i>Angelica gigas</i> Nakai Apiaceae (underground parts)	68 µM a,k	nd	nd	nd	MCE	
Xanthotoxin	<i>Angelica gigas</i> Nakai Apiaceae (underground parts)	54 µM a,k	nd	nd	nd	MCE	
Bergapten	<i>Angelica officinalis</i> L. Apiaceae (fruits)	25 µg mL ⁻¹ — 32.65 ± 6.10% b,e 100 µg mL ⁻¹ —nd	GAL 100 µg mL ⁻¹ −98.97 ± 0.24% b,e	25 µg mL ⁻¹ −86.69 ± 2.56% b,m 100 µg mL ⁻¹ —nd	GAL 100 µg mL ⁻¹ −80.31 ± 1.14% b,m	MCE	
Imperatorin	<i>Angelica officinalis</i> L. Apiaceae (fruits)	25 µg mL ⁻¹ — 18.76 ± 1.07% b,e 100 µg mL ⁻¹ −46.11 ± 0.92% b,e	GAL 100 µg mL ⁻¹ −98.97 ± 0.24% b,e	25 µg mL ⁻¹ — 37.46 ± 1.09% b,m 100 µg mL ⁻¹ — 83.98 ± 0.99% b,m	GAL 100 µg mL ⁻¹ −80.31 ± 1.14% b,m	MCE	[48,99,100]
Xanthotoxin	<i>Angelica officinalis</i> L. Apiaceae (fruits)	25 µg mL ⁻¹ — 38.23 ± 0.06% b,e 100 µg mL ⁻¹ −66.08 ± 2.88% b,e	GAL 100 µg mL ⁻¹ −98.97 ± 0.24% b,e	25 µg mL ⁻¹ −63.60 ± 1.78% b,m 100 µg mL ⁻¹ −88.04 ± 0.83% b,m	GAL 100 µg mL ⁻¹ −80.31 ± 1.14% b,m	MCE	
Heraclenol-2'-O-angelate	<i>Archangelica officinalis</i> L. Apiaceae (roots)	>1000 µM a,e	GAL 0.37 ± 1.1 µM a,e	7.5 ± 1.8 µM a,m	GAL 8.3 ± 2.6 µM a,m	BTLC by Marston et al. (2002)	[28,48,101]
Imperatorin	<i>Archangelica officinalis</i> L. Apiaceae (fruits)	156 ± 15 µM a,e	GAL 0.37 ± 1.1 µM a,e	14.4 ± 3.2 µM a,m	GAL 8.3 ± 2.6 µM a,m	BTLC by Marston et al. (2002)	
Isoimperatorin	<i>Citrus hystrix</i> DC. Rutaceae (peels of fruits)	nd	nd	23 ± 0.2 µM a,m	GAL 3.2 ± 0.2 µM a,m	MCE	
6',7'-Dihydroxybergamottin	<i>Citrus hystrix</i> DC. Rutaceae (peels of fruits)	nd	nd	15.4 ± 0.3 µM a,m	GAL 3.2 ± 0.2 µM a,m	MCE	[27,48]
6'-Hydroxy-7'-methoxybergamottin	<i>Citrus hystrix</i> DC. Rutaceae (peels of fruits)	nd	nd	11.2 ± 0.1 µM a,m	GAL 3.2 ± 0.2 µM a,m	MCE	
5,7-Dihydroxy-8-(3-methylbutanoyl)-6-[(E)-3,7-dimethylocta-2,6-dienyl]-4-phenyl-2H-chromen-2-one	<i>Mesua elegans</i> Kosterm. Clusiaceae (bark)	3.06 ± 0.04 µM a,e	TAC 0.074 ± 0.012 µM a,e	nd	nd	CE	
Mesuagenin A	<i>Mesua elegans</i> Kosterm. Clusiaceae (bark)	1.06 ± 0.04 µM a,e	TAC 0.074 ± 0.012 µM a,e	nd	nd	CE	[29,48]
Mesuagenin B	<i>Mesua elegans</i> Kosterm. Clusiaceae (bark)	0.70 ± 0.10 µM a,e	TAC 0.074 ± 0.012 µM a,e	nd	nd	CE	
Mesuagenin D	<i>Mesua elegans</i> Kosterm. Clusiaceae (bark)	8.73 ± 0.25 µM a,e	TAC 0.074 ± 0.012 µM a,e	nd	nd	CE	
Lucidafuranocoumarin A	<i>Peucedanum alsaticum</i> L. Apiaceae (fruits)	na	GAL 100 µg mL ⁻¹ −92.14 ± 2.49% b,k 1.82 ± 0.22 µg mL ⁻¹ a,k	100 µg mL ⁻¹ −40.66 ± 1.25% b,n	GAL 100 µg mL ⁻¹ −81.93 ± 2.52% b,n 22.16 ± 0.91 µg mL ⁻¹ a,n	MCE	[102]

Table 1. Cont.

Inhibitors	Source	Activity				Method	Ref.
		Value of Inhibition against AChE	Reference Standard for AChE	Value of Inhibition against BuChE	Reference Standard for BuChE		
Bergamottin	<i>Peucedanum alsaticum</i> L. Apiaceae (fruits)	100 µg mL ⁻¹ −4.00 ± 0.82% ^b	GAL 100 µg mL ⁻¹ −92.14 ± 2.49% ^{b,k} 1.82 ± 0.22 µg mL ⁻¹ a,k	100 µg mL ⁻¹ −17.65 ± 1.50% ^b	GAL 100 µg mL ⁻¹ −81.93 ± 2.52% ^{b,n} 22.16 ± 0.91 µg mL ⁻¹ a,n	MCE	
CHROMONES							
Sargachromanol G	<i>Sargassum siliquastrum</i> Sargassaceae (strains)	1.81 ± 0.020 µM ^{a,e}	BER 1.01 ± 0.01 µM ^{a,e} TAC 0.22 ± 0.004 µM ^{a,e}	10.79 ± 0.65 µM ^{a,m}	TAC 0.014 ± 0.0043 µM ^{a,m}	MCE	[48,59,60]
Sargachromanol I	<i>Sargassum siliquastrum</i> Sargassaceae (strains)	0.79 ± 0.07 µM ^{a,e}	BER 1.01 ± 0.01 µM ^{a,e} TAC 0.22 ± 0.004 µM ^{a,e}	13.69 ± 5.07 µM ^{a,m}	TAC 0.014 ± 0.0043 µM ^{a,m}	MCE	
DIARYLHEPTANOIDS							
(−)-Alpininoid B	<i>Alpinia officinarum</i> Hance Zingiberaceae (rhizomes)	100 µM—87.6 ± 0.1% ^{b,e} 2.6 ± 4.2 µM ^{a,e}	TAC 111.8 ± 4.6 µM ^{a,e}	100 µM—64.7 ± 1.4% ^{b,m} 35.2 ± 0.7 µM ^{a,m}	TAC 8.9 ± 2.4 µM ^{a,m}	MCE	
(4E) ⁻¹ ,7-Diphenyl-4-hepten-3-one	<i>Alpinia officinarum</i> Hance Zingiberaceae (rhizomes)	100 µM—98.0 ± 0.9% ^{b,e} 23.9 ± 2.6 µM ^{a,e}	TAC 111.8 ± 4.6 µM ^{a,e}	100 µM—62.3 ± 3.5% ^{b,m} 70.7 ± 2.5 µM ^{a,m}	TAC 8.9 ± 2.4 µM ^{a,m}	MCE	
Dihydroyashbushiketol	<i>Alpinia officinarum</i> Hance Zingiberaceae (rhizomes)	100 µM—36.2 ± 1.9% ^{b,e}	TAC 111.8 ± 4.6 µM ^{a,e}	100 µM—15.7 ± 2.1% ^{b,m}	TAC 8.9 ± 2.4 µM ^{a,m}	MCE	
(4E)-7-(4-Hydroxyphenyl)-1-phenyl-4-hepten-3-one	<i>Alpinia officinarum</i> Hance Zingiberaceae (rhizomes)	100 µM—57.9 ± 3.2% ^{b,e} 87.3 ± 3.4 µM ^{a,e}	TAC 111.8 ± 4.6 µM ^{a,e}	100 µM—41.1 ± 0.1% ^{b,m}	TAC 8.9 ± 2.4 µM ^{a,m}	MCE	[31,66]
(4E)-7-(4-Hydroxy-3-methoxyphenyl)-1-phenyl-hept-4-en-3-one	<i>Alpinia officinarum</i> Hance Zingiberaceae (rhizomes)	100 µM—76.6 ± 0.3% ^{b,e} 39.1 ± 2.3 µM ^{a,e}	TAC 111.8 ± 4.6 µM ^{a,e}	100 µM—43.7 ± 1.4% ^{b,m}	TAC 8.9 ± 2.4 µM ^{a,m}	MCE	
(5R)-7-(4-Hydroxy-3-methoxyphenyl)-5-methoxy-1-phenyl-3-heptanone	<i>Alpinia officinarum</i> Hance Zingiberaceae (rhizomes)	100 µM—35.3 ± 1.0% ^{b,e}	TAC 111.8 ± 4.6 µM ^{a,e}	100 µM—21.5 ± 0.6% ^{b,m}	TAC 8.9 ± 2.4 µM ^{a,m}	MCE	
Kaempferide	<i>Alpinia officinarum</i> Hance Zingiberaceae (rhizomes)	100 µM—67.2 ± 1.8% ^{b,e} 31.9 ± 2.0 µM ^{a,e}	TAC 111.8 ± 4.6 µM ^{a,e}	100 µM—47.6 ± 1.6% ^{b,m}	TAC 8.9 ± 2.4 µM ^{a,m}	MCE	
Galangin	<i>Alpinia officinarum</i> Hance Zingiberaceae (rhizomes)	100 µM—65.4 ± 4.5% ^{b,e} 70.1 ± 1.5 µM ^{a,e}	TAC 111.8 ± 4.6 µM ^{a,e}	100 µM—63.6 ± 3.1% ^{b,m} 61.4 ± 1.4 µM ^{a,m}	TAC 8.9 ± 2.4 µM ^{a,m}	MCE	
DITERPENES							
Dihydrotanshinone	<i>Salvia miltiorhiza</i> Bunge Lamiaceae (roots)	1 µM ^{a,d}	PHY 0.25 µM ^{a,d}	nd	nd	MCE	
Cryptotanshinone	<i>Salvia miltiorhiza</i> Bunge Lamiaceae (roots)	7 µM ^{a,d}	PHY 0.25 µM ^{a,d}	nd	nd	MCE	[38,103]
Tanshinone I	<i>Salvia miltiorhiza</i> Bunge Lamiaceae (roots)	>50 µM ^{a,d}	PHY 0.25 µM ^{a,d}	nd	nd	MCE	
Tanshinone IIA	<i>Salvia miltiorhiza</i> Bunge Lamiaceae (roots)	>140 µM ^{a,d}	PHY 0.25 µM ^{a,d}	nd	nd	MCE	
Scapaundulin C	<i>Scapania undulate</i> L. Scapaniaceae	>250 ng ^{c,e}	GAL >10 ng ^{c,e}	nd	nd	BTLC by Marston et al. (2002)	
Scapaundulin A	<i>Scapania undulate</i> L. Scapaniaceae	>250 ng ^{c,e}	GAL >10 ng ^{c,e}	nd	nd	BTLC by Marston et al. (2002)	
5α, 8α, 9α-Trihydroxy-13E-labden-12-one	<i>Scapania undulate</i> L. Scapaniaceae	>250 ng ^{c,e}	GAL >10 ng ^{c,e}	nd	nd	BTLC by Marston et al. (2002)	[104,105]
5α, 8α-Dihydroxy-13E-labden-12-one	<i>Scapania undulate</i> L. Scapaniaceae	>250 ng ^{c,e}	GAL >10 ng ^{c,e}	nd	nd	BTLC by Marston et al. (2002)	
(13S)-15-Hydroxy-labd-8(17)-en-19-oic acid	<i>Scapania undulate</i> L. Scapaniaceae	>500 ng ^{c,e}	GAL >10 ng ^{c,e}	nd	nd	BTLC by Marston et al. (2002)	

Table 1. Cont.

Inhibitors	Source	Activity				Method	Ref.
		Value of Inhibition against AChE	Reference Standard for AChE	Value of Inhibition against BuChE	Reference Standard for BuChE		
FATTY ACID							
(2E,4E,6R)-6-Hydroxydeca-2,4-dienoic acid.	<i>Lycopodiella cernua</i> L. Lycopodiaceae (whole plants)	0.22 ± 0.03 µM ^{a,k}	BER 0.10 ± 0.01 µM ^{a,k}	>30 µM ^{a,n}	BER 1.09 ± 0.17 µM ^{a,n}	MCE	[48,106]
FLAVONOIDS							
3-Methoxy quercetin	<i>Agrimonia pilosa</i> Ledeb. Rosaceae (leaves)	37.9 µM ^{a,e}	DEH 37.8 µM ^{a,e}	nd	nd	MCE	[48,107]
Quercetin	<i>Agrimonia pilosa</i> Ledeb. Rosaceae (leaves)	19.8 µM ^{a,e}	DEH 37.8 µM ^{a,e}	nd	nd	MCE	
Quercitrin	<i>Agrimonia pilosa</i> Ledeb. Rosaceae (leaves)	66.9 µM ^{a,e}	DEH 37.8 µM ^{a,e}	nd	nd	MCE	
Tiliroside	<i>Agrimonia pilosa</i> Ledeb. Rosaceae (leaves)	23.5 µM ^{a,e}	DEH 37.8 µM ^{a,e}	nd	nd	MCE	
Linarin	<i>Buddleja davidii</i> Franch. Buddlejaceae (leaves)	>10 ng ^{c,e}	HUP >1 ng ^{c,e}	nd	nd	BTLC by Marston [101,104] et al. (2002)	
Garcineflavonol A	<i>Garcinia atroviridis</i> Griff. ex T. Anderson Clusiaceae (stem bark)	100 µg mL ⁻¹ —68.45 ± 0.97% ^{b,e} 14.04 ± 0.77 µg mL ^{-1 a,e}	PHY 0.05 ± 0.01 µg mL ^{-1 a,e}	14.50 ± 0.47 µg mL ^{-1 a,m}	PHY 0.14 ± 0.015 µg mL ^{-1 a,m}	MCE	[48,108,109]
Quercetin	<i>Ginkgo biloba</i> L. Ginkgoaceae (leaves)	95.8 µg mL ^{-1 a,h}	CHL 12.4 µg mL ^{-1 a,h}	nd	nd	MCE	[48,110,111]
Quercetin-3-O-α-L-rhamnopyranosyl-(1 → 6)-β-D-glucopyranoside	<i>Ginkgo biloba</i> L. Ginkgoaceae (leaves)	73.1 µg mL ^{-1 a,h}	CHL 12.4 µg mL ^{-1 a,h}	nd	nd	MCE	
Quercetin-3-O-β-D-glucopyranoside	<i>Ginkgo biloba</i> L. Ginkgoaceae (leaves)	57.8 µg mL ^{-1 a,h}	CHL 12.4 µg mL ^{-1 a,h}	nd	nd	MCE	
Quercetin-3-O-α-L-rhamnopyranoside	<i>Ginkgo biloba</i> L. Ginkgoaceae (leaves)	110.9 µg mL ^{-1 a,h}	CHL 12.4 µg mL ^{-1 a,h}	nd	nd	MCE	
Quercetin-3-O-α-L-rhamnopyranosyl-(1 → 4)-O-α-L-rhamnopyranosyl-(1 → 2)-β-D-glucopyranoside	<i>Ginkgo biloba</i> L. Ginkgoaceae (leaves)	112.6 µg mL ^{-1 a,h}	CHL 12.4 µg mL ^{-1 a,h}	nd	nd	MCE	
Taxifolin	<i>Ginkgo biloba</i> L. Ginkgoaceae (leaves)	133.1 µg mL ^{-1 a,h}	CHL 12.4 µg mL ^{-1 a,h}	nd	nd	MCE	
Quercetin-3-O-neohesperidoside	<i>Lysimachia clethroides</i> Duby Primulaceae (whole plant)	6.98 ± 0.47 µM ^{a,e}	BER 1.01 ± 0.01 µM ^{a,e} TAC 0.22 ± 0.004 µM ^{a,e}	>40 µM ^{a,m}	TAC 0.014 ± 0.0043 µM ^{a,m}	MCE	[48,59,60]
Diplacone	<i>Paulownia tomentosa</i> Steud. Paulowniaceae (fruits)	7.2 ± 0.6 µM ^{a,f}	PHY 0.15 ± 0.03 µM ^{a,f}	1.4 ± 0.3 µM ^{a,m}	PHY 3.7 ± 0.6 µM ^{a,m}	MCEF	[34,48,112]
3'-O-Methyl diplacol	<i>Paulownia tomentosa</i> Steud. Paulowniaceae (fruits)	48.5 ± 2.1 µM ^{a,f}	PHY 0.15 ± 0.03 µM ^{a,f}	11.2 ± 2.1 µM ^{a,m}	PHY 3.7 ± 0.6 µM ^{a,m}	MCEF	
3'-O-Methyl diplacone	<i>Paulownia tomentosa</i> Steud. Paulowniaceae (fruits)	109.2 ± 8.4 µM ^{a,f}	PHY 0.15 ± 0.03 µM ^{a,f}	24.5 ± 1.2 µM ^{a,m}	PHY 3.7 ± 0.6 µM ^{a,m}	MCEF	
4'-O-Methyl diplacone	<i>Paulownia tomentosa</i> Steud. Paulowniaceae (fruits)	92.4 ± 4.1 µM ^{a,f}	PHY 0.15 ± 0.03 µM ^{a,f}	25.6 ± 1.6 µM ^{a,m}	PHY 3.7 ± 0.6 µM ^{a,m}	MCEF	
4'-O-Methyl diplacol	<i>Paulownia tomentosa</i> Steud. Paulowniaceae (fruits)	31.9 ± 1.2 µM ^{a,f}	PHY 0.15 ± 0.03 µM ^{a,f}	12.7 ± 1.3 µM ^{a,m}	PHY 3.7 ± 0.6 µM ^{a,m}	MCEF	
6-Geranyl-3',5,5',7-pentahydroxy-4'-methoxyflavane	<i>Paulownia tomentosa</i> Steud. Paulowniaceae (fruits)	15.6 ± 0.8 µM ^{a,f}	PHY 0.15 ± 0.03 µM ^{a,f}	3.8 ± 0.8 µM ^{a,m}	PHY 3.7 ± 0.6 µM ^{a,m}	MCEF	
6-Geranyl-3',5,5',7-tetrahydroxy-4'-methoxyflavanone	<i>Paulownia tomentosa</i> Steud. Paulowniaceae (fruits)	22.9 ± 1.6 µM ^{a,f}	PHY 0.15 ± 0.03 µM ^{a,f}	6.4 ± 0.9 µM ^{a,m}	PHY 3.7 ± 0.6 µM ^{a,m}	MCEF	
6-Geranyl-4',5,7-trihydroxy-3',5'-dimethoxyflavanone	<i>Paulownia tomentosa</i> Steud. Paulowniaceae (fruits)	316.3 ± 12.5 µM ^{a,f}	PHY 0.15 ± 0.03 µM ^{a,f}	80.00 ± 2.6 µM ^{a,m}	PHY 3.7 ± 0.6 µM ^{a,m}	MCEF	

Table 1. Cont.

Inhibitors	Source	Activity				Method	Ref.
		Value of Inhibition against AChE	Reference Standard for AChE	Value of Inhibition against BuChE	Reference Standard for BuChE		
Mimulone	<i>Paulownia tomentosa</i> Steud. Paulowniaceae (fruits)	91.5 ± 5.3 µM ^{a,f}	PHY 0.15 ± 0.03 µM ^{a,f}	20.6 ± 1.1 µM ^{a,m}	PHY 3.7 ± 0.6 µM ^{a,m}	MCEF	
Dihydrowogonin	<i>Prunus padus</i> var. <i>seoulensis</i> Nakai Rosaceae (leaves)	21.53 ± 0.32 µM ^{a,e}	TAC 0.22 ± 0.001 µM ^{a,e}	nd	nd	MCE	
Dihydrowogonin 7-O-glucoside	<i>Prunus padus</i> var. <i>seoulensis</i> Nakai Rosaceae (leaves)	15.49 ± 0.11 µM ^{a,e}	TAC 0.22 ± 0.001 µM ^{a,e}	nd	nd	MCE	
Genkwainin	<i>Prunus padus</i> var. <i>seoulensis</i> Nakai Rosaceae (leaves)	17.03 ± 0.77 µM ^{a,e}	TAC 0.22 ± 0.001 µM ^{a,e}	nd	nd	MCE	[48,59]
Rhamnocitrin	<i>Prunus padus</i> var. <i>seoulensis</i> Nakai Rosaceae (leaves)	18.26 ± 0.075 µM ^{a,e}	TAC 0.22 ± 0.001 µM ^{a,e}	nd	nd	MCE	
3,5,7-Trihydroxy-8-methoxyflavanone	<i>Prunus padus</i> var. <i>seoulensis</i> Nakai Rosaceae (leaves)	17.92 ± 0.63 µM ^{a,e}	TAC 0.22 ± 0.001 µM ^{a,e}	nd	nd	MCE	
Amentoflavone	<i>Selaginella doederleinii</i> Hieron Selaginellaceae (whole plant)	0.73 ± 0.009 µM ^{a,e}	TAC 1.26 ± 0.017 µM ^{a,e}	nd	nd	MCE	
Bilobetin	<i>Selaginella doederleinii</i> Hieron Selaginellaceae (whole plant)	5.76 ± 0.021 µM ^{a,e}	TAC 1.26 ± 0.017 µM ^{a,e}	nd	nd	MCE	
Isoginkgetin	<i>Selaginella doederleinii</i> Hieron Selaginellaceae (whole plant)	4.11 ± 0.019 µM ^{a,e}	TAC 1.26 ± 0.017 µM ^{a,e}	nd	nd	MCE	[48,113]
Robustaflavone	<i>Selaginella doederleinii</i> Hieron Selaginellaceae (whole plant)	6.16 ± 0.032 µM ^{a,e}	TAC 1.26 ± 0.017 µM ^{a,e}	nd	nd	MCE	
Kaempferol	<i>Spiranthes sinensis</i> Ames Orchidaceae (whole plant)	12.64 ± 0.31 ^{a,k}	GAL 0.19 ± 0.02 µg/mL ^{a,k}	nd	nd	MCE	
Quercetin	<i>Spiranthes sinensis</i> Ames Orchidaceae (whole plant)	8.63 ± 0.37 ^{a,k}	GAL 0.19 ± 0.02 µg/mL ^{a,k}	nd	nd	MCE	[48,114]
LANOSTANE TRITERPENES							
Methyl lucidenate E2	<i>Ganoderma lucidum</i> Karst. Ganodermataceae (fruiting bodies)	17.14 ± 2.88 µM ^{a,k}	BERCI 0.04 ± 0.01 µM ^{a,k}	>200 µM ^{a,n}	BERCI 18.97 ± 0.41 µM ^{a,n}	MCE	
n-Butyl lucidenate A	<i>Ganoderma lucidum</i> Karst. Ganodermataceae (fruiting bodies)	12.26 ± 0.68 µM ^{a,k}	BERCI 0.04 ± 0.01 µM ^{a,k}	>200 µM ^{a,n}	BERCI 18.97 ± 0.41 µM ^{a,n}	MCE	
Ganoderic acid E	<i>Ganoderma lucidum</i> Karst. Ganodermataceae (fruiting bodies)	18.35 ± 2.95 µM ^{a,k}	BERCI 0.04 ± 0.01 µM ^{a,k}	>200 µM ^{a,n}	BERCI 18.97 ± 0.41 µM ^{a,n}	MCE	
N-Butyl ganoderate H	<i>Ganoderma lucidum</i> Karst. Ganodermataceae (fruiting bodies)	9.40 ± 0.88 µM ^{a,k}	BERCI 0.04 ± 0.01 µM ^{a,k}	>200 µM ^{a,n}	BERCI 18.97 ± 0.41 µM ^{a,n}	MCE	
Lucidiol	<i>Ganoderma lucidum</i> Karst. Ganodermataceae (fruiting bodies)	31.03 ± 1.69 µM ^{a,k}	BERCI 0.04 ± 0.01 µM ^{a,k}	156.27 ± 6.12 µM ^{a,n}	BERCI 18.97 ± 0.41 µM ^{a,n}	MCE	[48,115]
Lucidenic acid N	<i>Ganoderma lucidum</i> Karst. Ganodermataceae (fruiting bodies)	25.91 ± 0.89 µM ^{a,k}	BERCI 0.04 ± 0.01 µM ^{a,k}	188.36 ± 3.05 µM ^{a,n}	BERCI 18.97 ± 0.41 µM ^{a,n}	MCE	
Lucidumol B	<i>Ganoderma lucidum</i> Karst. Ganodermataceae (fruiting bodies)	16.27 ± 0.51 µM ^{a,k}	BERCI 0.04 ± 0.01 µM ^{a,k}	>200 µM ^{a,n}	BERCI 18.97 ± 0.41 µM ^{a,n}	MCE	
n-Butyl lucidenate N	<i>Ganoderma lucidum</i> Karst. Ganodermataceae (fruiting bodies)	11.58 ± 0.36 µM ^{a,k}	BERCI 0.04 ± 0.01 µM ^{a,k}	>200 µM ^{a,n}	BERCI 18.97 ± 0.41 µM ^{a,n}	MCE	
LIGNANS							
Macelignan	<i>Myristica fragrans</i> Houltt. Myristicaceae (seeds)	4.16 ± 0.070 µM ^{a,e}	BER 1.01 ± 0.01 µM ^{a,e} TAC 0.22 ± 0.004 µM ^{a,e}	9.69 ± 0.98 µM ^{a,m}	TAC 0.014 ± 0.0043 µM ^{a,m}	MCE	[48,59,60]

Table 1. Cont.

Inhibitors	Source	Activity				Method	Ref.
		Value of Inhibition against AChE	Reference Standard for AChE	Value of Inhibition against BuChE	Reference Standard for BuChE		
(+)-(7R,8S)-Erythro-4,7,9'-trihydroxy-8-O-4'-neolignan-9-O-β-D-glucopyranoside	<i>Camelia sinensis</i> var. <i>sinensis</i> Theaceae (leaves and buds)	0.75 ± 0.04 μM ^{a,e}	HUP 0.29 ± 0.05 μM ^{a,e}	nd	nd	MCE	[48,116,117]
(7S,8S)-Threo-4,9,9'-trihydroxy-8-O-4'-neolignan-7-O-β-D-glucopyranoside	<i>Camelia sinensis</i> var. <i>sinensis</i> Theaceae (leaves and buds)	0.19 ± 0.02 μM ^{a,e}	HUP 0.29 ± 0.05 μM ^{a,e}	nd	nd	MCE	
STILBENOID							
Isoarundinin II	<i>Bletilla striata</i> Reichb. f. Orchidaceae (tuber)	25 μg mL ⁻¹ −0.9 ± 0.8% ^{b,e}	GAL 25 μg mL ⁻¹ −94.8 ± 0.9% ^{b,e}	25 μg mL ⁻¹ −39.3 ± 2.3% ^{b,m}	25 μg mL ⁻¹ GAL −64.2 ± 0.6% ^{b,m} 46.3 ± 5.8 μM ^{a,m} TAC 0.0101 ± 0.0005 μM ^{a,m}	MCE	[37,48]
PHENANTHRENES							
1-[(4-Hydroxyphenyl)methyl]-4-methoxy-2,7-phenanthrenediol	<i>Bletilla striata</i> Reichb. f. Orchidaceae (tuber)	25 μg mL ⁻¹ −19.1 ± 3.8% ^{b,e}	GAL 25 μg mL ⁻¹ −94.8 ± 0.9% ^{b,e}	25 μg mL ⁻¹ −96.6 ± 1.2% ^{b,m} 2.1 ± 0.3 μM ^{a,m}	25 μg mL ⁻¹ GAL −64.2 ± 0.6% ^{b,m} 46.3 ± 5.8 μM ^{a,m} TAC 0.0101 ± 0.0005 μM ^{a,m}	MCE	
1,8-bis(4-Hydroxybenzyl)-4-methoxyphenanthrene-2,7-diol	<i>Bletilla striata</i> Reichb. f. Orchidaceae (tuber)	25 μg mL ⁻¹ −16.1 ± 5.0% ^{b,e}	GAL 25 μg mL ⁻¹ −94.8 ± 0.9% ^{b,e}	25 μg mL ⁻¹ −95.4 ± 0.3% ^{b,m} 2.3 ± 0.4 μM ^{a,m}	25 μg mL ⁻¹ GAL −64.2 ± 0.6% ^{b,m} 46.3 ± 5.8 μM ^{a,m} TAC 0.0101 ± 0.0005 μM ^{a,m}	MCE	
2,7-Dihydroxy-1,3-bi(p-hydroxybenzyl)-4-methoxy-9,10-dihydrophenanthrene	<i>Bletilla striata</i> Reichb. f. Orchidaceae (tuber)	25 μg mL ⁻¹ −20.1 ± 3.5% ^{b,e}	GAL 25 μg mL ⁻¹ −94.8 ± 0.9% ^{b,e}	25 μg mL ⁻¹ −53.1 ± 1.2% ^{b,m} 44.6 ± 4.1 μM ^{a,m}	25 μg mL ⁻¹ GAL −64.2 ± 0.6% ^{b,m} 46.3 ± 5.8 μM ^{a,m} TAC 0.0101 ± 0.0005 μM ^{a,m}	MCE	
1-(p-Hydroxybenzyl)-4,7-dimethoxyphenanthrene-2,8-diol	<i>Bletilla striata</i> Reichb. f. Orchidaceae (tuber)	25 μg mL ⁻¹ −20.4 ± 4.5% ^{b,e}	GAL 25 μg mL ⁻¹ −94.8 ± 0.9% ^{b,e}	25 μg mL ⁻¹ −85.2 ± 2.9% ^{b,m} 6.4 ± 0.2 μM ^{a,m}	25 μg mL ⁻¹ GAL −64.2 ± 0.6% ^{b,m} 46.3 ± 5.8 μM ^{a,m} TAC 0.0101 ± 0.0005 μM ^{a,m}	MCE	
3-(4-Hydroxybenzyl)-4-methoxy-9,10-dihydrophenanthrene-2,7-diol	<i>Bletilla striata</i> Reichb. f. Orchidaceae (tuber)	25 μg mL ⁻¹ −9.6 ± 2.6% ^{b,e}	GAL 25 μg mL ⁻¹ −94.8 ± 0.9% ^{b,e}	25 μg mL ⁻¹ −65.7 ± 0.7% ^{b,m} 34.0 ± 1.4 μM ^{a,m}	25 μg mL ⁻¹ GAL −64.2 ± 0.6% ^{b,m} 46.3 ± 5.8 μM ^{a,m} TAC 0.0101 ± 0.0005 μM ^{a,m}	MCE	
9-(4'-Hydroxy-3'-methoxyphenyl)-10-(hydroxymethyl)-11-methoxy-5,6,9,10-tetrahydrophenanthro[2,3-b]furan-3-ol	<i>Bletilla striata</i> Reichb. f. Orchidaceae (tuber)	25 μg mL ⁻¹ −3.3 ± 1.8% ^{b,e}	GAL 25 μg mL ⁻¹ −94.8 ± 0.9% ^{b,e}	25 μg mL ⁻¹ −61.2 ± 1.3% ^{b,m} 35.8 ± 9.2 μM ^{a,m}	25 μg mL ⁻¹ GAL −64.2 ± 0.6% ^{b,m} 46.3 ± 5.8 μM ^{a,m} TAC 0.0101 ± 0.0005 μM ^{a,m}	MCE	[37,48]
Bleformin A	<i>Bletilla striata</i> Reichb. f. Orchidaceae (tuber)	25 μg mL ⁻¹ −18.5 ± 1.7% ^{b,e}	GAL 25 μg mL ⁻¹ −94.8 ± 0.9% ^{b,e}	25 μg mL ⁻¹ −70.0 ± 1.0% ^{b,m} 5.2 ± 0.4 μM ^{a,m}	25 μg mL ⁻¹ GAL −64.2 ± 0.6% ^{b,m} 46.3 ± 5.8 μM ^{a,m} TAC 0.0101 ± 0.0005 μM ^{a,m}	MCE	
Bleformin B	<i>Bletilla striata</i> Reichb. f. Orchidaceae (tuber)	25 μg mL ⁻¹ −9.9 ± 4.7% ^{b,e}	GAL 25 μg mL ⁻¹ −94.8 ± 0.9% ^{b,e}	25 μg mL ⁻¹ −75.7 ± 1.1% ^{b,m} 16.7 ± 2.4 μM ^{a,m}	25 μg mL ⁻¹ GAL −64.2 ± 0.6% ^{b,m} 46.3 ± 5.8 μM ^{a,m} TAC 0.0101 ± 0.0005 μM ^{a,m}	MCE	
Blestrin D	<i>Bletilla striata</i> Reichb. f. Orchidaceae (tuber)	25 μg mL ⁻¹ −6.8 ± 1.6% ^{b,e}	GAL 25 μg mL ⁻¹ −94.8 ± 0.9% ^{b,e}	25 μg mL ⁻¹ −69.0 ± 2.5% ^{b,m} 8.1 ± 0.5 μM ^{a,m}	25 μg mL ⁻¹ GAL −64.2 ± 0.6% ^{b,m} 46.3 ± 5.8 μM ^{a,m} TAC 0.0101 ± 0.0005 μM ^{a,m}	MCE	
Blestrin A	<i>Bletilla striata</i> Reichb. f. Orchidaceae (tuber)	25 μg mL ⁻¹ −8.4 ± 3.1% ^{b,e}	GAL 25 μg mL ⁻¹ −94.8 ± 0.9% ^{b,e}	25 μg mL ⁻¹ −64.0 ± 2.6% ^{b,m} 17.9 ± 4.7 μM ^{a,m}	25 μg mL ⁻¹ GAL −64.2 ± 0.6% ^{b,m} 46.3 ± 5.8 μM ^{a,m} TAC 0.0101 ± 0.0005 μM ^{a,m}	MCE	
Blestrin C	<i>Bletilla striata</i> Reichb. f. Orchidaceae (tuber)	25 μg mL ⁻¹ −4.9 ± 3.2% ^{b,e}	GAL 25 μg mL ⁻¹ −94.8 ± 0.9% ^{b,e}	25 μg mL ⁻¹ −64.3 ± 2.4% ^{b,m} 12.1 ± 3.4 μM ^{a,m}	25 μg mL ⁻¹ GAL −64.2 ± 0.6% ^{b,m} 46.3 ± 5.8 μM ^{a,m} TAC 0.0101 ± 0.0005 μM ^{a,m}	MCE	

Table 1. Cont.

Inhibitors	Source	Activity				Method	Ref.
		Value of Inhibition against AChE	Reference Standard for AChE	Value of Inhibition against BuChE	Reference Standard for BuChE		
Bletilol D	<i>Bletilla striata</i> Reichb. f. Orchidaceae (tuber)	25 µg mL ⁻¹ −5.7 ± 2.8% b,e	GAL 25 µg mL ⁻¹ −94.8 ± 0.9% b,e	25 µg mL ⁻¹ −31.6 ± 2.8% b,m	25 µg mL ⁻¹ −64.2 ± 0.6% b,m 46.3 ± 5.8 µM a,m TAC 0.0101 ± 0.0005 µM a,m	MCE	
Bletilol E	<i>Bletilla striata</i> Reichb. f. Orchidaceae (tuber)	25 µg mL ⁻¹ −5.1 ± 4.0% b,e	GAL 25 µg mL ⁻¹ −94.8 ± 0.9% b,e	25 µg mL ⁻¹ −8.0 ± 2.4% b,m	25 µg mL ⁻¹ −64.2 ± 0.6% b,m 46.3 ± 5.8 µM a,m TAC 0.0101 ± 0.0005 µM a,m	MCE	
Favanthrin	<i>Bletilla striata</i> Reichb. f. Orchidaceae (tuber)	25 µg mL ⁻¹ −13.3 ± 2.9% b,e	GAL 25 µg mL ⁻¹ −94.8 ± 0.9% b,e	25 µg mL ⁻¹ −56.7 ± 2.0% b,m 42.2 ± 5.1 µM a,m	25 µg mL ⁻¹ −64.2 ± 0.6% b,m 46.3 ± 5.8 µM a,m TAC 0.0101 ± 0.0005 µM a,m	MCE	
Pholidotol	<i>Bletilla striata</i> Reichb. f. Orchidaceae (tuber)	25 µg mL ⁻¹ −5.2 ± 3.2% b,e	GAL 25 µg mL ⁻¹ −94.8 ± 0.9% b,e	25 µg mL ⁻¹ −29.1 ± 1.3% b,m	25 µg mL ⁻¹ −64.2 ± 0.6% b,m 46.3 ± 5.8 µM a,m TAC 0.0101 ± 0.0005 µM a,m	MCE	
Shancidin	<i>Bletilla striata</i> Reichb. f. Orchidaceae (tuber)	25 µg mL ⁻¹ −15.2 ± 3.6% b,e	GAL 25 µg mL ⁻¹ −94.8 ± 0.9% b,e	25 µg mL ⁻¹ −72.8 ± 3.4% b,m 16.7 ± 2.0 µM a,m	25 µg mL ⁻¹ −64.2 ± 0.6% b,m 46.3 ± 5.8 µM a,m TAC 0.0101 ± 0.0005 µM a,m	MCE	
Shanciol F	<i>Bletilla striata</i> Reichb. f. Orchidaceae (tuber)	25 µg mL ⁻¹ −5.5 ± 1.8% b,e	GAL 25 µg mL ⁻¹ −94.8 ± 0.9% b,e	25 µg mL ⁻¹ −21.8 ± 3.1% b,m	25 µg mL ⁻¹ −64.2 ± 0.6% b,m 46.3 ± 5.8 µM a,m TAC 0.0101 ± 0.0005 µM a,m	MCE	
Cremaphenanthrene F	<i>Cremastra appendiculata</i> Makino Orchidaceae (tubers)	>200 µM a,e	GAL 0.39 ± 0.04 µM a,e	14.62 ± 2.15 µM a,m	1.12 ± 0.67 µM a,m	MCE	[44,48]
Cremaphenanthrene G	<i>Cremastra appendiculata</i> Makino Orchidaceae (tubers)	>200 µM a,e	GAL 0.39 ± 0.04 µM a,e	79.56 ± 0.78 µM a,m	1.12 ± 0.67 µM a,m	MCE	
PHENYLPROPANOIDS							
Lapathoside A	<i>Fallopia dentatoalata</i> Holub Polygonaceae (aerial part)	30.6 ± 4.7 µM a,e	TAC 0.1267 ± 0.0011 µM a,e	2.7 ± 1.7 µM a,m	0.0055 ± 0.0017 µM a,m	MCE	
Lapathoside B	<i>Fallopia dentatoalata</i> Holub Polygonaceae (aerial part)	>100 µM a,e	TAC 0.1267 ± 0.0011 µM a,e	10.9 ± 4.9 µM a,m	0.0055 ± 0.0017 µM a,m	MCE	
Smilaside G	<i>Fallopia dentatoalata</i> Holub Polygonaceae (aerial part)	>100 µM a,e	TAC 0.1267 ± 0.0011 µM a,e	17.1 ± 3.4 µM a,m	0.0055 ± 0.0017 µM a,m	MCE	[48,118,119]
Smilaside J	<i>Fallopia dentatoalata</i> Holub Polygonaceae (aerial part)	56.0 ± 2.4 µM a,e	TAC 0.1267 ± 0.0011 µM a,e	10.1 ± 4.6 µM a,m	0.0055 ± 0.0017 µM a,m	MCE	
Vanicoside B	<i>Fallopia dentatoalata</i> Holub Polygonaceae (aerial part)	32.3 ± 4.7 µM a,e	TAC 0.1267 ± 0.0011 µM a,e	7.5 ± 4.1 µM a,m	0.0055 ± 0.0017 µM a,m	MCE	
PHLOROTANNINS							
974-B	<i>Eisenia bicyclis</i> (Kjellman) Stechell Laminariaceae (leafy thalli)	1.95 ± 0.01 µM a,e	BER 0.22 ± 0.03 µM a,e	3.26 ± 0.08 µM a,m	11.74 ± 0.85 µM a,m	CE	[48,120]
PHTHALATES							
bis (7-Acetoxy-2-ethyl-5-methylheptyl) phthalate	<i>Lonicera quinquelocularis</i> Hard. Caprifoliaceae (whole plant)	1.65 ± 0.03 µM a,k	GAL 1.79 ± 0.061 µM a,k	5.98 ± 0.079 µM a,m	7.98 ± 0.01 µM a,m	MCE	[48,51,121]
Neopentyl-4-hydroxy-3,5-bis (3-methyl-2-butenyl) benzoate	<i>Lonicera quinquelocularis</i> Hard. Caprifoliaceae (whole plant)	3.43 ± 0.02 µM a,k	GAL 1.79 ± 0.061 µM a,k	9.84 ± 0.037 µM a,m	7.98 ± 0.01 µM a,m	MCE	
PHENOLIC ACIDS							
4-Hydroxybenzoic acid methyl ester	<i>Spiranthes sinensis</i> Ames Orchidaceae (whole plant)	42.89 ± 1.21 a,k	GAL 0.19 ± 0.02 µg/mL a,k	nd	nd	MCE	[48,114]
Ethyl ferulate	<i>Spiranthes sinensis</i> Ames Orchidaceae (whole plant)	19.97 ± 1.05 a,k	GAL 0.19 ± 0.02 µg/mL a,k	nd	nd	MCE	

Table 1. Cont.

Inhibitors	Source	Activity				Method	Ref.
		Value of Inhibition against AChE	Reference Standard for AChE	Value of Inhibition against BuChE	Reference Standard for BuChE		
3-(4-Tolyloxy)-propanoic acid	<i>Spiranthes sinensis</i> Ames Orchidaceae (whole plant)	15.31 ± 0.64 ^{a,k}	GAL 0.19 ± 0.02 µg/mL ^{a,k}	nd	nd	MCE	
POLYKETIDES							
Aspilactonol G	<i>Phaeospaeria</i> sp. LF5 (strain from <i>Huperzia serrata</i>)	>100 µM ^{a,k}	RIV 1.82 ± 0.13 µM ^{a,k} HUP 0.045 ± 0.01 µM ^{a,k}	nd	nd	MCE	
Aspilactonol H	<i>Phaeospaeria</i> sp. LF5 (strain from <i>Huperzia serrata</i>)	>100 µM ^{a,k}	RIV 1.82 ± 0.13 µM ^{a,k} HUP 0.045 ± 0.01 µM ^{a,k}	nd	nd	MCE	
Aspilactonol I	<i>Phaeospaeria</i> sp. LF5 (strain from <i>Huperzia serrata</i>)	6.26 ± 0.15 µM ^{a,k}	RIV 1.82 ± 0.13 µM ^{a,k} HUP 0.045 ± 0.01 µM ^{a,k}	nd	nd	MCE	
de-O-Methyladiaporthin	<i>Phaeospaeria</i> sp. LF5 (strain from <i>Huperzia serrata</i>)	21.18 ± 1.53 µM ^{a,k}	RIV 1.82 ± 0.13 µM ^{a,k} HUP 0.045 ± 0.01 µM ^{a,k}	nd	nd	MCE	
6,8-Dihydroxy-3-(10 <i>R</i> , 20 <i>R</i> -dihydroxypropyl)-isocoumarin	<i>Phaeospaeria</i> sp. LF5 (strain from <i>Huperzia serrata</i>)	>100 µM ^{a,k}	RIV 1.82 ± 0.13 µM ^{a,k} HUP 0.045 ± 0.01 µM ^{a,k}	nd	nd	MCE	
<i>E</i> - Δ^2 -Anhydromevalonic acid	<i>Phaeospaeria</i> sp. LF5 (strain from <i>Huperzia serrata</i>)	>100 µM ^{a,k}	RIV 1.82 ± 0.13 µM ^{a,k} HUP 0.045 ± 0.01 µM ^{a,k}	nd	nd	MCE	[48,122,123]
2-(1-Hydroxyethyl)-6-methylisonicotinic acid	<i>Phaeospaeria</i> sp. LF5 (strain from <i>Huperzia serrata</i>)	>100 µM ^{a,k}	RIV 1.82 ± 0.13 µM ^{a,k} HUP 0.045 ± 0.01 µM ^{a,k}	nd	nd	MCE	
6-Hydroxy-8-methoxy-3-methylisocoumarin	<i>Phaeospaeria</i> sp. LF5 (strain from <i>Huperzia serrata</i>)	>100 µM ^{a,k}	RIV 1.82 ± 0.13 µM ^{a,k} HUP 0.045 ± 0.01 µM ^{a,k}	nd	nd	MCE	
3-(Hydroxymethyl)-5-methylfuran-2(5H)-one	<i>Phaeospaeria</i> sp. LF5 (strain from <i>Huperzia serrata</i>)	>100 µM ^{a,k}	RIV 1.82 ± 0.13 µM ^{a,k} HUP 0.045 ± 0.01 µM ^{a,k}	nd	nd	MCE	
4-Methyl-5,6-dihydropyren-2-one	<i>Phaeospaeria</i> sp. LF5 (strain from <i>Huperzia serrata</i>)	>100 µM ^{a,k}	RIV 1.82 ± 0.13 µM ^{a,k} HUP 0.045 ± 0.01 µM ^{a,k}	nd	nd	MCE	
(<i>R</i>)-6-Hydroxymellein	<i>Phaeospaeria</i> sp. LF5 (strain from <i>Huperzia serrata</i>)	>100 µM ^{a,k}	RIV 1.82 ± 0.13 µM ^{a,k} HUP 0.045 ± 0.01 µM ^{a,k}	nd	nd	MCE	
Asterric acid	<i>Talaromyces aurantiacus</i> FL 15 (strain from leave <i>Huperzia serrata</i>)	66.7 ± 1.7 µM ^{a,e}	RIV 1.82 ± 0.13 µM ^{a,e} HUP 0.045 ± 0.01 µM ^{a,e}	>100 µM ^{a,m}	ns	MCE	
Ethyl asterrate	<i>Talaromyces aurantiacus</i> FL 15 (strain from leave <i>Huperzia serrata</i>)	20.1 ± 0.9 µM ^{a,e}	RIV 1.82 ± 0.13 µM ^{a,e} HUP 0.045 ± 0.01 µM ^{a,e}	>100 µM ^{a,m}	ns	MCE	[48,91,92]
Methyl asterrate	<i>Talaromyces aurantiacus</i> FL 15 (strain from leave <i>Huperzia serrata</i>)	23.3 ± 1.2 µM ^{a,e}	RIV 1.82 ± 0.13 µM ^{a,e} HUP 0.045 ± 0.01 µM ^{a,e}	>100 µM ^{a,m}	ns	MCE	
Sulochrin	<i>Talaromyces aurantiacus</i> FL 15 (strain from leave <i>Huperzia serrata</i>)	>100 µM ^{a,e}	RIV 1.82 ± 0.13 µM ^{a,e} HUP 0.045 ± 0.01 µM ^{a,e}	>100 µM ^{a,m}	ns	MCE	
POLYPHENOLS							
Broussonin A	<i>Anemarrhena asphodeloides</i> Bunge Asparagaceae (roots)	15.88 ± 1.02 µM ^{a,e}	BER 1.01 ± 0.01 µM ^{a,e} TAC 0.22 ± 0.004 µM ^{a,e}	7.50 ± 0.07 µM ^{a,m}	TAC 0.014 ± 0.0043 µM ^{a,m}	MCE	[48,59,60]
Mangiferin	<i>Anemarrhena asphodeloides</i> Bunge Asparagaceae (whole plant)	62.8 µM ^{a,g}	TAC nd ^{a,g}	nd	nd	MCE	[48,124]
Caffeoylated catechin	<i>Camellia sinensis</i> var. <i>assamica</i> Theaceae (leaves)	2.49 ± 0.43 µM ^{a,e}	HUP 0.088 ± 0.004 µM ^{a,e}	nd	d	MCE	
Epigallocatechin 3- <i>O</i> - <i>p</i> -coumaroate	<i>Camellia sinensis</i> var. <i>assamica</i> Theaceae (leaves)	11.41 ± 2.00 µM ^{a,e}	HUP 0.088 ± 0.004 µM ^{a,e}	nd	nd	MCE	[48,116]
Epigallocatechin-3- <i>O</i> -ferulate	<i>Camellia sinensis</i> var. <i>assamica</i> Theaceae (leaves)	62.26 ± 10.18 µM ^{a,e}	HUP 0.088 ± 0.004 µM ^{a,e}	nd	nd	MCE	

Table 1. Cont.

Inhibitors	Source	Activity				Method	Ref.
		Value of Inhibition against AChE	Reference Standard for AChE	Value of Inhibition against BuChE	Reference Standard for BuChE		
Creoside IV	<i>Codonopsis pilosula</i> Nannf Campanulaceae (roots)	7.30 ± 0.49 µM ^{a,e}	BER 1.01 ± 0.01 µM ^{a,e} TAC 0.22 ± 0.004 µM ^{a,e}	>40 ^{a,m}	TAC 0.014 ± 0.0043 µM ^{a,m}	MCE	[48,59,60]
Heyneanol A	<i>Vitis amurensis</i> Rupr. Vitaceae (roots)	1.66 ± 0.09 µM ^{a,f}	GAL 0.93 ± 0.07 µM ^{a,f}	1.75 ± 0.09 µM ^{a,l}	GAL 9.24 ± 1.32 µM ^{a,l}	MCE	[48,125]
Vitisin A	<i>Vitis amurensis</i> Rupr. Vitaceae (roots)	1.04 ± 0.05 µM ^{a,f}	GAL 0.93 ± 0.07 µM ^{a,f}	4.41 ± 0.39 µM ^{a,l}	GAL 9.24 ± 1.32 µM ^{a,l}	MCE	
SESQUITERPENE LACTONES							
Britannin	<i>Inula aucheriana</i> DC. Asteraceae (aerial parts)	300 µg mL ⁻¹ —25.2% ^{b,k}	DON	nd	nd	MCE	
Gaillardin	<i>Inula oculus-christi</i> L. Asteraceae (aerial parts)	300 µg mL ⁻¹ —67% ^{b,k}	DON	nd	nd	MCE	[48,126]
Pulchellin C	<i>Inula oculus-christi</i> L. Asteraceae (aerial parts)	300 µg mL ⁻¹ —10.9% ^{b,k}	DON	nd	nd	MCE	
Amberin	<i>Amberboa ramosa</i> Jafri. Asteraceae (whole plant)	17.5 ± 0.01 µM ^{a,e}	GAL 0.5 ± 0.01 µM ^{a,e} PHY 0.04 ± 0.0001 µM ^{a,e}	2.7 ± 0.02 µM ^{a,m}	GAL 8.2 ± 0.02 µM ^{a,m} PHY 0.82 ± 0.001 µM ^{a,m}	MCE	
Amberbin A	<i>Amberboa ramosa</i> Jafri. Asteraceae (whole plant)	8.6 ± 0.15 µM ^{a,e}	GAL 0.5 ± 0.01 µM ^{a,e} PHY 0.04 ± 0.0001 µM ^{a,e}	4.8 ± 0.15 µM ^{a,m}	GAL 8.2 ± 0.02 µM ^{a,m} PHY 0.82 ± 0.001 µM ^{a,m}	MCE	[48,127]
Amberbin B	<i>Amberboa ramosa</i> Jafri. Asteraceae (whole plant))	0.91 ± 0.015 µM ^{a,e}	GAL 0.5 ± 0.01 µM ^{a,e} PHY 0.04 ± 0.0001 µM ^{a,e}	2.5 ± 0.15 µM ^{a,m}	GAL 8.2 ± 0.02 µM ^{a,m} PHY 0.82 ± 0.001 µM ^{a,m}	MCE	
Amberbin C	<i>Amberboa ramosa</i> Jafri. Asteraceae (whole plant)	1.1 ± 0.08 µM ^{a,e}	GAL 0.5 ± 0.01 µM ^{a,e} PHY 0.04 ± 0.0001 µM ^{a,e}	17.9 ± 0.05 µM ^{a,m}	GAL 8.2 ± 0.02 µM ^{a,m} PHY 0.82 ± 0.001 µM ^{a,m}	MCE	
Zerumbone	<i>Zingiber zerumbet</i> L. Zingiberaceae (whole plant)	1 mg mL ⁻¹ ^{c,k}	TAC 10 mM ^{c,k}	nd	nd	BTLC by Rhee et al. (2001)	[16,128]
Silphiperfolene acetate	<i>Leontopodium alpinum</i> Cass. Asteraceae (sub-aerial parts)	200 µM —40.64 ± 7.09% ^{b,k}	GAL 3.2 µM ^{a,k} GAL 100 µM—89.30 ± 2.29% ^{b,k}	nd	nd	MCE	[93,95,129]
STEROIDS							
Leucisterol	<i>Leucas urticifolia</i> Vahl. Lamiaceae (whole plant)	83.6 ± 0.59 µM ^{a,k}	PHY 0.04 µM ^{a,k}	3.2 ± 0.85 µM ^{a,n}	PHY 0.93 ± 0.3 µM ^{a,n}	CE	[48,130]
STEROLS							
Haloxylon A	<i>Haloxylon recurvum</i> Bunge ex Boiss Chenopodiaceae (whole plant)	8.3 ± 0.02 µM ^{a,e}	GAL 0.5 ± 0.001 µM ^{a,e}	4.7 ± 0.01 µM ^{a,m}	GAL 8.5 ± 0.00 µM ^{a,m}	MCE	[48,131]
Haloxylon B	<i>Haloxylon recurvum</i> Bunge ex Boiss Chenopodiaceae (whole plant)	0.89 ± 0.002 µM ^{a,e}	GAL 0.5 ± 0.001 µM ^{a,e}	2.3 ± 0.001 µM ^{a,m}	GAL 8.5 ± 0.00 µM ^{a,m}	MCE	
TRIFLAVANONES							
Garcineflavanone A	<i>Garcinia atroviridis</i> Griff. ex T. Anders. Clusiaceae (stem bark)	100 µg mL ⁻¹ —80.15 ± 6.65% ^{b,e} 28.52 ± 5.23 µg mL ⁻¹ ^{a,e}	PHY 0.05 ± 0.01 µg mL ⁻¹ ^{a,e}	ns	PHY 0.14 ± 0.015 µg mL ⁻¹ ^{a,m}	MCE	[48,108,109]
TRITERPENOIDES							
Arbora-1,9(11)-dien-3-one	<i>Buxus hyrcana</i> Pojark. Buxaceae (leaves)	47.9 ± 1.2 µM ^{a,k}	GAL 0.53 ± 0.5 µM ^{a,k} HUP 1.7 ± 0.3 µM ^{a,k}	220.1 ± 1.0 µM ^{a,n}	GAL 8.7 ± 1.0 µM ^{a,n} HUP >1000 ± 3.0 µM ^{a,n}	MCE	[48,56–58]
Asiatic acid	<i>Centella asiatica</i> Urb Apiaceae (whole plant)	15.05 ± 0.05 µM ^{a,e}	PHY 0.05 ± 0.12 µM ^{a,e}	nd	nd	MCE	
Asiaticoside	<i>Centella asiatica</i> Urb Apiaceae (whole plant)	59.13 ± 0.18 µM ^{a,e}	PHY 0.05 ± 0.12 µM ^{a,e}	nd	nd	MCE	[48,132,133]
Madecassic acid	<i>Centella asiatica</i> Urb Apiaceae (whole plant)	17.83 ± 0.06 µM ^{a,e}	PHY 0.05 ± 0.12 µM ^{a,e}	nd	nd	MCE	
Madecassoside	<i>Centella asiatica</i> Urb Apiaceae (whole plant)	37.14 ± 0.04 µM ^{a,e}	PHY 0.05 ± 0.12 µM ^{a,e}	nd	nd	MCE	

Table 1. Cont.

Inhibitors	Source	Activity				Method	Ref.
		Value of Inhibition against AChE	Reference Standard for AChE	Value of Inhibition against BuChE	Reference Standard for BuChE		
Betulin	<i>Garcinia hombroniana</i> Pierre Clusiaceae (bark)	28.5 ± 0.78 µM ^{a,e}	PHY 0.04 ± 0.004 µM ^{a,e}	nd	PHY 0.09 ± 0.003 µM ^{a,m}	MCE	
Betulinic acid	<i>Garcinia hombroniana</i> Pierre Clusiaceae (bark)	24.2 ± 0.99 µM ^{a,e}	PHY 0.04 ± 0.004 µM ^{a,e}	19.1 ± 1.33 µM ^{a,m}	PHY 0.09 ± 0.003 µM ^{a,m}	MCE	
2β-Hydroxy-3α-O-caffeoyltaraxar-14-en-28-oic acid	<i>Garcinia hombroniana</i> Pierre Clusiaceae (bark)	13.5 ± 0.95 µM ^{a,e}	PHY 0.04 ± 0.004 µM ^{a,e}	10.6 ± 0.54 µM ^{a,m}	PHY 0.09 ± 0.003 µM ^{a,m}	MCE	[48,81]
Taraxerol	<i>Garcinia hombroniana</i> Pierre Clusiaceae (bark)	nd	PHY 0.04 ± 0.004 µM ^{a,e}	17.8 ± 1.73 µM ^{a,m}	PHY 0.09 ± 0.003 µM ^{a,m}	MCE	
21β-Hydroxyserrat-14-en-3,16-dione	<i>Lycopodiella cernua</i> L. Lycopodiaceae (whole plants)	10.67 ± 0.66 µM ^{a,k}	BER 0.10 ± 0.01 µM ^{a,k}	>30 µM ^{a,n}	BER 1.09 ± 0.17 µM ^{a,n}	MCE	
3β,21α-Diacetoxyserrat-14β-ol	<i>Lycopodiella cernua</i> L. Lycopodiaceae (whole plants)	0.91 ± 0.01 µM ^{a,k}	BER 0.10 ± 0.01 µM ^{a,k}	>30 µM ^{a,n}	BER 1.09 ± 0.17 µM ^{a,n}	MCE	[48,106]
3β,21β,29-Trihydroxyserrat-14-en-3β-yl p-dihydrocoumarate	<i>Lycopodiella cernua</i> L. Lycopodiaceae (whole plants)	1.69 ± 0.10 µM ^{a,k}	BER 0.10 ± 0.01 µM ^{a,k}	0.42 ± 0.01 µM ^{a,n}	BER 1.09 ± 0.17 µM ^{a,n}	MCE	
SESQUITERPENES							
1α-Acetoxy-6β,9β-difuroxyloxy-4β-hydroxydihydro-β-agarofuran	<i>Maytenus disticha</i> Urb. Celastraceae (seeds)	738.0 ± 0.007 µM ^{a,e}	GAL 10.0 ± 0.015 µM ^{a,e} CAR 45.0 ± 0.031 µM ^{a,e}	ns ^{a,m}	ns ^{a,m}	MCE	
6β-Acetoxy-9β-benzyloxy-1α,8α-dihydroxydihydro-β-agarofuran	<i>Maytenus disticha</i> Urb. Celastraceae (seeds)	500.0 ± 0.03 µM ^{a,e}	GAL 10.0 ± 0.015 µM ^{a,e} CAR 45.0 ± 0.031 µM ^{a,e}	ns ^{a,m}	ns ^{a,m}	MCE	
6β,8α-Diacetoxy-9β-furoxyloxy-1α-hydroxydihydro-β-agarofuran	<i>Maytenus disticha</i> Urb. Celastraceae (seeds)	740.0 ± 0.045 µM ^{a,e}	GAL 10.0 ± 0.015 µM ^{a,e} CAR 45.0 ± 0.031 µM ^{a,e}	ns ^{a,m}	ns ^{a,m}	MCE	[48,134]
1α,6β,14-Triacetoxy-9β-benzyloxydihydro-β-agarofuran	<i>Maytenus magellanica</i> Hook.f. Celastraceae (seeds)	695.0 ± 0.001 µM ^{a,e}	GAL 10.0 ± 0.015 µM ^{a,e} CAR 45.0 ± 0.031 µM ^{a,e}	ns ^{a,m}	ns ^{a,m}	MCE	
2α,3β,6β-Triacetoxy-1α,9β-dibenzyloxy-4β-hydroxydihydro-β-agarofuran	<i>Maytenus magellanica</i> Hook.f. Celastraceae (seeds)	30.0 ± 0.06 µM ^{a,e}	GAL 10.0 ± 0.015 µM ^{a,e} CAR 45.0 ± 0.031 µM ^{a,e}	ns ^{a,m}	ns ^{a,m}	MCE	
XANTHONES							
Bellidin	<i>Gentianella amarilla</i> ssp. <i>acuta</i> J.M.Gillett Gentianaceae (whole plants)	10 µM—17.5 ± 5.7% ^{b,e}	GAL 10 µM—96.82 ± 0.04% ^{b,e}	nd	nd	MCE BTLC by Marston et al. (2002)	
Bellidifolin	<i>Gentianella amarilla</i> ssp. <i>acuta</i> J.M.Gillett Gentianaceae (whole plants)	10 µM—21.9 ± 6.2% ^{b,e}	GAL 10 µM—96.82 ± 0.04% ^{b,e}	nd	nd	MCE BTLC by Marston et al. (2002)	
Corymbiferin 1-O-glucoside	<i>Gentianella amarilla</i> ssp. <i>acuta</i> J.M.Gillett Gentianaceae (whole plants)	10 µM—1.5 ± 1.2% ^{b,e}	GAL 10 µM—96.82 ± 0.04% ^{b,e}	nd	nd	MCE BTLC by Marston et al. (2002)	[42,48,101,135]
Corymbiferin 3-O-β-D-glucopyranoside	<i>Gentianella amarilla</i> ssp. <i>acuta</i> J.M.Gillett Gentianaceae (whole plants)	10 µM—17.6 ± 1.8% ^{b,e}	GAL 10 µM—96.82 ± 0.04% ^{b,e}	nd	nd	MCE BTLC by Marston et al. (2002)	
nor-Swertianolin	<i>Gentianella amarilla</i> ssp. <i>acuta</i> J.M.Gillett Gentianaceae (whole plants)	10 µM—4.4 ± 4.4% ^{b,e}	GAL 10 µM—96.82 ± 0.04% ^{b,e}	nd	nd	MCE BTLC by Marston et al. (2002)	
Swertianolin	<i>Gentianella amarilla</i> ssp. <i>acuta</i> J.M.Gillett Gentianaceae (whole plants)	10 µM—9.8 ± 3.9% ^{b,e}	GAL 10 µM—96.82 ± 0.04% ^{b,e}	nd	nd	MCE BTLC by Marston et al. (2002)	

Table 1. Cont.

Inhibitors	Source	Activity				Method	Ref.
		Value of Inhibition against AChE	Reference Standard for AChE	Value of Inhibition against BuChE	Reference Standard for BuChE		
Swertiabisxanthone-I	<i>Gentianella amarella</i> ssp. <i>acuta</i> J.M.Gillett Gentianaceae (whole plants)	10 μ M −20.9 \pm 3.3% ^{b,e}	GAL 10 μ M −96.82 \pm 0.04% ^{b,e}	nd	nd	MCE BTLC by Marston et al. (2002)	
Swertiabisxanthone-I 8'-O- β -D- glucopyranoside	<i>Gentianella amarella</i> ssp. <i>acuta</i> J.M.Gillett Gentianaceae (whole plants)	10 μ M −12.3 \pm 2.9% ^{b,e}	GAL 10 μ M −96.82 \pm 0.04% ^{b,e}	nd	nd	MCE BTLC by Marston et al. (2002)	
Triptexanthoside C	<i>Gentianella amarella</i> ssp. <i>acuta</i> J.M.Gillett Gentianaceae (whole plants)	10 μ M −43.7 \pm 3.3% ^{b,e} 13.8 \pm 1.6 μ M ^{a,e}	GAL 10 μ M −96.82 \pm 0.04% ^{b,e} GAL 0.35 \pm 0.02 μ M ^{a,e}	nd	nd	MCE BTLC by Marston et al. (2002)	
Veratriloside	<i>Gentianella amarella</i> ssp. <i>acuta</i> J.M.Gillett Gentianaceae (whole plants)	10 μ M −28.2 \pm 2.5% ^{b,e}	GAL 10 μ M −96.82 \pm 0.04% ^{b,e}	nd	nd	MCE BTLC by Marston et al. (2002)	
XANTHONOIDS							
Allanxanthone E	<i>Garcinia mangostana</i> L. Clusiaceae (seedcases)	15.0 \pm 1.2 μ M ^{a,f} 67.4 \pm 0.3 μ M ^{a,e}	PHY 0.043 \pm 0.002 μ M ^{a,f} 0.049 \pm 0.003 μ M ^{a,e}	11.0 \pm 0.4 μ M ^{a,m}	PHY 0.073 \pm 0.006 μ M ^{a,m}	MCEF	
α -Mangostin	<i>Garcinia mangostana</i> L. Clusiaceae (seedcases)	8.0 \pm 0.5 μ M ^{a,f} 6.3 \pm 0.6 μ M ^{a,e}	PHY 0.043 \pm 0.002 μ M ^{a,f} 0.049 \pm 0.003 μ M ^{a,e}	2.9 \pm 0.7 μ M ^{a,m}	PHY 0.073 \pm 0.006 μ M ^{a,m}	MCEF	
8-Deoxygartanin	<i>Garcinia mangostana</i> L. Clusiaceae (seedcases)	6.2 \pm 0.3 μ M ^{a,f} 11.0 \pm 0.6 μ M ^e	PHY 0.043 \pm 0.002 μ M ^{a,f} 0.049 \pm 0.003 μ M ^{a,e}	9.2 \pm 0.5 μ M ^{a,m}	PHY 0.073 \pm 0.006 μ M ^{a,m}	MCEF	
γ -Mangostin	<i>Garcinia mangostana</i> L. Clusiaceae (seedcases)	5.4 \pm 0.3 μ M ^{a,f} 2.5 \pm 3.3 μ M ^{a,e}	PHY 0.043 \pm 0.002 μ M ^{a,f} 0.049 \pm 0.003 μ M ^{a,e}	0.7 \pm 0.03 μ M ^{a,m}	PHY 0.073 \pm 0.006 μ M ^{a,m}	MCEF	[48,112,136]
Gudraxanthone	<i>Garcinia mangostana</i> L. Clusiaceae (seedcases)	11.7 \pm 0.7 μ M ^{a,f} 18.9 \pm 1.7 μ M ^{a,e}	PHY 0.043 \pm 0.002 μ M ^{a,f} 0.049 \pm 0.003 μ M ^{a,e}	9.0 \pm 1.2 μ M ^{a,m}	PHY 0.073 \pm 0.006 μ M ^{a,m}	MCEF	
9-Hydroxy- calabaxanthone	<i>Garcinia mangostana</i> L. Clusiaceae (seedcases)	>100 μ M ^{a,f} >100 μ M ^{a,e}	PHY 0.043 \pm 0.002 μ M ^{a,f} 0.049 \pm 0.003 μ M ^{a,e}	86.3 \pm 2.4 μ M ^{a,m}	PHY 0.073 \pm 0.006 μ M ^{a,m}	MCEF	
Mangostanol	<i>Garcinia mangostana</i> L. Clusiaceae (seedcases)	14.6 \pm 0.7 μ M ^{a,f} 6.3 \pm 5.4 μ M ^{a,e}	PHY 0.043 \pm 0.002 μ M ^{a,f} 0.049 \pm 0.003 μ M ^{a,e}	6.0 \pm 0.2 μ M ^{a,m}	PHY 0.073 \pm 0.006 μ M ^{a,m}	MCEF	
MISCELLANEOUS							
3-Methylbutyl hydrodisulfide	<i>Buthus martensii</i> Karsch Buthidae (whole body of scorpion)	40.93 \pm 3.21 μ M ^{a,e}	GAL 1.17 \pm 0.01 μ M ^{a,e} DON 0.049 \pm 0.004 μ M ^{a,e}	152.84 \pm 7.22 μ M ^{a,m}	GAL 18.78 \pm 1.81 μ M ^{a,m} DON 5.536 \pm 0.018 μ M ^{a,m}	MCE	[48,54,55]
2-Benzothiazolol	<i>Spiranthes sinensis</i> Ames Orchidaceae (whole plant)	37.67 \pm 0.52 ^{a,k}	GAL 0.19 \pm 0.02 μ g/mL ^{a,k}	nd	nd	MCE	[48,114]

Abbreviations in Table 1: nd—not determined; ns—not shown; ^a—inhibitory concentration for which enzyme activity is equal to half-maximal (IC₅₀)/(IC₅₀) \pm S.E.M.; ^b—percentage of inhibition against enzyme (χ μ g mL^{−1}-y%, χ μ M—y%); ^c—minimal inhibitory quantity (MIC); ^d—IC₅₀ against bovine acetylcholinesterase (bAChE); ^e—IC₅₀ against *Electrophorus electricus* acetylcholinesterase (eeAChE); ^f—IC₅₀ against human erythrocyte acetylcholinesterase (hAChE); ^g—IC₅₀ against mice hippocampus acetylcholinesterase; ^h—against *Nilaparvata lugens* acetylcholinesterase; ⁱ—IC₅₀ against rat cortical acetylcholinesterase; ^j—against *Torpedo californica* acetylcholinesterase; ^k—against acetylcholinesterase not specified in the publication; ^l—IC₅₀ against human butyrylcholinesterase; ^m—IC₅₀ against *Equus caballus* butyrylcholinesterase; ⁿ—against butyrylcholinesterase not specified in the publication. ALA—allanzanthane A; CAR—carvacrol; GAL—galanthamine; TAC—tacrine; HUP—huperzine A; BER—berberine; BERCl—berberine chloride; PHY—physostigmine (eserine); DEH—dehydroevodiamine; CHL—chlorpyrifos; DON—donepezil; NEO—neostigmine bromide; MCE—modified colorimetric Ellman’s method; CE—colorimetric Ellman’s method; BTLC—bioautography TLC; MCEF—modified colorimetric Ellman’s method and fluorescence measurement.

3. Activity

A comparison of the activity of individual isolated compounds is presented in Table 1. Based on the information provided in Table 1, higher activity against AChE relative to galanthamine (1) is exhibited by the alkaloids aconorine, berberine (7), coptisine (9), 1,2-dihydrogalanthamine, epiberberine, jadwarine-A, jatrorrhizine, *N*-allyl-*nor*-galanthamine (4), *N*-(14-methylallyl)-*nor*-galanthamine (5), sanguinine (6), phthalates (e.g., bis (7-acetoxy-2-ethyl-5-methylheptyl) phthalate) and sterols (haloxylon B); relative to berberine (7), sargachromanol I (chromones) shows stronger inhibitory activity; rela-

tive to dehydroevodiamine, tiliroside and quercetin (flavonoids) have stronger inhibitory activity; compared to huperzine A, (7*S*,8*S*)-threo-4,9,9'-trihydroxy-8-O-4'-neolignan-7-O- β -D-glucopyranoside (lignans) has stronger inhibitory activity; compared to physostigmine (eserine), discorhabdin G (alkaloids) has stronger inhibitory activity; relative to neostigmine bromide, 7,8-didehydroorientalidine TFA salt and orientalidine (alkaloids) have stronger inhibitory activity; and compared to tacrine, 7-*epi*-javaniside, six diarylheptanoids from *Alpinia officinarum* and amentoflavone (flavonoids) show stronger inhibitory activity.

In the case of BuChE inhibitors, stronger BuChE inhibitory activity relative to galanthamine (**1**) is shown not only by the alkaloids aconorine, angustidine (**2**), angustine, angustoline, deoxyvobtusine, harmane, hohenackerine, jadwarine-A, nauclefine and pyrroloquinolone A, but also the bibenzyls bulbocol and gymconopin D; the coumarins bergapten, imperatorin (**17**), heraclenol-2'-O-angelate (**18**) and xanthotoxin; the phthalate bis (7-acetoxy-2-ethyl-5-methylheptyl) phthalate; the polyphenols vitisin A and heyneanol A; twelve phenanthrenes from *Bletilla strata*; the sesquiterpene lactones amberin, amberbin A and amberbin B; and the sterols haloxylon A and haloxylon B. In comparison to berberine (**7**), stronger inhibitory activity is exerted by sargachromanol I (chromones), 3 β ,21 β ,29-trihydroxyserrat-14-en-3 β -yl p-dihydrocoumarate (triterpenoids) and compound 974-B (phlorotannins); relative to physostigmine, discorhabdin C and G (alkaloids) and diplacone (**30**) (flavonoids) show stronger inhibitory activity; relative to neostigmine bromide, alborine, isothebaine and *N*-methylisothebainium (alkaloids) have stronger inhibitory activity; and relative to tacrine, 7-*epi*-javaniside (alkaloids) has stronger inhibitory activity.

There are compounds that act more selectively and more potently on AChE versus (vs.) BuChE. The majority of them are alkaloids, including alborine, 9-O-demetil-2- α -hydroxyhomolycorine, 7,8-didehydromecambridine TFA salt, 7,8-didehydroorientalidine TFA salt, dihydroberberine (**8**), discorhabdin B, G and L, chlidanthine, hendersonine B, hydrohydrastinine, 10-hydroxy-infractopicrin, 11-hydroxygalanthine, infractopicrin, mucroniferanines H, narcissidine, orientalidine, sanguinine (**6**), sargachromanol G and I, and vincosamide from *Buxus hyrcana* (except 31-demethylcyclobuxoviridine and papillozine C). Additionally, ethyl asterrate, methyl asterrate (anthranoids), (–) alpininoid B (**23**), (4*E*)-1,7-diphenyl-4-hepten-3-one (**24**) and other diarylheptanoids from *Alpinia officinarum* (diarylheptanoids), sargachromanol G and I (chromones), (2*E*,4*E*,6*R*)-6-hydroxydeca-2,4-dienoic acid (fatty acid), quercetin-3-O-neohesperidoside (flavonoids), methyl lucidenate E2, n-butyl lucidenate A and, n-butyl ganoderate H, ganoderic acid E, garcineflavanone A, lucidanol, lucidenic acid, lucidumol B (lanostane triterpenes), macelignan (lignans), creoside IV (polyphenols), amberbin C (sesquiterpene lactones), 3 β ,21 α -diacetoxyserrat-14 β -ol and 21 β -hydroxyserrat-14-en-3,16-dione (triterpenoids) represent the same feature.

The following compounds are more selective and act more potently on BuChE vs. AChE: angustine, angustidine (**2**), angustoline, 31-demethylcyclobuxoviridine, harmane, isothebaine, lupanine, 2-methoxyatherosperminine, 4-methoxy-1-methyl-2-quinolone, narcipavline, nauclefine, pancratinine-C, papillozine C, pyrroloquinolone A, strictosamide (alkaloids), acetylvismione, bianthrone 1a, 2-geranylemodin, 3-geranyloxyemodin anthrone, 3-prenyloxyemodin, 3-prenyloxyemodin anthrone (anthranoids), bibenzyls from *Bletilla striata* (bibenzyls), bergapten, imperatorin (**17**), heraclenol-2'-O-angelate (**18**), xanthotoxin (coumarins), diplacone (**30**), 6-geranyl-3,3',5,5',7-pentahydroxy-4'-methoxyflavane, 6-geranyl-3',5,5',7-tetrahydroxy-4'-methoxyflavane, 3'-O-methyldiplacol, 3'-O-methyldiplacone, 4'-O-methyldiplacol, 4'-O-methyldiplacone (**33**), mimulone (flavonoids), heyneanol A, vitisin A (polyphenols), cremaphenanthrene F and phenanthrenes from *Bletilla striata* (**37,38**) (phenanthrenes), amberin, amberbin A, (sesquiterpene lactones), leucisterol (steroids) and 3 β ,21 β ,29-trihydroxyserrat-14-en-3 β -yl p-dihydrocoumarate (triterpenoids). On the basis of the IC₅₀ value (μ M) for galanthamine (**1**) obtained in the study and presented in Table 1, the median for AChE was determined, and it was IC₅₀ = 0.94 μ M, and for BuChE, it was 8.70 μ M. It was assumed that galanthamine (**1**) exhibits strong inhibition of AChE and BuChE, and the potency of other inhibitors was compared to the value of the determined median. Those with IC₅₀ under 1.5 μ M were considered strong, those under 20 μ M were medium-strong, and those between 20 and 100 μ M

were weak for AChE. For BuChE, those with IC_{50} under $10 \mu\text{M}$ were considered strong, those between 10 and $50 \mu\text{M}$ were medium-strong, and those in the range of 50 – $150 \mu\text{M}$ were weak.

From the presented tabular comparison (Table 1) of the results of the conducted studies (values of IC_{50}), it follows that the compounds belonging to the alkaloid group exhibit the strongest activity against AChE and therefore are discussed in more detail. Fourteen of them have strong inhibitory activity with an IC_{50} value $< 1.5 \mu\text{M}$, and forty-two have medium-strong activity below $20 \mu\text{M}$ (Table 1).

The best AChE inhibition result in the entire table (Table 1) was obtained for sanguinine ($IC_{50} = 0.007 \mu\text{M}$). This was confirmed in another independent study in which the compound was derived from a different plant material ($IC_{50} = 0.10 \mu\text{M}$). Strong activity against AChE was also detected for five other Amaryllidaceae alkaloids ($IC_{50} = 0.16 \mu\text{M}$, $0.18 \mu\text{M}$, $0.19 \mu\text{M}$, $0.67 \mu\text{M}$, $0.99 \mu\text{M}$).

The different values of the inhibition coefficient obtained for sanguinine (**6**) are probably due to the use of various origins of AChE in the two studies. Similarly, for the same Amaryllidaceae alkaloids, e.g., lycoramine, inconsistent results were observed, with potent activity against *Electric eel* AChE and inactivity or weak activity using human AChE (isolated from *Narcissus jonquilla* ‘Pipit’ and *Narcissus poeticus* ‘Pink Parasol’).

Stronger and more potent AChE inhibitory activity than galanthamine (**1**) was obtained for five other isoquinoline alkaloids of the protoberberine type ($IC_{50} = 0.52 \mu\text{M}$, $0.53 \mu\text{M}$, $0.51 \mu\text{M}$, $0.74 \mu\text{M}$, $0.80 \mu\text{M}$) isolated from *Mahonia bealei* and *Mahonia fortunei*, as well as medium-strong activity for three *Mahonia* alkaloids ($IC_{50} = 5.07$ – $13.3 \mu\text{M}$).

Values of the IC_{50} inhibition coefficient of AChE below $1.5 \mu\text{M}$ were demonstrated by alkaloids derived from the sponge *Latrunculia biformis* (discorhabdin G) and an alkaloid from *Lycopodium*, huperzine C, with a slightly weaker result than the known activity of huperzine A.

Fourteen alkaloids from Ranunculaceae exhibit strong or medium-strong AChE inhibition values ($IC_{50} = 2.51$ – $12.1 \mu\text{M}$), including an isoquinoline alkaloid, dihydroberberine (**8**), with $IC_{50} = 1.18 \mu\text{M}$ (from *Coptis chinensis*), and diterpenoid alkaloids, including aconorine (from *Aconitum laeve*) and jadwarine-A (from *Delphinium denudatum*), with a potential stronger than the reference galanthamine (**1**) (Table 1).

Similar moieties that are crucial for the binding of the inhibitor to the enzyme are also present in other strong and medium-strong inhibitors from other groups of compounds present in Table 1.

Lipophilic substituents will have a stronger affinity for the hydrophobic AChE ester part; hence, they show stronger binding to the enzyme and greater inhibition, which is described in more detail in the chemistry–structure–activity section [1,43].

A BuChE inhibition study showed inhibitory activity for thirty-one alkaloids with inhibition coefficients ranging from 10 to $50 \mu\text{M}$ and strong activity for alkaloids with inhibition coefficients below $10 \mu\text{M}$. Alkaloids isolated from *Nauclea officinalis* ($IC_{50} = 1.03 \mu\text{M}$, $4.98 \mu\text{M}$, $7.70 \mu\text{M}$), including angustidine (**2**), have the lowest inhibition coefficients of all the alkaloids listed in Table 1.

The group of alkaloids is distinguished by a strong inhibitory effect on BuChE: alkaloids isolated from *Papaver somniferum* ($IC_{50} = 2.80 \mu\text{M}$, $7.1 \mu\text{M}$), including one about thirty times more potent than neostigmine; two alkaloids stronger than galanthamine (**1**) from *Aconitum laeve* ($IC_{50} = 8.72 \mu\text{M}$, $9.94 \mu\text{M}$) and deoxyvobtusine ($IC_{50} = 6.20 \mu\text{M}$) from *Voacanga globosa*; two alkaloids more potent than physostigmine, i.e., discorhabdin G ($IC_{50} = 7.00 \mu\text{M}$) from *Latrunculia bocagei* and 2-methoxyatherosperminine from *Cryptocarya griffithiana* ($IC_{50} = 3.95 \mu\text{M}$); and two alkaloids more potent than tacrine from *Uncaria rynchophylla* (Table 1).

From the coumarin group, coumarins isolated from *Mesua elegans* ($IC_{50} = 0.70 \mu\text{M}$, $1.06 \mu\text{M}$, $3.06 \mu\text{M}$) have the strongest ability to inhibit AChE. Four of them exhibit medium activity with an IC_{50} value $< 10 \mu\text{M}$. Their activity against BuChE has not been studied. However, other presented coumarins displayed in the results seem to show BuChE inhibition (bergapten, imperatorin (**17**) and xanthotoxin (Table 1)). The IC_{50} values of coumarins

isolated from *Archangelicae officinalis* and *Citrus hystrix* (Table 1) prove their activity against BuChE (IC₅₀ from 7.5 to 23 µM) as well.

From all of the presented flavonoids, linarin from *Buddleja davidii* requires the minimal inhibitory quantity (10 ng) to inhibit AChE. Diplacone (30) and quercetin-3-O-neohesperidoside demonstrate the strongest activity against AChE, as determined by their IC₅₀ values (IC₅₀ = 7.2 µM, 6.98 µM). Medium-strong inhibitor values are reported for quercetin and tiliroside from *Agrimonia pilosa* and five flavonoids from *Prunus padus* var. *seoulensis* (IC₅₀ between 15.49 and 21.53 µM) (Table 1). Flavonoids isolated from *Paulownia tomentosa* show relatively medium or weak activity against AChE (values of IC₅₀ between 7.2 µM and 109.2 µM) and significant activity against BuChE (the strongest compounds demonstrated IC₅₀ = 1.4 µM, 3.8 µM). Garcineflavonol A (IC₅₀ = 14.50 µM) showed medium-strong activity against BuChE. Lanostane triterpenes from *Ganoderma lucidum* showed medium activity against AChE, ranging from 9.40 µM to 31.03 µM, and n-butyl ganoderate H reached a value of IC₅₀ = 9.40 µM. However, most of the results against BuChE are IC₅₀ > 200 µM, which may indicate the selective activity of these compounds on AChE. Conversely, cremaphenanthrene F (phenanthrenes) from *Cremastra appendiculata* shows more potent inhibition against BuChE vs. AChE. Two lignans from *Camelia sinensis* var. *sinensis* 'Huangjinya' revealed strong AChE inhibition, which was higher or slightly weaker than huperzine (Table 1). Strong activity against BuChE and medium-strong activity against AChE were achieved for another lignan: macelignan from *Myristica fragrans*. The phlorotannin compound 974-B reached satisfactory results for both cholinesterases (for AChE IC₅₀ = 1.95 µM and for BuChE IC₅₀ = 3.26 µM).

Similarly, phthalates from *Lonicera quinquelocularis* had IC₅₀ = 1.65 µM and 3.43 µM for AChE and IC₅₀ < 10 µM for BuChE. Among diterpenes, dihydrotanshinon I and cryptotanshinone (40) showed strong inhibition against AChE, and triptexanthoside C (45) (xanthones) showed significant inhibition. Xanthonoids from *Garcinia mangostana* had IC₅₀ on AChE from 2.5 µM, with six compounds having IC₅₀ < 20 µM, and IC₅₀ on BuChE from 0.7 µM, with six compounds having IC₅₀ < 12 µM. Anthranoids from *Psorospermum glaberrimum* demonstrated medium-strong activity toward BuChE (9.25–13.30 µM) and weak activity toward AChE. A fatty acid from *Lycopodiella cernua* has shown high inhibition of AChE (0.22 µM). Remarkable results are also shown by polyphenols from *Camellia sinensis* var. *assamica* (caffeoylated catechin) against AChE, as well as by polyphenols from *Vitis amurensis* (heyneanol A, vitsin A), which had strong activity against AChE and BuChE. Medium-strong inhibition of AChE by creoside IV from *Codonopsis pilosula* and strong inhibition against BuChE by brousosin A (*Anemarrhena asphodeloides*) were found. High inhibition values against AChE and BuChE were also observed for sesquiterpene lactones from *Amberboa ramosa* (amberin, amberbin A and amberbin B). Sterols (leucisterol, haloxylon A and haloxylon B) from *Haloxylon recurvum* have shown strong inhibition of both BuChE and AChE. A strong inhibition value against AChE and medium inhibition against BuChE were shown by chromones from *Sargassum siliquastrum* and one of the diarylheptanoids: (–)-alpininoid B (23) (Table 1). Terpenoids demonstrated strong (*Lycopodiella cernua*) or medium-strong (*Lycopodiella cernua* or *Garcinia hombroniana*) activity against AChE and BuChE. All results are presented in Table 1.

4. Analysis Methods

The studied compounds occur in materials of natural origin in the form of mixtures. To determine the change in enzyme activity due to a particular compound, it is necessary to purify samples or even fractionate them. Studies of inhibitory activity toward cholinesterases in scientific reports are performed according to different methods and procedures. Nevertheless, in most cases, analyses are based on Ellman's assay [48]. A summary of analysis methods used in the selected studies of cholinesterase inhibition is presented in Table 1. The description of the most important one is presented below.

The method should be simple, quick to perform, sensitive and inexpensive [77,137]. The analysis methods are based on a colorimetric assay using chromatographic techniques, TLC and fluorimetric and spectrophotometric measurements.

These methods are based on measuring changes in parameters indicative of enzyme activity before and after the introduction of the inhibitor to the system. Even slight changes in temperature, incubation time, pH, the concentration of substrates and the enzyme and the presence of other interfering compounds (detergents and heavy metal ions) can affect the accuracy of the results.

4.1. The Colorimetric Method of Ellman (1961)

This procedure is based on the result of the color reaction between the formed prethiocholine and the DTNB color developer (5,5'-dithiobis-(2-nitrobenzoic acid). Thiocholine is the product of the enzymatic reaction between acetylthiocholine (ATCI) and ChE. The intensity of the color of the product measured colorimetrically allows the determination of changes in enzyme activity. In the presence of an inhibitor, the change is suppressed, and we observe a lower-intensity color or complete inhibition [48].

Ellman's method, among others, was applied to study the inhibitory activity of hexane extracts of the roots of *Archangelicae officinalis* L. against AChE and BuChE using physostigmine as a standard and the following conditions: AChE (0.45 U mL^{-1}) in Tris-HCl buffer (pH 7.8); incubation of the enzyme at $4 \text{ }^\circ\text{C}$ for $t = 30 \text{ min}$; and incubation of the reaction mixture at $37 \text{ }^\circ\text{C}$ for 20 min, followed by measurements using an ELISA microplate reader ($\lambda = 412 \text{ nm}$). A weak result of inhibition was achieved for AChE (Angelica root hexane extract ($\text{IC}_{50} \text{ AChE} = 315 \pm 20 \text{ } (\mu\text{g mL}^{-1})$) and fruit hexane extract ($\text{IC}_{50} \text{ AChE} = 73 \pm 7 \text{ } (\mu\text{g mL}^{-1})$), but much higher inhibition was observed with regard to the BuChE root extract ($\text{IC}_{50} \text{ BuChE} = 16 \pm 5 \text{ } (\mu\text{g mL}^{-1})$) and fruit hexane extract ($\text{IC}_{50} \text{ BuChE} = 9 \pm 2 \text{ } (\mu\text{g mL}^{-1})$) [28].

4.2. Spectrophotometric Modification of Ellman's Method

Ding et al. (2013) described a modification used to determine the inhibitory activity of flavonoids and ginkgolides B and C from the leaves of *Ginkgo biloba* against AChE and BuChE [111]. Only flavonoids inhibit AChE (results in Table 1). In the method of Park and Choi (1991), the supernatant from the brown planthopper maggot was prepared (which contains ChE) [110]; the homogenized supernatant ($T = 4 \text{ }^\circ\text{C}$, $t = 30 \text{ min}$.) was prepared in phosphate buffer (pH = 7.0) and 0.1 % Triton X-100. Acetone solutions of the analyzed compounds and standard (chlorpyrifos) were mixed with the previously prepared solution containing the supernatant and analyzed in a 96-well microtiter plate after 1h. DTNB and ATCI were added. Then, the measurement of absorbance was performed ($\lambda = 405 \text{ nm}$ microplate reader). The activity is relative to the control reaction, assumed as 100 %, and to the test compounds replaced by the buffer. On the basis of the results, the IC_{50} was determined [110].

The spectrophotometric modification of Ellman's method described by Senol et al. (2010) was used to verify the inhibition of the methanol extract and isolated compounds (imperatorin (17), xanthotoxin and bergapten) from the fruits of *Angelica officinalis* L. [99]. The inhibition of both cholinesterases was tested using an ELISA microplate reader; galanthamine (1) as a standard; AChE from electric eel; and BuChE from horse serum. The potent inhibition of BuChE was observed for both the extract ($100 \text{ } \mu\text{g/mL}$ — $85.65 \pm 1.49\%$) and each of the compounds (Table 1) [100]. Many of the compounds were tested by using various modifications of the spectrophotometric method; they differed in the incubation time, the equipment used, the concentration of reactants and the wavelength measurement. The inhibitors belong to different groups of compounds (Table 1).

Cholinesterase inhibitory activity was also identified by using a TLC technique. By comparing the methods performed using the microplate and TLC, as described in Rhee et al. (2001), it can be assumed that TLC methods are more sensitive [16]. Due to the advantages of the TLC approach (simple, inexpensive and accurate measurement), this review focuses on methods using this technique.

4.3. TLC Modification of Ellman's Method

The modification of Ellman's method has been described by Rhee et al. (2001) [16,48]. As a result of the disruption of ATCI by AChE, choline is formed, which constitutes a colored compound (5-thio-2-nitrobenzoate anion) with DTNB. The color intensity of the product is measured spectrophotometrically. The bands of the tested extract are developed on the TLC plate, and the band pattern is sprayed with a mixture of DTNB and then ATCI in Tris-HCl buffer (Trizma hydrochloride with bovine serum, pH = 8); the AChE enzyme is then applied (3 U mL⁻¹; from electric eel). This results in a yellow background due to a diazo compound (5 min) with white trails, which indicates inhibition by the extract. The disadvantage of the method is the possibility of false-positive effects [16].

The modified method of Rhee et al. (2001) was used, inter alia, to evaluate the obtained compound (mahanimbine) and petroleum ether extract (10 mg mL⁻¹) from *Murraya koenigii*. The plates were developed with a mobile phase (petroleum ether: CHCl₃, 50: 50 (v/v)) and, after drying, were sprayed with DTNB/ATCI, followed by the implementation of the basic method. The enzyme activity was measured using a 96-well microplate reader [16,48,76]. The procedure described by Rhee et al. (2001) was also used to investigate the inhibitory activity against ChE by the extract and compounds (10-hydroxy-infractopicrin and infractopicrin) isolated from the toadstool *Cortinarius infractus*. For the measurement, the following compounds were used: AChE from bovine erythrocytes or equine serum BuChE and tacrine, physostigmine and galanthamine (1) as standards (>100 µM). The results were determined using a 96-well microplate reader [61].

4.4. TLC Bioautography by Marston

A properly made plate with applied spots of extracts was sprayed with a prepared mixture with the enzyme AChE or BuChE (T = 4 °C in Tris-hydrochloric acid, pH = 7.8, with bovine serum albumin as a stabilizer) and incubated (T = 37 °C, 20 min; increased humidity).

Then, in order to carry out the detection, a mixture containing, inter alia, Fast Blue Salt and alpha-naphthyl acetate prepared ex tempore was sprayed. After incubation (1–2 min.), a purple background due to the diazonium dye was obtained, while white spots indicated inhibition caused by the applied sample. The clear differences in the background color and band color indicate inhibition [101].

4.5. TLC Bioautography by Mroczek

A TLC plate with spots of the tested extracts (appropriately prepared) and the standard (galanthamine (1)) was developed with an adequate mobile phase (here, CHCl₃/MeOH/25 % NH₄OH 8:1:1 v/v/v) containing 2-naphthyl acetate. After developing and thoroughly drying (10 min), the plate was sprayed with the prepared mixture containing AChE (3 U mL⁻¹) in TRIS buffer (pH 7.8) and incubated (increased humidity, T = 37 °C).

Then, it was sprayed with a solution of Fast Blue B salt. White spots demonstrating inhibition were clearly visible on the dark purple background due to the azo compound and appeared quickly (1 min), and they were very persistent (for 24 h). The advantage of this method is the decreased usage of the enzyme and the shortened time required for its incubation (10 min) compared to other methods. The method is highly sensitive and fast [77].

This validation method was performed by the author for the determination of the inhibition of Amaryllidaceae AChE isolated from extracts from *Narcissus jonquilla* 'Pipit' and *Narcissus jonquilla* 'Havera' and purified extracts of *N. jonquilla* 'Baby Moon', *Crinum moorei* and *Scadoxus puniceus*. This procedure manages to achieve high sensitivity. The inhibitory activity of the isolated alkaloid was demonstrated, and it was indicated that dihydro-galanthamine has greater inhibition, approximately 42% higher than galanthamine (1) [77]. With the application of this method, the activity of alkaloids present in the extract from *Argemone mexicana* L. roots was proved; it was weak for magnoflorine and strong for berberine (7), palmatine and galanthamine (1), isolated for the first time from the Papaveraceae family [138]. Additionally, a two-dimensional thin-layer chromatography/high-

performance liquid chromatography/electrospray ionization time-of-flight mass spectrometry (TLC/HPLC/DAD/MS) system has been developed for both qualitative and quantitative analyses of active AChE inhibitors in plant samples [139]. The method of bioautography by Mroczek confirmed the inhibition of AChE by Amaryllidaceae alkaloids and determined their numerous occurrences in three cultivars of *Narcissus*: *N. jonquilla* 'Baby Moon', *N. 'Golden Ducat'* and *N. 'Cheerfulness'*; the alkaloids were and identified both by using a TLC plate assay and by using TLC/HPLC/DAD/MS [140]. These methods have also been used to demonstrate AChE inhibitory activity and to qualitatively evaluate Lycopodiaceae alkaloids, and they were successfully used to study neuroprotective polyphenols from two species of *Trifolium* as well [141,142].

4.6. Fluorimetric Methods

These are fluorescent techniques (quenching) that measure enzyme–inhibitor binding affinities. This type of pathway has been chosen to demonstrate the activity of flavonoids from *Paulownia tomentosa* fruits with minor modifications to the spectrophotometric method of Ellman (1961). As a reference standard, physostigmine (eserine) was used (Table 1). In addition, using the fluorescence assay method (decrease), the affinity of the compounds with the relevant enzyme was studied.

The results were based on the dependency of the constant affinity rate, proportional to the inhibitory activity. Spectrophotometer measurements of the fluorescence emission were taken with a camera (M Series Multi-Mode Microplate Readers) ($T = 18^\circ$ and 37°C) as the solution was titrated with a predetermined amount of a solution of hAChE (phosphate buffer (pH 8.0) (5 U mL^{-1})) with successive amounts of the tested flavonoids added. Studies have shown that the presence of a geranyl substituent at the C6 position in the structure of flavonoids is important for their ability to inhibit AChE [34].

The fluorimetric method was a part of the analysis of the *Mangosteen* seedcase extract outlined below [136]. To measure the compounds, the following steps were performed: the supernatant was centrifuged (12,000 rpm, 10 min.), a mixture with a buffer solution of ChE ($5\ \mu\text{L}$) was added to the extract solution ($20\ \mu\text{L}$), and the extract (CHCl_3 in MeOH) was incubated ($T = 37^\circ\text{C}$, $t = 30\text{ min.}$). The supernatant ($2\ \mu\text{L}$) was analyzed using ultra-performance liquid chromatography coupled with a photo-diode array detector and quadrupole time-of-flight mass spectrometry (UPLC/PDA/QTOF/MS), and the result was compared with that of the analysis without the enzyme. In the chromatogram, the peaks of mangostanol, allanxanthone E, gudraxanthone, γ -mangostin, 8-deoxygartanin and α -mangostin vanished (results in Table 1), so those compounds show an affinity for the enzyme. Then, the inhibitory activity of both cholinesterases was measured using a modification of Ellman's method (Table 1). Using a fluorescence technique (quenching), affinity toward AChE was compared with γ -mangostin (Table 1) and 9-hydroxycalabaxanthone ($\text{IC}_{50} > 100\ \mu\text{M}$). The first compound gained a much higher score. The authors supposed that the significant inhibition of AChE can respond to the presence of more than one prenyl group [136].

The methods presented in this review for determining cholinesterase inhibition by the investigated compounds can be described as qualitative and quantitative ones. Those based on the TLC technique (TLC bioautography) are more suitable for demonstrating inhibition by particular compounds (qualitative), and they are more sensitive compared to spectrophotometric methods (modifications of Ellman's method). Nevertheless, they are not suitable for the determination of the inhibition coefficient, or it is difficult to measure. Therefore, they do not offer the possibility to compare the potency of inhibition among inhibitors. Both of these advantages are realized by methods based on a combination of the TLC technique (TLC bioautography) with more advanced techniques, such as HPLC/DAD/MS (high performance liquid chromatography with photodiode array mass spectrometry), as mentioned in this article. Their use is increasingly observed in newer publications on cholinesterase inhibitors.

5. Conclusions

Reviewing the available publications, it can be concluded that methods for investigating cholinesterase inhibition have been mostly based on known procedures. These are generally modifications of previously used methods. They differ in parameters, which could affect the result of the activity of the enzyme and substrate, the incubation time, the method of analysis, the order of the addition of reactants and the type of assay.

It is important to study pure plant materials from respectively tested sources (heavy metal ions and detergents) and adequately purify the sample. The results (IC_{50}) of the same compound when determined relative to hAChE and eeAChE can differ [136]. In some of the publications, the type of cholinesterase used in the study is not described or this information is difficult to obtain.

It is only possible to compare the IC_{50} values of specific compounds when determined under relatively similar conditions, using the same methods and compared to the same reference compound, thereby concluding potency. In most cases, one method is used, and results are rarely confirmed by using another method. An increased number of studies examining the inhibitory effects on both cholinesterases would be advantageous. It is beneficial to enhance the awareness and understanding of the subject of IChEs and activity measurement methods. Some of the studies did not include designations of activity toward both cholinesterases. It would be useful to use several reference substances in one study, which would allow for a better comparison of the available inhibition results.

However, more recent studies include the determination of the inhibition of both cholinesterases by the studied compounds and also attempt to analyze the structure and enzyme–inhibitor interaction, which is highly beneficial. This review reveals that inhibitors more potent than galanthamine (1), acting against both cholinesterases, are still being discovered. At the same time, compounds exhibiting potent selective activity against one of the cholinesterases have emerged. According to the established criteria in the study, strong activity against AChE was shown by 27 compounds, medium-strong was shown by 93 compounds, and weak activity was shown by 77 compounds, while against BuChE, strong, medium-strong and weak activity was shown by 43, 68 and 22 inhibitors, respectively. The largest group of compounds with a strong effect on both AChE and BuChE, as shown by the tabular comparison, were alkaloids. Compounds from this group demonstrated the most potent inhibition of AChE. Especially strong inhibition results against both cholinesterases were demonstrated for alkaloids from the Amaryllidaceae and Papaveraceae families. The most potent BuChE inhibition was demonstrated by compounds from various groups: alkaloids, coumarins, flavonoids, phenylpropanoids, polyphenols, phenanthrenes, phthalates, sterols and steroids, triterpenoids, xanthonoids and also lignans or phlorotannins. The presented review, as well as a summary of the results of the inhibitors' structure analysis, may be beneficial in the determination and planning of further stages of research for the presented compounds. These data may also be helpful in the search and synthesis of new semi-synthetic or synthetic derivatives, as well as new biologically active substances.

Work on finding compound derivatives with more specific, preferable features that we find in plant materials has yielded positive results. The ability to modify them allows for even better parameters of the drug, such as greater activity, a better match to the receptor, mitigated side effects, a longer duration of action or a favorable method of production. The integration of phytochemistry and cooperative disciplines of molecular modeling and chemical synthesis provides an opportunity to find effective drugs. The studies conducted continuously demonstrate that compounds of natural origin are still abundant and carry a lot of possible solutions.

The observed persistent deficiency of effective therapies for neurological diseases, including AD, requires researchers to further search for new therapeutic substances. The presented review, conducted for the period from 2008 to 2022 years, shows that the search for and analysis of natural cholinesterase inhibitors have not been exhausted yet. After summarizing *in vitro* studies, the conclusion emerges that the potential for the use of

cholinesterase inhibitors in therapeutics has not been fully explored. Only some of them have been tested in vivo, and for several of them, clinical studies have been attempted. The results presented in this publication indicate that natural sources are a huge reservoir in the search for new therapeutic substances, including cholinesterase inhibitors.

Author Contributions: N.S.-W.: writing—original draft preparation, conceptualization and data curation; T.M.: writing—review and editing, conceptualization and supervision. All authors have read and agreed to the published version of the manuscript.

Funding: This research received no external funding.

Institutional Review Board Statement: Not applicable.

Informed Consent Statement: Not applicable.

Data Availability Statement: Not applicable.

Acknowledgments: The authors thank Patrycja Nawratowicz for help in translating the review into English.

Conflicts of Interest: The authors declare no conflict of interest.

Abbreviations

ACh	Acetylcholine
AChE	Acetylcholinesterase
AD	Alzheimer’s disease
ATCI	Acetylthiocholine
BuChE	Butyrylcholinesterase
ChE	Cholinesterase
DTNB	5,5'-Dithiobis-(2-nitrobenzoic acid)
eeAChE	Electrophors electricus acetylcholinesterase
e.g., (lat. exempli gratia)	For example
hAChE	Human erythrocyte acetylcholinesterase
IBuChE	Inhibitor of butyrylcholinesterase
IC ₅₀	Inhibitory concentration for which enzyme activity is equal to half-maximal
IChE	Inhibitor of cholinesterases
SAR	Structure–activity relationship
TLC/HPLC/DAD/MS	Thin-layer chromatography/high-performance liquid chromatography/electrospray ionization time-of-flight mass spectrometry
Tris-HCl	Trizma hydrochloride with bovine serum
UPLC-PDA-QTOF-MS	Ultra-performance liquid chromatography coupled with photo-diode array detector and quadrupole time-of-flight mass spectrometry
vs.	Versus

References

- Bukowska, B.; Pieniazek, D.; Hutnik, K.; Duda, W. Acetyl- and Butyrylcholinesterase—Structure, Functions and Their Inhibitors. *Curr. Top. Biophys.* **2007**, *30*, 11–23.
- Widy-Tyszkiewicz, E. Leki Układu Cholinergicznego. I. Leki Cholinomimetyczne. In *Farmakologia. Podstawy Farmakoterapii. Podręcznik dla Studentów Medycyny i Lekarzy*; Kostowski, W., Herman, Z., Eds.; Wydawnictwo Lekarskie PZWL: Warszawa, Poland, 2013; Volume 1, pp. 401–414.
- Bullock, R.; Lane, R. Executive dyscontrol in dementia, with emphasis on subcortical pathology and the role of butyrylcholinesterase. *Curr. Alzheimer Res.* **2007**, *4*, 277–293. [CrossRef] [PubMed]
- Rolinski, M.; Fox, C.; Maidment, I.; McShane, R. Cholinesterase inhibitors for dementia with Lewy bodies, Parkinson’s disease dementia and cognitive impairment in Parkinson’s disease. *Cochrane Database Syst. Rev.* **2012**, *3*, CD006504. [CrossRef] [PubMed]
- Vetulani, J. Leki Nootropowe i Prokognitywne. Farmakoterapia Choroby Alzheimerera. In *Farmakologia. Podstawy Farmakoterapii. Podręcznik dla Studentów Medycyny i Lekarzy*; Kostowski, W., Herman, Z., Eds.; Wydawnictwo Lekarskie PZWL: Warszawa, Poland, 2013; Volume 2, pp. 154–169.
- Sugimoto, H.; Yamanishi, Y.; Iimura, Y.; Kawakami, Y. Donepezil Hydrochloride (E2020) and Other Acetylcholinesterase Inhibitors. *Curr. Med. Chem.* **2000**, *7*, 303–339. [CrossRef]
- Research, C. *For D.E. and FDA’s Decision to Approve New Treatment for Alzheimer’s Disease*; FDA: Silver Spring, MD, USA, 2021.

8. Wright, C.I.; Geula, C.; Mesulam, M.-M. Neuroglial cholinesterases in the normal brain and in Alzheimer's disease: Relationship to plaques, tangles, and patterns of selective vulnerability. *Ann. Neurol.* **1993**, *34*, 373–384. [CrossRef]
9. Perry, E.K.; Perry, R.H.; Blessed, G.; Tomlinson, B.E. Changes in brain cholinesterases in senile dementia of alzheimer type. *Neuropathol. Appl. Neurobiol.* **1978**, *4*, 273–277. [CrossRef] [PubMed]
10. Pepeu, G.; Giovannini, M.G.; Bracco, L. Effect of cholinesterase inhibitors on attention. *Chem. Biol. Interact.* **2013**, *203*, 361–364. [CrossRef]
11. Little, J.T.; Walsh, S.; Aisen, P.S. An update on huperzine A as a treatment for Alzheimer's disease. *Expert Opin. Investig. Drugs* **2008**, *17*, 209–215. [CrossRef]
12. Macdonald, I.R.; Rockwood, K.; Martin, E.; Darvesh, S. Cholinesterase Inhibition in Alzheimer's Disease: Is Specificity the Answer? *J. Alzheimer's Dis.* **2014**, *42*, 379–384. [CrossRef]
13. Pinho, B.R.; Ferreres, F.; Valentão, P.; Andrade, P.B. Nature as a source of metabolites with cholinesterase-inhibitory activity: An approach to Alzheimer's disease treatment. *J. Pharm. Pharmacol.* **2013**, *65*, 1681–1700. [CrossRef]
14. Matławska, I.; Byłka, W.; Gawron-Gzella, A.; Sikorska, M.; Szauffer-Hajdrych, M.; Wojcińska, M.; Dudek-Makuch, M.; Witkowska-Banaszczak, E. *Farmakognozja. Podręcznik dla Studentów Farmacji*, 3rd ed.; Wydawnictwo Naukowe Uniwersytetu Medycznego im; Karola Marcinkowskiego w Poznaniu: Warszawa, Poland, 2008; ISBN 978-83-7597-004-3.
15. Berkov, S.; Ivanov, I.; Georgiev, V.; Codina, C.; Pavlov, A. Galanthamine biosynthesis in plant in vitro systems. *Eng. Life Sci.* **2014**, *14*, 643–650. [CrossRef]
16. Rhee, I.K.; van de Meent, M.; Ingkaninan, K.; Verpoorte, R. Screening for acetylcholinesterase inhibitors from Amaryllidaceae using silica gel thin-layer chromatography in combination with bioactivity staining. *J. Chromatogr. A* **2001**, *915*, 217–223. [CrossRef]
17. Gulcan, H.O.; Orhan, I.E.; Sener, B. Chemical and Molecular Aspects on Interactions of Galanthamine and Its Derivatives with Cholinesterases. *Curr. Pharm. Biotechnol.* **2015**, *16*, 252–258. [CrossRef]
18. McNulty, J.; Nair, J.J.; Little, J.R.; Brennan, J.D.; Bastida, J. Structure–activity studies on acetylcholinesterase inhibition in the lycorine series of Amaryllidaceae alkaloids. *Bioorg. Med. Chem. Lett.* **2010**, *20*, 5290–5294. [CrossRef] [PubMed]
19. Liew, S.Y.; Khaw, K.Y.; Murugaiyah, V.; Looi, C.Y.; Wong, Y.L.; Mustafa, M.R.; Litaudon, M.; Awang, K. Natural indole butyrylcholinesterase inhibitors from *Nauclea officinalis*. *Phytomedicine* **2015**, *22*, 45–48. [CrossRef] [PubMed]
20. Berkov, S.; Codina, C.; Viladomat, F.; Bastida, J. N-Alkylated galanthamine derivatives: Potent acetylcholinesterase inhibitors from *Leucojum aestivum*. *Bioorg. Med. Chem. Lett.* **2008**, *18*, 2263–2266. [CrossRef] [PubMed]
21. Sarikaya, B.B.; Kaya, G.I.; Onur, M.A.; Bastida, J.; Somer, N.U. Phytochemical investigation of *Galanthus woronowii*. *Biochem. Syst. Ecol.* **2013**, *51*, 276–279. [CrossRef]
22. Ortiz, J.E.; Garro, A.; Pigni, N.B.; Agüero, M.B.; Roitman, G.; Slanis, A.; Enriz, R.D.; Feresin, G.E.; Bastida, J.; Tapia, A. Cholinesterase-inhibitory effect and in silico analysis of alkaloids from bulbs of Hieronymiella species. *Phytomedicine* **2017**, *39*, 66–74. [CrossRef]
23. Song, H.-P.; Zhang, H.; Hu, R.; Xiao, H.-H.; Guo, H.; Yuan, W.-H.; Han, X.-T.; Xu, X.-Y.; Zhang, X.; Ding, Z.-X.; et al. A strategy to discover lead chemome from traditional Chinese medicines based on natural chromatogram-effect correlation (NCEC) and natural structure-effect correlation (NSEC): *Mahonia bealei* and *Mahonia fortunei* as a case study. *J. Chromatogr. B* **2021**, *1181*, 122922. [CrossRef]
24. Hirasawa, Y.; Kato, E.; Kobayashi, J.; Kawahara, N.; Goda, Y.; Shiro, M.; Morita, H. Lycoparins A–C, new alkaloids from *Lycopodium casuarinoides* inhibiting acetylcholinesterase. *Bioorg. Med. Chem.* **2008**, *16*, 6167–6171. [CrossRef]
25. Zhan, Z.-J.; Yu, Q.; Wang, Z.-L.; Shan, W.-G. Indole alkaloids from *Ervatamia hainanensis* with potent acetylcholinesterase inhibition activities. *Bioorg. Med. Chem. Lett.* **2010**, *20*, 6185–6187. [CrossRef] [PubMed]
26. Skalicka-Woźniak, K.; Orhan, I.E.; Cordell, G.A.; Nabavi, S.M.; Budzyńska, B. Implication of coumarins towards central nervous system disorders. *Pharmacol. Res.* **2016**, *103*, 188–203. [CrossRef] [PubMed]
27. Youkwon, J.; Sutthivaiyakit, S.; Sutthivaiyakit, P. Citrusosides A–D and Furanocoumarins with Cholinesterase Inhibitory Activity from the Fruit Peels of *Citrus hystrix*. *J. Nat. Prod.* **2010**, *73*, 1879–1883. [CrossRef] [PubMed]
28. Wszelaki, N.; Paradowska, K.; Jamróz, M.K.; Granica, S.; Kiss, A.K. Bioactivity-Guided Fractionation for the Butyrylcholinesterase Inhibitory Activity of Furanocoumarins from *Angelica archangelica* L. Roots and Fruits. *J. Agric. Food Chem.* **2011**, *59*, 9186–9193. [CrossRef] [PubMed]
29. Awang, K.; Chan, G.; Litaudon, M.; Ismail, N.H.; Martin, M.-T.; Gueritte, F. 4-Phenylcoumarins from *Mesua elegans* with acetylcholinesterase inhibitory activity. *Bioorg. Med. Chem.* **2010**, *18*, 7873–7877. [CrossRef] [PubMed]
30. Lv, H.; She, G. Naturally Occurring Diarylheptanoids—A Supplementary Version. *Rec. Nat. Prod.* **2012**, *13*, 321–333.
31. Lee, J.S.; Kim, J.H.; Han, Y.K.; Ma, J.Y.; Kim, Y.H.; Li, W.; Yang, S.Y. Cholinesterases inhibition studies of biological active compounds from the rhizomes of *Alpinia officinarum* Hance and in silico molecular dynamics. *Int. J. Biol. Macromol.* **2018**, *120*, 2442–2447. [CrossRef]
32. Xie, Y.; Yang, W.; Chen, X.; Xiao, J. Inhibition of flavonoids on acetylcholine esterase: Binding and structure–activity relationship. *Food Funct.* **2014**, *5*, 2582–2589. [CrossRef]
33. Ryu, H.W.; Curtis-Long, M.J.; Jung, S.; Jeong, I.Y.; Kim, D.S.; Kang, K.Y.; Park, K.H. Anticholinesterase potential of flavonols from paper mulberry (*Broussonetia papyrifera*) and their kinetic studies. *Food Chem.* **2012**, *132*, 1244–1250. [CrossRef]
34. Cho, J.K.; Ryu, Y.B.; Curtis-Long, M.J.; Ryu, H.W.; Yuk, H.J.; Kim, D.W.; Kim, H.J.; Lee, W.S.; Park, K.H. Cholinestrase inhibitory effects of geranylated flavonoids from *Paulownia tomentosa* fruits. *Bioorg. Med. Chem.* **2012**, *20*, 2595–2602. [CrossRef]
35. Katalinić, M.; Rusak, G.; Barović, J.D.; Šinko, G.; Jelić, D.; Antolović, R.; Kovarik, Z. Structural aspects of flavonoids as inhibitors of human butyrylcholinesterase. *Eur. J. Med. Chem.* **2010**, *45*, 186–192. [CrossRef] [PubMed]

36. Kovács, A.; Vasas, A.; Hohmann, J. Natural phenanthrenes and their biological activity. *Phytochemistry* **2008**, *69*, 1084–1110. [CrossRef] [PubMed]
37. Liu, Y.; Tu, Y.; Kang, Y.; Zhu, C.; Wu, C.; Chen, G.; Liu, Z.; Li, Y. Biological evaluation, molecular modeling and dynamics simulation of phenanthrenes isolated from *Bletilla striata* as butyrylcholinesterase inhibitors. *Sci. Rep.* **2022**, *12*, 13649. [CrossRef] [PubMed]
38. Ren, Y.; Houghton, P.J.; Hider, R.C.; Howes, M.-J.R. Novel Diterpenoid Acetylcholinesterase Inhibitors from *Salvia miltiorhiza*. *Planta Med.* **2004**, *70*, 201–204. [CrossRef]
39. Zhou, Y.; Li, W.; Xu, L.; Chen, L. In *Salvia miltiorrhiza*, phenolic acids possess protective properties against amyloid β -induced cytotoxicity, and tanshinones act as acetylcholinesterase inhibitors. *Environ. Toxicol. Pharmacol.* **2011**, *31*, 443–452. [CrossRef]
40. Raut, N.A.; Dhore, P.W.; Saoji, S.D.; Kokare, D.M. Chapter 9—Selected Bioactive Natural Products for Diabetes Mellitus. In *Studies in Natural Products Chemistry*; Atta-ur-Rahman, Ed.; Elsevier: Amsterdam, The Netherlands, 2016; Volume 48, pp. 287–322.
41. Urbain, A.; Marston, A.; Queiroz, E.F.; Ndjoko, K.; Hostettmann, K. Xanthones from *Gentiana campestris* as New Acetylcholinesterase Inhibitors. *Planta Med.* **2004**, *70*, 1011–1014. [CrossRef]
42. Urbain, A.; Marston, A.; Grilo, L.S.; Bravo, J.; Purev, O.; Purevsuren, B.; Batsuren, D.; Reist, M.; Carrupt, P.-A.; Hostettmann, K. Xanthones from *Gentianella amarella* ssp. *acuta* with Acetylcholinesterase and Monoamine Oxidase Inhibitory Activities. *J. Nat. Prod.* **2008**, *71*, 895–897. [CrossRef]
43. Fink, K.; Boratyński, J. Oddziaływania Niekowalencyjne Kation- π —Ich Rola w Przyrodzie. *Postepy Hig. Med. Dosw.* **2014**, *68*, 1276–1286. [CrossRef]
44. Liu, L.; Yin, Q.-M.; Gao, Q.; Li, J.; Jiang, Y.; Tu, P.-F. New biphenanthrenes with butyrylcholinesterase inhibitory activity from *Crematstra appendiculata*. *Nat. Prod. Res.* **2019**, *35*, 750–756. [CrossRef]
45. Ahmed, S.; Khan, S.T.; Zargaham, M.K.; Khan, A.U.; Khan, S.; Hussain, A.; Uddin, J.; Khan, A.; Al-Harrasi, A. Potential therapeutic natural products against Alzheimer’s disease with Reference of Acetylcholinesterase. *Biomed. Pharmacother.* **2021**, *139*, 111609. [CrossRef]
46. Santos, T.C.; dos Gomes, T.M.; Pinto, B.A.S.; Camara, A.L.; de Paes, A.M.A. Naturally Occurring Acetylcholinesterase Inhibitors and Their Potential Use for Alzheimer’s Disease Therapy. *Front. Pharmacol.* **2018**, *9*, 1192. [CrossRef] [PubMed]
47. Shah, A.A.; Dar, T.A.; Dar, P.A.; Ganie, S.A.; Kamal, M.A. A Current Perspective on the Inhibition of Cholinesterase by Natural and Synthetic Inhibitors. *Curr. Drug Metab.* **2017**, *18*, 96–111. [CrossRef] [PubMed]
48. Ellman, G.L.; Courtney, K.D.; Andres, V., Jr.; Featherstone, R.M. A new and rapid colorimetric determination of acetylcholinesterase activity. *Biochem. Pharmacol.* **1961**, *7*, 88–95. [CrossRef] [PubMed]
49. Senol, F.S.; Orhan, I.E.; Ustun, O. In vitro cholinesterase inhibitory and antioxidant effect of selected coniferous tree species. *Asian Pac. J. Trop. Med.* **2015**, *8*, 269–275. [CrossRef] [PubMed]
50. Mesquita, R.D.S.; Kyrylchuk, A.; Cherednichenko, A.; Sá, I.S.C.; Bastos, L.M.; da Silva, F.M.A.; Nunomura, R.D.C.S.; Grafov, A. In Vitro and In Silico Evaluation of Cholinesterase Inhibition by Alkaloids Obtained from Branches of *Abuta panurensis* Eichler. *Molecules* **2022**, *27*, 3138. [CrossRef] [PubMed]
51. Rocha, J.B.; Emanuelli, T.; Pereira, M.E. Effects of Early Undernutrition on Kinetic Parameters of Brain Acetylcholinesterase from Adult Rats. *Acta Neurobiol. Exp.* **1993**, *53*, 431–437.
52. Ahmad, H.; Ahmad, S.; Shah, S.A.A.; Khan, H.U.; Khan, F.A.; Ali, M.; Latif, A.; Shaheen, F.; Ahmad, M. Selective dual cholinesterase inhibitors from *Aconitum laeve*. *J. Asian Nat. Prod. Res.* **2017**, *20*, 172–181. [CrossRef]
53. Badaoui, M.I.; Magid, A.A.; Benkhaled, M.; Bensouici, C.; Harakat, D.; Voutquenne-Nazabadioko, L.; Haba, H. Pyrroloquinolone A, a new alkaloid and other phytochemicals from *Atractylis cancellata* L. with antioxidant and anticholinesterase activities. *Nat. Prod. Res.* **2019**, *35*, 2997–3003. [CrossRef]
54. Liu, Y.-M.; Fan, J.-J.; Wang, L.-N. Discovery of Guanidine Derivatives from *Buthus martensii* Karsch with Metal-Binding and Cholinesterase Inhibition Properties. *Molecules* **2021**, *26*, 6737. [CrossRef]
55. Cai, R.; Wang, L.-N.; Fan, J.-J.; Geng, S.-Q.; Liu, Y.-M. New 4-N-phenylaminoquinoline derivatives as antioxidant, metal chelating and cholinesterase inhibitors for Alzheimer’s disease. *Bioorg. Chem.* **2019**, *93*, 103328. [CrossRef]
56. Ata, A.; Iverson, C.D.; Kalhari, K.S.; Akhter, S.; Betteridge, J.; Meshkatsadat, M.H.; Orhan, I.; Sener, B. Triterpenoidal alkaloids from *Buxushyrcana* and their enzyme inhibitory, anti-fungal and anti-leishmanial activities. *Phytochemistry* **2010**, *71*, 1780–1786. [CrossRef] [PubMed]
57. Babar, Z.U.; Ata, A.; Meshkatsadat, M.H. New bioactive steroidal alkaloids from *Buxus hyrcana*. *Steroids* **2006**, *71*, 1045–1051. [CrossRef] [PubMed]
58. Ata, A.; Conci, L.J.; Orhan, I. Mucoralactone A: An Unusual Steroid from the Liquid Culture of *Mucor plumbeus*. *Heterocycles* **2006**, *68*, 2097. [CrossRef]
59. Baek, S.C.; Park, M.H.; Ryu, H.W.; Lee, J.P.; Kang, M.-G.; Park, D.; Park, C.M.; Oh, S.-R.; Kim, H. Rhamnocitrin isolated from *Prunus padus* var. *seoulensis*: A potent and selective reversible inhibitor of human monoamine oxidase A. *Bioorg. Chem.* **2018**, *83*, 317–325. [CrossRef] [PubMed]
60. Lee, J.P.; Kang, M.-G.; Lee, J.Y.; Oh, J.M.; Baek, S.C.; Leem, H.H.; Park, D.; Cho, M.-L.; Kim, H. Potent inhibition of acetylcholinesterase by sargachromanol I from *Sargassum siliquastrum* and by selected natural compounds. *Bioorg. Chem.* **2019**, *89*, 103043. [CrossRef]
61. Geissler, T.; Brandt, W.; Porzel, A.; Schlenzig, D.; Kehlen, A.; Wessjohann, L.A.; Arnold, N. Acetylcholinesterase inhibitors from the toadstool *Cortinarius infractus*. *Bioorg. Med. Chem.* **2010**, *18*, 2173–2177. [CrossRef]

62. Mehfooz, H.; Saeed, A.; Sharma, A.; Albericio, F.; Larik, F.A.; Jabeen, F.; Channar, P.A.; Flörke, U. Dual Inhibition of AChE and BChE with the C-5 Substituted Derivative of Meldrum's Acid: Synthesis, Structure Elucidation, and Molecular Docking Studies. *Crystals* **2017**, *7*, 211. [CrossRef]
63. Zhang, J.; Zhang, C.; Xu, F.-C.; Quesheng; Zhang, Q.-Y.; Tu, P.-F.; Liang, H. Cholinesterase inhibitory isoquinoline alkaloids from *Corydalis mucronifera*. *Phytochemistry* **2019**, *159*, 199–207. [CrossRef]
64. Hung, T.M.; Ngoc, T.M.; Youn, U.J.; Min, B.S.; Na, M.; Thuong, P.T.; Bae, K. Anti-Amnestic Activity of Pseudocoptisine from *Corydalis Tuber*. *Biol. Pharm. Bull.* **2008**, *31*, 159–162. [CrossRef]
65. Khaw, K.Y.; Choi, S.B.; Tan, S.C.; Wahab, H.A.; Chan, K.L.; Murugaiyah, V. Prenylated xanthenes from mangosteen as promising cholinesterase inhibitors and their molecular docking studies. *Phytomedicine* **2014**, *21*, 1303–1309. [CrossRef]
66. Othman, W.N.N.W.; Liew, S.Y.; Khaw, K.Y.; Murugaiyah, V.; Litaudon, M.; Awang, K. Cholinesterase inhibitory activity of isoquinoline alkaloids from three *Cryptocarya* species (Lauraceae). *Bioorg. Med. Chem.* **2016**, *24*, 4464–4469. [CrossRef] [PubMed]
67. Ahmad, S.; Ahmad, M.; Almeahadi, M.; Shah, S.A.A.; Khan, F.A.; Khan, N.M.; Khan, A.; Zainab; Halawi, M.; Ahmad, H. In Vitro and In Silico Investigation of Diterpenoid Alkaloids Isolated from *Delphinium chitralense*. *Molecules* **2022**, *27*, 4348. [CrossRef] [PubMed]
68. Ahmad, H.; Ahmad, S.; Ali, M.; Latif, A.; Shah, S.A.A.; Naz, H.; Rahman, N.U.; Shaheen, F.; Wadood, A.; Khan, H.U.; et al. Norditerpenoid alkaloids of *Delphinium denudatum* as cholinesterase inhibitors. *Bioorg. Chem.* **2018**, *78*, 427–435. [CrossRef]
69. López, S.; Bastida, J.; Viladomat, F.; Codina, C. Acetylcholinesterase Inhibitory Activity of Some Amaryllidaceae Alkaloids and Narcissus Extracts. *Life Sci.* **2002**, *71*, 2521–2529. [CrossRef] [PubMed]
70. Ortiz, J.E.; Pigni, N.B.; Andujar, S.A.; Roitman, G.; Suvire, F.D.; Enriz, R.D.; Tapia, A.; Bastida, J.; Feresin, G.E. Alkaloids from *Hippeastrum argentinum* and Their Cholinesterase-Inhibitory Activities: An in Vitro and in Silico Study. *J. Nat. Prod.* **2016**, *79*, 1241–1248. [CrossRef]
71. Botić, T.; Defant, A.; Zanini, P.; Žužek, M.C.; Frangež, R.; Janussen, D.; Kersken, D.; Knez, Ž.; Mancini, I.; Sepčić, K. Discorhabdin alkaloids from *Antarctic Latrunculia* spp. sponges as a new class of cholinesterase inhibitors. *Eur. J. Med. Chem.* **2017**, *136*, 294–304. [CrossRef]
72. Kolak, U.; Hacibekiroglu, I.; Boga, M.; Ozgokce, F.; Unal, M.; Choudhary, M.I.; Ayhan, U. Phytochemical Investigation of *Leontice leontopetalum* L. subsp. *ewersmannii* with Antioxidant and Anticholinesterase Activities. *Rec. Nat. Prod.* **2011**, *5*, 309–313.
73. Tang, Y.; Fu, Y.; Xiong, J.; Li, M.; Ma, G.-L.; Yang, G.-X.; Wei, B.-G.; Zhao, Y.; Zhang, H.-Y.; Hu, J.-F. Lycodine-Type Alkaloids from *Lycopodium casuarinoides*. *J. Nat. Prod.* **2013**, *76*, 1475–1484. [CrossRef]
74. Kubota, T.; Yahata, H.; Yamamoto, S.; Hayashi, S.; Shibata, T.; Kobayashi, J. Serratezomines D and E, new *Lycopodium* alkaloids from *Lycopodium serratum* var. *serratum*. *Bioorg. Med. Chem. Lett.* **2009**, *19*, 3577–3580. [CrossRef]
75. Guo, H.; Chen, Y.-H.; Wang, T.-M.; Kang, T.-G.; Sun, H.-Y.; Pei, W.-H.; Song, H.-P.; Zhang, H. A strategy to discover selective α -glucosidase/acetylcholinesterase inhibitors from five function-similar citrus herbs through LC-Q-TOF-MS, bioassay and virtual screening. *J. Chromatogr. B Analyt. Technol. Biomed. Life Sci.* **2021**, *1174*, 122722. [CrossRef]
76. Kumar, N.S.; Mukherjee, P.K.; Bhadra, S.; Saha, B.P.; Pal, B.C. Acetylcholinesterase inhibitory potential of a carbazole alkaloid, mahanimbine, from *Murraya koenigii*. *Phytotherapy Res.* **2009**, *24*, 629–631. [CrossRef]
77. Mroczek, T. Highly efficient, selective and sensitive molecular screening of acetylcholinesterase inhibitors of natural origin by solid-phase extraction-liquid chromatography/electrospray ionisation-octopole-orthogonal acceleration time-of-flight-mass spectrometry and novel thin-layer chromatography-based bioautography. *J. Chromatogr. A* **2009**, *1216*, 2519–2528. [CrossRef] [PubMed]
78. Šafratová, M.; Hošťálková, A.; Hulcová, D.; Breiterová, K.; Hrabcová, V.; Machado, M.; Fontinha, D.; Prudêncio, M.; Kuneš, J.; Chlebek, J.; et al. Alkaloids from *Narcissus poeticus* cv. Pink Parasol of various structural types and their biological activity. *Arch. Pharmacol Res.* **2017**, *41*, 208–218. [CrossRef]
79. Havlasová, J.; Safratova, M.; Siatka, T.; Štěpánková, Š.; Novák, Z.; Ločárek, M.; Opletal, L.; Hrabínova, M.; Jun, D.; Benešová, N.; et al. Chemical Composition of Bioactive Alkaloid Extracts from Some *Narcissus* Species and Varieties and their Biological Activity. *Nat. Prod. Commun.* **2014**, *9*, 1151–1155. [CrossRef]
80. Karakoyun, Ç.; Bozkurt, B.; Çoban, G.; Masi, M.; Cimmino, A.; Evidente, A.; Somer, N.U. A comprehensive study on narcissus tazetta subsp. tazetta L.: Chemo-profiling, isolation, anticholinesterase activity and molecular docking of amaryllidaceae alkaloids. *S. Afr. J. Bot.* **2020**, *130*, 148–154. [CrossRef]
81. Jamila, N.; Khairuddean, M.; Yeong, K.K.; Osman, H.; Murugaiyah, V. Cholinesterase inhibitory triterpenoids from the bark of *Garcinia hombroiana*. *J. Enzym. Inhib. Med. Chem.* **2014**, *30*, 133–139. [CrossRef]
82. Safa, N.; Trobec, T.; Holland, D.C.; Slazak, B.; Jacobsson, E.; Hawkes, J.A.; Frangež, R.; Sepčić, K.; Göransson, U.; Moodie, L.W.K.; et al. Spatial Distribution and Stability of Cholinesterase Inhibitory Protoberberine Alkaloids from *Papaver setiferum*. *J. Nat. Prod.* **2021**, *85*, 215–224. [CrossRef] [PubMed]
83. Ristovski, S.; Uzelac, M.; Kljun, J.; Lipec, T.; Uršič, M.; Jokhadar, Š.Z.; Žužek, M.C.; Trobec, T.; Frangež, R.; Sepčić, K.; et al. Organoruthenium Prodrugs as a New Class of Cholinesterase and Glutathione-S-Transferase Inhibitors. *ChemMedChem* **2018**, *13*, 2166–2176. [CrossRef] [PubMed]
84. Jiang, C.-S.; Ge, Y.-X.; Cheng, Z.-Q.; Song, J.-L.; Wang, Y.-Y.; Zhu, K.; Zhang, H. Discovery of new multifunctional selective acetylcholinesterase inhibitors: Structure-based virtual screening and biological evaluation. *J. Comput. Mol. Des.* **2019**, *33*, 521–530. [CrossRef] [PubMed]
85. Chen, S.-Q.; Jia, J.; Hu, J.-Y.; Wu, J.; Sun, W.-T.; Zheng, M.; Wang, X.; Zhu, K.-K.; Jiang, C.-S.; Yang, S.-P.; et al. Iboga-type alkaloids with Indolizidino[8,7-b]indole scaffold and bisindole alkaloids from *Tabernaemontana bufalina* Lour. *Phytochemistry* **2022**, *196*, 113089. [CrossRef]

86. Yu, P.; Chen, Z.; Liu, Y.; Gu, Z.; Wang, X.; Zhang, Y.; Ma, Y.; Dong, M.; Tian, Z. Bioactivity-Guided Separation of Anti-Cholinesterase Alkaloids from *Uncaria rhynchophylla* (Miq.) Miq. Ex Havil Based on HSCCC Coupled with Molecular Docking. *Molecules* **2022**, *27*, 2013. [CrossRef] [PubMed]
87. Decker, M. Novel inhibitors of acetyl- and butyrylcholinesterase derived from the alkaloids dehydroevodiamine and rutaecarpine. *Eur. J. Med. Chem.* **2005**, *40*, 305–313. [CrossRef] [PubMed]
88. Decker, M.; Krauth, F.; Lehmann, J. Novel tricyclic quinazolinimines and related tetracyclic nitrogen bridgehead compounds as cholinesterase inhibitors with selectivity towards butyrylcholinesterase. *Bioorg. Med. Chem.* **2006**, *14*, 1966–1977. [CrossRef] [PubMed]
89. Macabeo, A.P.G.; Vidar, W.S.; Chen, X.; Decker, M.; Heilmann, J.; Wan, B.; Franzblau, S.; Galvez, E.V.; Aguinaldo, M.A.M.; Cordell, G.A. Mycobacterium tuberculosis and cholinesterase inhibitors from *Voacanga globosa*. *Eur. J. Med. Chem.* **2011**, *46*, 3118–3123. [CrossRef]
90. Lenta, B.N.; Devkota, K.P.; Ngouela, S.; Boyom, F.F.; Naz, Q.; Choudhary, M.I.; Tsamo, E.; Rosenthal, P.J.; Sewald, N. Antiplasmodial and Cholinesterase Inhibiting Activities of some Constituents of *Psorospermum glaberrimum*. *Chem. Pharm. Bull.* **2008**, *56*, 222–226. [CrossRef]
91. Xiao, Y.; Liang, W.; Liu, D.; Zhang, Z.; Chang, J.; Zhu, D. Isolation and acetylcholinesterase inhibitory activity of asteric acid derivatives produced by *Talaromyces aurantiacus* FL15, an endophytic fungus from *Huperzia serrata*. *3 Biotech* **2022**, *12*, 60. [CrossRef]
92. Devidas, S.B.; Rahmatkar, S.N.; Singh, R.; Sendri, N.; Purohit, R.; Singh, D.; Bhandari, P. Amelioration of cognitive deficit in zebrafish by an undescribed anthraquinone from *Juglans regia* L.: An in-silico, in-vitro and in-vivo approach. *Eur. J. Pharmacol.* **2021**, *906*, 174234. [CrossRef]
93. Ingkaninan, K.; De Best, C.M.; Van Der Heijden, R.; Hofte, A.J.P.; Karabatak, B.; Irth, H.; Tjaden, U.R.; Van der Greef, J.; Verpoorte, R. High-Performance Liquid Chromatography with on-Line Coupled UV, Mass Spec-trometric and Biochemical Detection for Identification of Acetylcholinesterase Inhibitors from Natural Products. *J. Chromatogr. A* **2000**, *872*, 61–73. [CrossRef]
94. Rhee, I.K.; van Rijn, R.M.; Verpoorte, R. Qualitative determination of false-positive effects in the acetylcholinesterase assay using thin layer chromatography. *Phytochem. Anal.* **2003**, *14*, 127–131. [CrossRef]
95. Rollinger, J.M.; Hornick, A.; Langer, T.; Stuppner, H.; Prast, H. Acetylcholinesterase Inhibitory Activity of Scopolin and Scopoletin Discovered by Virtual Screening of Natural Products. *J. Med. Chem.* **2004**, *47*, 6248–6254. [CrossRef]
96. Se-Young, H.; Young-Pyo, C.; Soon-Jung, B.; Mee-Hee, J.; Young-Choong, K. An Acetylcholinesterase Inhibitor Isolated from *Corydalis* Tuber and Its Mode of Action. *Korean J. Pharmacogn.* **1996**, *27*, 91–95.
97. Kim, S.R.; Hwang, S.Y.; Jang, Y.P.; Park, M.J.; Markelonis, G.J.; Oh, T.H.; Kim, Y.C. Protopine from *Corydalis ternata* has Anticholinesterase and Antiamnesic Activities. *Planta Med.* **1999**, *65*, 218–221. [CrossRef] [PubMed]
98. Kang, S.Y.; Lee, K.Y.; Sung, S.H.; Park, M.J.; Kim, Y.C. Coumarins Isolated from *Angelica gigas* Inhibit Acetylcholinesterase: Structure–Activity Relationships. *J. Nat. Prod.* **2001**, *64*, 683–685. [CrossRef] [PubMed]
99. Şenol, F.S.; Orhan, I.; Celep, F.; Kahraman, A.; Doğan, M.; Yilmaz, G.; Şener, B. Survey of 55 Turkish *Salvia* taxa for their acetylcholinesterase inhibitory and antioxidant activities. *Food Chem.* **2010**, *120*, 34–43. [CrossRef]
100. Senol, F.S.; Skalicka-Woźniak, K.; Khan, M.T.H.; Orhan, I.E.; Sener, B.; Głowniak, K. An in vitro and in silico approach to cholinesterase inhibitory and antioxidant effects of the methanol extract, furanocoumarin fraction, and major coumarins of *Angelica officinalis* L. fruits. *Phytochem. Lett.* **2011**, *4*, 462–467. [CrossRef]
101. Marston, A.; Kissling, J.; Hostettmann, K. A rapid TLC bioautographic method for the detection of acetylcholinesterase and butyrylcholinesterase inhibitors in plants. *Phytochem. Anal.* **2002**, *13*, 51–54. [CrossRef]
102. Kozioł, E.; Sezor Desni, F.D.; Orhan, I.E.; Marcourt, L.; Budzynska, B.; Wolfender, J.-L.; Crawford, A.D.; Skalicka-Woźniak, K. High-performance counter-current chromatography isolation and initial neuroactivity characterization of furanocoumarin derivatives from *Peucedanum alsaticum* L. (Apiaceae). *Phytomedicine* **2019**, *15*, 259–264. [CrossRef]
103. Perry, N.S.L.; Houghton, P.J.; Jenner, P.; Keith, A.; Perry, E.K. *Salvia lavandulaefolia* essential oil inhibits cholinesterase in vivo. *Phytomedicine* **2002**, *9*, 48–51. [CrossRef]
104. Fan, P.; Hay, A.-E.; Marston, A.; Hostettmann, K. Acetylcholinesterase-Inhibitory Activity of Linarin from *Buddleja davidii*, Structure-Activity Relationships of Related Flavonoids, and Chemical Investigation of *Buddleja nitida*. *Pharm. Biol.* **2008**, *46*, 596–601. [CrossRef]
105. Kang, Y.-Q.; Zhou, J.-C.; Fan, P.-H.; Wang, S.-Q.; Lou, H.-X. Scapaundulin C, a novel labdane diterpenoid isolated from Chinese liverwort *Scapania undulate*, inhibits acetylcholinesterase activity. *Chin. J. Nat. Med.* **2015**, *13*, 933–936. [CrossRef]
106. Nguyen, V.T.; To, D.C.; Tran, M.H.; Oh, S.H.; Kim, J.A.; Ali, Y.; Woo, M.-H.; Choi, J.S.; Min, B.S. Isolation of cholinesterase and β -secretase 1 inhibiting compounds from *Lycopodiella cernua*. *Bioorg. Med. Chem.* **2015**, *23*, 3126–3134. [CrossRef] [PubMed]
107. Jung, M.; Park, M. Acetylcholinesterase Inhibition by Flavonoids from *Agrimonia pilosa*. *Molecules* **2007**, *12*, 2130–2139. [CrossRef] [PubMed]
108. Ahmed, T.; Gilani, A.-H. Inhibitory effect of curcuminoids on acetylcholinesterase activity and attenuation of scopolamine-induced amnesia may explain medicinal use of turmeric in Alzheimer’s disease. *Pharmacol. Biochem. Behav.* **2009**, *91*, 554–559. [CrossRef] [PubMed]
109. Tan, W.-N.; Khairuddean, M.; Wong, K.-C.; Khaw, K.-Y.; Vikneswaran, M. New cholinesterase inhibitors from *Garcinia atroviridis*. *Fitoterapia* **2014**, *97*, 261–267. [CrossRef]
110. Park, H.M.; Choi, S.Y. Changes in Esterase Activity and Acetylcholinesterase Sensitivity of Insecti-cide-Selected Strains of the Brown Planthopper (*Nilaparvata lugens* Stal). *Korean J. Appl. Entomol.* **1991**, *1*, 19–37.

111. Ding, X.; Ouyang, M.-A.; Liu, X.; Wang, R.-Z. Acetylcholinesterase Inhibitory Activities of Flavonoids from the Leaves of *Ginkgo biloba* against Brown Planthopper. *J. Chem.* **2013**, *2013*, 645086. [CrossRef]
112. Radić, Z.; Kalisiak, J.; Fokin, V.V.; Sharpless, K.B.; Taylor, P. Interaction kinetics of oximes with native, phosphorylated and aged human acetylcholinesterase. *Chem. Interact.* **2010**, *187*, 163–166. [CrossRef]
113. Zhang, F.; Li, S.; Liu, C.; Fang, K.; Jiang, Y.; Zhang, J.; Lan, J.; Zhu, L.; Pang, H.-Q.; Wang, G. Rapid screening for acetylcholinesterase inhibitors in *Selaginella doederleinii* Hieron by using functionalized magnetic Fe₃O₄ nanoparticles. *Talanta* **2022**, *243*, 123284. [CrossRef]
114. Zou, M.; Wang, R.; Yin, Q.; Liu, L. Bioassay-guided isolation and identification of anti-Alzheimer's active compounds from *Spiranthes sinensis* (Pers.) Ames. *Med. Chem. Res.* **2021**, *30*, 1849–1855. [CrossRef]
115. Lee, I.; Ahn, B.; Choi, J.; Hattori, M.; Min, B.; Bae, K. Selective cholinesterase inhibition by lanostane triterpenes from fruiting bodies of *Ganoderma lucidum*. *Bioorg. Med. Chem. Lett.* **2011**, *21*, 6603–6607. [CrossRef]
116. Wang, W.; Fu, X.-W.; Dai, X.-L.; Hua, F.; Chu, G.-X.; Chu, M.-J.; Hu, F.-L.; Ling, T.-J.; Gao, L.-P.; Xie, Z.-W.; et al. Novel acetylcholinesterase inhibitors from Zijuan tea and biosynthetic pathway of caffeoylated catechin in tea plant. *Food Chem.* **2017**, *237*, 1172–1178. [CrossRef]
117. Wu, H.-Y.; Ke, J.-P.; Wang, W.; Kong, Y.-S.; Zhang, P.; Ling, T.-J.; Bao, G.-H. Discovery of Neolignan Glycosides with Acetylcholinesterase Inhibitory Activity from Huangjinya Green Tea Guided by Ultra Performance Liquid Chromatography–Tandem Mass Spectrometry Data and Global Natural Product Social Molecular Networking. *J. Agric. Food Chem.* **2019**, *67*, 11986–11993. [CrossRef] [PubMed]
118. Wu, Y.; Su, X.; Lu, J.; Wu, M.; Yang, S.Y.; Mai, Y.; Deng, W.; Xue, Y. In Vitro and in Silico Analysis of Phytochemicals from *Fallopia dentatoalata* as Dual Functional Cholinesterase Inhibitors for the Treatment of Alzheimer's Disease. *Front. Pharmacol.* **2022**, *13*, 905708. [CrossRef] [PubMed]
119. Kim, J.H.; Lee, S.-H.; Lee, H.W.; Sun, Y.N.; Jang, W.-H.; Yang, S.-Y.; Jang, H.-D.; Kim, Y.H. (–)-Epicatechin derivate from *Orostachys japonicus* as potential inhibitor of the human butyrylcholinesterase. *Int. J. Biol. Macromol.* **2016**, *91*, 1033–1039. [CrossRef]
120. Choi, J.S.; Haulader, S.; Karki, S.; Jung, H.J.; Kim, H.R.; Jung, H.A. Acetyl- and butyryl-cholinesterase inhibitory activities of the edible brown alga *Eisenia bicyclis*. *Arch. Pharmacol. Res.* **2014**, *38*, 1477–1487. [CrossRef] [PubMed]
121. Difaraz, K.; Wang, Z.; Saeed, A.; Shafiullah, K. New antioxidant and cholinesterase inhibitory constituents from *Lonicera quinquelocularis*. *J. Med. Plants Res.* **2014**, *8*, 313–317. [CrossRef]
122. Ortiz, J.E.; Berkov, S.; Pigni, N.B.; Theoduloz, C.; Roitman, G.; Tapia, A.; Bastida, J.; Feresin, G.E. Wild Argentinian Amaryllidaceae, a New Renewable Source of the Acetylcholinesterase Inhibitor Galanthamine and Other Alkaloids. *Molecules* **2012**, *17*, 13473–13482. [CrossRef]
123. Xiao, Y.; Liang, W.; Zhang, Z.; Wang, Y.; Zhang, S.; Liu, J.; Chang, J.; Ji, C.; Zhu, D. Polyketide Derivatives from the Endophytic Fungus *Phaeosphaeria* sp. LF5 Isolated from *Huperzia serrata* and Their Acetylcholinesterase Inhibitory Activities. *J. Fungi* **2022**, *8*, 232. [CrossRef] [PubMed]
124. Jung, K.; Lee, B.; Han, S.J.; Ryu, J.H.; Kim, D.-H. Mangiferin Ameliorates Scopolamine-Induced Learning Deficits in Mice. *Biol. Pharm. Bull.* **2009**, *32*, 242–246. [CrossRef]
125. Jang, M.H.; Piao, X.L.; Kim, J.M.; Kwon, S.W.; Park, J.H. Inhibition of cholinesterase and amyloid- β aggregation by resveratrol oligomers from *Vitis amurensis*. *Phytotherapy Res.* **2008**, *22*, 544–549. [CrossRef]
126. Hajimehdipoor, H.; Mosaddegh, M.; Naghibi, F.; Haeri, A.; Hamzeloo-Moghadam, M. Natural sesquiterpen lactones as acetylcholinesterase inhibitors. *An. Acad. Bras. Cienc.* **2014**, *86*, 801–806. [CrossRef]
127. Ibrahim, M.; Farooq, T.; Hussain, N.; Hussain, A.; Gulzar, T.; Hussain, I.; Akash, M.S.H.; Rehmani, F.S. Acetyl and butyryl cholinesterase inhibitory sesquiterpene lactones from *Amberboa ramosa*. *Chem. Central J.* **2013**, *7*, 116. [CrossRef] [PubMed]
128. Bustamam, A.; Ibrahim, S.; Al-Zubairi, A.S.; Met, M.; Syam, M.M. Zerumbone: A Natural Compound with Anti-Cholinesterase Activity. *Am. J. Pharmacol. Toxicol.* **2008**, *3*, 209–211. [CrossRef]
129. Hornick, A.; Schwaiger, S.; Rollinger, J.M.; Vo, N.P.; Prast, H.; Stuppner, H. Extracts and constituents of *Leontopodium alpinum* enhance cholinergic transmission: Brain ACh increasing and memory improving properties. *Biochem. Pharmacol.* **2008**, *76*, 236–248. [CrossRef] [PubMed]
130. Fatima, I.; Ahmad, I.; Anis, I.; Malik, A.; Afza, N.; Iqbal, L.; Latif, M. New butyrylcholinesterase inhibitory steroid and peroxy acid from *Leucas urticifolia*. *Arch. Pharmacol. Res.* **2008**, *31*, 999–1003. [CrossRef] [PubMed]
131. Ahmed, E.; Nawaz, S.A.; Malik, A.; Choudhary, M.I. Isolation and Cholinesterase-Inhibition Studies of Sterols from *Haloxylon recurvum*. *Cheminform* **2006**, *37*, 573–580. [CrossRef]
132. Jusril, N.; Juhari, A.M.; Abu Bakar, S.; Saad, W.M.; Adenan, M. Combining In Silico and In Vitro Studies to Evaluate the Acetylcholinesterase Inhibitory Profile of Different Accessions and the Biomarker Triterpenes of *Centella asiatica*. *Molecules* **2020**, *25*, 3353. [CrossRef]
133. Tallini, L.R.; Osorio, E.H.; dos Santos, V.D.; Borges, W.D.S.; Kaiser, M.; Viladomat, F.; Zuanazzi, J.A.S.; Bastida, J. *Hippeastrum reticulatum* (Amaryllidaceae): Alkaloid Profiling, Biological Activities and Molecular Docking. *Molecules* **2017**, *22*, 2191. [CrossRef]
134. Alarcón-Enos, J.; Muñoz-Núñez, E.; Gutiérrez, M.; Quiroz-Carreño, S.; Pastene-Navarrete, E.; Acuña, C.C. Dyhydro- β -agarofurans natural and synthetic as acetylcholinesterase and COX inhibitors: Interaction with the peripheral anionic site (AChE-PAS), and anti-inflammatory potentials. *J. Enzym. Inhib. Med. Chem.* **2022**, *37*, 1845–1856. [CrossRef]

135. Di Giovanni, S.; Borloz, A.; Urbain, A.; Marston, A.; Hostettmann, K.; Carrupt, P.-A.; Reist, M. In vitro screening assays to identify natural or synthetic acetylcholinesterase inhibitors: Thin layer chromatography versus microplate methods. *Eur. J. Pharm. Sci.* **2008**, *33*, 109–119. [CrossRef] [PubMed]
136. Ryu, H.W.; Oh, S.-R.; Curtis-Long, M.J.; Lee, J.H.; Song, H.-H.; Park, K.H. Rapid Identification of Cholinesterase Inhibitors from the Seedcases of Mangosteen Using an Enzyme Affinity Assay. *J. Agric. Food Chem.* **2014**, *62*, 1338–1343. [CrossRef] [PubMed]
137. Hostettmann, K.; Borloz, A.; Urbain, A.; Marston, A. Natural Product Inhibitors of Acetylcholinesterase. *Curr. Org. Chem.* **2006**, *10*, 825–847. [CrossRef]
138. Kukula-Koch, W.; Mroczek, T. Application of hydrostatic CCC–TLC–HPLC–ESI-TOF-MS for the bioguided fractionation of anticholinesterase alkaloids from *Argemone mexicana* L. roots. *Anal. Bioanal. Chem.* **2015**, *407*, 2581–2589. [CrossRef] [PubMed]
139. Mroczek, T. Qualitative and quantitative two-dimensional thin-layer chromatography/high performance liquid chromatography/diode-array/electrospray-ionization-time-of-flight mass spectrometry of cholinesterase inhibitors. *J. Pharm. Biomed. Anal.* **2016**, *129*, 155–162. [CrossRef] [PubMed]
140. Smyrska-Wieleba, N. *Analiza Fitochemiczna oraz Ocena Aktywności Biologicznej Alkaloidów w Wybranych Gatunkach Rodzaju Narcissus spp.*; Medical University of Lublin: Lublin, Poland, 2021.
141. Mroczek, T.; Dymek, A.; Widelski, J.; Wojtanowski, K.K. The Bioassay-Guided Fractionation and Identification of Potent Acetylcholinesterase Inhibitors from *Narcissus* c.v. ‘*Hawera*’ Using Optimized Vacuum Liquid Chromatography, High Resolution Mass Spectrometry and Bioautography. *Metabolites* **2020**, *10*, 395. [CrossRef]
142. Maciejewska-Turska, M.; Zgórk, G. In-depth phytochemical and biological studies on potential AChE inhibitors in red and zigzag clover dry extracts using reversed-phase liquid chromatography (RP-LC) coupled with photodiode array (PDA) and electron spray ionization-quadrupole/time of flight-mass spectrometric (ESI-QToF/MS-MS) detection and thin-layer chromatography-bioautography. *Food Chem.* **2021**, *375*, 131846. [CrossRef] [PubMed]

Disclaimer/Publisher’s Note: The statements, opinions and data contained in all publications are solely those of the individual author(s) and contributor(s) and not of MDPI and/or the editor(s). MDPI and/or the editor(s) disclaim responsibility for any injury to people or property resulting from any ideas, methods, instructions or products referred to in the content.



Article

Impact of Hydrophobic Chains in Five-Coordinate Glucoconjugate Pt(II) Anticancer Agents

Alfonso Annunziata ¹, Paola Imbimbo ² , Maria Elena Cucciolo ^{2,3} , Giarita Ferraro ² , Vincenzo Langellotti ² ,
Alessandra Marano ², Massimo Melchiorre ^{2,3} , Gabriella Tito ² , Marco Trifuoggi ² , Daria Maria Monti ² ,
Antonello Merlino ² and Francesco Ruffo ^{2,3,*}

¹ Institute Parisien de Chimie Moléculaire, Campus Pierre et Marie Curie, Sorbonne Université, 4 Place Jussieu, 75005 Paris, France

² Dipartimento di Scienze Chimiche, Università degli Studi di Napoli Federico II (Complesso Universitario di Monte S. Angelo), Via Cintia 21, 80126 Napoli, Italy

³ Consorzio Interuniversitario di Reattività Chimica e Catalisi (CIRCC), Via Celso Ulpiani 27, 70126 Bari, Italy

* Correspondence: ruffo@unina.it

Abstract: This study describes new platinum(II) cationic five-coordinate complexes (**1-R,R'**) of the formula [PtR(NHC)(dmphen)(ethene)]CF₃SO₃ (dmphen = 2,9-dimethyl-1,10-phenanthroline), containing in their axial positions an alkyl group R (methyl or octyl) and an imidazole-based NHC-carbene ligand with a substituent R' of variable length (methyl or octyl) on one nitrogen atom. The Pt–carbene bond is stable both in DMSO and in aqueous solvents. In DMSO, a gradual substitution of dmphen and ethene is observed, with the formation of a square planar solvated species. Octanol/water partitioning studies have revealed the order of hydrophobicity of the complexes (**1-Oct,Me** > **1-Oct,Oct** > **1-Me,Oct** > **1-Me,Me**). Their biological activity was investigated against two pairs of cancer and non-cancer cell lines. The tested drugs were internalized in cancer cells and able to activate the apoptotic pathway. The reactivity of **1-Me,Me** with DNA and protein model systems was also studied using UV–vis absorption spectroscopy, fluorescence, and X-ray crystallography. The compound binds DNA and interacts in various ways with the model protein lysozyme. Remarkably, structural data revealed that the complex can bind lysozyme via non-covalent interactions, retaining its five-coordinate geometry.

Keywords: platinum(II); five-coordinate complexes; glycoconjugation; cytotoxic activity; DNA binding; protein X-ray structure; lipophilicity

Citation: Annunziata, A.; Imbimbo, P.; Cucciolo, M.E.; Ferraro, G.; Langellotti, V.; Marano, A.; Melchiorre, M.; Tito, G.; Trifuoggi, M.; Monti, D.M.; et al. Impact of Hydrophobic Chains in Five-Coordinate Glucoconjugate Pt(II) Anticancer Agents. *Int. J. Mol. Sci.* **2023**, *24*, 2369. <https://doi.org/10.3390/ijms24032369>

Academic Editor: Dmitry Aminin

Received: 17 November 2022

Revised: 17 January 2023

Accepted: 20 January 2023

Published: 25 January 2023



Copyright: © 2023 by the authors. Licensee MDPI, Basel, Switzerland. This article is an open access article distributed under the terms and conditions of the Creative Commons Attribution (CC BY) license (<https://creativecommons.org/licenses/by/4.0/>).

1. Introduction

Cisplatin [1] and its derivatives are successfully used in the clinical treatment of cancer diseases. However, their administration is often accompanied by side effects that seriously affect the quality of life of patients [2]. Current strategies to enhance their performance involve the accurate tailoring of the coordination environment of the compounds, to make their action selective towards target cells, improve their stability, facilitate transport in physiological fluids, increase internalization in cells, and favour accumulation in selected biological compartments. This variety of options has produced a plethora of platinum(II) and platinum(IV) complexes, respectively, square planar and octahedral, endowed with biologically active fragments [3,4], modular and stable ligands [5–10], or functions that can be interfaced with supramolecular structures [11].

Recently, our research group has contributed to this emerging area by proposing new five-coordinate platinum(II) glycoconjugate complexes [12–15] (**1**) with the following structural motifs (Figure 1):

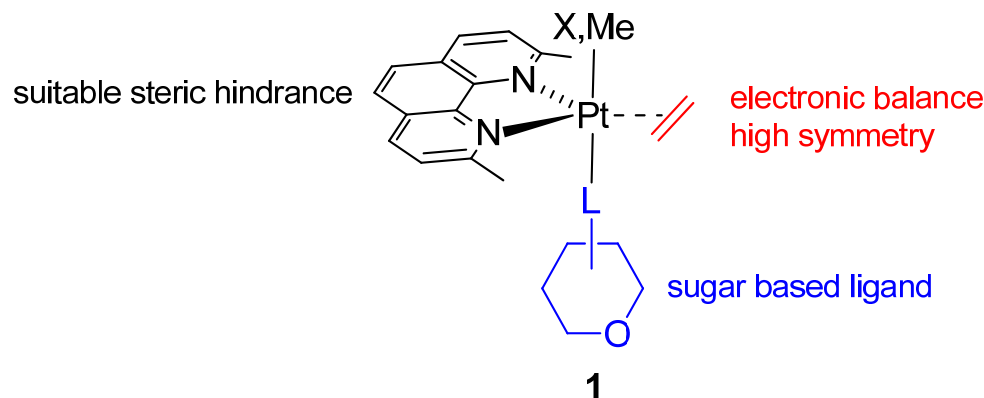


Figure 1. General structure of type 1 complexes.

We designed our structures aiming at conferring specific qualities to these agents, taking full advantage of the high versatility of the trigonal bipyramidal (*tbp*) scaffold. This coordinated saturation enhances their stability in biological milieu and hence, their chance at reaching the cellular target intact. This property is guaranteed by the simultaneous presence of the sterically hindered 2,9-dimethyl-1,10-phenanthroline (dmphen) and the π -acid ligand ethene, which balance the delicate electronic equilibrium within the equatorial plane of the trigonal bipyramid [16]. One axial position is occupied by a targeting ligand containing a sugar fragment. Glycoconjugation aims to selectively deliver the agent to cancer cells [17], exploiting the overexpression of glycosyl receptors, to satisfy their increased uptake of carbohydrates (“Warburg effect”), which is necessary to sustain cell growth and proliferation. Remarkable results were obtained with a *tbp* Pt(II) complex containing a glucoconjugate *N*-heterocyclic carbene ligand, which was demonstrated to be highly active and by far more selective for cancer cells, compared to cisplatin [14]. Carbene ligands are highly versatile synthetic platforms that can be variously decorated and confer good resistance to their complexes under hydrolytic conditions such as those of biological fluids [6].

The other apical position of the *tbp*, which in our previous structures hosted a halide (X) or a methyl (Me), can be further exploited to provide additional features to the complexes. This consideration inspired the possibility of adding further diversity, taking a cue from recent studies on the fine engineering of platinum agents. It has been demonstrated that the introduction of hydrophobic groups in the coordination sphere of metal complexes can have a positive impact on their cytotoxicity, cellular uptake, and selective transport in cellular targets [11,18–26]. This work aimed to verify the effect of fatty alkyl chains in the following family of type 1 complexes (Figure 2).

Hydrophobic *n*-octyl groups were added both in the apical position and in the carbene ligand, along with a simple methyl group. Thus, a set of four complexes spanning from the less aliphatic **1-Me,Me** to the more aliphatic **1-Oct,Oct** were synthesised and fully characterized. The ability of **1-Me,Me** to interact with model DNA and protein systems was demonstrated, and studies of cytotoxicity have disclosed that increasing the length of the chain enhances its antiproliferative activity.

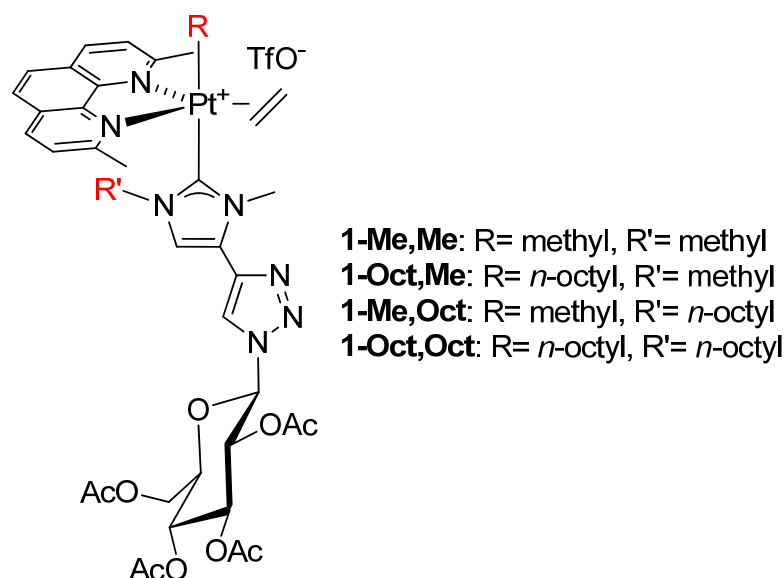
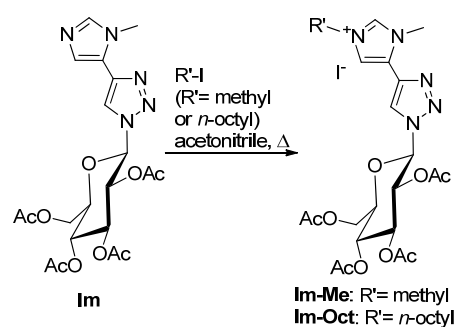


Figure 2. Structure of the complexes prepared within this study.

2. Results and Discussion

2.1. Synthesis and Characterization

The synthesis of the target platinum(II) complexes involved the initial preparation of pro-carbene imidazolium salts **Im-R** (Scheme 1).



Scheme 1. Synthesis of the pro-carbene species **Im-Me** and **Im-Oct**.

The imidazole precursor **Im** [12] was treated with an excess of the appropriate alkyl iodide to yield the pro-carbene precursor **Im-Me** or **Im-Oct** (Scheme 1). The alkylation was carried out in refluxing acetonitrile and the cationic products were isolated in a nearly quantitative yield by the removal of the solvent. A high-frequency shift of the NMR signals (Figures S1 and S2) of the three heterocyclic protons is indicative of the presence of a positive charge. For instance, Figure 3 compares the NMR spectra of **Im** and **Im-Oct** in deuteriochloroform.

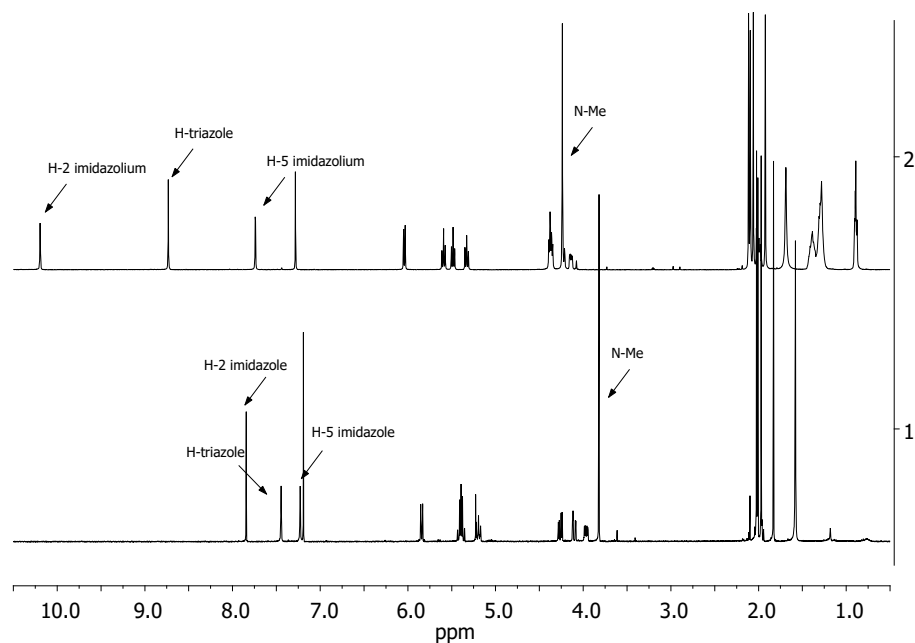
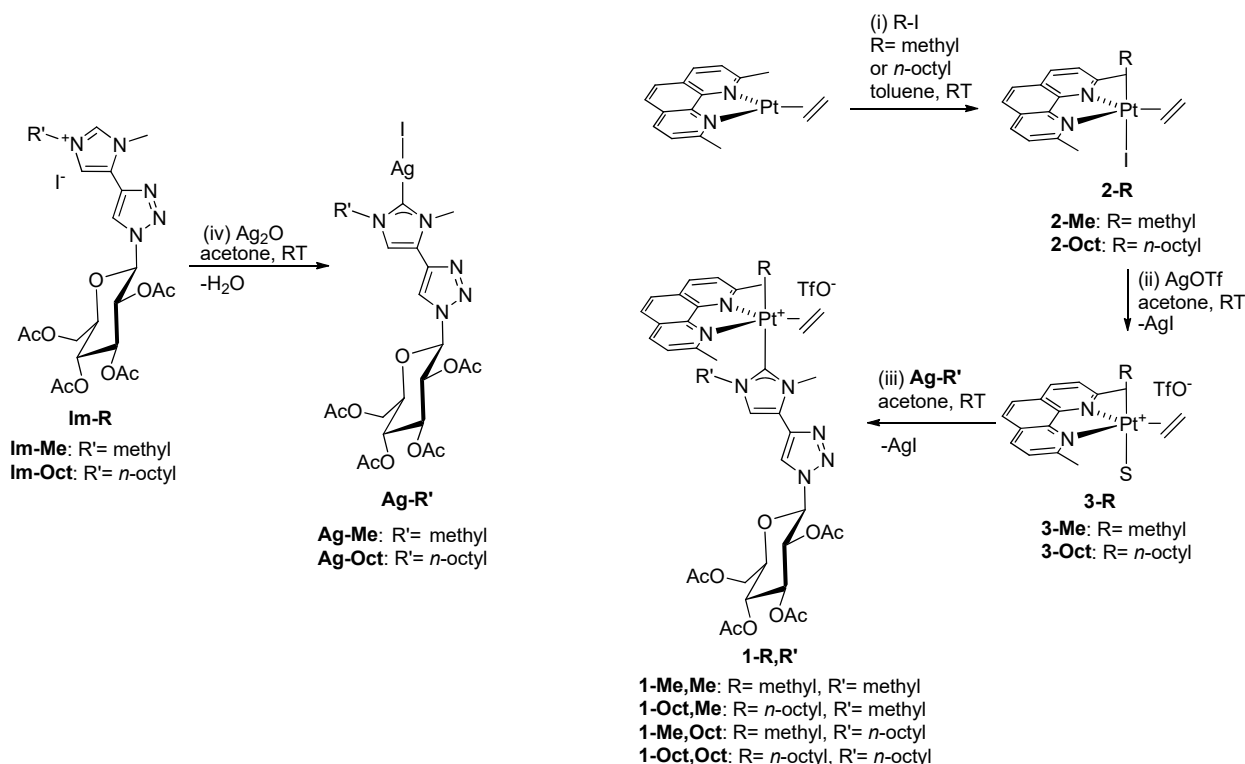


Figure 3. The ^1H NMR spectra of **Im** (trace 1) and **Im-Oct** (trace 2) in CDCl_3 .

The platinum precursors used to synthesise the glucoconjugated complexes were obtained through the oxidative addition (path i of Scheme 2) of methyl iodide or *n*-octyl iodide to the $\text{Pt}(0)$ precursor $[\text{Pt}(\text{dmphen})(\text{ethene})]$, affording the five-coordinate species **2-Me** and **2-Oct** in excellent yields as light yellow powders. Treatment with silver triflate in acetone promoted the formation of the solvato species **3-Me** and **3-Oct**. They were immediately reacted with the appropriate silver carbene complex **Ag-R'** (iii), obtained by treating the imidazolium salts **Im-R'** with silver oxide (iv). Transfer of the carbene ligand, assisted by the precipitation of Ag-I , completed the synthesis of the type **1-R,R'** complexes.



Scheme 2. Synthesis of the silver precursors (**Ag-R'**) and platinum **1-R,R'** complexes.

The products (complete names in Table S1) were characterized by ^1H and ^{13}C NMR spectroscopy (Figures S3–S12), which allowed for the unequivocal assessment of their structure, thanks to the following relevant observations. The two halves of dmphen are not equivalent due to the presence of the chiral sugar ligand. The four ethene protons resonate as an AA'BB' multiplet or accidentally as a singlet flanked by the expected satellites due to coupling with ^{195}Pt nuclei. The chemical shift was at a low frequency (2–2.5 ppm) due to the intense π -backdonation in the Pt–alkene bond. In accordance with this, olefin carbon signals were also detected at ca. 30 ppm. The signal of the methyl on platinum was at a low frequency in both the proton and carbon spectra, while the *n*-octyl chain gave rise to a crowded set of signals in the aliphatic region. Sugar protons showed the expected pattern of signals with H,H-couplings in accordance with their relative position in the glucose ring. Finally, as expected, the C(carbene)–Pt signal was found at a high frequency (173.8–172 ppm). Figure 4 displays the proton NMR spectrum of **1-Me,Oct**, in which some of the above evidence has been highlighted.

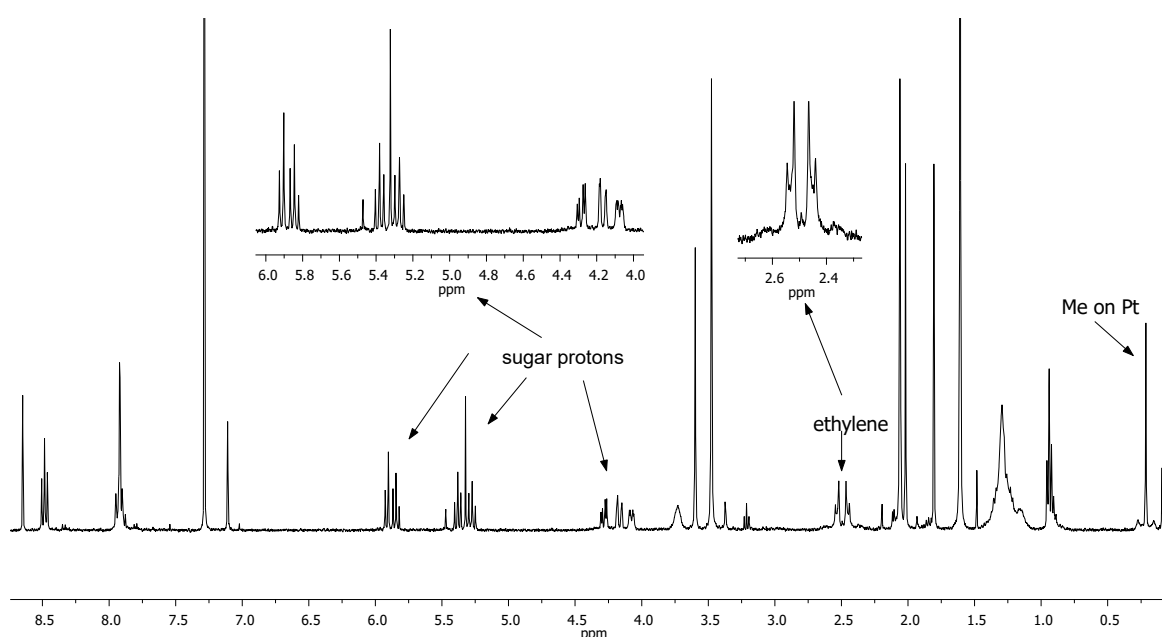


Figure 4. The ^1H NMR spectrum of **1-Me,Oct** in CDCl_3 .

2.2. In-Solution Stability of **1-R,R'** Complexes

The stability of the complexes in DMSO-d_6 , the solvent used to prepare stock solutions for biological experiments, was evaluated by recording their UV–vis absorptions and ^1H -NMR spectra over time.

UV–vis absorption spectra of **1-Me,Me** were recorded in DMSO for 5 h and then after 24 h and 7 days (Figure 5). The Pt complex showed a maximum of absorbance at 278 nm and two shoulders at 260 and 300 nm. The kinetic measurements highlight the poor stability of **1-Me,Me** in DMSO since, after just a few minutes, a variation in the spectral profile occurred. In fact, the λ_{max} experienced a blue shift from 278 to 269 nm, giving rise to an isosbestic point at 275 nm. In addition, a decrease in the absorbance of the shoulder at 300 nm is observed, together with an absorbance increase in the shoulder at 260 nm. These findings suggest that an exchange of metal ligands with DMSO occurs. The exchange continued over time and the spectra significantly changed from 0 to 7 days. It is highly probable that a slow release of ethene and dmphen can occur. This would lead to the formation of the square planar species of type **4-R,R'**, as reported in Scheme 3.

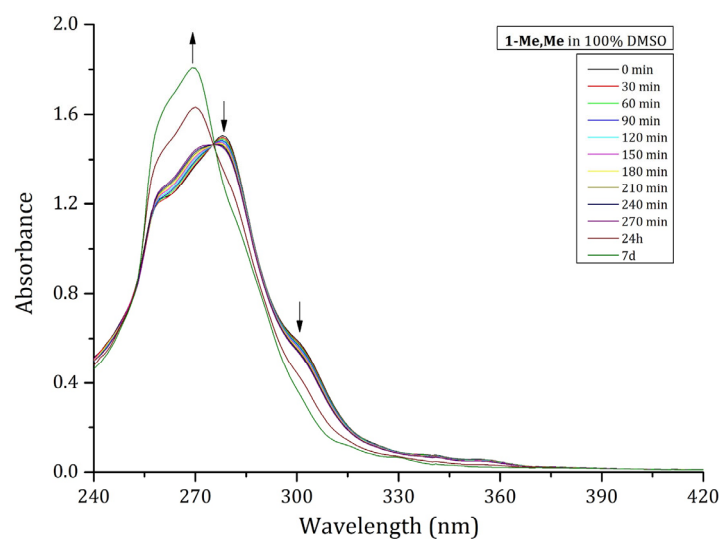
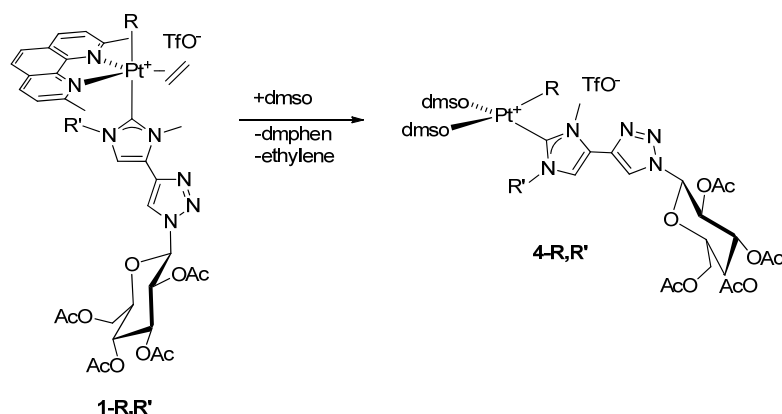


Figure 5. Time-course UV-vis spectra of 50 μM of **1-Me,Me** in DMSO.



Scheme 3. Reactivity of **1-R,R'** complexes in DMSO-d_6 .

The NMR data confirm (Figures S13–S16) this hypothesis and demonstrate that the progress of the process is influenced by the steric hindrance of the alkyl substituent on Pt: after 24 h, the molar ratios of **1-R,R'**/**4-R,R'** are, respectively, 1.8/1 for **1-Me,Me** and **1-Me,Oct** and 4.5/1 for **1-Oct,Me** and **1-Oct,Oct**. This finding indicates that the presence of the octyl chain on the platinum centre represents the major obstacle to exchange. In all cases, no cleavage of the Pt–carbene bond was detected. Figure 6 reports the ^1H NMR spectra of **1-Me,Oct** after dissolution, 1.5, 5, and 24 h.

Attempts to evaluate their stability in aqueous solutions were complicated due the poor solubility of the complexes in water. Only for **1-Me,Me** was it possible to prepare a solution in the mixed solvent $\text{D}_2\text{O}:\text{DMSO-d}_6$ 10:1. After 24 h, no appreciable changes in the NMR spectra of the complex were observed (Figure S17). To further study the stability of **1-Me,Me** in aqueous solvents, UV-vis absorption spectra over time were collected under the two experimental conditions (20% ethylene glycol, 0.1 M sodium acetate buffer at pH 4.0 and 0.6 M sodium nitrate and 2.0 M sodium formate, 0.1 M Hepes buffer at pH 7.5), used to obtain crystals of the adducts with the model protein hen egg white lysozyme (HEWL). HEWL has been used as a model system to study the interaction with proteins of several metallodrugs [27–30], including cisplatin [31–33], oxaliplatin [34,35], and carboplatin [31,32]. The **1-Me,Me** complex appeared more stable in these solutions than in DMSO (Figure S18A,B). Under the first condition, **1-Me,Me** showed three signals: a maximum at 275 nm and two minor peaks at 255 and 313 nm (Figure S18A). Over time, a red shift of the λ_{max} from 275 to 278 nm and of the peak at 313 nm, which shifted up to 317 nm, was observed. Under the other condition, spectra of **1-Me,Me** showed a λ_{max} at

277 nm and a minor peak at 300 nm (Figure S18B). Under this condition, the compound was stable over time and only a slight precipitation of the sample took place. Such results convinced us that five-coordinate compounds are the species administered to cells if DMSO stock solutions are immediately diluted in an aqueous medium.

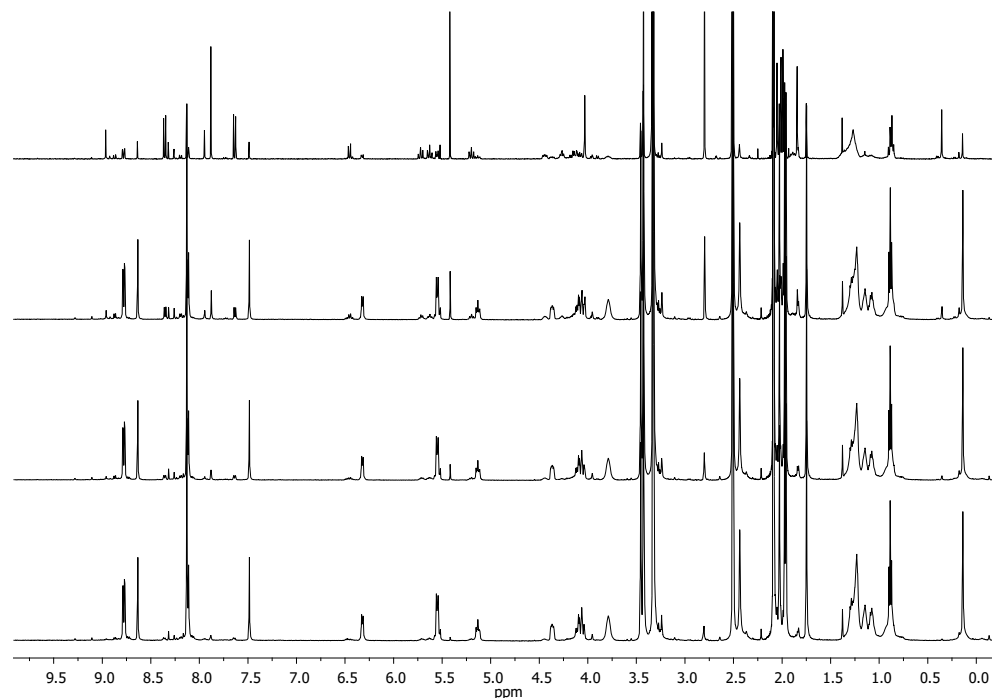


Figure 6. The ^1H NMR spectrum of **1-Me,Oct** in DMSO-d_6 after dissolution (bottom), 1.5, 5, and 24 h (up).

2.3. Partition Coefficients of **1-R,R'** Complexes

The partition coefficients in octanol/water ($\log P_{o/w}$) were measured using the shake-flask method [36], by calculating the equilibrium concentrations through UV spectra (Table 1).

Table 1. Octanol/water partition coefficients.

Complex	Log $P_{o/w}$
1-Me,Me	0.42
1-Me,Oct	0.74
1-Oct,Me	1.14
1-Oct,Oct	0.80

Complexes with the methyl group on the platinum centre are more hydrophilic than the ones with *n*-octyl. Among this first type of complexes, an increase in the length of its R group is connected to an increase in its hydrophobicity. Conversely, for complexes with *n*-octyl on platinum, there is an inversion of this trend. Therefore, the order of hydrophobicity of the complexes is the following: **1-Oct,Me** > **1-Oct,Oct** > **1-Me,Oct** > **1-Me,Me**. This tendency, although counterintuitive because it does not reflect the content of the carbon atoms in the complexes, has already been observed in other studies on platinum agents and has been attributed to the extent of ligand surface exposition [37,38].

2.4. Interaction with DNA

The interaction of Pt-based drugs with biological macromolecules deeply affects their biological activity. DNA represents a target for this kind of metallodrug, while proteins

are considered both as carriers and targets. To obtain information on the reactivity of the synthesised Pt compounds with DNA, fluorescence intercalation displacement assays [39] have been performed using ethidium bromide (EB) as the DNA intercalator. When bound to DNA, EB has an emission fluorescence of significant intensity. On the other hand, when it is displaced by a competitive DNA-binding molecule, it undergoes quenching by water molecules. Thus, if a molecule binds DNA by displacing EB, a significant reduction in the fluorescence intensity of the EB-DNA complex will be observed. Upon addition of **1-Me,Me** to the EB-DNA complex, a significant reduction in fluorescence intensity was found (Figure 7). This finding demonstrates that the complex binds DNA.

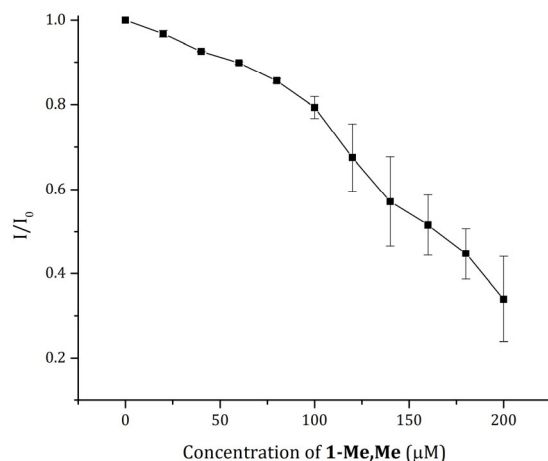


Figure 7. Fluorescence quenching of a 20 μM EB-DNA complex upon titration with a solution of **1-Me,Me** in 0.05 M of ammonium acetate at a pH of 7.5, reported as a function of the Pt compound concentration.

2.5. Interaction with Proteins

To obtain information on the reactivity of **1-Me,Me** with proteins, the X-ray structure of the adducts that the Pt compound forms with HEWL was solved. It was preventively verified that under these conditions, the complex does not degrade in the presence of the protein (Figure S18C,D).

The structures were obtained using crystals grown in 20% ethylene glycol, 0.1 M sodium acetate buffer at pH 4.0, and 0.6 M sodium nitrate (Structure **A**, Figure 8A) and in 2.0 M sodium formate and 0.1 M Hepes at pH 7.5 (Structure **B**, Figure 8B), refined at 1.25 and 1.33 Å resolutions, respectively (Table S2).

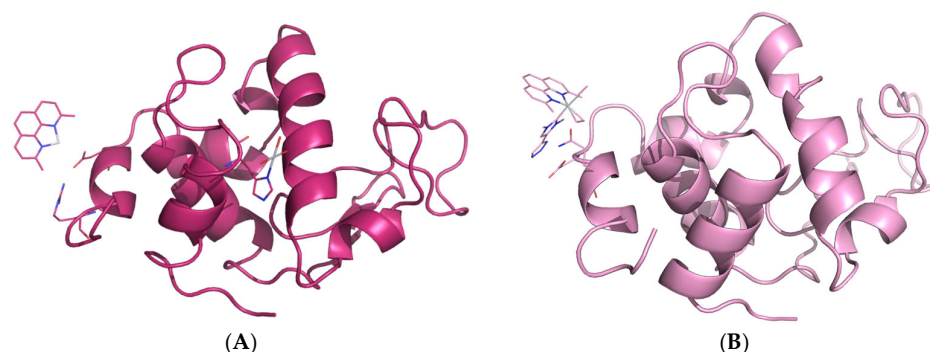


Figure 8. Overall structures of the adducts formed upon the reaction of **1-Me,Me** with HEWL in 20% ethylene glycol, 0.1 M sodium acetate buffer at pH 4.0, and 0.6 M sodium nitrate (Structure **A**) and in 2.0 M sodium formate and 0.1 M Hepes at pH 7.5 (Structure **B**).

In both cases, the Pt compound binding did not significantly affect the protein's tertiary structure. The root mean square deviation of the $\text{C}\alpha$ atoms from the structure of

the metal-free HEWL (PDB code 193L) [40] were within the range of 0.16–0.23 Å. However, under the two conditions, different results were obtained.

In Structure **A**, two Pt binding sites were observed (Figure 9A,B), close to the His15 and Asp119 side chains. In both these binding sites, Pt seems to adopt a square planar geometry, suggesting that the complex lost its 5C geometry. The definition of Pt ligands at these metal binding sites is not clear. In the final Structure **A**, at the His15 binding site, a Pt atom coordinated by water molecules was modelled, while close to Asp119, it appeared that a dmphen ligand could be present. Both His15 and Asp119 have already been identified as Pt binding sites [34,35,41,42]. In Structure **B**, a single Pt binding site was observed (Figure 9C). Notably, in this structure, a Pt-containing fragment non-covalently bound to the protein was found. This Pt-containing fragment retained its 5C geometry. In fact, the electron density map allowed for modelling all the ligands of the platinum centre, if the glucoconjugated part of the carbene ligand was excluded (Figure 9C). This finding agrees with the results of UV–vis absorption spectroscopy suggesting that **1-Me,Me** does not show any variation in its structure in the presence of the protein, under the crystallization conditions used to obtain Structure **B**.

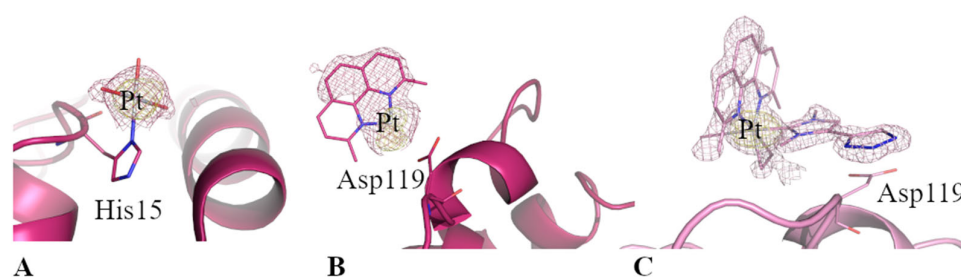


Figure 9. Pt binding sites in Structures **A** (panels **(A,B)**) and **B** (panel **(C)**). Atoms were placed where we were confident of their assignment. The 2Fo-Fc maps (violet) are shown at the 1.0 σ values. An anomalous difference electron density map (yellow) is shown at the 3 σ contour level. The Pt atoms are shown in grey.

2.6. Effects of Complexes on Cell Viability

To evaluate their biological activity, the effects of the four complexes on cell viability were evaluated in eukaryotic cell models. For this purpose, experiments were performed on two cancer cell lines, i.e., human epidermoid carcinoma cells (A431) and murine fibroblast BALB/c-3T3 transformed with the SV40 virus (SVT2), and on two non-cancer cell lines, i.e., immortalized human keratinocytes (HaCaT) and immortalized murine fibroblasts (BALB/c-3T3). Cells were incubated with increasing concentrations of **1,Me-Me**, **1,Oct-Me**, **1,Me-Oct**, and **1,Oct-Oct** (from 0.1 to 50 μ M). After 48 h of incubation, cytotoxicity was determined by MTT assay [43] and cell survival was expressed as the percentage of viable cells in the presence of each complex compared with that of the untreated cells (Figure S19).

The IC₅₀ values (the concentration of the complex able to reduce cell viability to 50%) and the selectivity indexes (SI) (the ratio between the IC₅₀ values of the non-cancer cell line and cancer cells) of the compounds are reported in Table 2.

Table 2. IC₅₀ values (μ M) obtained for Pt complexes on HaCaT, A431, BALB/c-3T3 and SVT2 cells after 48 h incubation. The selectivity indexes (SI) are indicated by the ratios between the IC₅₀ values of the immortalized cells and cancer cells.

	HaCaT	A431	SI	BALB-c/3T3	SVT2	SI
1-Me,Me	8.4 \pm 1.7	20 \pm 2	0.42	26 \pm 1	9.8 \pm 0.3	2.65
1-Me,Oct	8.0 \pm 0.1	7.3 \pm 0.4	1.1	8.3 \pm 0.4	7.6 \pm 1.1	1.09
1-Oct,Me	6.4 \pm 1.0	2.3 \pm 0.1	2.78	7.1 \pm 0.1	8.6 \pm 0.6	0.83
1-Oct,Oct	6.4 \pm 0.8	5.0 \pm 0.6	1.28	7.3 \pm 0.7	4.5 \pm 1.3	1.62

Overall, despite the IC_{50} values being in the low micromolar range, only a slight selectivity towards cancer cells was observed. Interestingly, in the case of the A431 cells, the IC_{50} values increased with hydrophilicity, with **1-Oct,Me** being the most active and **1-Me,Me** being the least. Moreover, the SI decreased with hydrophilicity, suggesting that the higher the hydrophobicity of the drug, the higher the selectivity observed. Indeed, in the case of the A431/HaCaT couple, it was pleasantly observed that greater activity of **1-Oct,Me** was accompanied by a higher SI (2.78). By contrast, in the case of SVT2, the highest SI was found for the most hydrophilic compound (**1-Me,Me**, SI of 2.65) with respect to **1-Oct,Me**, which showed the lowest SI value.

2.7. Cytotoxicity Pathways of **1-Me,Me** and **1-Oct,Me**

To further investigate the molecular mechanisms of cell death induced by the two complexes that showed the highest SI values, the effects of **1-Me,Me** and **1-Oct,Me** were analysed in cancer cells. In particular, SVT2 and A431 were incubated for 48 h with **1-Me,Me** and **1-Oct,Me**, using the IC_{50} value concentrations. At the end of incubation, uptake and cell death mechanisms were evaluated. As shown in Table 3, both complexes were able to enter cells, but **1-Oct,Me** was more internalized on A431 with respect to **1-Me,Me** on SVT2. This result is in agreement with the higher toxicity of **1-Oct,Me**, as it is better able to enter cells at a lower concentration. Finally, apoptosis was investigated by Western blot analyses using specific antibodies against pro-caspases 9 and 3. As shown in Figure 10, both complexes were able to induce the activation of apoptosis, as a significant decrease in pro-caspases 9 and 3 levels was observed in both cell lines.

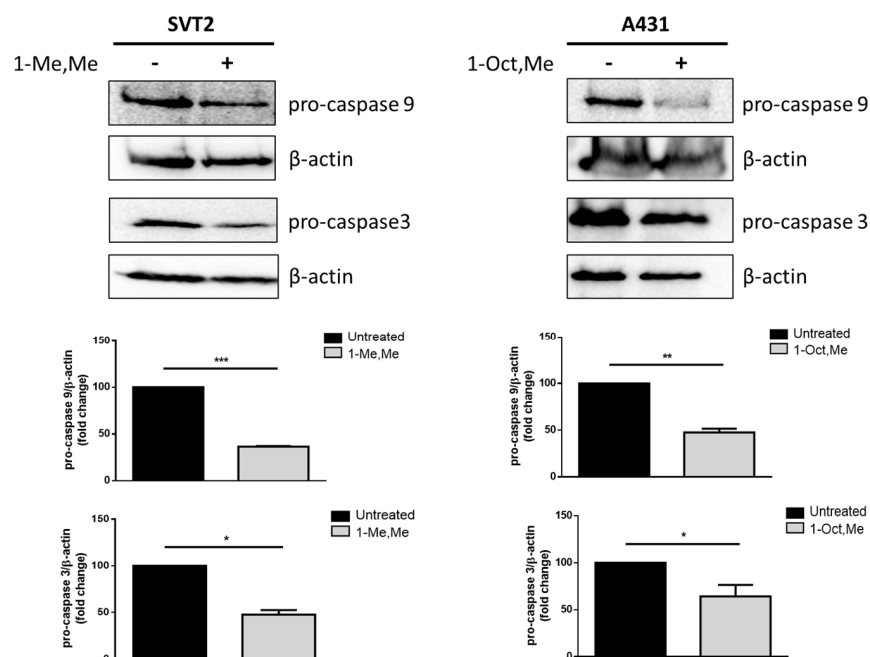


Figure 10. Apoptosis analysis in cancer cell lines. Cells were incubated with the molecule being tested, with each one at its IC_{50} value ($9.8 \mu\text{M}$ **1-Me,Me** on SVT2 and $2.3 \mu\text{M}$ **1-Oct,Me** on A431). After 48 h, protein extracts were analysed by Western blot using anti-pro-caspases 9 and 3. β -actin was used as the loading control. The densitometric analysis is reported below the Western blot images. Black bars, untreated cells; grey bars, treated cells. Data shown are the means \pm S.D. of three independent experiments. * indicates $p < 0.05$; ** indicates $p < 0.01$; *** indicates $p < 0.001$ with respect to untreated cells.

Table 3. The uptake of **1-Me,Me** and **1-Oct,Me** in cancer cells. Cells were incubated with either **1-Me,Me** or **1-Oct,Me**, with each one tested at its IC₅₀ value (9.8 μM **1-Me,Me** on SVT2 and 2.3 μM **1-Oct,Me** on A431). After 48 h, cells were analysed by ICP analysis, as described in the Materials and Methods section. Data shown are the means ± S.E. of three independent experiments.

Samples	Pt ng/10 ⁶ cells
Untreated SVT2	<0.0001
SVT2 incubated with 1-Me,Me	0.772 ± 0.010
Untreated A431	<0.0001
A431 incubated with 1-Oct,Me	14.3 ± 1.3

3. Materials and Methods

All solvents and reagents were purchased from Merck KGaA (Darmstadt, Germany) and used without any further purification. NMR spectra were recorded using a 400 Bruker Avance with Ultrashield or a 500 Varian Inova spectrometer at 298 K. Chemical shifts are given in parts per million (ppm, δ), referenced to the solvent peaks of CDCl₃ (¹H NMR δ = 7.26, ¹³C NMR δ = 77), DMSO-d₆ (¹H NMR δ = 2.50, ¹³C NMR δ = 39.52), and D₂O (¹H NMR δ = 4.79 ppm). Coupling constants are quoted in Hz (J). The ¹H NMR and ¹³C NMR splitting patterns were designated as singlet (s), doublet (d), triplet (t), quartet (q), double doublet (dd), and broad (br). Splitting patterns with a difficult interpretation or visualization were designated as multiplet (m). The compounds **Im-Me** [44], [Pt(dmphen)(ethene)] [45], and **2-Me** [44] were prepared according to procedures in the literature. In describing the NMR assignments, the scheme adopted for numbering the carbon atoms within the rings is reported as the following (Figure 11).

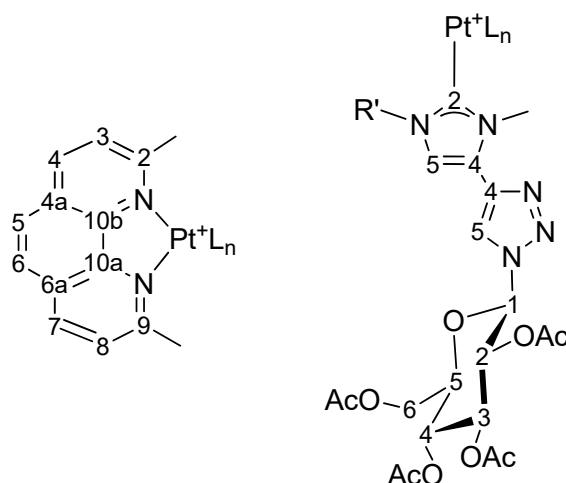


Figure 11. Numbering scheme for the carbon atoms within the rings.

For the ICP-MS analyses, high-purity water (resistivity of 18.2 MΩ cm) was obtained from a Milli-Q unit (Millipore, Burlington, MA, USA) and was used for the standard solution preparation and sample dilutions. Nitric acid (HNO₃, 69% v/v Ultratrace[®] ppb-trace analysis grade) was provided by Scharlab (Barcelona, Spain). A certified reference solution containing Pt at 100 mg/L of ultrapure grade for ICP by VWR Avantor[®] (Radnor Township, PA, USA) was used.

3.1. Synthesis of **Im-Oct**

n-Octyl iodide (0.85 mL, 4.7 mmol) was added to a solution of **Im** (0.15 g, 0.31 mmol) in 2 mL of acetonitrile. The light yellow solution was stirred under reflux for 3 h. The solvent was removed and the orange oil was washed with *n*-hexane. A white powder was obtained (yield: 97%). ¹H NMR (500 MHz, 298 K, CDCl₃): δ 10.17 (s, 1H, H2 imidazolium), 8.71 (s, 1H, H5 triazole), 7.72 (s, 1H, H5 imidazolium), 6.02 (d, 1H, ³J_{H1-H2} = 9.3 Hz, H1

glu), 5.57 (t, 1H, $^3J_{H2-H3} = 9.4$ Hz, H2 glu), 5.46 (t, 1H, $^3J_{H3-H4} = 9.5$ Hz, H3 glu), 5.31 (t, 1H, $^3J_{H4-H5} = 9.8$ Hz, H4 glu), 4.41–4.30 (m, 3H, H6 glu, and NCH₂), 4.22 (s, 3H, nMe), 4.19 (dd, 1H, $^2J_{H6-H6'}$ overlapped, $^3J_{H5-H6} = 1.8$ Hz, H6' glu), 4.15–4.08 (m, 1H, H5 glu), 2.09 (s, 3H, OAc), 2.07 (s, 3H, OAc), 2.04 (s, 3H, OAc), 2.02–1.93 (m, 2H, CH₂), 1.90 (s, 3H, OAc), 1.47–1.17 (m, 10H, CH₂), and 0.95–0.77 (m, 3H, Me). ¹³C NMR (125 MHz, 298 K, CDCl₃): δ 170.6 (CO), 169.9 (CO), 169.4 (CO), 169.0 (CO), 137.7 (C2 imidazole), 134.1 (C4 imidazole), 126.4 (C4 triazole), 124.0 (C5 triazole), 120.2 (C5 imidazole), 85.8 (C1 glu), 75.3, 72.6, 70.5, and 67.6 (C2–C5 glu), 61.5 (C6 glu), 50.7 (NCH₂), 36.7 (nMe), 31.7, 30.2, 29.1, 29.0, 26.3, and 22.6 (6 CH₂), 20.9 (OAc), 20.6 (x2, OAc), 20.4 (OAc), and 14.1 (Me).

3.2. Synthesis of 2-Oct

n-Octyl iodide (0.5 mL, 2.7 mmol) was added to a suspension of [Pt(dmphen)(ethene)] (0.43 g, 1.0 mmol) in 5 mL of dry toluene and the mixture was stirred at room temperature. After 1 h, *n*-hexane was added to complete the precipitation of a yellow solid, which was recovered and washed with *n*-hexane. The solid was dissolved in dichloromethane, and the solution was filtered on a thin pad of FLORISIL[®] (100–200 mesh) and crystallized with *n*-hexane (light brown solid—yield: 65%). ¹H NMR (500 MHz, 298 K, CDCl₃): δ 8.31 (d, 2H, $J = 8.2$ Hz, H4 and H7 dmphen), 7.85 (s, 2H, H5 and H6 dmphen), 7.77 (d, 2H, $J = 8.2$ Hz, H3 and H8 dmphen), 3.33 (s, 6H, Me dmphen), 3.31 (dd, 2H, $J_{Pt} = 85.2$ Hz, H ethene—partially overlapped), 2.22 (dd, 2H, $J_{Pt} = 62.0$ Hz, ethene), 1.14–0.7 (m, 12H, H_{aliphatic}), 0.75 (t, 3H, $J = 7.3$ Hz, Me aliphatic), and 0.36–0.23 (m, 2H). ¹³C NMR (125.7 MHz, 298 K, CDCl₃): δ 161.2 (x2, C2 and C9 dmphen), 145.2 (x2, C10a and C10b dmphen), 137.3 (x2, C4 and C7 dmphen), 128.5 (x2, C4a and C6a dmphen), 126.1 (x2, C5 and C6 dmphen), 125.8 (x2, C3 and C8 dmphen), 31.7, 31.0 (x2), 30.7 and 30.3 (5 CH₂), 29.2 (x2, Me dmphen), 28.9 (x2) (ethene, $J_{Pt} = 382$ Hz), 22.6 (CH₂), 19.6 (PtCH₂, $J_{Pt} = 638$ Hz), and 14.1 (Me).

3.3. Synthesis of Ag-R' Complexes

The appropriate **Im-R'** precursor (0.30 mmol) was dissolved in 6 mL of acetone. Then, silver(I) oxide (0.046 g, 0.20 mmol) was added. The colourless mixture was stirred for 2 h in the dark. The light yellow mixture was filtered on a Celite[®] to remove the excess of silver oxide and the resulting colourless solution was used in situ as described in the following paragraph.

3.4. Synthesis of 1-R,R' Complexes

The appropriate type **2-R** complex (0.30 mmol) was suspended in 6 mL of acetone. Then, thallium triflate (0.10 g, 0.30 mmol) was added and the yellow mixture was stirred for 15 min. The suspension was centrifuged to separate the thallium chloride. The resulting solution, containing the type **3-R** complex, was treated with the solution of **Ag-R'** prepared as described above. The mixture was stirred for 60 h in the dark. The resulting solution was filtered on a Celite[®] to separate the silver iodide. The solvent was removed and a solid was obtained. The crude residue was dissolved in dichloromethane and filtered on a pad of basic activated aluminium oxide. The solution was treated with diethyl ether until the precipitation of a solid and subsequently washed again with diethyl ether. The products were obtained as yellow/light brown solids. **1-Me,Me** (yellow solid—yield: 55%). ¹H NMR (500 MHz, 298 K, CDCl₃): δ 8.49 (s, 1H, H5 triazole), 8.47 (d, $^3J_{H4-H5}$ or $H7-H6 = 8.1$, 1H, H4 or H7 dmphen), 8.45 (d, $^3J_{H7-H8}$ or $H4-H5 = 8.1$, 1H, H7 or H4 dmphen), 7.94–7.86 (m, 4H, H3, H5, H6, H8 dmphen), 7.08 (s, 1H, H5 imidazole), 5.85 (d, 1H, $^3J_{H1-H2} = 9.4$ Hz, H1 glu), 5.75 (t, 1H, $^3J_{H2-H3} = 9.4$ Hz, H2 glu), 5.35 (t, 1H, $^3J_{H3-H4} = 9.4$ Hz, H3 glu), 5.24 (t, 1H, $^3J_{H4-H5} = 9.8$ Hz, H4 glu), 4.25 (dd, 1H, $^2J_{H6-H6'} = 12.6$ Hz, $^3J_{H5-H6} = 4.6$ Hz, H6 glu), 4.13 (dd, 1H, $^2J_{H6'-H6} = 12.6$ Hz, $^3J_{H5-H6'} = 1.9$ Hz, H6' glu), 4.05–4.00 (m, 1H, H5 glu), 3.56 (s, 3H, N-Me), 3.45 (s, 6H, Me dmphen), 3.33 (s, 3H, N-Me), 2.48 (AA'BB', 4 H, $J_{Pt} = 68.4$ Hz, ethene), 2.03 (s, 6H, OAc), 1.99 (s, 3H, OAc), 1.78 (s, 3H, OAc), and 0.18 (s, 3H, $J_{Pt} = 45.7$ Hz, PtMe). ¹³C NMR (100 MHz, 298 K, CDCl₃): δ 172.1 (C carbene), 170.7 (CO), 170.1 (CO), 169.4 (CO), 168.8 (CO), 161.3 and 161.2 (C2 and C9 dmphen), 145.9 (x2, C10a and C10b

dmphen), 138.9 and 138.8 (C4 and C7 dmphen), 135.9 (C4 imidazole), 128.7 (x2, C4a and C6a dmphen), 126.7 and 126.6 (C5 and C6 dmphen), 126.1 and 126.0 (C3 and C8 dmphen), 125.6 (C4 triazole), 124.5 and 122.0 (C5 triazole and C5 imidazole), 121.0 (q, CF₃, $J_{C-F} = 321$ Hz), 85.1 (C1 glu), 74.8, 73.4, 70.0 and 67.7 (C2–C5 of glu), 61.5 (C6 of glu), 37.2 (nMe), 36.4 (nMe), 30.1 (x2, ethene, $J_{Pt} = 355$ Hz), 28.7 (x2, Me dmphen), 20.8 (OAc), 20.7 (x2, OAc), 20.3 (OAc), and -6.6 (PtMe, $J_{Pt} = 464$ Hz). Calculated for C₃₉H₄₆F₃N₇O₁₂PtS: C, 43.01; H, 4.26; and N, 9.00. Found: C, 43.28; H, 4.33; and N, 8.87. **1-Me,Oct** (yellow solid—yield: 63%). ¹H NMR (400 MHz, 298 K, CDCl₃): δ 8.62 (s, 1H, H5 triazole), 8.47 (d, ³ J_{H4-H5} or $H7-H6 = 8.7$, 1H, H4 or H7 dmphen), 8.45 (d, 1H, ³ J_{H7-H8} or $H4-H5 = 8.7$, H7 or H4 dmphen), 7.96–7.82 (m, 4H, H3, H5, H6, H8 dmphen), 7.09 (s, 1H, H5 imidazole), 5.89 (d, 1H, ³ $J_{H1-H2} = 9.4$ Hz, H1 glu), 5.82 (t, 1H, ³ $J_{H2-H3} = 9.2$ Hz, H2 glu), 5.36 (t, 1H, ³ $J_{H3-H4} = 9.2$ Hz, H3 glu), 5.25 (t, 1H, ³ $J_{H4-H5} = 9.7$ Hz, H4 glu), 4.26 (dd, 1H, ² $J_{H6-H6'} = 12.7$ Hz, ³ $J_{H5-H6} = 4.5$ Hz, H6 glu), 4.14 (dd, 1H, ² $J_{H6'-H6} = 12.7$, ³ $J_{H5-H6'} = 2.3$ Hz, H6' glu), 4.09–4.01 (m, 1H, H5 glu), 3.70 (br, 2H, NCH₂), 3.57 (s, 3H, nMe), 3.45 (s, 6H, Me dmphen), 2.47 (AA'BB', 4 H, $J_{Pt} = 68.4$ Hz, ethene), 2.04 (s, 3H, OAc), 2.03 (s, 3H, OAc), 1.99 (s, 3H, OAc), 1.78 (s, 3H, OAc), 1.40–1.10 (m, 12H, CH₂), 0.92 (t, 3H, Me), and 0.19 (s, 3H, $J_{Pt} = 46.5$ Hz, PtMe). ¹³C NMR (100 MHz, 298 K, CDCl₃): δ 172.0 (C carbene), 170.7 (CO), 170.1 (CO), 169.4 (CO), 168.7 (CO), 161.1 and 161.0 (C2 and C9 dmphen), 145.9 (x2, C10a and C10b dmphen), 138.8 and 138.7 (C4 and C7 dmphen), 135.8 (C4 imidazole), 128.7 and 128.6 (C4a and C6a dmphen), 126.7 and 126.5 (C5 and C6 dmphen), 126.4 and 126.2 (C3 and C8 dmphen), 126.1 (C4 triazole), 124.7 (C5 triazole), 121.0 (q, CF₃, $J_{C-F} = 321$ Hz), 118.9 (C5 imidazole), 85.0 (C1 glu), 74.7, 73.4, 69.9 and 67.6 (C2–C5 glu), 61.5 (C6 glu), 49.5 (NCH₂), 36.4 (nMe), 31.8 (CH₂), 30.6 (CH₂), 30.1 and 30.0 (ethene), 29.3 (CH₂), 29.2 (CH₂), 28.7 (x2, Me dmphen), 26.8 (CH₂), 22.7 (CH₂), 20.7 (OAc), 20.6 (x2, OAc), 20.3 (OAc), 14.1 (Me), and -6.6 (PtMe, $J_{Pt} = 466$ Hz). Calculated for C₄₆H₆₀F₃N₇O₁₂PtS: C, 46.54; H, 5.09; and N, 8.26. Found: C, 46.39; H, 5.14; and N, 8.20. **1-Oct,Me** (light brown solid—yield 62%). ¹H NMR (400 MHz, 298 K, CDCl₃): δ 8.49 (d, 1H, ³ J_{H4-H3} or $H7-H8 = 6.9$, H4 or H7 dmphen), 8.49 (s, 1H, H5 triazole), 8.47 (d, 1H, ³ J_{H7-H8} or $H4-H3 = 6.8$, H7 or H4 dmphen), 7.96–7.86 (m, 4H, H3, H5, H6, H8 dmphen), 7.06 (s, 1H, H5 imidazole), 5.85 (d, 1H, ³ $J_{H1-H2} = 9.3$ Hz, H1 glu), 5.75 (t, 1H, ³ $J_{H2-H3} = 9.4$ Hz, H2 glu), 5.35 (t, 1H, ³ $J_{H3-H4} = 9.3$ Hz, H3 glu), 5.24 (t, 1H, ³ $J_{H4-H5} = 9.7$ Hz, H4 glu), 4.25 (dd, 1H, ² $J_{H6-H6'} = 12.6$ Hz, ³ $J_{H5-H6} = 4.7$ Hz, H6 glu), 4.13 (dd, 1H, ³ $J_{H5-H6'} = 1.8$ Hz, H6' glu), 4.06–4.00 (m, 1H, H5 glu), 3.52 (s, 3H, N-Me), 3.46 (s, 6H, Me dmphen), 3.29 (s, 3H, N-Me), 2.37 (s, 4 H, $J_{Pt} = 75.5$ Hz, ethene), 2.03 (s, 6H, OAc), 1.99 (s, 3H, OAc), 1.78 (s, 3H, OAc), 1.13 (t, 2H, ³ $J = 7$ Hz, $J_{Pt} = 62.2$ Hz, Pt-CH₂), 1.10–0.92 (m, 8H, CH₂), 0.90–0.80 (m, 2H, CH₂), 0.77 (t, 3H, Me), and 0.56 (br, 2H, CH₂). ¹³C NMR (100 MHz, 298 K, CDCl₃): δ 173.8 (C carbene), 170.8 (CO), 170.1 (CO), 169.4 (CO), 168.8 (CO), 161.0 and 160.9 (C2 and C9 dmphen), 145.8 and 145.7 (C10a and C10b dmphen), 138.8 and 138.7 (C4 and C7 dmphen), 135.9 (C5 imidazole), 128.8 (x2, C4a and C6a dmphen), 126.8 and 126.7 (C5 and C6 dmphen), 126.1 and 125.9 (C3 and C8 dmphen), 125.7 (C4 triazole), 124.4 and 122.0 (C5 triazole and C4 imidazole), 121.0 (q, CF₃, $J_{C-F} = 317$ Hz), 85.1 (C1 glu), 74.8, 73.3, 70.0 and 67.6 (C2–C5 glu), 61.5 (C6 glu), 37.1 (nMe), 36.4 (nMe), 33.3 (CH₂), 31.8 (CH₂), 30.9 and 30.8 (ethene), 30.0, 29.2, 29.1 and 28.9 (x2) (3 CH₂ and Me dmphen), 22.6 (CH₂), 20.7 (OAc), 20.6 (x2, OAc), 20.3 (OAc), 14.1 (Me), and 13.8 (PtCH₂, $J_{Pt} = 458$ Hz). Calculated for C₄₆H₆₀F₃N₇O₁₂PtS: C, 46.54; H, 5.09; and N, 8.26. Found: C, 46.73; H, 4.99; and N, 8.35. **1-Oct,Oct** (light brown solid—yield 71%). ¹H NMR (400 MHz, 298 K, CDCl₃): δ 8.61 (s, 1H, H5 triazole), 8.49 (d, 1H, ³ J_{H4-H3} or $H7-H8 = 8.7$ Hz, H4 or H7 dmphen), 8.47 (d, ³ J_{H7-H8} or $H4-H3 = 8.9$ Hz, 1H, H7 or H4 dmphen), 7.98–7.82 (m, 4H, H3, H5, H6, H8 dmphen), 7.06 (s, 1H, H5 imidazole), 5.89 (d, 1H, ³ $J_{H1-H2} = 9.4$ Hz, H1 glu), 5.82 (t, 1H, ³ $J_{H2-H3} = 9.2$ Hz, H2 glu), 5.35 (t, 1H, ³ $J_{H3-H4} = 9.2$ Hz, H3 glu), 5.25 (t, 1H, ³ $J_{H4-H5} = 9.7$ Hz, H4 glu), 4.26 (dd, 1H, ² $J_{H6-H6'} = 12.7$ Hz, ³ $J_{H5-H6} = 4.6$ Hz, H6 glu), 4.14 (dd, 1H, ³ $J_{H5-H6'} = 2.1$ Hz, H6' glu), 4.09–3.99 (m, 1H, H5 glu), 3.65 (br, 2H, N-CH₂), 3.53 (s, 3H, N-Me), 3.46 (s, 6H, Me dmphen), 2.36 (s, 4 H, $J_{Pt} = 73$ Hz, ethene), 2.04 (s, 3H, OAc), 2.03 (s, 3H, OAc), 1.99 (s, 3H, OAc), 1.78 (s, 3H, OAc), 1.40–1.20 (m, 10H, CH₂), 1.13 (t, 2H, Pt-CH₂), 1.10–0.90 (m, 10H, CH₂), 0.91 (t, 3H, ³ $J = 7$ Hz, Me), 0.77 (t, 3H, Me), and 0.55 (br, 2H, CH₂). ¹³C NMR (125 MHz, 298 K,

CDCl₃): δ 173.6 (C carbene, $J_{Pt} = 702$ Hz), 170.8 (CO), 170.1 (CO), 169.4 (CO), 168.8 (CO), 160.8 (x2, C2 and C9 dmphen), 145.8 (x2, C10a and C10b dmphen), 138.7 and 138.6 (C4 and C7 dmphen), 135.8 (C4 imidazole), 128.8 and 128.7 (C4a and C6a dmphen), 126.8 and 126.6 (C5 and C6 dmphen), 126.6 and 126.3 (C3 and C8 dmphen), 126.1 (C4 triazole), 124.8 (C5 triazole), 118.9 (C5 imidazole), 85.0 (C1 glu), 74.7, 73.5, 69.9 and 67.7 (C2–C5 glu), 61.5 (C6 glu), 49.4 (NCH₂), 36.4 (nMe), 33.3 (CH₂), 31.8 (x2, CH₂), 30.9 (x2, ethene), 30.6, 29.9, 29.4, 29.3, 29.2, 29.1 and 28.9 (x2) (6 CH₂ and Me dmphen), 26.8 (CH₂), 22.7 (x2, CH₂), 20.8 (OAc), 20.7 (x2, OAc), 20.4 (OAc), 14.2 (Me), 14.1 (Me), and 13.7 (PtCH₂). Calculated for C₅₃H₇₄F₃N₇O₁₂PtS: C, 49.53; H, 5.80; and N, 7.63. Found: C, 49.32; H, 5.71; and N, 7.52.

3.5. In-Solution Stability of 1-R,R' Complexes

The stability of the **1-R,R'** complexes in DMSO was studied by dissolving 5 mg of each complex in 250 μ L of DMSO-d₆ and then diluting 200 μ L of this solution with 300 μ L of DMSO-d₆. The stability of the **1-R,R'** complexes in aqueous solvents was studied by dissolving 5 mg of each complex in 250 μ L of DMSO-d₆ and then diluting 50 μ L of this solution with 500 μ L of D₂O. The ¹H-NMR spectra of the resulting solutions were recorded over time.

UV–vis absorption spectra of **1-Me,Me** were collected at 25 °C on a JASCO V-750 UV–vis spectrophotometer in the range of 240–500 nm, using a platinum compound concentration of 50 μ M in 100% DMSO as well as under the crystallization conditions of 20% ethylene glycol, 0.1 M sodium acetate buffer at pH 4.0, and 0.6 M sodium nitrate and 2.0 M sodium formate and 0.1 M Hepes at pH 7.5, in the absence and in the presence of HEWL. The HEWL:**1-Me,Me** molar ratio was 1:3. Each measurement was repeated three times.

3.6. Partition Coefficients

Partition coefficients for the platinum complexes were determined in triplicate in an *n*-octanol/water system, with different ratios (1:1, 1:2, 2:1). Each complex was dissolved in *n*-octanol at the concentrations 16.7, 12.5, or 10 μ M and subsequently, an appropriate volume of water was added. The mixtures were shaken mechanically for 1 h to ensure the distribution between the two solvent phases. The samples were then centrifuged (13,000 rpm, 10 min). Afterwards, the platinum concentration was determined in the octanol phases by UV–vis spectrophotometry, after collecting a calibration line for each complex. Results are expressed as the logarithm of the partition coefficient of octanol/water ($\log P_{o/w}$), which is the logarithm of the concentration of platinum in the *n*-octanol divided by its concentration in the aqueous layer.

3.7. DNA Binding Assays

The ethidium bromide (EB) displacement assay was performed on a HORIBA Fluoro Max-4 spectrofluorometer equipped with a thermostat bath. Calf thymus DNA was incubated with EB in 0.05 M of ammonium acetate at pH 7.5, at a DNA:EB molar ratio of 1:5 for 30 min in the dark at room temperature. Then, the fluorescence quenching of this complex was evaluated by adding to it increasing amounts of Pt compounds dissolved in DMSO (20 mM). Samples were equilibrated for 5 min before collecting each spectrum. The other experimental settings comprised the following: a 1.0 cm quartz cell, 5.0 nm excitation/emission slit, 560–750 nm range, and 50 nm minutes^{−1} scanning speed. Data were obtained as the average of three independent measurements.

3.8. Crystallization of the Adducts Formed by the Reaction of 1-Me,Me with HEWL

HEWL crystals were grown using the hanging drop vapour diffusion method and the following reservoirs:

- (a) 20% ethylene glycol, 0.10 M sodium acetate at pH 4.0, and 0.60 M sodium nitrate
- (b) 2.0 M sodium formate and 0.1 M HEPES at pH 7.5.

The crystals of the protein adduct with **1-Me,Me** were obtained by the soaking procedure. The HEWL crystals were soaked in a solution consisting of 83% reservoir, 17% DMSO, and 3.3 mM **1-Me,Me**.

3.9. Structure Solution and Refinement of Structures A and B

The structures of the Pt–HEWL adducts were solved by the molecular replacement method, using the HEWL coordinates deposited in the PDB under the accession code 193L [40] as a model. Refinements were carried out with a CCP4 REFMAC5 [46], and the model building, adjustments, and inspection of the electron density maps was manually carried out using WinCoot [47].

The Pt binding sites were unambiguously identified by comparing 2Fo–Fc, residual Fo–Fc, and anomalous difference electron density maps. The two structures were refined to the R -factor/ R_{free} values of 0.187/0.219 and 0.184/0.218, respectively. The details of the crystallographic and refinement parameters are given in Table S2. The refined models and structure factors were deposited in the Protein Data Bank under the accession codes 8BOY and 8BOV. The coordinates and structure factors, including anomalous data, were provided to the reviewers and editor for the review process.

3.10. Cell Culture and Cytotoxicity

The immortalized human keratinocytes (HaCaT) were from Innoprot. Human The A431 epidermoid carcinoma, murine BALB/c-3T3, and SVT2 fibroblasts were from ATCC. Cells were cultured in Dulbecco's modified Eagle's medium (DMEM) (Sigma-Aldrich, St. Louis, MO, USA), supplemented with 10% foetal bovine serum (HyClone), 2 mM L-glutamine, and antibiotics, all from Sigma-Aldrich, under a 5% CO₂-humidified atmosphere at 37 °C. To test the effects of the complexes on cell viability, cells were seeded at a density of 2.5×10^3 cells per well in 96-well plates. After 24 h, cells were incubated with increasing concentrations (from 0.1 to 50 µM) of the four complexes. After 48 h, cell viability was assessed by the MTT assay, as previously reported in [43]. Cell viability was expressed as the percentage of viable cells in the presence of the Pt complexes compared to the controls, represented by untreated cells and cells supplemented with identical volumes of DMSO. Each sample was tested in three independent analyses, each carried out in triplicate.

3.11. Uptake Experiments

To study the uptake of the complexes, SVT2 and A431 were incubated for 48 h in the presence of **1-Me,Me** and **1-Oct,Me**, respectively, at their IC₅₀ concentrations. At the end of incubation, Pt determination was performed by inductively coupled plasma mass spectrometry (ICP-MS, Aurora M90; Bruker, Ettlingen/Leipzig, Germany) in the "Normal Sensitivity" mode. Calibration curves for the quantification of Pt ranged from 0.1 to 100 µg/L and were constructed daily by the analysis of the standard solutions prepared immediately before analysis. All standards used for analysis were prepared in HNO₃ solution (2%, v/v). The internal standards were ⁸⁹Y and ¹¹⁵In in both the calibration curve and sample analyses. The linearity was acceptable with an R² value greater than 0.9996. The treatment of the cells involved a wet digestion: after centrifugation, cell samples were wet digested with 1 mL of ultrapure HNO₃ (67–69%, v/v). The mixture was gently boiled over a water bath (90 °C) for 3 h until a clear solution was obtained. After cooling, HNO₃ solution (2%, v/v) was added up to a final volume of 10 mL. The obtained solutions were analysed by ICP-MS. Under this condition, the quantification limit for Pt was equal to 0.001 ng Pt/10⁶ cells.

3.12. Western Blot Analysis

The SVT2 were seeded on six-well plates at a density of 2.5×10^5 cells/well, whereas A431 was seeded at a density of 3×10^5 cells/well. After 24 h, cells were treated with 9.8 µM of **1-Me,Me** or 2.3 µM **1-Oct,Me**. After 48 h of incubation, Western blot analyses were performed by using pro-caspase 9 (Cell Signaling Technology, Danvers, MA, USA) and pro-

caspase 3 (Abcam, Cambridge, MA, USA) antibodies, as reported by Del Giudice et al. [48] Protein intensity levels were normalized using β -actin (Sigma-Aldrich, St. Louis, MO, USA). The chemiluminescence detection system was purchased from Bio-Rad (Hercules, CA, USA).

3.13. Statistical Analysis

All experiments were performed in triplicate. The results are presented as the mean of the results obtained after three independent experiments and compared by one-way ANOVA according to Bonferroni's method (post hoc), obtained using GraphPad Prism for Windows, version 6.01.

4. Conclusions

This study demonstrates the versatility of platinum(II) anticancer agents with a coordination number of five. Previous studies on methyl/carbene complexes with trigonal bipyramidal geometry [14] have demonstrated that their structural diversity is enriched by introducing variable-length alkyl groups in strategic positions of the coordination environment. This allows for a comparison of biological activity among complexes with different lipophilicity, revealing different behaviours of the drug being tested, depending on the cell system being analysed. The tested drug was internalized in cancer cells and able to activate the apoptotic pathway. One might speculate that the activity of the complexes may reside in the different compositions of their plasma membranes. Accordingly, changes in the structural arrangements of membrane lipids may influence their lipid core and consequently their overall surface properties [49,50]. The structural study also revealed a variety of interactions between the metal fragment and the model protein HEWL. In one of these, the metal complex retained its 5C geometry and established non-covalent interactions with the protein. These data, along with the observation that the same complex is stable for days in an aqueous solvent, demonstrate the great structural robustness of this class of compounds and encourage further study towards understanding and optimization.

Supplementary Materials: The following supporting information can be downloaded at: <https://www.mdpi.com/article/10.3390/ijms24032369/s1>.

Author Contributions: Conceptualization, D.M.M., A.M. (Antonello Merlino) and F.R.; methodology, A.A., M.M., V.L., G.T. and M.T.; validation, G.F., P.I., M.E.C., A.M. (Alessandra Marano) and M.T.; investigation, A.A., G.F., V.L., A.M. (Alessandra Marano), M.M., P.I. and G.T.; data curation, A.A., M.E.C., G.F., V.L., A.M. (Alessandra Marano), M.M., G.T. and M.T.; writing—original draft preparation, A.A., P.I., D.M.M., A.M. (Antonello Merlino) and F.R.; writing—review and editing, M.M., D.M.M., A.M. (Antonello Merlino) and F.R.; supervision, F.R.; funding acquisition, D.M.M. and F.R. All authors have read and agreed to the published version of the manuscript.

Funding: This research was funded by the Università di Napoli Federico II, grant number "000023_AL-TRI_CDA_75_2021_FRA_RUFFO".

Institutional Review Board Statement: Not applicable.

Informed Consent Statement: Not applicable.

Data Availability Statement: Data is contained within the article or supplementary material.

Conflicts of Interest: The authors declare no conflict of interest.

References

1. Rosenberg, B.; Vancamp, L.; Trosko, J.E.; Mansour, V.H. Platinum Compounds: A New Class of Potent Antitumour Agents. *Nature* **1969**, *222*, 385–386. [CrossRef] [PubMed]
2. Oun, R.; Moussa, Y.E.; Wheate, N.J. Oun, R.; Moussa, Y.E.; Wheate, N.J. The side effects of platinum-based chemotherapy drugs: A review for chemists. *Dalton Trans.* **2018**, *47*, 6645–6653. [CrossRef] [PubMed]
3. Johnstone, T.C.; Suntharalingam, K.; Lippard, S.J. The Next Generation of Platinum Drugs: Targeted Pt(II) Agents, Nanoparticle Delivery, and Pt(IV) Prodrugs. *Chem. Rev.* **2016**, *116*, 3436–3486. [CrossRef]

4. Kenny, R.G.; Marmion, C.J. Toward Multi-Targeted Platinum and Ruthenium Drugs—A New Paradigm in Cancer Drug Treatment Regimens? *Chem. Rev.* **2019**, *119*, 1058–1137. [CrossRef]
5. Wai-Yin Sun, R.; Lok-Fung Chow, A.; Li, X.-H.; Yan, J.J.; Sin-Yin Chui, S.; Che, C.-M. Luminescent cyclometalated platinum(II) complexes containing N-heterocyclic carbene ligands with potent in vitro and in vivo anti-cancer properties accumulate in cytoplasmic structures of cancer cells. *Chem. Sci.* **2011**, *2*, 728–736. [CrossRef]
6. Zhao, W.; Ferro, V.; Baker, M.V. Carbohydrate–N-heterocyclic carbene metal complexes: Synthesis, catalysis and biological studies. *Coord. Chem. Rev.* **2017**, *339*, 1–16. [CrossRef]
7. Bouché, M.; Bonnefont, A.; Achard, T.; Bellemin-Lapponnaz, S. Exploring diversity in platinum(IV) N-heterocyclic carbene complexes: Synthesis, characterization, reactivity and biological evaluation. *Dalton Trans.* **2018**, *47*, 11491–11502. [CrossRef] [PubMed]
8. Zou, T.; Lok, C.-N.; Wan, P.-K.; Zhang, Z.-F.; Fung, S.-K.; Che, C.-M. Anticancer metal-N-heterocyclic carbene complexes of gold, platinum and palladium. *Curr. Opin. Chem. Biol.* **2018**, *43*, 30–36. [CrossRef]
9. Cucciolito, M.E.; Trinchillo, M.; Iannitti, R.; Palumbo, R.; Tesauro, D.; Tuzi, A.; Ruffo, F.; D’Amora, A. Sugar-Incorporated N-Heterocyclic-Carbene-Containing Complexes: Synthesis, Characterization, and Cytotoxic. *Eur. J. Inorg. Chem.* **2017**, *316*, 4855–4961. [CrossRef]
10. Rehm, T.; Rothmund, M.; Bär, A.; Dietel, T.; Kempe, R.; Kostrhunova, H.; Brabec, V.; Kasparkova, J.; Schobert, R. N,N-Dialkylbenzimidazol-2-ylidene platinum complexes—effects of alkyl residues and ancillary cis-ligands on anticancer activity. *Dalton Trans.* **2018**, *47*, 17367–17381. [CrossRef] [PubMed]
11. Datta, P.; Bang, S.; Yue, Z.; Beach, T.; Stilgenbauer, M.; Wang, H.; Bowers, D.J.; Kurokawa, M.; Xiao, H.; Zheng, Y.-R. Engineering liposomal nanoparticles of cholesterol-tethered amphiphilic Pt(IV) prodrugs with prolonged circulation time in blood. *Dalton Trans.* **2020**, *49*, 8107–8113. [CrossRef]
12. Cucciolito, M.E.; D’Amora, A.; De Feo, G.; Ferraro, G.; Giorgio, A.; Petruk, G.; Monti, D.M.; Merlino, A.; Ruffo, F. Five-Coordinate Platinum(II) Compounds Containing Sugar Ligands: Synthesis, Characterization, Cytotoxic Activity, and Interaction with Biological Macromolecules. *Inorg. Chem.* **2018**, *57*, 3133–3143. [CrossRef]
13. Cucciolito, M.E.; De Luca Bossa, F.; Esposito, R.; Ferraro, G.; Iadonisi, A.; Petruk, G.; D’Elia, L.; Romanetti, C.; Traboni, S.; Tuzi, A.; et al. C-Glycosylation in platinum-based agents: A viable strategy to improve cytotoxicity and selectivity. *Inorg. Chem. Front.* **2018**, *5*, 2921–2933. [CrossRef]
14. Annunziata, A.; Cucciolito, M.E.; Esposito, R.; Imbimbo, P.; Petruk, G.; Ferraro, G.; Pinto, V.; Tuzi, A.; Monti, D.M.; Merlino, A.; et al. A highly efficient and selective antitumor agent based on a glucoconjugated carbene platinum(II) complex. *Dalton Trans.* **2019**, *48*, 7794–7800. [CrossRef]
15. Annunziata, A.; Cucciolito, M.E.; Esposito, R.; Ferraro, G.; Monti, D.M.; Merlino, A.; Ruffo, F. Five-Coordinate Platinum(II) Compounds as Potential Anticancer Agents. *Eur. J. Inorg. Chem.* **2020**, *2020*, 918–929. [CrossRef]
16. Albano, V.G.; Natile, G.; Panunzi, A. Five-coordinate alkene complexes of palladium(II) and platinum(II). *Coord. Chem. Rev.* **1994**, *133*, 67–114. [CrossRef]
17. Pettenuzzo, A.; Pigot, R.; Luca, R. Metal-based glycoconjugates and their potential in targeted anticancer chemotherapy. *Metallo drugs* **2015**, *1*, 36–61. [CrossRef]
18. Konkankit, C.C.; Vaughn, B.A.; Huang, Z.; Boros, E.; Wilson, J.J. Systematically altering the lipophilicity of rhenium(I) tricarbonyl anticancer agents to tune the rate at which they induce cell death. *Dalton Trans.* **2020**, *49*, 16062–16066. [CrossRef] [PubMed]
19. Stilgenbauer, M.; Jayawardhana, A.M.D.S.; Datta, P.; Yue, Z.; Gray, M.; Nielsen, F.; Bowers, D.J.; Xiao, H.; Zheng, Y.-R. A spermine-conjugated lipophilic Pt(IV) prodrug designed to eliminate cancer stem cells in ovarian cancer. *Chem. Commun.* **2019**, *55*, 6106–6109. [CrossRef] [PubMed]
20. Jayawardhana, A.M.D.S.; Stilgenbauer, M.; Datta, P.; Qiu, Z.; McKenzie, S.; Wang, H.; Bowers, D.; Kurokawa, M.; Zheng, Y.-R. Fatty acid-like Pt(IV) prodrugs overcome cisplatin resistance in ovarian cancer by harnessing CD36. *Chem. Commun.* **2020**, *56*, 10706–10709. [CrossRef]
21. Bavetsias, V.; Lanigan, R.M.; Ruda, G.F.; Atrash, B.; McLaughlin, M.G.; Tumber, A.; Mok, N.Y.; Le Bihan, Y.-V.; Dempster, S.; Boxall, K.J.; et al. 8-Substituted Pyrido [3,4-d]pyrimidin-4(3H)-one Derivatives As Potent, Cell Permeable, KDM4 (JMJD2) and KDM5 (JARID1) Histone Lysine Demethylase Inhibitors. *J. Med. Chem.* **2016**, *59*, 1388–1409. [CrossRef] [PubMed]
22. Awuah, S.G.; Zheng, Y.-R.; Bruno, P.M.; Hemann, M.T.; Lippard, S.J. A Pt(IV) Pro-drug Preferentially Targets Indoleamine-2,3-dioxygenase, Providing Enhanced Ovarian Cancer Immuno-Chemotherapy. *J. Am. Chem. Soc.* **2015**, *137*, 14854–14857. [CrossRef]
23. Johnstone, T.C.; Lippard, S.J. The Effect of Ligand Lipophilicity on the Nanoparticle Encapsulation of Pt(IV) Prodrugs. *Inorg. Chem.* **2013**, *52*, 9915–9920. [CrossRef] [PubMed]
24. Varbanov, H.; Valiahdhi, S.M.; Legin, A.A.; Jakupec, M.A.; Roller, A.; Galanski, M.S.; Keppler, B.K. Synthesis and characterization of novel bis(carboxylato)dichloridobis(ethylamine)platinum(IV) complexes with higher cytotoxicity than cisplatin. *Eur. J. Med. Chem.* **2011**, *46*, 5456–5464. [CrossRef]
25. Renfrew, A.K.; Juillerat-Jeanneret, L.; Dyson, P.J. Adding diversity to ruthenium(II)–arene anticancer (RAPTA) compounds via click chemistry: The influence of hydrophobic chains. *J. Organomet. Chem.* **2011**, *696*, 772–779. [CrossRef]

26. Silva, H.; Barra Carolina, V.; Rocha Fillipe, V.; Frézard, F.; Lopes Miriam, T.P.; Fontes, A.R.S. Novel Platinum(II) Complexes of Long Chain Aliphatic Diamine Ligands with Oxalato as the Leaving Group. Comparative Cytotoxic Activity Relative to Chloride Precursors. *J. Braz. Chem. Soc.* **2010**, *21*, 1961–1967. [CrossRef]
27. Messori, L.; Merlino, A. Cisplatin binding to proteins: A structural perspective. *Coord. Chem. Rev.* **2016**, *315*, 67–89. [CrossRef]
28. Messori, L.; Merlino, A. Protein metalation by metal-based drugs: X-ray crystallography and mass spectrometry studies. *Chem. Commun.* **2017**, *53*, 11622–11633. [CrossRef] [PubMed]
29. Merlino, A.; Marzo, T.; Messori, L. Protein Metalation by Anticancer Metallodrugs: A Joint ESI MS and XRD Investigative Strategy. *Chem.–A Eur. J.* **2017**, *23*, 6942–6947. [CrossRef]
30. Merlino, A. Recent advances in protein metalation: Structural studies. *Chem. Commun.* **2021**, *57*, 1295–1307. [CrossRef]
31. Tanley, S.W.; Schreurs, A.M.; Kroon-Batenburg, L.M.; Meredith, J.; Prendergast, R.; Walsh, D.; Bryant, P.; Levy, C.; Helliwell, J.R. Structural studies of the effect that dimethyl sulfoxide (DMSO) has on cisplatin and carboplatin binding to histidine in a protein. *Acta Crystallogr. D Biol. Crystallogr.* **2012**, *68*, 601–612. [CrossRef]
32. Tanley, S.W.; Schreurs, A.M.; Kroon-Batenburg, L.M.; Helliwell, J.R. Re-refinement of 4g4a: Room-temperature X-ray diffraction study of cisplatin and its binding to His15 of HEWL after 14 months chemical exposure in the presence of DMSO. *Acta Crystallogr. F Struct. Biol. Commun.* **2016**, *72*, 253–254. [CrossRef] [PubMed]
33. Ferraro, G.; Pica, A.; Russo Krauss, I.; Pane, F.; Amoresano, A.; Merlino, A. Effect of temperature on the interaction of cisplatin with the model protein hen egg white lysozyme. *JBC J. Biol. Inorg. Chem.* **2016**, *21*, 433–442. [CrossRef]
34. Messori, L.; Marzo, T.; Merlino, A. The X-ray structure of the complex formed in the reaction between oxaliplatin and lysozyme. *Chem. Commun.* **2014**, *50*, 8360–8362. [CrossRef] [PubMed]
35. Marasco, D.; Messori, L.; Marzo, T.; Merlino, A. Oxaliplatin vs. cisplatin: Competition experiments on their binding to lysozyme. *Dalton Trans.* **2015**, *44*, 10392–10398. [CrossRef]
36. OECD. *Test No. 107: Partition Coefficient (n-Octanol/Water): Shake Flask Method*; OECD Publishing: Paris, France, 1995.
37. Oldfield, S.P.; Hall, M.D.; Platts, J.A. Calculation of Lipophilicity of a Large, Diverse Dataset of Anticancer Platinum Complexes and the Relation to Cellular Uptake. *J. Med. Chem.* **2007**, *50*, 5227–5237. [CrossRef] [PubMed]
38. Pizarro, A.M.; McQuitty, R.J.; Mackay, F.S.; Zhao, Y.; Woods, J.A.; Sadler, P.J. Cellular Accumulation, Lipophilicity and Photocytotoxicity of Diazido Platinum(IV) Anticancer Complexes. *ChemMedChem* **2014**, *9*, 1169–1175. [CrossRef] [PubMed]
39. Tse, W.C.; Boger, D.L. A Fluorescent Intercalator Displacement Assay for Establishing DNA Binding Selectivity and Affinity. *Acc. Chem. Res.* **2004**, *37*, 61–69. [CrossRef] [PubMed]
40. Vaney, M.C.; Maignan, S.; Riès-Kautt, M.; Ducruix, A. High-Resolution Structure (1.33 Å) of a HEW Lysozyme Tetragonal Crystal Grown in the APCF Apparatus. Data and Structural Comparison with a Crystal Grown under Microgravity from SpaceHab-01 Mission. *Acta Crystallogr. Sect. D* **1996**, *52*, 505–517. [CrossRef] [PubMed]
41. Tanley, S.W.; Starkey, L.V.; Lamplough, L.; Kaenket, S.; Helliwell, J.R. The binding of platinum hexahalides (Cl, Br and I) to hen egg-white lysozyme and the chemical transformation of the PtI6 octahedral complex to a PtI3 moiety bound to His15. *Acta Crystallogr. F Struct. Biol. Commun.* **2014**, *70*, 1132–1134. [CrossRef] [PubMed]
42. Tanley, S.W.; Schreurs, A.M.; Kroon-Batenburg, L.M.; Helliwell, J.R. Re-refinement of 4xan: Hen egg-white lysozyme with carboplatin in sodium bromide solution. *Acta Crystallogr. F Struct. Biol. Commun.* **2016**, *72*, 251–252. [CrossRef]
43. Ferraro, G.; Imbimbo, P.; Marseglia, A.; Illiano, A.; Fontanarosa, C.; Amoresano, A.; Olivieri, G.; Pollio, A.; Monti, D.M.; Merlino, A. A thermophilic C-phycoyanin with unprecedented biophysical and biochemical properties. *Int. J. Biol. Macromol.* **2020**, *150*, 38–51. [CrossRef] [PubMed]
44. Annunziata, A.; Ferraro, G.; Cucciolito, M.E.; Imbimbo, P.; Tuzi, A.; Monti, D.M.; Merlino, A.; Ruffo, F. Halo complexes of gold(i) containing glycoconjugate carbene ligands: Synthesis, characterization, cytotoxicity and interaction with proteins and DNA model systems. *Dalton Trans.* **2022**, *51*, 10475–10485. [CrossRef] [PubMed]
45. De Felice, V.; Funicello, M.; Panunzi, A.; Ruffo, F. Stable five-coordinate [Pt(N N')(olefin)(R)X] complexes formed by oxidative addition to [Pt(N N')(olefin)] precursors. *J. Organomet. Chem.* **1991**, *403*, 243–252. [CrossRef]
46. Murshudov, G.N.; Skubak, P.; Lebedev, A.A.; Pannu, N.S.; Steiner, R.A.; Nicholls, R.A.; Winn, M.D.; Long, F.; Vagin, A.A. REFMAC5 for the refinement of macromolecular crystal structures. *Acta Crystallogr. D Biol. Crystallogr.* **2011**, *67*, 355–367. [CrossRef]
47. Emsley, P.; Lohkamp, B.; Scott, W.G.; Cowtan, K. Features and development of Coot. *Acta Crystallogr. D Biol. Crystallogr.* **2010**, *66*, 486–501. [CrossRef]
48. Del Giudice, R.; Imbimbo, P.; Pietrocola, F.; Martins, I.; De Palma, F.D.E.; Bravo-San Pedro, J.M.; Kroemer, G.; Maiuri, M.C.; Monti, D.M. Autophagy Alteration in ApoA-I Related Systemic Amyloidosis. *Int. J. Mol. Sci.* **2022**, *23*, 3498. [CrossRef]
49. Ruggieri, S.; Roblin, R.; Black, P.H. Lipids of whole cells and plasma membrane fractions from Balb/c3T3, SV3T3, and concanavalin A-selected revertant cells. *J. Lipid Res.* **1979**, *20*, 772–783. [CrossRef]
50. Preta, G. New Insights Into Targeting Membrane Lipids for Cancer Therapy. *Front. Cell Dev. Biol.* **2020**, *8*, 571237. [CrossRef]

Disclaimer/Publisher’s Note: The statements, opinions and data contained in all publications are solely those of the individual author(s) and contributor(s) and not of MDPI and/or the editor(s). MDPI and/or the editor(s) disclaim responsibility for any injury to people or property resulting from any ideas, methods, instructions or products referred to in the content.



Article

Effect of Arylazo Sulfones on DNA: Binding, Cleavage, Photocleavage, Molecular Docking Studies and Interaction with A375 Melanoma and Non-Cancer Cells

Chrysoula Mikra ^{1,†}, Achilleas Mitrakas ^{2,3,†} , Virginia Ghizzani ⁴, Katerina R. Katsani ⁵, Maria Koffa ², Michael Koukourakis ³, George Psomas ⁶ , Stefano Protti ⁴ , Maurizio Fagnoni ^{4,*} and Konstantina C. Fylaktakidou ^{1,*}

¹ Laboratory of Organic Chemistry, Faculty of Chemistry, Aristotle University of Thessaloniki, 54124 Thessaloniki, Greece

² Laboratory of Cellular Biology and Cell Cycle, Molecular Biology and Genetics Department, Democritus University of Thrace, University Campus, Dragana, 68100 Alexandroupolis, Greece

³ Department of Radiotherapy and Oncology, Democritus University of Thrace, University General Hospital of Alexandroupolis, 68100 Alexandroupolis, Greece

⁴ PhotoGreen Lab, Department of Chemistry, University of Pavia, V. Le Taramelli 12, 27100 Pavia, Italy

⁵ Laboratory of Biochemistry and Molecular Virology, Molecular Biology and Genetics Department, Democritus University of Thrace, Dragana, 68100 Alexandroupolis, Greece

⁶ Laboratory of Inorganic Chemistry, Faculty of Chemistry, Aristotle University of Thessaloniki, 54124 Thessaloniki, Greece

* Correspondence: fagnoni@unipv.it (M.F.); kfylakta@chem.auth.gr (K.C.F.)

† These authors contributed equally to this work.

Citation: Mikra, C.; Mitrakas, A.; Ghizzani, V.; Katsani, K.R.; Koffa, M.; Koukourakis, M.; Psomas, G.; Protti, S.; Fagnoni, M.; Fylaktakidou, K.C. Effect of Arylazo Sulfones on DNA: Binding, Cleavage, Photocleavage, Molecular Docking Studies and Interaction with A375 Melanoma and Non-Cancer Cells. *Int. J. Mol. Sci.* **2023**, *24*, 1834. <https://doi.org/10.3390/ijms24031834>

Academic Editors: Philippe Pourquier and Martin Hohenegger

Received: 8 November 2022

Revised: 4 January 2023

Accepted: 12 January 2023

Published: 17 January 2023

Abstract: A set of arylazo sulfones, known to undergo N–S bond cleavage upon light exposure, has been synthesized, and their activity in the dark and upon irradiation towards DNA has been investigated. Their interaction with calf-thymus DNA has been examined, and the significant affinity observed (most probably due to DNA intercalation) was analyzed by means of molecular docking “in silico” calculations that pointed out polar contacts, mainly via the sulfonyl moiety. Incubation with plasmid pBluescript KS II revealed DNA cleavage that has been studied over time and concentration. UV-A irradiation considerably improved DNA damage for most of the compounds, whereas under visible light the effect was slightly lower. Moving to in vitro experiments, irradiation was found to slightly enhance the death of the cells in the majority of the compounds. Naphthylazosulfone **1** showed photo-disruptive effect under UV-A irradiation (IC₅₀ ~13 μM) followed by derivatives **14** and **17** (IC₅₀ ~100 μM). Those compounds were irradiated in the presence of two non-cancer cell lines and were found equally toxic only upon irradiation and not in the dark. The temporal and spatial control of light, therefore, might provide a chance for these novel scaffolds to be useful for the development of phototoxic pharmaceuticals.

Keywords: arylazo sulfones; DNA binding; DNA cleavage; DNA photocleavage; A375 melanoma cells; molecular docking; radicals; N–S bond homolysis



Copyright: © 2023 by the authors. Licensee MDPI, Basel, Switzerland. This article is an open access article distributed under the terms and conditions of the Creative Commons Attribution (CC BY) license (<https://creativecommons.org/licenses/by/4.0/>).

1. Introduction

A wide variety of small organic molecules have been designed and investigated for their interaction with structural features of DNA, aiming to target the transcriptional machinery of cancer cells and lead to apoptosis. Indeed, DNA modification may inhibit cancer progression, and this can be achieved via several pathways, including hydrolysis of phosphodiester and oxidation of the deoxyribose sugar or the nucleotide bases [1,2]. In this context, the affinity of a small molecule with DNA is examined as the initial step [3] by means of spectroscopic analyses able to provide an evaluation of the changes in the DNA moiety while interacting with the examined compound [4]. Thus, intercalation of

the “host” with DNA, minor and major groove binding can be revealed, indicating its important physicochemical approach that is a prerequisite for possible effective damage.

Although most DNA-cleaving compounds are metal complexes, a significant number of research publications are devoted to organic molecules, also referred to as artificial “metal-free nucleases”, aiming to identify differentiated mechanisms of action. Such compounds exhibit very diversified molecular structures, including, among the recent ones, simple oximes and hydroxylamines [5], coumarin oxime ethers [6], imidazo-phenanthrolines [7] and their carbohydrate conjugates [8], indolo-pyrimidines [9], pyridine [10] and naphthoquinone thiazole hybrids [11] and benzothiazole derivatives [12,13], bis- and tetrakis-1,2,3-triazole derivatives [14], naphthalenophanes [15], selenylated oxadiazoles [16], 2-styryl-4-aminoquinazoline [17], calixarene-benzazole [18] and indolyl derivatives [19], azaenedienes [20], and the natural product Shishijimicin A [21].

The challenge to find DNA binding molecules that do not interfere with the functions of normal cells and/or to overcome multidrug resistance to chemotherapeutics is the most desirable goal. In this direction, due to the high spatial and temporal control, photochemotherapy [22–24] and photodynamic therapy [25–28] allow the minimally invasive treatment of several kinds of cancer and other nonmalignant diseases. Such impressive selectivity is due to the role of light, which acts as a counterpart to small organic molecules that can be excited by the energy offered by light and affect the biological target. Thus, a photosensitizer activatable under UV-B and UV-A irradiation is the requirement in photochemotherapy and a photosensitizer in combination with UV-A/visible and NIR irradiations with concomitant participation of oxygen reactive species (mainly singlet oxygen) characterize the photodynamic one.

However, to overcome multidrug resistance to chemotherapeutics, combinations of photochemotherapy and chemotherapy were investigated for the treatment of cutaneous T-cell lymphoma [29], whereas combinations of chemotherapy and photodynamic therapy were applied to study the synergistic effects in various cancer cells [30] and for better therapeutic efficacy in prostate [31] and breast cancer [32], advanced gastric adenocarcinoma [33], etc. Additionally, photosensitizers are increasingly used for the inactivation of bacteria and other microorganisms [34–36], with the scientist suspecting effectiveness that will not reach the dead ends of antibiotics because of the multiple biological targets of the process [37,38].

Recently, the concept of a *dyedauxiliary* group was introduced [39]. This moiety may be incorporated within an organic molecule to induce a bathochromic shift and make it colored. At the same time, these groups bear a chemical bond that is labile upon visible (or UV) light excitation, thus causing the photorelease of reactive intermediates (e.g., radicals) [39,40].

Barton esters, which hold a photolabile N–O bond, have been employed in radical addition chain reactions for the synthesis of natural products as well as in the C–X (X = sulfur, selenium, halogen, nitrogen) bond formation [41–44] (Figure 1A), path *a*). The DNA photocleavage induced by these *O*-acyl thiohydroxamate esters has been previously investigated [45–47]. Indeed, the N–O bond homolysis of Barton esters generated arylloxyl (oxygen-centered) radicals (Figure 1A, path *b*) known to attack a thymidine model, providing, along with the photobiological experiments, evidence of the efficiency of the oxygen-centered reactive intermediates under chemical conditions [48]. In analogy with *O*-acyl thiohydroxamate esters, *N*-aryloxynaphthalimides exhibited good intercalation and DNA photocleavage upon UV-A exposure [49,50].

The concept of using photolabile N–O bonds is general, as in the case of functionalized oximes that are employed in chemistry for the creation of carbon, nitrogen, and oxygen-centered radicals [51–54] and as photoinitiators in polymerizations [55]. Oxime carboxylates have been applied to the DNA photocleavage of various substrates under UV-B and UV-A irradiation [56–60], along with oxime sulfonates [61,62] and oxime carbamates [63]. It should be noted that all the above-described compounds showed affinity to DNA, which is a prerequisite for DNA photocleavage, and they are classified as “true” DNA photo-cleavers because they show no evidence of DNA cleavage in the dark.

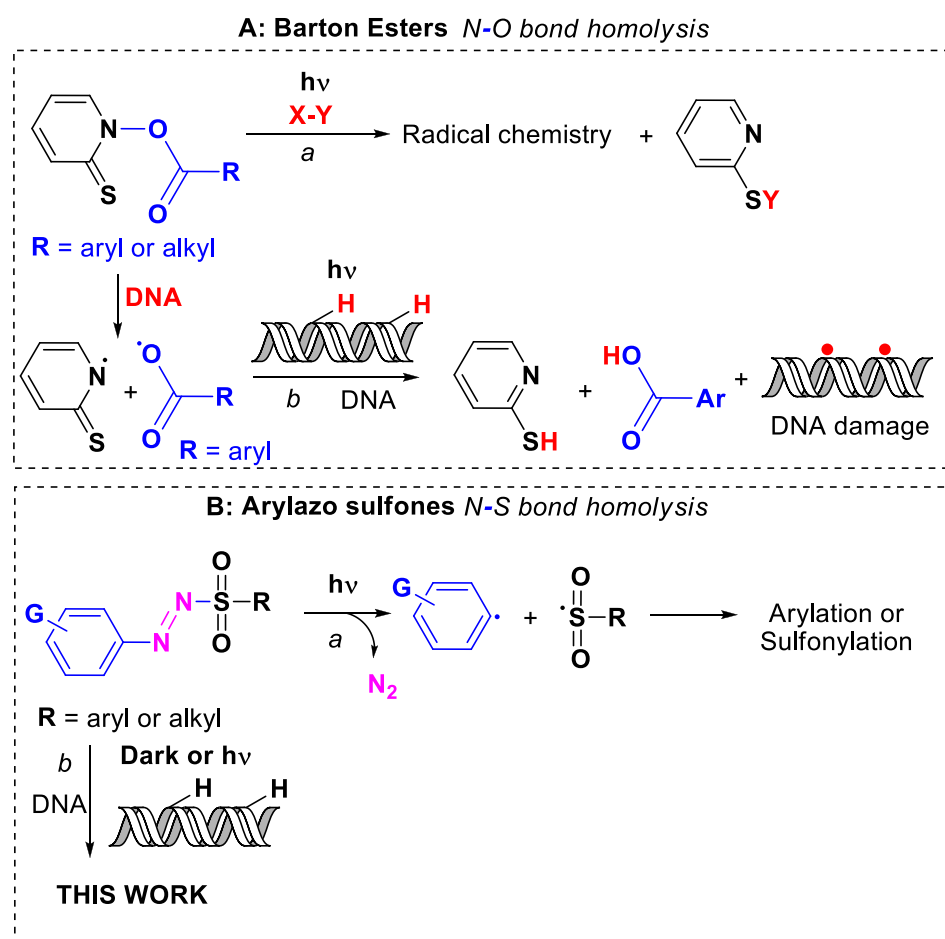


Figure 1. Light-induced homolysis: (A) of an N–O bond in Barton esters in synthesis (path *a*) and in chemical biology (path *b*); (B) of an N–S bond in arylazo sulfones in synthesis (path *a*) and in chemical biology (path *b*, this work).

Recently, our team has extensively studied a class of colored shelf-stable derivatives containing a *dyedauxiliary* group, namely arylazo sulfones (Ar–N = N–SO₂–R'). Such derivatives underwent the N–S bond homolysis upon visible light irradiation (Figure 1B, path *a*) and the ensuing loss of a molecule of nitrogen facilitates the formation of Ar' and R'–S'O₂ reactive radicals that have been exploited in the preparation of, among the others, arylstannanes [64], (hetero)arylphosphonates [65], aryl selenides and tellurides [66], symmetrical (hetero)biaryls [67], arylboronates [68], sulfonyl fluorides [69], stilbenes and vinyl sulfones [70], trifluoromethylthiolates [71], and (*E*)-vinyl sulfones [72]. Additionally, arylazo sulfones were able to initiate the polymerization of a broad range of electron-poor olefins [73], or to cause covalent functionalization (arylation) of reduced graphene oxide nanosheets [74] and simultaneous photografting of both aryl and methanesulfonyl groups on a gold surface [75].

We were eager, within this manuscript, to investigate whether the rich photochemistry of arylazo sulfones might have an effect on biomolecules and live cells, which are, to the best of our knowledge, yet totally unexplored. For this reason, using a well-established methodology, we have synthesized a set of arylazo sulfones (**1–14**, **16**, Figure 2) with compounds bearing various electron-donating and withdrawing groups on the aryl group. The results have been compared with those obtained with compounds bearing a different azo moiety, including an arylazo sulfide (**15**) and a triazene (**17**). A DNA binding profile of the total set of seventeen compounds has been studied using calf-thymus (CT) DNA and UV–vis and fluorescence spectroscopy as well as viscosity experiments. The DNA cleavage (in dark) and photocleavage (under UV-A and visible light irradiations) were

studied using plasmid DNA pBluescript SK II and visualized via agarose gel electrophoresis (Figure 1B, path *b*). The highly malignant A375 melanoma cells were the model cells that provided initial results on cell cultures under dark, UV-A [76,77], and visible light exposure. Additionally, two non-cancer cell lines have been used as a control for the activity; HFL1, a fibroblast cell line that was isolated from the lung of a white, normal embryo, and HaCaT cell lines, human immortalized keratinocytes.

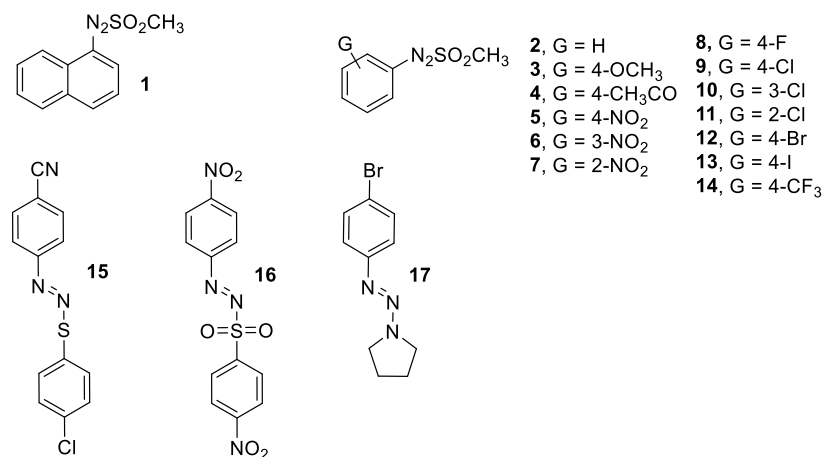


Figure 2. Arylazo sulfones (1–14, 16), arylazo sulfide (15), and triazene (17) prepared and investigated in this work.

2. Results and Discussion

2.1. Synthesis and Characterization of Arylazo Sulfones

A representative set of arylazo sulfones (mesylates 1–14 and *p*-nitrophenylsulfonate 16, Figure 2) have been prepared according to a reported procedure [64]. As hinted at above, two further derivatives where the sulfone moiety has been replaced by a thioaryl group and a piperidine moiety (azosulfide 15 and triazene 17, respectively) were likewise prepared for the sake of comparison (copies of the NMR spectra of compounds 15 and 16 are available in Supporting Information, S.1, part S.1.a,b and S.1.c,d, respectively).

The seventeen compounds were preliminarily divided into four groups (A–D). Group A contained hydrogen, carbon, and oxygen substituents on the aromatic moiety of arylazo mesylates (1–4), Group B contained all nitro-substituted derivatives (5–7) and *p*-nitrophenylazo (*p*-nitrophenyl)sulfone (16), Group C contained all halogenated compounds (8–13), and Group D contained the remaining compounds (14, 15, and 17).

2.2. CT DNA Binding Studies of Arylazo Sulfones

The interaction of compounds 1–17 with calf-thymus DNA (CT DNA) was investigated *in vitro* by UV–vis spectroscopy and viscosity measurements and via their ability to displace ethidium bromide (EB) from the EB-DNA adduct, which was examined by fluorescence emission spectroscopy.

The structural changes induced by the interaction of CT DNA with the examined compounds have been investigated by means of UV–vis spectroscopy, which was exploited to measure DNA-binding constants (K_b). In most cases, the bands observed in the UV–vis spectra of the compounds (see the representative case of compound 1 shown in Figure 3a) exhibited, in the presence of increasing amounts of CT DNA, slight hyperchromism or even hypochromism accompanied by a slight red-shift (Table 1). These features may be attributed to the interaction of the compounds with CT DNA, whereas the interaction mode may not be safely interpreted, necessitating the performance of other experiments such as DNA-viscosity measurements.

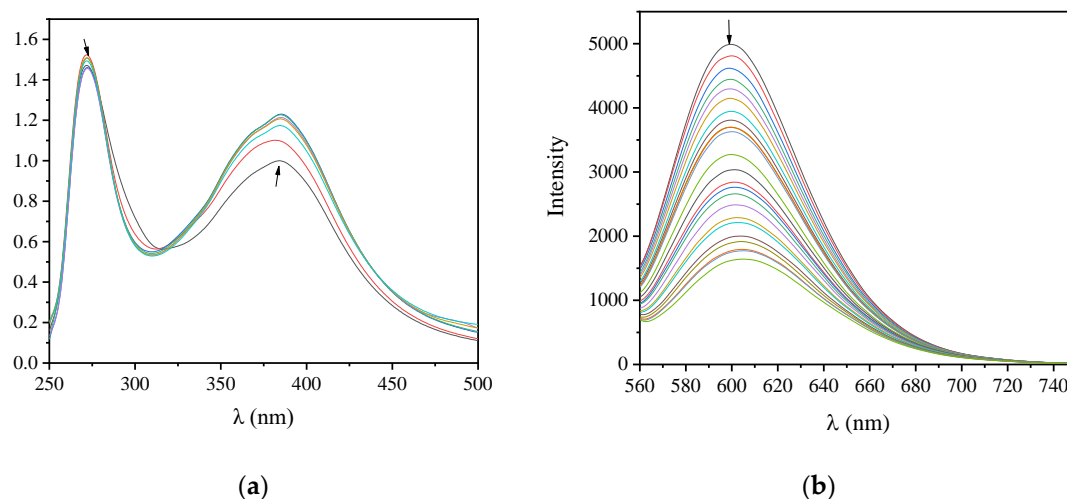


Figure 3. (a) UV-vis spectra of compound **1** (2.5×10^{-4} M) in DMSO in the presence of increasing amounts of CT DNA. The arrows show the changes upon increasing amounts of CT DNA. (b) Fluorescence emission spectra ($\lambda_{\text{exc}} = 540$ nm) for EB-DNA conjugate ($[\text{EB}] = 20 \mu\text{M}$, $[\text{DNA}] = 26 \mu\text{M}$) in buffer solution (150 mM NaCl and 15 mM trisodium citrate at pH = 7.0) in the presence of increasing amounts of compound **9**. The arrow shows the changes in intensity upon increasing amounts of compound **9**.

Table 1. Spectral features of the UV-vis spectra of compounds **1–17** upon addition of CT DNA. UV-band (λ , nm) (percentage of observed hyper-/hypo-chromism ($\Delta A/A_0$, %), blue-/red-shift of the λ_{max} ($\Delta\lambda$, nm)) and the corresponding DNA-binding constants (K_b , M^{-1}).

Groups	No of Compound	Band (nm) ($\Delta A/A_0$ (%) ¹ , $\Delta\lambda$ (nm) ²)	K_b (M^{-1})
Group A	1	272 (+2, +1); 385 (+17, 0)	$3.73(\pm 0.24) \times 10^5$
	2	300 (+2, +1)	$1.12(\pm 0.15) \times 10^5$
	3	347 (−4, +1)	$5.04(\pm 0.16) \times 10^5$
	4	387 (−68, +11); 489 (+54, +6)	$6.08(\pm 0.15) \times 10^5$
Group B	5	288 (+6, −2); 359 (sh) ³ (−43, +20)	$9.31(\pm 0.18) \times 10^3$
	6	269 (+8, +2)	$2.87(\pm 0.10) \times 10^7$
	7	289 (+2, +3)	$4.59(\pm 0.10) \times 10^5$
	16	274 (+6, +3)	$1.05(\pm 0.08) \times 10^6$
Group C	8	301 (+1, +1)	$2.67(\pm 0.27) \times 10^5$
	9	298 (+2, +0)	$3.81(\pm 0.35) \times 10^5$
	10	290 (+8, −1)	$1.31(\pm 0.08) \times 10^6$
	11	308 (+4, +1)	$6.41(\pm 0.32) \times 10^5$
	12	312 (+0.5, +2)	$9.13(\pm 0.15) \times 10^5$
Group D	13	330 (+8, −1)	$6.02(\pm 0.44) \times 10^5$
	14	279 (+12, 0)	$7.42(\pm 0.10) \times 10^5$
	15	280 (+23, +8)	$1.02(\pm 0.04) \times 10^5$
	17	322 (−3, +0)	$3.82(\pm 0.30) \times 10^5$

¹ “+” denotes hyperchromism, “−” denotes hypochromism; ² “+” denotes red-shift, “−” denotes blue-shift; ³ “sh” = shoulder.

The values of K_b of the compounds (Table 1) were determined with the Wolfe-Shimer equation (SI, Part S.2.1, Equation (1)) [78] and the plots $[\text{DNA}]/(\epsilon_A - \epsilon_f)$ versus $[\text{DNA}]$ (SI, Figure Part S.3). The K_b of the compounds **1–17** (in the order 10^5 – 10^6 M^{-1}) are higher than that of the classical intercalator EB ($=1.23(\pm 0.07) \times 10^5$ M^{-1}) [79] and show the magnitude of their interaction with CT DNA.

Among the compounds of Group A, compound **4** (the *p*- CH_3CO -substituted) presents the highest K_b value ($=6.08(\pm 0.15) \times 10^5$ M^{-1}) whereas among the NO_2 derivatives in

Group B, the *m*-NO₂-isomer **6** exhibited the strongest affinity ($K_b = 2.87(\pm 0.10) \times 10^7 \text{ M}^{-1}$) and the highest DNA binding constant observed in the present work. A similar behavior was observed for *m*-chloro derivative **10**, Group C ($K_b = 1.31(\pm 0.08) \times 10^6 \text{ M}^{-1}$). As concerning the effect of a halogen atom as the substituent, *p*-Br-derivative **12** bears the highest K_b value ($=9.13(\pm 0.15) \times 10^5 \text{ M}^{-1}$).

Any changes in the DNA structure upon the addition of a studied compound have also been monitored via viscosity experiments (SI, Part S.2.2) that provide information about the mode of interaction due to their sensitivity to the relative DNA length changes (L/L_0) [80]. More broadly speaking, when a compound intercalates into DNA, the distance between the DNA base pairs increases at the intercalation site to facilitate the insertion of the hosted compound. Thus, the relative DNA length increases, leading to an increase in DNA viscosity, whose value is often proportional to the strength of the interaction [81]. In the case of non-classical intercalation (i.e., electrostatic interaction or groove-binding), the relative DNA length suffers rather than a slight shortening, and accordingly, a slight decrease in the DNA viscosity may be induced [81]. Within this context, the viscosity of a CT DNA solution (0.1 mM) was monitored upon the addition of increasing amounts of the compounds (up to the value of $r = 0.36$, Figure 4). Initially and up to the r -value of 0.1, the viscosity of the CT DNA solution remains practically stable, suggesting an external interaction with the compounds (obviously groove-binding). For r -values above 0.1, the observed increase in DNA viscosity could be attributed to an intercalative interaction [60–63].

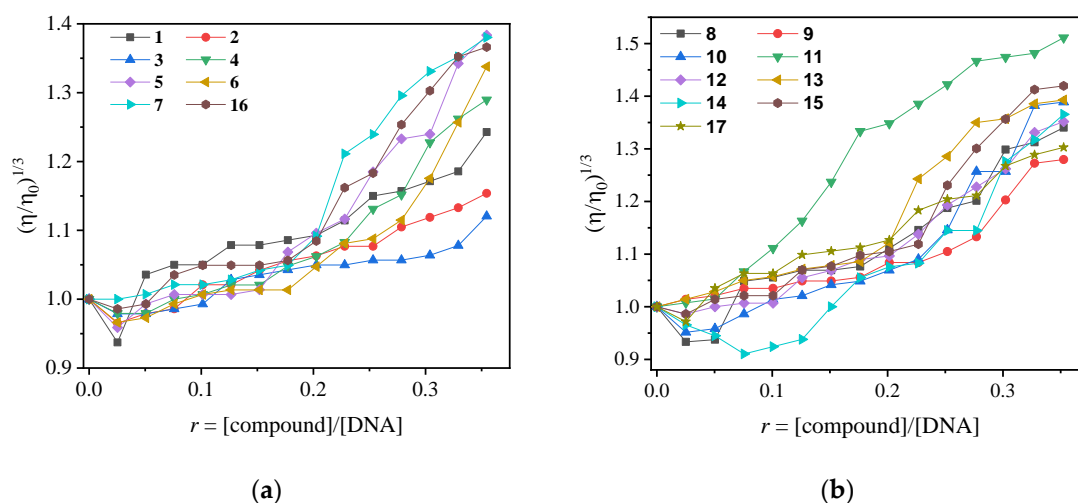


Figure 4. Relative viscosity $(\eta/\eta_0)^{1/3}$ of CT DNA (0.1 mM) in buffer solution (150 mM NaCl and 15 mM trisodium citrate at pH 7.0) in the presence of increasing amounts of compounds 1–17 ($r = [\text{compound}]/[\text{DNA}] = 0\text{--}0.36$). (a) Groups A and B; (b) Groups C and D.

EB is a fluorescent dye that intercalates DNA and forms an adduct with an intense fluorescent emission band at 592–593 nm, when excited at 540 nm [82]. When a compound that intercalates into DNA equally or more strongly than EB is added to the EB-DNA solution, changes in the EB-DNA emission band may be observed and are often monitored to examine the competition of the compound with EB for the DNA intercalation site [82]. Thus, the fluorescence emission spectra of 1 h pretreated EB-DNA ($[\text{EB}] = 20 \mu\text{M}$, $[\text{DNA}] = 26 \mu\text{M}$) were recorded in the presence of increasing amounts of the compounds (see the case of compound **9** in Figure 3b) and a significant decrease in the fluorescence emission band of EB-DNA at 592 nm (up to 67.5% for compound **9**, Figure 5b, Table 2) revealed that the compounds are able to displace EB for the EB-DNA adduct. Thus, an intercalative mode of interaction of the complexes with CT DNA can be indirectly proposed [83].

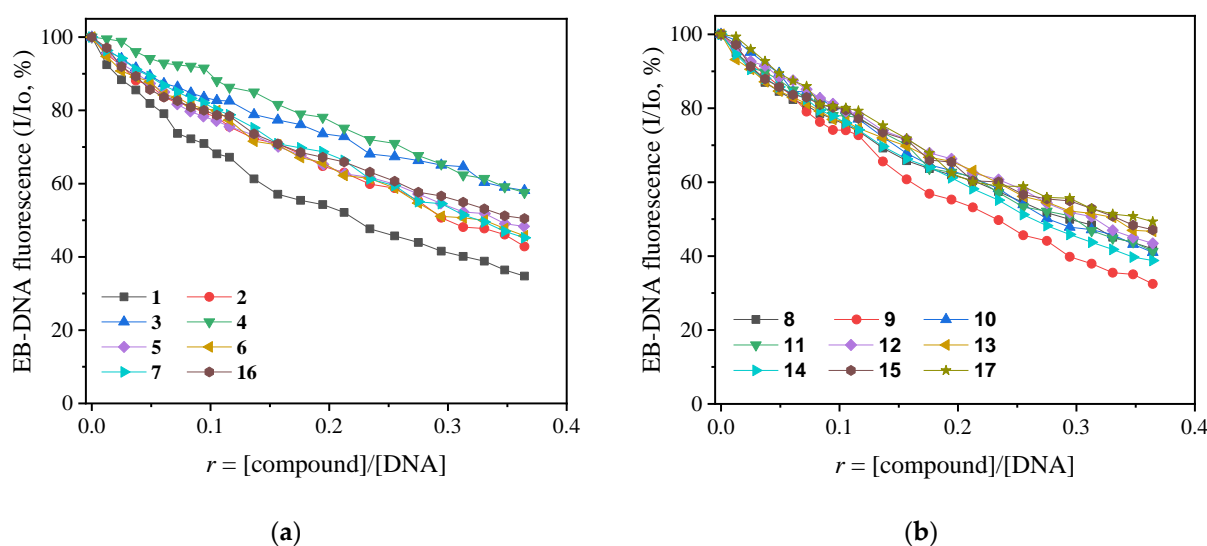


Figure 5. Plot of EB–DNA relative fluorescence emission intensity at $\lambda_{\text{emission}} = 592 \text{ nm}$ (%) versus r ($r = [\text{compound}]/[\text{DNA}]$) in the presence of compounds 1–17. (a) Groups A and B; (b) Groups C and D; (up to 34.8 % of the initial EB–DNA fluorescence emission intensity for 1, 42.9 % for 2, 59.2 % for 3, 57.6 % for 4, 48.4 % for 5, 45.8 % for 6, 45.2 % for 7, 42.0 % for 8, 32.5 % for 9, 41.0 % for 10, 41.3 % for 11, 43.4 % for 12, 46.7 % for 13, 38.8 % for 14, 47.1 % for 15, 50.5 % for 16, 49.3 % for 17).

Table 2. Data of the EB–DNA competitive studies of compounds 1–17. Percentage of EB–DNA fluorescence quenching ($\Delta I/I_0$, %), EB–DNA Stern–Volmer constants (K_{SV} , M^{-1}), and EB–DNA quenching constants (k_q , $M^{-1}s^{-1}$) for compounds 1–17.

Groups	Compound	($\Delta I/I_0$, %)	K_{SV} (M^{-1})	k_q , $M^{-1} s^{-1}$
Group A	1	65.2	$2.40(\pm 0.03) \times 10^4$	$1.04(\pm 0.01) \times 10^{12}$
	2	57.1	$3.51(\pm 0.06) \times 10^4$	$1.53(\pm 0.03) \times 10^{12}$
	3	41.8	$4.41(\pm 0.08) \times 10^4$	$1.92(\pm 0.03) \times 10^{12}$
	4	42.4	$8.51(\pm 0.26) \times 10^4$	$3.70(\pm 0.11) \times 10^{12}$
Group B	5	51.6	$3.58(\pm 0.06) \times 10^4$	$1.56(\pm 0.02) \times 10^{12}$
	6	54.2	$3.41(\pm 0.07) \times 10^4$	$1.48(\pm 0.03) \times 10^{12}$
	7	54.8	$1.31(\pm 0.03) \times 10^4$	$5.70(\pm 0.14) \times 10^{11}$
	16	49.5	$3.31(\pm 0.05) \times 10^4$	$1.44(\pm 0.02) \times 10^{12}$
Group C	8	58.0	$8.40(\pm 0.13) \times 10^4$	$3.65(\pm 0.05) \times 10^{12}$
	9	67.5	$5.88(\pm 0.13) \times 10^4$	$2.56(\pm 0.06) \times 10^{12}$
	10	59	$4.65(\pm 0.12) \times 10^4$	$2.02(\pm 0.05) \times 10^{12}$
	11	58.7	$4.20(\pm 0.08) \times 10^4$	$1.83(\pm 0.04) \times 10^{12}$
	12	56.5	$3.90(\pm 0.11) \times 10^4$	$1.70(\pm 0.05) \times 10^{12}$
Group D	13	53.3	$3.69(\pm 0.07) \times 10^4$	$1.60(\pm 0.03) \times 10^{12}$
	14	61.2	$4.37(\pm 0.11) \times 10^4$	$1.90(\pm 0.05) \times 10^{12}$
	15	52.9	$3.61(\pm 0.08) \times 10^4$	$1.57(\pm 0.03) \times 10^{12}$
	17	50.7	$3.77(\pm 0.05) \times 10^4$	$1.64(\pm 0.02) \times 10^{12}$

The Stern–Volmer (K_{SV}) constants (Table 2) of the complexes were calculated with the Stern–Volmer equation (SI, Part S.2.3, Equation (2)) and the corresponding S–V plots (Figure Part S.4). K_{SV} are relatively high, compounds 4 and 8 exhibit the highest values (8.40×10^4 and $8.51 \times 10^4 M^{-1}$, respectively), suggesting a tight binding to DNA. In addition, the EB–DNA quenching constants (k_q) of the compounds (Table 2) were calculated with Equation (3) (SI, Part S.2.3) (considering $\tau_0 = 23 \text{ ns}$ as the fluorescence lifetime value) [84] and are higher than the value $10^{10} M^{-1}s^{-1}$ [83]. Therefore, a static quenching mechanism may be proposed for the quenching of the fluorescence induced by the compounds [82], suggesting subsequently the interaction of the compounds with the fluorophore.

2.3. DNA Interactions of Arylazo Sulfones with Plasmid DNA pBluescript SK II

2.3.1. DNA Cleavage Experiments

All compounds, at DMSO solutions $\leq 10\%$, were incubated with plasmid DNA pBluescript SK II (500 ng). To confirm the stability of the examined compounds in DMSO, NMR experiments in DMSO- d_6 and other deuterated media (DMSO- d_6 /D $_2$ O and CD $_3$ OD, $t = 48$ h) were carried out. The compounds were found to be stable in DMSO, the solvent used for their storage (SI, Part S.5). It should be noted that the samples immediately after their preparation in DMSO were kept at 4 °C, in the fridge.

The chosen concentration for the experiments in the dark was 100 μ M, and the estimated incubation time was 30 and 150 min. According to the protocol used, the compounds are incubated for 30 min before irradiation, and then the irradiation lasts for two hours. As can be seen in Figure 6 (and S.I. Part S.6.1), incubation of the compounds in the dark for 30 and 150 min (A and B, respectively, for plots with the same color, in Figure 6), most of the compounds show their cleavage activity within the first 30 min. A slight increase over time has been observed for only a few compounds (e.g., 1, 6, 7, 9, and 13).

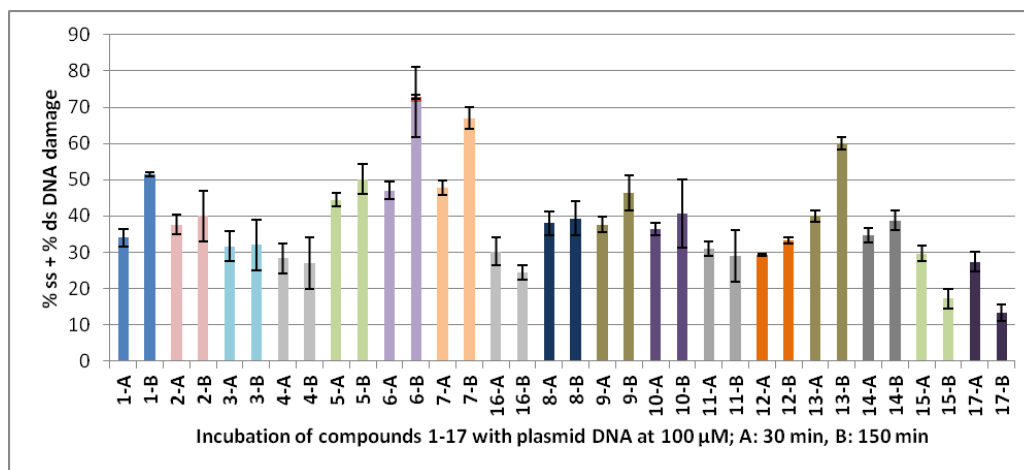


Figure 6. Plots of DNA cleavage of compounds 1–17 in dark. Explanation of the horizontal axis codes: 1-A: The first number corresponds to the number of the compound in the text (compound 1 in the example). A means incubation of the compound with plasmid DNA for 30 min and concentration 100 μ M. B means incubation of the compound with plasmid DNA for 150 min and concentration 100 μ M. Pictures of the agarose gel electrophoresis of representative experiment of each compound under conditions A and B are given in SI, Part S.6.1. ds % is given always in red and on the top of the ss % plot.

Having completed the control experiments in the dark, we proceeded to the irradiations of all compounds at 100 μ M.

2.3.2. DNA Photo-Cleavage Experiments

All compounds at a concentration of 100 μ M were mixed with pBluescript SK II, incubated for 30 min, and then irradiated for 120 min, either at 365 nm or with visible light [Figure 7a–d; each set of three same-colored plots indicates the average number of the % ss and % ds (photo)cleavage; the latter is always depicted on the top of the ss plot and in red]. The second column of each triad affords the result of the UV-A irradiation on each compound of the group, and the third column is the visible light irradiation result. The first column was added for comparison of the effect in dark (Figure 6 under the same concentrations and irradiation time; pictures of the agarose gel electrophoresis of representative experiment of each compound under UV-A and under visible irradiation are given in SI, Part S.6.2)]. UV-A irradiation caused obviously a stronger DNA photocleavage than upon visible light for most of the compounds (Group A, compounds 1 and 2; Group B, compounds 5, 7, and 16; Groups C and D, all compounds). This is probably due to the

significant absorption of the compounds in the UV-A region (SI, Part S.7) and the higher energy offered by UV-A irradiation compared to visible light. Nitro derivatives proved to be very effective, and a lower concentration had to be examined. Gratingly, particularly for compound 5, it was found very active even at a concentration of 25 μM (SI, Part S.6.3) and led to a cleavage of 50% of the plasmid between 10 and 25 μM .

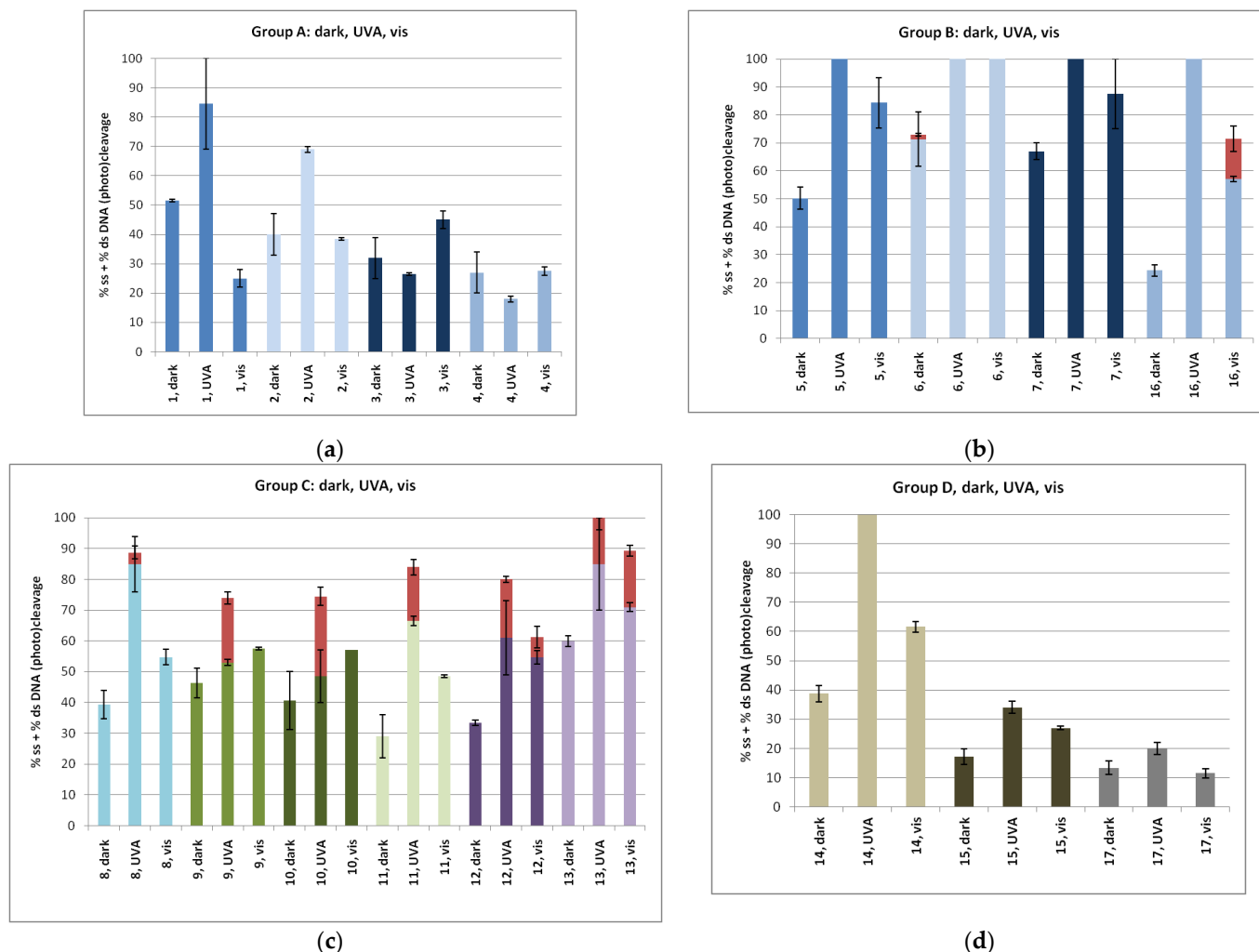


Figure 7. Plots of DNA cleavage and photocleavage for (a) Group A, (b) Group B, (c) Group C, and (d) Group D. For each compound, all three experiments at concentration 100 μM are depicted in the order: dark, UV-A, visible. Pictures of the agarose gel electrophoresis of representative experiment of each compound under UV-A and visible irradiation are given in SI, Part S.6.2. ds % is given always in red and on the top of the ss % plot.

Mechanistic studies for compound 1 under UV-A showed that the DNA photocleavage has been reduced both under argon and under air in the presence of scavengers of singlet oxygen (such as histidine and NaN_3) and in the presence of hydroxyl radical scavengers (DMSO and KI), indicating that, among different ROS, singlet oxygen is effectively formed (SI, Part S.8). Similar behavior towards various scavengers has been observed for compound 5. In visible light, the singlet oxygen formation was obvious.

2.4. Molecular Docking “In Silico” Calculations of DNA/Arylazo Sulfones

Molecular docking studies for all derivatives 1–17 were performed, utilizing the AutoDock Vina program. The scope was to identify the polar contacts and calculate the energy of their DNA binding. In Table 3, all calculated energy binding values as well as DNA base interactions are provided. We may see that in Group A naphthyl derivative (1)

shows the highest binding energy, meaning that probably the planarity offered by the extra aromatic ring increases stacking with DNA base pairs. Additionally, polar interactions are developed with the participation of both oxygen atoms that constitute the sulfonyl moiety (Figure 8a), whereas in compounds 2–4, the polar interaction involves only one oxygen atom (SI: Part S.9.1, Group A).

Table 3. “In silico” energy binding calculations towards DNA of compounds 1–17.

Groups	Compound	Energy (Kcal/mol)	Interactions (PyMol) Polar Contacts
Group A	1	−7.8	DG16, DG10
	2	−6.2	DA17
	3	−6.8	DG16, DA17
	4	−7.1	DG16, DA17
Group B	5	−7.2	DA17, DG10
	6	−7.3	DG10, DG12, DG14
	7	−7.3	DG10, DG14, DG16
	16	−8.9	DA16
Group C	8	−6.6	DA17, DG10
	9	−6.5	DG16, DA17
	10	−6.7	DG10, DA17
	11	−6.0	DG10, DA17
	12	−6.5	DG16, DA17
	13	−6.6	DG10, DA17
Group D	14	−7.3	DA5
	15	−7.3	No Polar Contacts
	17	−7.1	No Polar Contacts

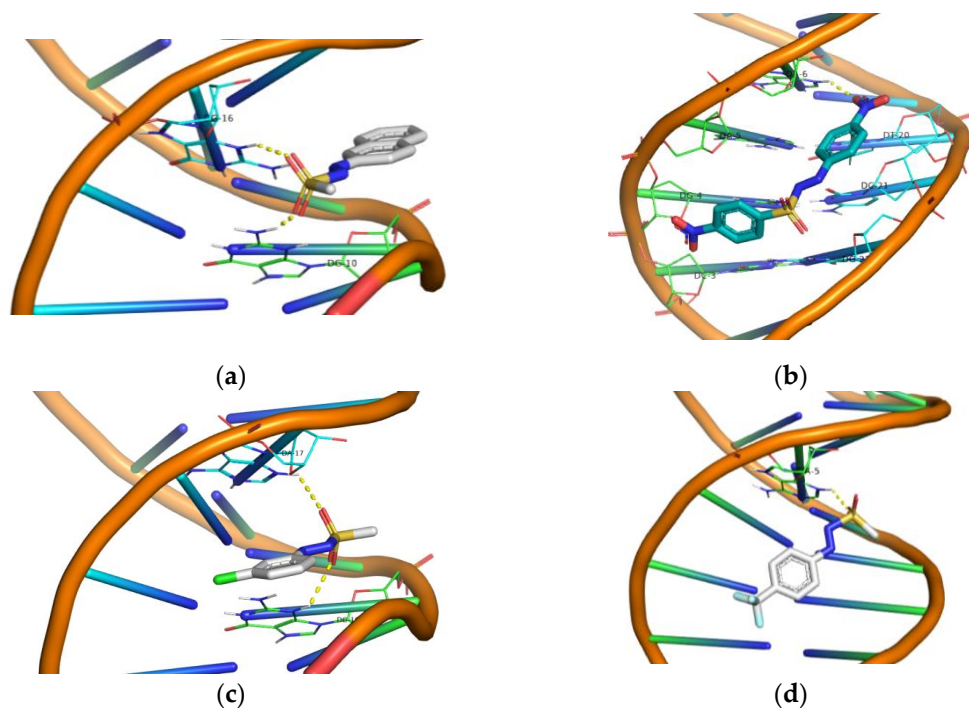


Figure 8. 3D structures of the polar contacts of selected compounds of each group. (a) Compound 1 of Group A; (b) compound 16 of Group B; (c) compound 10 of Group C; (d) compound 14 of Group D. See Figures S.9.1–S.9.4 for further details.

Compound 4 exhibits also comparable energy binding with the naphthylazo sulfone 1, and it seems to give superior values in UV binding experiments (K_b , Table 1) and in

competitive studies with EB (K_{SV} and K_Q , Table 2). In viscosity experiments up to $r \sim 0.25$, compound **1** shows better interaction that is inversed in favor of compound **4** at higher r values (Figure 4). In cleavage and photocleavage experiments, compound **1** was superior to the remaining derivatives (Figure 7a).

In Group B, compound **16** shows the highest binding energy, with *p*-, *m*- and *o*-derivatives showing quite similar values, albeit lower than **16** (Table 3, Figure 8b, SI: Part S.9.2, Group B). We may observe, however, that the lack of the *p*-nitro-phenylsulfonyl aromatic ring in compounds **5–7** allows them to possess more polar contacts. This is more obvious for the *m*- and *o*- derivatives (**6** and **7**, respectively) where both nitro as well as sulfonyl moieties develop polar contacts to DNA (SI: Part S.9.2, Group B). In all DNA affinity calculations using spectroscopic techniques, compounds **5** and **6** were found to have a stronger effect than compounds **7** and **16**, with the exception of the viscosity experiments, in which compounds **5**, **7**, and **16** exhibited almost equally high values up to $r \sim 0.36$. As for DNA photocleavage, it is not safe to arrive at conclusions due to the high reactivity of the compounds at the concentrations used in the experiments (Figure 7b). DNA photocleavage is a complex phenomenon that requires not only a good affinity to DNA for the photo-derived radicals to attack DNA but also the generation of those radicals, which needs an efficient intersystem crossing of the photosensitizer to its triplet state, which is a physico-chemical property of each individual compound [85].

The compounds of Group C seem to exhibit quite similar energy bindings (Table 3, Figure 8c, SI: Part S.9.3, Group C) and this is observed in the DNA cleavage and photocleavage experiments, with the exception of compound **13** (Figure 7c). Finally, in Group D, it seems that polar interactions are important for DNA cleavage and photocleavage since those that lack such interactions show very poor activity (Table 3, Figures 8d and 7d, SI: Part S.9.4, Group D). However, their spectroscopically calculated bindings to CT-DNA were comparable to most of the compounds.

2.5. Cell Culture Experiments of Arylazo Sulfones with Melanoma Cell Lines

Highly malignant melanoma cell lines have been used for cell culture experiments. Control experiments have been performed in dark and under irradiation of the cells without the presence of any arylazo sulfone. A second set of control experiments provided information about the effect of the presence of 1% DMSO in the culture media, which was the final concentration of DMSO in the solutions with the dissolved tested compounds. As shown, the presence of 1% DMSO was well tolerated by the cells (Figure 9). For the photodamage experiments, the cells were incubated individually with each of the seventeen compounds (100 μ M and 50 μ M) for 1 h and then irradiated under UV-A light for 1 h. Cell culture media with the compounds were then removed, and viability was measured after 24 h.

In Group A, it was observed that compound **1** induced satisfactory photodamage, causing death in about 80% of the cells. By taking into account the “phototoxicity” caused by the 1% DMSO alone (after normalization), the death of the cells is $\sim 60\%$ (Figure 9a). This is the first indication that naphthyl-azo methylsulfone (**1**) is a “true” photo-disrupting compound that is activated only in the presence of irradiation. Compound **3** exhibited the same percentage of dead cells regardless of the use of irradiation, reaching its IC_{50} at 100 μ M (Figure 9a). However, derivatives **2** and **4** were able to cause some minor cell damage when used in the dark, with the latter responding to irradiation, albeit to a lesser extent than compound **1**. When the concentration of the compounds was reduced to 50 μ M, compound **1** continued to cause the same high rate of cell death, but the activity of derivative **3** was reduced, whereas that of derivatives **2** and **4** remained the same (SI: Part S.10.1, Group A).

As far as the nitro group-containing derivatives (Group B) are concerned, compound **5** reached its IC_{50} concentration at 100 μ M. Irradiation did not cause any additional damage. Under the dark, the effect of compounds **6**, **7**, and **16** was weak; however, irradiation improved the effect on derivative **16**. Lower compound concentrations reduced their effect in the dark while retaining or increasing the photochemical effect (Figure 9b, SI: Part S.10.2, Group B). The effect of all halogenated compounds of Group C on melanoma cells was

weak; however, here again, lowering the concentration favored the photochemically over the chemically (in the dark) caused death of the cells (Figure 9c, SI: Part S.10.3, Group C).

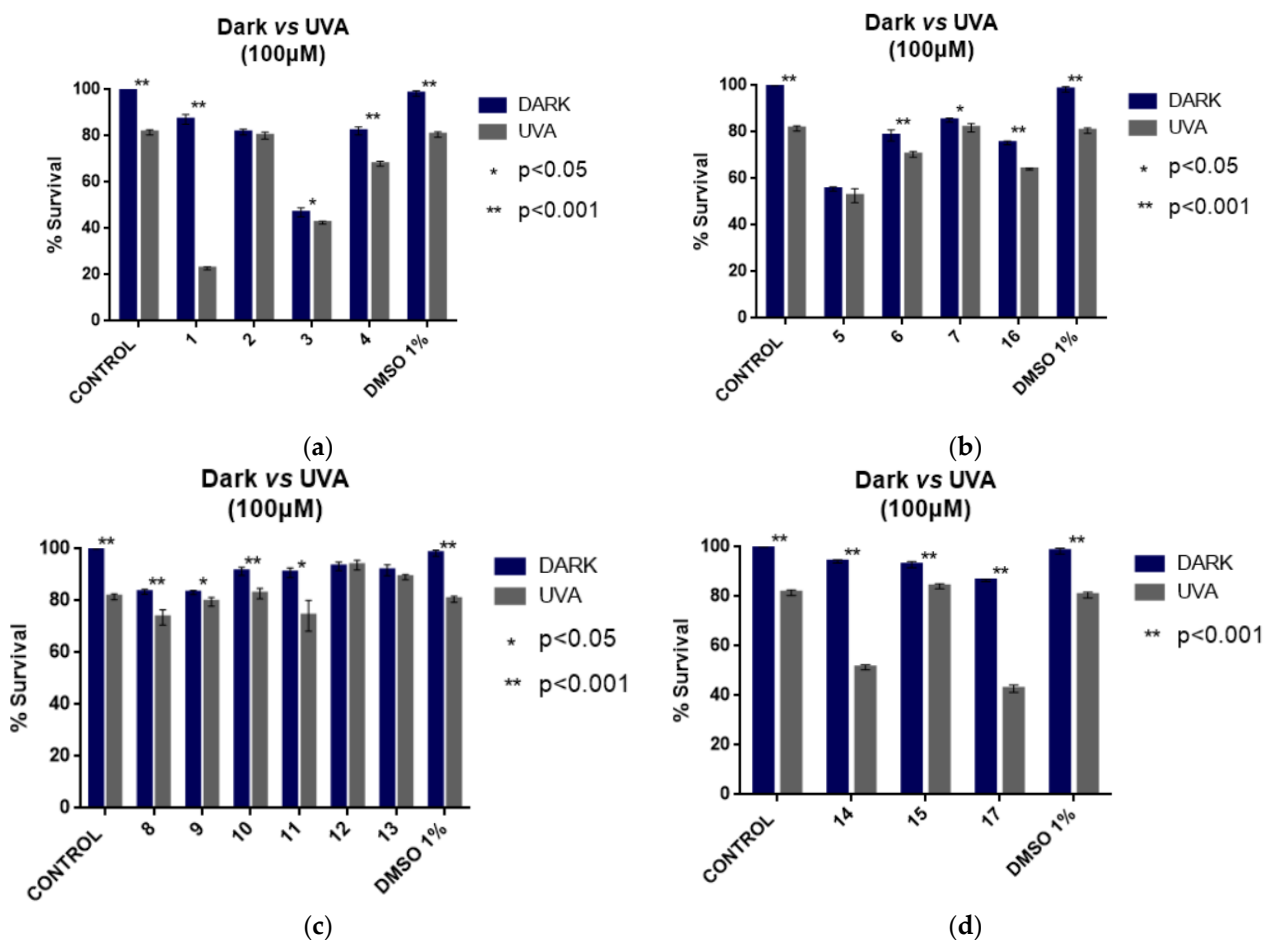


Figure 9. A375 melanoma cell culture viability experiments. Effectiveness of compounds 1–17 in dark and under UV-A irradiation; (a) Group A; (b) Group B; (c) Group C; (d) Group D.

It was very interesting to note that among compounds 14, 15, and 17 of Group D, compound 14 and derivative 17 showed equal activity, with both compounds reaching their IC_{50} at this concentration. Compound 14, apart from the exhibited photo-disruptive activity on melanoma cells, showed the highest DNA-binding constant (K_b , Table 1), EB-DNA Stern–Volmer and EB-DNA quenching constants (K_{SV} , k_q , Table 2), DNA cleavage and photocleavage (Figure 8d) and “in silico” calculated energy bindings (Table 3). No activity has been observed in the dark. Photo-reactivity was decreased when the concentration was lowered to 50 μ M (Figure 9d, SI: Part S.10.4, Group D). Compound 15, which contained sulfur stripped of oxygen atoms, exhibited no activity, not only in cells but also towards plasmid DNA (Figure 7). Even though more experimentation is required, it seems that the azosulfone moiety is important for showing the examined biological activities. The exchange of sulfur to nitrogen showed that the derived compounds should be considered as a different class of possible photosensitizers, as experiments with plasmid DNA and most importantly cell culture experiments indicated most probably a different mechanism with the cells which are in due course.

Concluding the results of the cell cultures with melanoma cells, it was found that compounds 1, 14, and 17 exhibited only photochemical activity, with the two last compounds showing an IC_{50} of 100 μ M and derivatives 3 and 5 having a chemical activity with the same IC_{50} . Derivative 1, however, was superior to all, and therefore for its IC_{50} to be determined, A365 melanoma cells were incubated with six different concentrations of 1

(0, 5, 10, 25, 50, 100, 200 μM) following the same procedure, in the dark and under UV-A irradiation (Figure 10).

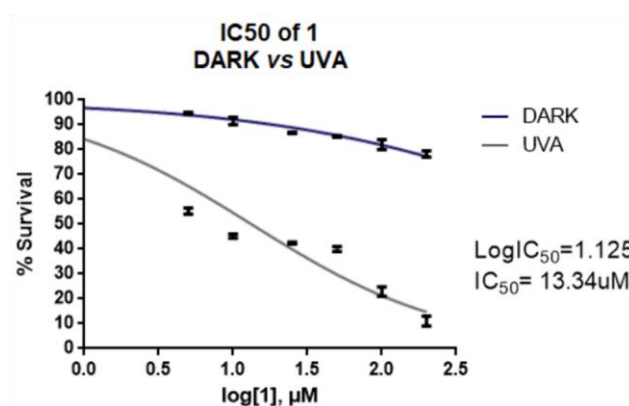


Figure 10. IC₅₀ determination for the effect of compound 1 on melanoma cells.

The results were very encouraging. Cells' viability without irradiation was greater than 50% even at higher concentrations than 200 μM , whereas the IC₅₀ under UV-A irradiation was 13.34 μM .

2.6. Cell Culture Experiments of the Photoactive Arylazo Sulfones 1, 14 and 17 with Non-Cancer Cell Lines

In order to perform a control experiment with non-cancer cells, two different cell lines were used; HFL1, a fibroblast cell line that was isolated from the lung of a white, normal embryo, and HaCaT cell lines, human immortalized keratinocytes (Figure 11a,b, respectively). Cells were incubated with 13.4 μM of compound 1 and 100 μM of compounds 14 and 17. The experimental procedure was the same as the procedure followed for A375 cell lines. As can be seen in Figure 11, in these preliminary results, compounds 1 and 17 were less toxic for the fibroblast cell line than the keratinocyte ones. Nevertheless, the photodamage in keratinocytes was comparable to that in melanoma cells (Figures 9a and 10 for compound 1 and Figure 9d for compounds 14 and 17). The damage was attributed to the UV-A irradiation in combination with the compound. The compounds themselves were found non-toxic for the cells in dark. Thus, it seems that the advantage of the spatial and temporal control driven by light, in conjunction with the novelty of the arylazosulfone scaffold, may be useful for the development of phototoxic pharmaceuticals.

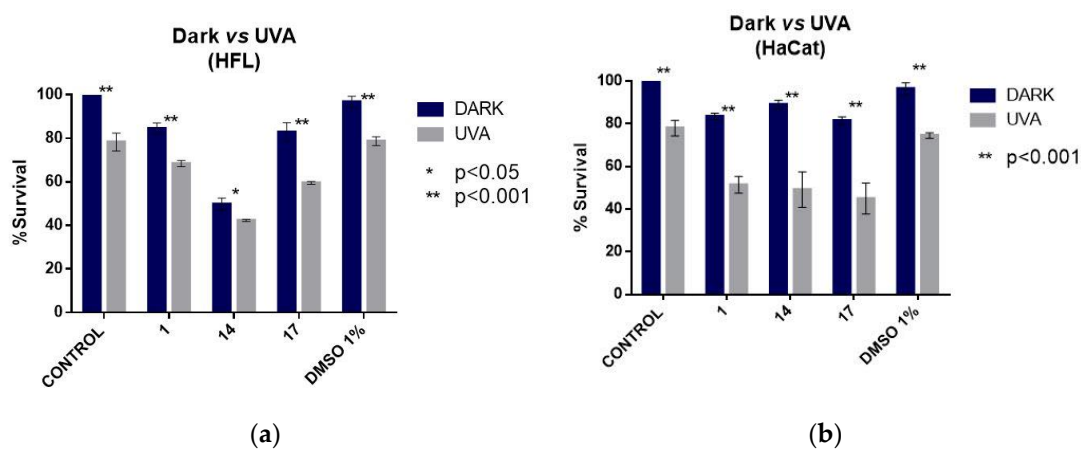


Figure 11. Non-cancer cell lines experiments with compounds 1, 14, and 17 in dark and under UVA; (a) Effect on HFL1 fibroblast cell line; (b) Effect on human immortalized keratinocytes.

3. Materials and Methods

All commercially available reagent-grade chemicals and solvents were used without further purification. Trisodium citrate, NaCl, CT DNA, and EB were purchased from Sigma-Aldrich Co., and all solvents were from Chemlab. DNA stock solution was prepared by dilution of CT DNA to buffer (containing 150 mM NaCl and 15 mM trisodium citrate at pH 7.0) followed by exhaustive stirring at 4 °C for 3 days and kept at 4 °C for no longer than a week. The stock solution of CT DNA gave a ratio of UV absorbance at 260 and 280 nm (A_{260}/A_{280}) of ~1.90, indicating that the DNA was sufficiently free of protein contamination [86]. The DNA concentration per nucleotide was determined by the UV absorbance at 260 nm after 1:20 dilution using $\epsilon = 6600 \text{ M}^{-1} \text{ cm}^{-1}$ [87]. The supercoiled plasmid pBluescript SK II was synthesized and tested not to contain nicked and/or linear strands. All samples containing pBluescript SK II were irradiated at pH 6.8 with Philips $2 \times 9\text{W}/10/2\text{P}$ UV-A lamps at 365 nm or white light OSRAM DULUX S BLUE. NMR spectra were recorded on an Agilent 500/54 (500 MHz for ^1H) (Agilent Technologies, Santa Clara, CA, USA) and on a Bruker (300 MHz for ^1H) spectrometer using DMSO- d_6 , D_2O , CDCl_3 , and CD_3OD as solvents. UV-vis spectra were recorded on a Hitachi U-2001 dual-beam spectrophotometer (Hitachi, Tokyo, Japan). Viscosity experiments were carried out using an ALPHA L Fungilab rotational viscometer (Fungilab, Barcelona, Spain) equipped with an 18 mL LCP spindle and the measurements were performed at 100 rpm. Fluorescence spectra were recorded in solution on a Hitachi F-7000 fluorescence spectrophotometer (Hitachi, Tokyo, Japan).

Arylazo sulfones **1–14** were prepared from the corresponding diazonium salts by following a known procedure [64]. Spectroscopic data for compounds **1**, **11**, **12** [88], **2–4** [40], **5**, **6–9**, **14** [64], **10** [67], **13** [89] were in accordance with the literature. Compound **17** was synthesized from 4-bromoaniline by following a known procedure [90]. Spectroscopic data for **17** were in accordance with the literature [91].

Synthesis of 4-(((4-chlorophenyl)thio)diazenyl)benzonitrile (**15**).

Compound **15** was prepared by adapting a known procedure [92]. 4-aminobenzonitrile (11.4 mol) was suspended in MeCN:H₂O 2:1 (5 mL), and the resulting mixture was cooled to 0 °C. Conc. HCl (3.8 mL) was then added, and the so-obtained mixture was further cooled to −5 °C. A solution of NaNO₂ (17 mmol) in water (5 mL) was added dropwise, and the mixture was treated with sodium acetate (25% *w/w*) until pH = 5. 4-chlorothiophenol (11.4 mmol) in ethanol (20 mL) was then added dropwise, and the resulting orange precipitate was collected by filtration and purified by recrystallization from ethanol, to afford 1.81 g of **15** (orange solid, 58% yield, mp (dec.): 111.3–112 °C).

15. ^1H NMR (300 MHz, CDCl_3) δ : 7.47–7.50 (d, 2H, $J = 6\text{ Hz}$), 7.58–7.63 (m, 4H), 7.71–7.74 (d, 2H, $J = 6\text{ Hz}$). ^{13}C NMR (75 MHz, CDCl_3) δ : 113.5, 118.4, 122.4, 129.7, 131.5, 132.9, 133.4, 136.4, 153.5. Anal. Calcd for $\text{C}_{13}\text{H}_8\text{ClN}_3\text{S}$: C, 57.04; H, 2.95; N, 15.35. Found: C, 57.1; H, 3.0; N, 15.2.

Synthesis of 1-(4-nitrophenyl)-2-((4-nitrophenyl)sulfonyl)diazene (**16**).

Compound **16** was prepared by adapting a known procedure [63]. 4-nitrophenyldiazonium tetrafluoroborate (1.89 g, 8 mmol) and sodium 4-nitrobenzenesulfinate [93] (1.77 g, 8.5 mmol) were suspended in CH_2Cl_2 (20 mL). The resulting mixture was stirred overnight, then filtered, and the obtained solution was evaporated to give a dark yellow residue, that was purified by dissolving in CH_2Cl_2 and precipitated by adding cold n-hexane, to afford 336 mg of **16** (yellow solid, 12.5% yield, mp (dec.): 129–130 °C).

16. ^1H NMR (300 MHz, CD_3COCD_3) δ : 8.60 (d, $J = 8.9\text{ Hz}$, 2H), 8.49 (d, $J = 9.0\text{ Hz}$, 2H), 8.33 (d, $J = 8.9\text{ Hz}$, 2H), 8.11 (d, $J = 9.0\text{ Hz}$, 2H). ^{13}C NMR (75 MHz, CD_3COCD_3) δ : 153.3, 153.2, 152.7, 139.1, 133.6, 126.6, 126.5, 125.8. Anal. Calcd for $\text{C}_{12}\text{H}_8\text{N}_4\text{O}_6\text{S}$: C, 42.86; H, 2.40; N, 16.66. Found: C, 43.0; H, 2.5; N, 16.5.

3.1. Interaction with CT DNA

The interaction of the compounds with CT DNA was evaluated in vitro using their solutions in DMSO (1 mM) due to their low solubility in water. These studies were

performed in the presence of aqueous buffer solutions, where the mixing of each solution never exceeded 5% DMSO (*v/v*) in the final solution. Control experiments were undertaken to assess the effect of DMSO on the data, and no changes were observed in the spectra of CT DNA. The interaction of the compounds with CT DNA was investigated by UV–vis spectroscopy and viscosity measurements, and the evaluation of their EB-displacing ability was studied by fluorescence emission spectroscopy. Detailed procedures and equations regarding the *in vitro* study of the interaction of the compounds with CT DNA are given in the Supporting Information File (SI, Parts S.2–S.4).

3.2. DNA Cleavage and Photo-Cleavage Experiments

Compounds 1–17 were individually incubated with plasmid DNA at the desired concentration in Eppendorf vials and/or irradiated with UV-A or visible light (365 nm–18 W, or white light 400–700 nm–18 W) and in 10 cm distance under aerobic conditions at room temperature for 2 h. Conditions of the photobiological reaction and gel electrophoresis, quantification of DNA cleaving activity, and calculation of ss% and ds% damage protocols have been described previously [60]. All experiments were performed at least twice.

3.3. Molecular Docking Studies

Organic compounds were fully optimized at the B3LYP/6-31g* level of theory with the LanL2DZ basis set for iodine in the case of compound 13 as implemented in the Gaussian 09 [94] suite of programs (Revision B.01). The crystal data of the B-DNA dodecamer d(CGCGAATTCGCG)2 (PDB 1D:1BNA) were downloaded from the Protein Data Bank [95]. The docking analysis was performed using the AutoDock Vina program [96]. The DNA was adapted for docking by removing water molecules and polar hydrogens, and Gasteiger charges were added by Autodock 4.2 Tools (ADT) before performing docking calculations. A grid box with a size of 60 × 80 × 114 with 0.375 Å spacing was used to encompass the whole DNA. The rigid docking protocol and 100 runs of the Lamarckian genetic algorithm for searching ligand conformations were performed. PyMOL [97] was used for the representation of the docking results and interactions between DNA and compounds.

3.4. Cell Culture Experiments

A375 (CRL-1619TM) cell line was used to test the cytotoxic effect of the compounds [76]. Cells were cultured under aseptic conditions using DMEM basal medium (31885-023; Gibco, MD, USA) supplemented with 10% fetal bovine serum (FB1000/500, Biosera, London, UK), 100 units/ml penicillin, 100 ug/mL streptomycin (15140-122, Gibco), and 2 mM L-glutamine (25030; Gibco). The cell line was maintained at standard conditions (37 °C, 5% CO₂) in a humidified atmosphere and was used at 70–90% confluency. Five thousand cells were seeded per well. A UV-A lamp was placed 10 cm over the 96-well plate. After 1 h incubation with 50 μM and 100 μM of each compound, 1 h irradiation with UV-A (365 nm) followed. Then, compounds were removed, and a cytotoxicity assay was performed 24 h later. Resazurin Cell Viability Assay (CA035, Canvax, Valladolid, Spain) was used for fluorescence measurements according to the manufacturer's guidelines. Essentially, a non-irradiated 96-well plate was used as a control, under the same conditions. Incubation with 10% resazurin (7 h) was followed by fluorescence measurement at $\lambda_{em} = 590$ nm and $\lambda_{ex} = 530/560$ nm in a VarioSkan lux reader (Thermo, MT, USA).

HFL1, a fibroblast cell line, was isolated from the lung of a white, normal embryo, as were HaCaT cell lines, human immortalized keratinocytes. Cells were cultured under aseptic conditions using DMEM basal medium (31885-023; Gibco) supplemented with 10% fetal bovine serum (FB1000/500, Biosera, UK), 100 units/ml penicillin, 100 ug/mL streptomycin (15140-122, Gibco), and 2 mM L-glutamine (25030; Gibco). Cell lines were maintained at standard conditions (37 °C, 5% CO₂) in a humidified atmosphere and were used at 70–90% confluency. Five thousand cells were seeded per well. Cells were incubated with 13.4 μM of compound 1 and 100 μM of compounds 14 and 17. The experimental procedure was the same as the procedure that was followed for A375 cell lines.

4. Conclusions

A set of arylazosulfone derivatives has been synthesized, and their biological evaluation has been investigated in relation to their strong UV-A and visible light absorption and the lability of their N–S bond. Thus, their ability to photocleave DNA as well as their cytotoxic effect on the highly malignant melanoma cells A375 as well as on two non-cancer cell lines has been studied.

The affinity of sulfones to calf-thymus DNA has been studied to prove their ability to interact with biological materials via polar contacts and Van der Waals forces. The interaction of compounds 1–17 with CT DNA revealed their tight binding to CT DNA via partial intercalation. It was found that the *m*-substitution (in the case of NO₂- and Cl-derivatives) leads to higher DNA-binding constants. Molecular docking calculations have indicated moderate energy bindings and polar contacts for most of the compounds.

Incubation of the compounds with plasmid DNA showed DNA cleavage for several derivatives, whereas application of light led to considerable DNA photocleavage, especially in the UV-A region. The derivatives that exhibited the best photocleavage activity were compounds 1, 5–14, and 16, the vast majority of which had a nitro- or halogen-aromatic substituent.

Cell cultures with the melanoma cells showed that derivatives 3 and 5 exhibited chemical activity with an IC₅₀ of ~100 μM. On the other hand, compounds 1, 14, and 17 exhibited only photochemical activity with an IC₅₀ of ~13, 100, and 100 μM, respectively. The same was evident for the two non-cancer cell lines. Derivatives 14 and 17, and, most importantly, naphthyl derivative 1, exerted a small effect in the dark on cells, but they killed them in concentrations as low as 100, 100, and ~13 μM, respectively. Thus, they might be lead compounds for the development of novel derivatives able to act under photodynamic effects and to be used in the development of phototoxic pharmaceuticals.

Supplementary Materials: The following supporting information can be downloaded at: <https://www.mdpi.com/article/10.3390/ijms24031834/s1>.

Author Contributions: Conceptualization, S.P. and M.F.; methodology, M.K. (Maria Koffa), M.K. (Michael Koukourakis), G.P., S.P., M.F. and K.C.F.; software, C.M. and K.C.F.; validation, C.M., A.M., V.G., K.R.K., M.K. (Maria Koffa), G.P., S.P., M.F. and K.C.F.; investigation, C.M., A.M. and V.G.; resources, K.R.K., M.K. (Maria Koffa), M.K. (Michael Koukourakis), G.P., S.P., M.F. and K.C.F.; data curation, C.M., A.M., V.G., K.R.K., M.K. (Maria Koffa), G.P., S.P., M.F. and K.C.F.; writing—original draft preparation, K.C.F.; writing—review and editing, K.R.K., M.K. (Maria Koffa), G.P., S.P., M.F. and K.C.F.; supervision, S.P., M.F. and K.C.F.; project administration, S.P., M.F. and K.C.F. All authors have read and agreed to the published version of the manuscript.

Funding: This research received no external funding.

Institutional Review Board Statement: Not applicable.

Informed Consent Statement: Not applicable.

Data Availability Statement: Not applicable.

Acknowledgments: The authors would like to thank the editorial board for a free waiver for the manuscript. Special thanks owed to Konstantinos Meliopoulos for preparing plasmid DNA, Christos Kakouratos and Erasmia Xanthopoulou, members of Prod. M.I. Koukourakis' laboratory for technical assistance on HFL1 cell line and Molecular Physiology Aglaia Pappa at MBG, DUTH for providing the HaCat cell line. A.M. was funded by the project "InTechThrace: Integrated Technologies in biomedical research: multilevel biomarker analysis in Thrace" (MIS Code 5047285), under the Operational Program "Competitiveness, Entrepreneurship & Innovation" (EPAnEK), co-funded by the European Regional Development Fund (ERDF) and national resources (Partnership Agreement 2014–2020).

Conflicts of Interest: The authors declare no conflict of interest.

References

1. Ali, A.; Bhattacharya, S. DNA binders in clinical trials and chemotherapy. *Bioorg. Med. Chem.* **2014**, *22*, 4506–4521. [CrossRef] [PubMed]
2. Portugal, J. Challenging transcription by DNA-binding antitumor drugs. *Biochem. Pharmacol.* **2018**, *155*, 336–345. [CrossRef] [PubMed]
3. Paul, A.; Bhattacharya, S. Chemistry and biology of DNA-binding small molecules. *Curr. Sci.* **2012**, *102*, 212–231.
4. Sirajuddin, M.; Ali, S.; Badshah, A. Drug-DNA interactions and their study by UV-Visible, fluorescence spectroscopies and cyclic voltametry. *J. Photochem. Photobiol. B Biol.* **2013**, *124*, 1–19. [CrossRef] [PubMed]
5. Fernandes, L.; Fischer, F.L.; Ribeiro, C.W.; Silveira, G.P.; Sá, M.M.; Nome, F.; Terenzi, H. Metal-free artificial nucleases based on simple oxime and hydroxylamine scaffolds. *Bioorg. Med. Chem. Lett.* **2008**, *18*, 4499–4502. [CrossRef]
6. Reddy, D.S.; Kongot, M.; Netalkar, S.P.; Kurjogi, M.M.; Kumar, R.; Avecilla, F.; Kumar, A. Synthesis and evaluation of novel coumarin-oxime ethers as potential anti-tubercular agents: Their DNA cleavage ability and BSA interaction study. *Eur. J. Med. Chem.* **2018**, *150*, 864–875. [CrossRef]
7. Obalı, A.Y.; Akçaalan, S.; Arslan, E.; Obalı, İ. Antibacterial activities and DNA-cleavage properties of novel fluorescent imidazo-phenanthroline derivatives. *Bioorg. Chem.* **2020**, *100*, 103885. [CrossRef]
8. Gratal, P.; Arias-Pérez, M.S.; Gude, L. 1H-imidazo[4,5-f][1,10]phenanthroline carbohydrate conjugates: Synthesis, DNA interactions and cytotoxic activity. *Bioorg. Chem.* **2022**, *125*, 105851. [CrossRef]
9. Bhat, R.; Begum, N.S. Synthesis, characterization and molecular docking studies of new indol(1H-3-yl)pyrimidine derivatives: Insights into their role in DNA interaction. *Nucleosides Nucleotides Nucleic Acids* **2021**, *40*, 619–634. [CrossRef]
10. Eryılmaz, S.; Türk Çelikoğlu, E.; İdil, Ö.; İnkaya, E.; Kozak, Z.; Mısı, E.; Gül, M. Derivatives of pyridine and thiazole hybrid: Synthesis, DFT, biological evaluation via antimicrobial and DNA cleavage activity. *Bioorg. Chem.* **2020**, *95*, 103476. [CrossRef]
11. Doğan, A.; Özdemir, S.; Yalçın, M.S.; Sari, H.; Nural, Y. Naphthoquinone-thiazole hybrids bearing adamantane: Synthesis, antimicrobial, DNA cleavage, antioxidant activity, acid dissociation constant, and drug-likeness. *J. Res. Pharm.* **2021**, *25*, 292–304. [CrossRef]
12. Mishra, V.R.; Ghanavatkar, C.W.; Mali, S.N.; Chaudhari, H.K.; Sekar, N. Schiff base clubbed benzothiazole: Synthesis, potent antimicrobial and MCF-7 anticancer activity, DNA cleavage and computational study. *J. Biomol. Struct. Dyn.* **2020**, *38*, 1772–1785. [CrossRef]
13. Katrahalli, U.; Chanabasappa Yallur, B.; Manjunatha, D.H.; Krishna, P.M. BSA interaction and DNA cleavage studies of anti-bacterial benzothiazol-2-yl-malonaldehide. *J. Mol. Struct.* **2019**, *1196*, 96–104. [CrossRef]
14. Nural, Y.; Ozdemir, S.; Yalcin, M.S.; Demir, B.; Atabey, H.; Seferoglu, Z.; Ece, A. New bis- and tetrakis-1,2,3-triazole derivatives: Synthesis, DNA cleavage, molecular docking, antimicrobial, antioxidant activity and acid dissociation constants. *Bioorg. Med. Chem. Lett.* **2022**, *55*, 128453. [CrossRef]
15. Caron, C.; Duong, X.N.T.; Guillot, R.; Bombard, S.; Granzhan, A. Interaction of Functionalized Naphthalenophanes with Abasic Sites in DNA: DNA Cleavage, DNA Cleavage Inhibition, and Formation of Ligand–DNA Adducts. *Chem.—Eur. J.* **2019**, *25*, 1949–1962. [CrossRef]
16. Rafique, J.; Farias, G.; Saba, S.; Zapp, E.; Bellettini, I.C.; Momoli Salla, C.A.; Bechtold, I.H.; Scheide, M.R.; Santos Neto, J.S.; Monteiro de Souza Junior, D.; et al. Selenylated-oxadiazoles as promising DNA intercalators: Synthesis, electronic structure, DNA interaction and cleavage. *Dye. Pigment.* **2020**, *180*, 108519. [CrossRef]
17. Wei, X.W.; Yuan, J.M.; Huang, W.Y.; Chen, N.Y.; Li, X.J.; Pan, C.X.; Mo, D.L.; Su, G.F. 2-Styryl-4-aminoquinazoline derivatives as potent DNA-cleavage, p53-activation and in vivo effective anticancer agents. *Eur. J. Med. Chem.* **2020**, *186*, 111851. [CrossRef]
18. Ozkan, S.C.; Aksakal, F.; Yilmaz, A. Synthesis of novel calix[4]arene: P-benzazole derivatives and investigation of their DNA binding and cleavage activities with molecular docking and experimental studies. *RSC Adv.* **2020**, *10*, 38695–38708. [CrossRef]
19. Rathod, A.S.; Biradar, J.S. Synthesis of Some Indolyl Derivatives under Solvent Free Conditions, Their Cytotoxicity, and DNA Cleavage Studies. *Russ. J. Gen. Chem.* **2020**, *90*, 135–141. [CrossRef]
20. Danilkina, N.A.; Rumyantsev, A.M.; Lyapunova, A.L.; D'Yachenko, A.S.; Khlebnikov, A.F.; Balova, I.A. 10-Membered Azaenediyne Fused to a Benzothiophene through the Nicholas Macrocyclization: Synthesis and DNA Cleavage Ability. *Synlett* **2019**, *30*, 161–166. [CrossRef]
21. Zhang, H.; Li, R.; Ba, S.; Lu, Z.; Pitsinos, E.N.; Li, T.; Nicolaou, K.C. DNA Binding and Cleavage Modes of Shishijimicin A. *J. Am. Chem. Soc.* **2019**, *141*, 7842–7852. [CrossRef] [PubMed]
22. Marrani, E.; Foeldvari, I.; Lopez, J.A.; Cimaz, R.; Simonini, G. Comparing ultraviolet light A photo(chemo)therapy with Methotrexate protocol in childhood localized scleroderma: Evidence from systematic review and meta-analysis approach. *Semin. Arthritis Rheum.* **2018**, *48*, 495–503. [CrossRef] [PubMed]
23. Garritsen, F.M.; Brouwer, M.W.D.; Limpens, J.; Spuls, P.I. Photo(chemo)therapy in the management of atopic dermatitis: An updated systematic review with implications for practice and research. *Br. J. Dermatol.* **2014**, *170*, 501–513. [CrossRef] [PubMed]
24. Pinto, M.N.; Mascharak, P.K. Light-assisted and remote delivery of carbon monoxide to malignant cells and tissues: Photochemotherapy in the spotlight. *J. Photochem. Photobiol. C Photochem. Rev.* **2020**, *42*, 100341. [CrossRef]
25. de Souza da Fonseca, A.; de Paoli, F.; Mencalha, A.L. Photodynamic therapy for treatment of infected burns. *Photodiagnosis Photodyn. Ther.* **2022**, *38*, 102831. [CrossRef]

26. Yaqoob, M.D.; Xu, L.; Li, C.; Leong, M.M.L.; Xu, D.D. Targeting mitochondria for cancer photodynamic therapy. *Photodiagnosis Photodyn. Ther.* **2022**, *38*, 102830. [CrossRef]
27. Heerfordt, I.M.; Philipsen, P.A.; Wulf, H.C. Bringing the gentle properties of daylight photodynamic therapy indoors: A systematic review of efficacy and safety. *Photodiagnosis Photodyn. Ther.* **2022**, *39*, 102858. [CrossRef]
28. Mazur, A.; Koziarowska, K.; Dynarowicz, K.; Aebisher, D.; Bartusik-Aebisher, D. Photodynamic Therapy for Treatment of Disease in Children—A Review of the Literature. *Children* **2022**, *9*, 695. [CrossRef]
29. Morita, A.; Tateishi, C.; Ikumi, K.; Hayashi, D.; Nakada, A.; Nishihara, H.; Torii, K.; Nishida, E.; Tsuruta, D. Comparison of the Efficacy and Safety of Bexarotene and Photo(Chemo)Therapy Combination Therapy and Bexarotene Monotherapy for Cutaneous T-Cell Lymphoma. *Dermatol. Ther.* **2022**, *12*, 615–629. [CrossRef]
30. Hu, S.; Dong, C.; Wang, J.; Liu, K.; Zhou, Q.; Xiang, J.; Zhou, Z.; Liu, F.; Shen, Y. Assemblies of indocyanine green and chemotherapeutic drug to cure established tumors by synergistic chemo-photo therapy. *J. Control. Release* **2020**, *324*, 250–259. [CrossRef]
31. Ghosh, S.; Gul, A.R.; Xu, P.; Lee, S.Y.; Rafique, R.; Kim, Y.H.; Park, T.J. Target delivery of photo-triggered nanocarrier for externally activated chemo-photodynamic therapy of prostate cancer. *Mater. Today Chem.* **2022**, *23*, 100688. [CrossRef]
32. Zamani, M.; Aghajanzadeh, M.; Jashnani, S.; Darvishzad, S.; Khoramabadi, H.; Shirin Shahangian, S.; Shirini, F. Combination of chemo and photo dynamic therapy using pH triggered bio-coated spinels for treatment of breast cancer. *J. Mol. Liq.* **2022**, *358*, 119211. [CrossRef]
33. Ma, C.-H.; Ma, H.-H.; Deng, X.-B.; Yu, R.; Song, K.-W.; Wei, K.-K.; Wang, C.-J.; Li, H.-X.; Chen, H. Photodynamic Therapy in Combination with Chemotherapy, Targeted, and Immunotherapy As a Successful Therapeutic Approach for Advanced Gastric Adenocarcinoma: A Case Report and Literature Review. *Photobiomodulation Photomed. Laser Surg.* **2022**, *40*, 308–314. [CrossRef]
34. Wang, Y.; Xu, Y.; Guo, X.; Wang, L.; Zeng, J.; Qiu, H.; Tan, Y.; Chen, D.; Zhao, H.; Gu, Y. Enhanced antimicrobial activity through the combination of antimicrobial photodynamic therapy and low-frequency ultrasonic irradiation. *Adv. Drug Deliv. Rev.* **2022**, *183*, 114168. [CrossRef]
35. Ferrisse, T.M.; Dias, L.M.; de Oliveira, A.B.; Jordão, C.C.; de Oliveira Mima, E.G.; Pavarina, A.C. Efficacy of curcumin-mediated antibacterial photodynamic therapy for oral antiseptics: A systematic review and network meta-analysis of randomized clinical trials. *Photodiagnosis Photodyn. Ther.* **2022**, *39*, 102876. [CrossRef]
36. Sales, L.S.; Miranda, M.L.; de Oliveira, A.B.; Ferrisse, T.M.; Fontana, C.R.; Milward, M.; Brighenti, F.L. Effect of the technique of photodynamic therapy against the main microorganisms responsible for periodontitis: A systematic review of in-vitro studies. *Arch. Oral Biol.* **2022**, *138*, 105425. [CrossRef]
37. Maisch, T. Resistance in antimicrobial photodynamic inactivation of bacteria. *Photochem. Photobiol. Sci.* **2015**, *14*, 1518–1526. [CrossRef]
38. Hamblin, M.R. Antimicrobial photodynamic inactivation: A bright new technique to kill resistant microbes. *Curr. Opin. Microbiol.* **2016**, *33*, 67–73. [CrossRef]
39. Qiu, D.; Lian, C.; Mao, J.; Fagnoni, M.; Protti, S. Dyedauxiliary Groups, an Emerging Approach in Organic Chemistry. The Case of Arylazo Sulfones. *J. Org. Chem.* **2020**, *85*, 12813–12822. [CrossRef]
40. Crespi, S.; Fagnoni, M. Generation of Alkyl Radicals: From the Tyranny of Tin to the Photon Democracy. *Chem. Rev.* **2020**, *120*, 9790–9833. [CrossRef]
41. Coyle, R.; Fahey, K.; Aldabbagh, F. Barton esters for initiator-free radical cyclisation with heteroaromatic substitution. *Org. Biomol. Chem.* **2013**, *11*, 1672–1682. [CrossRef] [PubMed]
42. Coyle, R.; McArdle, P.; Aldabbagh, F. Tandem reactions via barton esters with intermolecular addition and vinyl radical substitution onto indole. *J. Org. Chem.* **2014**, *79*, 5903–5907. [CrossRef]
43. Saraiva, M.F.; Couri, M.R.C.; Le Hyaric, M.; de Almeida, M.V. The Barton ester free-radical reaction: A brief review of applications. *Tetrahedron* **2009**, *65*, 3563–3572. [CrossRef]
44. Protti, S.; Ravelli, D.; Fagnoni, M. Designing Radical Chemistry by Visible-Light Promoted Homolysis. *Trends Chem.* **2022**, *4*, 305–317. [CrossRef]
45. Blom, P.; Xiang, A.X.; Kao, D.; Theodorakis, E.A. Design, synthesis, and evaluation of N-aryloxy-2-thiopyridones as DNA photocleaving reagents. *Bioorg. Med. Chem.* **1999**, *7*, 727–736. [CrossRef] [PubMed]
46. Theodorakis, E.A.; Xiang, X.; Blom, P. Photochemical cleavage of duplex DNA by N-benzoyloxy-2-thiopyridone linked to 9-aminoacridine. *Chem. Commun.* **1997**, *5*, 1463–1464. [CrossRef]
47. Theodorakis, E.A.; Wilcoxon, K.M. N-Aroyloxy-2-thiopyridones as efficient oxygen-radical generators: Novel time-controlled DNA photocleaving reagents. *Chem. Commun.* **1996**, *16*, 1927–1928. [CrossRef]
48. Theodorakis, E.A.; Xiang, X.; Lee, M.; Gibson, T. On the Mechanism of Photo-induced Nucleic Acid Cleavage Using N-Aroyloxy-2-thiopyridones. *Tetrahedron Lett.* **1998**, *39*, 3383–3386. [CrossRef]
49. Qian, X.; Yao, W.; Chen, G.; Huang, X.; Mao, P. N-Aroyloxynaphthalimides as novel highly efficient DNA photocleavers: Substituent effects. *Tetrahedron Lett.* **2001**, *42*, 6175–6178. [CrossRef]
50. Xu, Y.; Huang, X.; Qian, X.; Yao, W. N-Aroyloxylthioxo-naphthalimides as DNA photocleavers of aroyloxyl oxygen radicals: Synthesis, evaluation, and substituents' effect. *Bioorg. Med. Chem.* **2004**, *12*, 2335–2341. [CrossRef]
51. Alonso, R.; Campos, P.J.; Rodríguez, M.A.; Sampedro, D. Photocyclization of iminyl radicals: Theoretical study and photochemical aspects. *J. Org. Chem.* **2008**, *73*, 2234–2239. [CrossRef]

52. Lalevée, J.; Allonas, X.; Fouassier, J.P.; Tachi, H.; Izumitani, A.; Shirai, M.; Tsunooka, M. Investigation of the photochemical properties of an important class of photobase generators: The O-acyloximes. *J. Photochem. Photobiol. A Chem.* **2002**, *151*, 27–37. [CrossRef]
53. Alonso, R.; Caballero, A.; Campos, P.J.; Rodríguez, M.A. Photochemistry of acyloximes: Synthesis of heterocycles and natural products. *Tetrahedron* **2010**, *66*, 8828–8831. [CrossRef]
54. Walton, J.C. Functionalised oximes: Emergent precursors for carbon-, nitrogen- and oxygen-centred radicals. *Molecules* **2016**, *21*, 63. [CrossRef]
55. Pang, Y.; Fan, S.; Wang, Q.; Oprych, D.; Feilen, A.; Reiner, K.; Keil, D.; Slominsky, Y.L.; Popov, S.; Zou, Y.; et al. NIR-Sensitized Activated Photoreaction between Cyanines and Oxime Esters: Free-Radical Photopolymerization. *Angew. Chem.—Int. Ed.* **2020**, *59*, 11440–11447. [CrossRef]
56. Karamtzioti, P.; Papastergiou, A.; Stefanakis, J.G.; Koumbis, A.E.; Anastasiou, I.; Koffa, M.; Fylaktakidou, K.C. O-Benzoyl pyridine aldoxime and amidoxime derivatives: Novel efficient DNA photo-cleavage agents. *Medchemcomm* **2015**, *6*, 719–726. [CrossRef]
57. Hwu, J.R.; Tsay, S.C.; Hong, S.C.; Hsu, M.H.; Liu, C.F.; Chou, S.S.P. Relationship between structure of conjugated oxime esters and their ability to cleave DNA. *Bioconjug. Chem.* **2013**, *24*, 1778–1783. [CrossRef]
58. Bindu, P.J.; Mahadevan, K.M.; Satyanarayan, N.D.; Ravikumar Naik, T.R. Synthesis and DNA cleavage studies of novel quinoline oxime esters. *Bioorg. Med. Chem. Lett.* **2012**, *22*, 898–900. [CrossRef]
59. Chowdhury, N.; Dutta, S.; Dasgupta, S.; Singh, N.D.P.; Baidya, M.; Ghosh, S.K. Synthesis, photophysical, photochemical, DNA cleavage/binding and cytotoxic properties of pyrene oxime ester conjugates. *Photochem. Photobiol. Sci.* **2012**, *11*, 1239–1250. [CrossRef]
60. Pasolli, M.; Dafnopoulos, K.; Andreou, N.P.; Gritzapis, P.S.; Koffa, M.; Koumbis, A.E.; Psomas, G.; Fylaktakidou, K.C. Pyridine and p-nitrophenyl oxime esters with possible photochemotherapeutic activity: Synthesis, DNA photocleavage and DNA binding studies. *Molecules* **2016**, *21*, 864. [CrossRef]
61. Andreou, N.P.; Dafnopoulos, K.; Tortopidis, C.; Koumbis, A.E.; Koffa, M.; Psomas, G.; Fylaktakidou, K.C. Alkyl and aryl sulfonyl p-pyridine ethanone oximes are efficient DNA photo-cleavage agents. *J. Photochem. Photobiol. B Biol.* **2016**, *158*, 30–38. [CrossRef] [PubMed]
62. Papastergiou, A.; Perontsis, S.; Gritzapis, P.; Koumbis, A.E.; Koffa, M.; Psomas, G.; Fylaktakidou, K.C. Evaluation of O-alkyl and aryl sulfonyl aromatic and heteroaromatic amidoximes as novel potent DNA photo-cleavers. *Photochem. Photobiol. Sci.* **2016**, *15*, 351–360. [CrossRef] [PubMed]
63. Gritzapis, P.S.; Varras, P.C.; Andreou, N.P.; Katsani, K.R.; Dafnopoulos, K.; Psomas, G.; Peitsinis, Z.V.; Koumbis, A.E.; Fylaktakidou, K.C. P-Pyridinyl oxime carbamates: Synthesis, DNA binding, DNA photocleaving activity and theoretical photodegradation studies. *Beilstein J. Org. Chem.* **2020**, *16*, 337–350. [CrossRef] [PubMed]
64. Lian, C.; Yue, G.; Mao, J.; Liu, D.; Ding, Y.; Liu, Z.; Qiu, D.; Zhao, X.; Lu, K.; Fagnoni, M.; et al. Visible-Light-Driven Synthesis of Arylstannanes from Arylazo Sulfones. *Org. Lett.* **2019**, *21*, 5187–5191. [CrossRef] [PubMed]
65. Qiu, D.; Lian, C.; Mao, J.; Ding, Y.; Liu, Z.; Wei, L.; Fagnoni, M.; Protti, S. Visible Light-Driven, Photocatalyst-Free Arbusov-Like Reaction via Arylazo Sulfones. *Adv. Synth. Catal.* **2019**, *361*, 5239–5244. [CrossRef]
66. Liu, J.; Tian, M.; Li, Y.; Shan, X.; Li, A.; Lu, K.; Fagnoni, M.; Protti, S.; Zhao, X. Metal-Free Synthesis of Unsymmetrical Aryl Selenides and Tellurides via Visible Light-Driven Activation of Arylazo Sulfones. *Eur. J. Org. Chem.* **2020**, *2020*, 7358–7367. [CrossRef]
67. Di Terlizzi, L.; Scaringi, S.; Raviola, C.; Pedrazzani, R.; Bandini, M.; Fagnoni, M.; Protti, S. Visible Light-Driven, Gold(I)-Catalyzed Preparation of Symmetrical (Hetero)biaryls by Homocoupling of Arylazo Sulfones. *J. Org. Chem.* **2022**, *87*, 4863–4872. [CrossRef]
68. Blank, L.; Fagnoni, M.; Protti, S.; Rueping, M. Visible-Light Promoted Formation of C-B and C-S Bonds under metal and photocatalyst-free conditions. *Synthesis* **2019**, *51*, 1243–1252. [CrossRef]
69. Bui, T.T.; Tran, V.H.; Kim, H.K. Visible-Light-Mediated Synthesis of Sulfonyl Fluorides from Arylazo Sulfones. *Adv. Synth. Catal.* **2022**, *364*, 341–347. [CrossRef]
70. Chawla, R.; Jaiswal, S.; Dutta, P.K.; Yadav, L.D.S. A photocatalyst-free visible-light-mediated solvent-switchable route to stilbenes/vinyl sulfones from β -nitrostyrenes and arylazo sulfones. *Org. Biomol. Chem.* **2021**, *19*, 6487–6492. [CrossRef]
71. Li, A.; Li, Y.; Liu, J.; Chen, J.; Lu, K.; Qiu, D.; Fagnoni, M.; Protti, S.; Zhao, X. Metal-Free Trifluoromethylthiolation of Arylazo Sulfones. *J. Org. Chem.* **2021**, *86*, 1292–1299. [CrossRef]
72. Chawla, R.; Jaiswal, S.; Dutta, P.K.; Yadav, L.D.S. Photocatalyst-free visible light driven synthesis of (E)-vinyl sulfones from cinnamic acids and arylazo sulfones. *Tetrahedron Lett.* **2020**, *61*, 151898. [CrossRef]
73. Nitti, A.; Martinelli, A.; Batteux, F.; Protti, S.; Fagnoni, M.; Pasini, D. Blue light driven free-radical polymerization using arylazo sulfones as initiators. *Polym. Chem.* **2021**, *12*, 5747–5751. [CrossRef]
74. Lombardi, L.; Kovtun, A.; Mantovani, S.; Bertuzzi, G.; Favaretto, L.; Bettini, C.; Palermo, V.; Melucci, M.; Bandini, M. Visible-Light Assisted Covalent Surface Functionalization of Reduced Graphene Oxide Nanosheets with Arylazo Sulfones. *Chem.—Eur. J.* **2022**, *28*, e202200333. [CrossRef]
75. Médard, J.; Decorse, P.; Mangeney, C.; Pinson, J.; Fagnoni, M.; Protti, S. Simultaneous Photografting of Two Organic Groups on a Gold Surface by using Arylazo Sulfones as Single Precursors. *Langmuir* **2020**, *36*, 2786–2793. [CrossRef]


76. Panagopoulos, A.; Balalas, T.; Mitrakas, A.; Vrazas, V.; Katsani, K.R.; Koumbis, A.E.; Koukourakis, M.I.; Litinas, K.E.; Fylaktakidou, K.C. 6-Nitro-Quinazolin-4(3H)-one Exhibits Photodynamic Effects and Photodegrades Human Melanoma Cell Lines. A Study on the Photoreactivity of Simple Quinazolin-4(3H)-ones. *Photochem. Photobiol.* **2021**, *97*, 826–836. [CrossRef]
77. Hansda, S.; Ghosh, G.; Ghosh, R. 9-phenyl acridine photosensitizes A375 cells to UVA radiation. *Heliyon* **2020**, *6*, e04733. [CrossRef]
78. Wolfe, A.; Shimer, G.H.; Meehan, T. Polycyclic Aromatic Hydrocarbons Physically Intercalate into Duplex Regions of Denatured DNA. *Biochemistry* **1987**, *26*, 6392–6396. [CrossRef]
79. Dimitrakopoulou, A.; Dendrinou-Samara, C.; Pantazaki, A.A.; Alexiou, M.; Nordlander, E.; Kessissoglou, D.P. Synthesis, structure and interactions with DNA of novel tetranuclear, [Mn₄(II/II/II/IV)] mixed valence complexes. *J. Inorg. Biochem.* **2008**, *102*, 618–628. [CrossRef]
80. Luis García-Giménez, J.; González-Álvarez, M.; Liu-González, M.; Macías, B.; Borrás, J.; Alzuet, G. Toward the development of metal-based synthetic nucleases: DNA binding and oxidative DNA cleavage of a mixed copper(II) complex with N-(9H-purin-6-yl)benzenesulfonamide and 1,10-phenanthroline. Antitumor activity in human Caco-2 cells and Jurkat T lymphocy. *J. Inorg. Biochem.* **2009**, *103*, 923–934. [CrossRef]
81. Liu, J.; Zhang, H.; Chen, C.; Deng, H.; Lu, T.; Ji, L. Interaction of macrocyclic copper(II) complexes with calf thymus DNA: Effects of the side chains of the ligands on the DNA-binding behaviors. *Dalt. Trans.* **2003**, *1*, 114–119. [CrossRef]
82. Lakowicz, J.R. *Principles of Fluorescence Spectroscopy*; Springer: New York, NY, USA, 2006; ISBN 978-0-387-31278-1.
83. Wilson, W.D.; Ratmeyer, L.; Zhao, M.; Streckowski, L.; Boykin, D. The Search for Structure-Specific Nucleic Acid-Interactive Drugs: Effects of Compound Structure on RNA versus DNA Interaction Strength. *Biochemistry* **1993**, *32*, 4098–4104. [CrossRef] [PubMed]
84. Heller, D.P.; Greenstock, C.L. Fluorescence lifetime analysis of DNA intercalated ethidium bromide and quenching by free dye. *Biophys. Chem.* **1994**, *50*, 305–312. [CrossRef] [PubMed]
85. Pang, E.; Zhao, S.; Wang, B.; Niu, G.; Song, X.; Lan, M. Strategies to construct efficient singlet oxygen-generating photosensitizers. *Coord. Chem. Rev.* **2022**, *472*, 214780. [CrossRef]
86. Marmur, J. A procedure for the isolation of deoxyribonucleic acid from micro-organisms. *J. Mol. Biol.* **1961**, *3*, 208–218. [CrossRef]
87. Reichmann, M.E.; Rice, S.A.; Thomas, C.A.; Doty, P. A Further Examination of the Molecular Weight and Size of Desoxyribose Nucleic Acid. *J. Am. Chem. Soc.* **1954**, *76*, 3047–3053. [CrossRef]
88. Malacarne, M.; Protti, S.; Fagnoni, M. A Visible-Light-Driven, Metal-free Route to Aromatic Amides via Radical Arylation of Isonitriles. *Adv. Synth. Catal.* **2017**, *359*, 3826–3830. [CrossRef]
89. Di Terlizzi, L.; Cola, I.; Raviola, C.; Fagnoni, M.; Protti, S. A Dyedauxiliary Group Strategy for the α -Functionalization of Ketones and Esters. *ACS Org. Inorg. Au* **2021**, *1*, 68–71. [CrossRef]
90. Nan, G.; Ren, F.; Luo, M. Suzuki–Miyaura cross-coupling reaction of 1-aryltriazenes with arylboronic acids catalyzed by a recyclable polymer-supported N-heterocyclic carbene–palladium complex catalyst. *Beilstein J. Org. Chem.* **2010**, *28*, 70. [CrossRef]
91. Disli, A.; Yildirim, Y. New Synthesis Of Phenylthioglycolic Acids Via Related Tri-azene Compounds. *Org. Prep. Proc. Int.* **1998**, *30*, 349–352. [CrossRef]
92. Novi, M.; Petrillo, G.; Dell’Erba, C. An SRN1 approach to some aromatic nitriles diazosulfides. *Tetrahedron Lett.* **1987**, *28*, 1345–1348. [CrossRef]
93. Zhou, X.; Luo, J.; Liu, J.; Peng, S.; Deng, G.-J. Pd-Catalyzed desulfitative Heck coupling with dioxygen as the terminal oxidant. *Org. Lett.* **2011**, *13*, 1432–1435.
94. Frisch, M.J.; Trucks, G.; Schlegel, H.; Scuseria, G.E.; Robb, M.; Cheeseman, J.; Scalmani, G.; Barone, V.; Mennucci, B.; Petersson, G. *Gaussian 09*; Revision B.01; Gaussian Inc.: Wallingford, CT, USA, 2009.
95. Drew, H.R.; Dickerson, R.E. Structure of a B-DNA dodecamer. III. Geometry of hydration. *J. Mol. Biol.* **1981**, *151*, 535–556. [CrossRef]
96. Trott, O.; Olson, A.J. Software news and update AutoDock Vina: Improving the speed and accuracy of docking with a new scoring function, efficient optimization, and multithreading. *J. Comput. Chem.* **2010**, *31*, 455–461.
97. Schrödinger LLC. *The PyMOL Molecular Graphics System*; Version 1.2r3pre; Schrödinger LLC: New York, NY, USA, 2022.

Disclaimer/Publisher’s Note: The statements, opinions and data contained in all publications are solely those of the individual author(s) and contributor(s) and not of MDPI and/or the editor(s). MDPI and/or the editor(s) disclaim responsibility for any injury to people or property resulting from any ideas, methods, instructions or products referred to in the content.



Article

Combined Administration of Pravastatin and Metformin Attenuates Acute Radiation-Induced Intestinal Injury in Mouse and Minipig Models

Jung Moon Kim ^{1,2}, Hyewon Kim ¹, Su Hyun Oh ¹, Won Il Jang ¹, Seung Bum Lee ¹ , Mineon Park ¹, Soyeon Kim ¹, Sunhoo Park ¹, Sehwan Shim ^{1,*} and Hyosun Jang ^{1,*}

¹ Laboratory of Radiation Exposure & Therapeutics, National Radiation Emergency Medical Center, Korea Institute of Radiological and Medical Science, Seoul 01812, Republic of Korea

² Department of Veterinary Surgery, College of Veterinary Medicine, Konkuk University, Seoul 05029, Republic of Korea

* Correspondence: ssh3002@kirams.re.kr (S.S.); hsjang@kirams.re.kr (H.J.);
Tel.: +82-2-3399-5873 (S.S.); +82-2-970-1302 (H.J.)

Abstract: Radiation-induced gastrointestinal (GI) damage is one of the critical factors that serve as basis for the lethality of nuclear accidents or terrorism. Further, there are no Food and Drug Administration-approved agents available to mitigate radiation-induced intestinal injury. Although pravastatin (PS) has been shown to exhibit anti-inflammatory and epithelial reconstructive effects following radiation exposure using mouse and minipig models, the treatment failed to improve the survival rate of high-dose irradiated intestinal injury. Moreover, we previously found that metformin (MF), a common drug used for treating type 2 diabetes mellitus, has a mitigating effect on radiation-induced enteropathy by promoting stem cell properties. In this study, we investigated whether the combined administration of PS and MF could achieve therapeutic effects on acute radiation-induced intestinal injury in mouse and minipig models. We found that the combined treatment markedly increased the survival rate and attenuated histological damage in a radiation-induced intestinal injury mouse model, in addition to epithelial barrier recovery, anti-inflammatory effects, and improved epithelial proliferation with stem cell properties. Furthermore, in minipig models, combined treatment with PS and MF ameliorates gross pathological damage in abdominal organs and attenuated radiation-induced intestinal histological damage. Therefore, the combination of PS and MF effectively alleviated radiation-induced intestinal injury in the mouse and minipig models. We believe that the combined use of PS and MF is a promising therapeutic approach for treating radiation-induced intestinal injury.

Citation: Kim, J.M.; Kim, H.; Oh, S.H.; Jang, W.I.; Lee, S.B.; Park, M.; Kim, S.; Park, S.; Shim, S.; Jang, H. Combined Administration of Pravastatin and Metformin Attenuates Acute Radiation-Induced Intestinal Injury in Mouse and Minipig Models. *Int. J. Mol. Sci.* **2022**, *23*, 14827. <https://doi.org/10.3390/ijms232314827>

Academic Editor: Dmitry Aminin

Received: 27 September 2022

Accepted: 24 November 2022

Published: 27 November 2022

Publisher's Note: MDPI stays neutral with regard to jurisdictional claims in published maps and institutional affiliations.



Copyright: © 2022 by the authors. Licensee MDPI, Basel, Switzerland. This article is an open access article distributed under the terms and conditions of the Creative Commons Attribution (CC BY) license (<https://creativecommons.org/licenses/by/4.0/>).

Keywords: pravastatin; metformin; radiation-induced intestinal injury; minipigs; epithelial regeneration; inflammation

1. Introduction

Radiotherapy, mainly used to treat cancer, induces radiation-induced gastrointestinal (GI) damage, and presents a major limitation in the treatment of abdominal and pelvic cancers. It can cause GI symptoms that affect the quality of life, including abdominal pain, anorexia, vomiting, diarrhea, weight loss, and dehydration [1,2]. Furthermore, it is predicted to be a mandatory factor for survival in the event of nuclear accidents or radiological terrorism [3,4]. GI damage in acute radiation syndrome is characterized by nausea, diarrhea, and endotoxemia. Delayed radiation damage leads to chronic inflammation and fibrotic changes [5,6]. Although various therapeutic agents have been reported to minimize these effects on healthy tissues, practical medication options are lacking. Therefore, it is necessary to develop a suitable mitigating agent for radiation-induced intestinal injuries.

Statins inhibit 3-hydroxy-3-methyl-glutaryl coenzyme A reductase and are widely used as lipid-controlling drugs [7,8]. The beneficial effects of statins include modulation

of the immune system, reduction of vascular inflammation with improved endothelial dysfunction, and inhibition of oxidative stress [8]. Statins exhibit a therapeutic effect on radiation-induced damage, and various studies have demonstrated their anti-inflammatory effect by regulating endothelial function after ionizing radiation [9–11]. In particular, pravastatin (PS) has therapeutic effects on radiation-induced intestinal damage [10,12–14]. The anti-inflammatory, anti-fibrotic, and barrier reconstructive effects of PS following radiation exposure have been revealed using mouse and minipig models [10,13,14]. A clinical study also showed that statin treatment was associated with a reduction in acute GI syndrome following pelvic radiotherapy [15]. Although the above-mentioned outcomes proved certain effects of PS on the prevention and treatment of radiation-induced enteropathy, it is noteworthy that radiation damage is triggered by multiple complicated crosstalk mechanisms. Thus, a single therapeutic strategy may fail; for instance, PS treatment failed to improve the survival rate of high-dose irradiated enteropathy.

Metformin (MF), a biguanide derivative, is the most extensively used drug for the treatment of type 2 diabetes mellitus. It not only lowers blood glucose levels but also has notable properties such as anti-oxidative and anti-inflammatory effects, which have been demonstrated in several studies [16–18]. Recent studies have shown that MF can protect healthy tissues from radiation-induced damage [17,19]. Furthermore, MF can stimulate the restoration of damaged DNA by upregulating AMP-activated protein kinase [20]. Although many studies have confirmed that MF is effective for radiation-induced injury, most studies have focused on protective purposes rather than the mitigating effects. Nevertheless, in our previous study, we found that MF mitigated radiation-induced enteropathy by promoting stem cell properties [21].

Although many studies have been conducted using mice and rats in the medical industry, several anatomical and physiological differences between humans and rodents exist [22]. Over a long period of time, minipigs have evolved from little-known alternative animal models compared with dogs and primates to promising models in the toxicology and drug development fields [23]. The minipig model mimics the human GI tract anatomy and physiology (e.g., transit time, pH value, and microbiota) [24]. Therefore, minipigs are an appropriate animal model in evaluating oral bioavailability [25]. It is a potentially more useful animal model than are rodent models in evaluating radiation-induced GI damage. As the body thickness of a minipig resembles that of a young human, the radiation absorption patterns of minipigs are similar to those of humans [26]. Therefore, the minipig model is a useful animal model for clinical therapeutic studies on radiation-induced GI damage [14,27].

A single therapy with PS or MF did not show survival effects in lethal dose irradiation. Surprisingly, the combined treatment of PS and MF notably increased the survival rate in the lethal dose-irradiated mouse model. In the minipig model, combined treatment with PS and MF improved gross pathological damage in abdominal organs and attenuated radiation-induced intestinal histological damage. Collectively, the results indicated that the combined administration of PS and MF in mouse and minipig models achieved superior therapeutic effects on acute radiation-induced intestinal injury compared to a single treatment with PS or MF.

2. Results

2.1. Effects of Combined PS and MF Treatment on Survival Rate and Radiation-Induced Intestinal Injury in the Mouse Model

To examine the effects of the combination of PS and MF on the outcome of radiation-induced intestinal injury, we performed focal irradiation of the mouse abdomen using Xrad-320 with a lethal dose of 15 Gy for survival analysis and a sublethal dose of 13.5 Gy for the therapeutic effects of radiation-induced intestinal injury. As shown in Figure 1A, MF treatment did not show a significant difference in the survival rate compared with the IR group; however, PS treatment slightly, but not significantly, increased the survival rate compared with the IR group (Figure 1A). In particular, the combination of PS and MF significantly improved the survival rate compared to the IR group (Figure 1A). In sub-lethal dose irradiation, the groups of PS, MF, and the combination of PS and MF treatment showed

significantly increased body weight compared with the IR group (Figure 1B). There were no significant differences in body weight between the IR + PS, IR + MF, and IR + PS/MF groups (Figure 1B). Six days after irradiation, histological evaluation was performed to demonstrate the therapeutic effects of the combination of PS and MF on radiation-induced intestinal injury. hematoxylin and eosin (H&E) staining of the small intestine showed crypt and villus destruction, loss of epithelial layers, inflammatory cell accumulation in the mucosa and submucosa, and thickness of the submucosa in the IR group. While this histological damage was partially attenuated in the PS- or MF-treated group, the combination treatment of PS and MF improved the histological damage (Figure 1C). Villi lengths and crypt numbers were increased in the IR + PS, IR + MF, and IR + PS/MF groups compared with those in the IR group. In particular, the combination treatment with PS and MF improved the most in the groups (Figure 1D,E). Further, we evaluated the histological scores, including epithelial layer destruction, crypt damage, vascular dilation, and inflammation. The combination treatment of PS and MF significantly decreased the histological scores compared to the single treatment with PS or MF (Figure 1F). These results indicate that the combination treatment of PS and MF improved the survival rate under lethal dose radiation exposure and effectively alleviated radiation-induced intestinal injury.

2.2. Effect of Combined PS and MF Treatment on Epithelial Barrier Damage and Inflammatory Response in Radiation-Induced Intestinal Injury

Epithelial tight junctions are physical components of epithelial integrity that preserve intestinal homeostasis by controlling paracellular permeability [28,29]. In particular, claudin3 (CLDN3) is highly sensitive to radiation exposure, and rapid disruption of CLDN3 induces loss of epithelial integrity in the irradiated intestine [27,30]. Previously, we identified that PS improves radiation-induced barrier destruction by regulating intercellular junction molecules, including tight junctions [14]. The immunostaining of Cldn3 was also strongly expressed in the epithelium of the small intestinal tissue under the PS, MF, and combination treatment in PS and MF groups (Figure 2A). Moreover, we identified that mRNA levels of Cldn3 significantly increased in the IR + PS and IR + PS/MF groups than in the IR group (Figure 2C). There were no marked differences between IR + MF and IR groups. As villin is an enterocyte marker involved in the regulation of epithelial integrity, we evaluated villin expression. Villin protein was broadly expressed in the enterocytes of the IR + PS, IR + MF, and IR + PS/MF groups (Figure 2B). Additionally, mRNA levels of villin were significantly higher in the IR + PS, IR + MF, and IR + PS/MF groups than in the IR group (Figure 2D).

Radiation-induced intestinal injury is characterized by an inflammatory response, with increased leukocyte infiltration and (pro-)inflammatory cytokine expression. We examined the anti-inflammatory effects of the combined PS and MF treatment on the irradiated intestines. The increased expression of myeloperoxidase (MPO), a neutrophil marker, corresponds to the severity of inflammation in intestinal diseases. Eosinophils also play a critical role in intestinal inflammation and radiation-induced intestinal damage by releasing cytokines and chemokines [31,32]. The number of cells positive for Mpo and eosinophils increased in the IR group, and these inflammatory cells markedly decreased in the IR + PS and IR + PS/MF groups (Figure 2E,F). In contrast, MF treatment slightly decreased the number of active neutrophils and eosinophils in the irradiated intestines (Figure 2E,F). Interleukin (IL) 1 β and monocyte chemoattractant protein 1 (MCP1) are well-known pro-inflammatory cytokines that cause inflammation [12,33]. The mRNA levels of Il1 β and Mcp1 were markedly increased in the irradiated intestine compared with those in the healthy intestine (Figure 2G,H). However, these pro-inflammatory cytokines (Il1 β and Mcp1) mRNA levels considerably decreased in the PS-treated and combined PS and MF-treated groups compared with those of the IR group. These data suggest that the combination treatment with PS and MF restores barrier integrity with epithelial reconstruction and inhibits inflammation in radiation-induced intestinal injury.

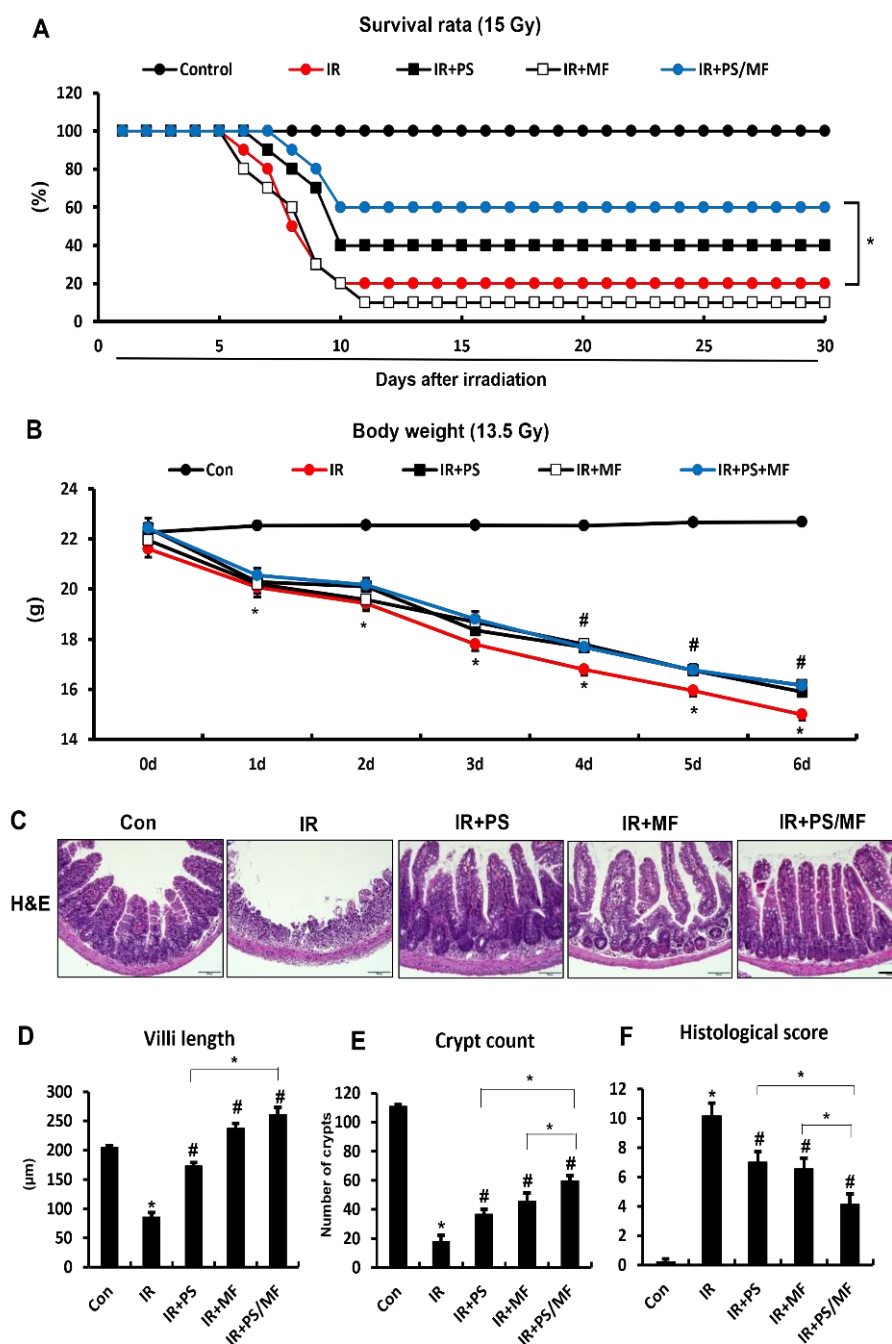


Figure 1. Effects of combined pravastatin and metformin treatment on survival rate and radiation-induced intestinal injury in the mouse model. **(A)** Survival Rate of control (Con), irradiated (IR), pravastatin-treated IR (IR + PS), metformin-treated IR (IR + MF), combined PS and MF-treated IR (IR + PS/MF) mice after abdominal irradiation of lethal dose of 15Gy. n = 10 mice per group **(B)** Body weights of Con, IR, IR + PS, IR + MF, IR + PS/MF groups after abdominal radiation of sub-lethal dose of 13.5 Gy. **(C)** Hematoxylin & Eosin (H&E) stain, **(D)** villi length, and **(E)** crypt count of 13.5 Gy irradiated small intestine after 6 days. Bar = 100 µm. **(F)** Histological score defined by the degree of maintenance of epithelial architecture, crypt damage, vascular dilation, and infiltration of inflammatory cells in the lamina propria (0 = none, 1 = mild, 2 = moderate, 3 = high) of small intestine from Con, IR, IR + PS, IR + MF, IR + PS/MF groups. Data are presented as the mean ± standard error of the mean; n = 5–6 mice per group. * *p* < 0.05 compared to the control; # *p* < 0.05 compared to the IR group.

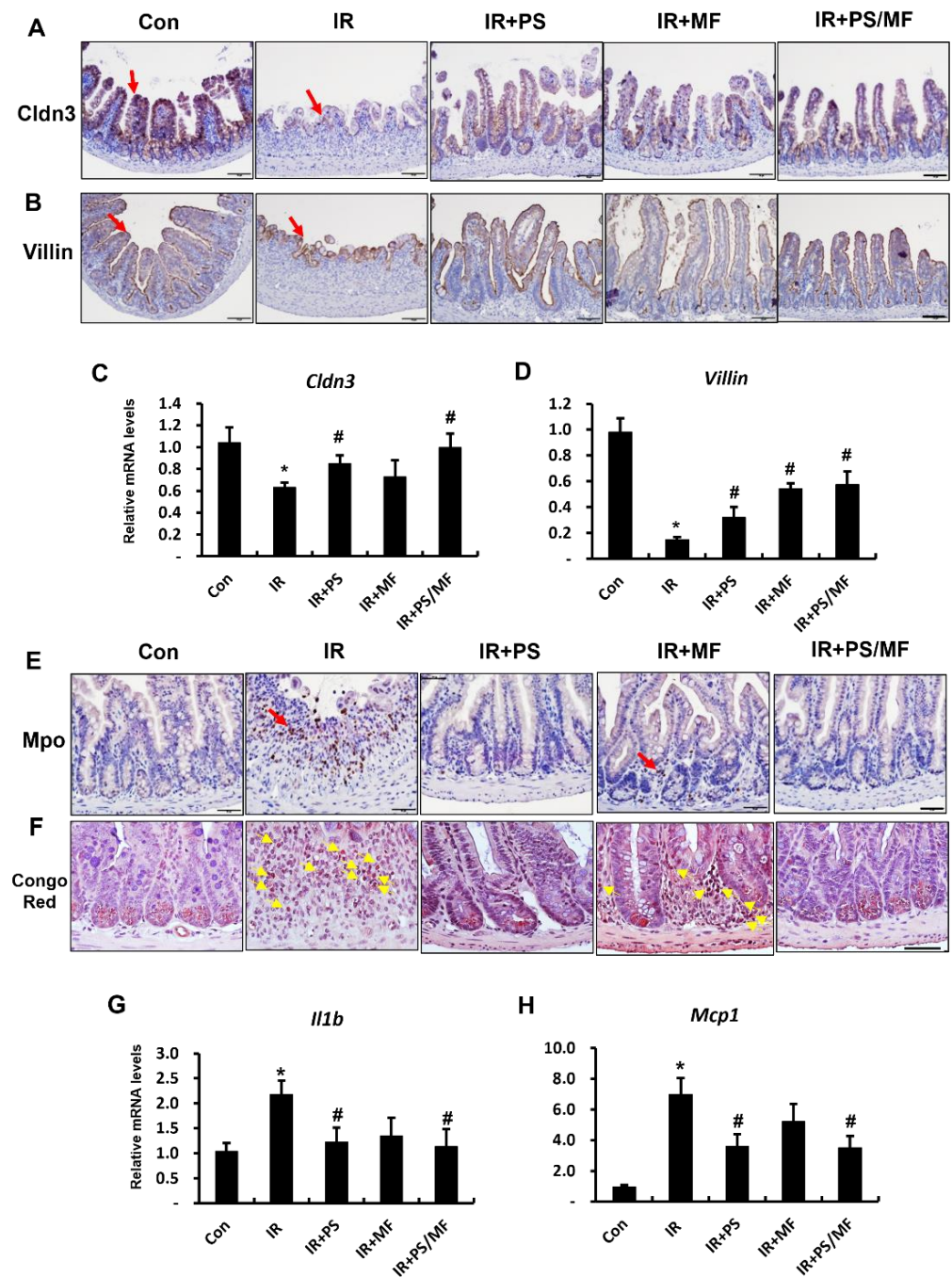


Figure 2. Effect of combined pravastatin and metformin treatment on epithelial barrier damage and inflammatory response in radiation-induced intestinal injury. Immunohistochemical analysis of (A) claudin 3 (Cldn3) and (B) villin in intestine tissue of control (Con), irradiated (IR), pravastatin-treated IR (IR + PS), metformin-treated IR (IR + MF), combined PS and MF-treated IR (IR + PS/MF) groups. Red arrows indicate Cldn3 and villin positive cells. Bar = 100 μ m. mRNA levels of (C) Cldn3 and (D) villin of the intestine from Con, IR, IR + PS, IR + MF, IR + PS/MF groups. (E) Immunohistochemical analysis of myeloperoxidase (MPO) and (F) congo red stain for eosinophils. Red arrows indicate MPO positive cells. Yellow arrows indicate eosinophils. Bar = 50 μ m. mRNA levels of (G) interleukin 1b (Il-1b) and (H) monocyte chemoattractant protein 1 (Mcp1) of the intestine from Con, IR, IR + PS, IR + MF, IR + PS/MF groups. Data are presented as the mean \pm standard error of the mean; n = 5–6 mice per group. * $p < 0.05$ compared to the control; # $p < 0.05$ compared to the IR group.

2.3. Effect of Combined PS and MF Treatment on Epithelial Cell Proliferation in Radiation-Induced Intestinal Injury

As the GI tract has a rapid self-renewal rate, intestinal stem cells are sensitive to radiation exposure. Impaired intestinal stem cells by radiation retard epithelial cell proliferation and regeneration of the intestine [34,35]. In our previous study, we found that MF treatment promoted stem cell properties and increased epithelial proliferation [21]. Therefore, we assessed the epithelial proliferation capacity and intestinal stem cell ability in the combined PS and MF treatment under radiation exposure. Ki-67 is a marker of the active state of proliferating cells and is used to identify regeneration crypts [36]. The number of Ki-67 positive cells was markedly lower in the IR group than in the control group. However, Ki-67 positive cells increased in the PS, MF, and combination of PS and MF-treated groups compared with the IR group (Figure 3A). In particular, treatment with MF alone and combined treatment with PS and MF markedly increased the Ki-67 positive cells in the irradiated intestine. The protein and mRNA expression of olfactomedin 4 (Olfm4), an active-state intestinal stem cell marker, considerably decreased in the IR group. The MF alone and the combination of PS and MF treatment markedly increased the expression of Olfm4 compared with the IR group. However, there was no significant difference in the Olfm4 mRNA levels between the IR + PS and IR groups (Figure 3C). We also evaluated another intestinal stem cell marker, leucine-rich repeat containing G protein-coupled receptor 5 (Lgr5), which is highly sensitive to radiation [37]. In the small intestine of irradiated mice, the mRNA levels of Lgr5 were notably reduced compared with those in the control group. There was a remarkable increase in Lgr5 expression in the group treated with MF alone or in combination with PS and MF. Overall, the combination of PS and MF treatment enhanced epithelial proliferation by promoting intestinal stem cell properties during radiation-induced intestinal injury.

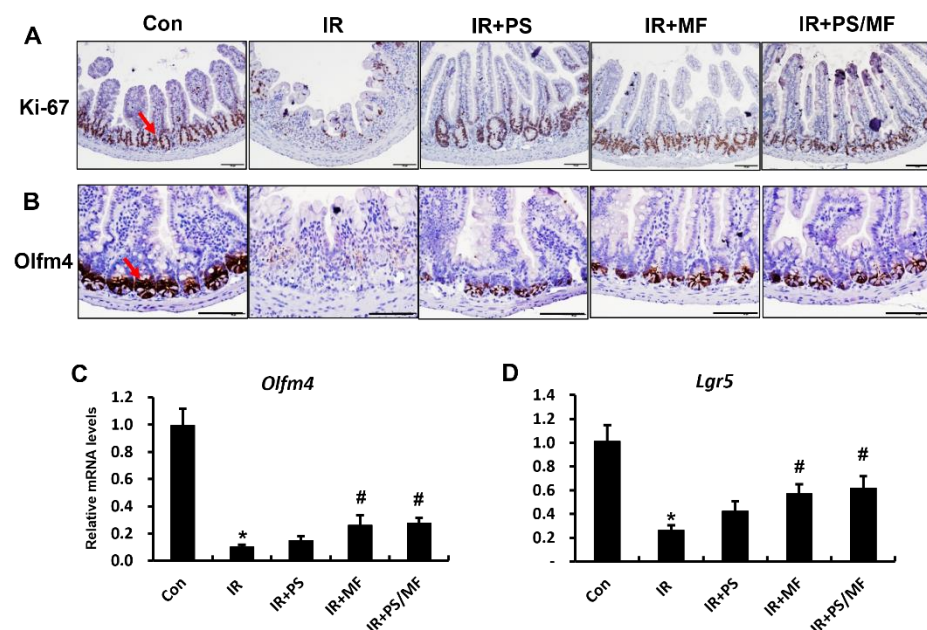


Figure 3. Effect of combined pravastatin and metformin treatment on epithelial cell proliferation in radiation-induced intestinal injury. Immunohistochemical analysis of (A) Ki-67 and (B) olfactomedin 4 (Olfm4) in small intestine of control (Con), irradiated (IR), pravastatin-treated IR (IR + PS), metformin-treated IR (IR + MF), combined PS and MF-treated IR (IR + PS/MF) groups. Bar = 100 μ m Red arrows indicate Ki-67 and Olfm4 positive cells. mRNA levels of (C) Olfm4 and (D) leucine rich repeat containing G protein coupled receptor 5 (Lgr5) of Con, IR, IR + PS, IR + MF, IR + PS/MF groups. Data are presented as the mean \pm standard error of the mean; n = 5–6 mice per group. * $p < 0.05$ compared to the control; # $p < 0.05$ compared to the IR group.

2.4. Effect of Combined PS and MF Treatment on Radiation-Induced Damage in a Minipig Model: Gross Morphology of Abdominal Organs

The minipig model is similar in anatomy and physiology to the human GI tract, including transit time, pH value, microbiota [24], and the radiation absorption patterns in humans [26]. Therefore, minipigs are an appropriate animal model to evaluate the effects of oral pharmaceutical treatment on radiation-induced intestinal injury. We tested whether the combination treatment of PS and MF was also effective in abdominally irradiated minipigs. After anesthetizing the minipigs, they were placed in lateral recumbency, and the abdomen was irradiated with a total dose of 15 Gy. A schematic of minipig modeling and treatment is shown in Figure 4A. After 2 weeks, there was no significant difference in body weight between the groups (Figure 4B). Necropsy was performed 2 weeks after irradiation. We investigated the gross pathology of the abdominal lesions. Abdominal irradiated minipigs showed an enlarged stomach due to poor peristalsis, spleen atrophy, thin wall, and edematous small intestine, and congested blood vessels around the intestine (Figure 4C). On the contrary, the IR + PS, IR + MF, and IR + PS/MF groups improved these pathological changes to a gross appearance close to the normal condition (Figure 4C). On gross appearance of the intestine, the IR group showed a thin and dilated intestinal wall with accumulating gas and a congested change in the vessels in the intestinal wall (Figure 4D). The other groups showed alleviation of these pathological changes (Figure 4D). In spleen morphology, atrophic changes by irradiation improved the PS, MF, and combination of PS and MF treatments (Figure 4E). Overall, the combined treatment with PS and MF alleviated the pathophysiological changes caused by radiation exposure.

2.5. Effect of Combined PS and MF Treatment on Histological Damage of the Intestine in the Irradiated Minipig Model

To verify the effects of combined treatment with PS and MF on radiation-induced GI injury, we performed H&E and periodic acid-Schiff (PAS) staining of intestinal tissue in a minipig model. Histological analysis showed that the irradiated small intestine displayed congested vessels, crypt loss, accumulation of inflammatory cells, a decreased number of goblet cells, and disruption of epithelial continuity (Figure 5A,B). In contrast, PS treatment improved crypt regeneration, epithelial integrity, inflammatory cell infiltration, and goblet cell maturation in the small intestine. MF treatment also recovered the loss of crypts and epithelium with goblet cells, but partial vessel congestion and inflammatory cell infiltration were observed. In particular, the combined treatment with PS and MF resulted in complete epithelial continuity and goblet cell maturation in the epithelial layers (Figure 5A,B). In the large intestine, irradiated minipigs showed severe crypt and epithelial layer loss, inflammatory cell infiltration, and goblet cell loss (Figure 5C,D). PS and MF treatment partially attenuated the histological damage caused by irradiation (Figure 5C,D). In particular, the combined treatment with PS and MF resulted in complete epithelial layers with mature goblet cells and crypt regeneration (Figure 5C,D). Overall, the combined treatment of PS and MF improves histological damage compared to monotherapy with PS or MF.

2.6. Effect of Combined PS and MF Treatment on Inflammatory Response and Epithelial Integrity in Irradiated Minipig Model

In our previous study on radiation-induced intestinal injury in a mouse model, leukocyte infiltration and production of inflammatory cytokines increased, resulting in an inflammatory response in the irradiated intestine. To classify inflammation occurring in the small intestine of minipig models, we performed immunohistochemical analysis of CD68 for monocytes and Congo red staining for eosinophils. As shown in Figure 6A and 6B, the number of CD68-positive cells and eosinophils in the IR group was significantly higher than that in the IR + PS, IR + MF, and IR + PS/MF groups (Figure 6A,B). IL6, IL1 β , matrix metalloproteinase 9 (MMP9), and monocyte chemoattractant protein 1 (MCP1) are representative inflammatory cytokines in the irradiated intestine [12,33]. PS treatment or combined treatment with PS and MF significantly decreased the mRNA levels of IL6, IL1 β , MMP9, and MCP1 compared with those in the IR group (Figure 6C). MF treatment also

decreased the levels of these inflammatory cytokines, except MMP9 (Figure 6C). However, there were considerable differences in the expression of inflammatory cytokines between the IR + MF and IR + PS/MF groups. As the combined treatment of PS and MF affected epithelial proliferation in the mouse model, we also investigated epithelial proliferative ability in the minipig model. The expression of Ki-67 was higher in the IR + PS, IR + MF, and IR + PS/MF groups than in the IR group (Figure 6D). The mucosal barrier is composed of tight junction molecules (CLDN3 and ZO1), adherent junction molecules (E-cadherin), and desmosomes (DSG2) [29]. The expression of DSG2 protein was increased in the IR + PS, IR + MF, and IR + PS/MF groups compared with that in the IR group (Figure 6E). The mRNA levels of CLDN3, ZO1, E-cadherin, and DSG2 were notably higher in the IR + PS, IR + MF, and IR + PS/MF groups than in the IR group (Figure 6F). In particular, these junction molecules were most highly expressed in the IR + PS/MF group compared with the other groups (Figure 6E). These results suggest that the combined treatment of PS and MF in minipigs, as in mice, has a better effect on epithelial proliferation and epithelial junction molecules recovery than when used individually.

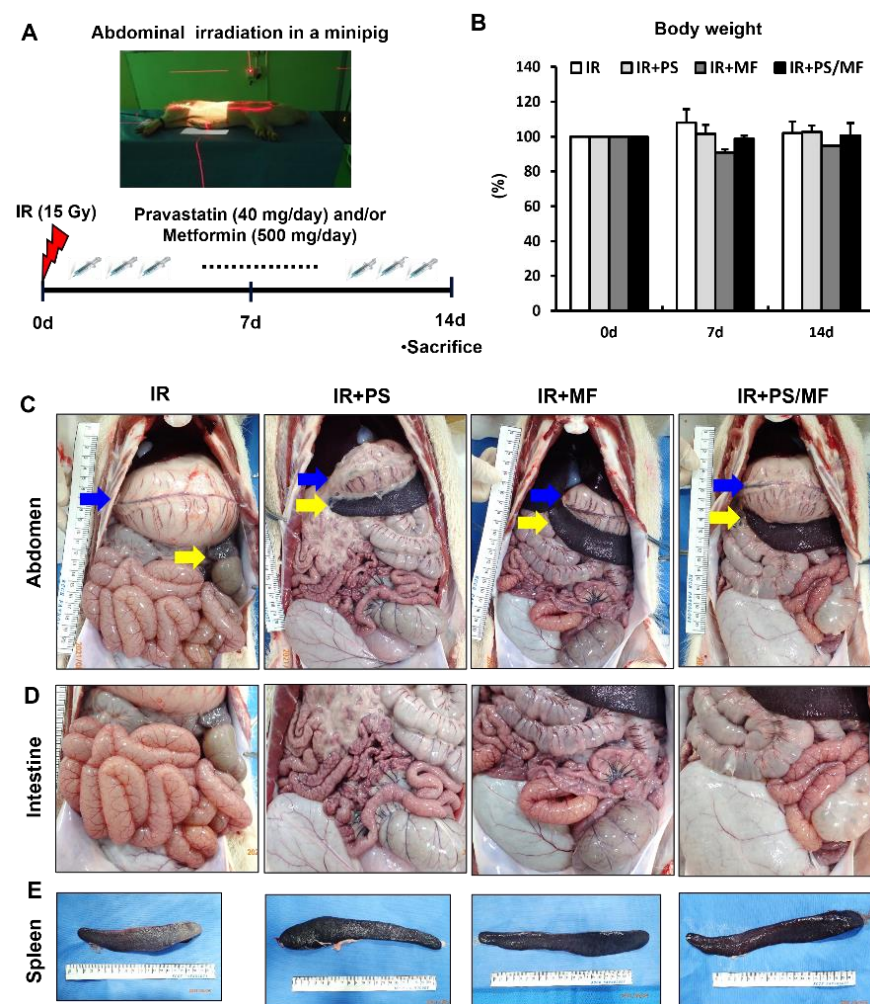


Figure 4. Effect of combined pravastatin and metformin treatment on radiation-induced damage in a minipig model: gross morphology of abdominal organs. (A) Schematic diagram of the minipig experimental protocol. Minipigs were treated with combination of pravastatin (PS) and metformin (MF) by oral administration after receiving a single dose of 15Gy gamma-ray radiation to the whole abdomen. (B) Body weights of minipig in irradiated (IR), PS-treated IR (IR + PS), MF-treated IR (IR + MF), combined PS and MF-treated IR (IR+PS/MF) groups after 15Gy irradiation. (C) Gross pathology of abdominal organs, (D) intestine, and (E) spleen at 14 days after irradiation of IR, IR + PS, IR + MF, IR + PS/MF groups. Blue arrows indicate stomach. Yellow arrows indicate spleen.

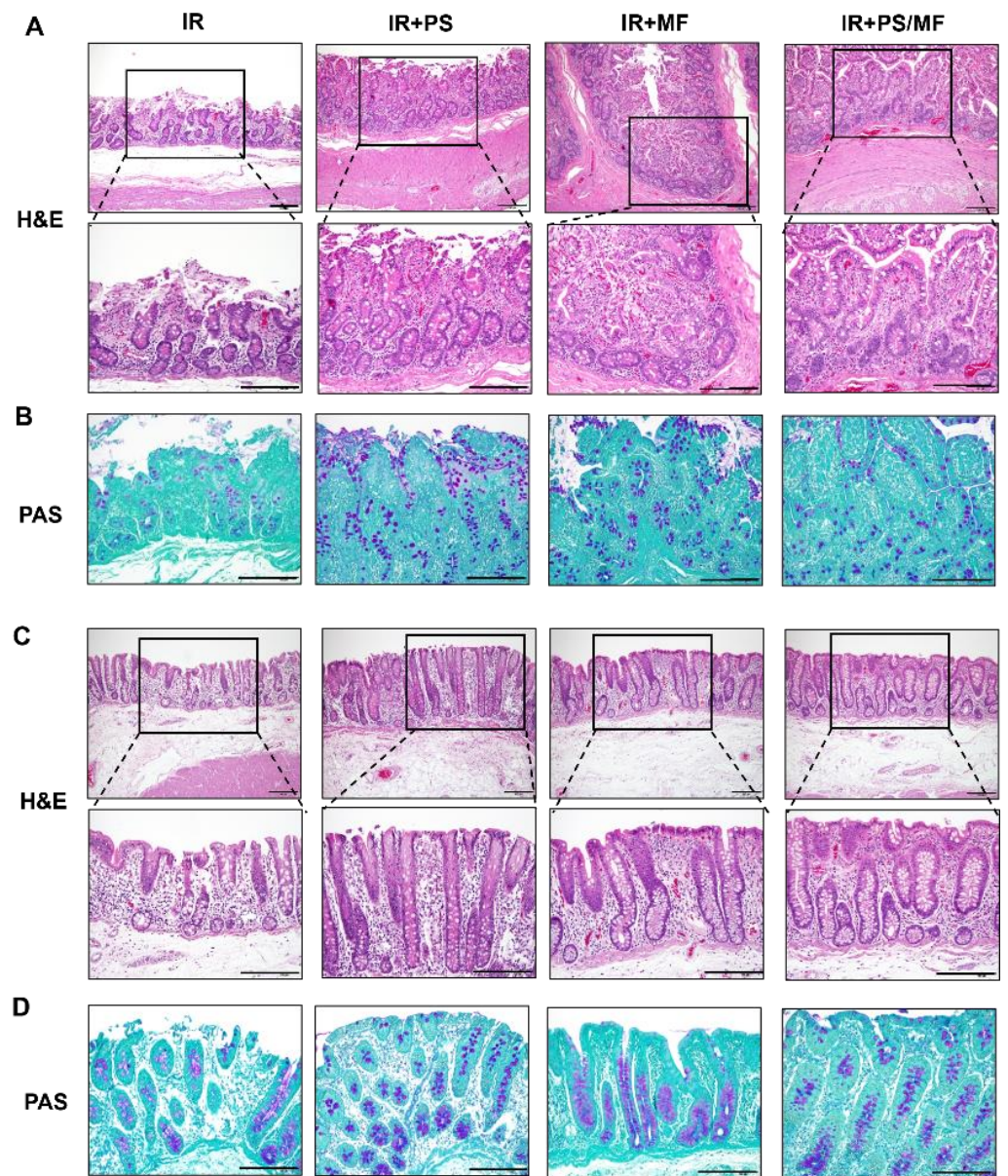


Figure 5. Effect of combined pravastatin and metformin treatment on histological damage of the intestine in the irradiated minipig model. **(A)** Hematoxylin & Eosin (H&E) staining of small intestinal tissues harvested from irradiated (IR), pravastatin-treated IR (IR + PS), metformin-treated IR (IR + MF), combined PS and MF-treated IR (IR + PS/MF) minipigs. Bar = 200 μ m. **(B)** Periodic Acid Schiff (PAS) staining of small intestinal tissues harvested from IR, IR + PS, IR + MF, IR + PS/MF groups. Bar = 200 μ m. **(C)** H&E staining and **(D)** PAS staining of large intestinal tissues harvested from IR, IR + PS, IR + MF, IR + PS/MF groups. Bar = 200 μ m.

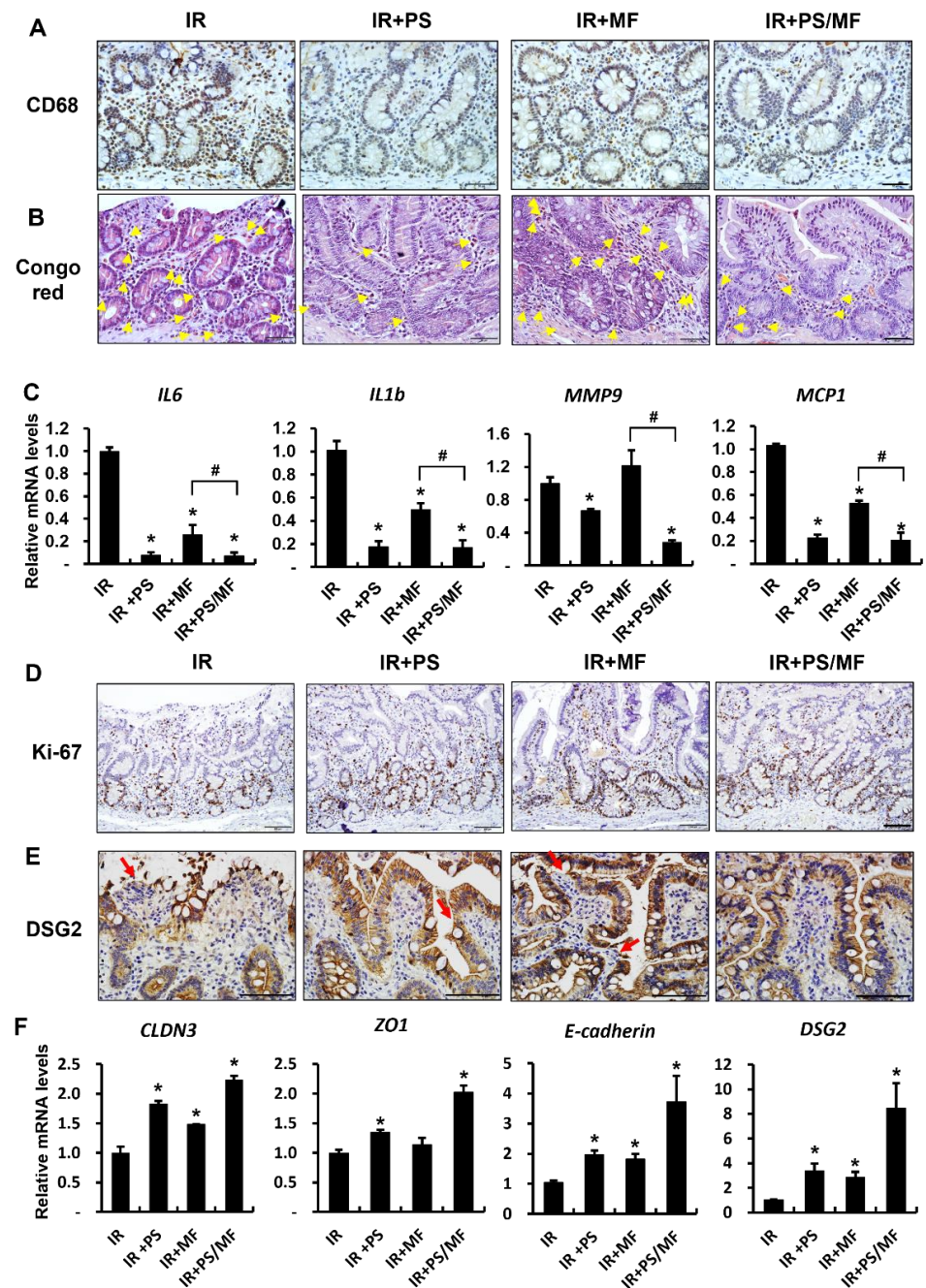


Figure 6. Effect of combined pravastatin and metformin treatment on inflammatory response and epithelial integrity in irradiated minipig model. (A) Immunohistochemical analysis of CD68 and (B) congo red stain in small intestine of irradiated (IR), pravastatin-treated IR (IR + PS), metformin-treated IR (IR + MF), combined PS and MF-treated IR (IR + PS/MF) minipigs. Yellow arrows indicate eosinophils. Bar = 50 μ m. (C) mRNA levels of inflammatory cytokines, such as interleukin (IL) 6, IL1b, matrix metalloproteinase 9 (MMP9), and monocyte chemoattractant protein 1 (MCP1) in the small intestine of IR, IR+PS, IR+MF, IR+PS/MF groups. Immunostaining of (D) Ki-67 and (E) desmoglein 2 (DSG2) in the small intestine. Red arrows indicate defective DSG2 expression in the epithelium. Bar = 100 μ m. (F) mRNA levels of intercellular junction molecules, such as claudin 3 (CLDN3), zonula occludens 1 (ZO1), E-cadherin, and DSG2 in the small intestine of IR, IR + PS, IR+MF, IR+PS/MF groups. Data are presented as the mean \pm standard error of the mean; n = 4 per group. * $p < 0.05$ compared to the IR group; # $p < 0.05$ compared to the IR + MF group.

3. Discussion

As radiation-induced GI injury limits the survival of casualties from nuclear accidents or terrorism, GI damage is a critical factor responsible for mortality in humans and other mammals [38]. Radiation exposure of over 10 Gy mainly leads to GI injury with clinical symptoms, such as diarrhea, dehydration, sepsis, and intestinal bleeding, with eventual mortality within 10–15 days post exposure [39]. Furthermore, no Food and Drug Administration-approved agents are available to mitigate radiation-induced intestinal injury [40]. In this study, the combined treatment of PS and MF was more effective in alleviating radiation-induced intestinal injury than a single treatment. These data suggest that combined treatment of PS and MF may be used as a powerful therapeutic agent for radiation-induced enteropathy.

The anti-inflammatory effect of PS in radiation-induced GI injury has been demonstrated in mice and minipigs [10,12–14]. Recently, we reported that PS directly regulated epithelial barrier function and attenuated radiation-induced enteropathy in minipig models [14]. MF is a drug used worldwide for treatment of type 2 diabetes, and its various effects have been widely studied. The protective effects of MF on radiation-induced GI damage have been previously reported [17,19,20]. We also identified the stem cell preservative effects of MF in a radiation-induced intestinal injury mouse model [21]. However, a single therapy with PS or MF did not show survival effects in lethal dose irradiation in our data. To overcome this limitation, we used a combination of PS and MF for radiation-induced intestinal injury in mouse and minipig models in this study. We found that the combined treatment of PS and MF notably increased the survival rate compared with the single treatment or IR group in the lethal dose-irradiated mouse model. Histological analysis showed that the combined treatment of PS and MF dramatically attenuated histological damage, including villus length, crypt number, and histological score, compared with the other groups.

Furthermore, using minipig models, we investigated the therapeutic effects of combination treatment with PS and MF. Several *in vivo* experiments have been designed using rodents; however, there are limitations due to differences in anatomical, physiological, histopathological, and sensitivity to radiation between humans and rodents. We adjusted minipig models because not only is the GI function of minipigs similar to that of humans, but also the response to radiation exposure is highly similar to that of humans, which has been reported in several studies [41,42]. Therefore, minipigs are an appropriate animal model for the evaluation of pharmaceutical oral bioavailability following radiation damage. In the minipig model, combined treatment with PS and MF improved gross pathological damage in abdominal organs, including the stomach, intestine, and spleen, and attenuated radiation-induced intestinal histological damage.

Barrier damage with intercellular junction disruption is a well-known cause of radiation-induced intestinal injury [14,43]. Damaged intestinal epithelium increases permeability and promotes systemic influx of bacterial pathogens, resulting in inflammation and endotoxemia [34,44]. Clinical studies have shown that radiotherapy received patients exhibit increased intestinal permeability and tight junction disruption [43]. PS directly enhances intercellular junctions, including CLDN3, ZO1, and DSG2, in differentiated epithelial cells upon radiation exposure [14]. Tao et al. reported that adenosine monophosphate-activated kinase activation by MF accelerates tight junction molecules such as ZO1 and occludin and alleviates colitis [16]. In this study, while single treatment with MF did not markedly increase *Cldn3* expression, single treatment with PS enhanced tight junction expression in the mouse model. In particular, the combined treatment of PS and MF markedly increased intercellular junction molecules, including CLDN3, ZO1, E-cadherin, and DSG2, compared with the single treatment groups in the mouse and minipig models. Therefore, combined treatment with PS and MF enhanced radiation-induced barrier damage by maintaining the effects of PS.

Radiation-induced intestinal injury results in inflammatory reaction with increased levels of inflammatory cytokines and chemokines, such as IL6, IL1 β , MMP9, and MCP1 [12,14].

IL6 is an important mediator of the acute inflammatory phase [45]. IL1 β , an inflammatory cytokine, is produced immediately following radiation exposure in epithelial and endothelial cells [46]. MMP9 is mainly produced by neutrophils and is the most abundantly expressed protease in inflamed tissues [47]. MCP1 is a chemokine that regulates migration and infiltration of monocytes and macrophages. Leukocyte infiltration in inflamed tissues is an important component of the progression of inflammatory processes. Neutrophils migrate into damaged tissue, generating a respiratory burst and contributing to the progression of the inflammatory response [48]. Eosinophils are pro-inflammatory leukocytes that comprise a small percentage of circulating blood cells [49]. Eosinophils also contribute to the inflammatory process by releasing various cytokines and chemokines, which are derived in concert with other inflammatory and immune cells during radiation exposure. PS has potent anti-inflammatory effects on radiation-induced intestinal injury [10,12,13]. Here, we also found that PS treatment showed anti-inflammatory effects, including inhibition of leukocyte infiltration and decreased inflammatory cytokine and chemokine expression in irradiated intestinal tissue. MF treatment did not inhibit the inflammatory response in the irradiated mouse model. In the mouse and minipig models, combined treatment with PS and MF effectively attenuated intestinal inflammation. Therefore, the combined treatment with PS and MF showed anti-inflammatory effects in radiation-induced intestinal injury by retaining the effects of PS.

The intestinal epithelium is one of the most rapidly proliferating tissues. Intestinal stem cells located in the crypt drive a processes of epithelium turnover and intestinal regeneration and generate precursors for specialized differentiated cells [50,51]. Therefore, these intestinal stem cells are reported to be responsible for intestinal regeneration after radiation damage [52]. The pathology of lethal GI tract damage is mainly involved in the depletion of the pool of intestinal stem cells, which impairs the regeneration of the villi-crypt structure and intestinal function [34,35]. MF was previously shown to mitigate radiation-induced enteropathy by promoting stem cell properties and epithelial proliferation in a mouse model and an ex vivo system [21]. In this study, we also identified that MF activated stem cell properties and alleviated radiation-induced intestinal injury in mice and minipig models. The combined treatment with PS and MF sustained the activated stem cell properties of MF in radiation-induced intestinal injury. Therefore, the combined treatment with PS and MF resulted in stem cell properties and epithelial regeneration in radiation-induced intestinal injury.

In conclusion, our findings highlight that the combination of PS and MF was more effective in alleviating radiation-induced enteropathy than a single treatment. Additionally, we suggest that minipigs may serve as an outstanding animal model for studying radiation-induced GI injury. Thus, the combined use of PS and MF is a promising therapeutic approach for treating radiation-induced enteropathy.

4. Material and Methods

4.1. Animal

4.1.1. Mice

Male C57BL/6 mice (6-week-old) were obtained from DooYeol Biotech (Seocho-gu, Seoul, Republic of Korea) and sustained under specific pathogen free conditions at the animal facility of the Korea Institute of Radiological and Medical Sciences (KIRAMS). The mice were housed in a temperature-controlled room with a 12 h light/dark cycle, and food and water were provided ad libitum. The mice were acclimated for 1 week before the commencement of the experiments and were assigned to the following groups: (1) control, (2) irradiation (IR), (3) IR with PS treatment (IR + PS), (4) IR with MF treatment (IR + MF), and (5) IR with combined PS and MF treatment (IR + PS/MF). All animal experiments were approved by and performed in accordance with the guidelines of the Institutional Animal Care and Use Committee (IACUC) of KIRAMS (kirams 2021-0018).

4.1.2. Minipigs

Eight male Gottingen minipigs (PWG Genetics Korea, PyungTek, Republic of Korea), weighing 20–25 kg each, were used in this study. The minipigs were physically examined for health before the experiments. They were housed indoors in individual cages and provided with dry pig food and filtered water. The minipigs were housed under environmentally controlled conditions at 22 ± 1 °C and $50 \pm 10\%$ relative humidity, with a 12 h light/dark cycle. The minipig care procedures were performed in accordance with the Guide for the Care and Use of Laboratory Animals of the Institute of Laboratory Animal Resources. All the animal experiments were approved by the IACUC of KIRAMS (kirams 2020-0090). Minipigs were randomized before treatment initiation in all experiments.

4.2. Irradiation and Treatment

4.2.1. Irradiation and Treatment in Mice

The animals were anesthetized with an intraperitoneal injection of alfaxalone (85 mg/kg; Alfaxan[®]; Careside, Gyeonggi-do, Republic of Korea) and xylazine (10 mg/kg; Rompun[®]; Bayer Korea, Seoul, Republic of Korea). They were irradiated with a single exposure to 15 Gy or 13.5 Gy of whole abdominal lesion at a dose rate of 2 Gy/min using an X-RAD 320 X-ray irradiator (Softex, Gyeonggi-do, Republic of Korea). After exposure, the animals were orally administered 30 mg/kg/day PS (Prastan[®]; Yunjin Pharm, Seoul, Republic of Korea) and/or 500 mg/kg/day MF (Diabex, Daewoong Pharm. Co., Ltd., Seoul, Republic of Korea) for 30 d in the 15 Gy irradiated model and 6 d in the 13.5 Gy irradiated model.

4.2.2. Irradiation and Treatment in Minipigs

The minipigs were anesthetized using an intramuscular injection of Zoletil 50 (4 mg/kg; Virbac, Republic of Korea) and xylazine (2.3 mg/kg; Rompun[®]; Bayer Korea, Seoul, Republic of Korea). The minipigs were randomly divided into four groups: IR, IR + PS, IR + MF, and IR + PS/MF. These minipigs were irradiated with 15 Gy at the abdominal lesions. For radiation exposure, minipigs were placed bilaterally in lateral recumbency. The mean dose rate at the center of the field was 1.12 Gy/min. The cranial landmark is located at the end of the xiphoid process. The irradiated field size was 20 × 30 cm under a 60 Co gamma-ray irradiation unit (Gamma Beam 100-80, 780; Best Theratronics, Ontario, Canada). The distance between the radiation source and spine was 80 cm. After irradiation, the minipigs were housed individually and provided dry food and filtered water. All minipigs were treated with a twice-daily oral dose of 40 mg/day PS (Prastan[®]; Yunjin Pharm, Seoul, Republic of Korea) and/or 500 mg/day MF (Diabex, Daewoong Pharm. Co., Ltd., Republic of Korea) for 2 weeks. On days 13 and 14, the minipigs were sacrificed.

4.3. Histological Analysis of the Intestinal Tissue

Intestinal tissues of mice and minipigs were fixed with 10% neutral buffered formalin solution, embedded in paraffin wax, and sectioned transversely at a thickness of 4 µm. The slides were stained with H&E and Congo red. Histological scores were quantified in the H&E-stained slides and assessed by the degree of the epithelial maintenance, crypt damage, vascular dysfunction, and inflammation with infiltration of inflammatory cells. To investigate radiation-induced goblet cell damage, the slides were stained with PAS. For immunohistochemical analysis, the slides were subjected to antigen retrieval for 20 min and then treated with 0.3% hydrogen peroxide in methyl alcohol for 20 min to block endogenous peroxidase activity. After washing with PBS, the slides were blocked with 10% normal goat serum (Vector ABC Elite kit; Vector Laboratories, Burlingame, CA, USA) and incubated with primary antibodies, such as anti-Cldn3 (Invitrogen, Carlsbad, CA, USA), villin (Abcam, Cambridge, UK), Mpo (Abcam), ki-67 (Acris), Olfm4 (Invitrogen), and CD68 (Abcam) antibodies. Additionally, the slides were incubated with horseradish peroxidase-conjugated secondary antibody (Dako, Carpinteria, CA, USA) for 60 min. The peroxidase reaction was developed using diaminobenzidine substrate (Dako) prepared according to the manufacturer's instructions, and the slides were counterstained with hematoxylin.

4.4. RNA Extraction, Reverse Transcription-Polymerase Chain Reaction (RT-PCR), and Real-Time PCR Quantification

Small intestine tissues of mice and minipigs were immediately snap-frozen and stored at -80°C until RNA extraction was performed. Total RNA was isolated from the intestinal tissues using the TRIzol reagent (Invitrogen, Carlsbad, CA, USA) according to the manufacturer's protocol. cDNA was synthesized using the AccuPower RT premix (Bioneer, Daejeon, Republic of Korea) according to the manufacturer's protocol. Real-time RT-PCR was performed using a LightCycler 480 system (Roche, San Francisco, CA, USA). The mRNA expression levels of gene, determined using LightCycler 480 system software (Roche), were normalized to those of glyceraldehyde 3-phosphate dehydrogenase. Cycle threshold values were used to calculate the relative mRNA expression using the $2^{-\Delta\Delta\text{Ct}}$ method. The primer sequences are listed in Table 1.

Table 1. The primer sequences.

Species	Primer	Forward (5'–3')	Reverse (5'–3')
Mouse	<i>Cldn3</i>	AAGCCGAATGGACAAAGAA	CTGGCAAGTAGCTGCAGTG
	<i>Villin</i>	CACCTTTGGAAGCTTCTTCG	CTCTCGTTGCCTTGAACCTC
	<i>Il-1β</i>	GCAACTGTTCTGAACTCA	CTCGGAGCCTGTAGTGCAG
	<i>Mcp-1</i>	GCAGTTAACGCCCCACTCA	CCCAGCCTACTCATTGGGATCA
	<i>Olfm4</i>	GCTGGAAGTGAAGGAGATGC	ACAGAAGGAGCGCTGATGTT
	<i>Lgr5</i>	TCAGTCAGCTGCTCCCGAAT	CGTTTCCC GCAAGACGTAAC
	<i>Gapdh</i>	AAGATGGTGATGGGCTTCCCC	TGGCAAAGTGGAGATTGTTGCC
Minipig	<i>IL-6</i>	TTCAGTCCAGTCGCCTTCT	GTGGCATCACCTTTGGCATCTTCTT
	<i>IL-1b</i>	ACCTGGACCTTGGTTCTC	GGATTCTTCATCGGCTTC
	<i>MMP-9</i>	AAGACGCAGAAGGTGGATTC	AACTCACACGCCAGAAGAAG
	<i>MCP-1</i>	TCTCCAGTCACCTGCTGCTA	AGGCTTCGGAGTTTGGTTTT
	<i>CLDN3</i>	GCCAAGATCCTCTACTCCGC	GAGAGCTGCCTAGCATCTGG
	<i>ZO1</i>	GAGGATGGTCACACCGTGGT	GGAGGATGCTGTTGTCTCGG
	<i>E-cadherin</i>	AAATGCTAGCTGGTGGGGAC	GCCTCCCATTGCTAACACCT
	<i>DSG2</i>	TCTTCCAGGCAGGGTCAAAC	CCAGGATCACAGTGCTTGGT
	<i>GAPDH</i>	GAAGGTCGGAGTGAACGGAT	CATGGGTAGAATCATACTGGAACA

4.5. Statistical Analysis

All quantitative data are expressed as the mean \pm standard error of the mean. Statistical significance of differences was evaluated by performing Kaplan–Meier analysis followed by log-rank test for survival data and one-way analysis of variance with Tukey's multiple comparison test for other data. Statistical significance was set at $p < 0.05$.

Author Contributions: J.M.K., W.I.J., S.P., S.S. and H.J. conceived and designed the experiments. J.M.K., H.K., S.H.O., S.B.L., M.P., S.K., S.S. and H.J. performed the experiments in these studies. J.M.K., S.S. and H.J. analyzed the data. J.M.K. and H.J. wrote the paper. All authors have read and agreed to the published version of the manuscript.

Funding: This research was supported by a grant from the Korea Institute of Radiological and Medical Sciences (KIRAMS), funded by the Ministry of Science and ICT (MSIT), Republic of Korea (grant numbers 50535-2022 and 50612-2022). This research was also supported by a grant from the National Research Foundation of Korea (NRF), funded by the Ministry of Science and ICT (MSIT), Republic of Korea (grant number 2020R1C1C1012154).

Institutional Review Board Statement: Not applicable.

Informed Consent Statement: Not applicable.

Data Availability Statement: Not applicable.

Conflicts of Interest: The authors declare no conflict of interest.

References

- Andreyev, J. Gastrointestinal complications of pelvic radiotherapy: Are they of any importance? *Gut* **2005**, *54*, 1051–1054. [CrossRef] [PubMed]
- Lu, L.; Li, W.; Chen, L.; Su, Q.; Wang, Y.; Guo, Z.; Lu, Y.; Liu, B.; Qin, S. Radiation-induced intestinal damage: Latest molecular and clinical developments. *Futur. Oncol.* **2019**, *15*, 4105–4118. [CrossRef] [PubMed]
- Citrin, D.; Cotrim, A.P.; Hyodo, F.; Baum, B.J.; Krishna, M.C.; Mitchell, J.B. Radioprotectors and mitigators of radiation-induced normal tissue injury. *Oncologist* **2010**, *15*, 360–371. [CrossRef] [PubMed]
- Yang, H.; Hu, W.; Wang, W.; Chen, P.; Ding, W.; Luo, W. Replanning during intensity modulated radiation therapy improved quality of life in patients with nasopharyngeal carcinoma. *Int. J. Radiat. Oncol.* **2013**, *85*, e47–e54. [CrossRef]
- Dubois, A.; Walker, R.I. Prospects for management of gastrointestinal injury associated with the acute radiation syndrome. *Gastroenterology* **1988**, *95*, 500–507. [CrossRef] [PubMed]
- Damman, C.J.; Surawicz, C.M. The gut microbiota: A microbial arsenal protecting us from infectious and radiation-induced diarrhea. *Gastroenterology* **2009**, *136*, 722–724. [CrossRef] [PubMed]
- Rosenson, R.S. Non-lipid-lowering effects of statins on atherosclerosis. *Curr. Cardiol. Rep.* **1999**, *1*, 225–232. [CrossRef] [PubMed]
- Meyer, N.; Brodowski, L.; Richter, K.; von Kaisenberg, C.S.; Schröder-Heurich, B.; von Versen-Höynck, F. Pravastatin promotes endothelial colony-forming cell function, angiogenic signaling and protein expression in vitro. *J. Clin. Med.* **2021**, *10*, 183. [CrossRef]
- Gaugler, M.-H.; Vereycken-Holler, V.; Squiban, C.; Vandamme, M.; Vozenin-Brotans, M.-C.; Benderitter, M. Pravastatin limits endothelial activation after irradiation and decreases the resulting inflammatory and thrombotic responses. *Radiat. Res.* **2005**, *163*, 479–487. [CrossRef]
- Haydont, V.; Bourcier, C.; Pocard, M.; Lusinchi, A.; Aigueperse, J.; Mathé, D.; Bourhis, J.; Vozenin-Brotans, M.-C. Pravastatin Inhibits the Rho/CCN2/extracellular matrix cascade in human fibrosis explants and improves radiation-induced intestinal fibrosis in rats. *Clin. Cancer Res.* **2007**, *13*, 5331–5340. [CrossRef]
- Holler, V.; Buard, V.; Gaugler, M.-H.; Guipaud, O.; Baudelin, C.; Sache, A.; Perez, M.d.R.; Squiban, C.; Tamarat, R.; Milliat, F. Pravastatin limits radiation-induced vascular dysfunction in the skin. *J. Invest. Dermatol.* **2009**, *129*, 1280–1291. [CrossRef] [PubMed]
- Jang, H.; Lee, J.; Park, S.; Myung, H.; Kang, J.; Kim, K.; Kim, H.; Jang, W.-S.; Lee, S.-J.; Shim, S.; et al. Pravastatin attenuates acute radiation-induced enteropathy and improves epithelial cell function. *Front. Pharmacol.* **2018**, *9*, 1215. [CrossRef] [PubMed]
- Jang, H.; Kwak, S.Y.; Park, S.; Kim, K.; Kim, Y.H.; Na, J.; Kim, H.; Jang, W.S.; Lee, S.J.; Kim, M.J.; et al. Pravastatin Alleviates Radiation Proctitis by Regulating Thrombomodulin in Irradiated Endothelial Cells. *Int. J. Mol. Sci.* **2020**, *21*, 1897. [CrossRef] [PubMed]
- Kwak, S.Y.; Jang, W.I.; Park, S.; Cho, S.S.; Lee, S.B.; Kim, M.-J.; Park, S.; Shim, S.; Jang, H. Metallothionein 2 activation by pravastatin reinforces epithelial integrity and ameliorates radiation-induced enteropathy. *EBioMedicine* **2021**, *73*, 103641. [CrossRef]
- Wedlake, L.J.; Silia, F.; Benton, B.; Lalji, A.; Thomas, K.; Dearnaley, D.P.; Blake, P.; Tait, D.; Khoo, V.S.; Andreyev, H.J.N. Evaluating the efficacy of statins and ACE-inhibitors in reducing gastrointestinal toxicity in patients receiving radiotherapy for pelvic malignancies. *Eur. J. Cancer* **2012**, *48*, 2117–2124. [CrossRef]
- Tao, L.; Li, D.; Liu, H.; Jiang, F.; Xu, Y.; Cao, Y.; Gao, R.; Chen, G. Neuroprotective effects of metformin on traumatic brain injury in rats associated with NF- κ B and MAPK signaling pathway. *Brain Res. Bull.* **2018**, *140*, 154–161. [CrossRef]
- Mortezaee, K.; Shabeeb, D.; Musa, A.E.; Najafi, M.; Farhood, B. Metformin as a radiation modifier; implications to normal tissue protection and tumor sensitization. *Curr. Clin. Pharmacol.* **2019**, *14*, 41–53. [CrossRef]
- Pålsson-McDermott, E.M.; O'Neill, L.A. Targeting immunometabolism as an anti-inflammatory strategy. *Cell Res.* **2020**, *30*, 300–314. [CrossRef]
- Bagheri, H.; Rezapoor, S.; Najafi, M.; Safar, H.; Shabeeb, D.; Cheki, M.; Shekarchi, B.; Motevaseli, E. Metformin protects the rat small intestine against radiation enteritis. *Jundishapur J. Nat. Pharm. Prod.* **2019**, *14*, e67352. [CrossRef]
- Najafi, M.; Cheki, M.; Hassanzadeh, G.; Amini, P.; Shabeeb, D.; Musa, A.E. Protection from radiation-induced damage in rat's ileum and colon by combined regimens of melatonin and metformin: A histopathological study. *Anti-Inflamm. Anti-Allergy Agents Med. Chem.* **2020**, *19*, 180–189. [CrossRef]
- Jang, H.; Kim, S.; Kim, H.; Oh, S.H.; Kwak, S.Y.; Joo, H.-W.; Lee, S.B.; Jang, W.I.; Park, S.; Shim, S. Metformin Protects the Intestinal Barrier by Activating Goblet Cell Maturation and Epithelial Proliferation in Radiation-Induced Enteropathy. *Int. J. Mol. Sci.* **2022**, *23*, 5929. [CrossRef] [PubMed]
- Vigneulle, R.M.; Rao, S.; Fasano, A.; MacVittie, T.J. Structural and functional alterations of the gastrointestinal tract following radiation-induced injury in the rhesus monkey. *Am. J. Dig. Dis.* **2002**, *47*, 1480–1491.
- Heining, P.; Ruysschaert, T. The use of minipig in drug discovery and development: Pros and cons of minipig selection and strategies to use as a preferred nonrodent species. *Toxicol. Pathol.* **2016**, *44*, 467–473. [CrossRef] [PubMed]
- Henze, L.J.; Koehl, N.J.; O'Shea, J.P.; Kostewicz, E.S.; Holm, R.; Griffin, B.T. The pig as a preclinical model for predicting oral bioavailability and in vivo performance of pharmaceutical oral dosage forms: A PEARRL review. *J. Pharm. Pharmacol.* **2019**, *71*, 581–602. [CrossRef]
- Augustine, A.D.; Gondré-Lewis, T.; McBride, W.; Miller, L.; Pellmar, T.C.; Rockwell, S. Animal models for radiation injury, protection and therapy. *Radiat. Res.* **2005**, *164*, 100–109. [CrossRef]
- Jones, S.; George, R.; West, J.; Verrelli, D. The relative effectiveness of fission neutrons for gastrointestinal death in miniature pigs. *Radiat. Res.* **1972**, *50*, 504–518. [CrossRef]
- Shim, S.; Jang, W.-S.; Lee, S.-J.; Jin, S.; Kim, J.; Lee, S.-S.; Bang, H.Y.; Jeon, B.S.; Park, S. Development of a new minipig model to study radiation-induced gastrointestinal syndrome and its application in clinical research. *Radiat. Res.* **2014**, *181*, 387–395. [CrossRef]

28. Schulzke, J.D.; Ploeger, S.; Amasheh, M.; Fromm, A.; Zeissig, S.; Troeger, H.; Richter, J.; Bojarski, C.; Schumann, M.; Fromm, M. Epithelial tight junctions in intestinal inflammation. *Ann. N. Y. Acad. Sci.* **2009**, *1165*, 294–300. [CrossRef]
29. Turner, J.R. Intestinal mucosal barrier function in health and disease. *Nat. Rev. Immunol.* **2009**, *9*, 799–809. [CrossRef]
30. Shukla, P.K.; Gangwar, R.; Manda, B.; Meena, A.S.; Yadav, N.; Szabo, E.; Balogh, A.; Lee, S.C.; Tigyi, G.; Rao, R. Rapid disruption of intestinal epithelial tight junction and barrier dysfunction by ionizing radiation in mouse colon in vivo: Protection by N-acetyl-L-cysteine. *Am. J. Physiol. Liver Physiol.* **2016**, *310*, G705–G715. [CrossRef]
31. Radnai, B.; Sturm, E.M.; Stančić, A.; Jandl, K.; Labocha, S.; Ferreirós, N.; Grill, M.; Hasenoehrl, C.; Gorkiewicz, G.; Marsche, G. Eosinophils contribute to intestinal inflammation via chemoattractant receptor-homologous molecule expressed on Th2 cells, CRTH2, in experimental Crohn's disease. *J. Crohn's Colitis* **2016**, *10*, 1087–1095. [CrossRef] [PubMed]
32. Takemura, N.; Kurashima, Y.; Mori, Y.; Okada, K.; Ogino, T.; Osawa, H.; Matsuno, H.; Aayam, L.; Kaneto, S.; Park, E.J. Eosinophil depletion suppresses radiation-induced small intestinal fibrosis. *Sci. Transl. Med.* **2018**, *10*, eaan0333. [CrossRef] [PubMed]
33. Eder, P.; Adler, M.; Dobrowolska, A.; Kamhieh-Milz, J.; Witowski, J. The role of adipose tissue in the pathogenesis and therapeutic outcomes of inflammatory bowel disease. *Cells* **2019**, *8*, 628. [CrossRef] [PubMed]
34. Saha, S.; Bhanja, P.; Liu, L.; Alfieri, A.A.; Yu, D.; Kandimalla, E.R.; Agrawal, S.; Guha, C. TLR9 agonist protects mice from radiation-induced gastrointestinal syndrome. *PLoS ONE* **2012**, *7*, e29357. [CrossRef]
35. Saha, S.; Aranda, E.; Hayakawa, Y.; Bhanja, P.; Atay, S.; Brodin, N.P.; Li, J.; Asfaha, S.; Liu, L.; Taylor, Y. Macrophage-derived extracellular vesicle-packaged WNTs rescue intestinal stem cells and enhance survival after radiation injury. *Nat. Commun.* **2016**, *7*, 13096. [CrossRef] [PubMed]
36. Otsuka, K.; Suzuki, K. Differences in radiation dose response between small and large intestinal crypts. *Radiat. Res.* **2016**, *186*, 302–314. [CrossRef]
37. Kim, C.-K.; Yang, V.W.; Bialkowska, A.B. The role of intestinal stem cells in epithelial regeneration following radiation-induced gut injury. *Curr. Stem Cell Rep.* **2017**, *3*, 320–332. [CrossRef] [PubMed]
38. Singh, V.K.; Newman, V.L.; Berg, A.N.; MacVittie, T.J. Animal models for acute radiation syndrome drug discovery. *Expert Opin. Drug Discov.* **2015**, *10*, 497–517. [CrossRef]
39. Leibowitz, B.J.; Wei, L.; Zhang, L.; Ping, X.; Epperly, M.; Greenberger, J.; Cheng, T.; Yu, J. Ionizing irradiation induces acute haematopoietic syndrome and gastrointestinal syndrome independently in mice. *Nat. Commun.* **2014**, *5*, 3494. [CrossRef]
40. Rios, C.I.; Cassatt, D.R.; Dicarolo, A.L.; Macchiarini, F.; Ramakrishnan, N.; Norman, M.K.; Maidment, B.W. Building the strategic national stockpile through the NIAID Radiation Nuclear Countermeasures Program. *Drug Dev. Res.* **2014**, *75*, 23–28. [CrossRef]
41. Van der Laan, J.W.; Brightwell, J.; McAnulty, P.; Ratky, J.; Stark, C. Regulatory acceptability of the minipig in the development of pharmaceuticals, chemicals and other products. *J. Pharmacol. Toxicol. Methods* **2010**, *62*, 184–195. [CrossRef] [PubMed]
42. Jang, H.; Kim, J.-s.; Shim, S.; Jang, W.-s.; Lee, S.-J.; Myung, J.K.; Lee, S.-S.; Park, S. Acute radiation syndrome in an irradiated minipig model for patients with radiation exposure. *J. Radiat. Prot. Res.* **2017**, *42*, 146–153. [CrossRef]
43. Nejdofors, P.; Ekelund, M.; Weström, B.R.; Willén, R.; Jeppsson, B. Intestinal permeability in humans is increased after radiation therapy. *Dis. Colon Rectum* **2000**, *43*, 1582–1587. [CrossRef] [PubMed]
44. Saha, S.; Bhanja, P.; Kabarriti, R.; Liu, L.; Alfieri, A.A.; Guha, C. Bone marrow stromal cell transplantation mitigates radiation-induced gastrointestinal syndrome in mice. *PLoS ONE* **2011**, *6*, e24072. [CrossRef] [PubMed]
45. Nishimoto, N.; Kishimoto, T. Interleukin 6: From bench to bedside. *Nat. Clin. Pract. Rheumatol.* **2006**, *2*, 619–626. [CrossRef]
46. Liu, W.; Ding, I.; Chen, K.; Olschowka, J.; Xu, J.; Hu, D.; Morrow, G.R.; Okunieff, P. Interleukin 1beta (IL1B) signaling is a critical component of radiation-induced skin fibrosis. *Radiat. Res.* **2006**, *165*, 181–191. [CrossRef]
47. Baugh, M.D.; Perry, M.J.; Hollander, A.P.; Davies, D.R.; Cross, S.S.; Lobo, A.J.; Taylor, C.J.; Evans, G.S. Matrix metalloproteinase levels are elevated in inflammatory bowel disease. *Gastroenterology* **1999**, *117*, 814–822. [CrossRef]
48. Williams, M.R.; Azcutia, V.; Newton, G.; Alcaide, P.; Luscinskas, F.W. Emerging mechanisms of neutrophil recruitment across endothelium. *Trends Immunol.* **2011**, *32*, 461–469. [CrossRef]
49. Al-Haddad, S.; Riddell, R.; Wanders, A.; Winqvist, O.; Carlson, M.; Lampinen, M. Eosinophil granulocytes are activated during the remission phase of ulcerative colitis. Commentary. *Gut* **2005**, *54*, 1674–1675. [CrossRef]
50. Li, L.; Clevers, H. Coexistence of quiescent and active adult stem cells in mammals. *Science* **2010**, *327*, 542–545. [CrossRef]
51. Barker, N. Adult intestinal stem cells: Critical drivers of epithelial homeostasis and regeneration. *Nat. Rev. Mol. Cell Biol.* **2014**, *15*, 19–33. [CrossRef] [PubMed]
52. Hua, G.; Thin, T.H.; Feldman, R.; Haimovitz-Friedman, A.; Clevers, H.; Fuks, Z.; Kolesnick, R. Crypt base columnar stem cells in small intestines of mice are radioresistant. *Gastroenterology* **2012**, *143*, 1266–1276. [CrossRef] [PubMed]



Article

Diastereoselective Synthesis of Novel Spiro-Phosphacoumarins and Evaluation of Their Anti-Cancer Activity

Valeriia V. Sennikova ¹, Alena V. Zalaltdinova ¹ , Yulia M. Sadykova ¹ , Ayrat R. Khamatgalimov ^{1,*} , Almir S. Gazizov ^{1,*} , Alexandra D. Voloshina ¹ , Anna P. Lyubina ¹, Syumbelya K. Amerhanova ¹, Julia K. Voronina ² , Elena A. Chugunova ¹ , Nurbol O. Appazov ³ , Alexander R. Burilov ¹ and Michail A. Pudovik ¹

- ¹ Arbuzov Institute of Organic and Physical Chemistry, FRC Kazan Scientific Center, Russian Academy of Sciences, Arbuzova str. 8, 420088 Kazan, Russia
² N.S. Kurnakov Institute of General and Inorganic Chemistry, Russian Academy of Sciences, Leninsky Ave. 31, 119991 Moscow, Russia
³ Korkyt Ata Kyzylorda State University, 29A Aiteke Bi St., Kyzylorda 120014, Kazakhstan
* Correspondence: ayrat_kh@iopc.ru (A.R.K.); agazizov@iopc.ru (A.S.G.)

Abstract: Herein we present the regio- and diastereoselective synthesis of novel pyrrolidine-fused spiro-dihydrophosphacoumarins via intermolecular [3 + 2] cycloaddition reaction. The presented approach is complementary to existing ones and provides an easy entry to the otherwise inaccessible derivatives. Additionally, the unprecedented pathway of the reaction of 4-hydroxycoumarin with azomethine ylides is described. The anti-cancer activity of the obtained compounds was tested in vitro, the most potent compound being 2.6-fold more active against the HuTu 80 cell line than the reference 5-fluorouracil, with a selectivity index > 32.

Keywords: phosphacoumarin; azomethine ylide; cycloaddition; anti-cancer; cytotoxicity; quantum chemistry

Citation: Sennikova, V.V.; Zalaltdinova, A.V.; Sadykova, Y.M.; Khamatgalimov, A.R.; Gazizov, A.S.; Voloshina, A.D.; Lyubina, A.P.; Amerhanova, S.K.; Voronina, J.K.; Chugunova, E.A.; et al.

Diastereoselective Synthesis of Novel Spiro-Phosphacoumarins and Evaluation of Their Anti-Cancer Activity. *Int. J. Mol. Sci.* **2022**, *23*, 14348. <https://doi.org/10.3390/ijms232214348>

Academic Editor: Dmitry Aminin

Received: 27 October 2022

Accepted: 15 November 2022

Published: 18 November 2022

Publisher's Note: MDPI stays neutral with regard to jurisdictional claims in published maps and institutional affiliations.



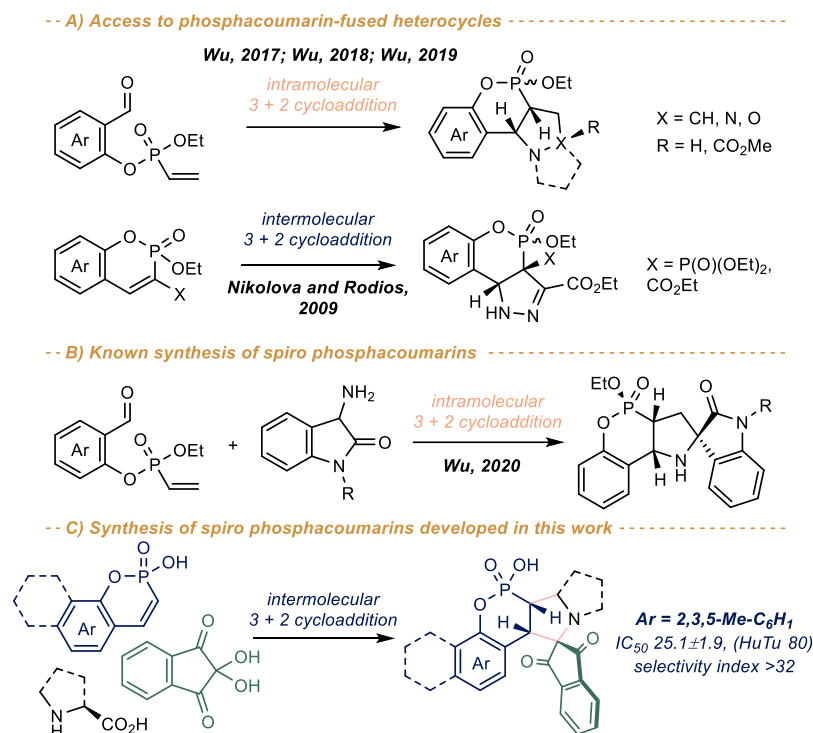
Copyright: © 2022 by the authors. Licensee MDPI, Basel, Switzerland. This article is an open access article distributed under the terms and conditions of the Creative Commons Attribution (CC BY) license (<https://creativecommons.org/licenses/by/4.0/>).

1. Introduction

Coumarins and dihydrocoumarins are ubiquitous in nature and have attracted considerable attention due to their biological properties [1–3]. Among known activities of coumarins, their anti-cancer properties [4,5] have gained an increasing interest and represent an emerging area of research, as indicated by recent reviews [6,7]. A number of substituted coumarins have been synthesized and tested in attempts to enhance their activity and pharmacological properties. The phosphorus-containing analogues of coumarins, the phosphacoumarins, have recently appealed as promising compounds possessing interesting structural, chemical and biological properties [8,9]. Various approaches to these compounds exist [8,10–12], which have been summarized in a recent review paper [13]. Despite the ongoing research in this field, the synthesis of heterocycle annelated and spiro derivatives of phosphacoumarins and dihydrophosphacoumarins is still scarce (see [14] for the review).

The approach to the pyrazolidin-3-on-, pyrrolidine- and isoxazolidine-fused phosphacoumarins via intramolecular 1,3-dipolar cycloaddition of salicylaldehyde-derived vinylphosphonates has been developed by Wu and coworkers (Scheme 1A) [15–17]. Earlier, Nikolova and Rodios reported the synthesis of pyrazole-fused phosphacoumarins using intermolecular [3 + 2] cycloaddition of phosphacoumarins with ethyl diazoacetate [18]. The only synthesis of oxindole spiro phosphacoumarins has been described by Wu [19], which also involved the intramolecular [3 + 2] cycloaddition of vinylphosphonates (Scheme 1B). This is in sharp contrast to parent coumarins, for which a number of spiro derivatives are known [20,21], including rather complex polycyclic [22] and even fullerene-fused ones [23].

As a result of our ongoing research in this area [24–26], herein we report a highly diastereoselective synthesis of spiro dihydrophosphacoumarins via intramolecular [3 + 2] cycloaddition of phosphacoumarins with some azomethine ylides (Scheme 1C). The proposed approach is complementary to that reported by Wu [19] and provides an easy entry to the novel pyrrolidine-fused spiro-phosphacoumarins derivatives, which are inaccessible via Wu’s method. The mechanism of the reaction and its regio- and diastereoselectivity was explored using quantum chemistry calculations. The cytotoxicity of the obtained compounds towards normal and cancer cell lines was also tested, the most potent compound being 3-fold more active than reference 5-fluorouracil and exhibiting a selectivity index > 32.

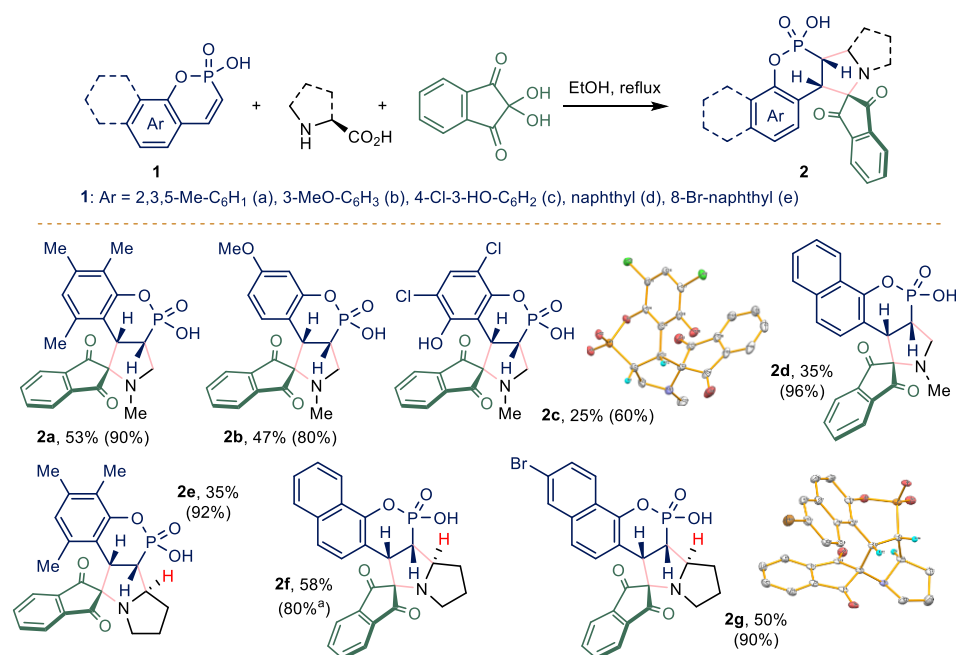


Scheme 1. Synthesis of heterocycle-fused phosphacoumarins via [3 + 2] cycloaddition reactions [15–18] (A), the only reported synthesis of spiro phosphacoumarins [19] (B) and the complementary approach developed in this work (C).

2. Results and Discussion

2.1. Chemistry

We started our research with the optimization of reaction conditions using phosphacoumarin **1a**, ninhydrin and sarcosine as model compounds. Pleasingly, simple refluxing of reactants in ethanol provided the target compound **2a** with a *ca* 90% yield according to ³¹P NMR data (Scheme 2). Additionally, the reaction proceeded in a highly regio- and diastereoselective manner (*dr* > 95: 5), which was also evidenced by ³¹P NMR data. We succeeded in the isolation of the single diastereomer from the reaction mixture with a 53% yield. Convinced of the possibility of the formation of the desired spiro dihydrophosphacoumarins, we further extended the reaction scope using phosphacoumarins **1b–e**. The reaction proceeded smoothly, providing target spiro compounds with a 60–96% yield according to NMR data. However, isolated yields were considerably lower due to the degradation of phosphacoumarins **2** during silica gel column purification, leading to the formation of highly polar compounds. Unfortunately, we were not able to isolate and identify these byproducts.



Scheme 2. Synthesis of spiro pyrrolidinophosphacoumarins **2**. Isolated yield is given, yield according to ³¹P NMR is given in parenthesis. ^a Isolated as a mixture of diastereomers with *dr* 12: 1 (see discussion in the text).

Presumably, the electron-donating groups in aromatic moiety promote the reaction, whereas electron withdrawing chlorine substituent clearly lowers the yield of the compound **2c**. In all cases, the target compounds were formed as single regioisomers with an excellent diastereoselectivity (*dr* > 95: 5). The configuration of the compound **2c** was determined to be *SS/RR* with X-ray analysis.

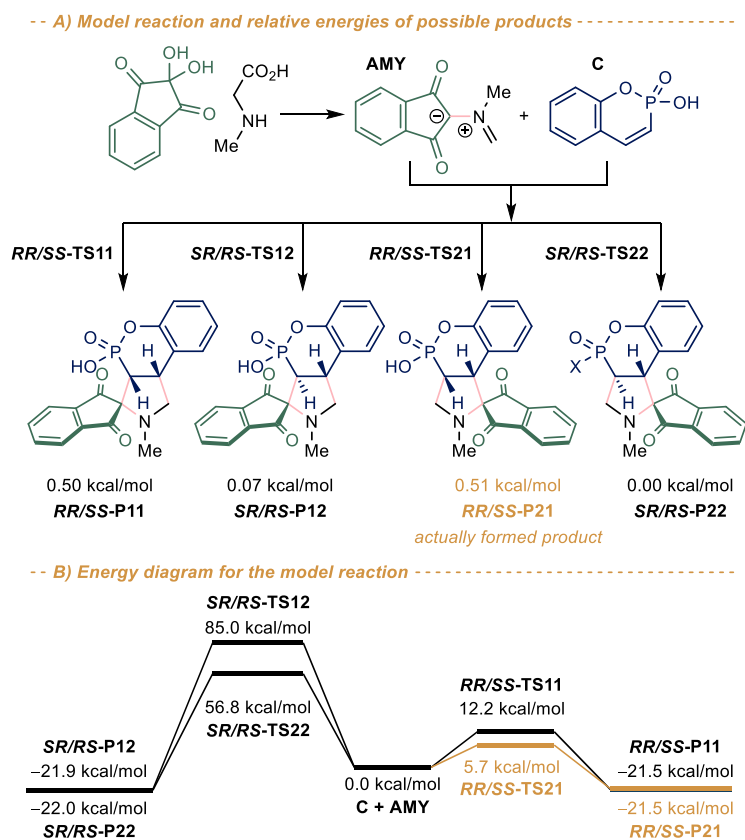
We also tested *L*-proline as an amino acid component in this reaction, which also furnished tetracyclic spiro phosphacoumarins **2e–g**. Despite one more stereocenter being present in these cases, the diastereoselectivity of the reaction remained fairly high (*dr* > 95: 5 according to ³¹P NMR data). Fortunately, we were able to grow crystals which were suitable for x-ray analysis of the compound **2g**, which allowed us to assign *SRS/RSR* configuration to the obtained diastereomers.

Despite the ³¹P NMR data of the reaction mixtures in all cases indicating the presence of single desired product, the compound **2f** was isolated as a mixture of diastereomers (*dr* 12: 1, see Supporting Information, Figure S31). This may be explained by the relatively low sensitivity of the ³¹P NMR method, not allowing the detection of very low concentrations (*ca* 2–3%) of the second diastereomer in the reaction mixtures. However, the reaction mixture could be enriched with this unobservable diastereomer during work-up, which is presumably the case for the compound **2f**.

2.2. Quantum Chemistry Studies

In order to gain more insight into the regio- and diastereoselectivity of the reaction of phosphacoumarins with azomethine ylides, quantum chemistry studies were carried out using unsubstituted phosphacoumarin **C** as the model compound (Scheme 3A). The first stage of the reaction, i.e., the formation of azomethine ylide **AMY** from ninhydrin and sarcosine, is a well-known process (see, e.g., [27,28]) and therefore was not modelled. The second stage is the [3 + 2] dipolar cycloaddition of intermediate **AMY** and compound **C**. In principle, two regioisomeric products may be formed at this stage. Since each one can exist as two diastereomers, this gives four possible final products in total. So, to identify the most preferred regioisomer of the reaction, the quantum chemistry calculations of the reagents **C** and **AMY**, the products **P** as well as the corresponding transition states **TS** were performed. Analysis of quantum chemical results shows that for the charged

species taking solvation model with a protic ethanol solvent into account play a crucial role in stabilizing the intermediates and products of [3 + 2]-cycloaddition (see Table S2 in Supporting Information).



Scheme 3. (A) Model [3 + 2] cycloaddition of phosphacoumarin **C** with ninhydrin-derived azomethine ylide **AMY** alongside relative energies of the possible isomeric products (ΔE , kcal/mol); (B) Energy diagram (ΔE , kcal/mol) as obtained from quantum chemistry calculations (PW6B95D/def2-TZVPD//B3LYP/6-31 + G*, Gaussian16). The sum of the total energies of reactants (**C** + **AMY**) is taken as zero.

According to the obtained quantum chemistry data, the reaction under study is exothermic (thermal effects are 21.5–22.0 kcal/mol for all expected reaction pathways) with the compound **SR/RS-P22** being slightly lower in energy compared to all the others (Scheme 3A, see also Supporting Information, Table S1). This is somewhat counterintuitive, since one would expect isomers **RR/SS-P21** and **SR/RS-P22** to be much more unfavourable due to sterical hindrance caused by the ninhydrin moiety. However, the energy difference appeared to be *ca* 0.1–0.5 kcal/mol only. Obviously, the preferable formation of the **RR/SS-P21** isomer cannot be attributed to its thermodynamic stability.

On the other hand, the calculated transition state energies differ significantly for all products (Scheme 3B, see also Supporting Information, Table S2). The transition state energies for the **SR/RS**-diastereomers are significantly higher than for their **SS/RR**-counterparts for both regioisomers. Taking into account the energy difference (*ca* 51–73 kcal/mol), the barriers can be considered prohibitively high for the **SR/RS**-diastereomers formation. On the other hand, the barrier for the formation of the **SS/RR-P21** diastereomer is *ca* 7 kcal/mol lower compared to that of the **SS/RR-P11**-diastereomer. According to the Arrhenius equation, 1 kcal/mol difference in activation energies results in more than a 6-fold difference in reaction rates at room temperature. Thus, the formation of the compound **SS/RR-P21** is much more preferable. These results are in complete agreement with the experimental observations. Thus, the high regio- and diastereoselectivity of the reaction

may be attributed to the faster formation of the *SS/RR-P21*-isomer, which appears to be a product of a kinetic control.

2.3. Biological Studies

2.3.1. In Vitro Cytotoxicity

Next, the obtained compounds were tested for cytotoxicity against normal and cancer human cell lines at concentrations of 1–100 μM . The compounds **2f** and **2g** were excluded from these studies, however, due to their extremely low solubility in water. As seen from Table 1, all of the tested compounds exhibit low cytotoxicity against MCF-7 cancer cell line, whereas the cytotoxicity against M-HeLa cells is comparable to that of the reference compound 5-fluorouracil. Notably, some of the compounds appeared to be non-toxic to normal cells in the studies' concentrations range. Similarly, the cytotoxicity of the obtained compounds against HuTu 80 cancer cells is either lower or comparable to the cytotoxicity of 5-fluorouracil.

Table 1. Cytotoxic effects of phosphacoumarins **2** on the cancer and normal human cell lines ¹.

Cmpd	Cancer Cell Line						Normal Cell Line
	M-HeLa		MCF-7		HuTu 80		Chang Liver
	IC ₅₀ , μM	SI	IC ₅₀ , μM	SI	IC ₅₀ , μM	SI	IC ₅₀ , μM
2a	52.6 \pm 4.1	>15	82.3 \pm 7.5	>10	25.1 \pm 1.9	>32	>800
2b	59.7 \pm 4.6	1	>100	ns	53.4 \pm 4.2	1.2	62.0 \pm 5.5
2c	>100	ns	77.6 \pm 6.2	ns	100 \pm 8.4	ns	>100
2d	60 \pm 5.4	ns	92.2 \pm 8.3	ns	82.6 \pm 7.6	ns	57.0 \pm 4.3
2e	>100	ns	>100	ns	>100	ns	>100
5-fluorouracil	62.0 \pm 4.7	1.4	16.7 \pm 1.3	5	65.2 \pm 5.6	1.3	86.3 \pm 6.5

¹ Three independent experiments were carried out; "ns" means no selectivity.

The remarkable exception is the phosphacoumarin **2a**. Its cytotoxicity against HuTu 80 cell line is *ca* 2.6-fold higher than the cytotoxicity of the reference compound, whereas the cytotoxicity against the Chang liver normal cell line is more than 10-fold lower, which gives a selectivity index > 32. For the M-HeLa cells, the cytotoxicity of compound **2a** was somewhat higher than that of the reference compound (52.6 \pm 4.1 vs. 62.0 \pm 4.7), with a selectivity index > 15. Finally, although the activity against MCF-7 cell line was considerably lower compared to the 5-fluorouracil, the selectivity index still remained above 10. Since compounds with a selectivity index > 10 are considered highly selective [29], the phosphacoumarin **2a** is a promising lead for further studies.

2.3.2. Cell Cycle Analysis

Taking into account the high potency and selectivity of the compound **2a**, some additional experiments were carried out to study in more details its anti-cancer action. The mechanism of action of cytotoxic agents is often associated with cell cycle arrest, which leads to a slowing down of cell proliferation. So, we have performed a cell cycle analysis for the HuTu 80 cells using flow cytometry. According to the obtained data, the presence of compound **2a** at concentrations of IC₅₀/2 (12.5 μM) and IC₅₀ (25 μM) after 24 h leads to an increase in the number of cells in the G1/G0 phase up to 79.0% and 81.0%, respectively, compared with the control of 77% (Figure 1). Meanwhile, the proportion of cells in S phase decreased almost by half (8.2% vs. 4.7%). Taken together, these results indicate that the compound **2a** treatment induces G0/G1 phase arrest and reduces the S phase of the cell cycle, leading to an inhibition in the proliferation of HuTu 80 cells.

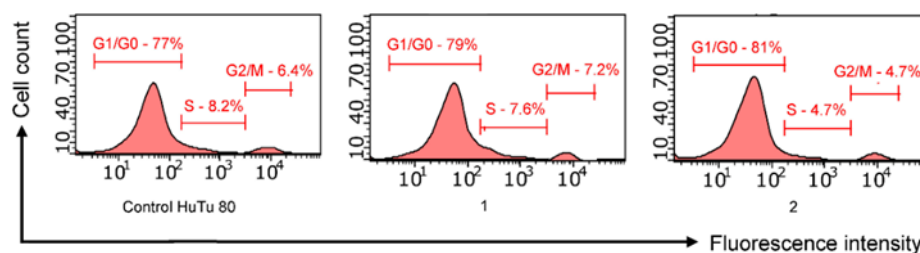


Figure 1. Effect of compound **2a** on cell cycle of HuTu 80 by flow cytometry. 1-**2a** at IC₅₀/2 concentration (12.5 μM); 2-**2a** at IC₅₀ concentration (25 μM).

2.3.3. Induction of Apoptotic Effects

Apoptosis is one of the most important mechanisms used to screen for new anticancer agents. The ability of the lead compound **2a** to induce apoptosis in HuTu 80 cells was determined by flow cytometry using annexin V-Alexa Fluor 647. Cells were incubated in the presence of **2a** at concentrations of IC₅₀/2 and IC₅₀ (Figure 2). It can be seen that after a 24-h incubation, the test compound begins to induce apoptosis in HuTu 80 cells. The most active apoptotic effects are manifested at an IC₅₀/2 concentration (12.5 μM) in the early apoptosis stage (Figure 3).

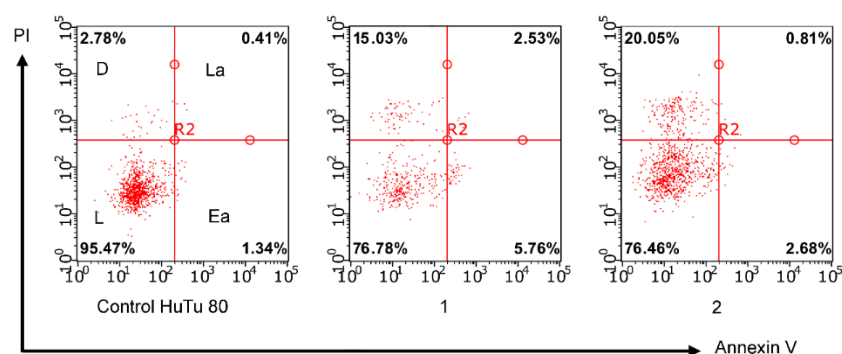


Figure 2. Apoptotic effects of compounds **2a** on HuTu 80 cells. 1-**2a** at IC₅₀/2 concentration (12.5 μM); 2-**2a** at IC₅₀ concentration (25 μM).

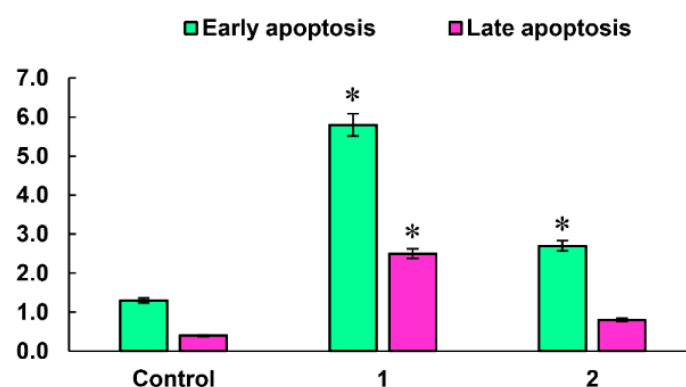


Figure 3. Representative histograms for the numbers of cells (% of total) in the early and late stages of apoptosis for the control and experimental groups. 1-**2a** at IC₅₀/2 concentration (12.5 μM); 2-**2a** at IC₅₀ concentration (25 μM). The values are presented as the mean ± SD; (*) $p < 0.05$ compared to control.

2.3.4. Mitochondrial Membrane Potential

The possibility of apoptosis through the mitochondrial pathway was assessed by flow cytometry using the JC-10 fluorescent dye (in the Mitochondria Membrane Potential Kit). In normal cells with a high membrane potential, JC-10 accumulates in the mitochondrial

matrix, where it forms aggregates with a red fluorescence. However, in apoptotic cells, a decrease in the membrane potential occurs. JC-10 diffuses from mitochondria and turns into a monomeric form, emitting a green fluorescence, which is recorded by a flow cytometer (Figure 4). After treatment with lead compound **2a** at concentrations of $IC_{50}/2$ and IC_{50} , the intensity of the green fluorescence significantly increased compared to the control (Figure 5). The results obtained indicated a significant decrease in the mitochondrial membrane potential of HuTu 80 cells. As in the experiment with V-Alexa Fluor 647, the cytotoxic effect of compound **2a** was more pronounced at $IC_{50}/2$ concentration. The results described above suggest that the mechanism of action of the leader of compound **2a** can be associated with the induction of apoptosis proceeding via the mitochondrial pathway.

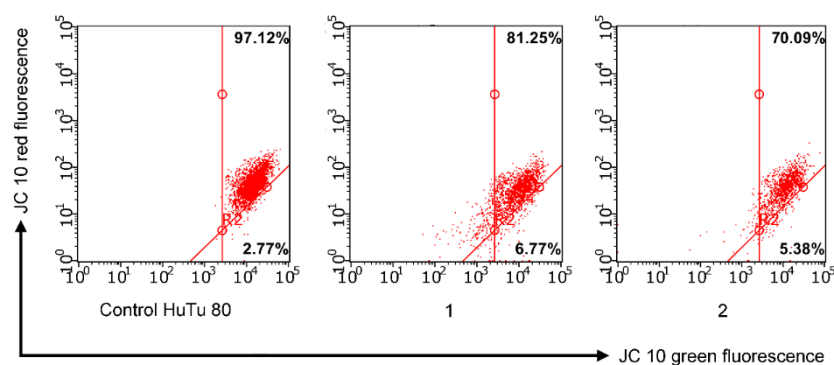


Figure 4. Flow cytometry analysis of HuTu 80 cells treated with compound **2a**. 1–**2a** at $IC_{50}/2$ concentration (12.5 μM); 2–**2a** at IC_{50} concentration (25 μM).

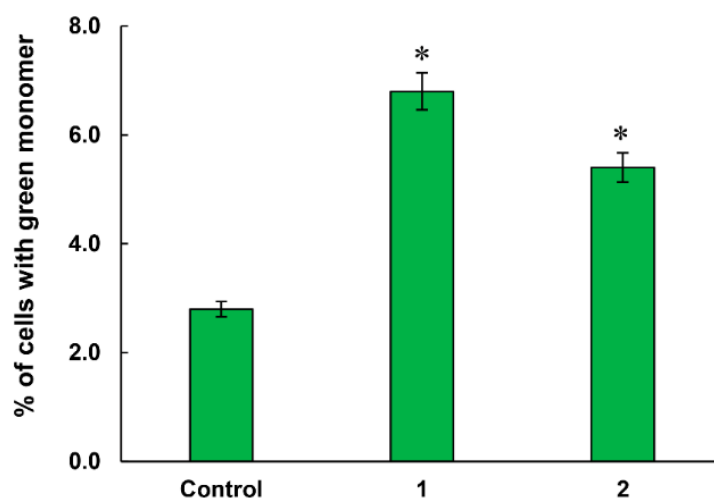


Figure 5. Quantitative determination of % cells with green monomers; 1–**2a** at $IC_{50}/2$ concentration (12.5 μM); 2–**2a** at IC_{50} concentration (25 μM). Values are presented as mean ± SD; (*) $p < 0.05$ compared to control.

An increase in the production of reactive oxygen species (ROS) by compounds also characterizes the development of apoptosis along the mitochondrial pathway. Mitochondria are a potential source and target of ROS. ROS leads to dysfunction of the mitochondria and, consequently, to irreversible cell damage. In this regard, the effect of the lead compound **2a** in HuTu 80 cells on ROS production was investigated using a flow cytometry assay and the CellROX[®] Deep Red flow cytometry kit. The data presented in Figure 6 show a significant increase in CellROX[®] Deep Red fluorescence intensity dominated by $IC_{50}/2$. This indicates an increase in ROS production in the presence of compound **2a**.

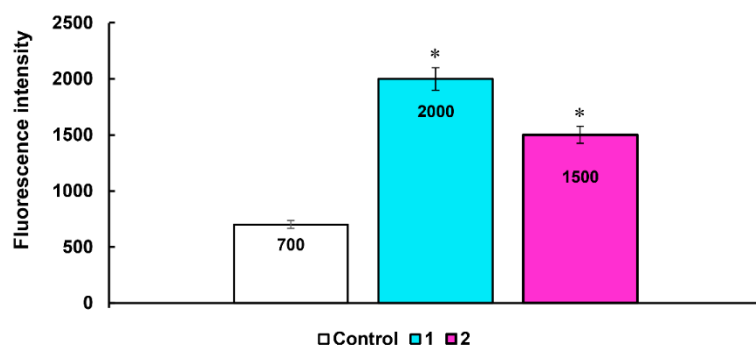


Figure 6. Induction of ROS production by lead compound **2a**. 1–**2a** at concentration $IC_{50}/2$ (12.5 μ M); 2–**2a** at concentration IC_{50} (25 μ M); (*) $p < 0.05$ compared to control.

3. Materials and Methods

3.1. Quantum Chemistry Calculations

All calculations were performed with Becke's three parameter hybrid exchange functional [30] and the gradient-corrected nonlocal correlation functional of Lee et al. [31] (B3LYP) in combination with the standard 6–31 + G* basis set [32–34] in the Gaussian16 package [35]. All geometry optimizations were performed without symmetry constraints (see Supporting Information, Table S3 for optimized cartesian coordinates). Since the method and the basis set used are known to have many limitations [36], geometry optimization was followed by a single-point calculation with PW6B95D functional [37] and def2-TZVPD basis set [38] to improve energies. Additionally, the Polarizable Continuum Model with the CPCM polarizable conductor calculation model was used in single-point calculations as a solvation model with the molecule of interest inside a cavity in a continuous, homogenous dielectric medium. Ethanol was used as a solvent in the used solvation model.

To ensure the calculated geometries correspond to true minima, vibrational analyses were performed using the same level of theory and the structure was accepted only if all eigenvalues of the Hessian matrix were positive. The transition states were confirmed by the presence of one negative eigenvalue in the Hessian matrix of the second derivatives. Additionally, the intrinsic reaction coordinate (IRC) was traced to ensure the transition state really connects the species involved in the reaction. The energy diagram was created with the aid of the Energy Diagram Plotter (CDXML) program [39].

3.2. Chemistry

3.2.1. General Methods

IR spectra were recorded on a UR-20 spectrometer in a 400–3600 cm^{-1} range in KBr. 1H NMR spectra were recorded on a Bruker MSL 400 spectrometer (399.93 MHz) with respect to the signals of residual protons in the deuterated solvent ($CDCl_3$, DMSO- d_6 , D_2O , CF_3COOD). The ^{13}C NMR spectra were recorded on a Bruker Avance 600 (151 MHz) spectrometer relative to the signals of residual protons from the deuterated solvent ($CDCl_3$, DMSO- d_6 , D_2O , CF_3COOD) (see Supporting information, Figures S3–S30, S32–S36 for the copies of NMR spectra). The ^{31}P NMR spectra were recorded on a Bruker Avance 600 (151 MHz) spectrometer. Elemental analysis was performed on a Carlo Erba device EA 1108. The melting points were determined in glass capillaries on a Stuart SMP 10 instrument.

The X-ray diffraction data for the crystals were collected on a Bruker D8 Venture diffractometer equipped with a CCD detector (Mo- $K\alpha$, $\lambda = 0.71073 \text{ \AA}$, graphite monochromator). Semi-empirical absorption correction was applied by the SADABS program [40]. The structures were solved by direct methods and refined by the full-matrix least squares in the anisotropic approximation for non-hydrogen atoms. The calculations were carried out by the SHELX-2014 program package [41] using Olex2 1.2 [42]. Crystallographic data for the structures reported in this paper have been deposited with the Cambridge Crystallographic Data Center (CCDC 2179367, 2179368, see Supporting information, Tables S4

and S5 and Figures S1 and S2 for the detailed data). Starting phosphacoumarins **1** were obtained by reported procedures [43].

3.2.2. General Procedure for the Synthesis of Compounds **2**

To a refluxing solution of phosphacoumarin **1** (1.8 mmol) in ethanol (5 mL), a mixture of ninhydrin (0.32 g, 1.8 mmol) and appropriate aminoacid (1.8 mmol) was added in one portion. The reaction mixture was refluxed until full consumption of starting materials (^{31}P NMR control, *ca* 12 h). The target compounds **2** were isolated in a pure form in two ways. In case of compounds **2a–d** the solvent was removed in a vacuum and the residue was purified by gradient-elution column chromatography using DCM: ethanol as eluent. In the case of compounds **2e–g**, the precipitate formed was filtered off, washed thoroughly with distilled water and dried in vacuum.

(3aS,9bS)-4-hydroxy-2,6,7,9-tetramethyl-2,3,3a,9b-tetrahydrospiro[benzo [5,6][1,2]oxaphosphinino [3,4-c]pyrrole-1,2'-indene]-1',3'-dione 4-oxide (2a)

Yield 0.25 g (53%), yellow solid, m.p. > 300 °C. IR (ν , cm^{-1}): 1080 (C-O), 1232 (P = O), 1460 (CH_2), 1596 (C-C_{Ar}), 1705 (C = O), 1744 (C = O), 2939 (CH_3). ^1H NMR (600 MHz, D₂O): 1.64 (s, 3H), 1.94 (s, 3H), 2.04 (s, 3H), 2.31 (s, 3H), 2.58 (s, 1H), 3.03–3.13 (m, 1H), 3.53–3.60 (m, 1H), 3.85–3.95 (m, 1H), 4.41 (dd, 1H, PCH, $^3J_{\text{HH}}$ 11.74 Hz, $^2J_{\text{PH}}$ 17.08 Hz), 6.19 (s, 1H), 7.36 (d, 1H, $^3J_{\text{HH}}$ 7.71 Hz), 7.72 (t, 1H, $^3J_{\text{HH}}$ 7.56 Hz), 7.85 (t, 1H, $^3J_{\text{HH}}$ 7.55 Hz), 7.99 (d, 1H, $^3J_{\text{HH}}$ 7.69 Hz). ^{13}C NMR (151 MHz, D₂O): 11.0, 18.8, 24.8, 35.7 (d, $^1J_{\text{PC}}$ 229.4 Hz), 49.0 (d, $^2J_{\text{PC}}$ 10.6 Hz), 56.8, 80.1, 118.4 (d, $^2J_{\text{PC}}$ 14.1 Hz), 122.3, 123.4, 125.7, 126.6, 134.0, 137.1, 138.0, 138.4, 141.2, 141.4, 151.1 (d, $^3J_{\text{PC}}$ 6.3 Hz), 201.0, 201.9 (s). ^{31}P NMR (243 MHz, D₂O): 22.7. MS (MALDI TOF), *m/z*: 434 [M + Na]⁺. Calcd. (%) for C₂₂H₂₄NO₅P: C, 63.92; H, 5.19; O, 20.01 N, 3.39; P, 7.49. Found: C, 64.23; H, 5.39; O, 19.75; N, 3.19; P, 7.43.

(3aS,9bS)-4-hydroxy-7-methoxy-2-methyl-2,3,3a,9b-tetrahydrospiro[benzo [5,6][1,2]oxaphosphinino [3,4-c]pyrrole-1,2'-indene]-1',3'-dione 4-oxide (2b)

Yield 0.36 g (47%), yellow solid, m.p. > 300 °C. IR (ν , cm^{-1}): 1081 (C-O), 1162 (O-CH₃), 1229 (P = O), 1504 (CH_2), 1618 (C-C_{Ar}), 1705 (C = O), 1742 (C = O), 2930 (CH_3). ^1H NMR (600 MHz, D₂O): 2.18 (s, 3H, NCH₃); 3.03–3.12 (m, 1H, CH₂); 3.37–3.44 (mp, 1H, CH); 3.54 (s, 3H, OCH₃); 3.70–3.79 (m, 1H, CH₂) 4.05–4.12 (m, 1H, PCH); 5.97 (d, 1H, CH, $^3J_{\text{HH}}$ 8.19 Hz); 6.17 (d, 1H, CH, $^3J_{\text{HH}}$ 8.43 Hz); 6.44 (s, 1H, CH); 7.34 (d, 1H, CH, $^3J_{\text{HH}}$ 7.54 Hz); 7.73 (t, 1H, CH, $^3J_{\text{HH}}$ 7.15 Hz); 7.85 (t, 1H, CH, $^3J_{\text{HH}}$ 7.49 Hz); 7.96 (d, 1H, CH, $^3J_{\text{HH}}$ 7.57 Hz). ^{13}C NMR (100.6 MHz, D₂O): 35.7 (s); 35.81 (d, $^1J_{\text{PC}}$ 136.4 Hz); 52.0 (d, $^2J_{\text{PC}}$ 4.4 Hz); 56.0 (s); 57.3 (s); 80.8 (s); 106.2 (d, $^2J_{\text{PC}}$ 4.3 Hz); 109.8 (s); 115.2 (s); 115.4 (s); 122.8 (s); 124.1 (s); 130.8 (s); 137.7 (s); 138.4 (s); 142.1 (d, $^3J_{\text{PC}}$ 2.3 Hz); 153.7 (d, $^3J_{\text{PC}}$ 5.9 Hz); 160.2 (s); 202.7 (s); 203.5 (s). ^{31}P NMR (242.9 MHz, D₂O): 21.3. MS (MALDI-TOF) *m/z*: 420 [M + Na]⁺. Calcd. (%) for C₂₀H₁₈NO₆P: C, 60.15; H, 4.54; O, 24.04; N, 3.51; P, 7.76. Found: C, 60.23; H, 4.39; O, 23.95; N, 3.27; P, 7.52.

(3aS,9bS)-6,8-dichloro-4,9-dihydroxy-2-methyl-2,3,3a,9b-tetrahydrospiro[benzo [5,6][1,2]oxaphosphinino [3,4-c]pyrrole-1,2'-indene]-1',3'-dione 4-oxide (2c)

Yield 0.17 g (25%), yellow solid, m.p. > 300 °C. IR (ν , cm^{-1}): 1078 (C-Cl), 1229 (P = O), 1456 (CH_2), 1591 (C-C_{Ar}), 1703 (C = O), 1736 (C = O), 2871 (CH_3). ^1H NMR (399.93 MHz, D₂O): 2.21 (s, 3H, NCH₃); 3.01–3.15 (m, 1H, CH₂); 3.37–3.44 (m, 1H, CH); 3.64–3.75 (m, 1H, CH₂); 4.36–4.46 (m, 1H, PCH); 7.25 (s, 1H, CH); 7.54 (d, 1H, CH, $^3J_{\text{HH}}$ 7.86 Hz); 7.85 (t, 1H, CH, $^3J_{\text{HH}}$ 7.18 Hz); 7.94 (t, 1H, CH, $^3J_{\text{HH}}$ 7.76 Hz); 8.01 (d, 1H, CH, $^3J_{\text{HH}}$ 7.48 Hz). ^{13}C NMR (100.6 MHz, D₂O): 34.4 (d, $^1J_{\text{PC}}$ 128.6 Hz); 46.5 (s); 56.9 (s); 78.6 (s); 114.6 (d, $^2J_{\text{PC}}$ 15.2 Hz); 115.5 (s); 122.2 (s); 123.4 (s); 129.0 (s); 137.4 (s); 139.9 (s); 142.4 (s); 148.0 (d, $^3J_{\text{PC}}$ 4.9 Hz); 202.2 (s); 203.1 (s). ^{31}P NMR (161.9 MHz, D₂O): 21.2. MS (MALDI-TOF) *m/z*: 492 [M + K]⁺. Calcd. (%) for C₁₉H₁₄NCl₂O₆P: C, 50.24; H, 3.11; O, 21.14; Cl, 15.61; N, 3.08; P, 6.82. Found: C, 50.23; H, 3.39; O, 20.95; N, 3.17; P, 6.41.

(3a'S,11a'S)-11'-hydroxy-2'-methyl-1',2',3a',11a'-tetrahydrospiro[indene-2,3'-naphtho [2',1':5,6] oxaphosphinino [3,4-c]pyrrole]-1,3-dione 11'-oxide (2d)

Yield 0.25 g (34.7%), yellow solid, m.p. > 300 °C. IR (ν , cm^{-1}): 1243 (P = O), 1466 (CH_2), 1596 (C-C_{Ar}), 1703 (C = O), 1749 (C = O). ^1H NMR (399.93 MHz, D₂O): 2.25 (s, 3H,

NCH₃); 3.23–3.33 (m, 1H, CH₂); 3.51–3.58 (m, 1H, CH); 3.84–3.96 (m, 1H, CH₂); 4.97 (dd, 1H, PCH, ³J_{HH} 11.87 Hz, ²J_{PH} 16.02 Hz); 7.04–7.09 (m, 2H, CH); 7.13 (t, 1H, CH, ³J_{HH} 7.56 Hz); 7.19 (t, 1H, CH, ³J_{HH} 7.84 Hz); 7.40 (t, 1H, CH, ³J_{HH} 7.62 Hz); 7.42–7.52 (m, 3H, CH); 7.59 (d, 1H, CH, ³J_{HH} 8.87 Hz); 7.64 (d, 1H, CH, ³J_{HH} 7.73 Hz). ¹³C NMR (100.6 MHz, D₂O): 35.6 (d, ¹J_{PC} 136.9 Hz); 47.7 (d, ²J_{PC} 4.35 Hz); 56.7 (s); 80.6 (s); 116.4 (d, ²J_{PC} 15.5 Hz); 120.5 (d, ³J_{PC} 10.1 Hz); 121.3 (d, ³J_{PC} 9.0 Hz); 122.9 (s); 123.3 (s); 124.7 (s); 127.1 (s); 128.6 (s); 130.1 (s); 130.5 (s); 131.5 (s); 136.4 (s); 137.2 (s); 140.2 (s); 141.7 (s); 151.2 (d, ³J_{PC} 6.1 Hz); 202.2 (s); 203.0 (s). ³¹P NMR (161.9 MHz, D₂O): 23.6. MS (MALDI-TOF) *m/z*: 420 [M + 1]⁺, 442 [M + Na]⁺. Calcd: (%) for C₂₃H₁₈NO₅P: C, 65.87; H, 4.33; O, 19.08; N, 3.34; P, 7.39. Found: C, 65.65; H, 4.31; O, 19.01; N, 3.21; P, 7.40.

(6*aS*,6*bR*,11*aS*)-6-hydroxy-1,3,4-trimethyl-6*a*,6*b*,7,8,9,11*a*-hexahydrospiro[benzo [5,6][1,2]oxaphosphinino [3,4-*a*]pyrrolizine-11,2'-indene]-1',3'-dione 6-oxide (**2e**)

Yield 0.28 g (35%), white solid, m.p. > 300 °C. IR (ν, cm⁻¹): 1252 (P = O), 1460 (CH₂), 1591 (C-C_{Ar}), 1708 (C = O), 1751 (C = O), 2929 (CH₃). ¹H NMR (399.93 MHz, D₂O): 1.82 (s, 3H, CH₃); 1.97 (s, 3H, CH₃); 2.01 (s, 3H, CH₃); 2.10–2.29 (m, 2H, CH₂); 2.44–2.57 (m, 2H, CH₂); 2.87–3.00 (m, 1H, CH₂); 3.72–3.80 (m, 1H, CH); 4.23–4.32 (m, 1H, CH₂); 4.95 (dd, 1H, PCH, ³J_{HH} 11.50 Hz, ²J_{PH} 18.93 Hz); 5.51 (s, 1H, CH); 6.26 (s, 1H, CH); 7.49–7.52 (m, 1H, CH); 7.81 (td, 1H, CH, ³J_{HH} 6.35 Hz); 7.87 (td, 1H, CH, ³J_{HH} 7.58 Hz); 8.00–8.04 (m, 1H, CH). ¹³C NMR (100.6 MHz, D₂O): 10.7 (s); 18.4 (s); 18.7 (s); 23.5 (s); 29.5 (d, ³J_{PC} 3.4 Hz) 41.5 (d, ¹J_{PC} 135.1 Hz); 47.1 (d, ²J_{PC} 5.2 Hz); 50.4 (s); 72.0 (s); 77.1 (s); 115.6 (d, ²J_{PC} 14.2 Hz); 122.9 (s); 123.9 (s); 125.9 (d, ³J_{PC} 3.3 Hz); 127.3 (s); 134.3 (s); 137.3 (s); 138.1 (s); 139.5 (s); 139.9 (s); 141.0 (s); 150.5 (d, ³J_{PC} 6.8 Hz); 192.9 (s); 193.8 (s). ³¹P NMR (161.9 MHz, D₂O): 19.0. MS (MALDI-TOF) *m/z*: 460 [M + Na]⁺. Calcd: (%) for C₂₄H₂₄NO₅P: C, 65.90; H, 5.53; O, 18.29; N, 3.20; P, 7.08. Found: C, 65.65; H, 5.31; O, 18.11; N, 3.11; P, 7.00.

(8*a'S*,8*b'R*,13*a'S*)-8'-hydroxy-8*a'*,8*b'*,9',10',11',13*a'*-hexahydrospiro[indene-2,13'-naphtho [2',1':5,6][1,2]oxaphosphinino [3,4-*a*]pyrrolizine]-1,3-dione 8'-oxide (**2f**)

Yield 0.44 g (58%), white solid, m.p. > 300 °C. IR (ν, cm⁻¹): 1223 (P = O), 1465 (CH₂), 1594 (C-C_{Ar}), 1715 (C = O), 1753 (C = O). ¹H NMR (399.93 MHz, CF₃COOD): 2.29–2.41 (m, 1H, CH₂); 2.50–2.62 (m, 1H, CH₂); 2.65–2.73 (m, 1H, CH₂); 2.87–2.96 (m, 1H, CH₂); 3.82–3.92 (m, 1H, CH₂); 3.98–4.09 (m, 1H, CH₂); 4.25–4.35 (m, 1H, CH); 4.39–4.45 (m, 1H, CH); 5.06–5.18 (m, 1H, PCH); 7.39 (d, 1H, CH, ³J_{HH} 8.94 Hz); 7.71–7.82 (m, 2H, CH); 7.86–7.95 (m, 2H, CH); 8.05 (d, 1H, CH, ³J_{HH} 8.97 Hz); 8.11–8.18 (m, 2H, CH); 8.47 (d, 1H, CH, ³J_{HH} 7.31 Hz). ¹³C NMR (100.6 MHz, CF₃COOD): 7.5 (s); 23.2 (s); 25.4 (s); 37.2 (d, ¹J_{PC} 140.9 Hz); 42.9 (s); 51.0 (s); 61.5 (s); 68.5 (d, ³J_{PC} 4.5 Hz); 72.3 (s); 77.4 (d, ²J_{PC} 11.9 Hz); 105.6 (d, ²J_{PC} 11.0 Hz); 115.7 (d, ³J_{PC} 5.7 Hz); 121.0 (s); 121.9 (s); 122.1 (s); 122.2 (s); 123.0 (s); 123.8 (s); 126.1 (s); 126.6 (s); 126.9 (s); 127.4 (s); 127.9 (s); 143.8 (d, ³J_{PC} 6.8 Hz); 147.2 (s); 192.6 (s). ³¹P NMR (161.9 MHz, CF₃COOD): 18.9. MS (ESI) *m/z*: 448 [M + 3]⁺. Calcd: (%) for C₂₅H₂₀NO₅P: C, 67.41; H, 4.53; O, 17.96; N, 3.14; P, 6.95. Found: C, 67.65; H, 4.31; O, 18.01; N, 3.01; P, 6.85.

(8*a'S*,8*b'R*,13*a'S*)-4'-bromo-8'-hydroxy-8*a'*,8*b'*,9',10',11',13*a'*-hexahydrospiro[indene-2,13'-naphtho [2',1':5,6][1,2]oxaphosphinino [3,4-*a*]pyrrolizine]-1,3-dione 8'-oxide (**2g**)

Yield 0.23 g (50%), white solid, m.p. > 300 °C. IR (ν, cm⁻¹): 1085 (C-Br), 1251 (P = O), 1500 (CH₂), 1588 (C-C_{Ar}), 1713 (C = O), 1755 (C = O), 2926 (CH₃). ¹H NMR (399.93 MHz, DMSO-d₆): 1.73–1.84 (m, 1H, CH₂); 1.87–1.94 (m, 1H, CH₂); 2.05–2.16 (m, 2H, CH₂); 2.87–2.97 (m, 2H, CH₂); 3.47–3.55 (m, 1H, CH); 4.75–4.83 (m, 1H, CH); 5.19–5.26 (m, 1H, PCH); 7.09 (d, 1H, CH, ³J_{HH} 8.85 Hz); 7.30–7.36 (m, 2H, CH); 7.43 (d, 1H, CH, ³J_{HH} 9.26 Hz); 7.62 (d, 1H, CH, ³J_{HH} 8.92 Hz); 7. (td, 1H, CH, ³J_{HH} 6.55 Hz); 7.71 (td, 1H, CH, ³J_{HH} 8.61 Hz); 7.78 (d, 1H, CH, ³J_{HH} 7.58 Hz); 7.89 (d, 1H, CH, ³J_{HH} 2.1 Hz). ¹³C NMR (100.6 MHz, DMSO-d₆): 24.0 (s); 29.0 (s); 41.4 (d, ¹J_{PC} 131.9 Hz); 45.4 (s); 48.7 (s); 69.9 (s); 77.7 (s); 117.2 (d, ²J_{PC} 14.9 Hz); 117.7 (s); 119.7 (s); 122.5 (d, ³J_{PC} 3.0 Hz); 122.9 (s); 123.7 (s); 125.4 (s); 129.3 (s); 129.6 (s); 130.2 (s); 130.7 (s); 131.5 (s); 136.4 (s); 137.4 (s); 140.1 (s); 141.5 (s); 152.2 (d, ³J_{PC} 6.3 Hz). ³¹P NMR (161.9 MHz, DMSO-d₆): 20.06. MS (ESI) *m/z*: 520 [M-1]. Calcd: (%) for C₂₅H₁₉NBrO₅P: C, 57.27; H, 3.65; O, 15.26; Br, 15.24; N, 2.67; P, 5.91. Found: C, 57.25; H, 3.61; O, 15.01; Br, 15.31; N, 2.61; P, 5.85.

1-methyl-1,3-dihydro-4*H*-spiro[chromeno [4,3-*b*]pyrrole-2,2'-indene]-1',3',4-trione (**4**)

Yield 0.25 g (25%), orange solid, m.p. > 300 °C. IR (ν , cm^{-1}): 1511 (CH_2), 1594 (C-C_{Ar}), 1614 ($\text{C}=\text{C}$), 1707 ($\text{C}=\text{O}$), 1750 ($\text{C}=\text{O}$). ^1H NMR (399.93 MHz, CDCl_3): 3.25 (s, 3H, NCH_3); 3.28 (s, 2H, CH_2); 7.24–7.30 (m, 1H, CH); 7.43 (d, 1H, CH, $^3J_{\text{HH}}$ 8.04 Hz); 7.57 (t, 1H, CH, $^3J_{\text{HH}}$ 8.12 Hz); 7.99 (d, 1H, CH, $^3J_{\text{HH}}$ 8.11 Hz); 7.97–8.04 (m, 2H, CH); 8.10–8.15 (m, 2H, CH). ^{13}C NMR (100.6 MHz, CDCl_3): 35.0 (s); 36.2 (s); 78.0 (s); 96.0 (s); 113.2 (s); 118.4 (s); 123.1 (s); 123.4 (s); 124.6 (s); 132.0 (s); 137.1 (s); 141.1 (s); 155.0 (s); 158.1 (s); 159.3 (s); 196.5. MS (ESI) m/z : 330 [M-1]. Calcd: (%) for $\text{C}_{20}\text{H}_{13}\text{NO}_4$: C, 72.50; H, 3.95; O, 19.32; N, 4.23. Found: C, 72.10; H, 3.91; O, 19.31; N, 4.15.

3.3. Biological Studies

3.3.1. Cell Toxicity Assay (MTT-Test)

The toxic effect on cells was determined using the colorimetric method of cell proliferation MTT (Thiazolyl Blue Tetrazolium Bromide, Sigma). For this, 10 μL of MTT reagent in Hank's balanced salt solution (HBSS) (final concentration 0.5 mg/ml) was added to each well. The plates were incubated at 37 °C for 2–3 h in an atmosphere humidified with 5% CO_2 . Absorbance was recorded at 540 nm using an Invitrologic microplate reader (Russia). Experiments for all compounds were repeated three times. The M-HeLa clone 11 human, epithelioid cervical carcinoma, strain of HeLa, clone of M-HeLa; human duodenal cancer cell line (HuTu 80); human breast adenocarcinoma cells (MCF-7) and Chang liver cell line (Human liver cells) from the N. F. Gamaleya Research Center of Epidemiology and Microbiology and the Type Culture Collection of the Institute of Cytology (Russian Academy of Sciences) were used in the experiments. The cells were cultured on a standard nutrient medium "Igla" produced by the Moscow Institute of Poliomyelitis and Viral Encephalitis. M.P. Chumakov by PanEco, with the addition of 10% fetal calf serum and 1% nonessential amino acids (NEAA).

The cells were sown on a 96-well panel from Eppendorf at a concentration of 5×10^3 cells per well with a volume of 100 μL medium, and cultured in a CO_2 incubator at 37 °C. In 48 h after planting the cells, the culture medium was taken into the wells, and 100 μL solutions of the studied drug in the specified dilutions were added to the wells. Dilutions of the compounds were prepared directly in growth medium supplemented with 5% DMSO to improve solubility. The cytotoxic effect of the test compounds was determined at concentrations of 0.1–100 μM . The calculation of the IC_{50} , the concentration of the drug causing inhibition of cell growth by 50%, was performed using the program: MLA—"Quest Graph™ IC_{50} Calculator". AAT Bioquest, Inc., Pleasanton, CA, USA, <https://www.aatbio.com/tools/ic50-calculator> (accessed on 25 January 2022).

3.3.2. Induction of Apoptotic Effects by Test Compounds (Flow Cytometry Assay)

Cell Culture. HuTu 80 cells at 1×10^6 cells/well in a final volume of 2 mL were seeded into six-well plates. After 24 h of incubation, various concentrations of compound **2a** were added to wells.

Cell Apoptosis Analysis. The cells were harvested at 2000 rpm for 5 min and then washed twice with ice-cold PBS, followed by resuspension in binding buffer. Next, the samples were incubated with 5 μL of annexin V- Alexa Fluor 647 (Sigma-Aldrich, St. Louis, MO, USA) and 5 μL of propidium iodide for 15 min at room temperature in the dark. Finally, the cells were analyzed by flow cytometry (Guava easy Cyte, MERCK, Rahway, NJ, USA) within 1 h. The experiments were repeated three times.

3.3.3. Mitochondrial Membrane Potential

Cells were harvested at 2000 rpm for 5 min and then washed twice with ice-cold PBS, followed by resuspension in JC-10 (10 $\mu\text{g}/\text{mL}$) and incubation at 37 °C for 10 min. After the cells were rinsed three times and suspended in PBS, the JC-10 fluorescence was observed by flow cytometry (Guava easy Cyte, MERCK, Rahway, NJ, USA).

3.3.4. Detection of Intracellular ROS

HuTu 80 cells were incubated with compound **2a** at concentrations of IC₅₀ for 24 h. ROS generation was investigated using flow cytometry assay and CellROX[®] Deep Red flow cytometry kit. For this HuTu 80 cells were harvested at 2000 rpm for 5 min and then washed twice with ice-cold PBS, followed by resuspension in 0.1 mL of medium without FBS, to which was added 0.2 µL of CellROX[®] Deep Red and incubated at 37 °C for 30 min. After being washed three times, the cells were suspended in PBS, and the production of ROS in the cells was immediately monitored using a flow cytometer Guava easy Cyte, MERCK, Rahway, NJ, USA).

3.3.5. Statistical Analysis

The IC₅₀ values were calculated using the online calculator MLA—Quest Graph™ IC50 Calculator AAT Bioquest, Inc., Pleasanton, CA, USA, 25 January 2022. The statistical analysis was performed using the Mann-Whitney test ($p < 0.05$). Tabular and graphical data contains averages and standard errors.

4. Conclusions

In conclusion, a series of novel pyrrolidine-fused spiro dihydrophosphacoumarins were obtained via intermolecular [3 + 2] cycloaddition of phosphacoumarins with ninhydrin-based azomethine ylides. The reaction proceeded in a highly regioselective manner, leading to the formation of up to three stereocentres with excellent diastereoselectivity. The mechanism of the reaction was studied with quantum chemistry methods. The obtained results were in a good agreement with the experimental data and indicate that the preferential formation of a single regio- and diastereoisomer is due to kinetic reasons. Additionally, a novel pathway of the reaction of 4-hydroxycoumarin with azomethine ylides has been revealed, which will be a subject for further research. The anti-cancer activities of spiro phosphacoumarins were tested *in vitro*. The compound possessing three methyl groups in aromatic moiety appeared to be the most potent against all tested cancer cell lines (M-HeLa, HuTu 80 and MCF-7). Its cytotoxicity was up to 2.6-fold higher than the cytotoxicity of a reference compound. At the same time, its cytotoxicity against normal cell lines (Chang liver) was much lower, thus giving the selectivity index ranging from 10 (M-HeLa cell line) to >32 (HuTu 80 cell line). The more detailed studies of the anti-cancer activity of the lead compound revealed that it arrests the cell cycle at the G1/G0 phase and leads to an increased level of ROS in HuTu 80 cells, as well as decreasing the mitochondrial potential. Thus, the death of cancer cells presumably occurs via an intrinsic mitochondrial apoptosis pathway.

Supplementary Materials: The following supporting information can be downloaded at: <https://www.mdpi.com/article/10.3390/ijms232214348/s1>.

Author Contributions: Synthesis—V.V.S., A.V.Z., Y.M.S., E.A.C. and N.O.A.; quantum chemistry studies, writing—review and editing—A.R.K.; writing—original draft preparation, conceptualization—A.S.G.; biological studies—A.P.L. and S.K.A.; biological studies supervision—A.D.V.; X-ray studies—J.K.V.; project administration, supervision—A.R.B. and M.A.P. All authors have read and agreed to the published version of the manuscript.

Funding: Synthetic work: quantum chemistry computations, NMR, MS research and biological studies were conducted by V.V., A.V., Y.M., A.R., A.S., A.D., A.P., S.K., E.A., N.O., A.R. and M.A. at the Arbuzov Institute of Organic and Physical Chemistry, and were funded by the government assignment for the FRC Kazan Scientific Center of RAS. X-ray studies were conducted by J.K. at the N.S. Kurnakov Institute of General and Inorganic Chemistry and were supported by the Ministry of Science and Higher Education of Russia as part of the state assignment of the Kurnakov Institute of General and Inorganic Chemistry of the Russian Academy of Sciences.

Institutional Review Board Statement: Not applicable.

Informed Consent Statement: Not applicable.

Data Availability Statement: The data presented in this study are contained within the article or in Supplementary Materials, or are available upon request from the corresponding authors Ayrat Khamatgalimov or Almir Gazizov.

Acknowledgments: The authors are grateful to the Assigned Spectral-Analytical Center of FRC Kazan Scientific Center of RAS for technical assistance in the research.

Conflicts of Interest: The authors declare no conflict of interest.

References

- Balewski, Ł.; Szulta, S.; Jalińska, A.; Kornicka, A. A Mini-Review: Recent Advances in Coumarin-Metal Complexes with Biological Properties. *Front. Chem.* **2021**, *9*, 781779. [CrossRef] [PubMed]
- Srikrishna, D.; Godugu, C.; Dubey, P.K. A Review on Pharmacological Properties of Coumarins. *Mini-Rev. Med. Chem.* **2018**, *18*, 113–141. [CrossRef]
- Annunziata, F.; Pinna, C.; Dallavalle, S.; Tamborini, L.; Pinto, A. An Overview of Coumarin as a Versatile and Readily Accessible Scaffold with Broad-Ranging Biological Activities. *Int. J. Mol. Sci.* **2020**, *21*, 4618. [CrossRef] [PubMed]
- Kaur, M.; Kohli, S.; Sandhu, S.; Bansal, Y.; Bansal, G. Coumarin: A Promising Scaffold for Anticancer Agents. *Anticancer. Agents Med. Chem.* **2015**, *15*, 1032–1048. [CrossRef]
- Thakur, A.; Singla, R.; Jaitak, V. Coumarins as anticancer agents: A review on synthetic strategies, mechanism of action and SAR studies. *Eur. J. Med. Chem.* **2015**, *101*, 476–495. [CrossRef] [PubMed]
- Wu, Y.; Xu, J.; Liu, Y.; Zeng, Y.; Wu, G. A Review on Anti-Tumor Mechanisms of Coumarins. *Front. Oncol.* **2020**, *10*, 592853. [CrossRef] [PubMed]
- Rawat, A.; Vijaya Bhaskar Reddy, A. Recent advances on anticancer activity of coumarin derivatives. *Eur. J. Med. Chem. Reports* **2022**, *5*, 100038. [CrossRef]
- Li, X.; Zhang, D.; Pang, H.; Shen, F.; Fu, H.; Jiang, Y.; Zhao, Y. Synthesis of a Diverse Series of Phosphacoumarins with Biological Activity. *Org. Lett.* **2005**, *7*, 4919–4922. [CrossRef]
- Alexieva, V.; Karanov, E.; Nikolova, R.; Bojilova, A. Plant growth regulating activity of some phosphorus derivatives of coumarin. *Bulg. J. Plant Physiol.* **1995**, *21*, 45.
- Kim, C.-E.; Ryu, T.; Kim, S.; Lee, K.; Lee, C.-H.; Lee, P.H. Gold-Catalyzed Hydroarylation of Aryl Alkynylphosphonates for the Synthesis of Phosphacoumarins. *Adv. Synth. Catal.* **2013**, *355*, 2873–2883. [CrossRef]
- Hariri, M.; Darvish, F.; Mengue Me Ndong, K.-P.; Sechet, N.; Chacktas, G.; Boosaliki, H.; Tran Do, M.L.; Mwande-Maguene, G.; Lebibi, J.; Burirov, A.R.; et al. Gold-Catalyzed Access to Isophosphinoline 2-Oxides. *J. Org. Chem.* **2021**, *86*, 7813–7824. [CrossRef] [PubMed]
- Hariri, M.; Darvish, F.; Ndong, K.-P.M.M.; Babouri, R.; Babouri, R.; Mwande-Maguene, G.; Burirov, A.R.; Licznar-Fajardo, P.; Pirat, J.-L.; Ayad, T.; et al. Biologically relevant surrogates of coumarins: 2-phenyl H-isophosphinoline 2-oxides with antibacterial activity. *GSC Biol. Pharm. Sci.* **2021**, *16*, 283–296. [CrossRef]
- Balašova, A.; Žalubovskis, R. Synthetic Methods toward Phosphacoumarins (microreview). *Chem. Heterocycl. Compd.* **2022**, *58*, 310–312. [CrossRef]
- Koleva, A.I.; Petkova-Yankova, N.I.; Nikolova, R.D. Synthesis and Chemical Properties of 3-Phosphono-coumarins and 1,2-Benzoxaphosphorins as Precursors for Bioactive Compounds. *Molecules* **2019**, *24*, 2030. [CrossRef] [PubMed]
- Huang, T.; Wang, Q.; Kong, D.; Wu, M. Diastereoselective catalyst-free construction of isoxazolidine-cis-fused phospho dihydrocoumarins via an intramolecular Nitron–Vinylphosphonate dipolar cycloaddition. *Tetrahedron Lett.* **2019**, *60*, 150913. [CrossRef]
- Jiang, J.; Wu, M.; Zhu, Z.; Kong, D. Catalyst-Free Intramolecular 1,3-Dipolar Cycloaddition of Ethyl (2-Formylphenyl) Vinylphosphonates: A Highly Stereoselective Access to Phosphadihydrocoumarin-Fused Pyrrolizidines/Pyrrolidines. *Synthesis* **2017**, *49*, 3731–3739. [CrossRef]
- Wu, M.; Jiang, J.; Zhu, Z.; Wang, Q.; Kong, D. One-Pot Catalyst-Free Domino Condensation/Intramolecular 1,3-Dipolar Cycloaddition: Highly Stereoselective Access to Phosphadihydrocoumarin-Fused N,N-Bicyclic Pyrazolidin-3-ones. *Synthesis* **2018**, *50*, 139–145. [CrossRef]
- Petkova, N.I.; Nikolova, R.D.; Bojilova, A.G.; Rodios, N.A.; Kopf, J. Synthesis of heterocyclic methylenebisphosphonates by 1,3-dipolar cycloaddition of ethyl diazoacetate to 1,2-benzoxaphosphorin-3-phosphonates. *Tetrahedron* **2009**, *65*, 1639–1647. [CrossRef]
- Huang, T.; Liu, L.; Wang, Q.; Wu, M.; Kong, D. 1,3-Dipolar Cycloaddition of 3-Amino Oxindole-Based Azomethine Ylides and O-Vinylphosphonylated Salicylaldehydes for Diastereoselective Synthesis of Oxindole Spiro-P,N-polycyclic Heterocycles. *Synthesis* **2020**, *52*, 1387–1397. [CrossRef]
- Li, D.-F.; Gu, Y.; Zhang, J.-R.; Liu, K.; Zhao, L.-M. Diastereoselective Construction of Spiro-furo[3,2-c]benzopyranoxindoles through a Cu(OTf)₂/AcOH Cooperative Promoted Bicyclization Reaction. *J. Org. Chem.* **2019**, *84*, 879–887. [CrossRef]
- Kowalczyk-Dworak, D.; Albrecht, Ł. α,β -Unsaturated butenolides in an organocatalytic doubly annulative cascade for the preparation of 3,4-dihydrocoumarins. *Org. Biomol. Chem.* **2019**, *17*, 2624–2628. [CrossRef]

22. Ming, Y.-C.; Lv, X.-J.; Liu, M.; Liu, Y.-K. Synthesis of Chiral Polycyclic Tetrahydrocarbazoles by Enantioselective Aminocatalytic Double Activation of 2-Hydroxycinnamaldehydes with Dienals. *Org. Lett.* **2021**, *23*, 6515–6519. [CrossRef]
23. Hussain, M.; Niu, C.; Wang, G.-W. Palladium-catalyzed synthesis of [60]fullerene-fused furochromenones and further electrochemical functionalization. *Org. Chem. Front.* **2020**, *7*, 1249–1254. [CrossRef]
24. Sadykova, Y.M.; Sadikova, L.M.; Zalaltdinova, A.V.; Sultanova, Z.N.; Burirov, A.R.; Pudovik, M.A. 2H-Benzo[e]-1,2-oxaphosphorine Related Heterocycles as Precursors for the Synthesis of Unsymmetrical Bicyclic Phosphonates. *Russ. J. Gen. Chem.* **2018**, *88*, 1941–1943. [CrossRef]
25. Sadykova, Y.M.; Zalaltdinova, A.V.; Smailov, A.K.; Trofimova, L.M.; Voronina, J.K.; Burirov, A.R.; Pudovik, M.A. Synthesis of unsymmetrical cage phosphonates from heterocyclic systems based on 2H-1,2-benzoxaphosphinine. *Chem. Heterocycl. Compd.* **2020**, *56*, 1605–1610. [CrossRef]
26. Zalaltdinova, A.V.; Sadykova, Y.M.; Smailov, A.K.; Trofimova, L.M.; Burirov, A.R.; Pudovik, M.A. New intramolecular cyclization of 2 H-benzo[e]-1,2-oxaphosphorinine derivatives—A way to the synthesis of unsymmetrical cage phosphonates. *Phosphorus. Sulfur. Silicon Relat. Elem.* **2022**, *197*, 549–550. [CrossRef]
27. Das, S. Recent applications of ninhydrin in multicomponent reactions. *RSC Adv.* **2020**, *10*, 18875–18906. [CrossRef] [PubMed]
28. Filatov, A.S.; Wang, S.; Khoroshilova, O.V.; Lozovskiy, S.V.; Larina, A.G.; Boitsov, V.M.; Stepanov, A.V. Stereo- and Regioselective 1,3-Dipolar Cycloaddition of the Stable Ninhydrin-Derived Azomethine Ylide to Cyclopropenes: Trapping of Unstable Cyclopropene Dipolarophiles. *J. Org. Chem.* **2019**, *84*, 7017–7036. [CrossRef]
29. Peña-Morán, O.; Villarreal, M.; Álvarez-Berber, L.; Meneses-Acosta, A.; Rodríguez-López, V. Cytotoxicity, Post-Treatment Recovery, and Selectivity Analysis of Naturally Occurring Podophyllotoxins from *Bursera fagaroides* var. *fagaroides* on Breast Cancer Cell Lines. *Molecules* **2016**, *21*, 1013. [CrossRef]
30. Becke, A.D. Density-functional thermochemistry. III. The role of exact exchange. *J. Chem. Phys.* **1993**, *98*, 5648–5652. [CrossRef]
31. Lee, C.; Yang, W.; Parr, R.G. Development of the Colle-Salvetti correlation-energy formula into a functional of the electron density. *Phys. Rev. B* **1988**, *37*, 785–789. [CrossRef] [PubMed]
32. Hehre, W.J.; Ditchfield, R.; Pople, J.A. Self-Consistent Molecular Orbital Methods. XII. Further Extensions of Gaussian-Type Basis Sets for Use in Molecular Orbital Studies of Organic Molecules. *J. Chem. Phys.* **1972**, *56*, 2257–2261. [CrossRef]
33. Ditchfield, R.; Hehre, W.J.; Pople, J.A. Self-Consistent Molecular-Orbital Methods. IX. An Extended Gaussian-Type Basis for Molecular-Orbital Studies of Organic Molecules. *J. Chem. Phys.* **1971**, *54*, 724–728. [CrossRef]
34. Petersson, G.A.; Bennett, A.; Tensfeldt, T.G.; Al-Laham, M.A.; Shirley, W.A.; Mantzaris, J. A complete basis set model chemistry. I. The total energies of closed-shell atoms and hydrides of the first-row elements. *J. Chem. Phys.* **1988**, *89*, 2193–2218. [CrossRef]
35. Frisch, M.J.; Trucks, G.W.; Schlegel, H.B.; Scuseria, G.E.; Robb, M.A.; Cheeseman, J.R.; Scalmani, G.; Barone, V.; Petersson, G.A.; Nakatsuji, H.; et al. *Gaussian 16; Revision B.01*; Gaussian Inc.: Wallingford, CT, USA, 2016.
36. Bursch, M.; Mewes, J.-M.; Hansen, A.; Grimme, S. Best-Practice DFT Protocols for Basic Molecular Computational Chemistry. *Angew. Chem. Int. Ed.* **2022**, *61*, e202205735. [CrossRef]
37. Zhao, Y.; Truhlar, D.G. Design of Density Functionals That Are Broadly Accurate for Thermochemistry, Thermochemical Kinetics, and Nonbonded Interactions. *J. Phys. Chem. A* **2005**, *109*, 5656. [CrossRef]
38. Rappoport, D.; Furche, F. Property-optimized Gaussian basis sets for molecular response calculations. *J. Chem. Phys.* **2010**, *133*, 134105. [CrossRef]
39. Li, Y. Energy Diagram Plotter (CDXML). Available online: https://github.com/liyuanhe211/Energy_Diagram_Plotter_CDXML (accessed on 10 September 2022).
40. Sheldrick, G.M. *SADABS, Program for Empirical Absorption Correction of Area Detector Data*; University of Gottingen: Gottingen, Germany, 1997.
41. Sheldrick, G.M. SHELXT—Integrated space-group and crystal-structure determination. *Acta Crystallogr. Sect. A Found. Adv.* **2015**, *71*, 3. [CrossRef]
42. Dolomanov, O.V.; Bourhis, L.J.; Gildea, R.J.; Howard, J.A.K.; Puschmann, H. OLEX2: A complete structure solution, refinement and analysis program. *J. Appl. Crystallogr.* **2009**, *42*, 339–341. [CrossRef]
43. Sadykova, Y.M.; Sadikova, L.M.; Badrtdinova, A.R.; Dobrynin, A.B.; Burirov, A.R.; Pudovik, M.A. Condensation of 2-Ethoxyvinylphosphonic Acid Dichloroanhydride with 2,3,5-Trimethylphenol. Novel Method for Preparation of Phosphacoumarins. *Phosphorus. Sulfur. Silicon Relat. Elem.* **2015**, *190*, 2267–2272. [CrossRef]



Article

Novel Regioisomeric Analogues of Naphthyl-*N*-Acylhydrazone Derivatives and Their Anti-Inflammatory Effects

Dayana da Costa Salomé ¹, Rosana Helena Coimbra Nogueira de Freitas ², Carlos Alberto Manssour Fraga ²
and Patricia Dias Fernandes ^{1,*}

- ¹ Laboratório de Farmacologia da Dor e da Inflamação, Programa de Pesquisa em Descoberta de Fármacos, Instituto de Ciências Biomédicas, Universidade Federal do Rio de Janeiro, Rio de Janeiro 21941-901, Brazil
- ² Laboratório de Avaliação e Síntese de Substâncias Bioativas (LASSBio), Programa de Pesquisa em Descoberta de Fármacos, Instituto de Ciências Biomédicas, Universidade Federal do Rio de Janeiro, Rio de Janeiro 21941-901, Brazil
- * Correspondence: patricia.dias@icb.ufrj.br; Tel.: +55-21-3938-0388 (ext. 115)

Abstract: Background: When homeostasis is disturbed it can result in a pathological event named inflammation. The main drugs used in the treatment consist of non-steroidal and steroidal anti-inflammatory drugs. However, the side effects remain an obstacle during the treatments. In this study, we aimed to evaluate three new regioisomers analogues of naphthyl-*N*-acylhydrazone derivatives. Methods: Acute models of inflammation in vivo (formalin-induced licking and carrageenan-induced inflammation) as well as in vitro were used to evaluate the effects of LASSBio-2039, LASSBio-2040, and LASSBio-2041. Results: All three substances (at 1, 10 or 30 $\mu\text{mol/kg}$) presented significant effects in the in vivo model reducing leukocyte migration, nitric oxide (NO) and interleukin-1 β production. It was observed that only LASSBio-2039 significantly reduced cell migration in vitro. None of the LASSBios affected inducible nitric oxide synthase activity nor presented nitric oxide (NO) scavenger effect. No toxic effect was observed, either in vivo or in vitro. The new regioisomers analogues of naphthyl-*N*-acylhydrazone derivatives presented significant anti-inflammatory activity, suggesting LASSBio-2039 has a direct effect in leukocytes migratory capacity. Conclusions: Taken together, the data indicate that these substances present promising effects for the development of a prototype for new drugs.

Keywords: anti-inflammatory substance; *N*-acylhydrazone; naphthyl-*N*-acylhydrazone; LASSBio-1524 analogues

Citation: da Costa Salomé, D.; de Freitas, R.H.C.N.; Fraga, C.A.M.; Fernandes, P.D. Novel Regioisomeric Analogues of Naphthyl-*N*-Acylhydrazone Derivatives and Their Anti-Inflammatory Effects. *Int. J. Mol. Sci.* **2022**, *23*, 13562. <https://doi.org/10.3390/ijms232113562>

Academic Editor: Dmitry Aminin

Received: 13 October 2022

Accepted: 3 November 2022

Published: 5 November 2022

Publisher's Note: MDPI stays neutral with regard to jurisdictional claims in published maps and institutional affiliations.



Copyright: © 2022 by the authors. Licensee MDPI, Basel, Switzerland. This article is an open access article distributed under the terms and conditions of the Creative Commons Attribution (CC BY) license (<https://creativecommons.org/licenses/by/4.0/>).

1. Introduction

The definition of inflammation has been continuously adapted. Recently, it was characterized as a tissue response to an emergent stimulus. This reaction can be macro and/or microscopically identified and there is involvement of a variety of cells. Altogether, these events can lead to necrosis, edema, fibrosis, malignancy and/or infection. An excessive inflammatory response not controlled can evolve into several diseases such as arthritis, osteoporosis [1], asthma [2], Alzheimer's disease [3], cardiovascular disease [4], cancer [5] and obesity [6]. Thus, the search and development of new anti-inflammatory substances that could reduce or eliminate the inflammatory process continues to be an objective for several groups. Although there is a wide variety of anti-inflammatory drugs, there are concomitantly a wide variety of side effects that can limit their use. Thus, the continuous search for new chemical entities with anti-inflammatory potential and lower incidence of side effects remains a goal for researchers in this area.

Derivatives LASSBio-1524 (1) and LASSBio-1760 (2) have already been described as powerful anti-inflammatory prototypes with action in several acute and chronic models of inflammation [7–9]. These two compounds present the *N*-acylhydrazone (NAH) subunit,

widely described as a privileged subunit [10], useful for discovering new drug candidates due to its peptidomimetic nature and superior stability to chemical and metabolic hydrolysis [11].

The bioisosteric relationship of 4-nitrophenyl fragment by 4-phenylboronic acid subunit was previously characterized by comparing the anti-inflammatory profiles of compounds 1 and 2 [8]. An isomeric exchange was performed in the naphthyl subunit of LASSBio-1760 (2), with NAH linked to position α of the naphthyl subunit to generate LASSBio-2039 (3) (Figure 1). Additionally, two LASSBio-1524 (1) regioisomers were proposed, with the exchange of the nitro group of LASSBio-1524 from para-position to meta position (LASSBio-2040, 3) or to the ortho position (LASSBio-2041, 5).

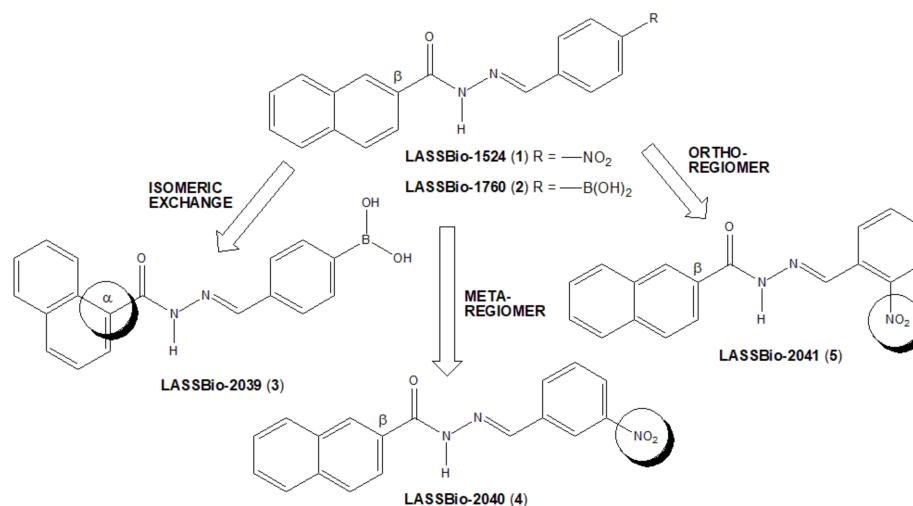


Figure 1. Design concept of novel naphthyl-*N*-acylhydrazone derivatives (3–5).

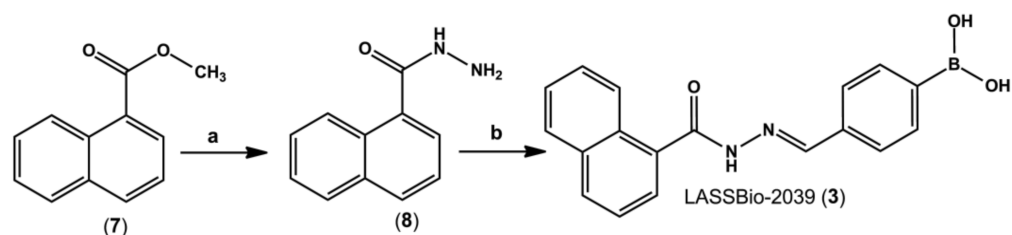
The changes introduced in new regioisomeric analogues (4) and (5) were purposed to avoid the potential toxicity produced by nitroaromatic derivatives [12]. The main idea was exchanging the position of the nitro group from a more accessible para-position to a more hindered meta- and ortho-position, respectively, in order to prevent access to the CYP reductase enzyme [13]. Moreover, it is well-known from the literature that the β -substituted naphthyl group is more susceptible to oxidative metabolism to form toxic metabolites than the corresponding α -substituted naphthyl, as learned from the discovery of β -blocker propranolol from its precursor pronetalol [14]. So, we proposed the exchange of the β -naphthyl group present in LASSBio-1760 (2) to the α -naphthyl group in LASSBio-2039 (3), in order to reduce the potential toxicity of this new drug candidate.

Thus, in this study, we described the synthesis and anti-inflammatory actions of a new small series of naphthyl-*N*-acylhydrazones (3–5), planned as regioisomeric analogues of LASSBio-1524 (1) and LASSBio-1760 (2).

2. Results

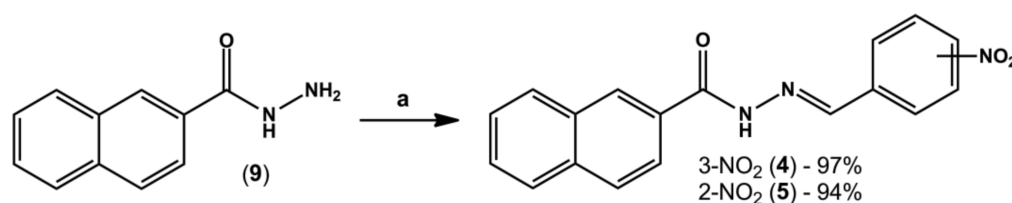
2.1. Chemistry

LASSBio-2039 (3) were synthesized from 1-naphthoic acid, which underwent Fischer esterification reaction in methanol, sulfuric acid at reflux to generated methyl 1-naphthoate (7) [15,16]. Next, hydrazinolysis reaction of ester (7), performed by reflux of an ethanolic solution containing anhydrous hydrazine hydrate, generated 1-naphthohydrazide (8) in 70% yield [17,18]. The final step consisted of acid catalyzed condensation of 1-naphthohydrazide (8) with 4-formylphenylboronic acid to furnish *N*-acylhydrazone LASSBio-2039 (3) in 92% yield [8] (Scheme 1).



Scheme 1. Reagents and conditions: (a) $\text{NH}_2\text{NH}_2 \cdot \text{H}_2\text{O}$ 100%, EtOH, reflux, 6 h, 83%; (b) 4-formylphenylboronic acid, EtOH, cat. HCl 20%, rt, 3 h, 92%.

2-Naphthohydrazide (9), the key intermediate for the synthesis of compounds 4 and 5, was prepared as previously described by Cordeiro et al. [8]. So, NAH derivatives 4 and 5 were obtained by adding, respectively, 3- or 2-nitrobenzaldehyde to 2-naphthohydrazide (9) under acid catalysis and at room temperature [17]. Both *N*-acylhydrazones (4–5) were obtained in very high yields as described in Scheme 2.



Scheme 2. Reagents and conditions: (a) 3-nitrobenzaldehyde or 2-nitrobenzaldehyde, EtOH, cat. HCl 20%, rt, 3 h, 94–97%.

All NAH derivatives were obtained as a single diastereoisomer, the most stable, (*E*)-diastereoisomer. This statement can be confirmed and corroborated through the analysis of $^1\text{H-NMR}$ spectra of molecules, which shows signs referring to only one imine hydrogen. Furthermore, this spectroscopic characteristic was already described in the literature, and it is a strong indication of the formation of (*E*)-diastereoisomer [19–21].

The obtained *N*-acylhydrazone derivatives (3–5) were fully spectroscopically characterized and their degree of purity was determined by reversed-phase HPLC analysis to be greater than 95%, which was considered adequate for the next step of investigating their antinociceptive and anti-inflammatory actions.

2.2. LASSBios Did Not Induce Any *In Vitro* or *In Vivo* Toxic Effect

Pretreatment of mice with a single oral dose of any of LASSBios (at 30 $\mu\text{mol/kg}$) did not affect either bone marrow cell count or hemogram values (blood leukocyte cell count, hematocrit, red blood cell count, hemoglobin, and hematocrit values) (Figure 2).

We did not observe alterations to respiration and no ulcers were observed in the stomach after 5 days. Additionally, there were no alterations in normal activity, such as food and water intake (Figure 3), grooming, and loss of righting reflex. The incubation of J774.A1 macrophage cell line with concentrations of 1, 10 or 30 μM of each LASSBio did not affect cell viability, even after 24 h incubation.

2.3. LASSBio-2039, LASSBio-2040 and LASSBio-2041 Did Present Antinociceptive Effect in an Inflammatory Pain Model

Figure 4 shows the effects of pretreatment of mice with LASSBio-2039, LASSBio-2040 or LASSBio-2041 one hour before formalin injection into the hind paw. Mice receiving the vehicle remained linking the formalin-injected paw during 22 ± 3 s and 2356 ± 29 s, for the first and second phases, respectively. The pretreatment of animals with acetylsalicylic acid (ASA, 1100 $\mu\text{mol/kg}$) or morphine (15 $\mu\text{mol/kg}$) resulted in 14% and 53% reduction in the first phase, respectively, and an inhibition in 40% and 15% in the second phase, respectively.

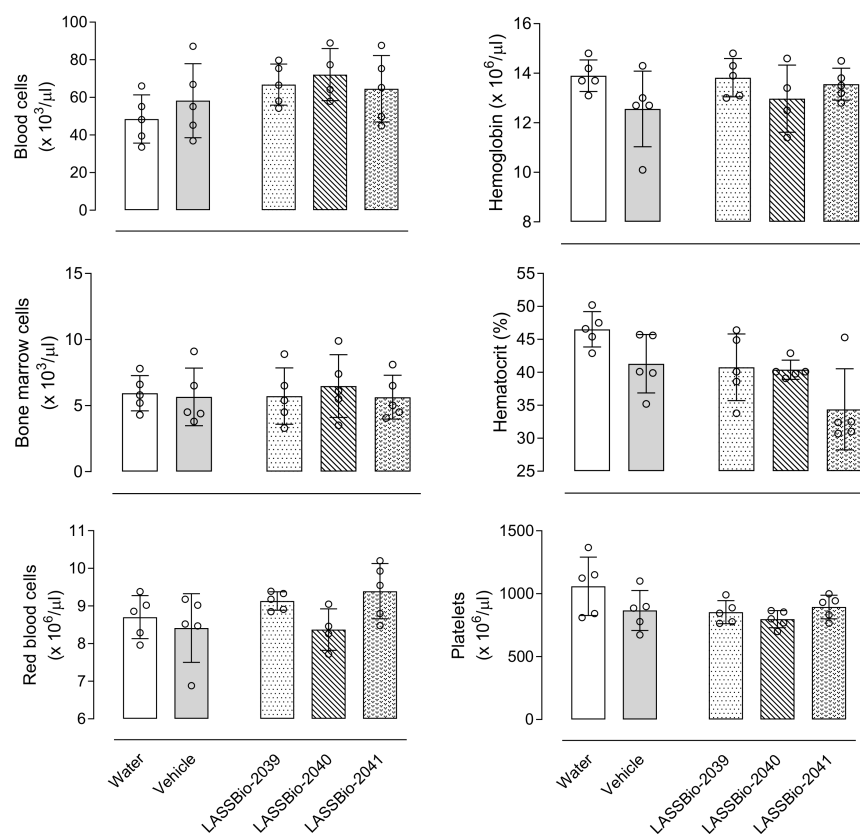


Figure 2. LASSBio-2039, LASSBio-2040 and LASSBio-2041 did not affect blood, bone marrow or red blood cells or platelet count nor hemoglobin and hematocrit levels. Mice were orally treated with each of the substances (30 $\mu\text{mol}/\text{kg}$), water or vehicle. After 24 h bone marrow and blood were collected to measurements. Results are expressed as mean \pm standard deviation ($n = 5-7$).

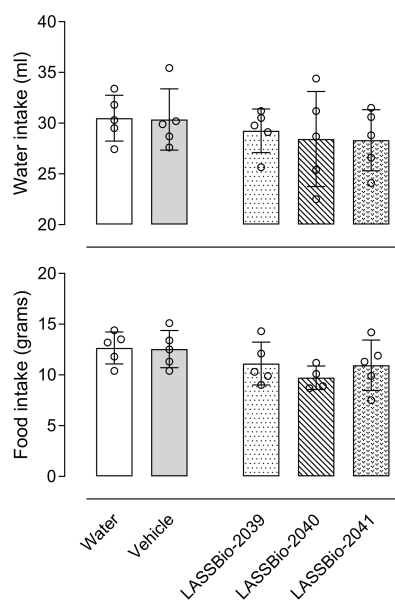


Figure 3. LASSBio-2039, LASSBio-2040 and LASSBio-2041 did not affect food and water intake. Mice were orally treated with each of the substances (30 $\mu\text{mol}/\text{kg}$), water or vehicle. After 24 h the amount of water (in mL) or food (in grams) ingested were evaluated. Results are expressed as mean \pm standard deviation ($n = 5-7$).

When LASSBio-2039 (1, 10 or 30 $\mu\text{mol}/\text{kg}$) was used, a reduction of 38%, 45% and 48%, respectively, was observed in the licking response of the first phase and 46%, 51% and 51% inhibition in the second phase of the model. When compared with the original substance, LASSBio-1760, similar effects can be observed. It is important to note that neither LASSBio-2040 nor LASSBio-2041 affected the time of reaction in any dose tested.

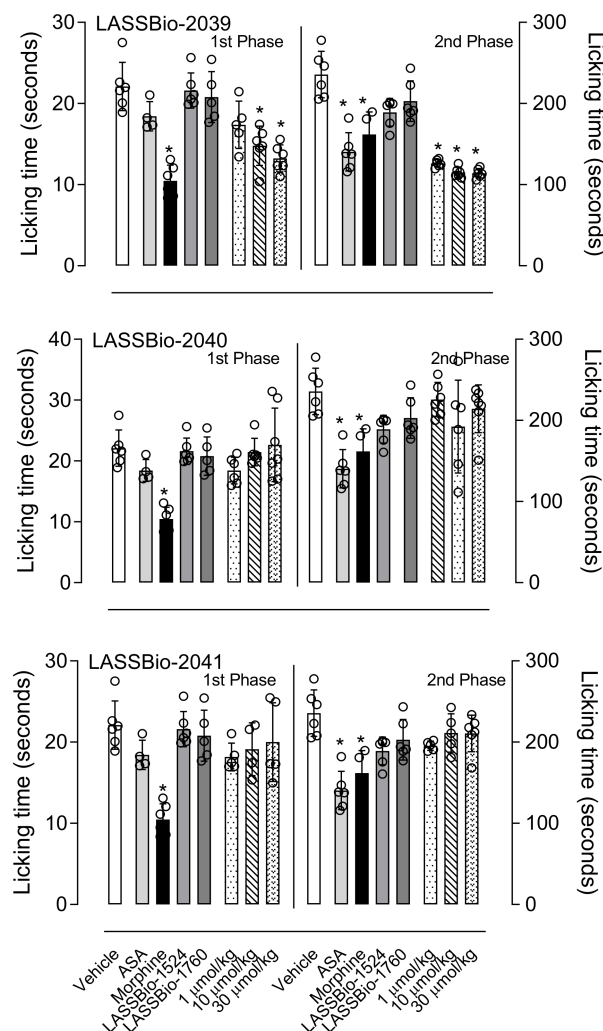


Figure 4. LASSBio-2039, LASSBio-2040 and LASSBio-2041 effects in an inflammatory pain model. Mice were orally treated with each of the substances with three different doses, acetylsalicylic acid (1100 $\mu\text{mol}/\text{kg}$), morphine (15 $\mu\text{mol}/\text{kg}$), LASSBio-1524 or LASSBio-1760 (30 $\mu\text{mol}/\text{kg}$) or vehicle. One hour later the nociceptive response was induced by intraplantar injection of formalin (2.5%) in right hind paw. Results are expressed as mean \pm standard deviation ($n = 5-7$). Statistical analyses were calculated in GraphPad Prism 8.0 (San Diego, CA, USA) using analyses of variance (ANOVA) followed by Tukey post-test with $p < 0.01$ (*) when comparing treated groups with vehicle-treated group. Data for the original compounds (LASSBio-1524 and LASSBio-1760) are original, independent duplicates of past results and have not been published previously.

2.4. LASSBios Reduced Inflammatory Parameters in an Acute Model of Inflammation

The injection of carrageenan (0.5%) into the subcutaneous air pouch induced a 35-fold increase in leukocyte migration toward the pouch ($167.3 \pm 25.5 \times 10^6$ cells/mL versus $4.6 \pm 1.9 \times 10^6$ cell/mL in animals that receives only saline in SAP). Dexamethasone (a steroidal anti-inflammatory drug, 6.5 $\mu\text{mol}/\text{kg}$) significantly reduced in 72% the number of leukocytes in the SAP ($34 \pm 2 \times 10^6$ cells/mL). When mice were pre-treated with LASSBio-2039 (1, 10 or 30 $\mu\text{mol}/\text{kg}$), a dose-dependent reduction was observed (58%, 63% and 66%,

respectively) in cell migration. Similarly, both LASSBio-2040 and LASSBio-2041 presented significant effects. LASSBio-2040 reduced by 48%, 69% and 73%; LASSBio-2041 inhibited in 29%, 62% and 68% for the doses of 1, 10, 30 $\mu\text{mol/kg}$, respectively. It is interesting to note that the dose of 1 $\mu\text{mol/kg}$ of LASSBios presented an inhibitory effect similar to that observed with dexamethasone. When compared with the original substances (LASSBio-1524 and LASSBio-1760, at 30 $\mu\text{mol/kg}$), it can be noted that the new compounds were most effective in reducing cell migration than the original molecules, since the lower dose used showed an effect comparable to the dose used from the LASSBio-1524 and LASSBio-1760 (Figure 5, left graphs).

We next decided to evaluate the capacity of each of the LASSBios in reducing protein extravasation induced by carrageenan injected in the SAP. This phlogistic agent induced a 7-fold increase in the amount of protein extravasated to the exudate ($212.6 \pm 50.7 \mu\text{g/mL}$ protein in carrageenan-injected group versus $33.7 \pm 19.3 \mu\text{g/mL}$ in vehicle-treated group receiving saline in the SAP). Pre-treatment of mice with dexamethasone caused a 71% reduction in the protein extravasated. It is interesting to observe that all three LASSBios significantly reduced protein extravasation with exception to a lower dose of LASSBio-2040. When comparing LASSBios, the most potent was LASSBio-2039. All three substances were also more potent than the original compound (Figure 5, right graphs).

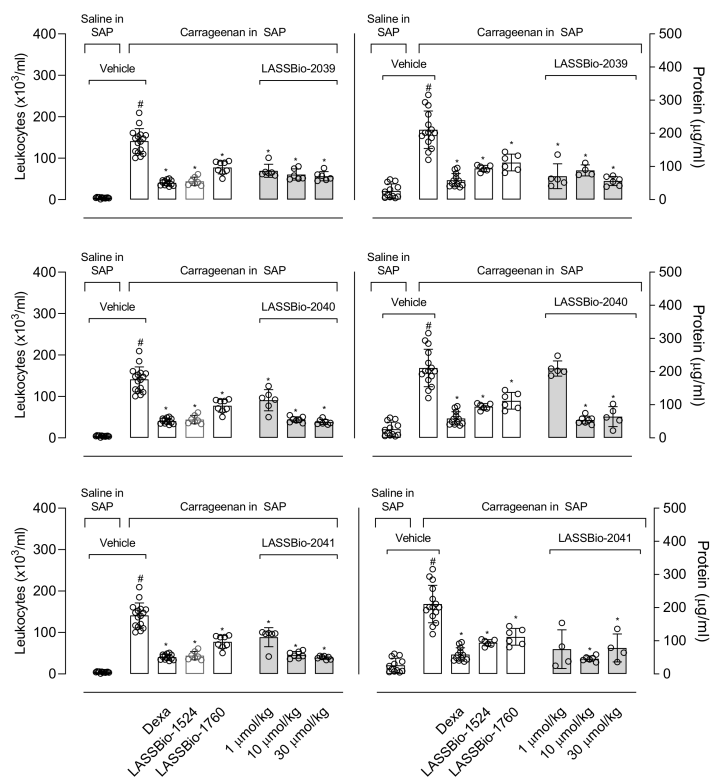


Figure 5. LASSBios reduce cell migration induced by carrageenan into the subcutaneous air pouch (SAP) and protein extravasated. Animals were pre-treated with vehicle, dexamethasone (6.5 $\mu\text{mol/kg}$) or LASSBios (doses of 1, 10 or 30 $\mu\text{mol/kg}$) 1 h before injection of saline (NaCl 0.9%) or carrageenan into the SAP. Results are expressed as media \pm SD ($n = 5\text{--}12$). Statistical significance was calculated in GraphPad Prism 8.0 (San Diego, CA, USA) using analyses of variance (ANOVA) followed by Tukey post-test with $p < 0.01$ (#) when comparing vehicle-treated group that received carrageenan injection into the SAP with vehicle-treated group that receives saline into the SAP or $p < 0.01$ (*) when comparing dexamethasone- or LASSBios-treated group that received carrageenan injection into the SAP with vehicle-treated group that receives carrageenan into the SAP. Data for the original compounds (LASSBio-1524 and LASSBio-1760) are original, independent duplicates of past results and have not been published previously.

2.5. LASSBios Inhibited Cytokines Production

Figure 6 shows that LASSBio-2039 significantly and dose-dependently reduced interleukin-1 β (IL-1 β), tumor necrosis factor- α (TNF- α) and interferon- γ (INF- γ) production. The dose of 30 $\mu\text{mol/kg}$ almost completely abolished cytokines production with values close to those observed in the control group. An increase in interleukin-10 (IL-10) production in those group of mice pretreated with LASSBio-2039 was also observed. It is interesting to note that pretreating mice with the higher dose resulted in a significant effect, even when compared with dexamethasone-treated mice. In those groups of mice pretreated with LASSBio-2040 or LASSBio-2041, a reduction in all three cytokines production was observed. Although in some groups these effects were significant, the inhibition caused by both compounds was not as intense when compared with LASSBio-2039.

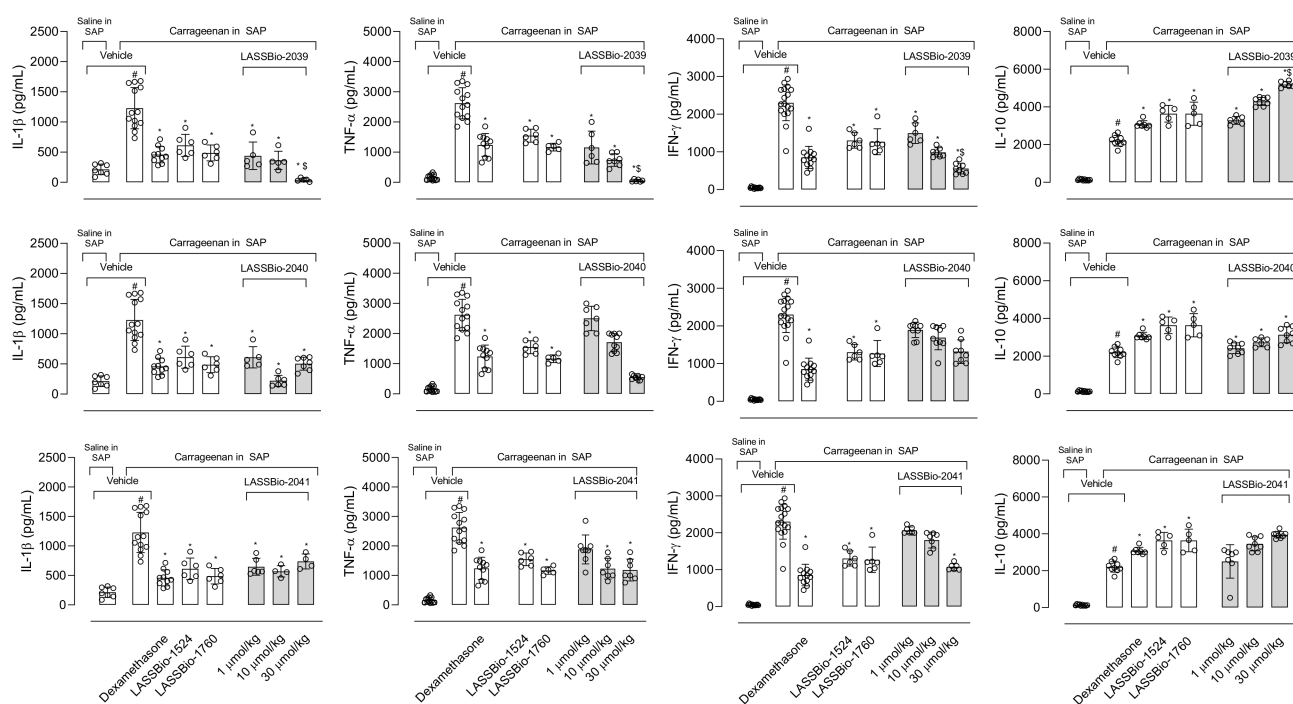


Figure 6. LASSBios reduce interleukin-1 β (IL-1 β), tumor necrosis factor- α (TNF- α), interferon- γ (INF- γ) and increase interleukin-10 (IL-10) produced in the inflammatory exudate. Animals were pretreated with vehicle, LASSBio-1524 or LASSBio-1760 (at 30 $\mu\text{mol/kg}$), dexamethasone (6.5 $\mu\text{mol/kg}$) or LASSBios (doses of 1, 10 or 30 $\mu\text{mol/kg}$) 1 h before injection of saline (NaCl 0.9%) or carrageenan into the SAP. Results are expressed as media \pm SD ($n = 5$ –12). Where no error bar is shown it is because it is smaller than the symbol. Statistical significance was calculated in GraphPad Prism 8.0 (San Diego, CA, USA) using analyses of variance (ANOVA) followed by Tukey post-test with $p < 0.01$ (#) when comparing vehicle-treated group that received carrageenan injection into the SAP with vehicle-treated group that receives saline into the SAP. $p < 0.01$ (*) when comparing dexamethasone- or LASSBios-treated group that received carrageenan injection into the SAP with vehicle-treated group that receives carrageenan into the SAP. $p < 0.01$ (\$) when comparing LASSBio-2039-treated group that received carrageenan injection into the SAP with LASSBio-1760-treated group that receives carrageenan into the SAP. Data for the original compounds (LASSBio-1524 and LASSBio-1760) are original, independent duplicates of past results and have not been published previously.

We also measured the amount of nitric oxide (NO) produced in the inflammatory exudate. NO is an instable mediator that is rapidly conversed and decayed to nitrate when in biological fluids. In normal conditions, the level of this mediator is very low, as we can observe in the groups of animals that received saline injection in the SAP ($15.4 \pm 6.2 \mu\text{M}$ of NO). However, after an inflammatory insult such as carrageenan, a 12-fold increase was observed. The total amount of NO measured in exudates obtained from

the carrageenan group was $189.2 \pm 45.4 \mu\text{M}$. The pre-treatment of mice with dexamethasone resulted in an 86% reduction in NO produced. Our data show that LASSBio-2039 reduced by at least 75%, and the higher dose (30 $\mu\text{mol}/\text{kg}$) completely blocked the production of NO. When evaluating the results obtained with LASSBio-2040 and LASSBio-2041, it was observed that even with 1 $\mu\text{mol}/\text{kg}$, the reduction in NO production was 54% and 71%, respectively. The other two doses inhibited at least 70% of the mediator production. When compared with the original compounds, LASSBio-1524 and LASSBio-1760, data demonstrated the LASSBio-2039 was more potent than LASSBio-1760 in reducing NO production (at 30 $\mu\text{mol}/\text{kg}$) (Figure 7).

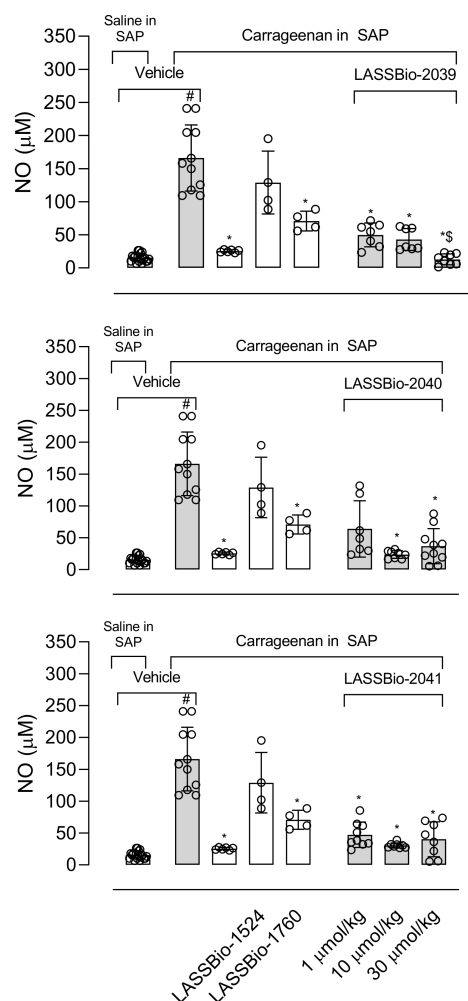


Figure 7. LASSBios reduce nitric oxide (NO) produced in the inflammatory exudate. Animals were pre-treated with vehicle, LASSBio-1524 or LASSBio-1760 (at 30 $\mu\text{mol}/\text{kg}$), dexamethasone (6.5 $\mu\text{mol}/\text{kg}$) or LASSBios (doses of 1, 10 or 30 $\mu\text{mol}/\text{kg}$) 1 h before injection of saline (NaCl 0.9%) or carrageenan into the SAP. Results are expressed as media \pm SD ($n = 5-12$). Where no error bar is shown it is because it is smaller than the symbol. Statistical significance was calculated in GraphPad Prism 8.0 (San Diego, CA, USA) using analyses of variance (ANOVA) followed by Tukey post-test with $p < 0.01$ (#) when comparing vehicle-treated group that received carrageenan injection into the SAP with vehicle-treated group that receives saline into the SAP. $p < 0.01$ (*) when comparing dexamethasone- or LASSBios-treated group that received carrageenan injection into the SAP with vehicle-treated group that receives carrageenan into the SAP. $p < 0.01$ (\$) when comparing LASSBio-2039-treated group that received carrageenan injection into the SAP with LASSBio-1760-treated group that receives carrageenan into the SAP. Data for the original compounds (LASSBio-1524 and LASSBio-1760) are original, independent duplicates of past results and have not been published previously.

2.6. LASSBios Also Reduced Inflammatory Parameters In Vitro

Data obtained using in vivo models indicated that all three LASSBios significantly reduced leukocyte migration and the production of cytokines and NO. These effects could be a direct result of the reduction in cell viability and/or reduction in the number of cells arriving in the inflammatory site, thus resulting in a reduced number of cells producing the mediators. To rule out these possibilities, we used a macrophage cell line (J774.A1) activated with lipopolysaccharide (LPS) and measured the production of NO, IL-1 β , TNF- α , IFN- γ and IL-10. As can be observed in Figure 8, non-LPS-activated cells produced low levels of cytokines. However, when activated with LPS, there was an increase of at least 10-fold.

Similar to data obtained in the SAP model, LASSBio-2039 (at 10 μ M) almost completely inhibited IL-1 β and TNF- α production. It was also observed that LASSBio-2040 and LASSBio-2041 significantly inhibited cytokines production. However, these effects were not as intense as those observed in the SAP model, suggesting that those effects could be a group of actions (reduction in cell migration and a direct effect in cytokines production by migrated cells).

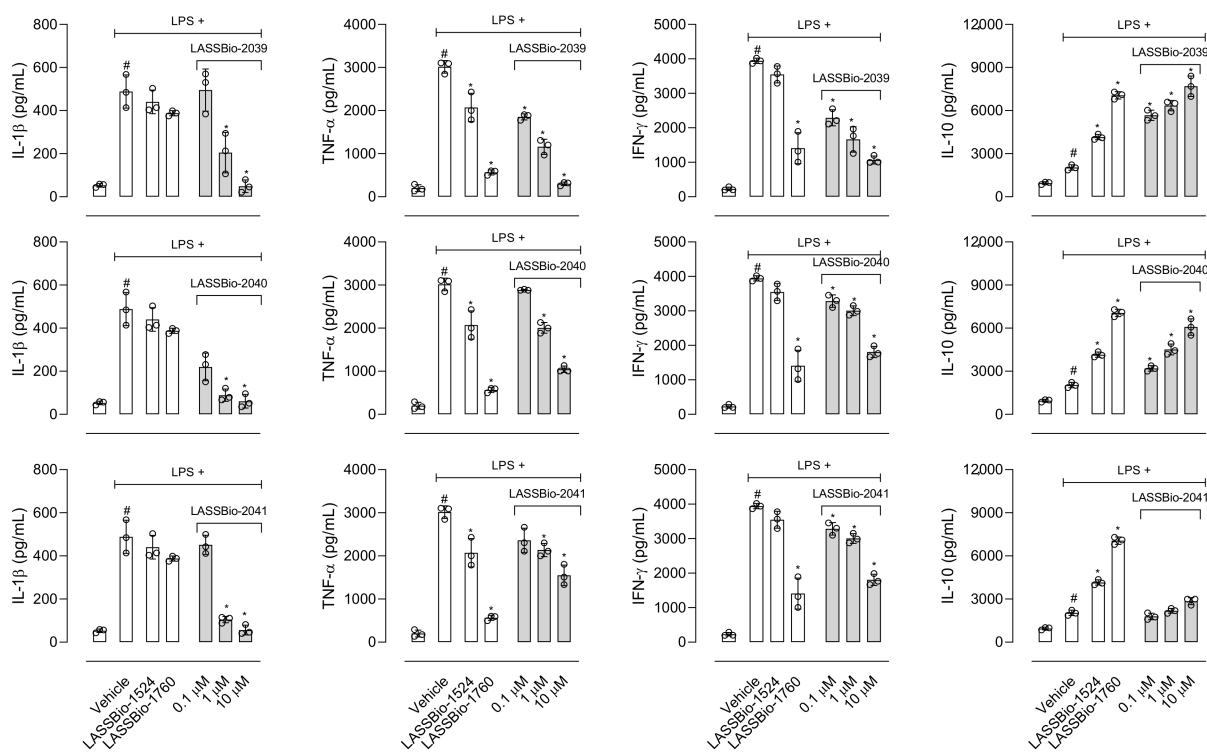


Figure 8. Effect of LASSBios in interleukin-1 β (IL-1 β), tumor necrosis factor- α (TNF- α), interferon- γ (IFN- γ) and interleukin-10 (IL-10) produced by J774.A1 cells line. Cells were incubated with vehicle, LASSBio-1524 or LASSBio-1760 (at 30 μ M), or LASSBios (0.1, 1 or 10 μ M) and after 1 h were activated with LPS (1 μ g/mL). Results are expressed as media \pm SD (n = 3). Where no error bar is shown it is because it is smaller than the symbol. Statistical significance was calculated in GraphPad Prism 8.0 (San Diego, CA, USA) using analyses of variance (ANOVA) followed by Tukey post-test with p < 0.01 (#) when comparing LPS-activated cells treated with vehicle and non-activated cells treated with vehicle. p < 0.01 (*) when comparing LPS-activated cells treated with LASSBios and LPS-activated cells treated with vehicle. Data for the original compounds (LASSBio-1524 and LASSBio-1760) are original, independent duplicates of past results and have not been published previously.

Then, we evaluated the ability of each compound to inhibit NO production in vitro. The data obtained (Figure 9) show that although LASSBio-2039 significantly reduced NO production when LPS-activated cells were incubated with 1 and 10 μ M, neither LASSBio-2040 nor LASSBio-2041 affected NO production with any of the concentrations used.

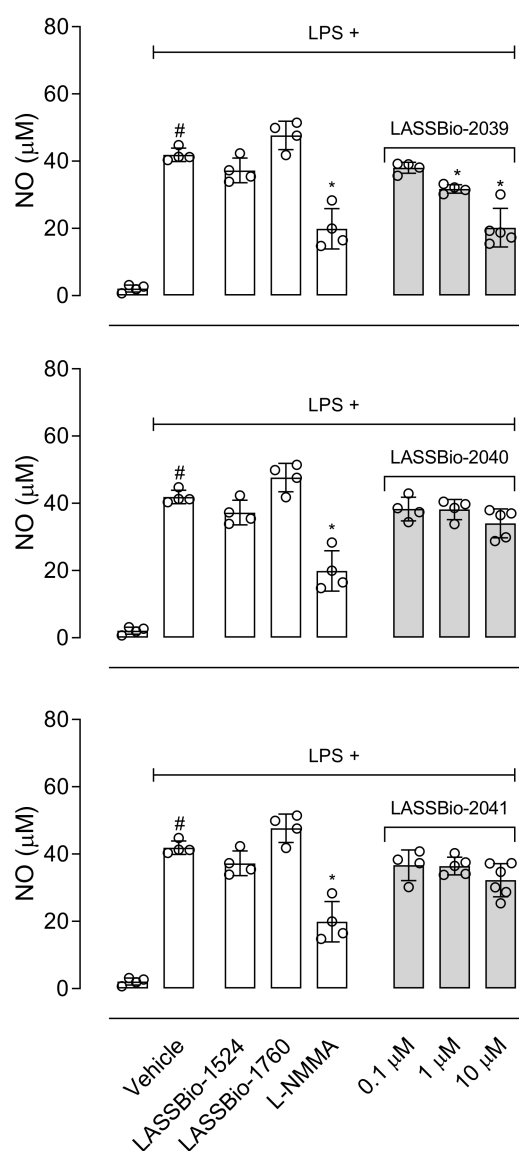


Figure 9. Effect of LASSBios in nitric oxide (NO) produced by J774.A1 cells line. Cells were incubated with vehicle, L-nitro mono methyl arginine (L-NMMA) or LASSBios (0.1, 1 or 10 µM) and after 1 h were activated with LPS (1 µg/mL). NO was measured 24 h later. Results are expressed as media ± SD ($n = 4-6$). Where no error bar is shown is because it is smaller than the symbol. Statistical significance was calculated in GraphPad Prism 8.0 (San Diego, CA, USA) using analyses of variance (ANOVA) followed by Tukey post-test with $p < 0.01$ (#) when comparing LPS-activated cells treated with vehicle and non-activated cells treated with vehicle. $p < 0.01$ (*) when comparing LPS-activated cells treated with LASSBios and LPS-activated cells treated with vehicle. Data for the original compounds (LASSBio-1524 and LASSBio-1760) are original, independent duplicates of past results and have not been published previously.

The data obtained so far are suggestive that LASSBio-2039 can inhibit NO production; however, we cannot conclude if this effect is due to inhibition in inducible nitric oxide synthase (iNOS) expression, its activity, or a direct NO-scavenger effect of each substance. Trying to elucidate these possibilities, we first incubated LPS-activated J774.A1 cells with LASSBios and after 8 h of activation, a period where protein synthesis of iNOS was finished and the enzyme begins its activity, LASSBios were added to culture medium. After 24 h of activation, the supernatants were collected, and NO was measured. Results shown in

Figure 10 demonstrated that none of LASSBios affected the NO production when added 8 h post-LPS activation, suggesting that their effects do not occur in enzyme activity.

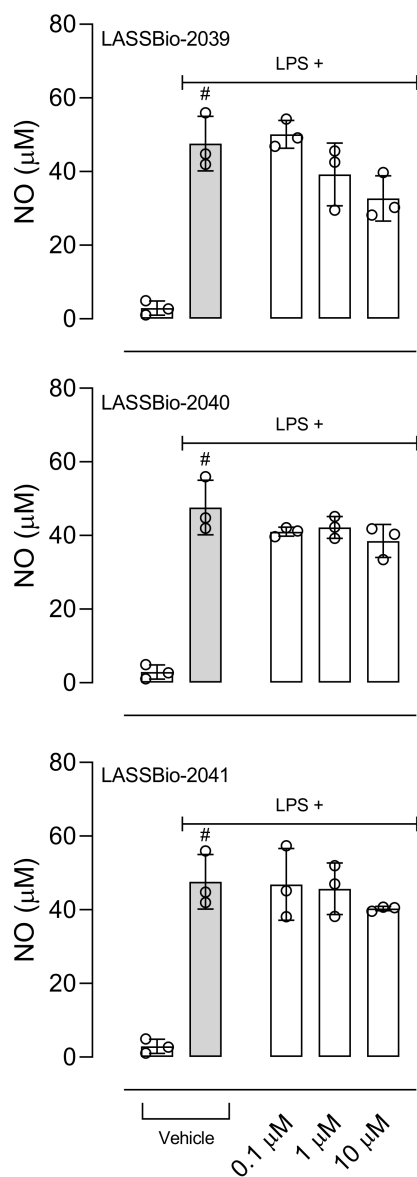


Figure 10. Effect of LASSBios in inducible nitric oxide synthase enzyme activity. J774.A1 cells were incubated with vehicle or lipopolysaccharide (LPS, 1 µg/mL) and after 8 h received LASSBios at different concentrations (0.1, 1 or 10 µM). Twenty-four hours after LPS activation NO accumulated in supernatant was measured. Results are expressed as media \pm SD ($n = 3$). Where no error bar is shown it is because it is smaller than the symbol. Statistical significance was calculated in GraphPad Prism 8.0 (San Diego, CA, USA) using analyses of variance (ANOVA) followed by Tukey post-test with $p < 0.01$ (#) when comparing LPS-activated cells treated with vehicle and non-activated cells treated with vehicle.

To rule out the possibility that LASSBios could act as a NO scavenger due to a direct interaction with the gas immediately after its production by cells, the NO donor SNAP was incubated with LASSBios. It was observed that none of substances showed ability in scavenger NO, thus reducing the levels of nitrite measured in the medium.

2.7. LASSBio-2039 Did Reduce Cell Migration In Vitro

As we observed a reduction in the number of leukocytes that migrated to SAP, we decided to assess whether this effect could be due to a direct action of LASSBios on cells, thus affecting their migratory capacity. Therefore, LASSBios were incubated with J774.A1 cells and their capacity in affect the wound healing of cells were evaluated after 24 h incubation. Figure 11 (left images) is a representative group of photos obtained at 0 or 24 h after LPS activation and showed that J774.A1 cells migrated into the wound area of the well. The values obtained in these groups were considered as 100% closed area. As can be seen in Figure 11 (right graph), only LASSBio-2039 significantly affected the migratory capacity of cells, thus reducing the percentage of area that became closed after 24 h incubation.

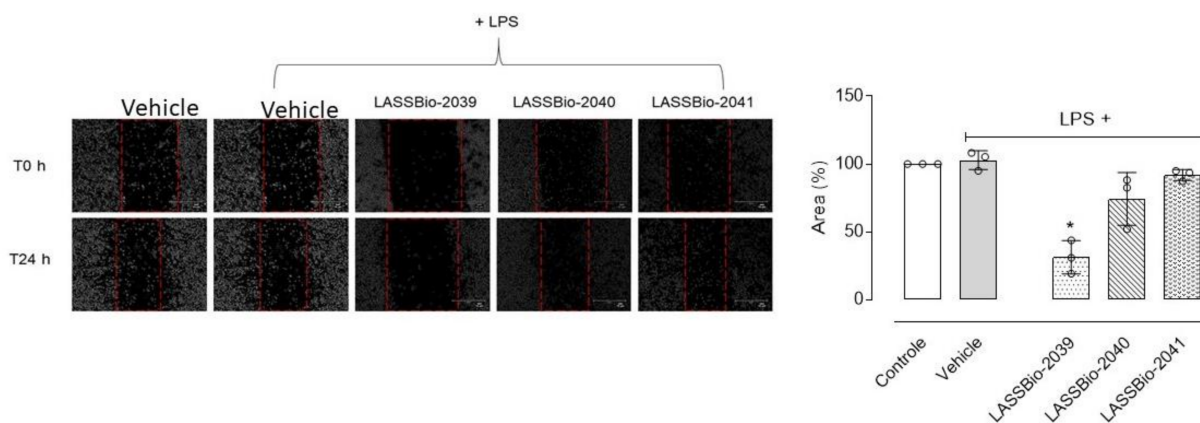


Figure 11. Effect of LASSBios in cell migration in vitro. J774.A1 cells were plated, and a wound area done. Cells were incubated with vehicle or LASSBios (10 μ M) 15 min before lipopolysaccharide (LPS, 1 μ g/mL) and after 24 h the area in each well was measured with the aid of ImageJ software (version 1.8.0.172, National Institute of Health, USA). Photos in the left are representative of 4 independent experiments and were obtained in a phase contrast microscope (EvoS500, ThermoFisher, Waltham, MA, USA), in 10 \times objective. Bars corresponds to 10 μ m. In the right is the graph with data obtained after four different experiments. Results are expressed as media \pm SD ($n = 4$). Statistical significance was calculated in GraphPad Prism 8.0 (San Diego, CA, USA) using analyses of variance (ANOVA) followed by Tukey post-test with $p < 0.01$ (*) when comparing LPS-activated cells treated with LASSBios and LPS-activated cells treated with vehicle.

3. Discussion

In this study, we aimed to evaluate the anti-inflammatory effects of three new molecules (named LASSBio-2039, LASSBio-2040 and LASSBio-2041). The advantage of these structures is based on the presence of a *N*-acylhydrazone (NAH) subunit, considered a privileged subunit [10] used for discovering new drug candidates [11].

Formalin injection into the hind paw causes a biphasic response, with the first phase (or neurogenic phase) occurring by an activation of nociceptors present in unmyelinated axons and the second phase (or inflammatory phase) occurring due to the release of mediators (i.e., histamine, prostaglandin, and serotonin) that can sensitize sensory neurons [22]. Drug-mediated reduction in paw licking occurs differently in both phases. Non-steroidal anti-inflammatory drugs act preferentially in the second phase through a peripheral action, whereas opioids act through a central action, inhibiting both phases [23–25]. Therefore, this model becomes suitable for the assessment of non-inflammatory or inflammatory pain. Our results showed that pre-treatment with LASSBio-2039 reduced the licking time in both phases and the result in the second phase suggests possible anti-inflammatory activity.

The remarkable effects of LASSBio-2039, even when compared with the original compound, LASSBio-1760, propelled us to continue investigating the anti-inflammatory effects. In this regard, we used the carrageenan-induced inflammation into the subcutaneous air pouch (SAP). This model is suitable for evaluating the local inflammatory response

in vivo. Carrageenan injected into the SAP stimulates an inflammatory response with influx of leukocytes, formation of exudate and accumulation of inflammatory mediators [10]. The migration of cells to the inflammatory site is involved in the development of several diseases. Therefore, inhibiting leukocyte recruitment enables effective control of the inflammatory process [26]. Pre-treatment with LASSBios caused a significant reduction in leukocyte migration. Some possibilities may be involved with this effect. Among them, the inhibition in the production or release of mediators involved with the chemotaxis process or even an action of LASSBios directly on the cells, preventing them from migrating to the inflammatory site.

The production of inflammatory mediators also stimulates the increase in vascular permeability. This step causes the passage of fluids and plasma proteins from the bloodstream to the tissue [27]. Our data showed that all three substances reduced the protein present in the exudate. This effect suggests that LASSBios may be acting by inhibiting the increase in vascular permeability, preventing the proteins from passing into the tissue. According to Lampugnani and collaborators [28], mediators induce the formation of radial stress fibers and the contraction of actomyosin, and this can result in the retraction of the intercellular junction, allowing the passage of fluids and plasma proteins from plasma to tissues. So, our results could suggest a direct effect against cells located in vascular lineage prevent them to contract, thus reducing protein leakage to tissue.

Interleukin-1 β (IL-1 β) participates in the inflammatory response through the activation of several molecules such as the cyclooxygenase-2 (COX-2) enzyme, nitric oxide (NO) and endothelial adhesion molecules that will act in the maintenance of inflammatory response [29,30]. Pre-treatment mice with LASSBios reduced the production of the cytokine in the exudate. The inhibition could lead to a decrease in the migration of cells to the inflammatory site and, therefore, a decrease in the arrival of activated cells, producing other mediators and recruiting more cells. This hypothesis is in accordance with Theofilis and collaborators [31] who found that cytokines can influence the expression of adhesion molecules that participate in the process of leukocyte diapedesis. Thus, controlling the production of this cytokine brings benefits for the treatment of various inflammatory diseases [32].

The production of NO plays a fundamental role in the development and maintenance of the inflammatory process. The increase in iNOS (inducible nitric oxide synthase enzyme) expression also occurs in response to activation by lipopolysaccharide (LPS) and the NO produced is one of the key molecules in the pathogenesis of several diseases, so the inhibition of this mediator becomes the target of several anti-inflammatory proposals [33]. Our results show that LASSBios significantly reduced the concentration of NO in the inflammatory exudate. It could be that once there was a reduction in the number of leukocytes, there would also be a reduction in the production of NO. However, the percentage of reduction in NO concentration is not proportional to the reduction in the number of cells that migrated. In this sense our hypothesis is that it may be that the inhibition observed in NO production could be due to the direct effect of LASSBios on the cells, either by inhibiting the production or the activity of the iNOS.

Among the substances that activate macrophages is LPS, which activates Toll-like receptor triggering production of a series of mediators [34,35]. Our data show that all LASSBios reduced IL-1 β production by LPS-activated cells. Our next step aimed to analyze the effects of LASSBios on NO production in LPS-activated macrophages. Our data indicate that only LASSBio-2039 reduced the NO production by activated macrophages. After 8 h of activation with LPS, there is a peak in the expression of the iNOS enzyme and that, despite this, the production of NO and this production remains for 24 h [36]. So, we evaluated the effect of LASSBios on NO production after 8 h of LPS activation; however, none of the LASSBios affected NO production. These results together suggest that the action of inhibiting the production of NO caused by LASSBio-2039 can happen through the reduction in the expression of iNOS and not by a reduction in the activity of this enzyme.

After obtaining positive results in reducing the production of inflammatory mediators *in vitro*, we choose to evaluate whether incubation with LASSBios would influence the process of cell migration. Our assay is advantageous because it mimics the process of cell migration *in vivo*, in addition to being considered a simple and inexpensive technique to analyze this process [37]. Only incubation with LASSBio-2039 inhibited the macrophage migration process *in vitro*. This result could be explained by the role of LASSBios in the inhibition of NO that is involved with the SRC-FAK pathway. Macrophages activated with LPS initiate the synthesis of a series of mediators, including the iNOS enzyme responsible for the synthesis of NO. The NO produced actively participates in the SRC-FAK cascade (steroid receptor co-activator-focal adhesion kinase). Studies indicate that this cascade is linked to the process of macrophage mobility, influencing their migratory capacity [38,39]. By understanding the importance of the SRC-FAK cascade in the migration process and how this cascade is highly dependent on NO, our hypothesis is that the effect caused by LASSBio-2039 to reduce cell migration may be occurring due to the reduction caused in the production of NO.

In 2011, LASSBio-1524 was synthesized with the aim of being an inhibitor of the IKK- β enzyme and this was confirmed from structure-based drug design trials. IKK- β is an important enzyme that participates in the activation of the signaling pathway of the nuclear transcription factor kappa B (Nf- κ B), the gene responsible for the transcription of several mediators and enzymes that participate in the development and maintenance of the inflammatory process [7]. In 2016, it was observed not only LASSBio-1524, but also LASSBio-1760 pronounced anti-inflammatory activity through reduced cell migration, reducing NO and TNF- α production. A reduction in the expression of phosphorylated Nf- κ B suggested that the anti-inflammatory effects of these compounds occur through the inhibition of the Nf- κ B signaling pathway [8]. The structural modifications performed for the synthesis of LASSBio-2039, LASSBio-2040 and LASSBio-2041 did not influence the anti-inflammatory activity presented by these compounds. When comparing all three new LASSBios with LASSBio-1524 or LASSBio-1760, only the LASSBio-2039 presented a significant effect when compared with the original molecule (LASSBio-1760). As the molecular target of LASSBio-1524 and LASSBio-1760 is the enzyme that participates in the activation of the Nf- κ B pathway, we can assume that the LASSBios tested in this study also act on the same molecular target. This signaling pathway can be activated by the cytokine IL-1 β and, once activated, initiates the synthesis of iNOS responsible for producing NO. We observed a reduction in the production of the cytokine, which may have decreased the activation of the Nf- κ B signaling pathway, which may cause a reduction in leukocyte migration, in NO, in vascular permeability and a consequent reduction in the concentration of protein in the inflammatory exudate.

The modifications carried out in all three new substances evaluated in this study demonstrated an absence of toxic effects observed in nitroaromatic derivatives [12]. These changes lead to changes in the position of the nitro group to a meta- and ortho-position (in LASSBios-2040 and 2041, respectively). It is also known that the presence of β -substituted naphthyl group confers susceptibility to metabolism with the formation of toxic metabolites [14]. So, the exchange of this group by a α -naphthyl group (in LASSBio-2039) may have influenced this *N*-acylhydrazone to act differently from the others, indicating LASSBio-2039 a pronounced activity in relation to LASSBio-2040 and LASSBio-2041. It is worth noting that the modification carried out in LASSBio-2039 in comparison to LASSBio-1760 resulted in a more pronounced effect, indicating that the addition of the α -naphthyl group resulted in an increase in activity.

It is also important to emphasize that unlike what is observed with anti-inflammatory drugs already on the market, the substances evaluated in this study did not demonstrate toxic effects, either for changes in the blood count, bone marrow, organs, or behavior, which makes them promising substances for testing in chronic disease models as yet untreated.

Taken together, the data demonstrated in this study suggest LASSBio-2039 with a significant anti-inflammatory profile in pre-clinical models of acute inflammation could be developed as a new substance that can be used as a source for the synthesis of new prototypes.

4. Materials and Methods

4.1. Chemistry

Reagents and solvents were purchased from commercial suppliers and have not been purified. Melting points were determined in a Quimis Q340.23 apparatus and are uncorrected. $^1\text{H-NMR}$ and $^{13}\text{C-NMR}$ spectra were recorded on Bruker AC-200, Bruker DRX-300 and Varian MR-400 (coupling constant (J) values were given in Hertz). Infrared spectra (IR) were carried out in the spectrophotometer apparatus Fourier transform IR Nicolet 6700 FT-IR using tablets of potassium bromide (KBr). Purity of the final product was determined by high-performance liquid chromatography (HPLC) on Shimadzu LC-20AD with Kromasil 100–5 C18 column (4.6 mm \times 250 mm), and Detector SPD-M20A (diode array). Analyte quantification was performed using a standardized wavelength, 254 nm, and acetonitrile and water 60% were used as the mobile phase.

Synthetic methodologies used to prepare methyl 1-naphthoate have been carefully described in previously published studies [15,16]. Moreover, 2-naphthohydrazide was prepared as previously described by Cordeiro et al. [8,9]. All the spectroscopical data can be accessed in the Supplementary Material.

4.2. Synthesis of 1-Naphthohydrazide (8)

Methyl 1-naphthoate (7) (1.4 g, 7.5 mmol) was solubilized in 50 mL of absolute ethanol in a round bottom flask. Then, 5 equivalents of hydrazine hydrate 100% (1.88 mL, 37.6 mmol) were slowly added under magnetic stirring. The mixture was refluxed for 6 h, then volume was partially reduced under reduced pressure. To the flask was added crushed ice and 10 mL of cold water, with precipitate formation. 1-naphthohydrazide (8) (11.6 g, 83%) was isolated by vacuum filtration in a Büchner funnel.

$^1\text{H-NMR}$ (300 MHz, $\text{DMSO-}d_6$) δ 9.71 (s, 1H, NH), 8.23–8.21 (m, 1H), 8.02–7.96 (m, 2H), 7.58–7.51 (m, 4H), 4.62 (s, 3H, NH_2); $^{13}\text{C-NMR}$ (75 MHz, $\text{DMSO-}d_6$) δ 168.00, 133.35, 133.12, 130.0, 129.96, 128.18, 126.64, 126.23, 125.42, 125.35, 124.99. IR (KBr, cm^{-1}) 3276 (ν N-H) 1645 (ν C=O).

4.3. General Procedure for the Synthesis of *N*-Acylhydrazone Derivatives (4) and (5)

In a round-bottom flask containing equimolar amounts of hydrazide (8 or 9, 0.3 g, 1.6 mmol) and the desired aromatic aldehyde (0.24 g, 1.6 mmol), three drops of 20% aq. HCl and 20 mL of absolute ethanol were added. The mixture was stirred at room temperature for three hours; however, in a few minutes intense formation of precipitates was already visible. The volume of ethanol was partially reduced under reduced pressure and then crushed ice and cold water were added to the flask. Finally, the solid was collected by vacuum filtration in a Büchner funnel.

4-((*E*)-(1-naphthoylimino)methyl)phenylboronic acid (LASSBio-2039, 3): White amorphous solid; 92%; m.p. $^{\circ}\text{C}$. $^1\text{H-NMR}$ (300 MHz, $\text{DMSO-}d_6$) δ 12.07 (s, NH), 8.36 (s, 1H), 8.21 (s, 2H, BOH_2), 8.10 (d, $J = 7.8$ Hz, 1H), 8.04–8.01 (m, 1H), 7.90 (d, $J = 7.9$ Hz, 2H), 7.78–7.72 (m, 3H), 7.64–7.59 (m, 4H). $^{13}\text{C-NMR}$ (75 MHz, $\text{DMSO-}d_6$) δ 170.73, 164.78, 147.90, 136.38, 135.62, 134.56, 133.17, 132.79, 130.55, 129.96, 128.39, 127.13, 126.49, 126.14, 125.91, 125.02. IR (KBr, cm^{-1}). **Purity** (HPLC): 99.5%.

(*E*)-*N*-(3-nitrobenzylidene)-2-naphthohydrazide (LASSBio-2040, 4): White amorphous solid; 97%; m.p. $^{\circ}\text{C}$. $^1\text{H-NMR}$ (500 MHz, $\text{DMSO-}d_6$) δ 12.32 (s, 1H), 8.61 (s, 1H), 8.57 (s, 2H), 8.27 (d, $J = 8.0$ Hz, 1H), 8.18 (d, $J = 7.6$ Hz, 1H), 8.10–8.06 (m, 2H), 8.02–8.00 (m, 2H), 7.76 (t, $J = 7.9$ Hz, 1H), 7.67–7.61 (m, 2H). $^{13}\text{C-NMR}$ (126 MHz, $\text{DMSO-}d_6$) δ 163.49, 148.28, 145.38, 136.26, 134.49, 133.49, 132.09, 130.54, 130.44, 129.02, 128.09, 127.78, 127.04, 124.36, 120.97. IR (KBr, cm^{-1}). **Purity** (HPLC): 99.2%.

(*E*)-*N*-(2-nitrobenzylidene)-2-naphthohydrazide (LASSBio-2041, 5): White amorphous solid; 94%; m.p. $^{\circ}\text{C}$. $^1\text{H-NMR}$ (300 MHz, $\text{DMSO-}d_6$) δ 12.41 (s, 1H), 8.93 (s, 1H), 8.59 (s,

1H), 8.18 (d, $J = 7.2$ Hz, 1H), 8.11–8.00 (m, 5H), 7.84 (t, $J = 7.7$ Hz, 1H), 7.71–7.63 (m, 3H). ^{13}C -NMR (75 MHz, DMSO- d_6) δ 163.43, 148.3, 142.99, 134.52, 133.82, 132.09, 130.75, 130.29, 129.02, 128.81, 128.4, 128.24, 128.1, 128.02, 127.77, 127.02, 124.75, 124.38. IR (KBr, cm^{-1}). **Purity** (HPLC): 98.8%.

4.4. Animals

Swiss Webster mice (25–30 g) were kindly donated by Instituto Vital Brazil (Niterói, Rio de Janeiro, Brazil). Mice were maintained in a room in a light-dark cycle of 12 h, 22 ± 2 °C from 60% to 80% humidity and with food and water provided ad libitum. Animals were acclimatized to the laboratory conditions for at least 1h before each test and were used only once throughout the experiments. All protocols were conducted in accordance with the Guidelines on Ethical Standards for Investigation of Experimental Pain in Animals [40] and followed the principles and guidelines adopted by the National Council for the Control of Animal Experimentation (CONCEA), approved by the Ethical Committee for Animal Research (# 31/19 and 34/19). All experimental protocols were performed during the light phase. Animal numbers per group were kept at a minimum and at the end of each experiment mice were sacrificed by ketamine/xylazine overdose.

4.5. Drugs, Reagents and Treatments

Acetylsalicylic acid (ASA), dexamethasone, L-NMMA (L-N^G-monomethyl arginine), Ara-C (cytosine arabinoside), MTT (3-(4,5-dimethyl-1-tiazol-2-yl)-2,5-diphenyltetrazole) and lipopolysaccharide were purchased from Sigma Aldrich (St. Louis, MO, USA). Ethanol and formalin were purchased from Merck Inc. (São Paulo, Brazil). Cytokines kits were purchased from BD Biosciences (Franklin Lakes, NJ, USA), protein kit (Kit Pierce BCA™ Protein Assay) was purchased from ThermoFisher Scientific, Inc. (Waltham, MA, USA). Morphine sulfate was kindly provided by Cristália (São Paulo, Brazil).

LASSBio-1524, LASSBio-1760, LASSBio-2039, LASSBio-2040 and LASSBio-2041 were dissolved in dimethylsulfoxide (DMSO) to prepare 100 $\mu\text{mol}/\text{mL}$ stock solutions. For use, solutions were prepared from each stock solution using tween as vehicle. Doses of 0.1 to 10 $\mu\text{mol}/\text{kg}$ (final volume of 0.1 mL per animal) were administered by gavage and final tween percentage did not exceed 1%. Acetylsalicylic acid, morphine, dexamethasone, and L-NMMA were used as references drugs. The doses of ASA, morphine, dexamethasone, and L-NMMA were chosen based on previous results obtained by our group when it was calculated the ED₅₀ or IC₅₀, the dose/concentration caused a 50% reduction in the effect in each procedure. The control group was given vehicle (Tween 80, Isofar, Rio de Janeiro, Brazil). All drugs and LASSBios were diluted just before their use. Data for LASSBio-1524 and LASSBio-1760 are original, independent duplicates of past results and have not been published previously.

4.6. Cell Culture

The mouse monocyte macrophage J774.A1 (ATCC # TIB-67) was grown in RPMI medium supplemented with 10% fetal bovine serum (from now on, named as RPMI) and kept in a 5% CO₂ incubator at 37 °C. An exchange of RPMI was carried out until cells reached 90% confluence and exponential growth. On the day of assays, cells were collected by scraping bottles and adhered in 96- or 12-well culture plates (2×10^6 cells/mL).

4.7. In Vitro Toxicity Test (Cell Viability)

In 96-well plates, J774.A1 cells (10^5 /well, final volume of 200 μL) were adhered at 37 °C, 5% CO₂. After 30 min incubation with LASSBio-1524 or LASSBio-1760 (30 μM), LASSBio-2039, LASSBio-2040 or LASSBio-2041 (0.1, 1 or 10 μM), LPS (1 $\mu\text{g}/\text{mL}$) was added to some groups. After 24 h of incubation (at 37 °C, 5% CO₂), supernatant was changed and MTT solution (5 mg/mL, 100 $\mu\text{L}/\text{well}$) was added. After 4 h of incubation (at 37 °C, 5% CO₂), supernatants were discarded and DMSO (100 $\mu\text{L}/\text{well}$) was added to solubilize the

MTT-formazan crystals formed [41]. Absorbance was measured at a wavelength of 570 nm. Control groups were composed by cells which received only RPMI plus DMSO.

4.8. *In vivo Toxicity Test*

Different groups of animals received an oral administration of 100 $\mu\text{mol/kg}$ of LASS-Bios. After 24 h, mice were euthanized with ketamine (50 mg/kg)/xylazine (20 mg/kg). Sample of blood was collected. The femur was removed, the ends were cut, and the bone marrow was washed with 1 mL of saline (NaCl 0.9%) and collected. Both samples of blood and bone marrow were submitted to a complete blood hemogram and cell count, respectively, in an automatic cell counter (PocH-100iV Diff, Sysmex, Kobe, Japan). Signs of acute toxicity, such as behavioral parameters (i.e., convulsion, hyperactivity, sedation, grooming, loss of righting reflexes, or increased or decreased respiration), as well as food and water intake, were observed over a 5-day period after a single oral dose of each substance (100 $\mu\text{mol/kg}$) administered to a group of ten animals of both sexes. After this period, the animals were sacrificed by ketamine/xylazine overdose, and their stomachs were removed. An incision was made along the great curvature, and the presence of ulcers or perforations and degree of hyperemia was observed and counted.

4.9. *Formalin-Induced Paw Licking Model*

The method was similar to previously described by Hunskaar and Hole [23,24] with modifications [42]. Briefly, mice received an intraplantar injection of formalin (20 μL , 2.5%) in one hind paw. Immediately they were individually placed in a box and the sum of the times each one remained licking the formalin-injected paw was recorded with the aid of a stopwatch at intervals of 5 min (first phase) or 15–30 min (second phase). Mice were pretreated with vehicle, ASA (1100 $\mu\text{mol/kg}$), morphine (15 $\mu\text{mol/kg}$), LASSBio-1524 or LASSBio-1760 (30 $\mu\text{mol/kg}$), LASSBios (1, 10 or 30 $\mu\text{mol/kg}$) for 1 h before formalin injection.

4.10. *Carrageenan-Induced Inflammation into the Subcutaneous Air Pouch (SAP)*

The protocol was based in Raymundo et al. [43]. A subcutaneous air pouch was induced in the mice's back through an injection of 10 mL of sterile air. After 3 days, a new injection of 7 mL of sterile air was performed on the animals' backs. On the 6th day, the animals were orally treated with vehicle, LASSBios (1, 10 or 30 $\mu\text{mol/kg}$), LASSBio-1524 or LASSBio-1760 (30 $\mu\text{mol/kg}$) or dexamethasone (6.5 $\mu\text{mol/kg}$) and after 60 min mice received an injection of saline or carrageenan (0.5%, 1 mL) into the SAP. After 24 h, the animals were euthanized, and the SAP washed with 1 mL of saline. The exudate was collected for leukocyte count and centrifuged at 1500 r.p.m., for 10 min, 4 °C. The supernatant was collected and stored at -20 °C for several dosages (see below).

4.11. *Quantification of Proteins and Cytokines*

To perform the quantification of proteins in the exudate obtained in the BAS the BCA Protein Assay Kit (Thermo Fisher Scientific, Inc., Waltham, MA, USA) was used. Quantification of cytokines was performed in the exudate collected from BAS and in the supernatant of J774.A1 cells, using an immunoenzymatic assay method (ELISA) with specific ELISA kits (BD OptEIA™ Set mouse, B&D, Albuquerque, NM, USA). Protocols were carried out according to the manufacturer's instructions.

4.12. *Quantification of Nitric Oxide (NO) Production*

When produced in biological fluids, NO interacts with hemoglobin and decays to nitrate (NO_3^-) and when its production occurs *in vitro* it interacts with oxygen decaying to nitrite (NO_2^-). As the technique does not quantify NO_3^- , it is necessary to convert the nitrate generated after NO production *in vivo* to nitrite. The protocol for converting nitrate to nitrite was described by Bartholomew [44] with adaptations made by Raymundo et al. [43].

Both the supernatant collected in the NO_3^- to NO_2^- conversion protocol and that collected from cell cultures were mixed, in equal parts, with the Griess reagent [45]. The

absorbance was read in a microplate reader (FlexStation, Molecular Devices, San Jose, CA, USA) at 540 nm. The sodium nitrite concentrations were calculated using a standard sodium nitrite curve.

4.13. Inducible Nitric Oxide (iNOS) Synthase Activity and NO-Scavenger Activity Assays

J774.A1 cells were plated in 96 well-plated and incubated with vehicle or lipopolysaccharide (LPS, 1 µg/mL). After 8 h incubation, different concentrations (0.1, 1 or 10 µM) of each LASSBio were added to different groups. Twenty-four hours after LPS activation, the supernatants were collected to NO measurement.

The NO donor, S-nitroso-N-acetyl-DL-penicillamine (SNAP, at 1 mM) was incubated with vehicle or LASSBios (10 µM) for 12 h at 37 °C. After incubation, an aliquot of 0.1 mL was used for nitrite measurement as previously cited.

4.14. Cell Migration In Vitro

To assess the effect of LASSBios on cell migration in vitro, J774.A1 cells were plated at 1×10^6 cells per well in 12-well plates (in a final volume of 2 mL) and after 3 h a healing was made in the well with the aid of a P20 tip. The wells were washed with RPMI to remove non-adherent cells. In order to inhibit cell proliferation, the anti-mitotic cytosine Arabinoside (AraC; 10^{-5} M, Sigma-Aldrich, USA) was added to wells. The cells were treated with LASSBios (0.1, 1 or 10 µM) and immediately after treatment and after 24 h, photographs of the wells were performed using an EvosM500 microscope (ThermoFisher). The healing area was measured with the aid of the ImageJ software. To obtain the results, three independent experiments were carried out.

4.15. Statistical Analysis

The experimental groups of the in vivo models were composed of 6 to 12 animals selected at random. The in vitro experiments were repeated at least three times on different days (and with a different cell lot) and each experimental group was carried out in triplicate. The results were expressed as mean \pm standard deviation (S.D.) and through the analysis of variance test (ANOVA), statistical significance was calculated followed by the Bonferroni post-test with the aid of the GraphPad Prisma 8.02 software. *p* values less than 0.05 ($* p < 0.05$) were considered significant.

5. Conclusions

Taken together, our data indicate that LASSBio-2039, LASSBio-2040 and LASSBio-2041 present anti-inflammatory effects, demonstrated in an acute model in vivo and in vitro. We can suggest that these substances could be further studied for the development of new drug prototypes.

Supplementary Materials: The following supporting information can be downloaded at: <https://www.mdpi.com/article/10.3390/ijms232113562/s1>.

Author Contributions: Conceptualization, P.D.F.; methodology, R.H.C.N.d.F. and D.d.C.S.; formal analysis, D.d.C.S. and P.D.F.; investigation, D.d.C.S.; resources, P.D.F. and C.A.M.F.; data curation, P.D.F.; writing—original draft preparation, P.D.F.; writing—review and editing, P.D.F. and C.A.M.F.; supervision, P.D.F. and C.A.M.F.; project administration, P.D.F.; funding acquisition, P.D.F. All authors have read and agreed to the published version of the manuscript.

Funding: This research was funded by Fundação Carlos Chagas Filho de Amparo a Pesquisa do Estado do Rio de Janeiro (FAPERJ), grant numbers E-26/010.001837/2015; SEI-260003/001182/2020; SEI-260003/012984/2021; SEI-260003/003464/2022, and Conselho Nacional de Desenvolvimento Científico e Tecnológico, grant number 308557/2021-2.

Institutional Review Board Statement: The animal study protocol was approved by Animal Experimentation Ethics Committee of the Health Sciences Center of UFRJ, Rio de Janeiro (# 31/19 and 34/19).

Informed Consent Statement: Not applicable.

Data Availability Statement: All data can be obtained directly with authors.

Acknowledgments: To Instituto Vital Brazil (Niterói, Rio de Janeiro, Brasil) for animal donation and Alan Minho for technical assistance.

Conflicts of Interest: The authors declare no conflict of interest.

References

- Rotta, D.; Fassio, A.; Rossini, M.; Giollo, A.; Viapiana, O.; Orsolini, G.; Bertoldo, E.; Gatti, D.; Adami, G. Osteoporosis in inflammatory arthritides: New perspective on pathogenesis and treatment. *Front. Med.* **2020**, *7*, 613720. [CrossRef]
- Maspero, J.; Adir, Y.; Al-Ahmad, M.; Celis-Preciado, C.A.; Colodenco, F.D.; Giavina-Bianchi, P.; Lababidi, H.; Ledanois, O.; Mahoud, B.; Perng, D.W.; et al. Type 2 inflammation in asthma and other airway diseases. *ERJ Open Res.* **2022**, *8*, 00576. [CrossRef]
- Qadri, M.A.R.M.; Khan, A.; Alshahrani, S.; Rashid, H.; Rashid, S.; Alsaffar, R.M.; Kamal, M.A.; Rehman, M.U. Inflammation and alzheimer's disease: Mechanisms and therapeutic implications by natural products. *Mediat. Inflamm.* **2021**, *2021*, 9982954.
- Sorriento, D.; Laccarino, G. Inflammation and cardiovascular diseases: The most recent findings. *Int. J. Mol. Sci.* **2019**, *20*, 3879. [CrossRef]
- Greten, F.R.; Grivennikov, S.I. Inflammation and cancer: Triggers, mechanisms, and consequences. *Immunity* **2019**, *51*, 27–41. [CrossRef]
- Kumar, D.P.; Koka, S.; Li, C.; Rajagopal, S. Inflammatory mediators in obesity. *Mediat. Inflamm.* **2019**, *2019*, 9481819. [CrossRef]
- Avila, C.M.; Lopes, A.B.; Gonçalves, A.S.; Da Silva, L.L.; Romeiro, N.C.; Miranda, A.L.P.; Sant'Anna, C.M.R.; Barreiro, E.J.; Fraga, C.A.M. Structure-based design and biological profile of (*E*)-*N*-(4-Nitrobenzylidene)-2-naphthohydrazide, a novel small molecule inhibitor of I κ B kinase- β . *Eur. J. Med. Chem.* **2011**, *46*, 1245–1253. [CrossRef]
- Cordeiro, N.M.; Freitas, R.C.N.; Fraga, C.A.M.; Fernandes, P.D. Discovery of novel orally active tetrahydronaphthyl-*n*-acylhydrazones with in vivo anti-TNF- α effect and remarkable anti-inflammatory properties. *PLoS ONE* **2016**, *11*, e0156271. [CrossRef]
- Cordeiro, N.M.; Freitas, R.C.N.; Fraga, C.A.M.; Fernandes, P.D. Therapeutic effects of anti-inflammatory *N*-acylhydrazones in the resolution of experimental colitis. *J. Pharmacol. Exp. Ther.* **2020**, *374*, 420–427. [CrossRef]
- Duarte, D.B.; Vasko, M.R.; Fehrenbacher, J.C. Models of inflammation: Carrageenan air pouch. *Curr. Protoc. Pharmacol.* **2016**, *72*, 561–569. [CrossRef]
- Thota, S.; Rodrigues, D.A.; Pinheiro, P.S.M.; Lima, L.M.; Fraga, C.A.M.; Barreiro, E.J. *N*-acylhydrazones as drugs. *Bioorg. Med. Chem. Lett.* **2018**, *28*, 2797–2806. [CrossRef]
- Hakimelahi, G.H.; Khodarahmi, G.A. The Identification of toxicophores for the prediction of mutagenicity, hepatotoxicity and cardiotoxicity. *J. Iran. Chem. Soc.* **2005**, *2*, 244–267. [CrossRef]
- Wang, Y.; Gray, J.P.; Heck, D.E.; Laskin, D.L.; Laskin, J.D. Role of cytochrome P450 reductase in nitrofurantoin-induced redox cycling and cytotoxicity. *Free Radic. Biol. Med.* **2008**, *44*, 1169–1179. [CrossRef]
- Black, J.W.; Duncan, W.A.M.; Shanks, R.G. Comparison of some properties of pronethalol and propranolol. *Br. J. Pharmacol.* **1997**, *120*, 283–284. [CrossRef]
- Houck, H.A.; Blasco, E.; Du Prez, F.E.; Barner-Kowollik, C. Light-stabilized dynamic materials. *J. Am. Chem. Soc.* **2019**, *141*, 12329–12337. [CrossRef]
- Shindo, K.; Osawa, A.; Kasai, Y.; Iba, N.; Saotome, A.; Misawa, N. Hydroxylations of substituted naphthalenes by *Escherichia coli* expressing aromatic dihydroxylating dioxygenase genes from polycyclic aromatic hydrocarbon-utilizing marine bacteria. *J. Mol. Catal. B Enzym.* **2007**, *48*, 77–83. [CrossRef]
- Lima, P.C.; Lima, L.M.; Silva, K.C.M.; Léda, P.H.O.; Miranda, A.L.P.; Fraga, C.A.M.; Barreiro, E.J. Synthesis and analgesic activity of novel *N*-acylarylhydrazones and isomers, derived from natural saffrole. *Eur. J. Med. Chem.* **2000**, *35*, 187–203. [CrossRef]
- Rai, G.; Kenyon, V.; Jadhav, A.; Schultz, L.; Armstrong, M.; Jameson, J.B.; Hoobler, E.; Leister, W.; Simeonov, A.; Holman, T.R.; et al. Discovery of potent and selective inhibitors of human reticulocyte 15-lipoxygenase-1. *J. Med. Chem.* **2010**, *53*, 7392–7404. [CrossRef]
- Lacerda, R.B.; Silva, L.L.; de Lima, C.K.F.; Miguez, E.; Miranda, A.L.P.; Laufer, S.A.; Barreiro, E.J.; Fraga, C.A.M. Discovery of novel orally active anti-inflammatory *N*-phenylpyrazolyl-*N*-glycinyld-hydrazones derivatives that inhibit TNF- α production. *PLoS ONE* **2012**, *7*, e46925.
- Lopes, A.B.; Miguez, E.; Kümmerle, A.E.; Rumjanek, V.M.; Fraga, C.A.M.; Barreiro, E.J. Characterization of amide bond conformers for a novel heterocyclic template of *N*-acylhydrazone derivatives. *Molecules* **2013**, *18*, 11683–11704. [CrossRef] [PubMed]
- Palla, G.; Pelizzi, C.; Predieri, G. Conformational study on *N*-acylhydrazones of aromatic aldehydes by NMR spectroscopy. *Gazz. Chim. Ital.* **1982**, *112*, 339–341.
- Parada, C.A.; Tambeli, C.H.; Cunha, F.Q.; Ferreira, S.H. The major role of peripheral release of histamine and 5-hydroxytryptamine in formalin-induced nociception. *Neuroscience* **2001**, *102*, 937–944. [CrossRef]
- Hunskar, S.; Fasmer, O.B.; Hole, K. Formalin test in mice, a useful technique for evaluating mild analgesia. *J. Neurosci. Methods* **1985**, *14*, 69–76. [CrossRef]
- Hunskar, S.; Hole, K. The formalin test in mice: Dissociation between inflammatory and non-inflammatory pain. *Pain* **1986**, *30*, 103–114. [CrossRef]
- Tassorelli, C.; Greco, R.; Wang, D.; Sandrini, G.; Nappi, G. Prostaglandins, glutamate and nitric oxide synthase mediate nitroglycerin-induced hyperalgesia in the formalin test. *Eur. J. Pharmacol.* **2006**, *534*, 103–107. [CrossRef]

26. Gupta, S.; Parent, C.A.; Bear, J.E. The principles of directed cell migration. *Nat. Rev. Mol. Cell Biol.* **2021**, *22*, 529–547.
27. Miskolci, V.; Klemm, L.C.; Huttenlocher, A. Cell migration guided by cell-cell contacts in innate immunity. *Trends Cell Biol.* **2021**, *31*, 86–94. [CrossRef]
28. Lampugnani, M.G.; Dejana, E.; Giampietro, C. Vascular endothelial (VE)-cadherin, endothelial adherens junctions, and vascular disease. *Cold Spring Harb. Perspect. Biol.* **2017**, *10*, a029322. [CrossRef]
29. Mantovani, A.; Dinarello, C.A.; Molgora, M.; Garlanda, C. Interleukin-1 and related cytokines in the regulation of inflammation and immunity. *Immunity* **2019**, *16*, 778–795. [CrossRef]
30. Szalecki, M.; Malinowska, A.; Prokop-Piotrkowska, M.; Janas, R. Interactions between the growth hormone and cytokines—A review. *Adv. Med. Sci.* **2018**, *63*, 285–289. [CrossRef]
31. Theofilis, P.; Sagris, M.; Oikonomou, E.; Antonopoulos, A.S.; Siasos, G.; Tsioufis, C.; Tousoulis, T. Inflammatory mechanisms contributing to endothelial dysfunction. *Biomedicines* **2021**, *9*, 781. [CrossRef] [PubMed]
32. Madej, M.P.; Töpfer, E.; Boraschi, D.; Italiani, P. Different regulation of interleukin-1 production and activity in monocytes and macrophages: Innate memory as an endogenous mechanism of IL-1 inhibition. *Front. Pharmacol.* **2017**, *8*, 335. [CrossRef] [PubMed]
33. Cinelli, M.A.; Do, H.T.; Miley, G.P.; Silverman, R.B. Inducible nitric oxide synthase: Regulation, structure, and inhibition. *Med. Res. Rev.* **2020**, *40*, 158–189. [CrossRef]
34. Olona, A.; Hateley, C.; Muralidharan, S.; Wenk, M.R.; Torta, F.; Behmoaras, J. Sphingolipid metabolism during Toll-like receptor 4 (TLR4)-mediated macrophage activation. *Br. J. Pharmacol.* **2021**, *178*, 4575–4587. [CrossRef] [PubMed]
35. Ciesielska, A.; Matyjek, M.; Kwiatkowska, K. TLR4 and CD14 trafficking and its influence on LPS-induced pro-inflammatory signaling. *Cell. Mol. Life Sci.* **2021**, *78*, 1233–1261. [CrossRef] [PubMed]
36. Pautz, A.; Li, H.; Kleinert, H. Regulation of NOS expression in vascular diseases. *Front. Biosci. Landmark Ed.* **2021**, *26*, 85–101.
37. Liang, C.C.; Park, A.Y.; Guan, J.L. In Vitro scratch assay: A convenient and inexpensive method for analysis of cell migration in vitro. *Nat. Protoc.* **2007**, *2*, 329–333. [CrossRef]
38. Gage, M.C.; Thippeswamy, T. Inhibitors of Src family kinases, inducible nitric oxide synthase, and NADPH oxidase as potential CNS drug targets for neurological diseases. *CNS Drugs* **2021**, *35*, 1–20. [CrossRef]
39. Cui, S.; Wu, Q.; Wang, J.; Li, M.; Qian, J.; Li, S. Quercetin inhibits LPS-induced macrophage migration by suppressing the iNOS/FAK/paxillin pathway and modulating the cytoskeleton. *Cell Adhes. Migr.* **2019**, *13*, 1–12. [CrossRef]
40. Zimmermann, M. Ethical guidelines for investigation of experimental pain in conscious animals. *Pain* **1983**, *16*, 109–110. [CrossRef]
41. Mosmann, T. Rapid colorimetric assay for cellular growth and survival: Application to proliferation and cytotoxicity assays. *J. Immunol. Methods* **1983**, *65*, 55–63. [CrossRef]
42. Gomes, N.M.; Rezende, C.M.; Fontes, S.P.; Matheus, M.E.; Fernandes, P.D. Antinociceptive activity of Amazonian Copaiba oils. *J. Ethnopharmacol.* **2007**, *109*, 486–492. [CrossRef]
43. Raymundo, L.J.R.P.; Guilhon, C.C.; Alviano, D.S.; Matheus, M.E.; Antonioli, A.R.; Cavalcanti, S.C.H.; Alves, P.B.; Alviano, C.S.; Fernandes, P.D. Characterisation of the anti-inflammatory and antinociceptive activities of the *Hyptis pectinata* (L.) Poit essential oil. *J. Ethnopharmacol.* **2011**, *134*, 725–732. [CrossRef]
44. Bartholomew, B. A rapid method for the assay of nitrate in urine using the nitrate reductase enzyme of *Escherichia coli*. *Food Chem. Toxicol.* **1984**, *22*, 541–543. [CrossRef]
45. Green, L.C.; Wagner, D.A.; Glogowski, J.; Skipper, P.L.; Wisnok, J.S.; Tannenbaum, S.R. Analysis of nitrate, nitrite, and [¹⁵N]nitrate in biological fluids. *Anal. Biochem.* **1982**, *126*, 131–138. [CrossRef]



Article

An Analysis of the Effects of In Vitro Photodynamic Therapy on Prostate Cancer Tissue by Histopathological Examination and Magnetic Resonance Imaging

David Aebisher ¹, Michał Osuchowski ², Dorota Bartusik-Aebisher ³, Magdalena Krupka-Olek ⁴,
Klaudia Dynarowicz ⁵ and Aleksandra Kawczyk-Krupka ^{4,*}

¹ Department of Photomedicine and Physical Chemistry, Medical College of the University of Rzeszów, University of Rzeszów, 35-959 Rzeszów, Poland

² Medical College of the University of Rzeszów, University of Rzeszów, 35-959 Rzeszów, Poland

³ Department of Biochemistry and General Chemistry, Medical College of the University of Rzeszów, 35-959 Rzeszów, Poland

⁴ Center for Laser Diagnostics and Therapy, Department of Internal Medicine, Angiology and Physical Medicine, Medical University of Silesia in Katowice, 41-902 Bytom, Poland

⁵ Center for Innovative Research in Medical and Natural Sciences, Medical College of the University of Rzeszów, 35-310 Rzeszów, Poland

* Correspondence: akawczyk@gmail.com

Citation: Aebisher, D.; Osuchowski, M.; Bartusik-Aebisher, D.; Krupka-Olek, M.; Dynarowicz, K.; Kawczyk-Krupka, A. An Analysis of the Effects of In Vitro Photodynamic Therapy on Prostate Cancer Tissue by Histopathological Examination and Magnetic Resonance Imaging. *Int. J. Mol. Sci.* **2022**, *23*, 11354. <https://doi.org/10.3390/ijms231911354>

Academic Editor: Dmitry Aminin

Received: 26 July 2022

Accepted: 22 September 2022

Published: 26 September 2022

Publisher's Note: MDPI stays neutral with regard to jurisdictional claims in published maps and institutional affiliations.



Copyright: © 2022 by the authors. Licensee MDPI, Basel, Switzerland. This article is an open access article distributed under the terms and conditions of the Creative Commons Attribution (CC BY) license (<https://creativecommons.org/licenses/by/4.0/>).

Abstract: Prostate cancer can significantly shorten the lifetime of a patient, even if he is diagnosed at an early stage. The development of minimally-invasive focal therapies such as photodynamic therapy to reduce the number of neoplastic cells while sparing delicate structures is extremely advantageous for treating prostate cancer. This study investigates the effect of photodynamic therapy performed in prostate tissue samples in vitro, using quantitative magnetic resonance imaging and histopathological analysis. Prostate tissue samples were treated with oxygenated solutions of Rose Bengal (RB) or protoporphyrin IX disodium salt (PpIX), illuminated with visible light, and then analyzed for changes in morphology by microscopy and by measurement of spin–lattice and spin–spin relaxation times at 1.5 Tesla. In the treated prostate tissue samples, histopathological images revealed chromatin condensation and swelling of the stroma, and in some cases, thrombotic necrosis and swelling of the stroma accompanied by pyknotic nuclei occurred. Several samples had protein fragments in the stroma. Magnetic resonance imaging of the treated prostate tissue samples revealed differences in the spin–lattice and spin–spin relaxation times prior to and post photodynamic action.

Keywords: prostate cancer; photodynamic therapy; magnetic resonance imaging; ex vivo

1. Introduction

Prostate cancer is the second most common malignant neoplasm in men [1–7]. According to the World Health Organization, prostate cancer had the highest incidence rate of 1 in 9.3 worldwide, assuming both sexes as the criterion and without the specified range of the criterion [8]. In prostate cancer, cell growth is a hormonal receptor-stimulated disease [9,10], and it is one of the few types of neoplasms for which no clear etiological factors can be indicated [11,12]. Histopathological examination is the basis for the diagnosis of prostate cancer, in which adenocarcinoma is mainly diagnosed. The acute and chronic forms of prostate disease include a complex set of diseases that can both lead to and result from cancer. Diseased states of the prostate require proper diagnosis and treatment, aided by introducing new focal therapies, such as photodynamic therapy (PDT), which is increasingly being applied as adjunctive therapy for cancer [13–21]. Deeper tumors are a challenge to treat by PDT due to the limited penetration of light into tissue. One of the conditions for carrying out PDT is the presence of a photosensitizer (PS) that elicits the cytotoxic photodynamic effect upon light absorption. Several photosensitizers have been approved

for clinical PDT and photodynamic diagnosis (PDD), and they are often porphyrin or chlorin derivatives. Tissue-based photosensitizers (PS) concentrate in cancer tissue, and local exposure to a PS-infused region causes the production of reactive oxygen species (ROS), which destroys cells via apoptotic, paraptotic, or necrotic mechanisms (Figure 1). Singlet oxygen ($^1\text{O}_2$), generated by a Type II energy transfer from the excited triplet PS to ground-state oxygen, is believed to be the most important ROS in tissue-based PDT and vascular PS, such as the Tookad[®] reactions via Type I processes, to generate hydroxyl radicals that damage tumor vasculature. Photodynamic therapy, used in prostate cancer, involves intravenous tissue or vascular PS injection, followed by a precise delivery of low-power laser light by optical fibers embedded in transparent plastic needles [22–24]. Due to the growing need to improve the diagnostic and therapeutic methods for prostate cancer (including PDT), in vitro experiments are useful. Currently, the development of PDT includes the synthesis of third-generation PSs that generate ROS as a result of near-infrared light absorption, lanthanide-doped upconversion nanoparticles that absorb infrared and emit visible light for deep tissue PDT, and the development of cell membrane-directed PS [25]. The in vitro results show that photosensitizers consistently and effectively reduce the viability of neoplastic cells [26,27].

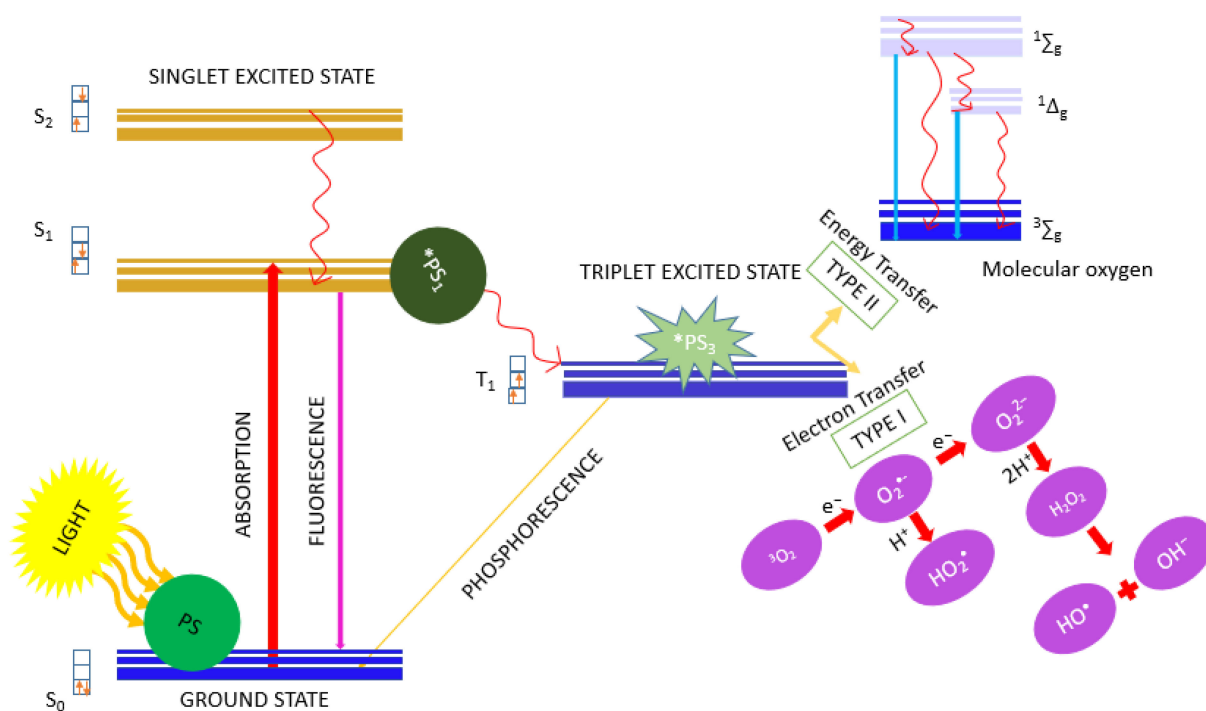


Figure 1. Type I and Type II pathways that elicit photodynamic action. The Jabłoński diagram above is a simplified graphical representation of Type I and Type II pathways that occur when a PS absorbs visible light. Singlet states are represented by S, and triplet states by T. The wavy arrows indicate internal conversion and intersystem crossing. Straight arrows illustrate transitions in which radiation is emitted or absorbed. S_0 —singlet ground state, S_1 —first singlet excited state, S_2 —second singlet excited state, PS—ground-state photosensitizer, *PS_1 —singlet excited-state photosensitizer, *PS_3 —triplet excited-state photosensitizer, $^1\Delta_g$ —singlet oxygen (excited state), $^1\Sigma_g$ —upper state excited, $^3\Sigma_g$ —triplet oxygen (ground state).

Magnetic resonance imaging (MRI) can be used to detect the differences between healthy and diseased tissue, track the progression or disappearance of disease, monitor a course of treatment at the tissue level, locate neoplastic lesions, measure their distribution and size, and indicate surgical sites [28,29]. Magnetic resonance imaging (MRI) is commonly used to detect and characterize prostate cancer before and after PDT. It is challenging to test tissue samples ex vivo when only using standard coils with large surfaces and vol-

umes. However, obtaining the relaxation times from individual measurements is extremely important and valuable in the context of comparing prostate cancer tissue samples before and after PDT [30,31]. The advantage of MRI is its excellent soft tissue contrast, which provides a powerful tool for delineating the prostate and prostate cancer. Furthermore, the 1.5-Tesla MRI has a high sensitivity for the detection of clinically significant prostate cancer and is routinely used in diagnostics [32,33]. In this study, we measured the spin–lattice (T_1) and spin–spin (T_2) relaxation times of prostate tissue samples prior to and post PDT. Spin–lattice mapping is a technique used to calculate the T_1 time of a local region of tissue and display them as a parametric map. The spin–lattice relaxation time reflects the changes in intracellular and extracellular compartments and is affected by collagen, protein, water (edema), lipids and iron content [34]. The spin–spin relaxation time, also referred to as transverse relaxation, is a time constant for the decay of transverse magnetization and is tissue specific regarding its ability to differentiate healthy from diseased tissue [35]. This study attempted to evaluate the effect of photodynamic therapy on prostate cancer tissue *ex vivo* by combining the clinical MRI measurements of T_1 , T_2 , and by histopathological analyses before and after PDT.

2. Results

2.1. Relaxation Time Measurements

The bar graph in Figure 2 shows the mean T_1 and T_2 values measured for healthy tissue and neoplastic tissue prior to the PDT procedure described in Section 4.3.

Table 1. Concentrations of photosensitizers used for PDT experiments, number of samples, and irradiation wavelength.

Prostate Tissue Sample Photosensitizer Concentrations			
Photosensitizer	Concentration [mM]	Wavelength of Light [nm]	Number of Samples
Rose Bengal (RB)	0.1	control, no light exposure	5
	control, 0 mM RB	532	5
	0.1	532	6
	0.2	532	6
	0.3	532	6
	0.4	532	6
	0.5	532	6
	Protoporphyrin IX disodium salt (PpIX)	3	control, no light exposure
control, 0 mM PpIX		410	5
3		410	15

The difference in the means for the T_1 and T_2 relaxation times between healthy and neoplastic prostate tissue prior to the PDT procedure were both statistically significant ($p < 0.03$). For healthy tissue, the mean value for T_1 was 1914.10 ± 52.43 ms, and 1506.48 ± 40.07 for the pre-PDT neoplastic tissue. For healthy tissue, the mean value for T_2 was 139.37 ± 15.07 ms, and 110.77 ± 16.84 ms for the neoplastic pre-PDT tissue.

Figure 3 presents the compiled mean values of the T_1 and T_2 relaxation times after the PDT procedure on the neoplastic prostate tissue samples as a function of RB concentration and for 3 mM PpIX. We found that the differences in the T_1 and T_2 relaxation times of neoplastic tissue prior to and after the PDT procedure with RB were statistically significant ($p < 0.03$). Additionally, differences in the T_1 and T_2 relaxation times of neoplastic tissue prior to and after the PDT procedure with 3 mM PpIX were statistically significant ($p < 0.03$).

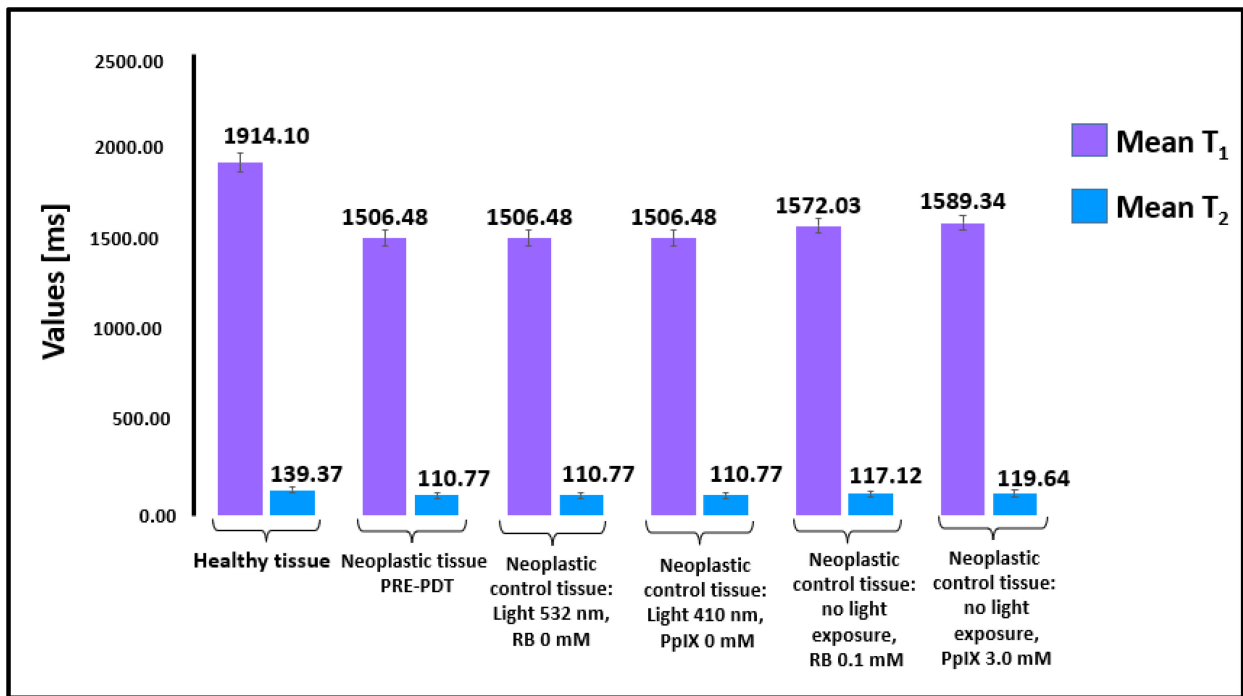


Figure 2. T₁ and T₂ relaxation times of healthy and neoplastic tissues (prior to the PDT procedure and control samples). Average T₁ and T₂ relaxation times between healthy (number of samples—65) and neoplastic prostate tissue (number of samples 65) were both statistically significant ($p < 0.03$). The number of samples in Figure 2 corresponds to the number of trials listed in Table 1.

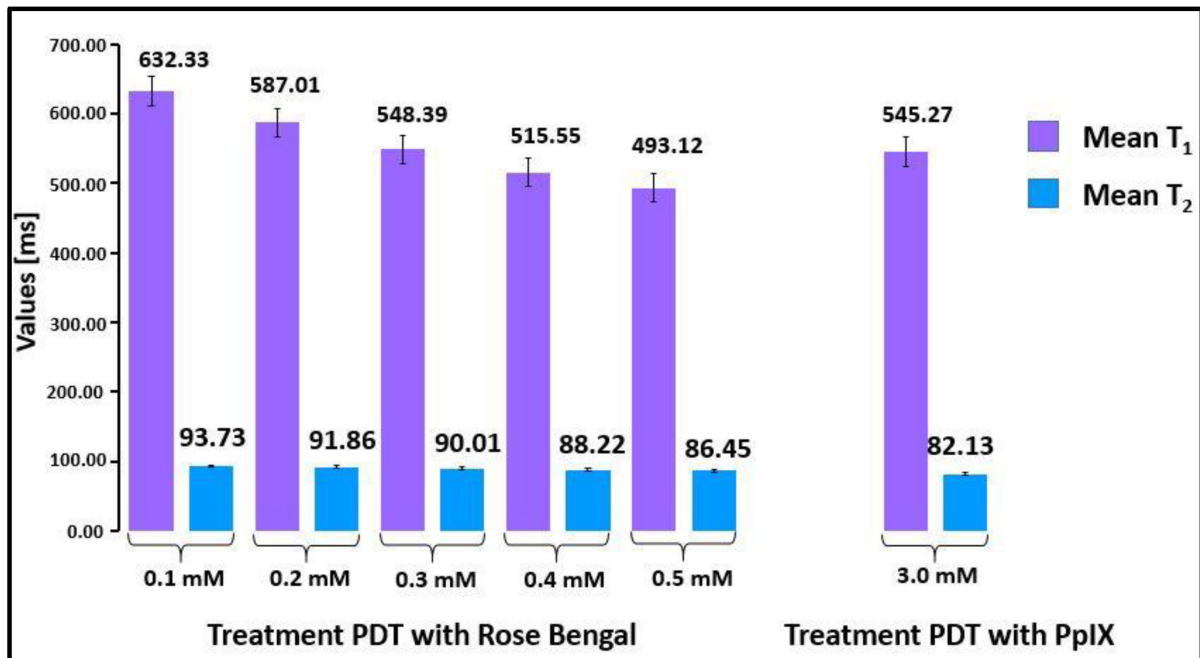


Figure 3. Mean values of T₁ and T₂ relaxation times for tissue treated with RB and PpIX. The difference in mean T₁ and T₂ relaxation times prior to and post PDT is statistically significant ($p < 0.03$). For comparison, the relaxation times measured for deionized water were T₁ = 3245.45 ± 23 ms and T₂ = 134.23 ± 11 ms. For 0.5 mM Rose Bengal, T₁ = 2994.68 ± 10 ms and T₂ = 129.32 ± 9 ms.

With an increase in the concentration of RB, the values of both relaxation times decreased. The measurement of relaxation times by clinical magnetic resonance imaging is a sufficient diagnostic tool for distinguishing neoplastic tissues before and after PDT.

2.2. Histopathological Analysis

Figure 4 shows the microscopic images at magnifications of 63× and 100× for prostate cancer tissue after being subjected to the PDT procedure with RB and PpIX. As a result of exposure of the tissues to oxygenated photosensitizer solution and light, we detected an architectural deformation of the nucleoli and chromatin, along with edema and the appearance of protein fragments. The data indicate that RB and PpIX inhibit the viability of prostate cancer cells. The histopathology images of neoplastic tissue show a distinct tumor structure with visible nucleoli and chromatin. Tissue after the PDT procedure with 0.1 mM and 0.2 mM RB shows discrete chromatin condensation and moderate stroma edema. Tissue after PDT with 0.3 mM RB shows moderate to relatively massive and enhanced chromatin condensation with architectural disturbances of the nucleoli. Tissue after PDT with 0.4 mM RB shows small pycnotic nuclei along with severe architectural damage to the membrane. Moderate chromatin condensation is visible with well-marked stroma edema. It was nearly impossible to identify the phase of prostate cancer after PDT with 0.5 mM RB due to severe architectural disturbances. Massive chromatin condensation, pyknotic nuclei, and significant architectural disturbances were visible. Tissue after PDT with 3 mM PpIX revealed cell damage and necrosis features that are easily identified and enhanced. The number of cancer cells was reduced, and there was swelling (arrows in Figure 4D–I) in the stroma and a significant amount of protein fragments.

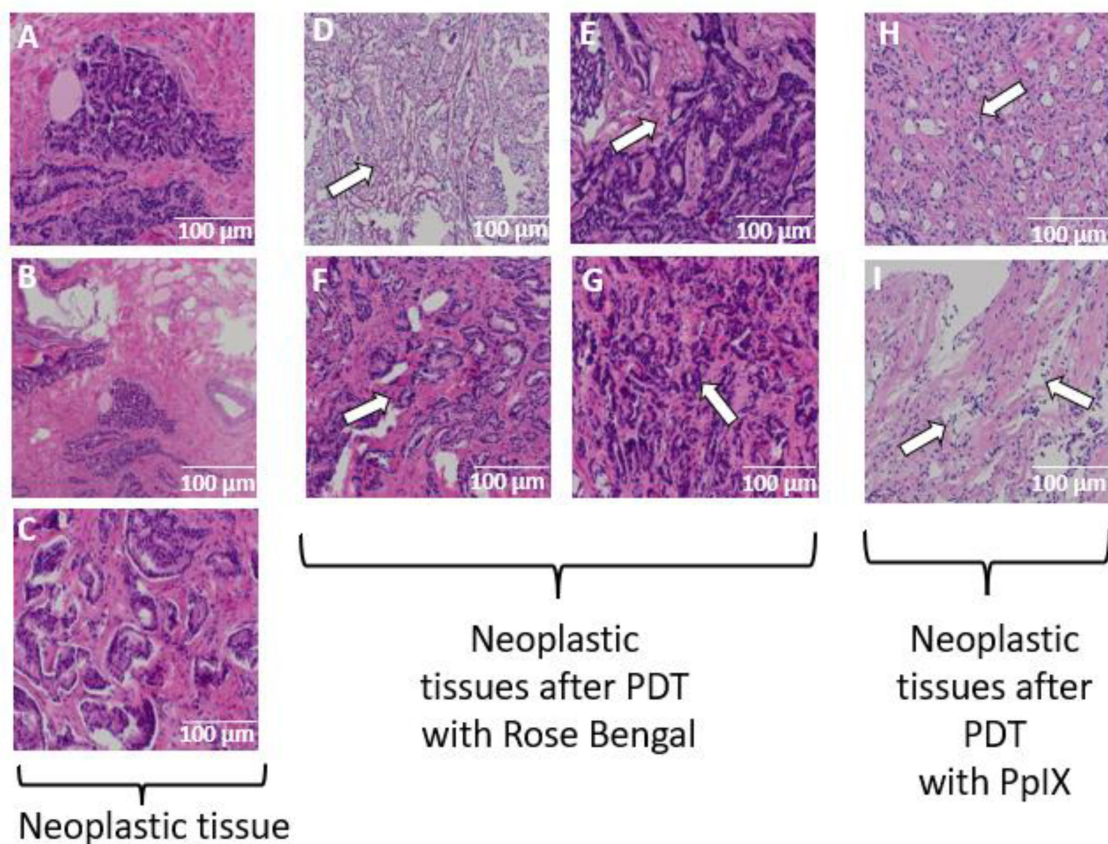


Figure 4. Prostate cancer tissue prior to (pictures A–C) and after the PDT procedure with (D) 0.2 mM RB, (E) 0.3 mM RB, (F) 0.4 mM RB, (G) 0.5 mM RB, (H,I) and 3 mM PpIX.

Figure 5 shows images from the histological analysis and T_1 and T_2 maps for the neoplastic tissue subjected to the PDT procedure using 0.4 mM.

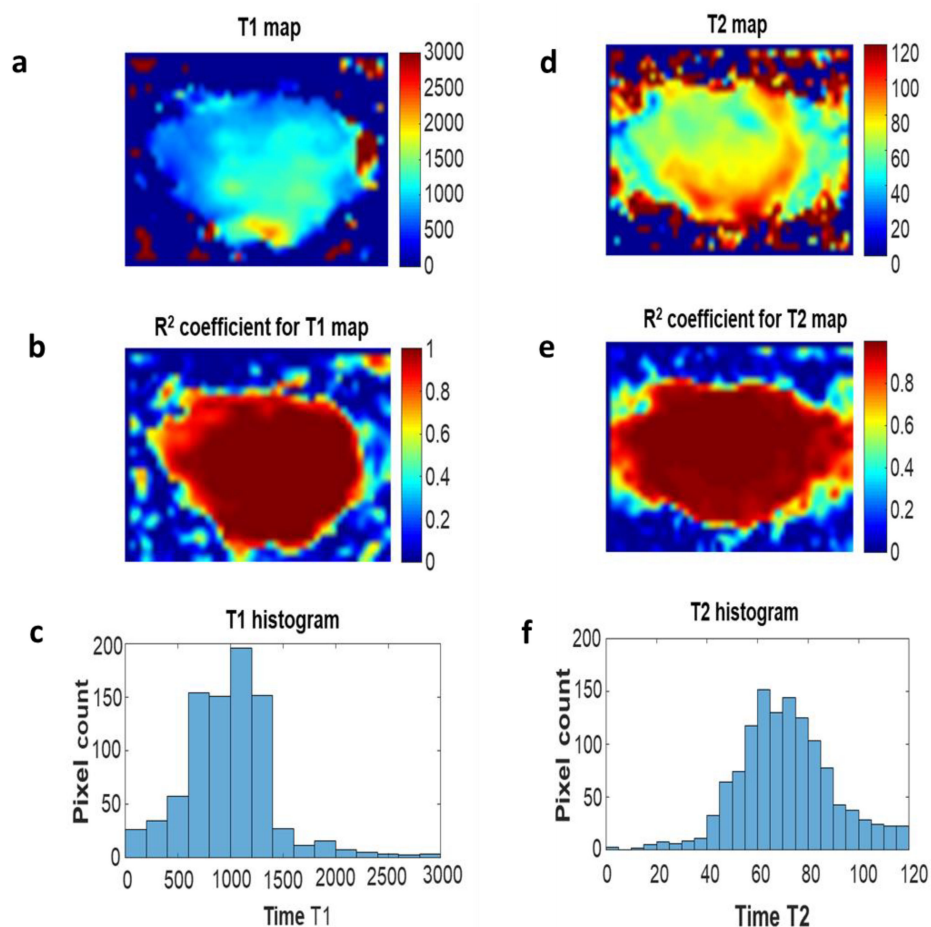


Figure 5. (a) Distribution of longitudinal relaxation time T_1 values in the prostate tissue section after PDT with 0.4 mM RB; (b) fit factor R^2 distribution; (c) a histogram of the values of T_1 times determined from the image (a); (d) distribution of T_2 transverse relaxation time values in the prostate cancer tissue section after PDT with 0.4 mM RB; (e) the distribution of the alignment factor, R_2 ; (f) a histogram of the T_2 time values determined from the image (d).

3. Discussion

By analyzing the effects of the PDT procedure on prostate cancer tissue samples *in vitro*, we have determined that RB and PpIX have different effects on the tissue structure. The effectiveness of PDT in cancer tissue is believed to be associated with the aggregation of PS in cells. However, the uptake of PpIX and RB in the cellular environment is still poorly understood. This can be explained by the lack of an analytical method that allows for precise dosimetry of PpIX and RB in tissue. Here, we demonstrate that the combination of PDT, histology, and the relaxation time measurement is very robust for monitoring the photodynamic action in prostate tissue.

PDT is under investigation for a variety of applications in oncology. PDT for prostate cancer may have a role as an adjuvant local modality, especially in locations where the risk of failure is high. Additionally, PDT can be delivered at the time of surgical resection. The use of MRI for monitoring PDT treatment can be transferred to the clinic. According to the literature, PDT destroys the tumor by three mechanisms. The first mechanism is that ROS can kill cancer cells directly. The second mechanism is targeting the tumor vasculature, which obstructs the supply of oxygen and essential nutrients. A third mechanism occurs when the immune system is activated by PDT, triggering an inflammatory and immune response against cancer cells [36].

Cancer cells grow rapidly in an uncontrolled manner and have abnormal, disorganized vascularization with a defective inner lining. As a consequence, the tumor endothelium is

leaky, and macromolecules may penetrate the extravascular space and be retained longer, compared to healthy tissues, due to impaired lymphatic drainage in the tumor tissue. This phenomenon is called the enhanced permeability and retention (EPR) effect and is often exploited for the treatment of cancer [37].

Additionally, the increased expression of some receptors on cancer cells helps to lower the pH inside the tumor and the number of macrophages that phagocytose the PS molecules [38]. Photodynamic therapy is a treatment that employs exogenously produced ROS to kill cancer cells generated from PS by light activation. Thus, the ROS generated by the PS is the key mechanism by which PDT elicits cell death and tissue destruction. The medical application of RB, a photosensitizer with high ROS generation capability, is limited due to its intrinsic toxicity and insufficient lipophilicity [39]. Protoporphyrin IX, induced by 5-ALA, promotes the generation of ROS and the induction of apoptosis via the activation of p53 and caspases in normal gastric cells but increases viability in gastric cancer cells. The molecular pathways involved in PpIX-induced cytotoxicity are not well-defined [40]. RB is reported to cause subcellular damage to the mitochondria, endoplasmic reticulum (ER), lysosomes, and the Golgi complex. Rose Bengal exerts long-term phototoxicity by activating both caspase-independent and dependent apoptotic pathways and autophagic cell death [41].

PpIX, a heme precursor, binds to the mitochondrial translocator protein and is transported to mitochondria to participate in heme metabolism. The application of porphyrin derivatives causes massive porphyrin accumulation in cancer cells [42–44]. In order to assess the effectiveness of PDT therapy in prostate cancer tissue *in vitro*, magnetic resonance imaging and microscopic examination of the histopathological specimens were used. Magnetic resonance imaging is able to distinguish the differences between tissue undergoing PDT therapy and healthy tissue. Submission of prostate cancer tissue to the PDT procedure generates a number of changes in the cellular and structural background due to the fact that the applied photosensitizer, through the accumulation in cells and exposure to laser light in the presence of oxygen, generates ROS, which directly or indirectly leads to cell apoptosis [45,46]. Photosensitizers are taken up by both healthy and diseased cells. In general, normal tissues are capable of eliminating or clearing a PS over time, while tumor tissues cannot do this due to non-existent lymphatics. This leads to some retention of PS in tumor tissue, which, when combined with localized activation light, gives PDT some additional selectivity. RB was shown to be toxic to cancer cells and to enter cancer preferentially, but not normal cells [47,48].

Prostate tissue, after extraction and freezing, does not change the morphology of cells. Many examinations, including those of the prostate, are performed intraoperatively and after the tumor is frozen. The histopathological examinations before and after freezing did not show any changes caused by freezing.

MRI can assist in the estimation of tumor volume. While MRI augments standard clinical and pathologic parameters in predicting advanced disease features and tumor volume, it is unable to reliably visualize small and well-differentiated cancers that may be prime candidates for either active surveillance or focal therapy. When it occasionally does highlight the area of a small, unifocal tumor, image-guided focal ablation may confidently target that region [49]. In 1980, the first endoscopic PDT procedure was performed for human lung cancer in a patient with poor cardiopulmonary function in whom surgery was not possible. This was an advanced squamous cell carcinoma obstructing the right main bronchus; PDT resulted in the opening of the bronchus. The second case was an early-stage squamous cell carcinoma of the right upper bronchus in March 1980 [50,51]. The variation in the initial tumor volumes (12–55 mm³) between different tumors within the same treatment condition could introduce variations in local tumor control [52]. Chang et al. discussed tumor size-dependent treatment with the use of ethyl pyropheophorbide a (MPPa) and N-methoxyl purpurinimide (NMPi) in an animal model, where high anticancer efficacy against small-size tumors was observed, indicating that early treatment with PDT is effective [53]. Small tumors (5–35 mm³) were found to respond well to a single round of

PDT, while large tumors (35–65 mm³) showed no response to the same treatment [54]. PDT with 5-ALA was performed on 14 patients with histologically proven prostate cancer. The concentration of 5-ALA was 20 mg/kg body weight taken orally. A significant reduction in the PSA levels was observed 6 weeks after interstitial PDT [55].

As a result of the PDT procedure on prostate cancer tissues, there was chromatin condensation, stromal edema, nucleolus architectonic disorders, presence of trace protein, and necrotic cell damage. In a study by Wang et al., in histopathological preparations of prostate cancer in mice, it was observed that the nuclei of cancer cells treated with PSMA-1-PDT conjugates were significantly smaller compared to the untreated tumors. This directly indicated damage to the neoplastic cells with PDT [56]. In an in vivo study in a mouse model of prostate cancer, the tumor size was reduced due to PDT. Degeneration, an increased number of apoptotic cells and partial necrosis were observed. By histological analysis, Liu et al. showed necrosis of prostate cancer cells after PDT treatment with Nano-gel-Ce6-SAHA. Inflammation of the inflammatory cells in the area of necrosis was also observed [57]. Zaak et al. observed necrosis, a reduced number of live cancer cells and an area of apoptosis and necrosis with apoptotic cells in the central part [58]. All published studies confirmed the efficacy of PDT by analyzing histological slides. Assessing PDT by MRI is an innovative way to analyze the effectiveness of PDT. In this experiment, the tissues treated with PDT had lower T₁ and T₂ values compared to tissues before the PDT treatment. The mean value for T₁ for the pre-PDT tissue was 1506.48 ± 40.07 ms and 629.31 ± 16.13 ms for the post-PDT tissue. The mean value of T₂ for the pre-PDT tissue was 110.77 ± 16.84 ms and 93.23 ± 16.87 ms for the post-PDT tissue. In research conducted by Wang et al., preparations after PDT had different T₁ and T₂ values compared to the preparations which were tested before PDT [56]. Similar results were obtained by Fei et al. [30]. Both T₁ and T₂ relaxation times decreased following PDT of prostate tissue in vitro. This may be due to the loss of water from tissue, and this effect increased as the mass of the sample size decreased. This decrease in T₁ and T₂ is not expected to occur under in vivo conditions, where processes such as edema and increased hypoxia tend to increase T₁ and T₂. In a recent study, the T₂ relaxation time measured following PDT of the brain in vivo [59] increased with a slight increase in T₁, which was attributed to tissue edema and swelling. In these experiments, loss of water from tissue was responsible for the decreases in T₁ and T₂. In agreement with this work, the literature shows that the changes in the T₁ and T₂ values before and after PDT therapy are significant, which makes MRI a non-invasive imaging method for monitoring PDT-induced changes.

4. Materials and Methods

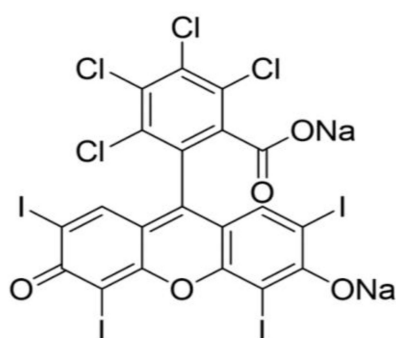
4.1. Prostate Tissue Samples

The prostate tissue samples were taken during prostatectomy at Clinical Hospital No. 1, Rzeszów, Poland. Immediately after removal, the prostate gland was evaluated in the Department of Pathomorphology, Clinical Hospital No. 1, Rzeszów, Poland. Tissues were collected from 30 patients diagnosed with advanced prostate cancer (well-differentiated prostate adenocarcinoma). As a result of the surgery, neoplastic tissue was removed along with a margin of healthy tissue. The healthy tissue margins that were collected served as controls in the experiments [60]. Controlled incisions were made, and a tissue fragment with hyperplasia features (healthy) and 2 or more tissue fragments suspected of a neoplastic lesion (diseased) were secured. Fragments with an average size of 8 × 4 × 4 mm³ were collected from the peripheral part of the organ (due to a much higher incidence of tumors in this area), and the second fragment was collected from the peripheral part of the organ with a high probability of benign nodular hypertrophy, with average dimensions of 5 × 3 × 2 mm³. The total samples collected from the 30 patients were 65 healthy and 65 neoplastic. Additionally, the healthy tissues were used as control samples. The remaining part of the prostate gland was fixed in formalin and subjected to standard histopathological evaluation. At the moment of acquiring the adenocarcinoma sample, the grade was not known but was determined later by a microscopic examination using the

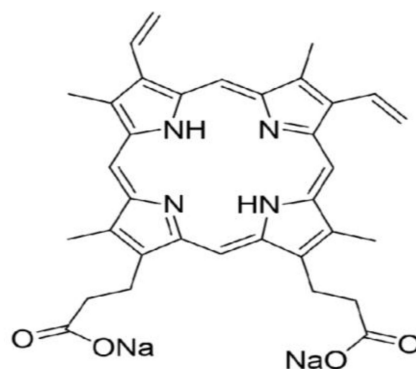
Gleason score. In this way, some samples were later identified as well-differentiated and some as poorly differentiated. For the PDT experiments, we chose samples with a Gleason score of 3 + 3 (grade 1) and 3 + 4 (grade 2) [61]. The secured tissue fragments intended for clinical trial were frozen in a cryostat at temperatures below $-17\text{ }^{\circ}\text{C}$ and then transported within 10 min to the tissue bank of the University of Rzeszów for storage at $-72\text{ }^{\circ}\text{C}$. On the day of the experiment, the tissues were thawed to room temperature [62,63]. In all cases, we did not find extended extracellular spaces or shrunken cells resulting from the freeze–thaw cycle. These features are more pronounced in tissues stored for longer durations. The study was conducted in accordance with the Helsinki Declaration and approved by the Ethics Committee of the University of Rzeszów (protocol code 9/11/2018 and date of approval: 8 November 2018).

4.2. Photosensitizers

In this experiment, the following photosensitizers were used: Rose Bengal (RB) disodium salt (95%) (Sigma Aldrich, St. Louis, MO, USA) at a concentration of 0.1 mM (5 samples were charged with 0.1 mM RB without illumination, 6 samples of 0.1 mM RB with illumination), 0 mM (5 samples, illuminated), 0.2 mM (6 samples, illuminated), 0.3 mM (6 samples, illuminated), 0.4 mM (6 samples, illuminated), and 0.5 mM (6 samples, illuminated); Protoporphyrin IX disodium salt (PpIX) (Sigma Aldrich, St. Louis, MO, USA) was used for 15 samples at a concentration of 3.0 mM PpIX with illumination, 5 samples with 3.0 mM PpIX without illumination, and 5 samples with 0 mM PpIX with illumination. The structures of RB and PpIX are depicted in Figure 6. Water for the preparation of the photosensitizer stock solutions was purified with a reverse osmosis water treatment system (AquaB Duo, Fresenius Medical Care, Singapore). The stock solutions of RB and PpIX were purged with oxygen (99%, STP & DIN Chemicals, Bielsko-Biała, Poland) for 10 min prior to their addition to the prostate tissue samples. The number of samples and the concentrations of photosensitizers used in addition to the prostate tissue samples that were either irradiated or kept in the dark are presented in Table 1.



Rose Bengal Sodium Salt



Protoporphyrin IX Disodium Salt

Figure 6. Structural formulas of photosensitizers (Rose Bengal Sodium Salt and Protoporphyrin IX Disodium Salt).

4.3. The PDT Procedure

The prostate tissue samples were individually warmed to room temperature and placed in the center of a plastic Petri dish for the addition of oxygenated photosensitizer stock solution. The stock solutions of RB (0.1 mM–0.5 mM) or PpIX (3 mM) were purged with oxygen for 10 min. Immediately after oxygenation, a volume of 0.1 mL of a given stock solution was topically spread on the tissue dropwise, allowing the solution to cover the entire surface of the prostate tissue sample. The photosensitizer-coated tissues were then covered and kept in the dark for 1 h prior to irradiation to allow the PS to penetrate into

the tissue [64,65]. After 1 h in the dark, the Petri dish containing the coated tissue samples was placed on a ring stand under a fiber optic cable that was connected to a solid-state laser via an SMA adapter and illuminated for 15 min. This distance of the light source from the tissue surface was selected to give an illumination area of $2.5 \times 2.5 \text{ cm}^2$, and the illumination of the samples did not cause the tissue to heat above $30 \text{ }^\circ\text{C}$, as measured with a CPR-411 temperature probe (Elmetron, Zabrze, Poland). The apparatus for tissue illumination is depicted in Figure 7. For the illumination of the RB-treated samples, a solid-state laser (LD Pumped All-Solid-State Green Laser, MGL-III-532 nm/300 mW, Cni Laser, Changchun, China) provided 532 nm light, and the PpIX treated samples were illuminated at 410 nm (LD Pumped All-Solid-State Green Laser, MGL-III-410 nm/300 mW, Cni Laser, Changchun, China).

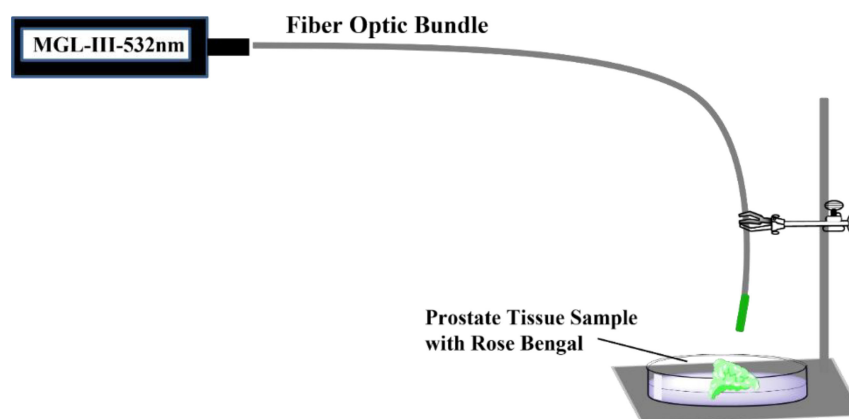


Figure 7. Experimental setup for illumination of RB-coated prostate tissue samples with an MGL-III 532 nm laser and Fiber Optic Bundle.

Immediately after 15 min of illumination, the tissue samples were cut in half, and one piece was sealed in an air-tight plastic tube for analysis by MRI, and the other was placed in a glass vial containing 10% buffered formalin solution (4% formaldehyde solution) for an eventual histopathological evaluation by microscopy. The control samples that were either treated with photosensitizer stock solution and not exposed to light or were exposed to light without photosensitizer were also divided into two pieces and stored in the same fashion.

Laser fluence was calculated using the formulas: energy [J] = power [W] \times time [s], and fluence = energy [J]/area [cm^2]. For example, 15 min (900 s) of irradiation on an area of 6.25 cm^2 with a 300 mW laser gives a fluence of 43.25 J/cm^2 .

4.4. Analysis of Prostate Tissue Samples by MRI

The spin–lattice and spin–spin relaxation times of the prostate tissue samples that were sealed in an air-tight plastic tube from the PDT procedure were measured with a 1.5 Tesla Magnetic Resonance 360 spectrometer with a dedicated transmit–receive coil (General Electric Healthcare, Milwaukee, WI, USA). For the measurements of T_1 , the repetition time-TR was tested in the range of 50–15,000 ms by gradually increasing the time. There were 12 total trials. The value of the TR time was successively selected from the range of values: 50, 100, 200, 300, 500, 1000, 1500, 2000, 3000, 5000, 10,000 and 15,000 (all measured in a time unit equal to a millisecond). The technical parameters used in the MRI examinations were the same for all stages of the examination. The scan matrix was 256×256 , and the field of view (FOV) was $6 \text{ cm} \times 6 \text{ cm}$ with a section thickness of 1 mm, spacing of 0.5 mm and NEX = 2. The echo-TE time was constant and equal to 3 ms. Maneuvering the TR-time values made it possible to obtain the fast spin-echo (FSE) sequence, on the basis of which the MR images of the tested samples and their parameters were obtained. Fast spin-echo (FSE) imaging reduces the examination time and improves SNR. The test protocol for determining the T_1 relaxation time consisted of the following steps: calibration of the system; recognition sequence—that is, locating an object in three planes (frontal, sagittal,

transverse, 3-plane); coronal sequence (T_1) of the fast spin-echo—FSE (with different values of the repetition time-TR).

For measuring the relaxation time T_2 , different spin-echo (TE) times were used. Different TE times (ranging from 1 ms to 250 ms) were used in 12 steps with the same scanning parameters, except for the repetition time, which was constant and amounted to 10,000 ms, and the echo time was in the range of 11.8–300 ms (11.8, 20, 42, 68, 85, 102, 130, 160, 200, 230, 250 ms). In this configuration, the repetition time was unchanged and amounted to 15×10^3 ms. The next steps of the measurement were the same as for the T_1 relaxation time (system calibration and recognition sequence), while step 3 was the T_2 FSE frontal sequence, not the T_1 FSE. MR scans were performed on pre-PDT and post-PDT tissues. The T_1 values could then be computed pixel-wise from a signal intensity versus a time curve fitting model. The T_2 values could then be computed pixel-wise from a signal intensity versus echo time curve fitting mode.

A region of interest (ROI) was selected in the imaged tissues to calculate the T_1 and T_2 values. The region of interest measurements were selected very close to the tissues (Figure 8).

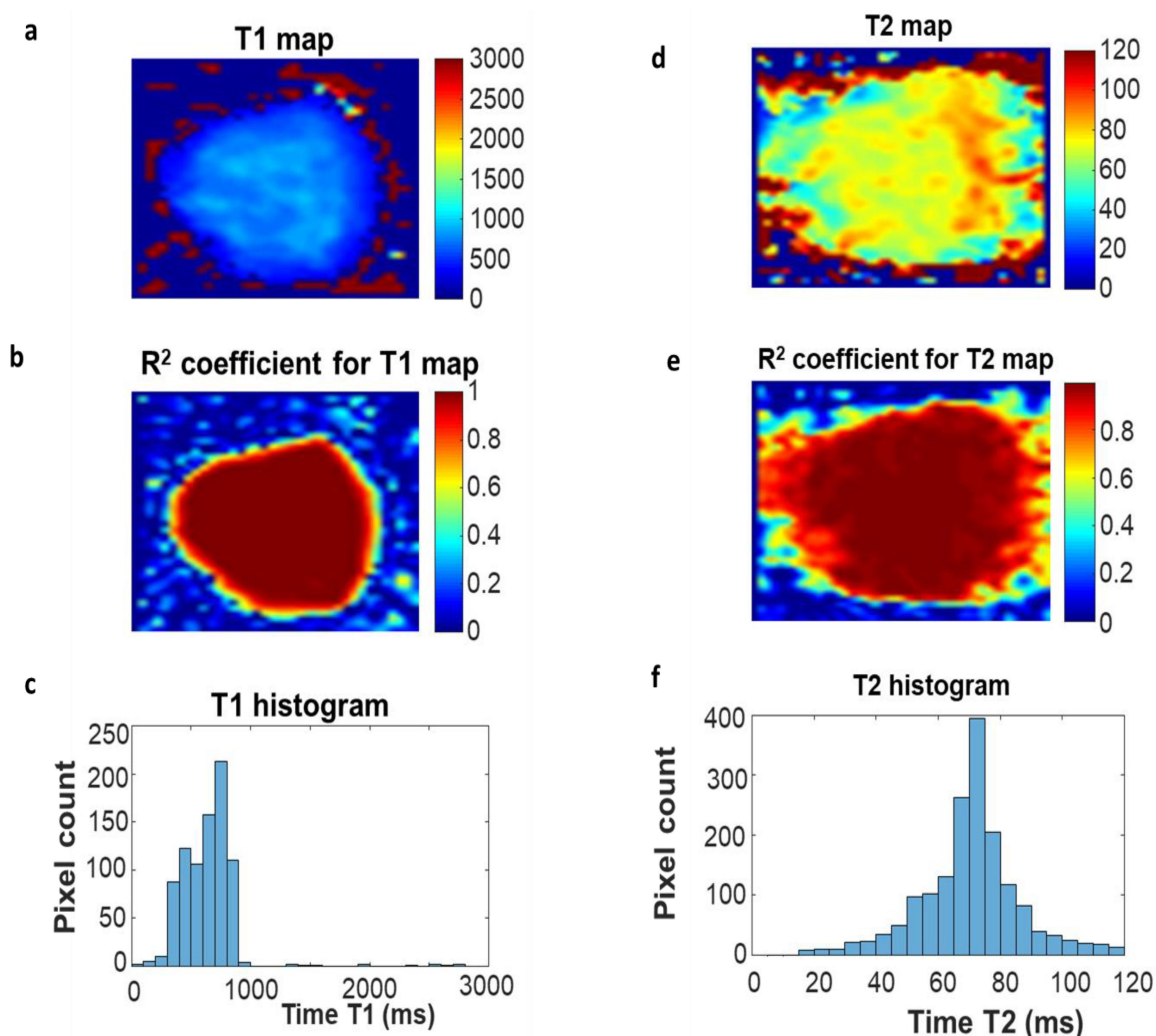


Figure 8. Selection of the area of interest for the measured samples: (a) distribution of the longitudinal relaxation time T_1 in the prostate tissue section before PDT; (b) distribution of the R^2 fit factor; (c) a histogram of the values of T_1 times determined from image (a); (d) distribution of transverse relaxation time T_2 values in a segment of the diseased tissue before PDT; (e) distribution of the R^2 fit factor; (f) a histogram of the values of T_2 times determined from the image (d).

Postprocessing was performed using a GE workstation (AW_4. 6, General Electric Healthcare, Milwaukee, WI, USA). When measuring all samples, the ROI was drawn by hand. The histograms were obtained from the marked ROI areas. On the abscissa of these graphs, the values of the longitudinal and transverse relaxation time, respectively, were recorded, while the percentage value of the signal was recorded on the ordinate axis. General Electric software AV4.6 was implemented to perform a statistical analysis of T_1 (at different TR values) and T_2 (at different TE values); the average values of the T_1 and transverse T_2 magnetization relaxation times were obtained. The signal intensity measurements were performed in the default GE software. The measuring of the intensity of the measurement was used to determine the relaxation times. The measured signal intensity (SI) for each tissue (normal, pre-PDT, and post-PDT) within the region of interest (ROI) range was used to calculate the relaxation times, T_1 and T_2 . These values were calculated in the software on the basis of the increase in the intensity of the magnetic resonance signal for T_1 relaxation and the decay of the signal for T_2 relaxation.

4.5. Statistical Significance

The data were analyzed using the Statistica 13.1 software (StatSoft Polska Sp.z o.o., Krakow, Poland). In order to compare the relaxation times, a student's *t*-test for dependent samples was used to calculate the *p*-value parameter. Values were considered significantly significant when the *p*-values were ≤ 0.05 .

4.6. Histopathological Preparations

Histological slides of the prostate tissue samples were prepared in the Clinical Department of Pathomorphology, Clinical Hospital No. 1. A tissue processor (Leica TP1020, Leica Biosystems, Deer Park, IL, USA), paraffin tissue embedder (Leica EG1150H, Leica Biosystems, Deer Park, IL, USA) and coverslipper (Leica CV5030, Leica Biosystems, Deer Park, IL, USA) were used.

The surgical material for the histopathological examinations was fixed for 24 h in a 10% buffered formalin solution (4% formaldehyde solution). After fixation of the prostate fragments, tissue sections were collected into cassettes. The tissue material from the cassettes was rinsed, dehydrated, passed through intermediate fluids and embedded in paraffin to obtain blocks. The sections were stained with hematoxylin and eosin. For this purpose, a universal device for staining the histopathological slides was used (Multistainer LEICA ST 5020, Leica Biosystems, Deer Park, IL, USA). The final step was to cover the sections with a coverslip; the space between the cover glass and the coverslip was filled with histofluid.

4.7. Microscopic Analysis

Histological image analysis was performed using a Leica DM1000 LED microscope (Leica DM1000 LED microscope, Leica Biosystems, Deer Park, IL, USA). The microscopic image unit was 100 μm . Microscopic images were obtained at magnifications of 40 \times and 100 \times .

5. Conclusions

The histopathological images of neoplastic prostate tissue samples subjected to the PDT procedure showed chromatin condensation, stromal edema and, in some cases, thrombotic necrosis accompanied by pyknotic nuclei occurred. Magnetic resonance imaging of prostate cancer tissue samples has been shown to be a helpful diagnostic tool in distinguishing pre- and post-PDT neoplastic tissue. Due to the fact that MRI provides information on the values of water relaxation times and their differences in healthy and neoplastic tissue, it is possible to assess the physico-chemical differences in tissues. The results of these experiments indicate the invaluable role of the usefulness of MRI relaxation times in tissue differentiation. The *in vitro* PDT therapy, using MRIs and histopathological analyses, enabled us to monitor the changes in neoplastic cells. It seems that the experiment may lead

to further exploration of the in vitro and in vivo monitoring of PDT by MRI. Preclinical and clinical applications of PDT have shown promising results in prostate cancer. Photodynamic approaches used in prostate cancer treatment can have severe side effects, and it is necessary to improve the treatment by developing new PSs and dosimetric analyses.

Author Contributions: Conceptualization, M.O., D.A. and D.B.-A.; methodology, M.O., D.A. and A.K.-K.; validation, A.K.-K., K.D. and D.B.-A.; formal analysis, M.O., M.K.-O. and D.A.; investigation, D.B.-A.; writing—original draft preparation, M.O., D.A., D.B.-A., K.D., A.K.-K.; writing—review and editing, D.A., M.O., K.D., A.K.-K., M.K.-O. and D.B.-A.; supervision, D.A. All authors have read and agreed to the published version of the manuscript.

Funding: This research received no external funding.

Institutional Review Board Statement: The study was conducted in accordance with the Declaration of Helsinki and approved by the Ethics Committee of the University of Rzeszów (protocol code 9/11/2018 and date of approval: 8 November 2018).

Informed Consent Statement: Informed consent was obtained from all subjects involved in the study.

Data Availability Statement: The data presented in this study are available on request from the corresponding author. The data are not publicly available due to ethical issues.

Conflicts of Interest: The authors declare no conflict of interest.

References

- Ni Raghallaigh, H.; Eeles, R. Genetic predisposition to prostate cancer: An update. *Fam. Cancer* **2022**, *21*, 101–114. [CrossRef] [PubMed]
- Cereda, V.; Falbo, P.T.; Manna, G.; Iannace, A.; Menghi, A.; Corona, M.; Semenova, D.; Calò, L.; Carnevale, R.; Frati, G.; et al. Hormonal prostate cancer therapies and cardiovascular disease: A systematic review. *Heart Fail. Rev.* **2022**, *27*, 119–134. [CrossRef] [PubMed]
- Yilmaz, M.; Toprak, T.; Suarez-Ibarrola, R.; Sigle, A.; Gratzke, C.; Miernik, A. Incidental prostate cancer after holmium laser enucleation of the prostate—A narrative review. *Andrologia* **2022**, *54*, e14332. [CrossRef] [PubMed]
- Jeong, S.H.; Kwak, C. Immunotherapy for prostate cancer: Requirements for a successful regime transfer. *Investig. Clin. Urol.* **2022**, *63*, 3–13. [CrossRef] [PubMed]
- Kamal, O.; Foster, B.R.; Young, D.J.; Hansel, D.E.; Coakley, F.V. MRI appearance of BRCA-associated prostate cancer. *Clin. Imaging* **2022**, *84*, 135–139.
- Prashar, J.; Schartau, P.; Murray, E. Supportive care needs of men with prostate cancer: A systematic review update. *Eur. J. Cancer Care* **2022**, *31*, e13541. [CrossRef]
- Osuchowski, M.; Bartusik-Aebischer, D.; Osuchowski, F.; Aebischer, D. Photodynamic therapy for prostate cancer—A narrative review. *Photodiagn. Photodyn. Ther.* **2021**, *33*, 102158. [CrossRef]
- World Health Organization. 2020. Available online: https://gco.iarc.fr/today/online-analysis-multi-bars?v=2020&mode=cancer&mode_population=countries&population=900&populations=900&key=cum_risk&sex=0&cancer=39&type=0&statistic=5&prevalence=0&population_group=0&ages_group%5B%5D=0&ages_group%5B%5D=17&nb_items=10&group_cancer=1&include_nmsc=0&include_nmsc_other=1&type_multiple=%257B%2522inc%2522%253Atrue%252C%2522mort%2522%253Afalse%252C%2522prev%2522%253Afalse%257D&orientation=horizontal&type_sort=0&type_nb_items=%257B%2522top%2522%253Atrue%252C%2522bottom%2522%253Afalse%257D (accessed on 25 February 2021).
- Merkens, L.; Sailer, V.; Lessel, D.; Janzen, E.; Greimeier, S.; Kirfel, J.; Perner, S.; Pantel, K.; Werner, S.; von Amsberg, G. Aggressive variants of prostate cancer: Underlying mechanisms of neuroendocrine transdifferentiation. *J. Exp. Clin. Cancer Res.* **2022**, *41*, 46. [CrossRef]
- Nugent, T.S.; Low, E.Z.; Fahy, M.R.; Donlon, N.E.; McCormick, P.H.; Mehigan, B.J.; Cunningham, M.; Gillham, C.; Kavanagh, D.O.; Kelly, M.E.; et al. Prostate radiotherapy and the risk of secondary rectal cancer—a meta-analysis. *Int. J. Colorectal Dis.* **2022**, *37*, 437–447. [CrossRef]
- Achard, V.; Putora, P.M.; Omlin, A.; Zilli, T.; Fischer, S. Metastatic Prostate Cancer: Treatment Options. *Oncology* **2022**, *100*, 48–59. [CrossRef]
- Ryman-Tubb, T.; Lothion-Roy, J.H.; Metzler, V.M.; Harris, A.E.; Robinson, B.D.; Rizvanov, A.A.; Jeyapalan, J.N.; James, V.H.; England, G.; Rutland, C.S.; et al. Comparative pathology of dog and human prostate cancer. *Vet. Med. Sci.* **2022**, *8*, 110–120. [CrossRef] [PubMed]
- Dougherty, T.J.; Marcus, S.L. Photodynamic therapy. *Eur. J. Cancer* **1992**, *28A*, 1734–1742. [CrossRef]
- Abrahamse, H.; Hamblin, M.R. New photosensitizers for photodynamic therapy. *Biochem. J.* **2016**, *473*, 347–364. [CrossRef] [PubMed]

15. Lui, H.; Anderson, R.R. Photodynamic therapy in dermatology. Shedding a different light on skin disease. *Arch. Dermatol.* **1992**, *128*, 1631–1636. [CrossRef] [PubMed]
16. Jori, G. Photodynamic therapy of microbial infections: State of the art and perspectives. *J. Environ. Pathol. Toxicol. Oncol.* **2006**, *25*, 505–519. [CrossRef] [PubMed]
17. Brown, S.B.; Brown, E.A.; Walker, I. The present and future role of photodynamic therapy in cancer treatment. *Lancet Oncol.* **2004**, *5*, 497–508. [CrossRef]
18. De Rosa, F.S.; Bentley, M.V. Photodynamic therapy of skin cancers: Sensitizers, clinical studies and future directives. *Pharm. Res.* **2000**, *17*, 1447–1455. [CrossRef]
19. Korbelik, M. PDT-associated host response and its role in the therapy outcome. *Lasers Surg. Med.* **2006**, *38*, 500–508. [CrossRef]
20. Lou, P.J.; Jäger, H.R.; Jones, L.; Theodossy, T.; Bown, S.G.; Hopper, C. Interstitial photodynamic therapy as salvage treatment for recurrent head and neck cancer. *Br. J. Cancer* **2004**, *91*, 441–446. [CrossRef]
21. Bown, S.G.; Rogowska, A.Z.; Whitelaw, D.E.; Lees, W.R.; Lovat, L.B.; Ripley, P.; Jones, L.; Wyld, P.; Gillams, A.; Hatfield, A.W. Photodynamic therapy for cancer of the pancreas. *Gut* **2002**, *50*, 549–557. [CrossRef]
22. Marberger, M.; Carroll, P.R.; Zelefsky, M.J.; Coleman, J.A.; Hricak, H.; Scardino, P.T.; Abenhaim, L.L. New treatments for localized prostate cancer. *Urology* **2008**, *72*, S36–S43. [CrossRef] [PubMed]
23. Azzouzi, A.R.; Lebdaï, S.; Benzaghrou, F.; Stief, C. Vascular-targeted photodynamic therapy with TOOKAD[®] Soluble in localized prostate cancer: Standardization of the procedure. *World J. Urol.* **2015**, *33*, 937–944. [CrossRef] [PubMed]
24. Allison, R.R.; Moghissi, K. Photodynamic Therapy (PDT): PDT Mechanisms. *Clin. Endosc.* **2013**, *46*, 24–29. [CrossRef]
25. Yano, T.; Wang, K.K. Photodynamic Therapy for Gastrointestinal Cancer. *Photochem. Photobiol.* **2020**, *96*, 517–523. [CrossRef] [PubMed]
26. Zhang, X.; Li, G.; Wu, D.; Li, X.; Hu, N.; Chen, J.; Chen, G.; Wu, Y. Recent progress in the design fabrication of metal-organic frameworks-based nanozymes and their applications to sensing and cancer therapy. *Biosens. Bioelectron.* **2019**, *137*, 178–198. [CrossRef] [PubMed]
27. Zhang, C.; Chen, W.; Zhang, T.; Jiang, X.; Hu, Y. Hybrid nanoparticle composites applied to photodynamic therapy: Strategies and applications. *J. Mater. Chem. B* **2020**, *8*, 4726–4737. [CrossRef] [PubMed]
28. Khoo, V.S.; Joon, D.L. New developments in MRI for target volume determination in radiotherapy. *Fr. J. Radiol.* **2006**, *79*, S2–S15. [CrossRef] [PubMed]
29. Colafati, G.S.; Voicu, I.P.; Carducci, C.; Miele, E.; Carai, A.; Di Loreto, S.; Marrazzo, A.; Cacchione, A.; Cecinati, V.; Tornesello, A.; et al. MRI features as a helpful tool to predict the molecular subgroups of medulloblastoma: State of the art. *Ther. Adv. Neurol. Disord.* **2018**, *11*, 1756286418775375. [CrossRef]
30. Fei, B.; Wang, H.; Meyers, J.D.; Feyes, D.K.; Oleinick, N.L.; Duerk, J.L. High-field magnetic resonance imaging of the response of human prostate cancer to Pc 4-based photodynamic therapy in an animal model. *Lasers Surg. Med.* **2007**, *39*, 723–730. [CrossRef]
31. Sandgren, K.; Nilsson, E.; Keeratijarut Lindberg, A.; Strandberg, S.; Blomqvist, L.; Bergh, A.; Frederick, B.; Axelsson, J.; Ögren, M.; Ögren, M.; et al. Registration of Histopathology for Magnetic Resonance Imaging of Prostate Cancer. *Phys. Imaging Radiat. Oncol.* **2021**, *18*, 19–25. [CrossRef]
32. Popita, C.; Popita, A.R.; Sitar-Taut, A.; Petrut, B.; Fetica, B.; Coman, I. 1.5-Tesla Multiparametric-Magnetic Resonance Imaging for the detection of clinically significant prostate cancer. *Clujul. Med.* **2017**, *90*, 40–48. [PubMed]
33. Fütterer, J.J.; Briganti, A.; De Visschere, P.; Emberton, M.; Giannarini, G.; Kirkham, A.; Taneja, S.S.; Thoeny, H.; Villeirs, G.; Villers, A. Can Clinically Significant Prostate Cancer Be Detected with Multiparametric Magnetic Resonance Imaging? A Systematic Review of the Literature. *Eur. Urol.* **2015**, *68*, 1045–1053. [CrossRef] [PubMed]
34. Haaf, P.; Garg, P.; Messroghli, D.; Broadbent, D.; Greenwood, J.; Plein, S. Cardiac T1 Mapping and Extracellular Volume (ECV) in Clinical Practice: A Comprehensive Review. *J. Cardiovasc. Magn. Reson.* **2016**, *18*, 8. [CrossRef] [PubMed]
35. Kim, P.K.; Hong, Y.J.; Im, D.J.; Suh, Y.J.; Park, C.H.; Kim, J.Y.; Chang, S.; Lee, H.J.; Hur, J.; Kim, Y.J.; et al. Myocardial T1 and T2 Mapping: Techniques and Clinical Applications. *Korean J. Radiol.* **2017**, *18*, 113–131. [CrossRef] [PubMed]
36. Hamblin, M.R.; Newman, E.L. On the mechanism of the tumour-localising effect in photodynamic therapy. *J. Photochem. Photobiol. B* **1994**, *23*, 3–8. [CrossRef]
37. Maeda, H.; Nakamura, H.; Fang, J. The epr effect for macromolecular drug delivery to solid tumors: Improvement of tumor uptake, lowering of systemic toxicity, and distinct tumor imaging in vivo. *Adv. Drug Deliv. Rev.* **2013**, *65*, 71–79. [CrossRef] [PubMed]
38. Boyle, R.W.; Dolphin, D. Structure and biodistribution relationships of photodynamic sensitizers. *Photochem. Photobiol.* **1996**, *64*, 469–485. [CrossRef]
39. Karthikeyan, K.; Babu, A.; Kim, S.J.; Murugesan, R.; Jeyasubramanian, K. Enhanced photodynamic efficacy and efficient delivery of Rose Bengal using nanostructured poly(amidoamine) dendrimers: Potential application in photodynamic therapy of cancer. *Cancer Nanotechnol.* **2011**, *2*, 95–103. [CrossRef]
40. Xu, H.; Sun, Y.; Zhang, Y.; Wang, W.; Dan, J.; Yao, J.; Chen, H.; Tian, F.; Sun, X.; Guo, S.; et al. Protoporphyrin IX Induces a Necrotic Cell Death in Human THP-1 Macrophages through Activation of Reactive Oxygen Species/c-Jun N-Terminal Protein Kinase Pathway and Opening of Mitochondrial Permeability Transition Pore. *Cell. Physiol. Biochem.* **2014**, *34*, 1835–1848. [CrossRef]
41. Panzarini, E.; Inguscio, V.; Dini, L. Overview of Cell Death Mechanisms Induced by Rose Bengal Acetate-Photodynamic Therapy. *Int. J. Photoenergy* **2011**, *2011*, 713726. [CrossRef]

42. Chung, J.; Chen, C.; Paw, B.H. Heme metabolism and erythropoiesis. *Curr. Opin. Hematol.* **2012**, *19*, 156–162. [CrossRef]
43. Li, Y.; Wang, P.; Zhao, P.; Zhu, S.; Wang, X.; Liu, Q. Apoptosis induced by sonodynamic treatment by protoporphyrin ix on mda-mb-231 cells. *Ultrasonics* **2012**, *52*, 490–496. [CrossRef] [PubMed]
44. Brieger, K.; Schiavone, S.; Miller, F.J., Jr.; Krause, K.H. Reactive oxygen species: From health to disease. *Swiss Med. Wkly.* **2012**, *142*, w13659. [CrossRef] [PubMed]
45. Sander, W.J.; Fourie, C.; Sabiu, S.; O'Neill, F.H.; Pohl, C.H.; O'Neill, H.G. Reactive oxygen species as potential antiviral targets. *Rev. Med. Virol.* **2022**, *32*, e2240. [CrossRef] [PubMed]
46. Sugita, N.; Iwase, Y.; Yumita, N.; Ikeda, T.; Umemura, S. Sonodynamically induced cell damage using rose bengal derivative. *Anticancer Res.* **2010**, *30*, 3361–3366. [PubMed]
47. Sugita, N.; Kawabata, K.; Sasaki, K.; Sakata, I.; Umemura, S. Synthesis of amphiphilic derivatives of rose bengal and their tumor accumulation. *Bioconjug. Chem.* **2007**, *18*, 866–873. [CrossRef] [PubMed]
48. Eggener, S.E.; Coleman, J.A. Focal treatment of prostate cancer with vascular-targeted photodynamic therapy. *ScientificWorldJournal* **2008**, *8*, 963–973. [CrossRef]
49. Kato, H.; Ono, J.; Konaka, C.; Kawate, N.; Yoneyama, K.; Kinoshita, K.; Nishimiya, K.; Sakai, H.; Noguchi, M.; Tomono, T.; et al. Clinical measurement of tumor fluorescence using a new diagnostic system with hematoporphyrin derivative, laser photoradiation, and a spectroscope. *Lasers Surg. Med.* **1984**, *4*, 49–58. [CrossRef] [PubMed]
50. Chung, P.S.; Ahn, J.C.; Lee, S.J.; Peijie, H.E.; Moon, J.H. Effect of Photodynamic Therapy in Melanoma Skin Cancer Cell Line A375: In vivo Study Crossref. *Med. Laser* **2014**, *3*, 27–30. [CrossRef]
51. Qiu, H.; Kim, M.M.; Penjweini, R.; Finlay, J.C.; Busch, T.M.; Wang, T.; Guo, W.; Cengel, K.A.; Simone, C.B.; Glatstein, E.; et al. A Comparison of Dose Metrics to Predict Local Tumor Control for Photofrin-mediated Photodynamic Therapy. *Photochem. Photobiol.* **2017**, *93*, 1115–1122. [CrossRef]
52. Huang, Z. A review of progress in clinical photodynamic therapy. *Technol. Cancer Res. Treat.* **2005**, *4*, 283–293. [CrossRef] [PubMed]
53. Chang, J.E.; Liu, Y.; Lee, T.H.; Lee, W.K.; Yoon, I.; Kim, K. Tumor Size-Dependent Anticancer Efficacy of Chlorin Derivatives for Photodynamic Therapy. *Int. J. Mol. Sci.* **2018**, *19*, 1596. [CrossRef] [PubMed]
54. Pigula, M.; Huang, H.C.; Mallidi, S.; Anbil, S.; Liu, J.; Mai, Z.; Hasan, T. Size-dependent Tumor Response to Photodynamic Therapy and Irinotecan Monotherapies Revealed by Longitudinal Ultrasound Monitoring in an Orthotopic Pancreatic Cancer Model. *Photochem. Photobiol.* **2019**, *95*, 378–386. [CrossRef] [PubMed]
55. Zaak, D.; Sroka, R.; Höppner, M.; Khoder, W.; Reich, O.; Tritschler, S.; Muschter, R.; Knüchel, R.; Hofstetter, A. Photodynamic therapy by means of 5-ALA induced PPIX in human prostate—Preliminary results. *Med. Laser Appl.* **2003**, *18*, 91–95. [CrossRef]
56. Wang, X.; Tsui, B.; Ramamurthy, G.; Zhang, P.; Meyers, J.; Kenney, M.E.; Kiechle, J.; Ponsky, L.; Basilion, J.P. Theranostic Agents for Photodynamic Therapy of Prostate Cancer by Targeting Prostate-Specific Membrane Antigen. *Mol. Cancer Ther.* **2016**, *15*, 1834–1844. [CrossRef] [PubMed]
57. Liu, N.; Liu, H.; Chen, H.; Wang, G.; Teng, H.; Chang, Y. Polyphotosensitizer nanogels for GSH-responsive histone deacetylase inhibitors delivery and enhanced cancer photodynamic therapy. *Colloids Surf. B Biointerfaces* **2020**, *188*, 110753. [CrossRef] [PubMed]
58. Zaak, D.; Sroka, R.; Stocker, S.; Bise, K.; Lein, M.; Höppner, M.; Frimberger, D.; Schneede, P.; Reich, O.; Kriegmair, M.; et al. Photodynamic therapy of prostate cancer by means of 5-aminolevulinic acid-induced protoporphyrin IX—In vivo experiments on the dunning rat tumor model. *Urol. Int.* **2004**, *72*, 196–202. [CrossRef] [PubMed]
59. Wang, H.; Fei, B. Diffusion-weighted MRI for monitoring tumor response to photodynamic therapy. *J. Magn. Reson. Imaging* **2010**, *32*, 409–417. [CrossRef]
60. Sooriakumaran, P.; Dev, H.S.; Skarecky, D.; Ahlering, T. The importance of surgical margins in prostate cancer. *J. Surg. Oncol.* **2016**, *113*, 310–315. [CrossRef]
61. Mottet, N.; van den Bergh, R.C.N.; Briers, E.; Van den Broeck, T.; Cumberbatch, M.G.; De Santis, M.; Fanti, S.; Fossati, N.; Gandaglia, G.; Gillessen, S.; et al. EAU-EANM-ESTRO-ESUR-SIOG Guidelines on Prostate Cancer-2020 Update. Part 1: Screening, Diagnosis, and Local Treatment with curative intent. *Eur. Urol.* **2021**, *79*, 243–262. [CrossRef] [PubMed]
62. Hubel, A.; Spindler, R.; Skubit, A.P. Storage of human biospecimens: Selection of the optimal storage temperature. *Biopreserv. Biobank.* **2014**, *12*, 165–175. [CrossRef] [PubMed]
63. Esteva-Socias, M.; Artiga, M.-J.; Bahamonde, O.; Belar, O.; Bermudo, R.; Castro, E.; Escámez, T.; Fraga, M.; Jauregui-Mosquera, L.; Novoa, I.; et al. In search of an evidence-based strategy for quality assessment of human tissue samples: Report of the tissue Biospecimen Research Working Group of the Spanish Biobank Network. *J. Transl. Med.* **2019**, *17*, 370. [CrossRef] [PubMed]
64. Mesquita, M.Q.; Ferreira, A.R.; Neves, M.d.G.P.M.S.; Ribeiro, D.; Fardilha, M.; Faustino, M.A.F. Photodynamic therapy of prostate cancer using porphyrinic formulations. *J. Photochem. Photobiol. B Biol.* **2021**, *223*, 112301. [CrossRef] [PubMed]
65. Martinez de Pinillos Bayona, A.; Woodhams, J.H.; Pye, H.; Hamoudi, R.A.; Moore, C.M.; MacRobert, A.J. Efficacy of photochemical internalisation using disulfonated chlorin and porphyrin photosensitisers: An in vitro study in 2D and 3D prostate cancer models. *Cancer Lett.* **2017**, *393*, 68–75. [CrossRef] [PubMed]



Article

Transcription Factor MAFB as a Prognostic Biomarker for the Lung Adenocarcinoma

Omar Samir ^{1,2}, Naohiro Kobayashi ³, Tepei Nishino ^{4,5}, Mennatullah Siyam ⁴, Manoj Kumar Yadav ^{4,6}, Yuri Inoue ^{4,7}, Satoru Takahashi ^{1,4,8,9,*} and Michito Hamada ^{1,4,*}

- ¹ Laboratory Animal Resource Center in Transborder Medical Research Center, Faculty of Medicine, University of Tsukuba, 1-1-1 Tennodai, Tsukuba 305-8575, Japan
- ² Department of Pathology, Faculty of Veterinary Medicine, Mansoura University, Mansoura 35516, Egypt
- ³ Department of General Thoracic Surgery, Faculty of Medicine, University of Tsukuba, 1-1-1 Tennodai, Tsukuba 305-8575, Japan
- ⁴ Department of Anatomy and Embryology, Faculty of Medicine, University of Tsukuba, 1-1-1 Tennodai, Tsukuba 305-8575, Japan
- ⁵ Department of Medical Education and Training, Tsukuba Medical Center Hospital, 1-3-1 Amakubo, Tsukuba 305-8558, Japan
- ⁶ Ph.D. Program in Human Biology, School of Integrative and Global Majors, University of Tsukuba, 1-1-1 Tennodai, Tsukuba 305-8575, Japan
- ⁷ Doctoral Program in Biomedical Sciences, Graduate School of Comprehensive Human Sciences, University of Tsukuba, 1-1-1 Tennodai, Tsukuba 305-8575, Japan
- ⁸ International Institute for Integrative Sleep Medicine (WPI-IIS), University of Tsukuba, 1-1-1 Tennodai, Tsukuba 305-8575, Japan
- ⁹ Life Science Center for Survival Dynamics, Tsukuba Advanced Research Alliance (TARA), University of Tsukuba, 1-1-1 Tennodai, Tsukuba 305-8577, Japan
- * Correspondence: satoruta@md.tsukuba.ac.jp (S.T.); hamamichi@md.tsukuba.ac.jp (M.H.); Tel.: +81-298-53-7516 (S.T.); +81-298-53-7516 (M.H.); Fax: +81-298-53-6965 (S.T.); +81-298-53-6965 (M.H.)

Citation: Samir, O.; Kobayashi, N.; Nishino, T.; Siyam, M.; Yadav, M.K.; Inoue, Y.; Takahashi, S.; Hamada, M. Transcription Factor MAFB as a Prognostic Biomarker for the Lung Adenocarcinoma. *Int. J. Mol. Sci.* **2022**, *23*, 9945. <https://doi.org/10.3390/ijms23179945>

Academic Editors: Dmitry Aminin and David Mu

Received: 25 July 2022

Accepted: 29 August 2022

Published: 1 September 2022

Publisher's Note: MDPI stays neutral with regard to jurisdictional claims in published maps and institutional affiliations.



Copyright: © 2022 by the authors. Licensee MDPI, Basel, Switzerland. This article is an open access article distributed under the terms and conditions of the Creative Commons Attribution (CC BY) license (<https://creativecommons.org/licenses/by/4.0/>).

Abstract: MAFB is a basic leucine zipper (bZIP) transcription factor specifically expressed in macrophages. We have previously identified MAFB as a candidate marker for tumor-associated macrophages (TAMs) in human and mouse models. Here, we analyzed single-cell sequencing data of patients with lung adenocarcinoma obtained from the GEO database (GSE131907). Analyzed data showed that general macrophage marker CD68 and macrophage scavenger receptor 1 (CD204) were expressed in TAM and lung tissue macrophage clusters, while transcription factor MAFB was expressed specifically in TAM clusters. Clinical records of 120 patients with lung adenocarcinoma stage I ($n = 57$), II ($n = 21$), and III ($n = 42$) were retrieved from Tsukuba Human Tissue Biobank Center (THB) in the University of Tsukuba Hospital, Japan. Tumor tissues from these patients were extracted and stained with anti-human MAFB antibody, and then MAFB-positive cells relative to the tissue area (MAFB⁺ cells/tissue area) were morphometrically quantified. Our results indicated that higher numbers of MAFB⁺ cells significantly correlated to increased local lymph node metastasis (nodal involvement), high recurrence rate, poor pathological stage, increased lymphatic permeation, higher vascular invasion, and pleural infiltration. Moreover, increased amounts of MAFB⁺ cells were related to poor overall survival and disease-free survival, especially in smokers. These data indicate that MAFB may be a suitable prognostic biomarker for smoker lung cancer patients.

Keywords: biomarker; cancer severity; cancer prognosis; MAFB; tumor-associated macrophages

1. Introduction

V-maf musculoaponeurotic fibrosarcoma oncogene homolog B (MAFB) belongs to the large Maf transcription factor family and is a bzip transcription factor that regulates target gene expression [1]. *Mafb* is expressed in several tissues and is associated with the differentiation of various cell types, such as kidney podocytes [2], keratinocytes [3], and pancreatic α -cells and β -cells [3,4].

In the hematopoietic cell lineage, a transcriptome analysis using multi-dendritic cell (DC) and macrophage subsets showed that the expression of *Mafb* is associated specifically with monocyte-macrophage lineage and not DC lineage [5]. An increase in *Mafb* expression was observed in anti-inflammatory M2-type macrophages in vitro [6]. Moreover, MAFB in macrophages plays an essential role in resolving inflammation in ischemic conditions, efferocytosis preventing autoimmunity, and inhibiting macrophage apoptosis in atherogenic conditions [7–9], indicating that MAFB regulates the homeostatic function of macrophages. Lung alveolar macrophages (AM) express a low level of MAFB [5]; however, exposure to cigarette smoke progressively increased the expression of *Mafb* in a mouse model [10]. Even though patients with chronic obstructive pulmonary disease also exhibit increased *Mafb* expression [11], the relationship between exposure to cigarette smoke, *Mafb* expression, and lung cancer remains largely unidentified.

Tumor-associated macrophages (TAM) are the major cell populations of the tumor microenvironment (TME) and promote tumor progression, metastasis, angiogenesis, and resistance to therapy [12]. A higher infiltration of TAMs is often associated with a high mortality rate in various cancers [13]. M2 macrophage markers such as CD163, CD68, CD206, and CD204 are TAM markers that are widely used to assess cancer progression [14]. However, distinguishing M1 and M2 macrophages within the TAM in vivo remains challenging [15]. Consistent with this, CD163 and CD206 are reported to be expressed on M1-like TAMs or DCs that stimulate T cell activity in gastrointestinal tumors and ovarian ascites [16,17]. CD204 is also expressed in dendritic cells [18] in angioblastic T cell lymphoma (AITL); however, CD204 was not expressed in TAM [19]. Even though CD68, CD163, and CD204 have been widely used to assess the severity and outcome of human cancers [14,20], opinion on what constitutes the definitive TAM marker remains controversial.

We have previously reported *Mafb* expression in M2-type TAMs in a mouse tumor model of Lewis lung carcinoma. Furthermore, we have shown a significant upregulation of MAFB in human lung carcinomas (stage I and stage III) [21]. However, the lack of expression of *Mafb* in AM, along with its cigarette smoke-induced increase in expression [5,10], led us to hypothesize that MAFB could be a potential TAM marker for lung cancer. Here, we analyzed the single-cell RNA sequence (scRNA-seq) data of human lung cancer previously reported to exhibit a lack of MAFB expression in AM but expressed specifically in another macrophage lineage. Further, the lung tissue of 120 patients with lung cancer was immunostained using an anti-MAFB antibody, and the association between MAFB and cancer-related parameters was analyzed. Our results indicated that *Mafb* is highly specific for TAM and is a potential prognostic marker. Moreover, MAFB was also identified as a prognostic marker that can predict the risk of mortality among smoker patients.

2. Results

2.1. MAFB Is Specifically Expressed in Monocytes/Macrophages but Not Alveolar Macrophages in Both Normal and Cancerous Tissue

It has been shown that in a mouse model, *Mafb* is not expressed in AM [5]. Expecting the same for humans, MAFB may be a more specific TAM marker in lung cancer than other M2 macrophage markers. Therefore, we compared the distribution of MAFB and other macrophage markers, *CD68* and *CD204*, using scRNA sequencing data of lung cancer patients, including normal lung, tumor tissue (stage I and III, $n = 7$), and advanced tumor tissue (stage IV, $n = 4$), as reported by Kim et al. (GSE131907) [22]. There were 34 clusters in all samples (Figure S2A). The myeloid series was extracted and analyzed using myeloid markers, *LYZ*, *MARCO*, *CD68*, and *FCGR3A* (Figure S2B). The extracted myeloid population had 18 (labeled 0–17) clusters, which were classified according to the expression of marker genes into AM, (cluster 0, 4, 10, 15), ML (cluster 2, 3, 5, 6, 9, 11, 13, 16), Mo (cluster 1, 8), and DC (cluster 7, 12, 14, 17) (Figures 1A and S3A). Interestingly, all macrophage populations were identified in normal lung, tumor, and advanced tumor samples. AM was found in cancer tissue; however, the number of AM decreased with advancement in cancer stage (Figure 1B).

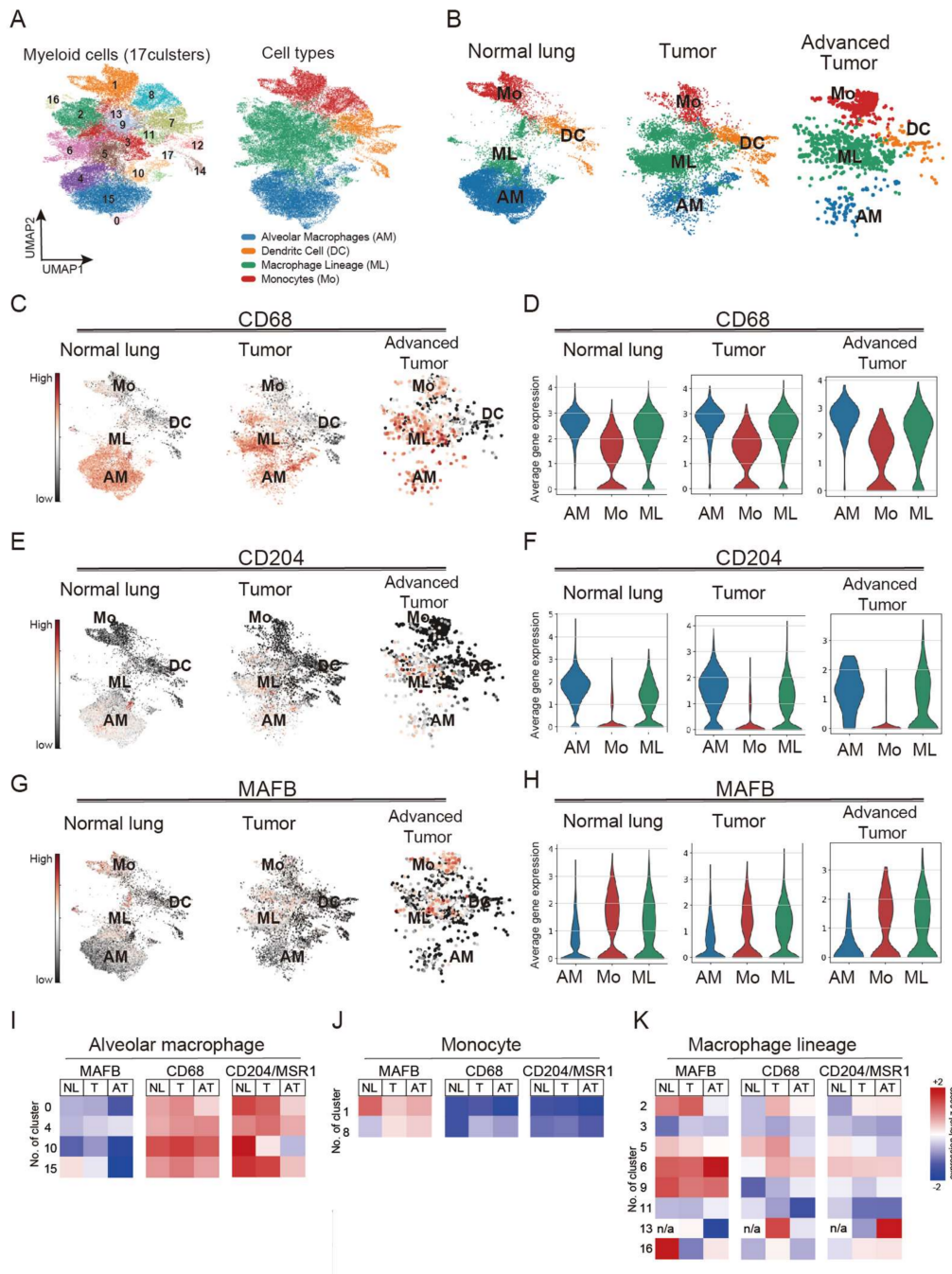


Figure 1. Single-cell RNA sequencing (scRNA-seq) analysis obtained from 44 patients with treatment-naive lung adenocarcinoma. Single-cell RNA raw data included normal lung tissue ($n = 11$), tumor tissue (stage I and III, $n = 7$), and advanced tumor tissue (stage IV, $n = 4$). Raw data were downloaded and processed using `sctransform` function in Seurat (v3). (A) Identified 17 clusters of the myeloid population. (B) monocytes (Mo), alveolar macrophages (AM), macrophages lineage (ML), and dendritic cells (DC) cluster distribution in normal lung tissues, tumors, and advanced tumors. (C,D) CD68 expression pattern in normal lung tissues, tumor, and advanced tumor. (E,F) CD204 expression pattern in normal lung tissues, tumor, and advanced tumor. (G,H) MAFB expression pattern in normal lung tissues, tumor, and advanced tumor. (I) Heatmap analysis of the expression of MAFB, CD68, and CD204 in AM. (J) Heatmap analysis of the expression of MAFB, CD68, and CD204 in monocytes. (K) Heatmap analysis of the expression of MAFB, CD68, and CD204 in macrophage lineage.

We further analyzed the expression patterns of *CD68* and *CD204* in normal lung and cancer tissues. Our results showed that *CD68* was expressed in ML and Mo clusters in normal lung and cancer tissues; however, strongly expressed in AM clusters (Figure 1C,D). *CD204* was also expressed in the ML clusters in tumor tissues and the AM clusters (Figure 1E,F). Compared to *CD68* and *CD204*, *MAFB* was markedly less expressed in AM and specifically expressed in ML and Mo in all data from normal lung and cancer tissues (Figure 1G,H). A heatmap analysis confirmed *MAFB* expression in myeloid clusters, and the results showed lower *MAFB* expression in all the AM clusters (0, 4, 10, 15) compared with expression levels of *CD68* and *CD204* (Figure 1I). A higher level of *MAFB* expression was observed in the Mo cluster, than *CD68* and *CD204*, suggesting that *MAFB* is expressed in infiltrating monocytes (Figure 1J). Consistently, the expression pattern of *CCR2*, a chemokine receptor for monocytes, was similar to that of *MAFB* in the monocyte clusters (Figure S3B). In the ML, *MAFB*, *CD68*, and *CD204* were all expressed in clusters 2, 5, and 6 of the stage I samples, while cluster 9 showed strong expression of *MAFB*. As for cluster 13, *CD68* was strongly expressed in stage I and *CD204* in the advanced tumor, but *MAFB* was not expressed (Figure 1K). These results indicate that *MAFB*, *CD68*, and *CD204* could be identified as markers of TAM but have different expression patterns among subsets of human macrophages.

2.2. Higher *MAFB*⁺ Cell Density May Be Associated with Poor Clinical Prognosis among Lung Cancer Patients

Cancer diagnostic TAM markers, *CD68*, *CD204*, *CD206*, and *CD163*, are expressed on lung tissue AM (Figures 1 and S3C); however, the poor *MAFB* expression on AM might significantly impact the assessment of cancer progression using TAM as an indicator. Therefore, to investigate whether the density of *MAFB*-positive cells is related to the clinical features of the tumor, we collected and analyzed cancer tissues from 120 patients with lung adenocarcinoma with or without nodal involvement (stage I, II, and III) admitted to the Tsukuba University Hospital between 2010 and 2019 (Table S1). The cancer tissues were immunostained using an anti-*MAFB* antibody, and the number of *MAFB*-positive cells relative to the tissue area was counted. The patients were ranked according to the *MAFB*⁺ cell density into low (25%) (low-*MAFB*⁺ group; $n = 30$, *MAFB*⁺ density ≤ 0.005), mid (49%) (mid *MAFB*⁺ group; $n = 59$, *MAFB*⁺ density = 0.006–0.016), and the higher (26%) (high-*MAFB*⁺ group; $n = 31$, *MAFB*⁺ density ≥ 0.017). The signals of *MAFB* staining differed significantly in each group (Figure 2A,B). Moreover, the high-*MAFB*⁺ group presented with significantly large tumors (Figure 2C). The correlation between the three groups, low-, mid-, and high- *MAFB*⁺ cell density with the recorded clinical features of the patients was analyzed using Fisher's exact test (Table 1).

The patients did not differ significantly in age < 70 years versus ≥ 70 years ($p = 0.22$), or smoking status (p -value = 0.30). The female-to-male ratios were significantly different in the mid-*MAFB*⁺ group (male: female, 21:38) and the high-*MAFB*⁺ group (male:female, 20:11, $p < 0.03$). No significant association between smoking habits and the *MAFB* cell population was identified; however, patients with smoking habits tended to cluster more in the high-*MAFB*⁺ group (never: former/current, 8:23). Most of the patients with stage I adenocarcinoma were grouped into the low-*MAFB*⁺ (stage I: stage III, 24:6), while a significant number of patients with stage III adenocarcinoma were grouped into the high-*MAFB*⁺ group (stage I:stage III, 3:28, $p < 0.01$). Similarly, clinical characteristics related to cancer recurrence, including nodal involvement, lymphatic permeation, and vessel invasion, were lower in tissues with low-*MAFB*⁺, while the high-*MAFB*⁺ group showed a significant correlation. Most of the tissues with low-*MAFB*⁺ showed no pleural infiltration. These findings suggest that higher *MAFB*⁺ cell density may be associated with poor clinical prognosis among patients with stages I, II, and III lung adenocarcinoma.

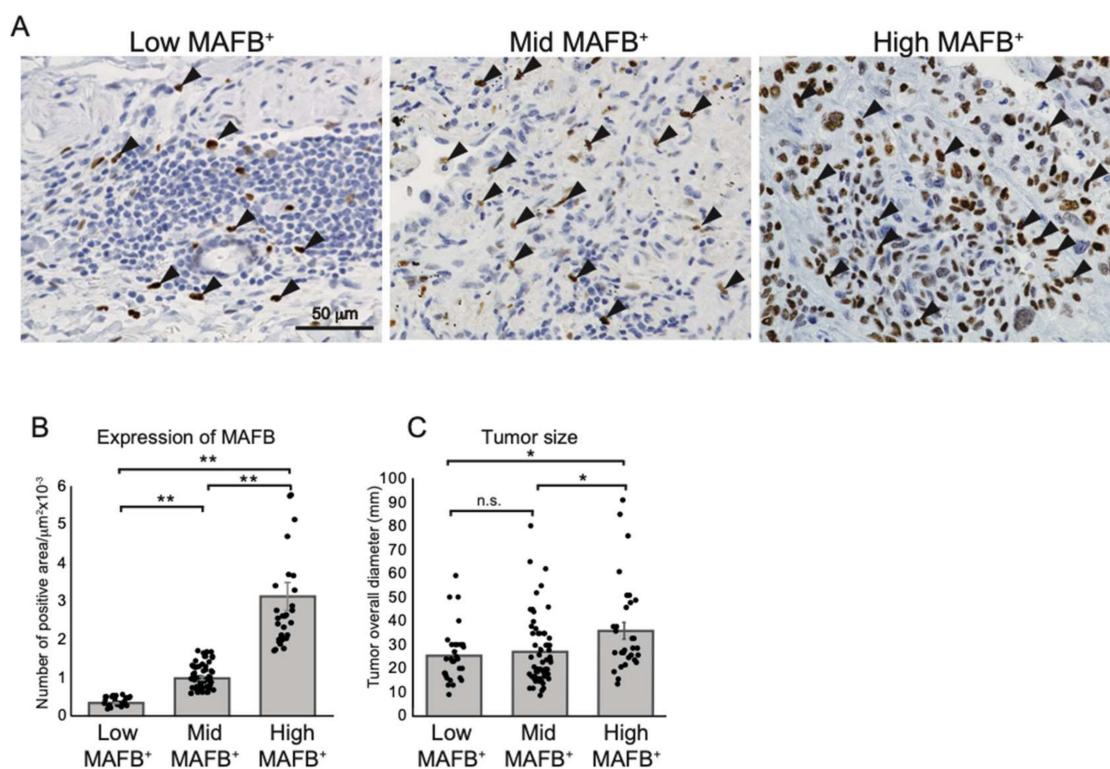


Figure 2. Grouping non-metastatic lung adenocarcinoma tissue according to MAFB⁺ cells density. (A) Representative data of immunohistochemical analysis of human lung adenocarcinomas with anti-human MAFB. Arrows point out the MAFB-positive cells. (B) MAFB-positive area relative to tissue area (MAFB/tissue area) was morphometrically quantified. Tissue samples were grouped into top 25% (high-MAFB⁺ group, MAFB expression area/tissue area = 0–0.005 (*n* = 30)), 25–50% (mid-MAFB⁺ group, MAFB expression area/tissue area = 0.006–0.016 (*n* = 59)), and bottom 25% (low-MAFB⁺ group, MAFB expression area/tissue area = 0.017–0.121 (*n* = 31)). (C) MAFB expression in three groups was tested for correlation to tumor sizes. Data are presented as means ± SEM; data is considered significant at * *p* < 0.05, ** *p* < 0.01.

Table 1. Correlation between MAFB⁺ cell density and the clinicopathological factors in non-metastatic lung adenocarcinoma.

Variables	Low-MAFB ⁺ (≤0.005) No of Case <i>n</i> = 30 (25%)	Mid-MAFB ⁺ (0.006–0.016) No of Case <i>n</i> = 59 (49%)	High-MAFB ⁺ (≥0.017) No of Case <i>n</i> = 31 (26%)	<i>p</i> -Value of Fisher’s Exact Test
Age (y)				
<70	20 (67%)	39 (66%)	15 (48%)	0.2249
≥70	10 (33%)	20 (34%)	16 (52%)	
Gender				
Male	15 (50%)	21 (36%) *	20 (65%) *	0.0302
Female	15 (50%)	38 (64%) *	11 (35%) *	
Smoking history				
Never	12 (40%)	25 (42%)	8 (26%)	0.3046
Former or current	18 (60%)	34 (58%)	23 (74%)	
Clinical Stage				
I (<i>n</i> = 57)	24 (42%) ***	30 (53%)	3 (5%) ***	<0.001
II + III (<i>n</i> = 63)	6 (10%) ***	29 (46%)	28 (44%) ***	

Table 1. Cont.

Variables	Low-MAFB ⁺ (≤ 0.005) No of Case $n = 30$ (25%)	Mid-MAFB ⁺ (0.006–0.016) No of Case $n = 59$ (49%)	High-MAFB ⁺ (≥ 0.017) No of Case $n = 31$ (26%)	<i>p</i> -Value of Fisher's Exact Test
Cancer Recurrence				
Negative	22 (73%) *	33 (56%)	10 (32%) *	0.006
Positive	8 (27%) *	26 (44%)	21 (68%) *	
Nodal involvement				
Negative (N–)	24 (80%) ***	32 (54%)	4 (13%) ***	<0.0001
Positive (N+)	6 (20%) ***	27 (46%)	27 (87%) ***	
Lymphatic permeation				
Ly(–)	26 (87%) ***	34 (58%)	12 (39%) **	<0.001
Ly(+)	4 (13%) ***	25 (42%)	19 (61%) **	
Vessel invasion				
V(–)	23 (77%) ***	26 (44%)	5 (16%) ***	<0.0001
V(+)	7 (23%) ***	33 (56%)	26 (84%) ***	
Pleural infiltration				
PL(–)	23 (77%) *	31 (53%)	13 (42%)	0.019
PL(+)	7 (23%) *	28 (47%)	18 (58%)	

According to density of cells expressing MAFB, 120 lung adenocarcinoma patients with stages I, II, and III were grouped into low-MAFB⁺, mid-MAFB⁺, and high-MAFB⁺ cell density groups. Correlation between MAFB expression and clinical factors among groups was recorded and statistically analyzed using Fisher's exact test, * $p < 0.05$, ** $p < 0.001$, *** $p < 0.0001$.

2.3. High-MAFB⁺ Cell Density Indicated a Higher Mortality Risk

Many studies have shown that TAM markers are associated with survival in lung cancer patients [13]. Therefore, we analyzed whether the MAFB⁺ cell density was associated with survival rates of the patients with non-metastatic (Stage I to III) lung adenocarcinoma. Figure 3A,B show the OS and DFS of low- (black line), mid- (green line), and high- (red line) MAFB⁺ cell density groups. The curves indicate that high-MAFB⁺ cell density indicated a higher mortality risk as the mean survival time (MST) for the low-, mid-, and high-MAFB⁺ groups were 114.7 months, 104.4 months, and 75.5 months ($p < 0.001$, log-rank test), respectively (Figure 3A).

In terms of DFS, the MST in the low-, mid-, and high-MAFB⁺ group was 96.4 months, 78.6 months, and 39.9 months ($p < 0.001$, log-rank test), respectively (Figure 3B). Compared with the MST of nodal involvement; negative (–) with an OS of 109.0 months and positive (+) with an OS of 92.4 months; the low-MAFB⁺ patients showed longer OS than patients with (–) nodal involvement and high-MAFB⁺ patients showed a 17 month shorter OS than patients with nodal involvement (Figures S4 and 3A,B).

Furthermore, Pearson correlation analysis showed that MAFB⁺ cell density was negatively correlated with OS or DFS (Figure 3C, R score: -0.37 , $p < 0.001$, D, R score: -0.38 , $p < 0.001$). Consistently, the univariate analysis using the Cox hazard test disclosed that the OS (low vs. Mid, $p = 0.0791$, low vs. high, $p = 0.0011$) and DFS (low vs. mid, $p = 0.0828$, low vs. high, $p = 0.0018$) was associated with MAFB expression and other factors except for sex and age (Table 2).

On the other hand, multivariate analysis suggested that MAFB expression was less influential than smoking history and nodal involvement. (Table 2).

These results suggest that grouping by the degree of MAFB expression allows a more detailed examination of hazard and mortality risk in patients with stage I to stage III lung adenocarcinoma. Thus, MAFB⁺ cell density may be an ideal predictor of the hazard ratio and DFS in these patients after surgery.

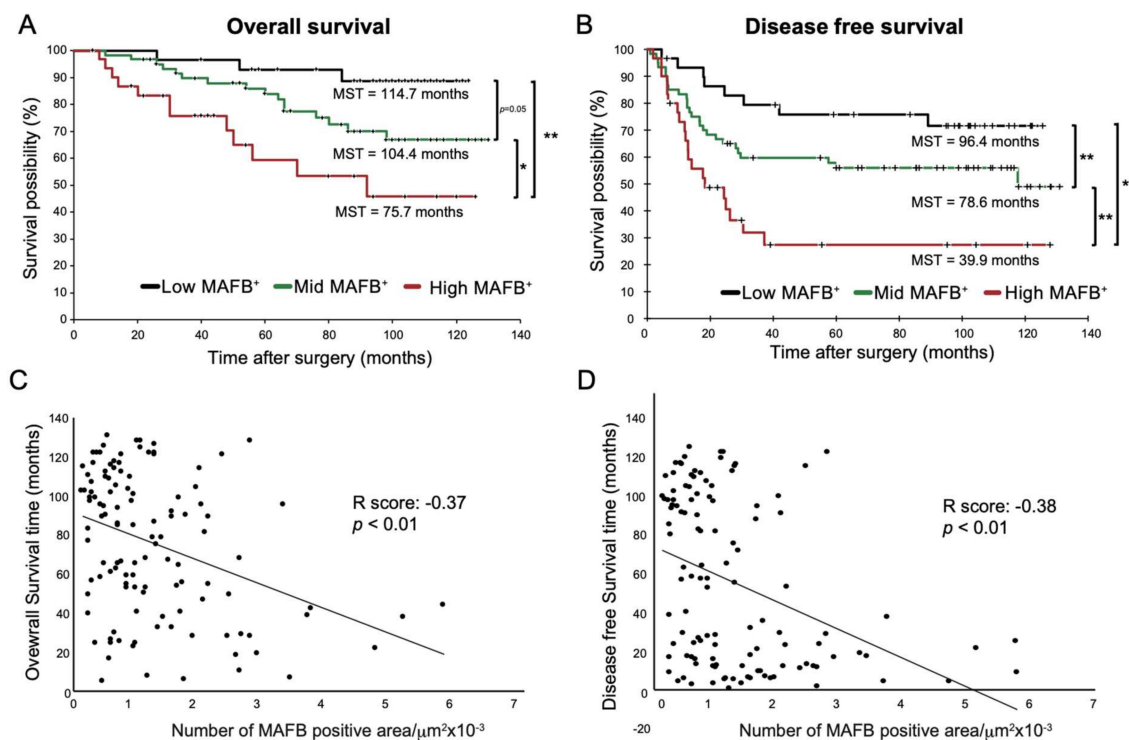


Figure 3. OS and DFS of low-, mid-, and high- in MAFB⁺ cells Kaplan–Meier analysis of (A) overall survival and (B) disease-free survival of the three groups: low-MAFB⁺, mid-MAFB⁺, and high-MAFB⁺. Difference in survival was compared using log-rank test. Pearson correlation analysis was performed between MAFB expression and (C) survival time (R score: -0.366 , $p = 0.000043$) and (D) disease-free survival (R score: -0.378 , $p = 0.000023$). Data are presented as means \pm SEM; data is considered significant at * $p < 0.05$; ** $p < 0.01$.

2.4. MAFB Could Be a Prognostic TAM Marker for Patients with Smoking Habits with Lung Adenocarcinoma

Univariate and multivariate analyses have revealed that smoking history and MAFB expression affect survival (Table 2). A previous study showed that cigarette smoke induces MAFB expression in lung macrophages in a mouse model [10]. Therefore, we decided to analyze whether there is any relationship between smoking and MAFB expression. We first checked the correlation between MAFB expression level and smoking index, but no association was observed (Figure S5). Next, we decided to ascertain whether the intensity of MAFB expression is related to survival in smokers and non-smokers. Our results showed that the OS rates of smokers ($n = 75$) were significantly lower compared to non-smokers ($n = 45$) (Figure S6A). Furthermore, we examined OS and DFS of low, mid, and high-MAFB⁺ in both smoking and non-smoking patients and found that the survival was significantly lower in the high-MAFB⁺ group only in smokers (Figure 4A).

The effects of cigarette smoking on men and women have long been a subject of controversy [19]. The samples included female smoker $n = 24$, female non-smoker $n = 40$, male smoker $n = 51$, and male non-smoker $n = 5$. Our results showed that female smokers had significantly lower OS rates (Figure S5B). In men, an accurate comparative analysis could not be performed as the number of non-smokers was only about 10% of smokers (Figure S6C). For women, we separately compared the survival curves for MAFB expression intensity for non-smokers and smokers. The results showed no significant difference in survival by MAFB expression intensity in the non-smoker group, but a dramatic difference in OS and DFS was observed in the smoker group. Since most of the men were smokers, we could not obtain data on survival curves for non-smokers; however, smokers showed a significant difference in DFS according to the intensity of MAFB (Figure 4C). These data

indicate that MAFB could be a prognostic TAM marker for patients with smoking habits with lung adenocarcinoma.

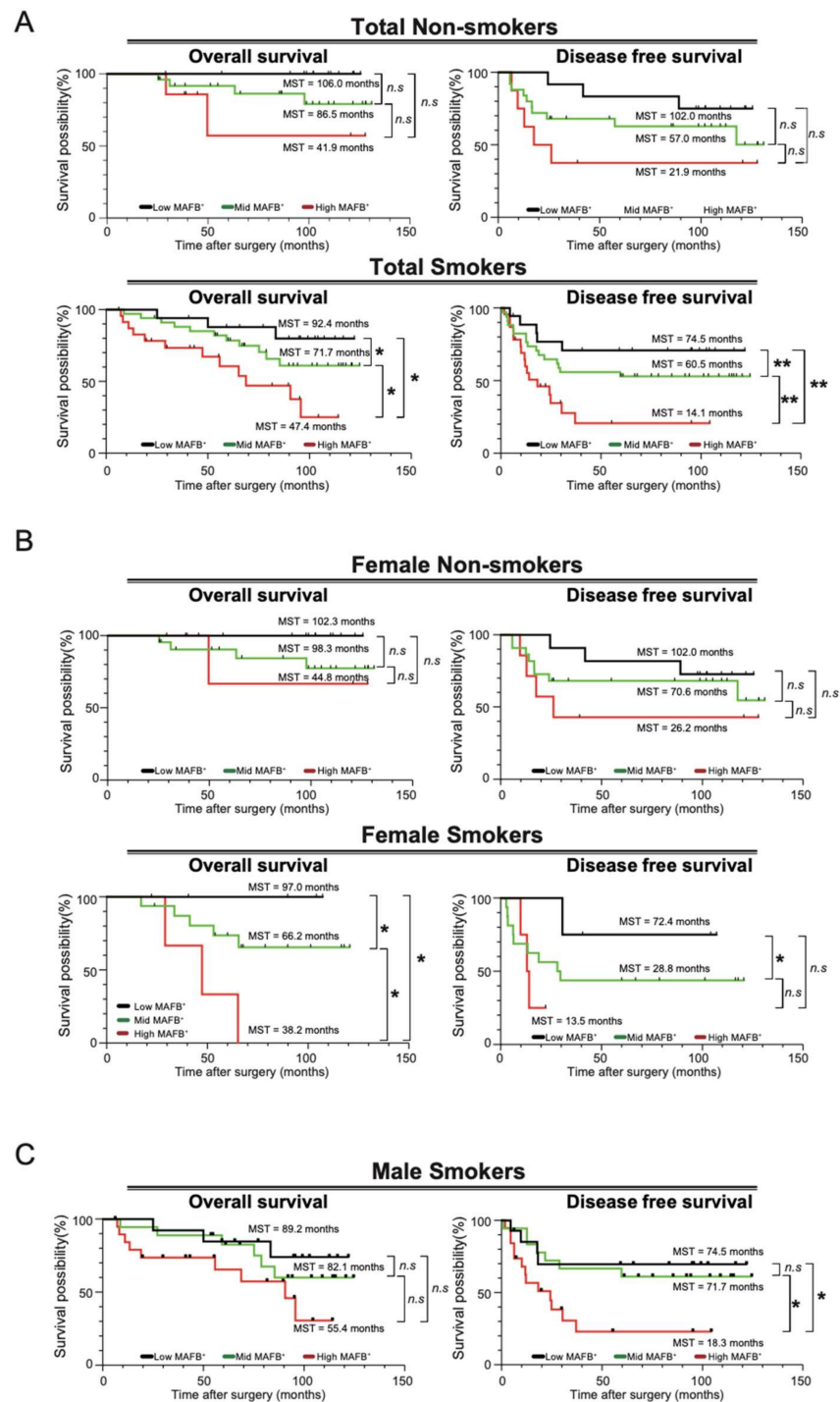


Figure 4. OS and DFS analysis in smokers and non-smoker patients. Kaplan–Meier analysis of (A) the overall survival and disease-free survival of the low-MAFB⁺, mid-MAFB⁺, and high-MAFB⁺ in the total smoking and non-smoking patients; (B) the overall survival and disease-free survival of the low-MAFB⁺, mid-MAFB⁺, and high-MAFB⁺ in female smoker and non-smoker groups; and (C) the overall survival and disease-free survival of the low-MAFB⁺, mid-MAFB⁺, and high-MAFB⁺ in male smoker and non-smoker groups. Difference in survival was compared using log-rank test. *, $p < 0.05$; **, $p < 0.01$.

Table 2. Univariate analysis of disease-free survival and overall survival in non-metastatic lung adenocarcinoma stages.

	Univariate Analysis				Multivariate Analysis			
	Disease-Free Survival		Overall Survival		Disease-Free Survival		Overall Survival	
	Hr (95% Ci)	<i>p</i> Value	Hr (95% Ci)	<i>p</i> Value	Hr (95% Ci)	<i>p</i> Value	Hr (95% Ci)	<i>p</i> Value
MAFB (low versus mid)	2.998 (0.9882–12.95)	0.0828	3.039 (1.001–13.13)	0.079	1.665 (0.5008–7.565)	0.4468	1.966 (0.5985–8.859)	0.3086
MAFB (low versus high)	7.423 (2.393–32.44)	0.0018	8.105 (2.620–35.36)	0.0011	1.773 (0.4873–8.669)	0.4230	2.001 (0.5587–9.646)	0.3263
Gender (male versus female)	1.856 (0.9236–3.847)	0.0861	1.826 (0.9081–3.790)	0.095				
Smoking (Yes versus No)	3.115 (1.369–8.376)	0.0122	0.3208 (1.368–8.390)	0.0123	3.106 (1.290–8.724)	0.0182	2.989 (1.231–8.437)	0.0235
Age (<70 versus ≥70)	1.010 (0.9697–1.058)	0.6397	1.013 (0.9715–1.062)	0.5578				
Pstage (I versus II + III)	7.500 (3.194–20.72)	<0.0001	8.464 (3.614–23.24)	<0.0001				
Nodal involvement (Yes versus No)	6.497 (2.880–16.71)	<0.0001	7.723 (3.411–19.85)	<0.0001	4.382 (1.555–13.88)	0.0078	5.304 (1.845–17.12)	0.0032
Lymphatic invasion (Yes versus No)	3.072 (1.522–6.398)	0.002	3.294 (1.626–6.887)	0.0011	1.049 (0.4812–2.384)	0.9064	1.094 (0.4918–2.522)	0.8285
Vessel invasion (Yes versus No)	5.444 (2.377–14.71)	0.0002	4.875 (2.136–13.14)	0.0005	1.843 (0.6468–5.939)	0.2753	1.370 (0.4730–4.458)	0.5786
Pleural infiltration (Yes versus No)	2.740 (1.350–5.803)	0.0062	2.644 (1.306–5.585)	0.008	1.228 (0.5665–2.793)	0.6108	1.216 (0.5498–2.805)	0.6363

Statistically significant differences between groups were determined using Cox proportional hazard model ($p < 0.05$). HR, hazard ratio; CI, confidence interval.

3. Discussion

TAMs and AMs are thought to coexist in the lung tissues from the early stages of cancer [22]. However, the cell-specific expression of MAFB remains largely unidentified. In our previous report, tumor samples from patients with lung adenocarcinoma showed MAFB expression in locations comparable to CD68- and CD204-positive TAMs and were abundant in severe stages of cancer [21]. In this study, the scRNA-seq analysis of patients with lung cancer showed MAFB expression in monocytes of tumor and advanced tumor tissue, while no other markers (CD204, CD68, CD206) were expressed (Figure 1J). In particular, in myeloid cluster 8, MAFB expression increased in tumors and advanced tumors. Similar expression patterns for CCR2 were observed in Figure S3B. CCR2 is the receptor for CCL2 which induces monocyte infiltration in tumors including lung cancer [23]; therefore, MAFB may be a potential indicator for monocyte infiltration. Although it is difficult to measure the actual percentage of monocyte infiltration, the CCR2-expressing cells in this analyzed data accounted for approximately 3% of the total cells in normal lung tissue and increased to 6% or 11% in tumors or advanced tumors, respectively (Figure S3B). This may indicate that TAM infiltration increases as the tumor stage advances, but it is difficult to clearly measure the extent of TAM infiltration considering conditions such as tumor removal site, sample preparation method, and individual differences. Further study is required to analyze whether MAFB can be established as a marker of invasion.

Moreover, unlike other TAM markers, MAFB was not expressed in AM. Our results were consistent with previous reports stating that *Mafb* was highly expressed in macrophage-colony stimulating factor (M-CSF)-derived macrophages but not expressed in the alveolar granulocyte macrophage-colony stimulating factor (GM-CSF)-derived macrophages. Since MAFB inhibits the self-renewal of macrophages, AMs have self-renewal ability [24]. Hence, our study suggests that MAFB shows a higher specificity to the macrophage/monocyte cell population than other cancer markers studied and could be used to identify patients with early stages of lung adenocarcinoma.

Previous studies have identified CD204⁺ TAMs as prognostic markers in non-small cell lung carcinoma (NSCLC), especially in lung adenocarcinoma [25], and the combined use of CD47 and CD68 was reported to predict the survival of eastern-Asian patients with NSCLC [26]. Further, CD68⁺CD163⁺ or CD68⁺CD206⁺ markers were used to identify M2-polarized TAMs in lung adenocarcinoma. The levels of M2 macrophages (CD68⁺CD206⁺) were positively associated with peritumoral lymphatic microvessel density, but nega-

tively associated with the patient's prognosis [27]. Moreover, the accumulation of CD163⁺ macrophages is closely correlated with a poor prognosis in lung cancer, and the increased density of CD68⁺CD163⁺ macrophages in tumor nests and stroma was associated with lymph node metastases [27]. However, no such association was observed with recurrence-free survival, OS, and TNM stages [14,28]. Similarly, CD68⁺CD163⁺M2 were also correlated with OS and DFS in NSCLC. A higher correlation was observed between increased infiltration of macrophages and clinical characteristics, including LUSC, EGFR status, and smoking habits [29]. However, the use of MAFB as a predictive marker for the survival of patients with non-metastatic lung adenocarcinoma remains unidentified. Our results showed that MAFB⁺ cell density correlated with clinicopathological characteristics in patients with stage I, II, and III lung adenocarcinoma. A higher MAFB⁺ cell density correlated with poor clinical outcomes, including poor pathologic stage, higher recurrence rate, nodal involvement, lymphatic permeation, and vessel invasion. An association with high hazards rate, poor OS, and DFS was also observed among these patients.

Smoking habits or sex differences did not show significant differences in their correlation with the OS and DFS in MAFB⁺ cells. However, one of the limitations of our study was the relatively small sample size of non-smoking males. Even though only Japanese patients were included in this study, our results were consistent with previous reports where the risk of lung cancer was comparable in both women and men exposed to tobacco smoke in patients from Germany and Italy [30]. Compared to squamous cells or small cell carcinomas, adenocarcinoma was reported to have a weak association with tobacco smoking in women from France [19]. Interestingly, smoking was significantly correlated with a higher density of CD68- and CD204-positive macrophages in tumor stroma [25,31]. It has also been reported that *Mafb* expression is upregulated in macrophages following exposure to cigarette smoke in a mouse model [10]. However, whether the increase in *MAFB* expression was observed in resident or infiltrating macrophages remained unclear. Our results indicate that *MAFB* was expressed in the monocyte-derived macrophages, but not tissue-resident macrophages, suggesting higher specificity of *MAFB* expression in TAMs than other markers, CD68 and CD204. Moreover, all patients with smoking habits showed higher MAFB⁺ cell density and were at risk of poor OS and DFS, suggesting that MAFB could be a prognostic TAM marker in smoking patients with early-stage lung adenocarcinomas. We suggest that the correlation between MAFB⁺ cells density with OS and DFS in smokers and/or non-smokers patients did not seem to be a sex-related relationship.

Our results suggest that MAFB⁺ cells could be a suitable predictor for severity and a prognostic marker for hazard rate, OS, and DFS in patients with non-metastatic lung adenocarcinoma. Moreover, we suggest that a higher MAFB⁺ cell density in patients with smoking habits could also be associated with poor overall and disease-free survival; however, this association is not sex-related.

4. Material and Methods

4.1. Single-Cell RNA Sequencing (scRNA-seq) Analysis

The single cell RNA-seq recently generated from 44 patients with treatment-naïve lung adenocarcinoma were analyzed (GEO database accession GSE131907). Single-cell RNA raw data included normal lung tissue ($n = 11$), tumor tissue (stage I and III, $n = 7$), and advanced tumor tissue (stage IV, $n = 4$).

The raw data was downloaded, and we used Scanpy (v1.7.2) for the following analyses. The initial cell number and gene number were 208,506 and 29,634, respectively. We extracted highly variable genes using “scanpy.pp.highly_variable_genes” function, and 2243 genes were extracted. We conducted dimension reduction with PCA using the “scanpy.tl.pca” function and UMAP using the “scanpy.pp.neighbors” function and the “scanpy.tl.umap” function. By clustering with the Leiden Method using the “sc.tl.leiden” function, cells were divided into 34 clusters and six clusters which contained myeloid cells (41,726 cells) were extracted. Dimension reduction and clustering were conducted on these extracted cells using the same method for all cells. For information about the parameters for these

analyses, please refer to our GitHub pages (<https://github.com/Teppei-Nishino/TAM>, accessed on 30 August 2022).

We clustered myeloid cell lineages, Alveolar Macrophages (AM), Dendritic cells (DC), Macrophage Lineage (ML), and Monocytes (Mo), and the analysis was performed using only these clusters. Statistical analysis and visualization were performed using functions from Scanpy.

4.2. Immunostaining of Human Cancer Tissues

We analyzed the cancerous tissues of patients with lung adenocarcinoma ($n = 120$) from the Tsukuba Human Tissue Biobank Center (THB) at the University of Tsukuba Hospital. Frozen human lung tumor tissues were sectioned ($5 \mu\text{m}$), stained, and visualized, as previously described [21], using 1:50 anti-MAFB (clone OT12A6; Lifespans Biosciences, Seattle, WA, USA). Means of three positively stained field areas relative to the tissue area (MAFB⁺ cells/tissue area) were morphometrically quantified (Supplementary Figure S1) using a BZ-X800 analyzer (Keyence, Itasca, IL, USA).

4.3. Evaluation of Clinicopathological Features

The clinical characteristics of patients with lung adenocarcinoma ($n = 120$) were retrieved from the clinical records of the University of Tsukuba. The following clinicopathological factors were considered: age (<70 years versus ≥ 70 years), sex (female vs. male), smoking history (non-smokers versus smokers), local metastasis to lymph nodes (nodal involvement; N0 versus N1), recurrence (positive vs. negative), pathological stage (I, II, and III), lymphatic permeation (present vs. absent), vascular invasion (present vs. absent), and pleural infiltration (present vs. absent). The UICC TNM staging system (The Union for International Cancer Control staging system for tumor size, lymphatic involvement, and metastasis) was used to classify the severity and extent of the cancer stage.

4.4. Statistical Analysis

Data are expressed as the mean \pm SEM and analyzed using Welch's *t*-test. The correlations between the grade of MAFB⁺ cells density and the clinicopathological factors were evaluated through Fisher's exact test. The Kaplan–Meier method was used to estimate the overall survival time and the disease-free survival, while the difference in survival was compared using the log-rank test, the two paired groups using the Wilcoxon test, and the different survival distributions using the Tarone–Ware test. In survival analysis, we used Dunn–Šidák correction to adjust the *p*-value, and the curve comparisons were calculated using the Cox hazard test. The following variables were considered, MAFB⁺ cells density, sex, age, smoking, cancer recurrence, tumor stage, nodal involvement, lymphatic permeation, vessel invasion, and pleural infiltration. The correlation between MAFB⁺ cell density and overall survival (OS) or disease-free survival (DFS) was evaluated using the Pearson correlation test. Differences were considered statistically significant at $p < 0.05$.

Supplementary Materials: The following supporting information can be downloaded at: <https://www.mdpi.com/article/10.3390/ijms23179945/s1>.

Author Contributions: Conceptualization, O.S. and M.H.; methodology, O.S. and M.K.Y.; software, O.S., M.H., M.S. and T.N.; validation, O.S., M.H. and M.S.; formal analysis, O.S.; investigation, O.S. and M.H.; resources, N.K.; data curation, O.S., M.H. and T.N.; writing—original draft preparation, O.S.; writing—review and editing, O.S., M.H., S.T., M.S., Y.I.; visualization, O.S. and M.H.; supervision, M.H. and S.T.; project administration, M.H. and S.T.; funding acquisition, M.H. and S.T. All authors have read and agreed to the published version of the manuscript.

Funding: This work was funded by the Ministry of Education and Sports of Japan and the Ministry of Education JSPS KAKENHI (grant numbers 26221004, 25860205, 23118504, 16K18398, 19K07499, and 19H00966), Research Grant of Princess Takamatsu Cancer Research Fund, the Culture, Sports, Science and Technology of Japan (MEXT), the Uehara Memorial Foundation, Takeda Science Foundation, and the World Premier International Research Center Initiative, MEXT, Japan.

Institutional Review Board Statement: This study was approved by the Tsukuba Clinical Research & Development Organization (T-CReDO), Department of Medicine, University of Tsukuba Hospital (R02-075). All methods were carried out following the guidelines and regulations described in the proposal submitted to the Ethics Committee.

Informed Consent Statement: For donations for scientific research, informed consent was signed by the donor before death or by relatives after death, according to local guidelines of University of Tsukuba Hospital. The anonymity of the cadavers was maintained.

Data Availability Statement: The datasets used and/or analyzed during the current study are available from the corresponding author upon reasonable request. All source code is available from our GitHub page (<https://github.com/Tepppei-Nishino/TAM>, accessed on 30 August 2022)).

Acknowledgments: We thank our laboratory co-workers from the Lab Animal Resource Center at the University of Tsukuba, Japan, for providing insights and assisting in the research. We also appreciate Tomoyo Takeuchi and Noriaki Sakamoto at Tsukuba Human Tissue Biobank Center (THB)/Tsukuba Pathological Analysis Support Service (T-PASS), the University of Tsukuba, Japan, for obtaining the human tissue sections.

Conflicts of Interest: The authors declare no conflict of interest.

Abbreviations

AM	Alveolar macrophages
bZIP	The basic leucine zipper
CD204	Cluster of differentiation 204
CD68	Cluster of differentiation 68
DC	Dendritic cells
DFS	Disease-free survival
FCGR3A	Fc gamma receptor IIIa gene
GEO	Gene expression omnibus
JSPS	Japan Society for the Promotion of Science
LY2	Lymphocyte antigen 2 gene
Maf	Musculoaponeurotic fibrosarcoma
MAFB	V-maf musculoaponeurotic fibrosarcoma oncogene homolog B
MARCO	Macrophage receptor with collagenous structure gene
MEXT	The Ministry of Education, Culture, Sports, Science, and Technology
ML	Macrophage lineage
Mo	Monocytes
MSR1	Macrophage scavenger receptor 1
Mφs	Macrophages
OS	Overall survival
PCA	Principal component analysis
PCs	Principal components
scRNA-seq	Single-cell RNA sequencing
SEM	Standard error of mean
SNN	Shared nearest neighbor
T-CReDO	Tsukuba clinical research and development organization
TAM	Tumor-associated macrophages
THP	Tsukuba Human Tissue Biobank Center
TME	Tumor microenvironment
TNM	Staging system based on tumor size, nodal involvement, and metastasis
UICC	The Union for International Cancer Control
UMAP	Uniform Manifold Approximation and Projection
UMIs	Unique molecular identifiers

References

- Kataoka, K.; Fujiwara, K.T.; Noda, M.; Nishizawa, M. MafB, a new Maf family transcription activator that can associate with Maf and Fos but not with Jun. *Mol. Cell. Biol.* **1994**, *14*, 7581–7591. [CrossRef] [PubMed]
- Sadl, V.S.; Jin, F.; Yu, J.; Cui, S.; Holmyard, D.; Quaggin, S.E.; Barsh, G.S.; Cordes, S.P. The Mouse Kreisler (Krrml1/MafB) Segmentation Gene Is Required for Differentiation of Glomerular Visceral Epithelial Cells. *Dev. Biol.* **2002**, *249*, 16–29. [CrossRef] [PubMed]
- Hang, Y.; Stein, R. MafA and MafB activity in pancreatic β cells. *Trends Endocrinol. Metab.* **2011**, *22*, 364–373. [CrossRef] [PubMed]
- Nishimura, W.; Kondo, T.; Salameh, T.; El Khattabi, I.; Dodge, R.; Bonner-Weir, S.; Sharma, A. A switch from MafB to MafA expression accompanies differentiation to pancreatic β -cells. *Dev. Biol.* **2006**, *293*, 526–539. [CrossRef] [PubMed]
- Gautier, E.L.; Shay, T.; Miller, J.; Greter, M.; Jakubzick, C.; Ivanov, S.; Helft, J.; Chow, A.; Elpek, K.G.; Gordonov, S.; et al. Gene-expression profiles and transcriptional regulatory pathways that underlie the identity and diversity of mouse tissue macrophages. *Nat. Immunol.* **2012**, *13*, 1118–1128. [CrossRef] [PubMed]
- Daassi, D.; Hamada, M.; Jeon, H.; Imamura, Y.; Tran, M.T.N.; Takahashi, S. Differential expression patterns of MafB and c-Maf in macrophages in vivo and in vitro. *Biochem. Biophys. Res. Commun.* **2016**, *473*, 118–124. [CrossRef]
- Tran, M.T.N.; Hamada, M.; Jeon, H.; Shiraishi, R.; Asano, K.; Hattori, M.; Nakamura, M.; Imamura, Y.; Tsunakawa, Y.; Fujii, R.; et al. MafB is a critical regulator of complement component C1q. *Nat. Commun.* **2017**, *8*, 1700. [CrossRef]
- Shichita, T.; Ito, M.; Morita, R.; Komai, K.; Noguchi, Y.; Ooboshi, H.; Koshida, R.; Takahashi, R.K.S.; Kodama, T.; Yoshimura, A. MAFB prevents excess inflammation after ischemic stroke by accelerating clearance of damage signals through MSR1. *Nat. Med.* **2017**, *23*, 723–732. [CrossRef]
- Hamada, M.; Nakamura, M.; Tran, M.T.N.; Moriguchi, T.; Hong, C.; Ohsumi, T.; Dinh, T.T.H.; Kusakabe, M.; Hattori, M.; Katsumata, T.; et al. MafB promotes atherosclerosis by inhibiting foam-cell apoptosis. *Nat. Commun.* **2014**, *5*, 3147. [CrossRef]
- Machiya, J.-I.; Shibata, Y.; Yamauchi, K.; Hirama, N.; Wada, T.; Inoue, S.; Abe, S.; Takabatake, N.; Sata, M.; Kubota, I. Enhanced Expression of MafB Inhibits Macrophage Apoptosis Induced by Cigarette Smoke Exposure. *Am. J. Respir. Cell Mol. Biol.* **2007**, *36*, 418–426. [CrossRef]
- Sato-Nishiwaki, M.; Aida, Y.; Abe, S.; Shibata, Y.; Kimura, T.; Yamauchi, K.; Kishi, H.; Igarashi, A.; Inoue, S.; Sato, M.; et al. Reduced Number and Morphofunctional Change of Alveolar Macrophages in MafB Gene-Targeted Mice. *PLoS ONE* **2013**, *8*, e73963. [CrossRef]
- Mantovani, A.; Marchesi, F.; Malesci, A.; Laghi, L.; Allavena, P. Tumour-associated macrophages as treatment targets in oncology. *Nat. Rev. Clin. Oncol.* **2017**, *14*, 399–416. [CrossRef] [PubMed]
- Mehraj, U.; Qayoom, H.; Mir, M.A. Prognostic significance and targeting tumor-associated macrophages in cancer: New insights and future perspectives. *Breast Cancer* **2021**, *28*, 539–555. [CrossRef] [PubMed]
- Ma, J.; Liu, L.; Che, G.; Yu, N.; Dai, F.; You, Z. The M1 form of tumor-associated macrophages in non-small cell lung cancer is positively associated with survival time. *BMC Cancer* **2010**, *10*, 112. [CrossRef] [PubMed]
- Murray, P.J.; Allen, J.E.; Biswas, S.K.; Fisher, E.A.; Gilroy, D.W.; Goerdts, S.; Gordon, S.; Hamilton, J.A.; Ivashkiv, L.B.; Lawrence, T.; et al. Macrophage Activation and Polarization: Nomenclature and Experimental Guidelines. *Immunity* **2014**, *41*, 14–20. [CrossRef] [PubMed]
- Cavnar, M.J.; Zeng, S.; Kim, T.; Sorenson, E.C.; Ocun, L.M.; Balachandran, V.P.; Seifert, A.M.; Greer, J.B.; Popow, R.; Crawley, M.H.; et al. KIT oncogene inhibition drives intratumoral macrophage M2 polarization. *J. Exp. Med.* **2013**, *210*, 2873–2886. [CrossRef]
- Segura, E.; Touzot, M.; Bohineust, A.; Cappuccio, A.; Chiochia, G.; Hosmalin, A.; Dalod, M.; Soumelis, V.; Amigorena, S. Human Inflammatory Dendritic Cells Induce Th17 Cell Differentiation. *Immunity* **2013**, *38*, 336–348. [CrossRef]
- Yi, H.; Yu, X.; Gao, P.; Wang, Y.; Baek, S.-H.; Chen, X.; Kim, H.L.; Subjeck, J.R.; Wang, X.-Y. Pattern recognition scavenger receptor SRA/CD204 down-regulates Toll-like receptor 4 signaling-dependent CD8 T-cell activation. *Blood* **2009**, *113*, 5819–5828. [CrossRef]
- Rusmaully, J.; Tvardik, N.; Martin, D.; Billmann, R.; C  n  e, S.; Antoine, M.; Blons, H.; Laurent-Puig, P.; Tr  daniel, J.; Wislez, M.; et al. Risk of lung cancer among women in relation to lifetime history of tobacco smoking: A population-based case-control study in France (the WELCA study). *BMC Cancer* **2021**, *21*, 711. [CrossRef]
- Mei, J.; Xiao, Z.; Guo, C.; Pu, Q.; Ma, L.; Liu, C.; Lin, F.; Liao, H.; You, Z.; Liu, L. Prognostic impact of tumor-associated macrophage infiltration in non-small cell lung cancer: A systemic review and meta-analysis. *Oncotarget* **2016**, *7*, 34217–34228. [CrossRef]
- Yadav, M.K.; Inoue, Y.; Nakane-Otani, A.; Tsunakawa, Y.; Jeon, H.; Samir, O.; Teramoto, A.; Kulathunga, K.; Kusakabe, M.; Nakamura, M.; et al. Transcription factor MafB is a marker of tumor-associated macrophages in both mouse and humans. *Biochem. Biophys. Res. Commun.* **2019**, *521*, 590–595. [CrossRef] [PubMed]
- Kim, N.; Kim, H.K.; Lee, K.; Hong, Y.; Cho, J.H.; Choi, J.W.; Lee, J.-I.; Suh, Y.-L.; Ku, B.M.; Eum, H.H.; et al. Single-cell RNA sequencing demonstrates the molecular and cellular reprogramming of metastatic lung adenocarcinoma. *Nat. Commun.* **2020**, *11*, 2285. [CrossRef] [PubMed]
- Schmall, A.; Al-Tamari, H.M.; Herold, S.; Kampschulte, M.; Weigert, A.; Wietelmann, A.; Vipotnik, N.; Grimminger, F.; Seeger, W.; Pullamsetti, S.S.; et al. Macrophage and Cancer Cell Cross-talk via CCR2 and CX3CR1 Is a Fundamental Mechanism Driving Lung Cancer. *Am. J. Respir. Crit. Care Med.* **2015**, *191*, 437–447. [CrossRef] [PubMed]

24. Cuevas, V.D.; Anta, L.; Samaniego, R.; Orta-Zavalza, E.; De La Rosa, J.V.; Baujat, G.; Domínguez-Soto, Á.; Sánchez-Mateos, P.; Escribese, M.M.; Castrillo, A.; et al. MAFB Determines Human Macrophage Anti-Inflammatory Polarization: Relevance for the Pathogenic Mechanisms Operating in Multicentric Carpotarsal Osteolysis. *J. Immunol.* **2017**, *198*, 2070–2081. [CrossRef] [PubMed]
25. Li, Z.; Maeda, D.; Yoshida, M.; Umakoshi, M.; Nanjo, H.; Shiraishi, K.; Saito, M.; Kohno, T.; Konno, H.; Saito, H.; et al. The intratumoral distribution influences the prognostic impact of CD68- and CD204-positive macrophages in non-small cell lung cancer. *Lung Cancer* **2018**, *123*, 127–135. [CrossRef]
26. Fu, F.; Zhang, Y.; Gao, Z.; Zhao, Y.; Wen, Z.; Han, H.; Li, Y.; Hu, H.; Chen, H. Combination of CD47 and CD68 expression predicts survival in eastern-Asian patients with non-small cell lung cancer. *J. Cancer Res. Clin. Oncol.* **2021**, *147*, 739–747. [CrossRef]
27. Zhang, B.; Yao, G.; Zhang, Y.; Gao, J.; Yang, B.; Rao, Z.; Gao, J. M2-Polarized tumor-associated macrophages are associated with poor prognoses resulting from accelerated lymphangiogenesis in lung adenocarcinoma. *Clinics* **2011**, *66*, 1879–1886. [CrossRef]
28. Jung, K.Y.; Cho, S.W.; A Kim, Y.; Kim, D.; Oh, B.-C.; Park, D.J.; Park, Y.J. Cancers with Higher Density of Tumor-Associated Macrophages Were Associated with Poor Survival Rates. *J. Pathol. Transl. Med.* **2015**, *49*, 318–324. [CrossRef]
29. Ao, L.; Che, X.; Qiu, X.; Li, Z.; Yang, B.; Wang, S.; Hou, K.; Fan, Y.; Qu, X.; Liu, Y. M2 macrophage infiltration into tumor islets leads to poor prognosis in non-small-cell lung cancer. *Cancer Manag. Res.* **2019**, *11*, 6125–6138. [CrossRef]
30. Kreuzer, M.; Boffetta, P.; Whitley, E.; Ahrens, W.; Gaborieau, V.; Heinrich, J.; Jöckel, K.H.; Kreienbrock, L.; Mallone, S.; Merletti, F.; et al. Gender differences in lung cancer risk by smoking: A multicentre case–control study in Germany and Italy. *Br. J. Cancer* **2000**, *82*, 227–233. [CrossRef]
31. Ohtaki, Y.; Ishii, G.; Nagai, K.; Ashimine, S.; Kuwata, T.; Hishida, T.; Nishimura, M.; Yoshida, J.; Takeyoshi, I.; Ochiai, A. Stromal Macrophage Expressing CD204 is Associated with Tumor Aggressiveness in Lung Adenocarcinoma. *J. Thorac. Oncol.* **2010**, *5*, 1507–1515. [CrossRef] [PubMed]



Article

Systems Drug Discovery for Diffuse Large B Cell Lymphoma Based on Pathogenic Molecular Mechanism via Big Data Mining and Deep Learning Method

Shan-Ju Yeh , Tsun-Yung Yeh and Bor-Sen Chen *

Laboratory of Automatic Control, Signal Processing and Systems Biology, Department of Electrical Engineering, National Tsing Hua University, Hsinchu 30013, Taiwan; m793281@gmail.com (S.-J.Y.); qpctotca@gmail.com (T.-Y.Y.)

* Correspondence: bschen@ee.nthu.edu.tw

Abstract: Diffuse large B cell lymphoma (DLBCL) is an aggressive heterogeneous disease. The most common subtypes of DLBCL include germinal center b-cell (GCB) type and activated b-cell (ABC) type. To learn more about the pathogenesis of two DLBCL subtypes (i.e., DLBCL ABC and DLBCL GCB), we firstly construct a candidate genome-wide genetic and epigenetic network (GWGEN) by big database mining. With the help of two DLBCL subtypes' genome-wide microarray data, we identify their real GWGENs via system identification and model order selection approaches. Afterward, the core GWGENs of two DLBCL subtypes could be extracted from real GWGENs by principal network projection (PNP) method. By comparing core signaling pathways and investigating pathogenic mechanisms, we are able to identify pathogenic biomarkers as drug targets for DLBCL ABC and DLBCL GCB, respectively. Furthermore, we do drug discovery considering drug-target interaction ability, drug regulation ability, and drug toxicity. Among them, a deep neural network (DNN)-based drug-target interaction (DTI) model is trained in advance to predict potential drug candidates holding higher probability to interact with identified biomarkers. Consequently, two drug combinations are proposed to alleviate DLBCL ABC and DLBCL GCB, respectively.

Keywords: diffuse large B cell lymphoma (DLBCL); deep neural network; drug discovery; drug combination

Citation: Yeh, S.-J.; Yeh, T.-Y.; Chen, B.-S. Systems Drug Discovery for Diffuse Large B Cell Lymphoma Based on Pathogenic Molecular Mechanism via Big Data Mining and Deep Learning Method. *Int. J. Mol. Sci.* **2022**, *23*, 6732. <https://doi.org/10.3390/ijms23126732>

Academic Editor: Dmitry Aminin

Received: 20 May 2022

Accepted: 15 June 2022

Published: 16 June 2022

Publisher's Note: MDPI stays neutral with regard to jurisdictional claims in published maps and institutional affiliations.



Copyright: © 2022 by the authors. Licensee MDPI, Basel, Switzerland. This article is an open access article distributed under the terms and conditions of the Creative Commons Attribution (CC BY) license (<https://creativecommons.org/licenses/by/4.0/>).

1. Introduction

Non-Hodgkin lymphoma (NHL), a lymphoid tissue malignancy, is one of the most prevalent cancers worldwide [1]. Diffuse large B-cell lymphoma (DLBCL) is the most common subtype of NHL in western countries [2]. Meanwhile, it is a biologically heterogeneous and aggressive disease. The survival rate is usually less than one year for patients without treatment. Along with the thriving of DNA array technology, gene expression profiling studies have confirmed the existence of DLBCL subtypes involving in germinal center B cells (GCB) DLBCL and activated B cells (ABC) DLBCL. It represents lymphomas caused at different stages of lymphatic differentiation. Moreover, DLBCL GCB is a lymphocyte from the germinal center, therefore, it expresses some genes often observed in germinal center B cells including BCL6 and CD10 [3]. The main pathological feature of DLBCL ABC is the NF κ B signaling pathway resulting in significant impacts on the cell proliferation and the regulation of apoptosis. It is noted that there is a large difference between DLBCL GCB and DLBCL ABC in terms of the clinical survival rate. The five-year survival rate of DLBCL GCB is about 60%, while the five-year survival rate of DLBCL ABC is about 35%. The pathogenesis of DLBCL in two subtypes is currently unknown.

The current standard therapy for DLBCL is R-CHOP, including five drugs, rituximab, cyclophosphamide, doxorubicin, vincristine, and prednisone. Among them, rituximab acts with CD20 to drive caspase-independent cell apoptosis death [4]. However, rituximab-induced hypogammaglobulinemia occurred [5]. For cyclophosphamide, it could target the

gene CD95 and trigger activation-induced cell death after activation [6]. One study indicates that patients treated with cyclophosphamide have a 4.5-fold increased risk of bladder cancer [7]. Doxorubicin, an anthracycline drug, has been implicated in cardiotoxicity. Its main mechanisms have something to do with DNA damage, membrane damage, oxidative stress, and the apoptosis pathways [8]. Targeting the p53 gene to participate in cell cycle arrest, DNA repair, or apoptosis [9], vincristine is widely used to treat malignant tumors; however, vocal cord paralysis caused by neurotoxicity has been found [10]. Prednisone, a glucocorticoid drug, inhibits NF κ B and other inflammatory transcription factors, while the long-term steroid therapy may induce osteoporosis and liver cancer [11,12]. Instead of using rituximab, novel anti-CD20 agents (i.e., obinutuzumab and ofatumumab) were suggested for B-chronic lymphocytic leukemia and follicular lymphoma as well [13]. In addition, several innovative treatments for DLBCL have been approved by the U.S. Food and Drug Administration (FDA) including the anti-CD79b antibody drug conjugate polatuzumab vedotin (Pola) with bendamustine and rituximab (Pola-BR) [14]; the oral nuclear transport (XPO1) inhibitor selinexor [15]; and the combination of the anti-CD19 monoclonal antibody tafasitamab with the immunomodulatory agent lenalidomide [16,17]. Considering the different side effects of current treatments, drug combinations with multi-targets therapies toward DLBCL are worth studying.

It usually takes more than 12 years to develop a novel drug. The average cost of the drug development is about USD 2.6 billion [18]. There are few drugs that start from actual human testing that ever make it to marketing [19]. Due to huge demand for new anticancer drugs and various combinations of cell-target based screenings [20], drug repositioning based on computational methods has become popular in drug discovery. Drug-target interaction (DTI) prediction facilitates the process of drug discovery. It is the exploration of new drugs that interact with a particular target. The computational methods for DTI can be broadly classified into ligand-based approaches, docking approaches, and chemogenomic approaches [21]. The concept of ligand-based approaches is to predict the interactions based on the similarities between the protein ligands. However, without using sequencing information, it is hard to discover possible novel interactions due to the limitation of known ligands and protein families [22]. Utilizing 3D structures of proteins as well as drugs, docking approaches are based on the simulations to predict DTI [23–25], while these tasks would be challenged for certain membrane proteins, the 3D structures of which are unavailable. For chemogenomic approaches, it combines the chemical space of drugs and the genomics space of proteins into feature vectors to overcome the drawbacks of ligand-based and docking approaches. Chemogenomic approaches is suitable for machine learning (ML) methods for prediction of DTI [26]. In ML methods, the knowledge about drugs and proteins are represented by feature vectors that are used to train models for predicting the interactions between new drugs and/or new targets [27]. Furthermore, different learning-based models have been developed for DTI predictions, such as deep belief neural networks [28,29], convolutional neural networks [30,31], multilayer perceptrons [32,33], and graph neural network [34–36]. From the viewpoint of application, taking advantage of a chemogenomic approach, we trained a deep neural network (DNN)-based DTI prediction framework in advance for obtaining potential drug candidates toward the identified biomarkers.

In this study, we propose systems biology methods including systems modeling, system identification, system order detection scheme, and a principal network projection method to identify essential biomarkers as drug targets based on investigating pathogenic molecular mechanisms. Afterward, for identified biomarkers, we follow system drug design procedure taking drug design specifications into account, such as drug-target interaction ability, drug regulation ability, and drug toxicity to suggest potential drug combinations for DLBCL GCB and DLBCL ABC, respectively. The corresponding systems drug discovery flowchart is shown in Figure 1. It is noted that we build a DNN-based DTI model in advance for helping us obtain drug candidates, which have higher interaction probability toward the identified biomarkers (drug targets). Consequently, both famotidine and chlorzoxazone are regarded as common molecular drugs, which contribute to

inhibiting tumor metastasis, migration, and invasion for DLBCL ABC and DLBCL GCB. Furthermore, etoposide is designed specifically for cancer cell DNA damage of DLBCL ABC, and methotrexate is designed specifically for abnormal cell cycle of DLBCL GCB.

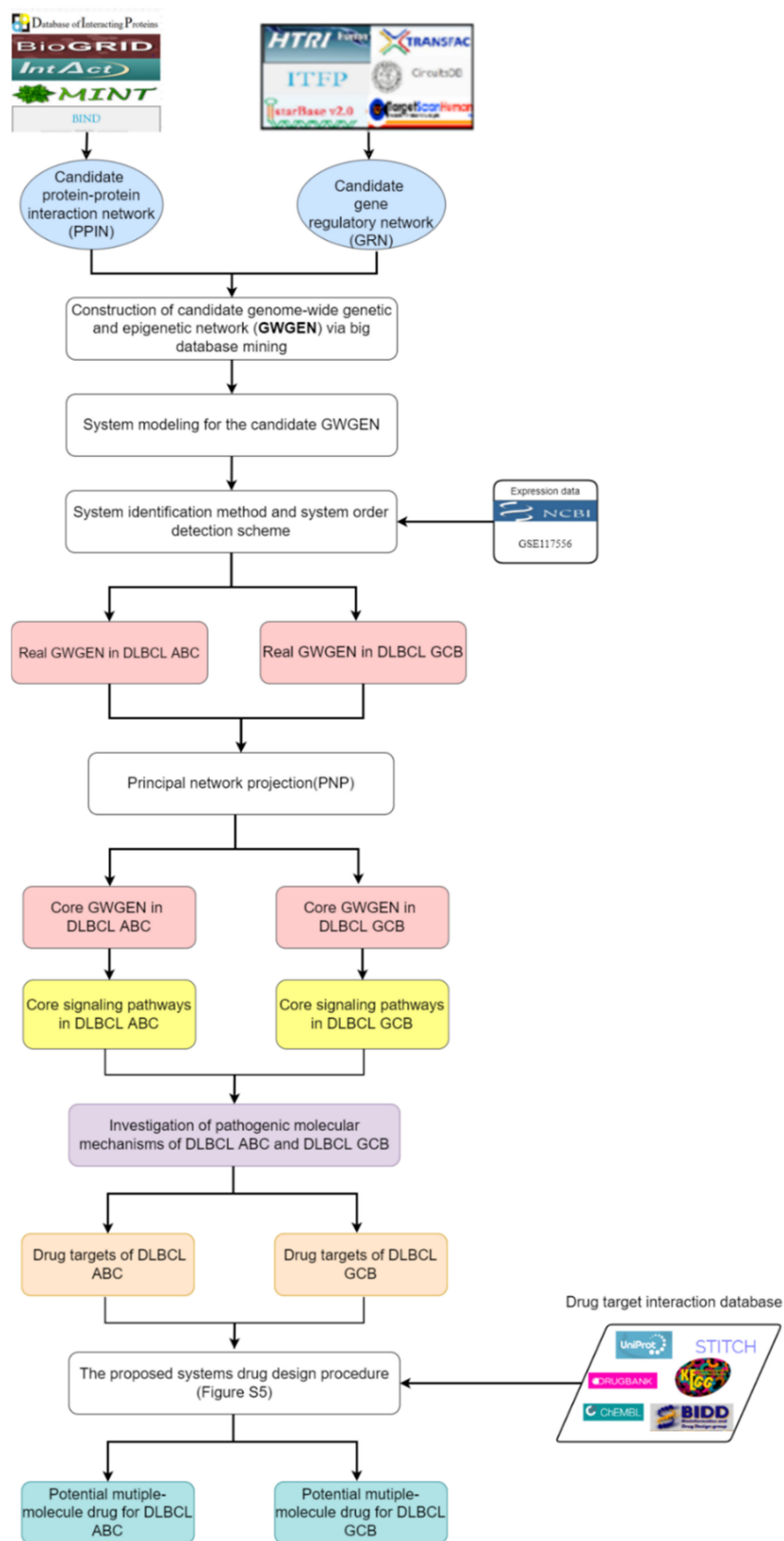


Figure 1. Flowchart of systems drug discovery based on systems biology approaches and drug design specifications.

2. Results

2.1. The Pathogenic Molecular Mechanisms in DLBCL ABC

From the core signaling pathways of DLBCL ABC in Figure 2, macrophage migration inhibitory factor (MIF) is found to be an important regulator of the innate immune system. MIF is classified as a pro-inflammatory cytokine [37]. MIF binds to CD74 on other immune cells to trigger an acute immune response [38]. Receptor CD74 (HLA class II histocompatibility antigen γ -chain receptor) in DLBCL ABC receives microenvironment factor MIF (macrophage migration inhibitory factor) to regulate TF STAT3 and MYC [39], respectively. The signaling transduction protein SRC, which was affected by phosphorylation, could transmit signals from CD74 to TF STAT3 in DLBCL ABC. Moreover, SRC was phosphorylated at the specific tyrosine residue by other tyrosine kinases, playing an important role in regulating embryonic development and cell growth [40]. Another signaling transduction protein, SORBS3, encodes a SH3 domain-containing adaptor protein. The presence of the SH3 domain is responsible for making the protein bind other cytoplasmic molecules, which are helpful for cytoskeletal organization, cell migration, gene expression and signaling. The constitutive activation of STAT3 signal promotes the growth, survival, angiogenesis and metastasis of tumor cells [41]; the overexpression of abnormally acetylated (activated) TF STAT3 can upregulate its target gene *HIF1A* [42], thereby promoting cellular functions, including cell proliferation as well as autophagy and inhibiting apoptosis [43]. At the same time, TF STAT3 would upregulate the target gene *ID2* [44] resulting in the promotion of cell cycle and epithelial-mesenchymal transition (EMT). Besides, it would upregulate the target gene *BCL2*, triggering the inhibition of autophagy and apoptosis. Upregulated by the acetylated STAT3, TF JDP2 is related to the inhibition of cell differentiation, cell cycle, and apoptosis. After being modified by the phosphorylation, the activated TF JDP2 would upregulate the DNA-methylated target gene *IL6*, which leads to promoting cell apoptosis and immune response against cancer [45].

Increased expression of SRC would trigger another core signaling pathway transmitting signals to TF FOXL1 through signaling transduction protein HIST1H2BA. FOXL1 plays an important role in regulating the expression of genes involved in cell metabolism, proliferation and differentiation. The overexpression of FOXL1 can upregulate miRNA MIR15A. The overexpression of MIR15A awakened by the upstream signals would inhibit the target genes *CCND1* and *ACTB* to promote their respective cellular functions. However, the total expression of *CCND1*, which is also activated by another TF NF κ B1 and miRNA MIR497, is upregulated. Moreover, the target gene *CCND1* can promote the cell cycle progression and the target gene *ACTB* can promote the cell apoptosis and metastasis.

In the next core signaling pathway, after the ligand MIF combining with the receptor CD64, the signals are transmitted to TF MYC via the signaling transduction proteins BIN2, ATL2, and AR in DLBCL ABC. It is known that BIN2 related pathways are immune system [46]. Moreover, it can facilitate cell movement and migration through podosomes that interact with cell membrane and mediate cytoskeleton. Among this core signaling pathway, AR, an androgen receptor, is a DNA-binding transcription factor that regulates gene expression of *BCL2* [47]. It can regulate gene expression in eukaryotes and affect cell proliferation and differentiation. MYC is a proto-oncogene, which plays an important role in cell cycle progression, apoptosis and metastasis [48]. Overexpressed TF MYC will promote the upregulation of the target gene *BCL2*, further inhibiting cell autophagy and apoptosis, and promoting immune response.

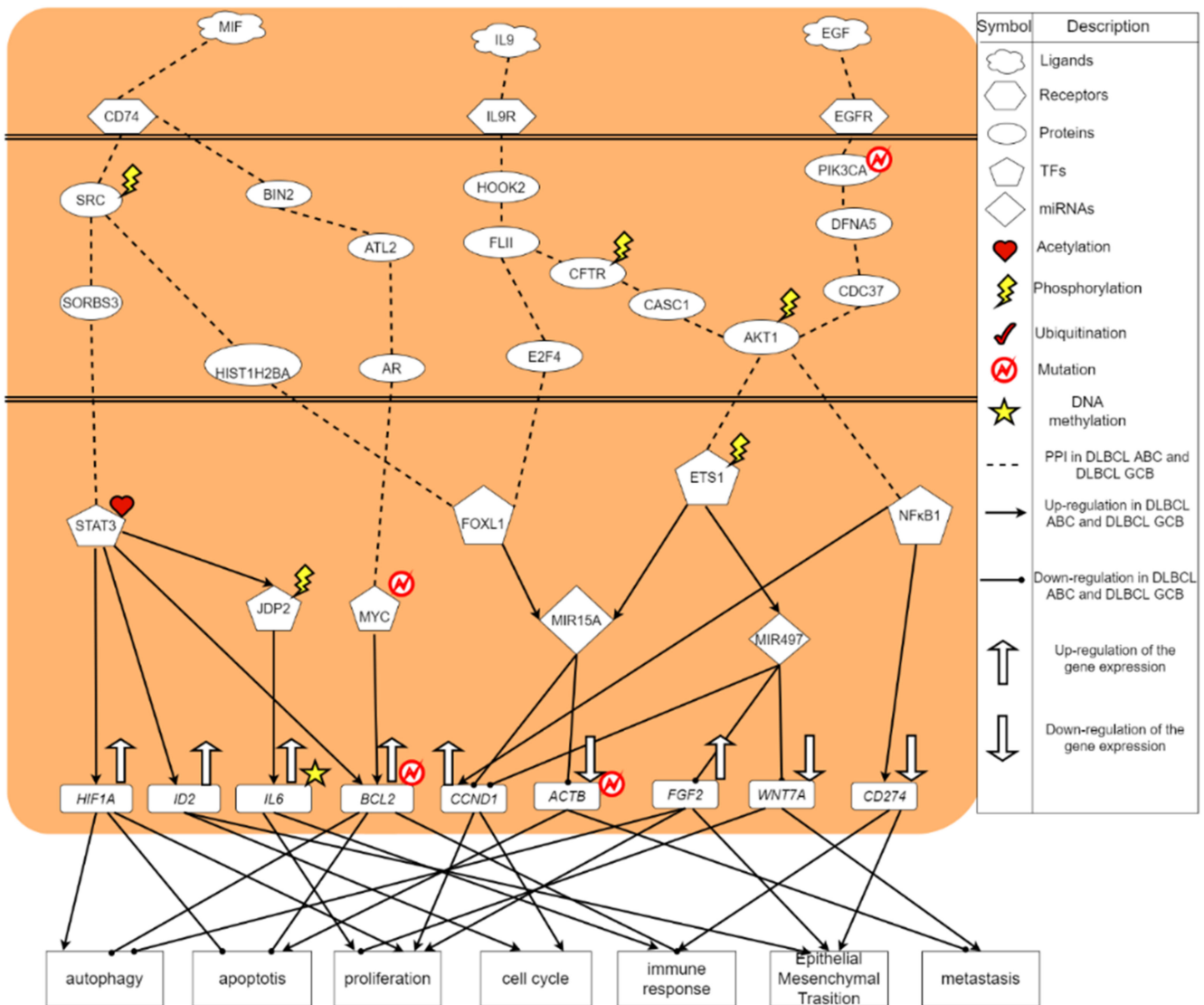


Figure 2. The core signaling pathways of DLBCL ABC. The black dotted line indicates protein–protein interactions in DLBCL ABC; the black arrow head of solid lines means activating cellular functions; the black circle head of solid lines means inhibiting cellular functions; the up arrow on the target gene indicates a high expression. The down arrow on the target gene indicates a low expression.

2.2. The Carcinogenic Molecular Mechanism in DLBCL GCB

The core signaling pathways of DLBCL GCB are shown in Figure 3. The microenvironment factor is a hepatocyte growth factor (HGF). HGF is secreted by mesenchymal cells and acts as a multifunctional cytokine on cells of primary epithelial origin [49]. Its ability to stimulate mitosis, cell movement and cytoplasmic matrix invasion makes it angiogenic, and plays a significant role in tumorigenesis and tissue regeneration [50]. The tyrosine kinase receptor MET receives the microenvironment factor HGF to regulate TF NFκB1, EZH2 and MYC, respectively. MET is an essential tyrosine kinase receptor for embryonic development, organ growth and wound healing. Through the signaling transduction proteins MAGEF1, IFT172 and GATA2, the mutated GATA2 protein will transmit the signal from MET to TF NFκB1. Among them, MAGEF1 can promote the degradation of proteasome and weaken the activity of some DNA repair and metabolic enzymes. In order to form cilia, IFT is necessary for the movement of other signaling proteins in the cilia [51]. Therefore, IFT172 plays a role in many different signaling pathways. IFT is considered to be a mediator of Hedgehog signaling and is one of the most important pathways in embryoge-

nesis. Furthermore, GATA2 plays an important role in regulating the transcription of genes related to the development and proliferation of hematopoietic and endocrine cells [52]. The mutation of GATA2 is associated with a variety of genetic and immune diseases, including myelodysplastic syndrome and acute myeloid leukemia [53]. The overexpressed NFκB1 can upregulate TF JUN. An improper activation of NFκB is related to many inflammatory diseases, while continuing to inhibit NFκB can cause abnormal immune cell development or delayed cell growth. This signal transduction event can lead to many biological processes such as inflammation, immunity, differentiation, cell growth, triggering growth, tumorigenesis and apoptosis. TF JUN was found to play an important role in cell proliferation [53]. In DLBCL GCB, TF JUN will downregulate the target gene *BCL6* and upregulate the target gene *FOXC1*, thereby correspondingly resulting in cell proliferation, autophagy, cell cycle, epithelial-mesenchymal transition (EMT) and cell metastasis.

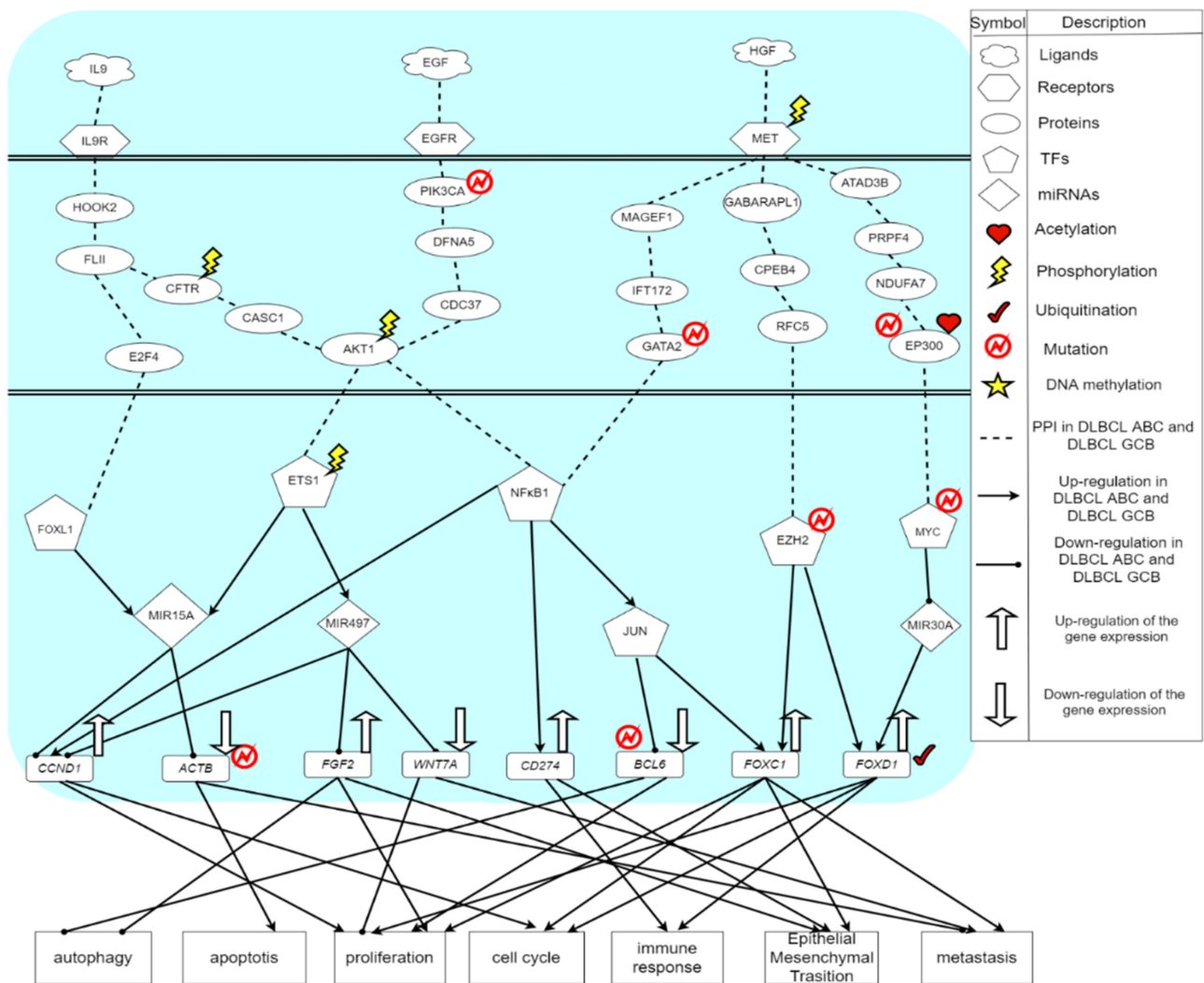


Figure 3. The core signaling pathways of DLBCL GCB: The dotted black line indicates protein–protein interactions of DLBCL GCB; the black arrow head of solid lines means activating cellular functions; the black circle head of solid lines means inhibiting cellular functions; the up arrow on the target gene indicates an up-regulation. The down arrow on the target gene indicates a down-regulation.

In addition, after receiving the signal from phosphorylated MET, the signaling transduction proteins GABARAPL1, CPEB4, and RFC5 transmit the signal to TF EZH2. GABARAPL1 is a protein related to autophagy [54]. CPEB4 is related to the cell cycle progression promoting the growth and proliferation of tumors [55]. RFC5 is involved in DNA replication and repair. TF EZH2 is responsible for healthy embryo development through the epigenetic

maintenance of genes, which take charge of regulating development and differentiation [56]. The mutation or overexpression of EZH2 is associated with a variety of cancers [57]. Blocking the activity of EZH2 may slow down tumor growth. It is known that EZH2 has become a target for inhibition as it was upregulated in a variety of cancers [58]. In Figure 2, the abnormally activated TF EZH2 can upregulate target gene *FOXC1*, further promoting cellular functions, including cell proliferation, cell cycle, epithelial-mesenchymal transition (EMT) and metastasis [59]. In addition, EZH2 will also upregulate *FOXD1*, causing cell proliferation, cell cycle and immune response.

In the next core signaling pathway, after HGF binding to MET, the signal will be transmitted to TF MYC via the signaling transduction proteins ATAD3B, PRPF4, NDUFA7, and EP300, where ATAD3B is a protein related to immunity, PRPF4 is involved in pre-mRNA splicing and modification [60], and NDUFA7-related pathways include respiration electronic transportation [61]. The mutant protein EP300 affected by acetylation can promote the transmission of upstream signals to downstream regulators. EP300 plays an important role in regulating cell growth and division, and promotes cell maturation and differentiation. One study indicates that EP300 protein is crucial for normal development of multicellular organisms before and after birth [62]. The expression of EP300 in DLBCL is significantly reduced. The mutations in EP300 usually remove or inactivate the histone acetyltransferase (HAT) coding domain of any gene [63]. In addition, study has pointed out that TF MYC was usually expressed constitutively in cancer [64], which led to an increased expression of many genes, some of which were involved in cell proliferation, in turn leading to cancer formation. The abnormally activated TF MYC will silence miRNA MIR30A [65]. Moreover, the low expression of MIR30A can negatively regulate the target gene *FOXD1*, thereby promoting cell proliferation, cell cycle and immune response.

Finally, from the results shown in Figures 1 and 2, although the cancer cells of DLBCL GCB have a stronger proliferative ability than the cancer cells of DLBCL ABC, we find that the ability of anti-apoptosis in DLBCL GCB is worse than DLBCL ABC. As a result, the cancer cells of DLBCL GCB are not conducive to spreading to other cell tissues. In other words, with stronger anti-apoptosis and anti-immune ability, DLBCL ABC will possess excessive cancer cell proliferation, which enhance the effect of metastasis and EMT. Therefore, DLBCL ABC has a higher mortality rate than GCB subtype.

2.3. The Common and Specific Carcinogenic Molecular Mechanism between DLBCL ABC and DLBCL GCB

In Figure 4, we have investigated the common and specific core signaling pathways between DLBCL ABC and DLBCL GCB. The microenvironment factor IL9 is a cell growth factor that can stimulate cell proliferation and prevent apoptosis [66]. Interleukin 9 receptor (IL9R) accepts IL9, a pleiotropic cytokine, belonging to the group of interleukins, through the signaling transduction proteins HOOK2, FLII, E2F4 in DLBCL ABC and DLBCL GCB, to upregulate TF FOXL1. In this core signaling pathway, the transduction signaling protein FLII plays a role in regulating cytoskeletal rearrangement involved in cell division and cell metastasis; E2F4 plays an important role in controlling the cell cycle and inhibiting tumor proteins. TF FOXL1 would regulate the expression of genes involved in cell metabolism, proliferation and differentiation [67].

The upregulated TF FOXL1 will overexpress MIR15A while MIR15A negatively regulates target genes *CCND1* and *ACTB*, respectively [68]. There have been studies showing that *ACTB* will mutate in DLBCL [69]. As for *CCND1*, it will cause cell proliferation and cell cycle progression [70]. After DNA replication, the replication chromosomes are separated into two independent cells. Generally speaking, the cell cycle can be divided into interphase (I) and mitosis (M). The stages of mitosis include prophase, prometaphase, metaphase, anaphase and telophase. The interphase (phase I) can usually be divided into the early stage of DNA synthesis (G1), the period of DNA synthesis (S) and the late stage of DNA synthesis (G2) [71]. The entire cell cycle can be expressed as: G1 phase → S phase → G2 phase → M phase. In G1 phase, the G1 checkpoint mechanism will prepare to ensure DNA

synthesis. Once the cell cycle checkpoint (Start or Restriction Point) is passed, the cell cycle is initiated and the process is irreversible, in which CCND1 is the most important cell cycle checkpoint [72]. DNA replication occurs in the S phase. During G2, the cells will prepare for mitosis, but in some cases the cells will jump out of the cell cycle and enter the so-called G0 phase. In G0 phase, the cells will leave the cycle and stop dividing. In fact, many cells in the human body are usually in the G0 phase, for example, nerve cells will never divide. The downregulation of ACTB will inhibit cell apoptosis and promote cell metastasis. Therefore, this core signaling pathway leads to the proliferation, the anti-apoptosis and the promotion of metastasis to exacerbate cancer progression in DLBCL patients. In addition, the receptor IL9R also transmits signals to TF ETS1 through signaling transduction proteins HOOK2, FLII, CFTR, CASC1, AKT1, where CFTR (cystic fibrosis transmembrane conductance regulator) is a membrane protein and chloride channel in vertebrates, which transport negatively charged particles called chloride ions into or out of the cell [73].

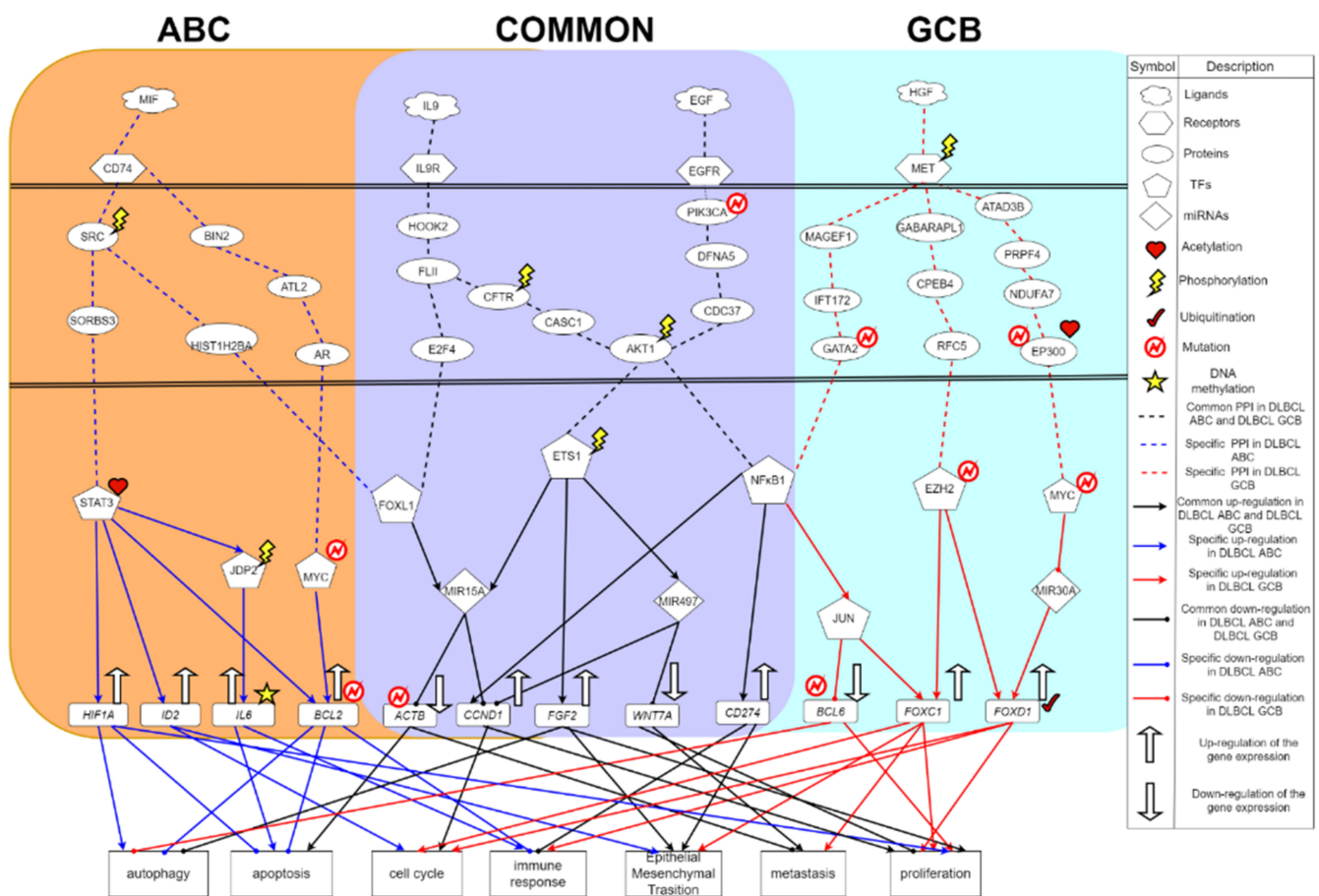


Figure 4. The common and specific core signaling pathways of DLBCL ABC and DLBCL GCB. This figure summarizes the genetic and epigenetic pathogenic molecular mechanisms of DLBCL ABC and DLBCL GCB. The core signaling pathways shown in the purple background are the common core signaling pathways of DLBCL ABC and DLBCL GCB. The blue line indicates specific core signaling pathways of DLBCL ABC; the red line indicates specific core signaling pathways of DLBCL GCB; the black line indicates common core signaling pathways of DLBCL ABC and DLBCL GCB; the arrow head of solid lines means activating cellular functions; the circle head of solid lines means inhibiting cellular functions. The up arrow on the target gene indicates an up-regulation. The down arrow on the target gene indicates a down-regulation.

For the next core signaling pathway in Figure 4, the epidermal growth factor receptor (EGFR) receives the microenvironmental factor EGF, and then the signal is transmitted

through the transduction proteins via the mutated PIK3CA, DFNA5, CDC37, and the phosphorylated AKT1 to TF ETS1, in which AKT1 is related to apoptosis [74]. It is found that AKT1 will phosphorylate AKT and inhibit apoptosis. ETS1 is a TF related to maintaining the proliferation of DLBCL and regulating the differentiation of germinal centers [75]. The overexpression of ETS1 will cause proliferation, survival and differentiation of lymphoma cells [76]. Modified by phosphorylation, the TF ETS1 will promote the expression of MIR15A and MIR497; meanwhile, ETS1 will upregulate the target gene FGF2. Furthermore, MIR497 will inhibit *CCND1* and *WNT7A*. It is known that *WNT7A* will promote cell proliferation and metastasis [77]. MIR15A will inhibit *CCND1* and *ACTB*. Although *CCND1* is inhibited by MIR15A and MIR497, *CCND1* is upregulated by another TF like NFκB1 as well. Hence, the total expression of *CCND1* in DLBCL is still upregulated, leading to subsequent cell proliferation and metastasis. In addition, *FGF2* can cause the inhibition of autophagy [78]. Autophagy is an orderly cell degradation and recycling process in all eukaryotes. There are generally three different forms of autophagy, including microautophagy, macroautophagy, and chaperone-mediated autophagy (CMA) [79]. One of their functions is to transport the cargo to the lysosome for degradation and recycling. *FGF2* will also promote cell proliferation and epithelial-mesenchymal transition (EMT). Therefore, this corresponding core signaling pathway will cause cell proliferation; simultaneously, autophagy and apoptosis will be inhibited, which further promote cancer cell metastasis and EMT in DLBCL. Moreover, the formation process of EMT will destroy the adhesion between normal cells improving the ability of migration and invasion for the cancer cells. It brings benefit to the cancer metastasis. This process not only accelerates the spread of cancer cells but also makes cancer cells spread intensely [79].

The microenvironment factor EGF (epidermal growth factor) plays an important role in regulating cell growth, proliferation and differentiation. After EGF binding to the receptor EGFR on the cell surface, the signals would be transmitted to TF NFκB1 through the signaling transduction proteins including the mutated PIK3CA, DFNA5, CDC37, and the phosphorylated AKT1. The role of PIK3CA is to promote the catalytic reaction of the message transmission [80]; and the mutation of PIK3CA will change the way of cells, regulating physiological responses to cause the formation of cancer. DFNA5 also has been found in other types of cancer such as stomach cancer, colorectal cancer, and breast cancer. Its characteristic is to induce apoptosis. Among this pathway, CDC37, a molecular chaperone protein, has a specific function in cell signaling transduction. It binds to a variety of kinases and regulates cyclin. Moreover, the TF NFκB1 will promote the upregulation of the target gene *CCND1*. Improper activation of NFκB is related to many inflammatory diseases, and continuous inhibition of NFκB will lead to poor development of immune cells or the delay of cell growth [81]. In summary, this signal transduction event is associated with many biological processes, such as inflammation, immunity, differentiation, and cell growth. It finally triggers cell growth, tumorigenesis and apoptosis. Besides, the upregulated *CCND1* further promotes cellular functions including cell proliferation and cell cycle progression. TF NFκB1 also upregulates the expression of target gene *CD274* (*PD-L1*), which in turn triggers cellular functions of EMT and immune responses [82].

2.4. Systems Drug Design Procedure Considering Drug-Target Interaction, Drug Regulation Ability, and Drug Toxicity

After investigating pathogenic molecular mechanisms, we identified two pools of essential biomarkers as drug targets for two subtypes of DLBCL shown in Table 1. The systems drug design procedure is in Figure S5. Firstly, we consider the drug-target interaction ability toward the identified biomarkers in terms of the application of DNN-based DTI model. Subsequently, filtered by drug regulation ability and drug toxicity, the number of predicted drug candidates would be narrowed down. For training DNN-based DTI model, there were 70% of the data as training set, including 10% of the data as validation set. The remaining 30% of the data were used as the testing set. To the architecture of DNN-based DTI model, it is a fully connected neural network consisting of one input

layer, four hidden layers and one output layer, of which four hidden layers have 512, 256, 128, 64 neurons, respectively. The dropout was added in each hidden layer for reducing overfitting. We used ReLU as the activation function for each hidden layer. In the output layer, we chose sigmoid to be the activation function for limiting the output value between zero and one. It is noted that the drugs with higher interaction probability (greater than 0.5) would be selected as drug candidates. Evaluating the robustness of hyperparameters including the number of nodes, dropout, and learning rate, we performed 10-fold cross validation. The corresponding 10-fold cross validation results could be found in Figure S6. The average accuracy of testing is 98.698% (standard deviation: 0.0659). Furthermore, we plot the receiver operating characteristic curve (ROC) in Figure S7. The area under ROC of the DNN-based DTI model is 0.99. Here, except for drug-target interaction, we regard drug regulation ability and drug toxicity as our drug design specifications as well. By referring to the connectivity map (CMap) [83], we could find the gene signatures after treating with more than 1300 compounds in numbers of cultivated cell lines. The goal here is to find the drugs owning the ability to reverse the abnormal gene expression. Meanwhile, according to the median lethal dose, which is looked up at DrugBank [84], we expect that the selected candidate small molecules could have less toxicity (Table S4). Consequently, we suggested famotidine, chlorzoxazone, and etoposide to be the potential multiple-molecule drug for alleviating DLBCL ABC (Table 2); famotidine, chlorzoxazone, and methotrexate as potential multiple-molecule drug for mitigating DLBCL GCB (Table 3).

Table 1. The biomarkers (drug targets) are identified for DLBCL ABC and DLBCL GCB.

Cancer	Biomarkers (Drug Targets)
DLBCL ABC	FOXL1 NFκB1 AKT1 MYC STAT3
DLBCL GCB	FOXL1 NFκB1 AKT1 MYC EZH2

Table 2. The multiple-molecule drug and the corresponding target proteins for DLBCL ABC.

Drugs	Targets				
	FOXL1	NFκB1	AKT1	MYC	STAT3
Famotidine		O	O		O
Chlorzoxazone	O	O			O
Etoposide		O		O	O

O: The drug targets to its potential target proteins.

Table 3. The multiple-molecule drug and the corresponding target proteins for DLBCL GCB.

Drugs	Targets				
	FOXL1	NFκB1	AKT1	MYC	EZH2
Famotidine		O	O		O
Chlorzoxazone	O	O			O
Methotrexate			O	O	O

O: The drug targets to its potential target proteins.

3. Discussion

Based on the core signaling pathways, we investigated the downstream carcinogenic pathogenesis and identified five significant biomarkers as drug targets for DLBCL ABC and DLBCL GCB, respectively (Table 1). Among these biomarkers, STAT3 and MYC can influence cancer cell survival and promote proliferation. The immune response of a human can be inhibited by NFκB1. Both AKT1 and EZH2 are associated with cancer metastasis and invasion, resulting in the deterioration of tumors. In contrast, FOXL1 can promote apoptosis and inhibit cancer cell metastasis. In order to reduce the ability of inhibiting apoptosis and promoting proliferation by HIF1A, to diminish the ability of promoting proliferation and

cell cycle by ID2, to decrease the ability of reducing apoptosis, and to reduce the ability of inhibiting autophagy and suppressing immunity by BCL2, STAT3 was selected as the biomarker to be inhibited. For enhancing the ability of promoting apoptosis and inhibiting metastasis caused by the target gene ACTB, FOXL1 was selected as a biomarker to be up-regulated. Moreover, to reduce the ability of inhibiting autophagy, promoting proliferation and EMT by FGF2, and to inhibit the ability of promoting cancer cell metastasis by WNT7A, AKT1 was selected as a biomarker to be inhibited. In addition, considering the significant impact of immune response on DLBCL ABC and GCB, NF κ B1 was selected as the drug target to be inhibited, thereby reducing the ability of both suppressing immune response by CD274 and promoting cell cycle and proliferation by CCND1. For the purpose of reducing the ability of promoting proliferation, metastasis, and EMT by FOXC1 and reducing the proliferation caused by FOXD1, EZH2 was selected as a biomarker to be down-regulated.

Using immunotherapy against cancer gains a lot of attention in recent years. Here, we selected NF κ B1 as a drug target to indirectly inhibit PD-L1 and block the related mechanisms having contribution to escape immunity. Among the proposed two multiple-molecule drugs, chlorzoxazone is a drug for treating muscle spasms [85]. It acts on the spinal cord by suppressing reflexes. One tumor related study has shown that it was used with other drugs to inhibit tumor growth, including tumor metastasis, migration, and invasion [86]. It is known that STAT3 and NF κ B1 are significant activators of carcinogenic signal transduction. Chlorzoxazone can effectively reduce the expression of STAT3, NF κ B1, and EZH2, and upregulate FOXL1, therefore, it might be an effective drug for DLBCL. In addition, famotidine could decrease the production of stomach acid. Its pharmacologic activity is used in the treatment of acid-related gastrointestinal conditions, including duodenal ulcer, esophageal adenocarcinoma and chronic gastroesophageal reflux disease in adults and children. Meanwhile, famotidine can inhibit the occurrence of cancer by inhibiting STAT3. Its drug targets include NF κ B1, AKT1, and EZH2 as well. Moreover, etoposide has been studied to replace the DLBCL current standard treatment with R-CHOP, including rituximab, cyclophosphamide, doxorubicin, vincristine and prednisone, among them, the disadvantage of doxorubicin is its cardiotoxicity [87]. Another study also mentioned that etoposide substituted could treat most of DLBCL patients who cannot receive anthracycline treatment [88]. Methotrexate, a chemotherapeutic drug and immunosuppressive agent, has been commonly applied in combination with other drugs for the treatment of breast cancer, leukemia, lung cancer, lymphoma, autoimmune disease, and ectopic pregnancy [89]. By down-regulating its target protein EZH2, methotrexate can treat cancers [89]. Note that dysregulation of EZH2 is closely related to oncogenesis of various tissue types. More and more evidences show that targeting EZH2 has great therapeutic potential in cancers [90]. Methotrexate can not only downregulate the expression of EZH2, but also interact with AKT1 and MYC. Hence, we suggest it as one of the small molecule drugs in our proposed drug combination.

Given the substantial costs and long development timeline of new drug discovery, the repurposing of old drugs to treat common and rare disease becomes an attractive proposition. In other words, drug repurposing is a strategy for identifying new uses for approved drugs that are outside the scope of known medical indication. In this study, by the proposed systems biology approaches and drug design specifications, we suggested multiple-molecule drugs (drug combinations) for DLBCL ABC and GCB, respectively. Those suggested small molecules are FDA approved. Although some studies have shown that etoposide and methotrexate were used in DLBCL, their combinations with famotidine and chlorzoxazone are still worth studying in the future in terms of synergistic and antagonistic effects. Leveraging computational biology methods, this study might provide new perspectives of understanding the pathogenic molecular mechanisms of DLBCL ABC and DLBCL GCB at a system level and give an alternative way to accelerate systems drug discovery for new therapeutics.

4. Materials and Methods

4.1. Overview of Systems Drug Discovery for DLBCL ABC and DLBCL GCB

The DLBCL microarray data is from the National Center for Biotechnology Information (NCBI) with accession number GSE117556. The corresponding platform is GPL14951. The dataset samples were divided into two subtypes, DLBCL ABC and DLBCL GCB, in which the ABC subtype has worse prognosis. There are 468 samples and 249 samples for DLBCL GCB and DLBCL ABC, respectively. The flowchart of systems drug discovery is in Figure 1. For identifying essential biomarkers as drug targets to alleviate DLBCL ABC and DLBCL GCB, we investigated the pathogenic molecular mechanisms based on the systems biology methods: (1) big database mining; (2) system modeling; (3) system identification and system order detection scheme; (4) principal network projection method.

Firstly, by big database mining, we constructed a candidate genome-wide genetic and epigenetic network (GWGEN), which is represented by a Boolean matrix (i.e., 0 or 1 if interaction is nonexistent or existent between two nodes). It is noted that both DLBCL ABC and DLBCL GCB shared the same candidate GWGEN. The candidate GWGEN consists of the candidate protein–protein interaction network (PPIN) and candidate gene regulatory network (GRN). For the candidate PPIN, we refer to the following database: DIP [91], IntAct [92], BioGRID [93], BIND [94], and MINT [95]. To the candidate GRN, we collect the pairs of transcription factors and target genes from ITFP [96] and HTRIdb [97]. Moreover, we look up databases including TargetScan [98], CircuitsDB [99], and StarBase2.0 [100] for the post-transcriptional regulations between miRNA, lncRNA and their target genes. After conducting system modeling for proteins, genes, miRNAs, and lncRNAs, we could evaluate system models' parameters by the system identification method with the help of microarray dataset in two subtypes of DLBCL. There might be false-positive interactions in the candidate GWGEN caused by various experimental conditions. Therefore, we performed a system order detection approach to prune these false-positive interactions for obtaining real GWGENs for DLBCL ABC and DLBCL GCB, respectively (Figures S1 and S2). The total number of nodes (i.e., transcription factors, receptors, proteins, miRNAs, lncRNAs) and their corresponding edges in the candidate GWGEN, real GWGEN of DLBCL ABC, and real GWGEN of DLBCL GCB are shown in Table S1. However, the real GWGENs were still too complicated to analyze. Applying principal network projection (PNP) method, from the real GWGENs, we could extract core GWGENs (Figures S3 and S4), which is comprised of the top 3000 nodes based on the descending order of projection value. The higher the projection value is, the more contribution provided by the node in the real GWGEN. Additionally, we did gene enrichment analyses by the Database for Annotation, Visualization and Integrated Discovery (DAVID) Bioinformatics Resources version 6.8 based on the genes in core GWGENs (Tables S2 and S3). Projecting the corresponding core GWGENs in the annotation of Kyoto Encyclopedia of Genes and Genomes (KEGG), we could further investigate the common and specific pathogenic molecular mechanisms and identify essential biomarkers as drug targets.

For suggesting potential drug candidates toward these identified drug targets, we followed systems drug design procedure shown in Figure S5. The drug design specifications include drug–target interaction probability, drug regulation ability, and drug toxicity. To estimate drug–target interaction probability, we trained a DNN-based DTI model in advance. We regard the drugs having higher predicted probability as drug candidates. Subsequently, the number of those predicted drug candidates would be narrowed down by considering drug regulation ability and toxicity. Here, we aim to find drugs having the ability to reverse abnormal gene expression with low toxicity. More details will be discussed in the following sections.

4.2. Constructing the System Models in the GWGEN to Identify Real GWGEN of DLBCL GCB and DLBCL ABC

To investigate the molecular mechanisms of DLBCL GCB and DLBCL ABC, we constructed the interactive and regulatory models in the candidate GWGEN, including protein–

protein interactions, transcriptional regulations, miRNA regulations, and lncRNA regulations. For the candidate PPIN (PPIN), the i -th protein is described in the following equation:

$$p_i[n] = \sum_{\substack{k=1 \\ k \neq i}}^{Y_i} \alpha_{ik} p_i[n] p_k[n] + \phi_{i,PPIN} + \eta_{i,PPIN}[n] \text{ for } i = 1, \dots, I, \text{ and } n = 1, \dots, N. \quad (1)$$

where α_{ik} is the interaction ability between the i -th protein and the k -th interactive protein; $p_i[n]$ denotes the expression level of the i -th protein for the sample n ; $p_k[n]$ represents the expression level of the k -th protein for the n data sample; Y_i indicates the total number of proteins interacting with the i -th protein and I denotes the total number of proteins in the candidate PPIN; N is the total number of data samples; $\phi_{i,PPIN}$ is the basal level of the i -th protein caused by some unknown interactions including phosphorylation and acetylation; $\eta_{i,PPIN}[n]$ represents the stochastic noise as a result of the modeling residue and measurement noise for the n data sample.

For the candidate gene regulatory network (GRN) in the candidate GWGEN, the systematic gene regulation model for the q -th gene of DLBCL cells to sample n can be governed by the following form:

$$g_q[n] = \sum_{\substack{j=1 \\ j \neq q}}^{J_q} A_{qj} z_j[n] + \sum_{w=1}^{W_q} B_{qw} x_w[n] - \sum_{h=1}^{H_q} C_{qh} d_h[n] g_q[n] + \phi_q + \eta_q[n] \quad (2)$$

for $q = 1, \dots, Q$ and $n = 1, \dots, N$.

where $g_q[n]$ represents the expression level of the q -th gene; J_q indicates the total number of TFs binding to the q -th gene; W_q represents the total number of lncRNAs binding to the q -th gene; H_q denotes the total number of miRNAs inhibiting the q -th gene; A_{qj} denotes the transcription regulatory ability from the j -th TF to the q -th gene; B_{qw} is the regulation ability from the w -th lncRNA to the q -th gene; $C_{qh} \geq 0$ represents the post-transcription regulatory ability, with which the h -th miRNA inhibits the q -th gene; $z_j[n]$, $x_w[n]$, and $d_h[n]$ indicate the expression of the j -th TF, the w -th lncRNA, and the h -th miRNA, respectively. Q is the total number of genes and N denotes the total number of data samples; ϕ_q represents the basal level of the q -th gene expression due to unknown regulations containing post-transcriptional modifications; $\eta_q[n]$ is the stochastic noise of the q -th gene for the data sample n caused by the model uncertainty and data noise. Furthermore, in the same way, the systematic models of the candidate lncRNA regulation network and the candidate miRNA regulation network can be referred to in the Supplementary Materials.

4.3. Using the System Identification Method and System Order Detection Approach to Build Real GWGENs of DLBCL GCB and DLBCL ABC

To estimate the unknown parameters for the PPI model in the candidate PPIN, we utilize a system identification method and system order detection approach on our systematic models with the help of genome-wide microarray data of patient samples. The PPI equation in Equation (1) could be rewritten as below:

$$p_i[n] = [p_i[n] p_1[n] \cdots p_i[n] p_{Y_i}[n] \ 1] \times \begin{bmatrix} \alpha_{i1} \\ \vdots \\ \alpha_{iY_i} \\ \phi_i \end{bmatrix} + \eta_i[n] \quad (3)$$

$$= \zeta_i[n] \cdot \varphi_{i,P} + \tau_i[n], \text{ for } i = 1, \dots, I \text{ and } n = 1, \dots, N.$$

where $\xi_i[n]$ determines the regression vector, which could be computed by the microarray data; $\varphi_{i,P}$ indicates the unknown parameter vector for the i -th protein. The Equation (3) of the i -th protein could be augmented for N samples as below:

$$\begin{bmatrix} p_i[1] \\ p_i[2] \\ \vdots \\ p_i[N] \end{bmatrix} = \begin{bmatrix} \xi_{i,P}[1] \\ \xi_{i,P}[2] \\ \vdots \\ \xi_{i,P}[N] \end{bmatrix} \cdot \varphi_{i,P} + \begin{bmatrix} \tau_i[1] \\ \tau_i[2] \\ \vdots \\ \tau_i[N] \end{bmatrix} \tag{4}$$

Furthermore, the Equation (4) could be simplified represented as:

$$P_i = \Xi_{i,P} \cdot \varphi_{i,P} + T_i \tag{5}$$

Therefore, the unknown parameters in the vector $\varphi_{i,P}$ could be estimated by solving the least square estimation problem:

$$\hat{\varphi}_{i,P} = \min_{\varphi_{i,P}} \frac{1}{2} \|\Xi_{i,P} \cdot \varphi_{i,P} - P_i\|_2^2 \tag{6}$$

where $\hat{\varphi}_{q,G}$ is the estimated vector including the estimated interaction parameters for the i -th protein.

In the same way, the gene regulation model in Equation (2) could be rewritten as below:

$$g_q[n] = \left[z_1[n] \cdots z_{J_q}[n] x_1[n] \cdots x_{W_q}[n] g_q[n] d_1[n] \cdots g_q[n] d_{H_q}[n] 1 \right] \times \begin{bmatrix} A_{q1} \\ \vdots \\ A_{qJ_q} \\ B_{q1} \\ \vdots \\ B_{qW_q} \\ -C_{q1} \\ \vdots \\ -C_{qH_q} \\ \phi_q \end{bmatrix} + \eta_q[n] \tag{7}$$

$$= \xi_q[n] \cdot \varphi_{q,G} + \tau_q[n], \text{ for } q = 1, \dots, Q \text{ and } n = 1, \dots, N.$$

where $\xi_q[n]$ indicates the regression vector, which could be obtained from the microarray data and $\varphi_{q,G}$ denotes the unknown parameters vector for the q -th gene. We could expand the Equation (7) for N samples as shown below:

$$\begin{bmatrix} g_q[1] \\ g_q[2] \\ \vdots \\ g_q[N] \end{bmatrix} = \begin{bmatrix} \xi_{q,G}[1] \\ \xi_{q,G}[2] \\ \vdots \\ \xi_{q,G}[N] \end{bmatrix} \cdot \varphi_{q,G} + \begin{bmatrix} \tau_q[1] \\ \tau_q[2] \\ \vdots \\ \tau_q[N] \end{bmatrix} \tag{8}$$

Moreover, the Equation (8) could be simplified in the following form:

$$G_q = \Xi_{q,G} \cdot \varphi_{q,G} + T_q \tag{9}$$

Hence, by solving the following constrained linear least square estimation problem, we could have the estimated regulatory parameters in the vector $\varphi_{q,G}$.

$$\hat{\varphi}_{q,G} = \min_{\varphi_{q,G}} \frac{1}{2} \|\Xi_{q,G} \cdot \varphi_{q,G} - G_q\|_2^2$$

$$\text{subject to } \begin{bmatrix} 0 & \cdots & \cdots & 0 & 0 & \cdots & \cdots & 0 & 1 & 0 & \cdots & 0 & 0 \\ \vdots & \ddots & & \vdots & \vdots & \ddots & & \vdots & 0 & \ddots & \ddots & \vdots & \vdots \\ \vdots & & \ddots & \vdots & \vdots & & \ddots & \vdots & \vdots & \ddots & \ddots & 0 & 0 \\ 0 & \cdots & \cdots & 0 & 0 & \cdots & \cdots & 0 & 0 & \cdots & 0 & 1 & 0 \end{bmatrix} \varphi_{q,G} \leq \begin{bmatrix} 0 \\ \vdots \\ \vdots \\ 0 \end{bmatrix} \quad (10)$$

$J_q \qquad \qquad \qquad W_q \qquad \qquad \qquad H_q$

where $\hat{\varphi}_{q,G}$ is the estimated vector including estimated regulatory parameters in the Equation (2). Meanwhile, the miRNA repression parameters C_{qh} are guaranteed to be positive (i.e., $C_{qh} \geq 0$) for $h = 1, \dots, H_q$.

It is noted that there are many false-positive interactions in the candidate GWGEN as a result of various experimental conditions in different databases. Here, we applied a system order detection approach in Equations (5) and (9) to prune the false-positive interactions. According to the Akaike information criterion (AIC) theory [101], the smallest AIC value would lead to the most accurate model. In other words, the smaller the AIC value we get, the closer we detect to the real system order. The formulas of AIC for determining the system order of interactions among the i -th protein and the q -th gene are given as below:

$$AIC(Y_i) = \log(\hat{\rho}_{i,P}^2) + \frac{2(Y_i+1)}{N}$$

$$\text{where } \hat{\rho}_{i,P} = \sqrt{\frac{(P_i - (\Xi_{i,P} \cdot \hat{\varphi}_{i,P}))^T (P_i - (\Xi_{i,P} \cdot \hat{\varphi}_{i,P}))}{N}}$$
(11)

$\hat{\rho}_{i,P}$ and Y_i denote the estimated residual error and the number (system order) of PPIs with the i -th protein, respectively; $\hat{\varphi}_{i,P}$ denotes the estimated interaction parameters of the i -th protein by solving (6). Based on the AIC theory, the real system order Y_i^* resulting in the smallest $AIC(Y_i^*)$.

$$AIC(J_q, W_q, H_q) = \log(\hat{\rho}_{q,G}^2) + \frac{2(\theta_{q,G}+1)}{N}$$

$$\text{where } \hat{\rho}_{q,G} = \sqrt{\frac{(G_q - (\Xi_{q,G} \cdot \hat{\varphi}_{q,G}))^T (G_q - (\Xi_{q,G} \cdot \hat{\varphi}_{q,G}))}{N}} \text{ and } \theta_{q,G} = J_q + W_q + H_q$$
(12)

$\hat{\rho}_{i,P}$ and $\theta_{q,G}$ represent the estimated residual error and the number of regulations on the q -th gene, respectively; $\hat{\varphi}_{q,G}$ is the estimated parameter vector of the q -th gene obtained by solving (9). It is noted that the real system order $J_q^* + W_q^* + H_q^*$ lead to the smallest $AIC(J_q^* + W_q^* + H_q^*)$. For each protein, gene, miRNA, and lncRNA, we used forward and backward search to find the real system order by AIC. The unimportant interactions among the candidate GWGEN, which are out of the system order, would be removed via the system order detection approach. By doing so, we could find the real GWGENs of DLBCL GCB and DLBCL ABC, respectively. The system identification method and system order detection approach could be applied to the lncRNA and miRNA system models as well (Supplementary Materials).

4.4. Extracting the Core GWGENs from the Real GWGENs by Principal Network Projection (PNP) Method

Although we have pruned the false-positive interactions from the candidate GWGEN by the system identification method and system order detection approach, the real GWGENs of DLBCL GCB and DLBCL ABC in Figures S1 and S2 are still too complex to investigate the common and specific pathogenic molecular mechanisms between DLBCL GCB and DLBCL ABC. Therefore, we utilize the PNP method to extract the core GWGENs from the real GWGENs of DLBCL GCB and DLBCL ABC. Before using the PNP method, we have to build a combined network matrix Z as follows:

$$Z = \begin{bmatrix}
 \hat{\alpha}_{11} & \dots & \hat{\alpha}_{1k} & \dots & \hat{\alpha}_{1K} & 0 & \dots & 0 & \dots & 0 & 0 & \dots & 0 & \dots & 0 \\
 \vdots & \ddots & \vdots & \ddots & \vdots & \vdots & \ddots & \vdots & \ddots & \vdots & \vdots & \ddots & \vdots & \ddots & \vdots \\
 \hat{\alpha}_{i1} & \dots & \hat{\alpha}_{ik} & \dots & \hat{\alpha}_{iK} & 0 & \dots & 0 & \dots & 0 & 0 & \dots & 0 & \dots & 0 \\
 \vdots & \ddots & \vdots & \ddots & \vdots & \vdots & \ddots & \vdots & \ddots & \vdots & \vdots & \ddots & \vdots & \ddots & \vdots \\
 \hat{\alpha}_{I1} & \dots & \hat{\alpha}_{Ik} & \dots & \hat{\alpha}_{IK} & 0 & \dots & 0 & \dots & 0 & 0 & \dots & 0 & \dots & 0 \\
 \hline
 \hat{A}_{11} & \dots & \hat{A}_{1j} & \dots & \hat{A}_{1J} & \hat{B}_{11} & \dots & \hat{B}_{1w} & \dots & \hat{B}_{1W} & -\hat{C}_{11} & \dots & -\hat{C}_{1h} & \dots & -\hat{C}_{1H} \\
 \vdots & \ddots & \vdots & \ddots & \vdots & \vdots & \ddots & \vdots & \ddots & \vdots & \vdots & \ddots & \vdots & \ddots & \vdots \\
 \hat{A}_{q1} & \dots & \hat{A}_{qj} & \dots & \hat{A}_{qJ} & \hat{B}_{q1} & \dots & \hat{B}_{qw} & \dots & \hat{B}_{qW} & -\hat{C}_{q1} & \dots & -\hat{C}_{qh} & \dots & -\hat{C}_{qH} \\
 \vdots & \ddots & \vdots & \ddots & \vdots & \vdots & \ddots & \vdots & \ddots & \vdots & \vdots & \ddots & \vdots & \ddots & \vdots \\
 \hat{A}_{Q1} & \dots & \hat{A}_{Qj} & \dots & \hat{A}_{QJ} & \hat{B}_{Q1} & \dots & \hat{B}_{Qw} & \dots & \hat{B}_{QW} & -\hat{C}_{Q1} & \dots & -\hat{C}_{Qh} & \dots & -\hat{C}_{QH} \\
 \hline
 \hat{\beta}_{11} & \dots & \hat{\beta}_{1j} & \dots & \hat{\beta}_{1J} & \hat{\lambda}_{11} & \dots & \hat{\lambda}_{1w} & \dots & \hat{\lambda}_{1W} & -\hat{\gamma}_{11} & \dots & -\hat{\gamma}_{1h} & \dots & -\hat{\gamma}_{1H} \\
 \vdots & \ddots & \vdots & \ddots & \vdots & \vdots & \ddots & \vdots & \ddots & \vdots & \vdots & \ddots & \vdots & \ddots & \vdots \\
 \hat{\beta}_{v1} & \dots & \hat{\beta}_{vj} & \dots & \hat{\beta}_{vJ} & \hat{\lambda}_{v1} & \dots & \hat{\lambda}_{vw} & \dots & \hat{\lambda}_{vW} & -\hat{\gamma}_{v1} & \dots & -\hat{\gamma}_{vh} & \dots & -\hat{\gamma}_{vH} \\
 \vdots & \ddots & \vdots & \ddots & \vdots & \vdots & \ddots & \vdots & \ddots & \vdots & \vdots & \ddots & \vdots & \ddots & \vdots \\
 \hat{\beta}_{V1} & \dots & \hat{\beta}_{Vj} & \dots & \hat{\beta}_{VJ} & \hat{\lambda}_{V1} & \dots & \hat{\lambda}_{Vw} & \dots & \hat{\lambda}_{VW} & -\hat{\gamma}_{V1} & \dots & -\hat{\gamma}_{Vh} & \dots & -\hat{\gamma}_{VH} \\
 \hline
 \hat{\sigma}_{11} & \dots & \hat{\sigma}_{1j} & \dots & \hat{\sigma}_{1J} & \hat{\delta}_{11} & \dots & \hat{\delta}_{1w} & \dots & \hat{\delta}_{1W} & -\hat{\omega}_{11} & \dots & -\hat{\omega}_{1h} & \dots & -\hat{\omega}_{1H} \\
 \vdots & \ddots & \vdots & \ddots & \vdots & \vdots & \ddots & \vdots & \ddots & \vdots & \vdots & \ddots & \vdots & \ddots & \vdots \\
 \hat{\sigma}_{m1} & \dots & \hat{\sigma}_{mj} & \dots & \hat{\sigma}_{mJ} & \hat{\delta}_{m1} & \dots & \hat{\delta}_{mw} & \dots & \hat{\delta}_{mW} & -\hat{\omega}_{m1} & \dots & -\hat{\omega}_{mh} & \dots & -\hat{\omega}_{mH} \\
 \vdots & \ddots & \vdots & \ddots & \vdots & \vdots & \ddots & \vdots & \ddots & \vdots & \vdots & \ddots & \vdots & \ddots & \vdots \\
 \hat{\sigma}_{M1} & \dots & \hat{\sigma}_{Mj} & \dots & \hat{\sigma}_{MJ} & \hat{\delta}_{M1} & \dots & \hat{\delta}_{Mw} & \dots & \hat{\delta}_{MW} & -\hat{\omega}_{M1} & \dots & -\hat{\omega}_{Mh} & \dots & -\hat{\omega}_{MH}
 \end{bmatrix} \in \mathfrak{R}^{(I^*+Q^*+V^*+M^*) \times (J^*+W^*+H^*)} \tag{13}$$

where the estimated parameters in (13) are obtained by solving the constrained linear least square estimation problem and conducting a system order detection approach based on AIC. The entry, which is pruned by AIC, would be padded with zero. The i -th row of Z denotes the interaction and regulation parameters of the i -th node in the real GWGEN. The PNP method is based on the singular value decomposition of Z shown as below:

$$Z = UKG^T \tag{14}$$

where $U \in \mathfrak{R}^{(I^*+Q^*+V^*+M^*) \times (I^*+Q^*+V^*+M^*)}$, $G \in \mathfrak{R}^{(J^*+W^*+H^*) \times (J^*+W^*+H^*)}$, $K = \text{diag}(k_1, \dots, k_r, \dots, k_{J^*+W^*+H^*}) \in \mathfrak{R}^{(I^*+Q^*+V^*+M^*) \times (J^*+W^*+H^*)}$ and K denotes the diagonal matrix which consists of $J^* + W^* + H^*$ singular values of Z in descending order (i.e., $k_1 \geq \dots \geq k_r \geq \dots \geq k_{J^*+W^*+H^*} \geq 0$). The normalization of singular values is defined as below:

$$E_r = \frac{k_r^2}{\sum_{r=1}^{J^*+W^*+H^*} k_r^2}, \quad \sum_{i=1}^{J^*+W^*+H^*} E_r = 1 \tag{15}$$

Here, we choose the top R normalized singular values of combined network matrix Z with the minimum R to satisfy $\sum_{r=1}^R E_r \geq 0.85$. It shows that we could use the top R singular vectors to construct 85% network structure as principal network structure. Afterwards, we project each node in the real GWGEN (i.e., each row in Z) to the top R singular vectors in G^T as below:

$$F(t, a) = d_{t,:} \cdot r_{a,:}^T, \text{ for } t = 1, \dots, I^* + Q^* + V^* + M^*, a = 1, \dots, R. \tag{16}$$

where $d_{t,:}$ denotes the t -th row vector of Z ; $r_{a,:}^T$ is the a -th singular vector of G^T . Subsequently, we compute the 2-norm projection value for each node in the following:

$$P(t) = \sqrt{\sum_{a=1}^R F^2(t, a)}, \text{ for } t = 1, \dots, I^* + Q^* + V^* + M^*, a = 1, \dots, R. \tag{17}$$

where $P(t)$ denotes the 2-norm projection value of each t -th node in the real GWGEN on the top R singular vectors. The greater a projection value is, the more significant the t -th node in the principal structure of the real GWGEN. If the projection value approaches zero, it means that the related t -th node is almost independent to the principal network structure. In other words, the greater the projection value of a node in real GWGEN is, the higher probability is that a node will be an important component in the principal network structure. Lastly, the core GWGENs of DLBCL ABC and DLBCL GCB could be extracted from the real GWGENs based on the top-rank 3000 projection values of the nodes. Moreover, the core GWGENs of DLBCL ABC and DLBCL GCB are shown in Figures S3 and S4.

4.5. Deep Neural Network (DNN)-Based Drug-Target Interaction (DTI) Model for Multiple-Molecule Drug Design

To train a DNN-based DTI model, the drug-target interaction dataset came from BindingDB [102]. We picked drugs that at least had four interactions. Hence, in the selected dataset, there are 80,291 known drug-target interactions between 38,015 drugs and 7292 proteins. In order to simply avoid a class imbalance issue, which would degrade the training performance or make the learning progress biased toward the majority class, we randomly chose the negative instance (unknown drug-target pair) in the same size as positive instance (known drug-target pair). We trained the model using 70% of the data containing 10% of the data as validation set. The remaining 30% of data were used as testing set. Delineating the drug-target pair in a numerical vector, we transformed them into a feature vector by PyBioMed Python package under python 2.7 environment [103]. The PyMolecule module in PyBioMed was responsible to transform the drug descriptors. The drug features include commonly used structural and physicochemical information. The PyProtein module in PyBioMed was applied to transform the target descriptors. The target features were computed based on the structural and physicochemical properties of proteins and peptide from amino acid sequence. The feature vector for each drug-target pair can be represented in the following form:

$$w_{drug-target} = [D, T] = [d_1, d_2, \dots, d_X, t_1, t_2, \dots, t_Y] \quad (18)$$

where $w_{drug-target}$ denotes a feature vector of drug-target pair, X and Y are the total number of drug features and target features, which are 363 and 996, respectively; D and T indicates the feature vector of the relevant drug-target pair; d_X is the x -th drug feature and t_Y is the y -th target feature. Since the drug and target features are measured in different scales, we performed normalization before training. Then, we applied principal component analysis (PCA) [104] to decrease the feature size from 1359 to 618. By doing so, we not only could remove noisy feature but also reduce memory consumption.

For the architecture of the DNN-based DTI model, the input layer contains 618 neurons, followed 512, 256, 128, and 64 neurons in the hidden layers, respectively. The output layer is with one neuron. The optimal hyperparameters were found based on 10-fold cross validation (Figure S6). Each layer of DNN-based DTI model could be simplified into a function as follows:

$$h_n = \sigma(w^T x_n + b) \quad (19)$$

where x_n denotes the input of the n -th drug-target feature vector, h_n indicates the output of each layer; w is the weighting matrix; b is the bias vector; σ is the activation function, by which sigmoid activation function is used for the output layer and ReLU [105] is used for the hidden layer. We added dropout on each hidden layer for reducing overfitting. Meanwhile, the model training would be terminated once the model performance stopped to improve on the validation set by early stopping function. Moreover, we chose the binary cross-entropy to be the cost function:

$$C_n(w, b) = -\frac{1}{N} \sum_{n=1}^N (p_n \log(\hat{p}_n) + (1 - p_n) \log(1 - \hat{p}_n))$$

$$L(w, b) = \frac{1}{N} \sum_{n=1}^N C_n(p_n, \hat{p}_n) \quad (20)$$

where $L(w, b)$ is the average of total loss; p_n denotes the n -th true positive instance (1) or true negative instance (0) of drug-target binding; \hat{p}_n denotes the n -th predicted probability of positive instance (1) or predicted probability of negative instance (0) of drug-target binding. For obtaining the optimal network parameter set ϕ^* , the cost function is in the following:

$$\phi^* = \arg \min_{\phi} L(\phi) \quad (21)$$

The above equation could be achieved by the backpropagation algorithm [106]. The updated weight and bias parameters for the j -th epoch is shown as below:

$$\phi^j = \phi^{j-1} - \eta \nabla L(\phi^{j-1}),$$

$$\text{where } \nabla L(\phi^{j-1}) = \begin{bmatrix} \frac{\partial L(\phi^{j-1})}{\partial w_1} \\ \vdots \\ \frac{\partial L(\phi^{j-1})}{\partial w_h} \\ \frac{\partial L(\phi^{j-1})}{\partial b_1} \\ \vdots \\ \frac{\partial L(\phi^{j-1})}{\partial b_h} \end{bmatrix}. \quad (22)$$

where η is the learning rate, which is 0.001; $\nabla L(\phi^{j-1})$ denotes the gradient of $L(\phi^{j-1})$.

Supplementary Materials: The following supporting information can be downloaded at: <https://www.mdpi.com/article/10.3390/ijms23126732/s1>.

Author Contributions: Conceptualization B.-S.C.; Methodology, S.-J.Y. and T.-Y.Y.; Software, T.-Y.Y.; Validation S.-J.Y. and T.-Y.Y.; Formal Analysis, S.-J.Y. and T.-Y.Y.; Investigation, T.-Y.Y.; Data Curation, T.-Y.Y.; Writing—Original Draft Preparation, S.-J.Y. and T.-Y.Y.; Writing—Review and Editing, S.-J.Y. and B.-S.C.; Visualization, T.-Y.Y.; Supervision, B.-S.C.; Funding Acquisition, B.-S.C. All authors have read and agreed to the published version of the manuscript.

Funding: This research was funded by Ministry of Science and Technology grant number MOST 107-2221-E-007-112-MY3.

Institutional Review Board Statement: Not applicable.

Informed Consent Statement: Not applicable.

Data Availability Statement: The DLBCL microarray data is from GSE117556 (<https://www.ncbi.nlm.nih.gov/geo/query/acc.cgi?acc=GSE117556>, accessed on 18 May 2022).

Conflicts of Interest: The authors declare no conflict of interest.

References

- Clarke, C.A.; Glaser, S.L.; Dorfman, R.F.; Bracci, P.M.; Eberle, E.; Holly, E.A.J.C.E.; Biomarkers, P. Expert review of non-Hodgkin's lymphomas in a population-based cancer registry: Reliability of diagnosis and subtype classifications. *Cancer Epidemiol. Biomark. Prev.* **2004**, *13*, 138–143. [CrossRef] [PubMed]
- Prochazka, V.; Jarošová, M.; Prouzova, Z.; Nedomova, R.; Papajik, T.; Indrák, K. Immune escape mechanisms in diffuse large B-cell lymphoma. *Int. Sch. Res. Not.* **2012**, *2012*, 208903. [CrossRef]
- Sehn, L.H.; Gascoyne, R.D. Diffuse large B-cell lymphoma: Optimizing outcome in the context of clinical and biologic heterogeneity. *Blood* **2015**, *125*, 22–32. [CrossRef] [PubMed]
- Salles, G.; Barrett, M.; Foà, R.; Maurer, J.; O'Brien, S.; Valente, N.; Wenger, M.; Maloney, D.G. Rituximab in B-cell hematologic malignancies: A review of 20 years of clinical experience. *Adv. Ther.* **2017**, *34*, 2232–2273. [CrossRef] [PubMed]
- Mok, C.C. Rituximab for the treatment of rheumatoid arthritis: An update. *Drug Des. Dev. Ther.* **2014**, *8*, 87. [CrossRef]

6. Al-Homsi, A.S.; Roy, T.S.; Cole, K.; Feng, Y.; Duffner, U. Post-transplant high-dose cyclophosphamide for the prevention of graft-versus-host disease. *Biol. Blood Marrow Transplant.* **2015**, *21*, 604–611. [CrossRef] [PubMed]
7. Travis, L.B.; Curtis, R.E.; Glimelius, B.; Holowaty, E.J.; Van Leeuwen, F.E.; Lynch, C.F.; Hagenbeek, A.; Stovall, M.; Banks, P.M.; Adami, J.; et al. Bladder and Kidney Cancer Following Cyclophosphamide Therapy for Non-Hodgkin's Lymphoma. *JNCI J. Natl. Cancer Inst.* **1995**, *87*, 524–531. [CrossRef] [PubMed]
8. Thorn, C.F.; Oshiro, C.; Marsh, S.; Hernandez-Boussard, T.; McLeod, H.; Klein, T.E.; Altman, R.B. Doxorubicin pathways: Pharmacodynamics and adverse effects. *Pharm. Genom.* **2011**, *21*, 440. [CrossRef]
9. Vayssade, M.; Faridoni-Laurens, L.; Bénard, J.; Ahomadegbe, J.-C. Expression of p53-family members and associated target molecules in breast cancer cell lines in response to vincristine treatment. *Biochem. Pharmacol.* **2002**, *63*, 1609–1617. [CrossRef]
10. Samoon, Z.; Shabbir-Moosajee, M. Vincristine-induced vocal cord palsy and successful re-treatment in a patient with diffuse large B cell lymphoma: A case report. *BMC Res. Notes* **2014**, *7*, 318. [CrossRef]
11. Kimberly, R.P. Mechanisms of action, dosage schedules, and side effects of steroid therapy. *Curr. Opin. Rheumatol.* **1991**, *3*, 373–379. [CrossRef]
12. Modlinski, R.; Fields, K.B. The effect of anabolic steroids on the gastrointestinal system, kidneys, and adrenal glands. *Curr. Sports Med. Rep.* **2006**, *5*, 104–109. [CrossRef]
13. Papageorgiou, S.G.; Thomopoulos, T.P.; Liaskas, A.; Vassilakopoulos, T.P. Monoclonal Antibodies in the Treatment of Diffuse Large B-Cell Lymphoma: Moving beyond Rituximab. *Cancers* **2022**, *14*, 1917. [CrossRef]
14. Sehn, L.H.; Herrera, A.F.; Flowers, C.R.; Kamdar, M.K.; McMillan, A.; Hertzberg, M.; Assouline, S.; Kim, T.M.; Kim, W.S.; Ozcan, M. Polatuzumab vedotin in relapsed or refractory diffuse large B-cell lymphoma. *J. Clin. Oncol.* **2020**, *38*, 155. [CrossRef]
15. Kalakonda, N.; Maerevoet, M.; Cavallo, F.; Follows, G.; Goy, A.; Vermaat, J.S.; Casasnovas, O.; Hamad, N.; Zijlstra, J.M.; Bakhshi, S. Selinexor in patients with relapsed or refractory diffuse large B-cell lymphoma (SADAL): A single-arm, multinational, multicentre, open-label, phase 2 trial. *Lancet Haematol.* **2020**, *7*, e511–e522. [CrossRef]
16. Salles, G.; Duell, J.; Barca, E.G.; Tournilhac, O.; Jurczak, W.; Liberati, A.M.; Nagy, Z.; Obr, A.; Gaidano, G.; André, M. Tafasitamab plus lenalidomide in relapsed or refractory diffuse large B-cell lymphoma (L-MIND): A multicentre, prospective, single-arm, phase 2 study. *Lancet Oncol.* **2020**, *21*, 978–988. [CrossRef]
17. Cheson, B.D.; Nowakowski, G.; Salles, G. Diffuse large B-cell lymphoma: New targets and novel therapies. *Blood Cancer J.* **2021**, *11*, 68. [CrossRef]
18. Mohs, R.C.; Greig, N.H. Drug discovery and development: Role of basic biological research. *Alzheimer's Dement. Transl. Res. Clin. Interv.* **2017**, *3*, 651–657. [CrossRef]
19. Takebe, T.; Imai, R.; Ono, S. The current status of drug discovery and development as originated in United States academia: The influence of industrial and academic collaboration on drug discovery and development. *Clin. Transl. Sci.* **2018**, *11*, 597–606. [CrossRef]
20. Bailón-Moscoso, N.; Romero-Benavides, J.C.; Ostrosky-Wegman, P. Development of anticancer drugs based on the hallmarks of tumor cells. *Tumor Biol.* **2014**, *35*, 3981–3995. [CrossRef]
21. Sachdev, K.; Gupta, M.K. A comprehensive review of feature based methods for drug target interaction prediction. *J. Biomed. Inform.* **2019**, *93*, 103159. [CrossRef]
22. Butina, D.; Segall, M.D.; Frankcombe, K. Predicting ADME properties in silico: Methods and models. *Drug Discov. Today* **2002**, *7*, S83–S88. [CrossRef]
23. Li, H.; Gao, Z.; Kang, L.; Zhang, H.; Yang, K.; Yu, K.; Luo, X.; Zhu, W.; Chen, K.; Shen, J. TarFisDock: A web server for identifying drug targets with docking approach. *Nucleic Acids Res.* **2006**, *34*, W219–W224. [CrossRef]
24. Cheng, A.C.; Coleman, R.G.; Smyth, K.T.; Cao, Q.; Soulard, P.; Caffrey, D.R.; Salzberg, A.C.; Huang, E.S. Structure-based maximal affinity model predicts small-molecule druggability. *Nat. Biotechnol.* **2007**, *25*, 71–75. [CrossRef]
25. Pujadas, G.; Vaque, M.; Ardevol, A.; Blade, C.; Salvado, M.; Blay, M.; Fernandez-Larrea, J.; Arola, L. Protein-ligand docking: A review of recent advances and future perspectives. *Curr. Pharm. Anal.* **2008**, *4*, 1–19. [CrossRef]
26. Bagherian, M.; Sabeti, E.; Wang, K.; Sartor, M.A.; Nikolovska-Coleska, Z.; Najarian, K. Machine learning approaches and databases for prediction of drug–target interaction: A survey paper. *Brief. Bioinform.* **2021**, *22*, 247–269. [CrossRef]
27. Nath, A.; Kumari, P.; Chaube, R. Prediction of human drug targets and their interactions using machine learning methods: Current and future perspectives. *Comput. Drug Discov. Des.* **2018**, *1762*, 21–30.
28. Wen, M.; Zhang, Z.; Niu, S.; Sha, H.; Yang, R.; Yun, Y.; Lu, H.J. Deep-learning-based drug–target interaction prediction. *J. Proteome Res.* **2017**, *16*, 1401–1409. [CrossRef]
29. Gao, K.Y.; Fokoue, A.; Luo, H.; Iyengar, A.; Dey, S.; Zhang, P. Interpretable drug target prediction using deep neural representation. In Proceedings of the IJCAI, Stockholm, Sweden, 13–19 July 2018; pp. 3371–3377.
30. Öztürk, H.; Özgür, A.; Ozkirimli, E.J.B. DeepDTA: Deep drug–target binding affinity prediction. *Bioinformatics* **2018**, *34*, i821–i829. [CrossRef]
31. Lee, I.; Keum, J.; Nam, H. DeepConv-DTI: Prediction of drug-target interactions via deep learning with convolution on protein sequences. *PLoS Comput. Biol.* **2019**, *15*, e1007129. [CrossRef]
32. You, J.; McLeod, R.D.; Hu, P. Predicting drug-target interaction network using deep learning model. *Comput. Biol. Chem.* **2019**, *80*, 90–101. [CrossRef] [PubMed]

33. Ezzat, A.; Wu, M.; Li, X.-L.; Kwok, C.-K. Drug-target interaction prediction via class imbalance-aware ensemble learning. *BMC Bioinform.* **2016**, *17*, 509. [CrossRef] [PubMed]
34. Li, Y.; Qiao, G.; Wang, K.; Wang, G. Drug–target interaction predication via multi-channel graph neural networks. *Brief. Bioinform.* **2021**, *23*, bbab346. [CrossRef] [PubMed]
35. Cheng, Z.; Yan, C.; Wu, F.; Wang, J. Drug-target interaction prediction using multi-head self-attention and graph attention network. *IEEE/ACM Trans. Comput. Biol. Bioinform.* **2021**, *1*, 33956632. [CrossRef]
36. Zhao, T.; Hu, Y.; Valsdottir, L.R.; Zang, T.; Peng, J. Identifying drug–target interactions based on graph convolutional network and deep neural network. *Brief. Bioinform.* **2020**, *22*, 2141–2150. [CrossRef]
37. Tillmann, S.; Bernhagen, J.; Noels, H. Arrest Functions of the MIF Ligand/Receptor Axes in Atherogenesis. *Front. Immunol.* **2013**, *4*, 115. [CrossRef]
38. Figueiredo, C.R.; Azevedo, R.A.; Mousdell, S.; Resende-Lara, P.T.; Ireland, L.; Santos, A.; Girola, N.; Cunha, R.L.O.R.; Schmid, M.C.; Polonelli, L.; et al. Blockade of MIF-CD74 Signalling on Macrophages and Dendritic Cells Restores the Antitumour Immune Response against Metastatic Melanoma. *Front. Immunol.* **2018**, *9*, 1132. [CrossRef]
39. Gil-Yarom, N.; Radomir, L.; Sever, L.; Kramer, M.P.; Lewinsky, H.; Bornstein, C.; Blecher-Gonen, R.; Barnett-Itzhaki, Z.; Mirkin, V.; Friedlander, G.; et al. CD74 is a novel transcription regulator. *Proc. Natl. Acad. Sci. USA* **2017**, *114*, 562–567. [CrossRef]
40. Roskoski, R. Src protein–tyrosine kinase structure and regulation. *Biochem. Biophys. Res. Commun.* **2004**, *324*, 1155–1164. [CrossRef]
41. Huang, X.; Meng, B.; Iqbal, J.; Ding, B.B.; Perry, A.M.; Cao, W.; Smith, L.M.; Bi, C.; Jiang, C.; Greiner, T.C.; et al. Activation of the STAT3 signaling pathway is associated with poor survival in diffuse large B-cell lymphoma treated with R-CHOP. *J. Clin. Oncol.* **2013**, *31*, 4520–4528. [CrossRef]
42. Pawlus, M.R.; Wang, L.; Hu, C.J. STAT3 and HIF1 α cooperatively activate HIF1 target genes in MDA-MB-231 and RCC4 cells. *Oncogene* **2014**, *33*, 1670–1679. [CrossRef]
43. Carmeliet, P.; Dor, Y.; Herbert, J.-M.; Fukumura, D.; Brusselmans, K.; Dewerchin, M.; Neeman, M.; Bono, F.; Abramovitch, R.; Maxwell, P.; et al. Role of HIF-1 α in hypoxia-mediated apoptosis, cell proliferation and tumour angiogenesis. *Nature* **1998**, *394*, 485–490. [CrossRef]
44. Wein, F.; Otto, T.; Lambertz, P.; Fandrey, J.; Hansmann, M.-L.; Küppers, R. Potential role of hypoxia in early stages of Hodgkin lymphoma pathogenesis. *Haematologica* **2015**, *100*, 1320–1326. [CrossRef]
45. Burger, R. Impact of interleukin-6 in hematological malignancies. *Transfus. Med. Hemotherapy* **2013**, *40*, 336–343. [CrossRef]
46. Sánchez-Barrena, M.J.; Vallis, Y.; Clatworthy, M.R.; Doherty, G.J.; Veprintsev, D.B.; Evans, P.R.; McMahon, H.T. Bin2 is a membrane sculpting N-BAR protein that influences leucocyte podosomes, motility and phagocytosis. *PLoS ONE* **2012**, *7*, e52401. [CrossRef]
47. Davey, R.A.; Grossmann, M. Androgen Receptor Structure, Function and Biology: From Bench to Bedside. *Clin. Biochem. Rev.* **2016**, *37*, 3–15.
48. Nguyen, L.; Papenhausen, P.; Shao, H. The Role of c-MYC in B-Cell Lymphomas: Diagnostic and Molecular Aspects. *Genes* **2017**, *8*, 116. [CrossRef]
49. Tjin, E.P.M.; Groen, R.W.J.; Vogelzang, I.; Derksen, P.W.B.; Klok, M.D.; Meijer, H.P.; van Eeden, S.; Pals, S.T.; Spaargaren, M. Functional analysis of HGF/MET signaling and aberrant HGF-activator expression in diffuse large B-cell lymphoma. *Blood* **2006**, *107*, 760–768. [CrossRef]
50. Lam, B.Q.; Dai, L.; Qin, Z. The role of HGF/c-MET signaling pathway in lymphoma. *J. Hematol. Oncol.* **2016**, *9*, 135. [CrossRef]
51. Haycraft, C.J.; Banizs, B.; Aydin-Son, Y.; Zhang, Q.; Michaud, E.J.; Yoder, B.K. Gli2 and Gli3 localize to cilia and require the intraflagellar transport protein polaris for processing and function. *PLoS Genet.* **2005**, *1*, e53. [CrossRef]
52. Lentjes, M.H.F.M.; Niessen, H.E.C.; Akiyama, Y.; de Bruïne, A.P.; Melotte, V.; van Engeland, M. The emerging role of GATA transcription factors in development and disease. *Expert Rev. Mol. Med.* **2016**, *18*, e3. [CrossRef]
53. Crispino, J.D.; Horwitz, M.S. GATA factor mutations in hematologic disease. *Blood* **2017**, *129*, 2103–2110. [CrossRef]
54. Chakrama, F.Z.; Seguin-Py, S.; Le Grand, J.N.; Fraichard, A.; Delage-Mourroux, R.; Despouy, G.; Perez, V.; Jouvenot, M.; Boyer-Guittaut, M. GABARAP1 (GEC1) associates with autophagic vesicles. *Autophagy* **2010**, *6*, 495–505. [CrossRef]
55. Zhong, X.; Xiao, Y.; Chen, C.; Wei, X.; Hu, C.; Ling, X.; Liu, X. MicroRNA-203-mediated posttranscriptional deregulation of CPEB4 contributes to colorectal cancer progression. *Biochem. Biophys. Res. Commun.* **2015**, *466*, 206–213. [CrossRef]
56. Béguelin, W.; Popovic, R.; Teater, M.; Jiang, Y.; Bunting, K.L.; Rosen, M.; Shen, H.; Yang, S.N.; Wang, L.; Ezponda, T.; et al. EZH2 is required for germinal center formation and somatic EZH2 mutations promote lymphoid transformation. *Cancer Cell* **2013**, *23*, 677–692. [CrossRef]
57. Bissierier, M.; Wajapeyee, N. Mechanisms of resistance to EZH2 inhibitors in diffuse large B-cell lymphomas. *Blood* **2018**, *131*, 2125–2137. [CrossRef]
58. Kim, K.H.; Roberts, C.W. Targeting EZH2 in cancer. *Nat. Med.* **2016**, *22*, 128–134. [CrossRef]
59. Elian, F.A.; Yan, E.; Walter, M.A. FOXC1, the new player in the cancer sandbox. *Oncotarget* **2017**, *9*, 8165–8178. [CrossRef] [PubMed]
60. Park, S.; Han, S.-H.; Kim, H.-G.; Jeong, J.; Choi, M.; Kim, H.-Y.; Kim, M.-G.; Park, J.-K.; Han, J.E.; Cho, G.-J.; et al. Suppression of PRPF4 regulates pluripotency, proliferation, and differentiation in mouse embryonic stem cells. *Cell Biochem. Funct.* **2019**, *37*, 608–617. [CrossRef] [PubMed]
61. Song, H.; Dang, X.; He, Y.-Q.; Zhang, T.; Wang, H.-Y. Selection of housekeeping genes as internal controls for quantitative RT-PCR analysis of the veined rapa whelk (*Rapana venosa*). *PeerJ* **2017**, *5*, e3398. [CrossRef] [PubMed]

62. Yao, T.-P.; Oh, S.P.; Fuchs, M.; Zhou, N.-D.; Ch'ng, L.-E.; Newsome, D.; Bronson, R.T.; Li, E.; Livingston, D.M.; Eckner, R. Gene Dosage-Dependent Embryonic Development and Proliferation Defects in Mice Lacking the Transcriptional Integrator p300. *Cell* **1998**, *93*, 361–372. [CrossRef]
63. Pasqualucci, L.; Dominguez-Sola, D.; Chiarenza, A.; Fabbri, G.; Grunn, A.; Trifonov, V.; Kasper, L.H.; Lerach, S.; Tang, H.; Ma, J.; et al. Inactivating mutations of acetyltransferase genes in B-cell lymphoma. *Nature* **2011**, *471*, 189–195. [CrossRef]
64. Dang, C.V. MYC on the Path to Cancer. *Cell* **2012**, *149*, 22–35. [CrossRef]
65. Ortega, M.; Bhatnagar, H.; Lin, A.P.; Wang, L.; Aster, J.C.; Sill, H.; Aguiar, R.C.T. A microRNA-mediated regulatory loop modulates NOTCH and MYC oncogenic signals in B- and T-cell malignancies. *Leukemia* **2015**, *29*, 968–976. [CrossRef]
66. Lv, X.; Feng, L.; Ge, X.; Lu, K.; Wang, X. Interleukin-9 promotes cell survival and drug resistance in diffuse large B-cell lymphoma. *J. Exp. Clin. Cancer Res.* **2016**, *35*, 106. [CrossRef]
67. Chen, A.; Zhong, L.; Lv, J. FOXL1 overexpression is associated with poor outcome in patients with glioma. *Oncol. Lett.* **2019**, *18*, 751–757. [CrossRef]
68. Ni, H.; Tong, R.; Zou, L.; Song, G.; Cho, W.C. MicroRNAs in diffuse large B-cell lymphoma. *Oncol. Lett.* **2016**, *11*, 1271–1280. [CrossRef]
69. Lohr, J.G.; Stojanov, P.; Lawrence, M.S.; Auclair, D.; Chapuy, B.; Sougnez, C.; Cruz-Gordillo, P.; Knoechel, B.; Asmann, Y.W.; Slager, S.L.; et al. Discovery and prioritization of somatic mutations in diffuse large B-cell lymphoma (DLBCL) by whole-exome sequencing. *Proc. Natl. Acad. Sci. USA* **2012**, *109*, 3879–3884. [CrossRef]
70. Vela-Chávez, T.; Adam, P.; Kremer, M.; Bink, K.; Bacon, C.M.; Menon, G.; Ferry, J.A.; Fend, F.; Jaffe, E.S.; Quintanilla-Martínez, L. Cyclin D1 positive diffuse large B-cell lymphoma is a post-germinal center-type lymphoma without alterations in the CCND1 gene locus. *Leuk Lymphoma* **2011**, *52*, 458–466. [CrossRef]
71. Vermeulen, K.; Van Bockstaele, D.R.; Berneman, Z.N. The cell cycle: A review of regulation, deregulation and therapeutic targets in cancer. *Cell Prolif.* **2003**, *36*, 131–149. [CrossRef]
72. Gennaro, V.J.; Stanek, T.J.; Peck, A.R.; Sun, Y.; Wang, F.; Qie, S.; Knudsen, K.E.; Rui, H.; Butt, T.; Diehl, J.A.; et al. Control of CCND1 ubiquitylation by the catalytic SAGA subunit USP22 is essential for cell cycle progression through G1 in cancer cells. *Proc. Natl. Acad. Sci. USA* **2018**, *115*, E9298. [CrossRef]
73. Hwang, T.-C.; Kirk, K.L. The CFTR ion channel: Gating, regulation, and anion permeation. *Cold Spring Harb. Perspect Med.* **2013**, *3*, a009498. [CrossRef]
74. Wang, J.; Xu-Monette, Z.Y.; Jabbar, K.J.; Shen, Q.; Manyam, G.C.; Tzankov, A.; Visco, C.; Wang, J.; Montes-Moreno, S.; Dybkær, K.; et al. AKT Hyperactivation and the Potential of AKT-Targeted Therapy in Diffuse Large B-Cell Lymphoma. *Am. J. Pathol.* **2017**, *187*, 1700–1716. [CrossRef]
75. Dittmer, J. The Biology of the Ets1 Proto-Oncogene. *Mol. Cancer* **2003**, *2*, 29. [CrossRef]
76. Bonetti, P.; Testoni, M.; Scandurra, M.; Ponzoni, M.; Piva, R.; Mensah, A.A.; Rinaldi, A.; Kwee, I.; Tibiletti, M.G.; Iqbal, J.; et al. Deregulation of ETS1 and FLI1 contributes to the pathogenesis of diffuse large B-cell lymphoma. *Blood* **2013**, *122*, 2233–2241. [CrossRef]
77. Ochoa-Hernández, A.B.; Ramos-Solano, M.; Meza-Canales, I.D.; García-Castro, B.; Rosales-Reynoso, M.A.; Rosales-Aviña, J.A.; Barrera-Chairez, E.; Ortiz-Lazareno, P.C.; Hernández-Flores, G.; Bravo-Cuellar, A.; et al. Peripheral T-lymphocytes express WNT7A and its restoration in leukemia-derived lymphoblasts inhibits cell proliferation. *BMC Cancer* **2012**, *12*, 60. [CrossRef]
78. Yuan, H.; Li, Z.-M.; Shao, J.; Ji, W.-X.; Xia, W.; Lu, S. FGF2/FGFR1 regulates autophagy in FGFR1-amplified non-small cell lung cancer cells. *J. Exp. Clin. Cancer Res.* **2017**, *36*, 72. [CrossRef]
79. Parzych, K.R.; Klionsky, D.J. An overview of autophagy: Morphology, mechanism, and regulation. *Antioxid. Redox Signal.* **2014**, *20*, 460–473. [CrossRef]
80. Cui, W.; Zheng, S.; Liu, Z.; Wang, W.; Cai, Y.; Bi, R.; Cao, B.; Zhou, X. PIK3CA expression in diffuse large B cell lymphoma tissue and the effect of its knockdown in vitro. *OncoTargets Ther.* **2017**, *10*, 2239–2247. [CrossRef]
81. Compagno, M.; Lim, W.K.; Grunn, A.; Nandula, S.V.; Brahmachary, M.; Shen, Q.; Bertoni, F.; Ponzoni, M.; Scandurra, M.; Califano, A.; et al. Mutations of multiple genes cause deregulation of NF-kappaB in diffuse large B-cell lymphoma. *Nature* **2009**, *459*, 717–721. [CrossRef]
82. Dong, P.; Xiong, Y.; Yue, J.; Hanley, S.J.B.; Watari, H. Tumor-Intrinsic PD-L1 Signaling in Cancer Initiation, Development and Treatment: Beyond Immune Evasion. *Front. Oncol.* **2018**, *8*, 386. [CrossRef] [PubMed]
83. Lamb, J. The Connectivity Map: A new tool for biomedical research. *Nat. Rev. Cancer* **2007**, *7*, 54–60. [CrossRef] [PubMed]
84. Wishart, D.S.; Feunang, Y.D.; Guo, A.C.; Lo, E.J.; Marcu, A.; Grant, J.R.; Sajed, T.; Johnson, D.; Li, C.; Sayeeda, Z.; et al. DrugBank 5.0: A major update to the DrugBank database for 2018. *Nucleic Acids Res.* **2018**, *46*, D1074–D1082. [CrossRef] [PubMed]
85. Roy, P.; Ghosh, A. Mechanochemical cocrystallization to improve the physicochemical properties of chlorzoxazone. *CrystEngComm* **2020**, *22*, 4611–4620. [CrossRef]
86. Sogawa, C.; Eguchi, T.; Tran, M.T.; Ishige, M.; Trin, K.; Okusha, Y.; Taha, E.A.; Lu, Y.; Kawai, H.; Sogawa, N.; et al. Antiparkinson Drug Bzotropine Suppresses Tumor Growth, Circulating Tumor Cells, and Metastasis by Acting on SLC6A3/DAT and Reducing STAT3. *Cancers* **2020**, *12*, 523. [CrossRef] [PubMed]
87. Prusila, R.E.I.; Peroja, P.; Jantunen, E.; Turpeenniemi-Hujanen, T.; Kuittinen, O.J.H.O. Treatment of diffuse large B-cell lymphoma in elderly patients: Replacing doxorubicin with either epirubicin or etoposide (VP-16). *Hematol. Oncol.* **2019**, *37*, 136–142. [CrossRef] [PubMed]

88. Moccia, A.A.; Schaff, K.; Hoskins, P.; Klasa, R.; Savage, K.J.; Shenkier, T.; Gascoyne, R.D.; Connors, J.M.; Sehn, L.H. R-CHOP with Etoposide Substituted for Doxorubicin (R-CEOP): Excellent Outcome in Diffuse Large B Cell Lymphoma for Patients with a Contraindication to Anthracyclines. *Blood* **2009**, *114*, 408. [CrossRef]
89. Huang, W.-Y.; Yang, P.-M.; Chang, Y.-F.; Marquez, V.E.; Chen, C.-C. Methotrexate induces apoptosis through p53/p21-dependent pathway and increases E-cadherin expression through downregulation of HDAC/EZH2. *Biochem. Pharmacol.* **2011**, *81*, 510–517. [CrossRef]
90. Han Li, C.; Chen, Y. Targeting EZH2 for cancer therapy: Progress and perspective. *Curr. Protein Pept. Sci.* **2015**, *16*, 559–570. [CrossRef]
91. Salwinski, L.; Miller, C.S.; Smith, A.J.; Pettit, F.K.; Bowie, J.U.; Eisenberg, D. The database of interacting proteins: 2004 update. *Nucleic Acids Res.* **2004**, *32*, D449–D451. [CrossRef]
92. Orchard, S.; Ammari, M.; Aranda, B.; Breuza, L.; Briganti, L.; Broackes-Carter, F.; Campbell, N.H.; Chavali, G.; Chen, C.; Del-Toro, N. The MIntAct project—IntAct as a common curation platform for 11 molecular interaction databases. *Nucleic Acids Res.* **2014**, *42*, D358–D363. [CrossRef]
93. Chatr-Aryamontri, A.; Breitkreutz, B.-J.; Oughtred, R.; Boucher, L.; Heinicke, S.; Chen, D.; Stark, C.; Breitkreutz, A.; Kolas, N.; O'Donnell, L. The BioGRID interaction database: 2015 update. *Nucleic Acids Res.* **2015**, *43*, D470–D478. [CrossRef]
94. Bader, G.D.; Betel, D.; Hogue, C.W. BIND: The biomolecular interaction network database. *Nucleic Acids Res.* **2003**, *31*, 248–250. [CrossRef]
95. Licata, L.; Briganti, L.; Peluso, D.; Perfetto, L.; Iannuccelli, M.; Galeota, E.; Sacco, F.; Palma, A.; Nardoza, A.P.; Santonico, E. MINT, the molecular interaction database: 2012 update. *Nucleic Acids Res.* **2012**, *40*, D857–D861. [CrossRef]
96. Zheng, G.; Tu, K.; Yang, Q.; Xiong, Y.; Wei, C.; Xie, L.; Zhu, Y.; Li, Y. ITFP: An integrated platform of mammalian transcription factors. *Bioinformatics* **2008**, *24*, 2416–2417. [CrossRef]
97. Bovolenta, L.A.; Acencio, M.L.; Lemke, N.J. HTRIdb: An open-access database for experimentally verified human transcriptional regulation interactions. *BMC Genom.* **2012**, *13*, 405. [CrossRef]
98. Agarwal, V.; Bell, G.W.; Nam, J.-W.; Bartel, D.P. Predicting effective microRNA target sites in mammalian mRNAs. *elife* **2015**, *4*, e05005. [CrossRef]
99. Friard, O.; Re, A.; Taverna, D.; De Bortoli, M.; Corá, D. CircuitsDB: A database of mixed microRNA/transcription factor feed-forward regulatory circuits in human and mouse. *BMC Bioinform.* **2010**, *11*, 435. [CrossRef]
100. Li, J.-H.; Liu, S.; Zhou, H.; Qu, L.-H.; Yang, J.-H. starBase v2. 0: Decoding miRNA-ceRNA, miRNA-ncRNA and protein–RNA interaction networks from large-scale CLIP-Seq data. *Nucleic Acids Res.* **2014**, *42*, D92–D97. [CrossRef]
101. Sakamoto, Y.; Ishiguro, M.; Kitagawa, G.J.D. *Akaike Information Criterion Statistics*; Reidel, D., Ed.; Springer: Dordrecht, The Netherlands, 1986; Volume 81, p. 26853.
102. Gilson, M.K.; Liu, T.; Baitaluk, M.; Nicola, G.; Hwang, L.; Chong, J. BindingDB in 2015: A public database for medicinal chemistry, computational chemistry and systems pharmacology. *Nucleic Acids Res.* **2016**, *44*, D1045–D1053. [CrossRef] [PubMed]
103. Dong, J.; Yao, Z.J.; Zhang, L.; Luo, F.; Lin, Q.; Lu, A.P.; Chen, A.F.; Cao, D.S. PyBioMed: A python library for various molecular representations of chemicals, proteins and DNAs and their interactions. *J. Cheminform.* **2018**, *10*, 16. [CrossRef] [PubMed]
104. Ringnér, M. What is principal component analysis? *Nat. Biotechnol.* **2008**, *26*, 303–304. [CrossRef] [PubMed]
105. Nwankpa, C.; Ijomah, W.; Gachagan, A.; Marshall, S. Activation functions: Comparison of trends in practice and research for deep learning. *arXiv* **2018**, arXiv:1811.03378.
106. Hecht-Nielsen, R. Theory of the backpropagation neural network. In *Neural Networks for Perception*; Elsevier: Amsterdam, The Netherlands, 1992; pp. 65–93.



Article

Kunitz-Type Peptides from Sea Anemones Protect Neuronal Cells against Parkinson's Disease Inductors via Inhibition of ROS Production and ATP-Induced P2X7 Receptor Activation

Aleksandra Kvetkina ¹, Evgeny Pisyagin ¹, Ekaterina Menchinskaya ¹, Ekaterina Yurchenko ¹, Rimma Kalina ¹, Sergei Kozlovskiy ¹, Leonid Kaluzhskiy ², Alexander Menshov ¹, Natalia Kim ¹, Steve Peigneur ³, Jan Tytgat ³, Alexis Ivanov ², Naira Ayyazyan ⁴, Elena Leychenko ¹ and Dmitry Aminin ^{1,*}

¹ G.B. Elyakov Pacific Institute of Bioorganic Chemistry, Far Eastern Branch, Russian Academy of Sciences, 690022 Vladivostok, Russia; kvetkina@gmail.com (A.K.); pisyagin@hotmail.com (E.P.); ekaterinamenchinskaya@gmail.com (E.M.); eyurch@piboc.dvo.ru (E.Y.); kalinarimma@gmail.com (R.K.); sergeimerx@gmail.com (S.K.); almenshov1990@gmail.com (A.M.); natalya_kim@mail.ru (N.K.); leychenko@gmail.com (E.L.)

² V.N. Orekhovich Institute of Biomedical Chemistry, 10, Pogodinskaya St., 119121 Moscow, Russia; leonid.kaluzhskiy@ibmc.msk.ru (L.K.); professor-ivanov@yandex.ru (A.L.)

³ Toxicology and Pharmacology, Campus Gasthuisberg O&N2, University of Leuven (KU Leuven), Herestraat 49, P.O. Box 922, B-3000 Leuven, Belgium; steve.peigneur@kuleuven.be (S.P.); jan.tytgat@kuleuven.be (J.T.)

⁴ L.A. Orbeli Institute of Physiology, National Academy of Sciences of Armenia, Yerevan 0028, Armenia; taipan@ysu.am

* Correspondence: daminin@piboc.dvo.ru

Citation: Kvetkina, A.; Pisyagin, E.; Menchinskaya, E.; Yurchenko, E.; Kalina, R.; Kozlovskiy, S.; Kaluzhskiy, L.; Menshov, A.; Kim, N.; Peigneur, S.; et al. Kunitz-Type Peptides from Sea Anemones Protect Neuronal Cells against Parkinson's Disease Inductors via Inhibition of ROS Production and ATP-Induced P2X7 Receptor Activation. *Int. J. Mol. Sci.* **2022**, *23*, 5115. <https://doi.org/10.3390/ijms23095115>

Academic Editor:
Chakraborty Ashok

Received: 6 April 2022

Accepted: 29 April 2022

Published: 4 May 2022

Publisher's Note: MDPI stays neutral with regard to jurisdictional claims in published maps and institutional affiliations.



Copyright: © 2022 by the authors. Licensee MDPI, Basel, Switzerland. This article is an open access article distributed under the terms and conditions of the Creative Commons Attribution (CC BY) license (<https://creativecommons.org/licenses/by/4.0/>).

Abstract: Parkinson's disease (PD) is a socially significant disease, during the development of which oxidative stress and inflammation play a significant role. Here, we studied the neuroprotective effects of four Kunitz-type peptides from *Heteractis crispa* and *Heteractis magnifica* sea anemones against PD inductors. The peptide HClQ1c9, which was obtained for the first time, inhibited trypsin less than other peptides due to unfavorable interactions of Arg17 with Lys43 in the enzyme. Its activity was reduced by up to 70% over the temperature range of 60–100 °C, while HClQ2c1, HClQ4c7, and HMIQ3c1 retained their conformation and stayed active up to 90–100 °C. All studied peptides inhibited paraquat- and rotenone-induced intracellular ROS formation, in particular NO, and scavenged free radicals outside the cells. The peptides did not modulate the TRPV1 channels but they affected the P2X7R, both of which are considered therapeutic targets in Parkinson's disease. HMIQ3c1 and HClQ4c7 almost completely inhibited the ATP-induced uptake of YO-PRO-1 dye in Neuro-2a cells through P2X7 ion channels and significantly reduced the stable calcium response in these cells. The complex formation of the peptides with the P2X7R extracellular domain was determined via SPR analysis. Thus, these peptides may be considered promising compounds to protect neuronal cells against PD inductors, which act as ROS production inhibitors and partially act as ATP-induced P2X7R activation inhibitors.

Keywords: Kunitz-type peptides; neuroprotective activity; sea anemones; TRPV1; P2X7R; Parkinson's disease (PD)

1. Introduction

Parkinson's disease (PD) is a common neurodegenerative disorder associated with dopaminergic neuron losses in the *substantia nigra*, resulting in such symptoms as resting tremor, muscular rigidity, and hypokinesia [1,2]. Numerous studies have shown that oxidative stress and neuroinflammation are key factors in the development and maintenance of the progressive neurodegeneration process in this disease.

The main characteristics of oxidative stress are increased levels of reactive oxygen species (ROS) and a decrease in, or dysfunction of, the antioxidant systems to counter free radicals [3–5]. The neurotoxins that produce irreversible PD-related effects via oxidative stress induction include paraquat, rotenone, 6-hydroxydopamine (6-OHDA), 1-methyl-4-phenyl-1,2,3,6-tetrahydropyridine (MPTP), and its active metabolite methyl-4-phenylpyridine (MPP⁺), which are the most widespread compounds [6]. All of these compounds exhibit neurotoxic activity due to the ROS formation inside the cells, including the inhibition of mitochondrial complex I, resulting in depletion of intracellular adenosine-5'-triphosphate (ATP) and cell death [7–12]. An exceptional feature is characterized for 6-OHDA, which is able to appear in catecholaminergic neurons and is rapidly and nonenzymatically oxidized by molecular oxygen into hydrogen peroxide and p-quinone [13].

Oxidative stress can modulate mechanisms involving activation of transient receptor potential (TRP) channels, in particular transient receptor potential vanilloid 1 (TRPV1) [14], and inflammatory response by the activation of signaling pathways, which induce the secretion of a high level of proinflammatory mediators [15,16] and is also accompanied by neuron damage [17]. Cell death tends to expand the consequences of neuroinflammatory processes via the release of biomolecules, such as ATP, activating purinergic receptors, including P2X7 (P2X7R). P2X7R is widely expressed in the regions of the central nervous system, such as the frontal cortex, hippocampus, amygdala, and striatum, involved in neurodegenerative diseases [18]. This receptor and its ligands play important roles in inflammation, tumorigenesis, development, and metastasis [19,20]. The activation of P2X7R by high concentrations of extracellular ATP results in the rapid influx of Na⁺ and Ca²⁺ and efflux of K⁺ [21]. Long-term activation induces the formation of non-selective pores, allowing the influx of the organic ions and fluorescent dyes up to 900 Da, which ultimately leads to cell death and the release of new portions of ATP in the extracellular milieu [22,23]. Therefore, the application of P2X7R antagonists will probably attenuate the processes of neuroinflammation and neurodegeneration [24–26].

Understanding the cellular mechanisms that make neurons vulnerable is one of the primary research directions [27]. At present, low-molecular antioxidants, dopamine precursors, and dopamine agonists are widely used for PD symptom elimination rather than delaying the degeneration of dopaminergic neuron [1]. Some peptides and proteins have been shown to reduce the destruction of dopamine neurons induced by oxidative stress [28–30]. In this context, peptides of the Kunitz/BPTI family are of great research interest. This structural group of peptides known as protease inhibitors is well-characterized and widespread among both venomous terrestrial and marine animals [31]. In snakes, spiders, scorpions, frogs, cone snails, and sea anemones, Kunitz peptides are encoded by multigene families and form a great diversity of peptide isoforms in the venomous secretion [32–37]. The primary function of most known Kunitz-type peptides is protease inhibition. Their structure is stabilized by three conserved intradomain disulfide bonds (CysI–CysVI, CysII–CysIV, CysIII–CysV) accompanied by the formation of two loops responsible for protease inhibition. Amino acid (a.a.) residues of the main protease-binding loop, in particular residues of reactive sites (P1-P1' positions), form the most contacts with the protease active site and contribute to the association energy of the protein–enzyme complex [38]. The presence of mutations in Kunitz-type peptides does not affect the spatial molecule structure but leads to the appearance of diverse biological activities toward various targets [39–42]. Recently, we demonstrated that Kunitz-type peptides of the sea anemone *Heteractis crispata* inhibit neuroblastoma cell death induced by 6-OHDA via ROS production reductions or anti-radical activity [43,44]. Furthermore, some of them demonstrated anti-inflammatory, antihistamine, and analgesic activities [45–50], which might also facilitate decreases in both inflammatory and oxidative stress processes inside neuronal cells.

This work is devoted to the study of the ability of a new Kunitz-type peptide from *H. crispera* as well as three known ones to protect neuronal cells from the actions of neurotoxins, which are the cause of PD, as well as to the search for possible mechanisms of their protective action.

2. Results

2.1. Expression and Purification of the Peptides

To study the neuroprotective activity, four peptides differing from each other by the presence of charged residues were chosen from combinatorial libraries of Kunitz-type peptides of the sea anemones *H. crispera* (HCIQ2c1, HCIQ4c7, and HCIQ1c9) and *H. magnifica* (HMIQ3c1) (Figure 1).

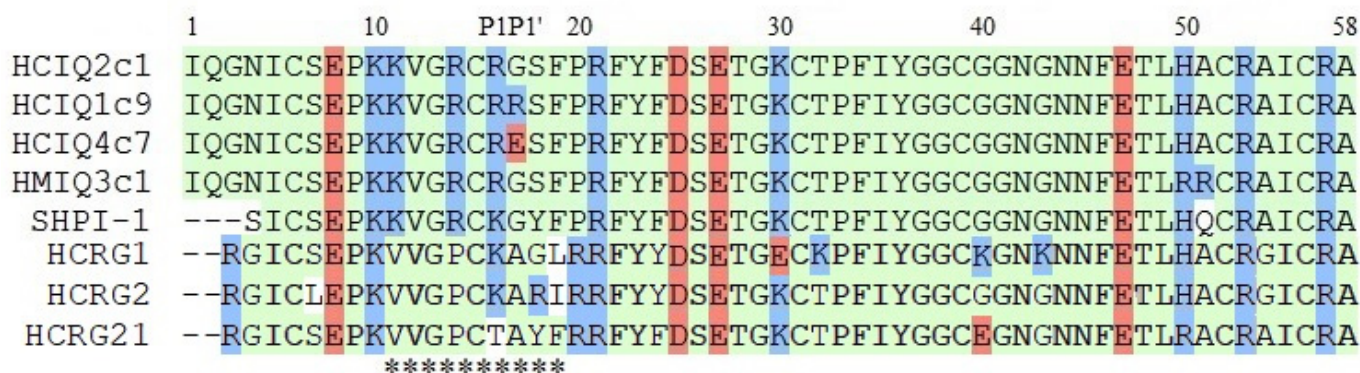


Figure 1. The alignment of sequences of peptides: HCIQ2c1 (UniProtKB ID: A0A6B7FBD3), HCIQ1c9 (A0A6B7FEJ3), HCIQ4c7 (A0A6B7FA07), HCRG1 (C0HJU6), HCRG2 (C0HJU7), and HCRG21 (P0DL86) from *H. crispera*; HMIQ3c1 (A0A3G2FQK2) from *H. magnifica*; and SHPI-1 (P31713) from *Stichodactyla helianthus*. P1-P1'—residues of the reactive sites of Kunitz-type peptides. The asterisks (*) below the sequences indicate the contact sites with proteases. Neutral, positively charged, and negatively charged residues are colored in green, blue, and red, respectively; non-similar residues are shown on white background.

The peptides HCIQ2c1, HCIQ4c7, and HMIQ3c1 were obtained as a result of their production in *Escherichia coli*, as previously described [43,51]. This technique was successfully used to obtain HCIQ1c9. The fusion proteins expressed in *E. coli* and purified by metal affinity chromatography had an expected molecular mass of about 23 kDa and were cleaved by CNBr. Targeted peptides were purified via RP-HPLC. The retention time of HCIQ1c9 on a reverse-phase column was 35.5 min (Figure 2a), which was close to the retention times of the previously obtained peptides [43,51]. The final yield of HCIQ1c9 was 9.02 mg/L of cell culture. The molecular masses of the peptides corresponded to the expected ones, while the molecular mass of HCIQ1c9 was 6429 Da (Figure 2b). The N-terminal sequences (15 a.a.) determined by the automated Edman degradation matched well with sequences deduced from cDNA.

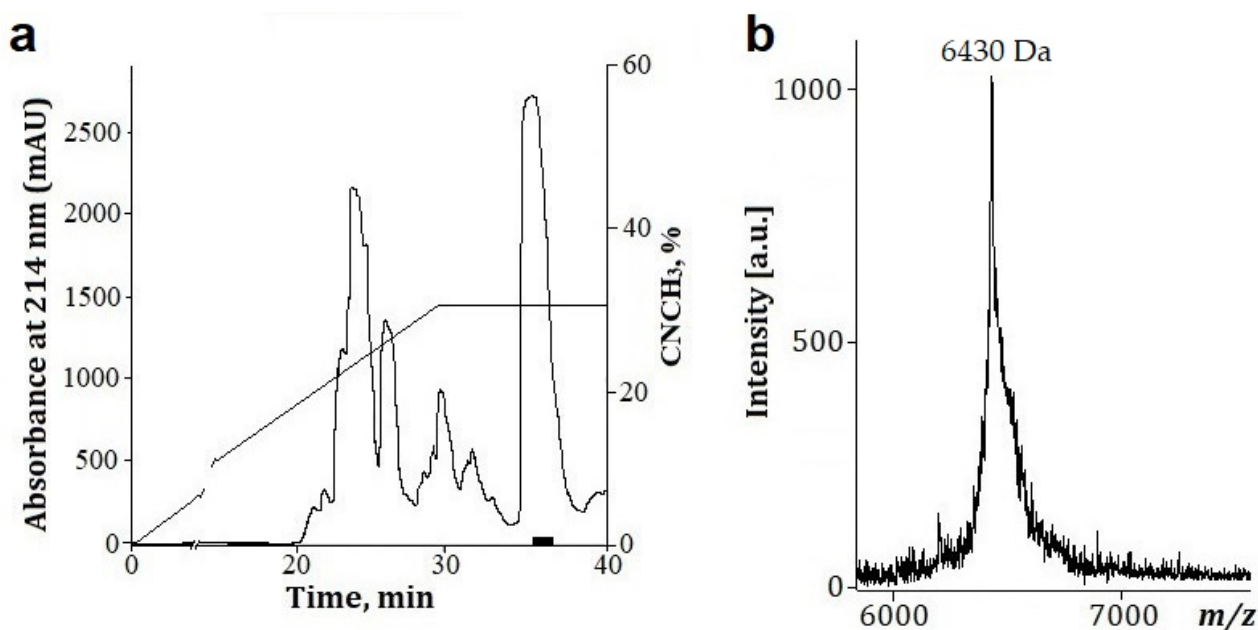


Figure 2. Isolation and molecular mass of HClQ1c9: (a) HPLC elution profile of HClQ1c9 on a Jupiter C4 reverse-phase column (10 × 250 mm), using a linear gradient of acetonitrile concentrations (0–70%) over 70 min with 0.1% TFA and a flow rate of 1.5 ml/min; (b) MALDI-TOF MS spectrum of HClQ1c9 after RP-HPLC.

To determine whether the obtained recombinant peptides had spatial structures, ^1H NMR spectroscopy was used. According to the ^1H NMR spectra, all peptides had pronounced spatial structures, as evidenced by the wide chemical shift dispersion of amide hydrogens to the field of 8–10 ppm and the presence of resonance signals below 0 ppm (Figure S1). Narrow signal lines may indicate that the peptide structures are stable, while the equal line width shows their homogeneity.

2.2. Calculation of the Peptides' Secondary Structures

To calculate secondary structural elements of peptides, circular dichroism (CD) spectroscopy was applied. CD spectroscopy is a fast, well-established, and widely used analytical technique to study secondary structures of proteins and their changes in different environments [52]. According to Figure 3, all spectra in the far UV region (190–240 nm) have similar profiles and are characterized by a positive maximum peak at 193 nm and negative minimum peaks at 202 and 225 nm. The peaks at 193 and 225 nm indicate the presence of α -helices and β -strands, respectively, while the small magnitude of the 225 nm peak and contribution of the signal at 215 nm suggest that the peptides are partially folded. Indeed, analysis of the spectra using the Provencher–Glockner method revealed that all peptides contain both α -helices and β -strands and an unordered structure. The peptides have an approximately equal content of secondary structural elements, while a slight increase in α -helices and decrease in β -structure were found in HClQ1c9 (Table 1), which might be reflected in the spatial structure and biological activity of the peptide. A comparison of peptide structures with the Kunitz-type peptides InhVJ from *H. crispa* [44] and SHPI-1 from *S. helianthus* [53], revealed similar values of secondary structural elements.

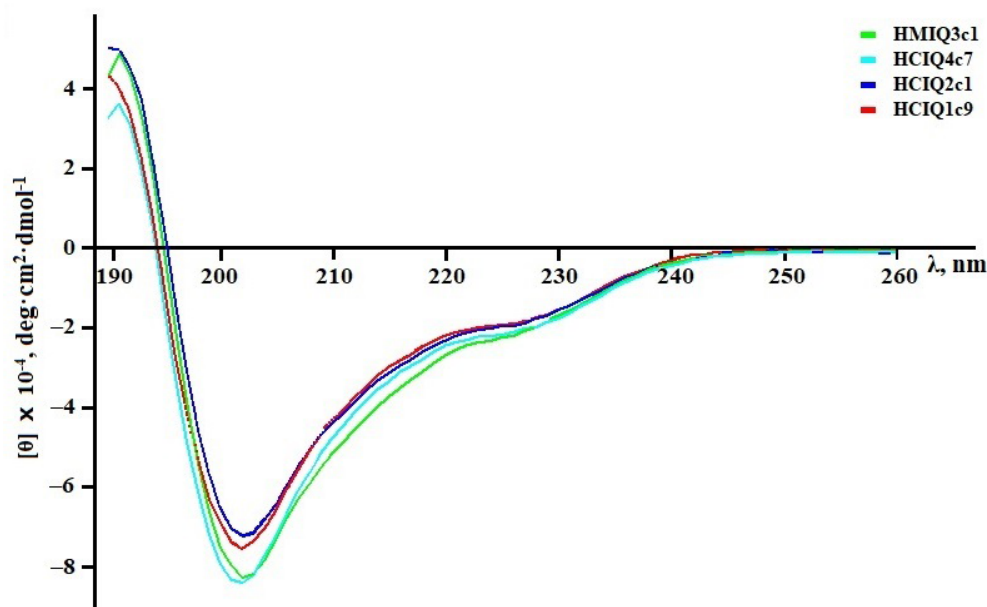


Figure 3. CD spectra of the peptides in deionized water in the far UV region.

Table 1. The peptide secondary structural elements.

Sample	α -Helix			β -Structure			β -Turn	Unordered Structure
	I	II	III	I	II	III		
HClQ2c1	7.1	13.9	21.0	17.4	6.9	24.3	19.0	35.7
HClQ4c7	7.1	13.9	21.0	17.5	6.9	24.4	18.9	35.7
HClQ1c9	10.6	16.2	26.8	14.2	5.7	19.9	19.3	34.0
HMIQ3c1	7.1	13.9	21.0	17.5	7.0	24.5	19.0	35.5
InhVJ	12.4	8.7	21.1	18.0	6.5	24.5	10.1	44.3
SHPI-1 *			20.0			21.8	18.2	40.0

I—Regular structure; II—irregular structure; III—summary value; * the data calculated using the CDSSR algorithm [54].

2.3. Trypsin-Inhibitory Constant Determination

As mentioned above, the main function of Kunitz-type peptides is the inhibition of proteases, in particular trypsin. To confirm the bioactive conformation of HClQ1c9, its ability to inhibit trypsin was determined. Like other Kunitz-type peptides in sea anemones, HClQ1c9 inhibited trypsin with an inhibitory constant (K_i) value 6.3×10^{-7} M. This is similar to HClQ4c7 (1.9×10^{-7} M) but one order higher than for HClQ2c1 (5.2×10^{-8} M) [43] and HMIQ3c1 (5.0×10^{-8} M) [51]. The decrease in trypsin-inhibitory activity of HClQ1c9 and HClQ4c7 in comparison with HClQ2c1 is probably associated with the substitution of Gly17 to Arg or Glu, respectively, at the P1' position (Figure 1), which is an important residue for serine protease inhibition [55].

2.4. Modeling of Peptide Complexes with Trypsin

To determine the residues that affect the nature of the interaction with trypsin, the 3D models of peptides and their complexes with bovine trypsin were generated. A 1.71 Å resolution X-ray structure of the bovine trypsin complex with SHPI-1 (PDB ID: 3M7Q [56]) was exploited as a template, since SHPI-1 is a close homolog of the peptides sharing 91 to 93% identity (Figure 1). The conformational analysis models revealed that 90–98% of the residues occupy the most favored regions of the Ramachandran plot, with no steric hindrance, reflecting sufficient model quality.

Despite point replacements between the peptides themselves and SHPI-1, the overall structures and interfaces of all obtained complexes were almost identical to the prototypical

trypsin complex with SHPI-1 (Figure 4a). The positively charged residue Lys13/Arg16 (SHPI-1/studied peptides) at position P1 makes salt bridges and H-bonds with the Asp171 at site 1 in trypsin, while Arg11/Arg14 at position P3 interacts with site 3 residues (Asn79, Thr80, Gln155, Trp 193, and Gly194). The interaction with the catalytic pocket is a characteristic if trypsin complexes with Kunitz-type inhibitors, whereby the complex stabilization by the P3 residue is substantially enhanced for sea anemone peptides versus BPTI or APPI because of Arg to Pro substitution [56]. The interfaces of HClQ2c1 or HMIQ3c1 are distinguished from SHPI-1 due to the presence of Ser18 instead of Tyr. According to the obtained results, Tyr15 from both SHPI-1 and Ser18 in peptides could make contacts with neighboring trypsin residues Tyr22, Phe24, and Tyr131, indicating their similar roles in complex formation (Figure 4b,c). The peptides HClQ1c9 and HClQ4c7 have oppositely charged residues Arg17 and Glu17 at position P1', respectively. Both Arg17 in HClQ1c9 and Glu17 in HClQ4c7 form an H-bond network with trypsin, but Glu17 makes salt bridges with Lys43, while the unfavorable closeness of Arg17 and Lys43 to each other lead to these residues being pushed off (unfavorable interaction) (Figure 4d–f).

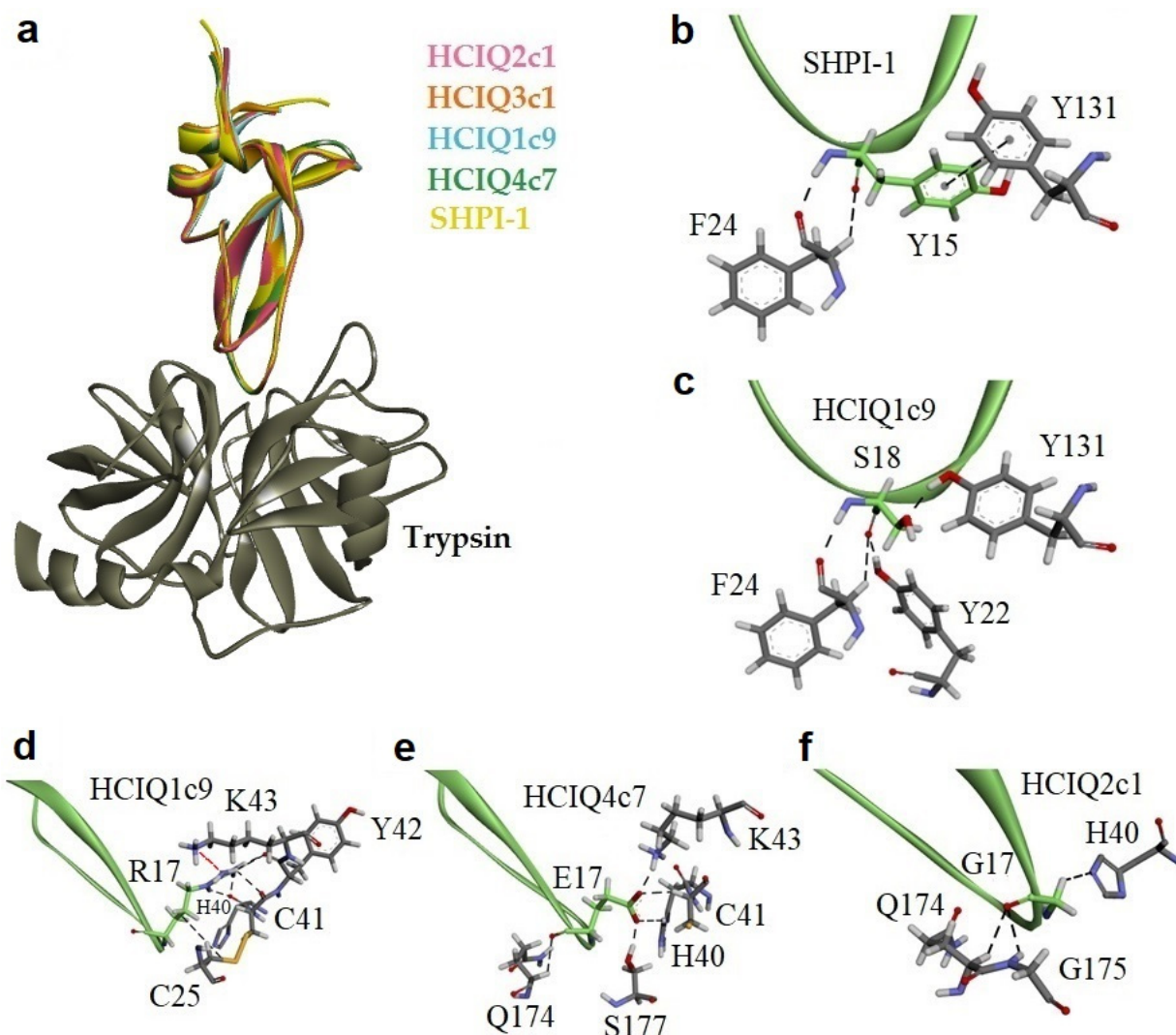


Figure 4. Comparative models of the peptide complexes with trypsin. (a) Ribbon representation of peptide complexes. Intermolecular interactions of residues at positions P1' (b,c) and P2' (d–f) with trypsin molecule. Residues are presented as sticks; hydrogen, oxygen, nitrogen, and sulfur atoms are colored in white, red, blue, and orange, respectively. Interactions are shown as dotted lines, unfavorable interactions between Arg17 of HClQ1c9 and Lys43 of trypsin are shown in red.

2.5. Temperature Effects on the Secondary Structure and Biological Activity of Peptides

The temperature effects on the secondary structure and biological activity of peptides were analyzed using both CD spectroscopy and a protease-inhibitory assay. The CD spectra of HClQ2c1 and HClQ4c7 as well as of HMIQ3c1 and HClQ1c9 solutions showed no significant changes after heating until 90 °C and 80 °C, respectively (Figure 5). Further heating of the solutions to 100 °C resulted in decreased positive peaks at 193 nm in HClQ2c1, HClQ4c7, and HMIQ3c1 spectra, as well as decreased spectral peaks at 202 and 225 nm in the HClQ1c9 spectrum, indicating a reduction in α -helices in the former and the initiation of protein unfolding in the latter. These data were confirmed by the trypsin-inhibitory activity results (Figure 6). HClQ2c1 and HMIQ3c1 were shown to inhibit trypsin completely at all temperature ranges, including at 100 °C, while HClQ4c7 activity was weakly decreased (by 7%) after heating to 100 °C. Regarding HClQ1c9, the heating of the solution in the range from 60 °C to 100 °C resulted in decreases in inhibitory activity of 30–70%. Thus, the obtained results indicated that HClQ2c1, HMIQ3c1, and HClQ4c7 have high thermostability, retaining their conformation on the secondary structural level and their biological activity until 90–100 °C.

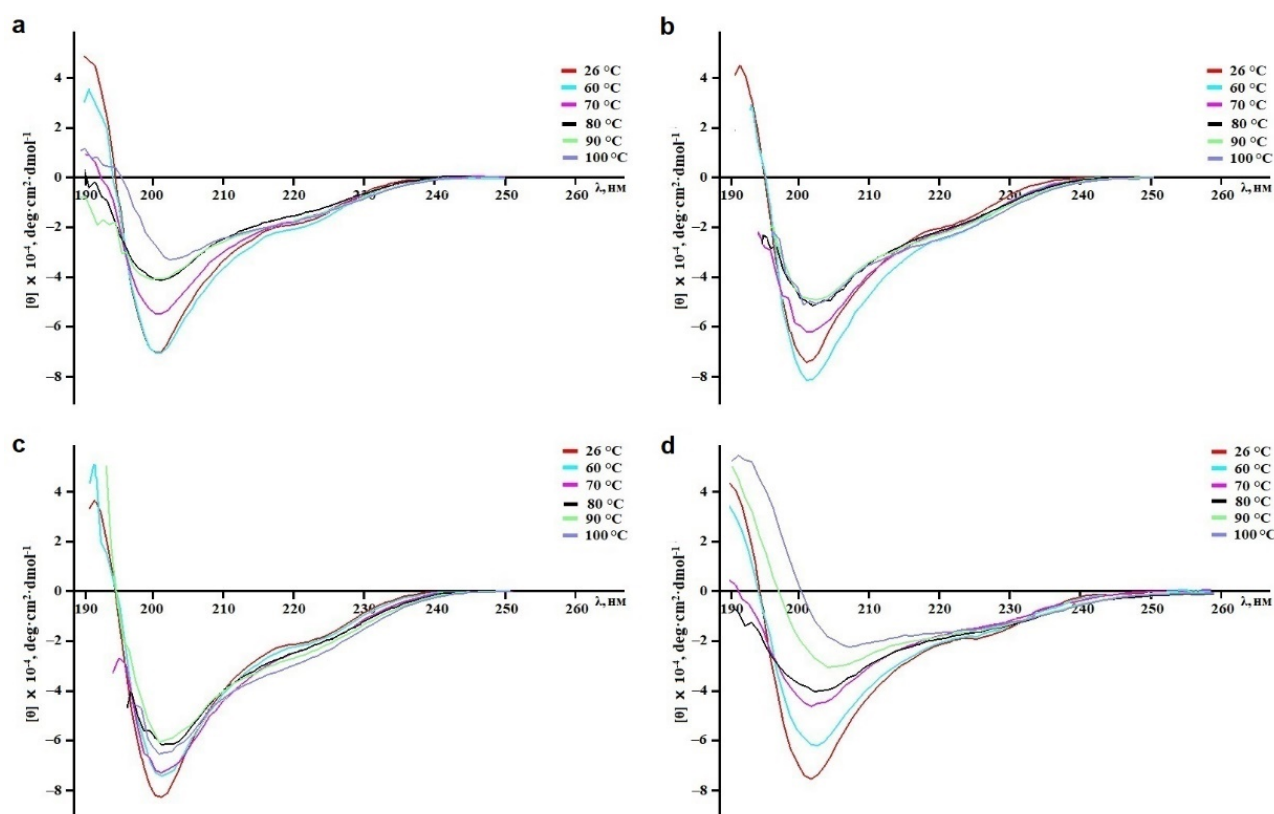


Figure 5. Evaluation of the thermal stability of peptides in deionized water via CD spectroscopy. Recordings of the CD spectra of HClQ2c1 (a), HMIQ3c1 (b), HClQ4c7 (c), and HClQ1c9 (d) were conducted in the far UV region (190–240 nm) after the solutions were incubated over a temperature range from 25 °C to 100 °C for 20–25 min.

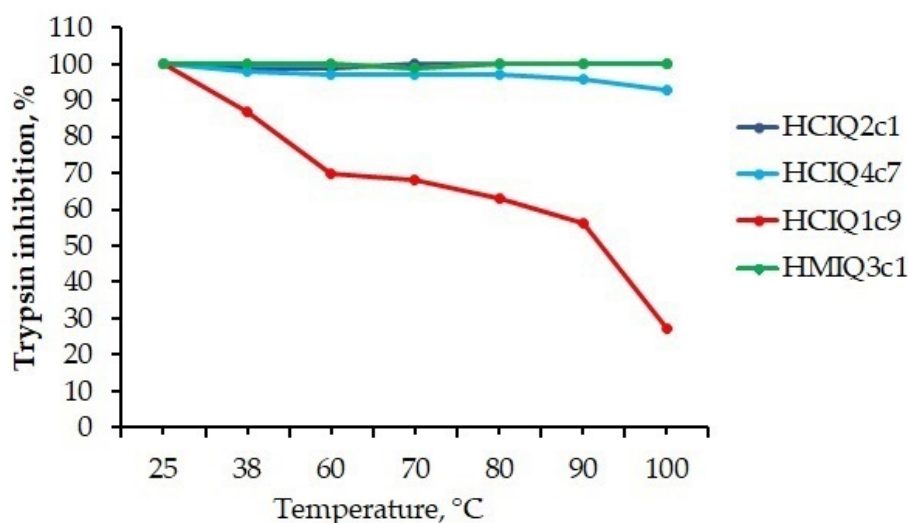


Figure 6. The effects of temperature on the trypsin-inhibitory activity levels of peptides. Peptides were incubated at the temperatures for 30 min and their residual activities were measured.

2.6. The Influence of the Peptides on 6-OHDA-, Paraquat-, Rotenone-, and MPP⁺-Induced Toxicity

The peptides were tested for cell viability in in vitro 6-OHDA-, rotenone-, paraquat-, and MPP⁺-induced Parkinson’s disease models. All peptides were non-toxic on Neuro-2a cells at a concentrations up to 10 μM (Figure S2). The viability of neurotoxin-treated cells was about 65% versus control (Figure 7). The peptide HClQ1c9 at concentrations from 0.1 to 10 μM did not influence the viability of 6-OHDA-treated cells in contrast to HClQ4c7 and HClQ2c1, increasing the cell viability in this model by 14% and 47%, respectively [43]. The peptides HClQ2c1 and HMIQ3c1 at concentrations up to 10 μM did not influence the viability of paraquat-treated cells, while HClQ4c7 and HClQ1c9 increased the cells viability in a dose-dependent manner, with the maximum activity levels of up to 6.7 ± 1.7% and 14.8 ± 3.3% at concentration of 1 and 0.1 μM, respectively (Figure 7a). Moreover, HClQ4c7 and HClQ1c9 increased the viability of rotenone-treated cells in a statistically significant manner (Figure 7b). The effect of HClQ4c7 on the cell viability did not depend on its concentration and reached 10.8 ± 1.4% at 0.1 μM, while HClQ1c9 increased the cell viability by up to 4.0 ± 0.6% at 1 μM. Regarding the MPP⁺-induced toxicity model, HClQ1c9 only revealed a cytoprotective effect; the peptide at a concentration of 10 μM increased the cell viability by up to 9.97 ± 2.9%.

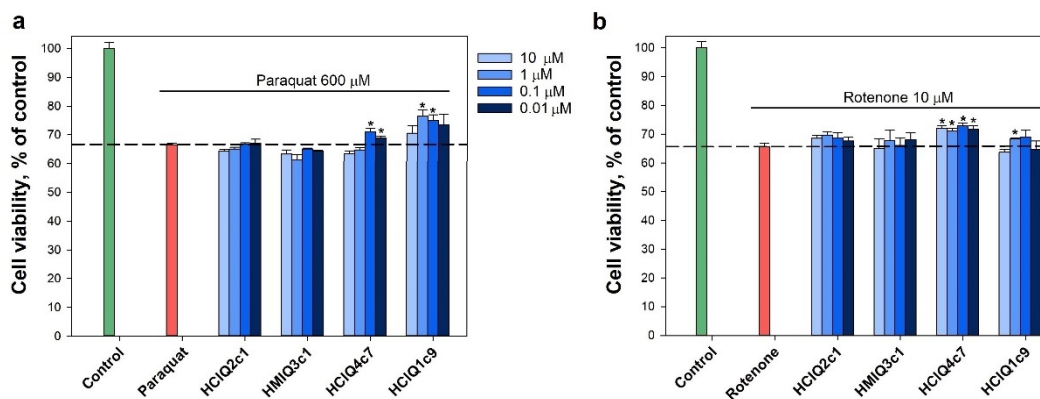


Figure 7. Effects of the peptides on neuroblastoma cell viability in the presence of 600 μM paraquat (a) and 10 μM rotenone (b). The data are shown as means ± SE; * — $p < 0.05$.

2.7. Effect of Peptides on Paraquat- and Rotenone-Induced ROS Formation

The peptides inhibited both rotenone- and paraquat-induced ROS formation (Figure 8a,b). The decrease in ROS levels caused by the peptides in the paraquat-induced cytotoxicity model was stronger than in the presence of rotenone. A reliable dose-dependent effect in the presence of paraquat was revealed for HMIQ3c1, with a maximum decrease in ROS levels (less than control level) of $36.9 \pm 7.9\%$ at a concentration of $0.01 \mu\text{M}$. HClQ2c1 and HClQ4c7 at the same concentrations decreased ROS levels by $30.7 \pm 1.8\%$ and $24.6 \pm 2.5\%$, respectively, while HClQ1c9 inhibited ROS levels by $29.3 \pm 5.6\%$ at a concentration of $1 \mu\text{M}$, a statistically significant result (Figure 8a). In the presence of rotenone, statistically significant decreases in ROS levels were revealed for HClQ2c1 and HClQ1c9 (by $22.0 \pm 7.3\%$ and $22.0 \pm 4.2\%$, respectively) at a concentration of $0.01 \mu\text{M}$, HClQ4c7 inhibited ROS by $17.3 \pm 1.7\%$ at a concentration of $1 \mu\text{M}$ (Figure 8b). In addition, all peptides decreased NO formation induced by paraquat in a statistically significant manner (Figure 8c). HClQ4c7 at a concentration of $0.01 \mu\text{M}$ showed a maximal effect, decreasing NO by $22.3 \pm 2.4\%$, which was less than the control level. In the rotenone-induced toxicity model, the peptides (except HClQ2c1) significantly decreased NO, while HClQ4c7 at a concentration of $0.1 \mu\text{M}$ decreased NO to the control level (by $20.5 \pm 0.1\%$), which was a statistically significant result (Figure 8d).

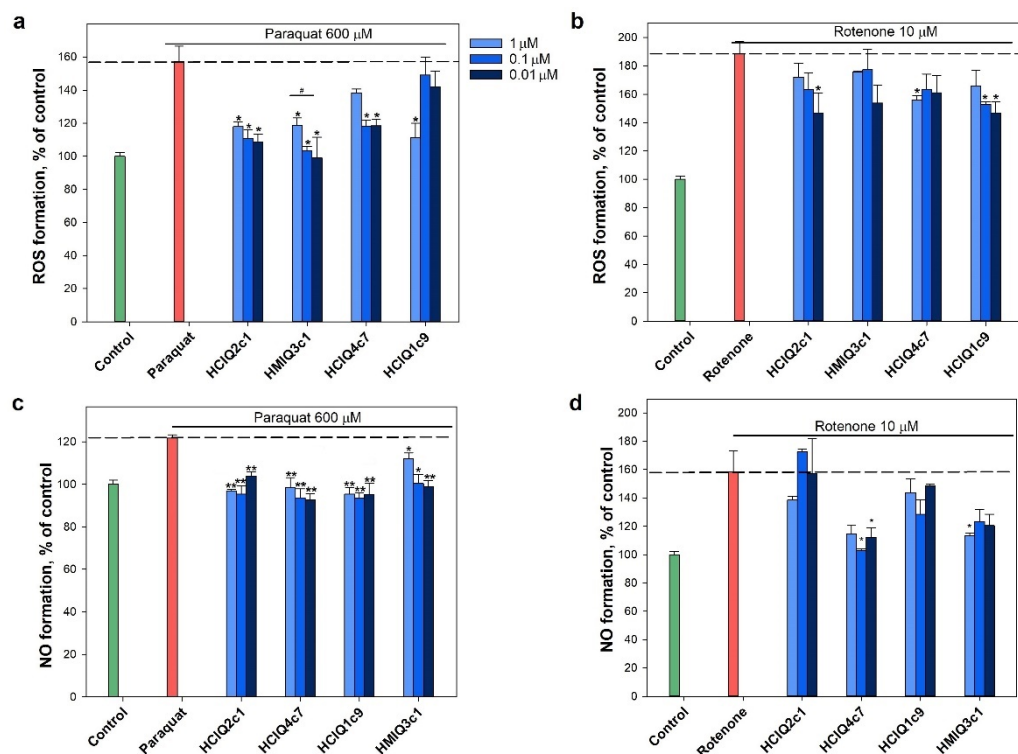


Figure 8. Effects of the peptides on intracellular ROS and NO formation. The effects of the peptides on ROS formation into Neuro-2a cells treated by $600 \mu\text{M}$ paraquat (a) and $10 \mu\text{M}$ rotenone (b). The effects of peptides on NO formation into the cells treated by $600 \mu\text{M}$ paraquat (c) and $10 \mu\text{M}$ rotenone (d). Cells were incubated with peptides for 1 h at $37 \text{ }^\circ\text{C}$, then 3 or 1 h with paraquat or rotenone, respectively. The data are shown as the means \pm SE; *— $p < 0.05$, **— $p < 0.01$, #— $p < 0.05$ when comparing concentrations of the same peptide.

2.8. Free Radical Scavenging of the Peptides

The studied peptides were tested for their ability to scavenge radicals using a DPPH radical scavenging cell-free assay. The obtained results revealed that all peptides reduced the DPPH radicals (Figure 9). The maximum antiradical effect was shown for HMIQ3c1, which scavenged $22.9 \pm 1.3\%$ of DPPH radicals.

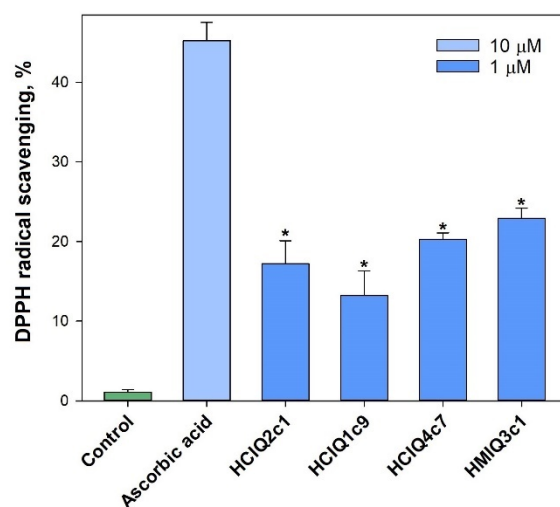


Figure 9. Scavenging activity levels of the peptides against DPPH radicals outside the cells. The data are shown as the mean \pm SE; *— $p < 0.05$.

2.9. Effects of the Peptides on TRPV1 Channels

The electrophysiological study of the peptides was carried out on TRPV1 channels expressed in *Xenopus laevis* oocytes. The activation of the TRPV1 channels was initiated via the application of 2 μ M capsaicin (CAP). The application of 10 μ M capsazepine (CZP) resulted in blocking of the channels. It was found that the peptides at a concentration of 10 μ M did not exert any effects on TRPV1 channels, either when the peptides were administered alone (Figure 10a) or during co-application together with capsaicin (Figure 10b).

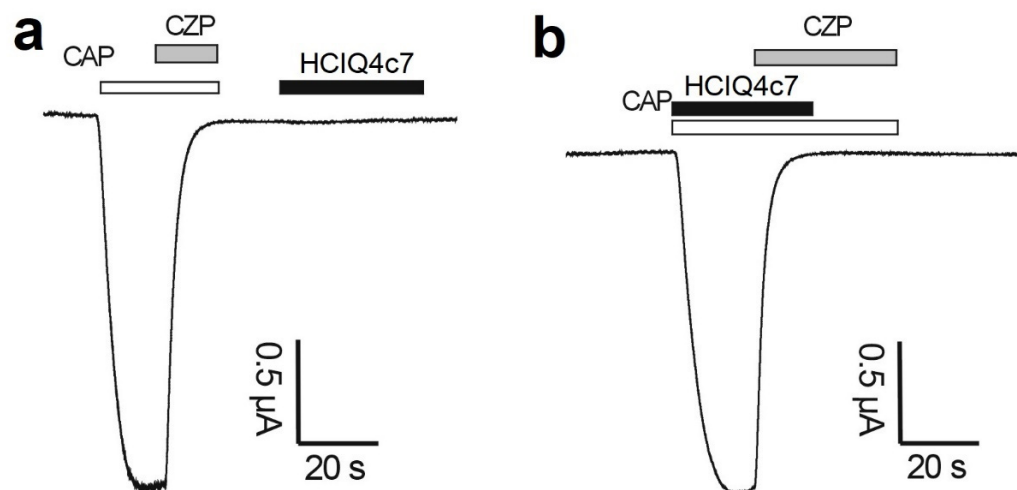


Figure 10. Effect of HClQ4c7 on TRPV1 channels expressed in *X. laevis* oocytes. Whole-cell current traces of capsaicin (CAP = 2 μ M) and capsazepine (CZP = 10 μ M). Applications of HClQ4c7 alone (a) or in the presence of capsaicin (b) are shown. The image was taken using pClamp Clampfit 10.0 (Molecular Devices, Downingtown, PA, USA) and Origin 7.5 software (Originlab, Northampton, MA, USA).

2.10. Effects of the Peptides on ATP-Induced Neuro-2a Cell Death

To establish whether 4 mM ATP leads to the death of Neuro-2a neuroblastoma cells, the cells were incubated with or without ATP for 48 h, and the percentage of viable cells was then determined via MTT assay. Incubation with 4 mM ATP led to a significantly increased percentage of total dead cells (up to $30.15 \pm 0.68\%$) compared with that in control cells (Figure 11a). To determine whether ATP-induced Neuro-2a cell death is caused by P2X7R activation, the cells were pre-incubated with or without 10 μ M A438079, which is

the inhibitor of P2X7R [57], and then were incubated in the absence or presence of 4 mM ATP for 48 h. Pre-incubation of cells with 10 μ M A438079 increased the cell viability by $21.3 \pm 0.5\%$ compared to the cells incubated with ATP alone, indicating that this process is partially mediated by P2X7R activation. The peptides (except HClQ2c1) had a slightly protective effect on ATP-induced cells. Statistically significant increases in cell viability were observed for HClQ4c7 (0.1 μ M), HClQ1c9 (0.01 μ M), and HMIQ3c1 (0.01 μ M), amounting to $4.7 \pm 0.74\%$, $5.96 \pm 0.72\%$, and $6.46 \pm 0.65\%$, respectively, as compared to cells incubated with ATP. Nevertheless, the dependence of the cytoprotective properties of peptides on the studied concentrations is not clearly shown.

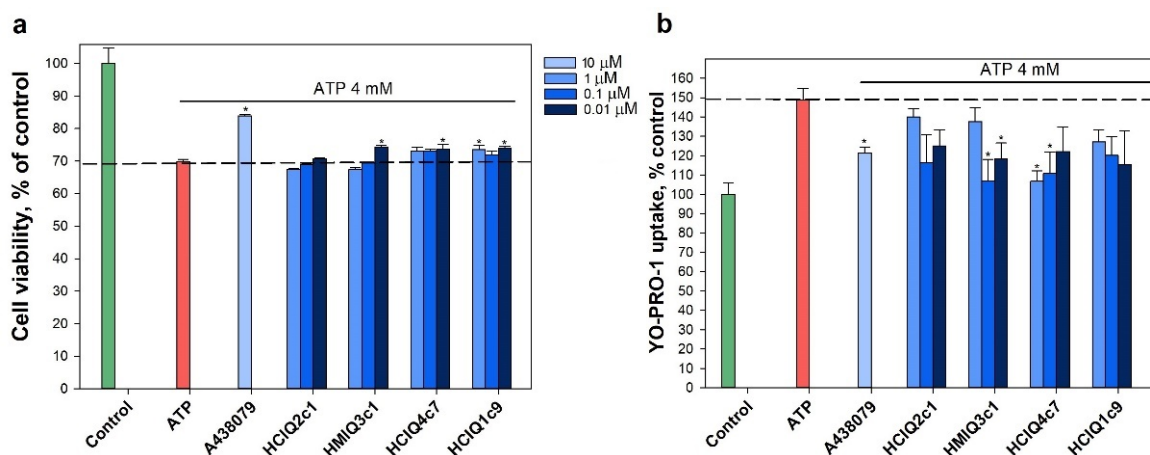


Figure 11. The effects of the peptides on ATP-induced Neuro-2a cell viability and activation of P2X7R. (a) Impact of the peptides on Neuro-2a cell viability in the presence of 4 mM ATP. The peptides were tested at concentrations of 0.01, 0.1, and 1.0 μ M. Cells were incubated with peptides for 1 h at 37 $^{\circ}$ C, then for 48 h with ATP. (b) Effects of the peptides (0.01, 0.1, and 1.0 μ M) on YO-PRO-1 uptake in Neuro-2a cells. ATP was used as a P2X7R agonist. A438079 (10 μ M) was used as a standard inhibitor of P2X7R. The peptide effects were evaluated against the effects of ATP. The data are shown as means \pm SE; *— $p < 0.05$ compared to the effect of ATP alone.

ATP (4 mM) increased the YO-PRO-1 dye penetration into Neuro-2a cells by $49.4 \pm 5.9\%$ (Figure 11b). HMIQ3c1 and HClQ4c7 at concentrations of 0.1 μ M and 1 μ M significantly reduced ATP-induced dye uptake by 28.1 ± 7.5 and $28.5 \pm 3.7\%$, respectively, showing superior results to A438079 ($18.5 \pm 3.2\%$). HClQ1c9 and HClQ2c1 also inhibited ATP-induced dye uptake, but their effects were not statistically significant. Therefore, HClQ4c7 and HMIQ3c1 were selected for further study.

2.11. Effects of the Peptides on ATP-Induced Ca^{2+} Influx into Neuro-2a

To determine whether HClQ4c7 and HMIQ3c1 inhibit the activation of P2X7R, the Ca^{2+} influx induced by channel gating (pore expansion) was measured. Neuro-2a cells were loaded with the Ca^{2+} -selective fluorescent probe Fluo-8, then cellular calcium responses were recorded. A large sustained increase in $[Ca^{2+}]_i$ was recorded after the addition of 1 mM ATP, indicating that it was also mediated through the purinergic receptor. This increase was significantly reduced in the presence of 10 μ M A438079 (Figure 12a). The peptides reduced the Ca^{2+} response at all tested concentrations (Figure 12b). A438079 decreased the calcium response by $47.7 \pm 4.4\%$ relative to the control level, while HClQ4c7 and HMIQ3c1 at a concentration of 10 μ M decreased the stable calcium response by $59.1 \pm 7.8\%$ and $40.6 \pm 2.6\%$, respectively. These data indicate that the peptides are capable of affecting the P2X7R activation.

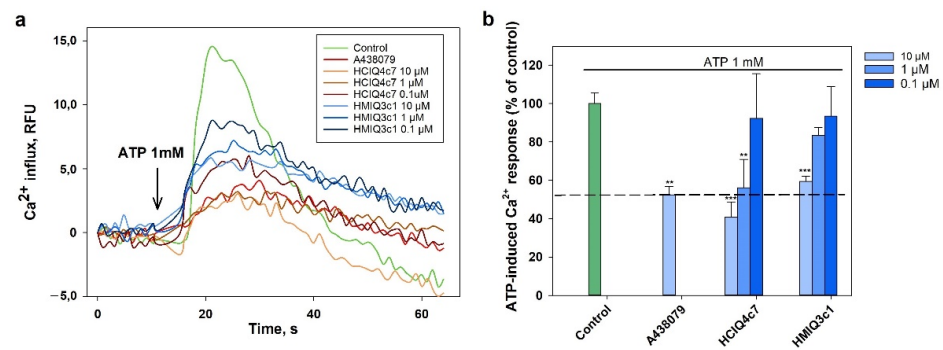


Figure 12. Influence of HClQ4c7 and HMIQ3c1 on ATP-induced calcium influx in Neuro-2a cells. (a) Representative time course of $[Ca^{2+}]_i$ increases induced by ATP (1 mM) alone or in the presence of the peptides or the P2X7R blocker A438079 (10 μ M) in Neuro-2a cells, as measured with Fluo-8. (b) Effect of pre-incubation of Neuro-2a cells with the peptides (0.1, 1.0, and 10.0 μ M) or A438079 (10 μ M) on Ca^{2+} influx caused by ATP (1 mM). The data are shown as the means \pm SE; **— $p < 0.01$, and ***— $p < 0.001$ compared to the effect of ATP alone.

2.12. Interaction of the Peptides with P2X7R Subunit

To reveal that HClQ4c7 and HMIQ3c1 influence P2X7R, their interactions with P2X7R were estimated using the surface plasmon resonance (SPR) method. For this purpose, 12.3 ng/mm² human recombinant P2X7R was immobilized on a Biacore 3000 optical biosensor chip. The direct binding of the peptides with P2X7R was detected and K_d values for the complexes of P2X7R with HClQ4c7 and HMIQ3c1 were calculated as 45.5 and 43.3 μ M, respectively. The dose–response curves from the SPR kinetic analysis are shown in Figure 13.

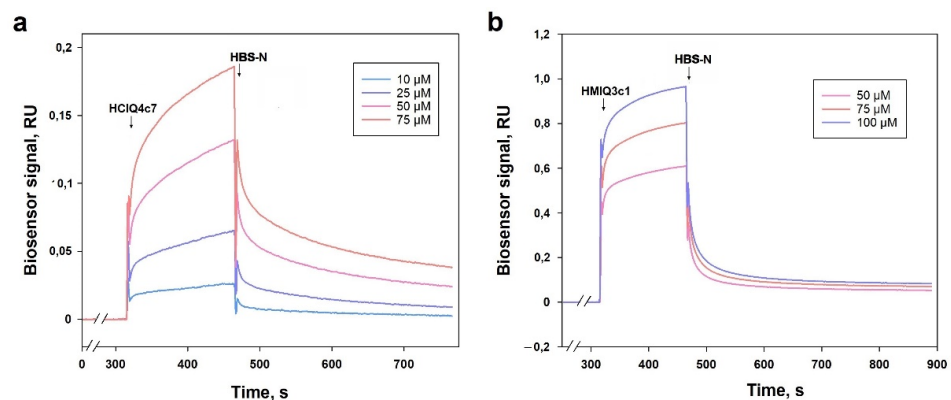


Figure 13. Binding sensorgrams of immobilized P2X7R with HClQ4c7 (a) and HMIQ3c1 (b) at 25 °C. Correspondence of line colors to the peptide concentrations is shown in frame. The injection times of the peptides and HEPES-buffered saline (HBS-N) are shown by a black arrow.

3. Discussion

Neurodegenerative disorders are socially significant diseases; they are some of the most common diseases globally among the elderly, and their frequency is steadily increasing. To date, there is growing evidence that in the development of neurodegenerative diseases, along with the degeneration of dopaminergic neurons (such as in PD), oxidative stress and inflammation play a significant role [5]. The focus of research in studying the etiology of these diseases is shifting to new targets, such as ion channels and enzymes. In this regard, the creation of drugs based on natural compounds with anti-inflammatory or antioxidant activity, specifically interacting with ion channels, enzymes, and other targets involved in neurodegenerative disorders, is vital for developing strategies for their treatment.

The peptides HClQ2c1 and HClQ4c7 from *H. crispata* and HMIQ3c1 from *H. magnifica* interact with several serine proteinases, including inflammatory ones, and they were also

described as the first Kunitz-type peptides with neuroprotective activity [43,51,58]. A new peptide, HClQ1c9, with Gly17Arg at position P1' of the reactive site was also found in a combinatorial library of *H. crispata* Kunitz-type peptides [43] and produced in *E. coli*. Thus, in this work four isoforms of Kunitz-type peptides with point a.a. substitutions were studied in various in vitro models.

Analysis of the superposition of 3D models of the peptides studied here and of SHPI-1 from *S. helianthus* indicated that the peptides have a spatial structure intrinsic of Kunitz folding. Despite the single replacements, the interfaces of the studied peptides and SHPI-1 are almost identical to SHPI-1. According to CD spectra, all peptides contain both α -helices and β -strands comparable with SHPI-1.

The active spatial conformation of the peptides was also confirmed by the presence of trypsin-inhibitory activity. As shown previously, HClQ2c1 and HMIQ3c1 inhibited trypsin at 10^{-8} M and HClQ4c7 (Gly17Glu) at 10^{-7} M. The peptide HClQ1c9 (Gly17Arg) also inhibited trypsin, with a K_i value (6.3×10^{-7} M) close to HClQ4c7. Thus, both negatively and positively charged residues at position P1' led to decreases in the trypsin-inhibitory activity of the peptides, with HClQ4c7 being a stronger trypsin inhibitor than HClQ1c9. This was due to the residue Glu17, which can make additional contact with Lys43 in trypsin, while Arg17 from HClQ1c9 experiences an unfavorable interaction with the trypsin residue.

One of the important characteristics of Kunitz-peptides is the strong stability of the domain structure thanks to the presence of three disulfide bonds. This feature allows them to maintain their protease-inhibitory activity over a wide range of temperatures and pH values. Indeed, the Kunitz peptide SdPI from the scorpion *Lychas mucronatus* [58] and BmTI-A from tick *Rhipicephalus microplus* [59] were shown to be thermostable, while Bm-SPI51 from the cocoon of the silkworm *Bombyx mori* is both heat- and pH-resistant [60]. Based on the CD spectra and residual trypsin activity levels, we revealed that HClQ2c1, HClQ4c7, and HMIQ3c1 are thermostable peptides retaining the conformation of the active molecules up to 90–100 °C, whereas the trypsin-inhibitory activity of HClQ1c9 is reduced by up to 70% in the temperature range of 60–100 °C, an observation that was confirmed by the CD spectrum.

Through our study, we demonstrated that the substitution of the residues at position P1' of the peptides contributes to their biological activity. Earlier, we revealed that HClQ2c1 has stronger neuroblastoma cell viability against 6-OHDA than HClQ4c7 with Gly17Glu substitution [43], while HMIQ3c1 with His50Arg and Ala51Arg substitutions did not affect 6-OHDA-induced cell toxicity [51]. Here, HClQ1c9 showed a maximum protective effect in the paraquat-induced cell death model, while HClQ4c7 was the best in the rotenone-induced cytotoxicity model. Furthermore, HClQ1c9 exhibited protective effects on cells in the presence of MPP⁺. Both rotenone and paraquat are known to induce oxidative stress in neuronal cells. Rotenone promotes mitochondrial complex I inhibition, resulting in an increase in ROS production, while paraquat induces redox cycling in the cytosol, altering the mitochondrial function indirectly [12]. The peptides inhibited ROS formation in the presence of both paraquat and rotenone. It was suggested that the inhibition of ROS formation is associated with the antiradical activity of the peptides. Indeed, these peptides interacted with free radicals, which may be one of the reasons for the reduced ROS levels. On the other hand, it is known that ion channels such as Kv and TRP and cell receptors such as P2X7 are actively involved in the regulation of neuronal processes, including inflammation, and are considered potential therapeutic targets for PD [61–63]. Recently, we showed that Kunitz-type peptides, namely HCRG1 and HCRG2, which are blockers of Kv channels, maintained ROS production in 6-OHDA-treated cells at the reference level [50]. Moreover, HCRG21, a blocker of TRPV1, showed significant neuroprotective action, decreasing ROS production below the control (up to 87%) [44]. The studied peptides were not active in either Kv [43] or TRPV1 channels, despite the high sequence homology with HCRG1, HCRG2, and HCRG21.

Cell death induced by oxidative stress is accompanied by the release of ATP, which at high concentrations activates P2X7R-associated channel opening, leading to osmotic swelling

and ultimately to cell death [22,23]. Therefore, the application of a P2X7R inhibitor can attenuate the progress of a neurodegenerative process. The studied peptides were found to inhibit the uptake of YO-PRO-1 staining, which is able to penetrate through the ion channels formed by P2X7R in Neuro-2a cells [22,64]. HMIQ3c1 and HCIQ4c7 demonstrated the best effects, almost completely inhibiting the ATP-induced YO-PRO-1 uptake. It should be noted, that both HMIQ3c1 and HCIQ4c7 at concentrations of 0.1 and 1 μ M, respectively, more effectively inhibited the dye penetration than 10 μ M A438079, a selective inhibitor of P2X7R. The peptide effect on P2X7R activation was confirmed by the results of Ca^{2+} influx measurements and SPR. Upon binding to ATP, P2X7Rs act as nonselective cation channels, resulting in a steady calcium influx response and increasing the intracellular concentration of calcium ($[\text{Ca}^{2+}]_i$). The obtained results showed that both peptides reduced Ca^{2+} influx and the Ca^{2+} response into Neuro-2a cells, with HCIQ4c7 more effectively decreasing the calcium response than A438079. Moreover, HCIQ4c7 and HMIQ3c1 bound to the P2X7R extracellular domain with similar K_d values, indicating the formation of stable complexes and excluding non-specific binding. This is direct evidence of the ability of the peptides to bind to the studied target, which may partially explain their neuroprotective activity in PD models.

One of the important requirements for potential neuroprotective compounds is their ability to pass through the blood–brain barrier (BBB), which restricts the entry of proteins and undesirable substances to cerebral tissues. Because most drugs do not cross the BBB, few treatments are available against neurodegenerative diseases, including PD.

It has been shown that the Kunitz domain in the β -amyloid precursor protein and Kunitz-type peptide from the bovine pancreas, BPTI, effectively crosses the BBB via low-density lipoprotein receptor-related protein (LRP) [65,66]. Moreover, short peptides create the basis for the BPTI sequence, which has been demonstrated to effectively cross the BBB [66]. The studied peptides have the same folds, including the pattern responsible for penetration through the BBB.

On the other hand, the BBB is known to become more permeable during the inflammatory process. As mentioned above, P2X7R is actively involved in the inflammatory process. The receptor associated with pannexin-1 and the P2X4 receptor are able to stimulate the ROS production induced by ATP, which leads to the activation of NLRP3 (NOD-, LRR-, and pyrin domain-containing protein 3) inflammasome and further release of proinflammatory cytokines IL-1 β and IL-18 [67]. The inflammation carried out by IL-1 β is found to promote the dysfunction and hyperpermeability of the BBB [68,69]. Taken together, the data allow us to assume that the studied peptides might be able to pass through the BBB, at least during inflammation.

Thus, the studied peptides are able to protect neuronal cells against PD inducers via the inhibition of ROS formation and ATP-induced P2X7R activation. However, the molecular mechanism of their interaction with P2X7R and passage through the BBB remains uncertain and requires further detailed study.

4. Materials and Methods

4.1. Expression and Isolation of Kunitz-Type Peptides

The pET32b(+)/*hciq1c9* construction was synthesized by JSC Eurogen (Russia). The Kunitz-type peptides HCIQ2c1, HCIQ4c7, and HMIQ3c1, as well as a new peptide HCIQ1c9, were obtained as described in [43,51]. The recombinant plasmids based on pET32b(+) and carrying the genes of the target peptides fused with thioredoxin were transformed into *E. coli*. The cells were cultured at 37 °C in Luria–Bertani medium containing 100 μ g/mL ampicillin until reaching the optical density (OD_{600}) of \sim 0.5. After induction with IPTG across a concentration range of 0.2–0.5 mM, the cells were incubated at 37 °C for 3 h. The presence of recombinant peptides was determined in 12% polyacrylamide gel by Laemmli's SDS-PAGE method [70]. Cell precipitates were resuspended in the starting buffer (400 mM NaCl, 20 mM Tris-HCl buffer, pH 8.0) and ultrasonicated on ice. Fusion proteins were purified under native conditions on a Ni-NTA agarose (Qiagen, Venlo,

The Netherlands) according to the manufacturer's instructions and cleaved using CNBr overnight at room temperature with a CNBr-to-protein molar ratio of 600:1 [71]. The recombinant peptides were purified from reaction mixture on a Jupiter C4 10 × 250 mm reverse-phase column (Phenomenex, Torrance, CA, USA) using a linear gradient of acetonitrile (from 0% to 70%) with 0.1% trifluoroacetic acid (TFA) over 70 min with a constant flow rate of 1.5 mL/min.

4.2. N-Terminal Amino Acid Sequence Analysis

HCIQ1c9 was treated using 6 M guanidine hydrochloride in 0.5 M Tris-HCl buffer, pH 8.5, containing 2 mM EDTA. Then, dithiothreitol was added and the mixture was incubated for 4 h at 40 °C. Thiol groups of cysteine residues were modified by 50% 4-vinylpyridine in isopropanol for 20 min at room temperature in the dark. The reaction mixture was separated on a Nucleosil C18 4.6 × 250 mm reverse-phase column (Phenomenex, Torrance, CA, USA) using a concentration gradient of acetonitrile (from 0% to 70%) with 0.1% TFA in 160 min, with a constant flow rate of 0.5 mL/min [49]. The N-terminal sequence of HCIQ1c9 (15 a.a.) was determined in duplicate via automatic Edman degradation on a Procise 492c LC sequencer (Applied Biosystems, Bedford, MA, USA) equipped with a Series 200 UV-Vis detector (Perkin Elmer, Waltham, MA, USA) for analysis of phenylthiohydantoyl amino acid derivatives according to the supplier's instructions.

4.3. MALDI-TOF MS Analysis

MALDI-TOF MS spectra of peptides were recorded using an Ultra Flex III MALDI-TOF/TOF mass spectrometer (Bruker, Bremen, Germany) with a nitrogen laser SmartBeam (355 nm), reflector, and potential LIFT tandem modes of operation. Sinapinic acid was used as the matrix. External calibration was employed using a peptide InhVJ with m/z 6107 [72] and its double-charged variant at m/z 3053.

4.4. One-Dimensional NMR Spectroscopy

The ^1H NMR spectra of peptides were acquired at 30 °C on a Bruker Avance III 700 MHz spectrometer (Bruker Biospin, Billerica, MA, USA) equipped with a triple-resonance z-gradient TXO probe. Peptides were dissolved in 90% H_2O /10% D_2O (Deutero GmbH, Kastellaun, Germany) over a concentration range of 1.5–2 mg/mL. Excitation sculpting with gradients [73] was applied to suppress strong solvent resonance, while the chemical shift of their signals was arbitrarily chosen as 4.7 ppm. TopSpin 3.6 (Bruker Biospin, Billerica, MA, USA) was used for the acquisition and processing of the spectra.

4.5. Circular Dichroism Spectroscopy

Circular dichroism (CD) spectra were recorded on a Chirascan-Plus CD spectropolarimeter (Applied Photophysics, Leatherhead, UK) in quartz cuvettes with an optical path length of 0.1 cm for the peptide spectrum region. The peptides were dissolved in deionized water (40 ng/mL) and incubated at temperatures ranging from 25 °C to 100 °C for 20–25 min before recording the CD spectra. The secondary structure elements were calculated using the Provencher–Glockner method [74] using advanced Provencher calculation programs from the CDPro software package (Leatherhead, UK) [75].

4.6. Trypsin-Inhibitory Activity

The trypsin-inhibitory activity of HCIQ1c9 was estimated according to the standard procedure using N- α -benzoyl-D,L-arginine p-nitroanilide (BAPNA) (Sigma-Aldrich, St. Louis, MO, USA) as a substrate. The trypsin inhibition constant was determined using Dyxon's method [76] using substrate concentrations of 0.6 and 1.2 mM. The trypsin concentration was 208 nM. The range of peptide concentrations was 0–20 μM . The constant was calculated based on the results of three parallel experiments. Computational error limits were in the range of 0.1–0.3%.

The temperature influence on the activity levels of peptides was assessed by measuring their residual inhibitory activity levels. After preincubation at temperatures ranging from 25 to 100 °C for 25 min, the peptide solutions were added to trypsin solution and the reaction mixtures were incubated for 10 min at 37 °C, then 1.2 mM BAPNA was added, followed by incubation at 37 °C for 30 min. The final concentration of the peptides was 7 µM. Substrate hydrolysis was measured at 410 nm. The residual activity was calculated based on the results of three parallel experiments according to the following equation [60]:

$$\% = (1 - \text{residual enzyme activity} / \text{enzyme activity without inhibitor}) \times 100$$

4.7. Modeling of Peptide–Trypsin Complexes

The comparative models of complex 3D structures were generated using the (PS)² web server [77]. The peptide sequences HClQ2c1 (UniProtKB ID: A0A6B7FBD3), HMIQ3c1 (A0A3G2FQK2), HClQ1c9 (A0A6B7FEJ3), HClQ4c7 (A0A6B7FA07), and bovine cationic trypsin (P00760) were used as input data and the spatial structure of homologous peptide SHPI-1 in complex with trypsin (PDB ID: 3M7Q [56]) was chosen as the template. The obtained models were further optimized using a fragment-guided molecular dynamics (FG-MD) algorithm [78] or UCSF Chimera 1.11.2rc software [79] using the Amber ff99SB protein force field and analyzed with the QMEAN server and other model quality assessment tools available within the SWISS-MODEL workspace [80]. The residues contributing to complex interfaces were identified using Discovery Studio 4.0 Visualizer (Accelrys Software Inc., San Diego, USA), PDBePISA [81], and CONSRANK web tools [82]. Visualization was performed using Discovery Studio 4.0 Visualizer software.

4.8. Cell Line and Culture Conditions

The murine neuroblastoma cell line Neuro-2a was purchased from ATCC (CCL-131, American Type Culture Collection, Manassas, VA, USA). Cells were cultured in Dulbecco's modified Eagle's medium (DMEM) (Biolot, St. Petersburg, Russia) containing 10% fetal bovine serum (Biolot, St. Petersburg, Russia) and 1% penicillin/streptomycin (Biolot, St. Petersburg, Russia) according to ATCC's instruction. Cells were incubated at 37 °C in a humidified atmosphere containing 5% CO₂ (*v/v*). Before the experiments, Neuro-2a cells at a concentration of 1 × 10⁴ cells/well were dispensed into 96-well plates and incubated for 24 h in a humidified atmosphere containing 5% CO₂ to allow cell attachment.

4.9. Cell Viability Assay (MTT Method)

Peptide stock solutions were prepared in deionized water at a concentration of 10 mM. All tested compounds were added to the plate wells at a volume of 20 µL and diluted in PBS to final concentrations of 0.01, 0.1, 1.0, and 10.0 µM.

Then, 20 µL of substance solution was loaded into the cells and incubated for 24 h followed by replacement of the medium with tested substances and 100 µL of fresh medium. Then, 10 µL of MTT (3-(4,5-dimethylthiazol-2-yl)-2,5-diphenyltetrazolium bromide) (Sigma-Aldrich, St. Louis, MO, USA) stock solution (5 mg/mL) was added to each well and the microplate was incubated for 4 h. Next, 100 µL of SDS-HCl solution (1 g SDS, 10 mL dH₂O, 17 µL 6N HCl) was added to each well followed by incubation for 4–18 h. The absorbance of the converted dye formazan was measured using a Multiskan FC microplate photometer (Thermo Scientific, Waltham, MA, USA) at a wavelength of 570 nm [83,84]. All experiments were repeated in triplicate. Cytotoxic activity was expressed as the percentage of cell viability.

4.10. In Vitro Paraquat-, Rotenone-, MPP⁺, 6-OHDA, and ATP-Induced Cytotoxicity Assays

At the end of the preincubation period, the cells were treated with peptides at concentrations of 0.01, 0.1, 1, and 10 µM for 1 h, after which 600 µM paraquat, 10 µM rotenone, 80 µM of 6-OHDA, 1 mM MPP⁺, or 4 mM ATP (Sigma-Aldrich, St. Louis, MO, USA) was added. The cells incubated with or without inductors were used as positive and negative

controls, correspondingly. Cell viability was measured after 24 h (with paraquat, rotenone and 6-OHDA) or 48 h (with ATP and MPP⁺) using the MTT assay [85–87]. The results are presented as a percentages, taking the cell viability when treated with the inductor as 100%.

4.11. ROS and NO Analyses in Paraquat- and Rotenone-Treated Cells

Neuro-2a cells were incubated with peptides at concentrations of 0.01, 0.1, and 1 μ M for 1 h. Then, paraquat (600 μ M) or rotenone (10 μ M) was added to each well and cells were incubated for 3 or 1 h, respectively. To study the ROS formation, the 2,7-dichlorodihydrofluorescein diacetate (H2DCF-DA) assay was performed according to the manufacturer's instructions (Molecular Probes, Eugene, OR, USA). H2DCF-DA solution was added to each well, such that the final concentration was 10 μ M, then the microplate was incubated for an additional 30 min at 37 °C.

To determine the NO production, a 4-amino-5-methylamino-2',7'-difluorofluorescein diacetate (DAF-FM) assay was performed according to the manufacturer's instructions (Invitrogen, Carlsbad, CA, USA). DAF-FM fluorescent probe solution was added to each well to a final concentration 5 μ M, then the microplate was further incubated for 40 min at 37 °C. In both cases, the fluorescence intensity was measured using a PHERAstar FS high-speed plate reader (BMG Labtech, Ortenberg, Germany) at $\lambda_{\text{ex}} = 485$ nm and $\lambda_{\text{em}} = 518$ nm. The data were processed using MARS Data Analysis v. 3.01R2 (BMG Labtech, Ortenberg, Germany). The results are presented as percentages of control with inductor data.

4.12. DPPH Radical Scavenging Activity

The 2,2-diphenyl-1-picrylhydrazyl (DPPH) radical scavenging activity of the peptides was tested as described in [88]. The peptides dissolved in MeOH were dispensed at a volume of 120 μ L into the wells of a 96-well microplate. Then, 30 μ L of the DPPH (Sigma-Aldrich, Steinheim, Germany) solution in MeOH (3.75 mM) was added to each well. The peptide concentration of the mixtures was 1 μ M. The mixtures were shaken and incubated at room temperature for 30 min, and the absorbance of the resulting solutions was measured at 520 nm with a Multiscan FC microplate reader (Thermo Scientific, Waltham, MA, USA). The results are presented as percentages of the negative control (MeOH) data. Ascorbic acid at 10 μ M was used as the positive control.

4.13. Expression of TRPV1 Channels in *Xenopus Laevis* Oocytes

To express TRPV1 in *Xenopus laevis* oocytes, the linearized plasmids were transcribed using a T7 or SP6 mMESSAGE-mMACHINE transcription kit (Ambion, Austin, TX, USA). The harvesting of stage V–VI oocytes from anaesthetized female *X. laevis* frogs was carried out as previously described [89]. Oocytes were injected with 50 nL of cRNA at a concentration of 1 ng/nL using a micro-injector (Drummond Scientific, Broomall, PA, USA). The oocytes were incubated in a solution containing 96 mM NaCl, 2 mM KCl, 1.8 mM CaCl₂, 2 mM MgCl₂, and 5 mM HEPES pH 7.4, supplemented with 50 mg/L gentamicin sulfate.

4.14. Electrophysiological Assay

The physiological activity in oocytes heterologously expressing the TRPV1 channels was measured using the two-electrode voltage-clamp technique, using a Geneclamp 500 amplifier (Molecular Devices, Austin, TX, USA) controlled by the pClamp database system (Axon Instruments, Union City, CA, USA). The measurements were performed at room temperature (18–22 °C). Whole-cell currents were recorded 1–4 days after the mRNA injection. The electrode resistance was 0.7–1.5 M Ω . The signal was amplified and preliminarily filtered using an amplifier-embedded Bessel filter (cutoff frequency 500 Hz) after digitization of the signal at 2000 Hz. Recordings obtained before the activation of the examined currents were used to subtract the capacitive and leakage currents. The cells were kept at a holding potential of –90 mV. TRPV1 currents were measured in ND96 solution using a protocol of –90 mV for 400 s. The recording chamber was perfused at a rate of 2 mL/min with the ND96 solution. Capsaicin (2 μ M) was used as an agonist and

capsazepine (10 μ M) was used as an antagonist of TRPV1. Capsaicin and capsazepine were purchased from Sigma-Aldrich (St. Louis, MO, USA). The use of the *X. laevis* animals was in accordance with the license number LA1210239 of the Laboratory of Toxicology and Pharmacology, University of Leuven (Belgium). The use of *X. laevis* animals was approved by the Ethical Committee for Animal Experiments of the University of Leuven (P186/2019). All animal care and experimental procedures agreed with the guidelines of the European Convention for the protection of vertebrate animals used for experimental and other scientific purposes (Strasbourg, 18.III.1986).

4.15. YO-PRO-1 Uptake Measurements

For the uptake measurements of the large cationic dye YO-PRO-1, the peptides at final concentrations of 0.01, 0.1, and 1.0 μ M were added to the culture medium with Neuro-2a cells and further incubated for 1 h at 37 °C with 5% CO₂. Then, the cells were washed once with Hanks' balanced salt solution (HBSS) (140 mM NaCl, 5 mM KCl, 0.8 mM MgCl₂, 2 mM CaCl₂, 10 mM glucose, 10 mM HEPES, pH 7.4) and filled with 180 μ L of the same buffer. YO-PRO-1 (Sigma-Aldrich, St. Louis, MO, USA) was loaded into the wells to a final concentration of 5 μ M, the cells were incubated for 15 min at 37 °C, then ATP was added to a final concentration of 4 mM and the plates were incubated for an additional 10 min. Then, the cells were washed three times with the buffer solution and the fluorescence intensity levels were measured with a PHERAstar FS plate reader (BMG, Germany) at $\lambda_{\text{ex}} = 480$ nm and $\lambda_{\text{em}} = 520$ nm. A438079 (10 μ M), a standard inhibitor of P2X₇R, was used as positive control. The effectiveness of the peptides was evaluated relative to the control with ATP.

4.16. Ca²⁺ Influx Measurement

Neuro-2a cells were pre-incubated with studied peptides for 1 h at 37 °C with 5% CO₂. Then, cells were washed twice with culture medium and loaded with 5 μ M Fluo-8 dye (Sigma-Aldrich, St. Louis, MO, USA) and 1 μ M Pluronic F-127 (Sigma-Aldrich, St. Louis, MO, USA) and incubated for 40 min at room temperature in HBSS saline at pH 7.4. Then, the cells were washed two times with the same solution but without the fluorescent dye and were incubated for 20–30 min at room temperature in the dark. In some experiments, Ca²⁺-free medium was used. Here, 140 mM NaCl, 5 mM KCl, 0.8 mM MgCl₂, 10 mM glucose, 10 mM HEPES, 5 mM EGTA, pH 7.4. ATP (1 mM final concentration) were added using a robotic microinjector (20 μ L/well), then 10 s later the baseline recording and additional readings were taken up to 50 s at 1 s intervals. The standard P2X₇R inhibitor A438079 (Sigma-Aldrich, St. Louis, MO, USA) was used as the inhibitory control. Ionomycin (Sigma-Aldrich, St. Louis, MO, USA) was used to generate a generic calcium signal in cells. Fluo-8 was excited at 488 nm, and the emission at 520 nm was measured with a PHERAstar plate reader (BMG LABTECH, Ortenberg, Germany).

4.17. Surface Plasmon Resonance

SPR analyses were performed based on using a Biacore 3000 optical biosensor (GE Healthcare, USA) running under the program "Biacore 3000 Control Software v.1.0". Recombinant human P2X₇R (sequence positions of 47–334 a.a.; complete extracellular domain, 36.8 kDa) (Abbeva LTD, Cambridge, UK) was covalently immobilized on the carboxymethylated surface of the Biacore CM5 sensor chip (Cytiva, Chicago, IL, USA), then activated by the 1:1 mixture of 0.2 M 1-ethyl-3-(3-dimethylaminopropyl)carbodiimide hydrochloride (EDC) and 0.05 M N-hydroxysuccinimide (NHS) via the injection of receptor solution (15 μ g/mL) in 10 mM sodium acetate (pH 5.0) for 10 min at a flow rate of 5 μ L/min. The reference channel without immobilized P2X₇R was used to correct the effects of the non-specific binding of peptides to the chip surface. The quantity of the immobilized hP2X₇R equaled 12300 RU (resonance units, 1 RU corresponds to 1 pg receptor bound per mm² of chip surface). HBS-N (10 mM HEPES, 150 mM NaCl, pH 7.4) (Cytiva, USA) was used as a running buffer for SPR assays. Peptide solutions in the HBS-N buffer over a concentration range of 5–100 μ M were passed through biosensor channels (working

and reference) at a flow rate of 10 $\mu\text{L}/\text{min}$ for 3 min at 25 $^{\circ}\text{C}$. Dissociation of the formed peptide–P2X7R complexes was registered at the same flow rate for no less than 6 min from the moment of sample injection. After each biosensor cycle, analytes were removed with two injections of regenerating solution (2 M NaCl, 1% CHAPS) at a flow rate of 30 $\mu\text{L}/\text{min}$ for 30 s.

SPR sensorgrams were processed in BIAevaluation Software v. 4.1.1 (GE Healthcare) using “1:1 binding (Langmuir)” and “two-state (conformational change) binding” data processing models.

The final kinetic parameters were obtained from the model of two-state (conformational change) binding. The equation describing the used model was as follows:

$$K_d = k_{\text{off}1}/k_{\text{on}1} \times (1 + k_{\text{on}2}/k_{\text{off}2}) - 1$$

where K_d is the equilibrium dissociation constant, $k_{\text{off}1}$ is the dissociation rate constant, $k_{\text{on}1}$ is the association rate constant, $k_{\text{on}2}$ is the forward rate constant for the $\text{CP} \leftrightarrow \text{CP}^*$ transition, $k_{\text{off}2}$ is the backward rate constant for transition $\text{CP} \leftrightarrow \text{CP}^*$, C is the compound, and P is the immobilized protein.

4.18. Statistics

All data were obtained from three independent replicates and calculated values were expressed as means \pm standard error of the mean (SEM). Student’s *t*-test was performed using SigmaPlot 14.0 (Systat Software Inc., San Jose, CA, USA) to determine statistical significance.

Supplementary Materials: The following supporting information can be downloaded at: <https://www.mdpi.com/article/10.3390/ijms23095115/s1>.

Author Contributions: A.K., E.P., E.M. and E.L. designed the experiments. A.K. and E.P. drafted the manuscript. A.K. carried out the peptide purification and trypsin-inhibitory constant analyses. R.K. performed the modeling, molecular docking of the molecules, and molecular mass determination. E.M., E.P. and E.Y. performed neuroprotective activity experiments. A.M. and N.K. assessed the NMR and CD spectra, respectively. S.K. and L.K. performed SPR experiments. S.P. performed electrophysiological experiments. E.L., J.T., A.I., N.A. and D.A. critically reviewed the manuscript. All authors have read and agreed to the published version of the manuscript.

Funding: The study of peptides’ effects on cell viability and ROS production was funded by RFBR and SC RA, project number 20-54-05006. The study of the peptides’ influence on ATP-induced P2X7R activation, Ca^{2+} influx measurements, and binding to P2X7R were supported by the Russian Science Foundation, Grant No. 21-74-00082. The study of the peptides’ influence on the TRPV1 channels was supported by RSF, No. 19-74-20088. J.T. was funded by grants GOC2319N, GOA4919N, and G0E7120N (F.W.O. Vlaanderen). S.P. was supported by KU Leuven funding (PDM/19/164) and grant 12W7822N (F.W.O. Vlaanderen).

Institutional Review Board Statement: Not applicable.

Informed Consent Statement: Not applicable.

Data Availability Statement: The additional data supporting the manuscript are available from the corresponding author upon request.

Acknowledgments: The study of the spatial structure of the peptides via ^1H NMR and CD spectroscopy and molecular mass determination was carried out on the equipment of The Far Eastern Center for Structural Molecular Research (NMR/MS) PIBOC FEB RAS. The SPR analysis was performed using the equipment of Human Proteome Core Facilities of the Institute of Biomedical Chemistry (Russia). We are grateful to Oleg Chernikov for the peptide sequencing and Pavel Dmitrenok for supervision of the peptide molecular mass determination.

Conflicts of Interest: The authors declare that there is no competing interest associated with the manuscript.

Sample Availability: Samples of the recombinant peptides are available from the authors.

References

- Dauer, W.; Przedborski, S. Parkinson's disease: Mechanisms and models. *Neuron* **2003**, *39*, 889–909. [CrossRef]
- Lees, A.J.; Hardy, J.; Revesz, T. Parkinson's disease. *Lancet* **2009**, *373*, 2055–2066. [CrossRef]
- Rivas-Arancibia, S.; Guevara-Guzmán, R.; López-Vidal, Y.; Rodríguez-Martínez, E.; Zanardo-Gomes, M.; Angoa-Pérez, M.; Raisman-Vozari, R. Oxidative stress caused by ozone exposure induces loss of brain repair in the hippocampus of adult rats. *Toxicol. Sci.* **2010**, *113*, 187–197. [CrossRef] [PubMed]
- Halliwell, B. Free radicals and antioxidants: Updating a personal view. *Nutr. Rev.* **2012**, *70*, 257–265. [CrossRef] [PubMed]
- Solleiro-Villavicencio, H.; Rivas-Arancibia, S. Effect of chronic oxidative stress on neuroinflammatory response mediated by CD4+T cells in neurodegenerative diseases. *Front. Cell. Neurosci.* **2018**, *12*, 114. [CrossRef]
- Blesa, J.; Phani, S.; Jackson-Lewis, V.; Przedborski, S. Classic and new animal models of Parkinson's disease. *J. Biomed. Biotechnol.* **2012**, *2012*, 845618. [CrossRef]
- Salari, S.; Bagheri, M. In vivo, in vitro and pharmacologic models of Parkinson's disease. *Physiol. Res.* **2019**, *68*, 17–24. [CrossRef]
- Lama, J.; Buhidma, Y.; Fletcher, E.J.R.; Duty, S. Animal models of Parkinson's disease: A guide to selecting the optimal model for your research. *Neuronal Signal.* **2021**, *5*, 1–24. [CrossRef]
- Zeng, X.S.; Geng, W.S.; Jia, J.J. Neurotoxin-induced animal models of Parkinson disease: Pathogenic mechanism and assessment. *ASN Neuro* **2018**, *10*, 1759091418777438. [CrossRef]
- Duty, S.; Jenner, P. Animal models of Parkinson's disease: A source of novel treatments and clues to the cause of the disease. *Br. J. Pharmacol.* **2011**, *164*, 1357–1391. [CrossRef]
- Sherer, T.B.; Kim, J.-H.; Betarbet, R.; Greenamyre, J.T. Subcutaneous rotenone exposure causes highly selective dopaminergic degeneration and α -synuclein aggregation. *Exp. Neurol.* **2003**, *179*, 9–16. [CrossRef] [PubMed]
- Miller, G.W. Paraquat: The red herring of Parkinson's disease research. *Toxicol. Sci.* **2007**, *100*, 1–2. [CrossRef] [PubMed]
- Soto-Otero, R.; Méndez-Álvarez, E.; Hermida-Ameijeiras, Á.; Muñoz-Patiño, A.M.; Labandeira-García, J.L. Autoxidation and neurotoxicity of 6-hydroxydopamine in the presence of some antioxidants: Potential implication in relation to the pathogenesis of Parkinson's disease. *J. Neurochem.* **2000**, *74*, 1605–1612. [CrossRef] [PubMed]
- Adhya, P.; Sharma, S.S. Redox TRPs in diabetes and diabetic complications: Mechanisms and pharmacological modulation. *Pharmacol. Res.* **2019**, *146*, 104271. [CrossRef] [PubMed]
- Chan, P.H. Reactive oxygen radicals in signaling and damage in the ischemic brain. *J. Cereb. Blood Flow Metab.* **2001**, *21*, 2–14. [CrossRef] [PubMed]
- Hsieh, H.L.; Yang, C.M. Role of redox signaling in neuroinflammation and neurodegenerative diseases. *BioMed Res. Int.* **2013**, *2013*, 484613. [CrossRef]
- Pajares, M.; Rojo, A.; Manda, G.; Boscá, L.; Cuadrado, A. Inflammation in Parkinson's disease: Mechanisms and therapeutic implications. *Cells* **2020**, *9*, 1687. [CrossRef]
- Sluyter, R.; Stokes, L. Significance of P2X7 receptor variants to human health and disease. *Recent Pat. DNA Gene Seq.* **2011**, *5*, 41–54. [CrossRef]
- Roger, S.; Jelassi, B.; Couillin, I.; Pelegrin, P.; Besson, P.; Jiang, L.H. Understanding the roles of the P2X7 receptor in solid tumour progression and therapeutic perspectives. *Biochim. Biophys. Acta Biomembr.* **2015**, *1848*, 2584–2602. [CrossRef]
- Rotondo, J.C.; Mazziotta, C.; Lanzillotti, C.; Stefani, C.; Badiale, G.; Campione, G.; Martini, F.; Tognon, M. The role of purinergic P2X7 receptor in inflammation and cancer: Novel molecular insights and clinical applications. *Cancers* **2022**, *14*, 1116. [CrossRef]
- Burnstock, G.; Kennedy, C. *P2X Receptors in Health and Disease*, 1st ed.; Elsevier Inc.: Amsterdam, The Netherlands, 2011; Volume 61, ISBN 9780123855268.
- Alves, L.A.; De Melo Reis, R.A.; De Souza, C.A.M.; De Freitas, M.S.; Teixeira, P.C.N.; Neto Moreira Ferreira, D.; Xavier, R.F. The P2X7 receptor: Shifting from a low- to a high-conductance channel—An enigmatic phenomenon? *Biochim. Biophys. Acta* **2014**, *1838*, 2578–2587. [CrossRef] [PubMed]
- Andrejew, R.; Oliveira-Giacomelli, Á.; Ribeiro, D.E.; Glaser, T.; Arnaud-Sampaio, V.F.; Lameu, C.; Ulrich, H. The P2X7 receptor: Central hub of brain diseases. *Front. Mol. Neurosci.* **2020**, *13*, 124. [CrossRef] [PubMed]
- Volonte, C.; Apolloni, S.; Skaper, D.S.; Burnstock, G. P2X7 receptors: Channels, pores and more. *CNS Neurol. Disord. Drug Targets* **2012**, *11*, 705–721. [CrossRef] [PubMed]
- Bartlett, R.; Stokes, L.; Sluyter, R. The P2X7 receptor channel: Recent developments and the use of P2X7 antagonists in models of disease. *Pharmacol. Rev.* **2014**, *66*, 638–675. [CrossRef] [PubMed]
- Jimenez-Mateos, E.M.; Smith, J.; Nicke, A.; Engel, T. Regulation of P2X7 receptor expression and function in the brain. *Brain Res. Bull.* **2019**, *151*, 153–163. [CrossRef]
- Hwang, O. Role of oxidative stress in Parkinson's Disease. *Exp. Neurobiol.* **2013**, *22*, 11–17. [CrossRef]
- Tunçel, N.; Korkmaz, O.T.; Tekin, N.; Şener, E.; Akyüz, F.; Inal, M. Antioxidant and Anti-Apoptotic Activity of Vasoactive Intestinal Peptide (VIP) Against 6-Hydroxy Dopamine Toxicity in the Rat Corpus Striatum. *J. Mol. Neurosci.* **2012**, *46*, 51–57. [CrossRef]
- Sun, S.Y.; An, C.N.; Pu, X.P. DJ-1 protein protects dopaminergic neurons against 6-OHDA/MG-132-induced neurotoxicity in rats. *Brain Res. Bull.* **2012**, *88*, 609–616. [CrossRef]

30. Yin, S.-M.; Zhao, D.; Yu, D.-Q.; Li, S.-L.; An, D.; Peng, Y.; Xu, H.; Sun, Y.-P.; Wang, D.-M.; Zhao, J.; et al. Neuroprotection by scorpion venom heat resistant peptide in 6-hydroxydopamine rat model of early-stage Parkinson's disease. *Acta Physiol. Sin.* **2014**, *66*, 658–666. [CrossRef]
31. Mourão, C.B.F.; Schwartz, E.F. Protease inhibitors from marine venomous animals and their counterparts in terrestrial venomous animals. *Mar. Drugs* **2013**, *11*, 2069–2112. [CrossRef]
32. Droctove, L.; Ciolek, J.; Mendre, C.; Chorfa, A.; Huerta, P.; Carvalho, C.; Gouin, C.; Lancien, M.; Blanchet, G.; De Pauw, E.; et al. A new Kunitz-type snake toxin family associated with an original mode of interaction with the vasopressin 2 receptor. *Br. J. Pharmacol.* **2022**. [CrossRef] [PubMed]
33. Yuan, C.H.; He, Q.Y.; Peng, K.; Diao, J.B.; Jiang, L.P.; Tang, X.; Liang, S.P. Discovery of a distinct superfamily of Kunitz-type toxin (KTT) from tarantulas. *PLoS ONE* **2008**, *3*, e3414. [CrossRef]
34. Isaeva, M.P.; Chausova, V.E.; Zelepuga, E.A.; Guzev, K.V.; Tabakmakher, V.M.; Monastyrnaya, M.M.; Kozlovskaya, E.P. A new multigene superfamily of Kunitz-type protease inhibitors from sea anemone *Heteractis Cris. Peptides* **2012**, *34*, 88–97. [CrossRef] [PubMed]
35. Elliger, C.A.; Richmond, T.A.; Lebaric, Z.N.; Pierce, N.T.; Sweedler, J.V.; Gilly, W.F. Diversity of conotoxin types from *Conus californicus* reflects a diversity of prey types and a novel evolutionary history. *Toxicon* **2011**, *57*, 311–322. [CrossRef]
36. Chen, Z.; Luo, F.; Feng, J.; Yang, W.; Zeng, D.; Zhao, R.; Cao, Z.; Liu, M.; Li, W.; Jiang, L.; et al. Genomic and structural characterization of Kunitz-type peptide LmKTT-1a highlights diversity and evolution of scorpion potassium channel toxins. *PLoS ONE* **2013**, *8*, e60201. [CrossRef]
37. You, D.; Hong, J.; Rong, M.; Yu, H.; Liang, S.; Ma, Y.; Yang, H.; Wu, J.; Lin, D.; Lai, R. The first gene-encoded amphibian neurotoxin. *J. Biol. Chem.* **2009**, *284*, 22079–22086. [CrossRef]
38. Ranasinghe, S.; McManus, D.P. Structure and function of invertebrate Kunitz serine protease inhibitors. *Dev. Comp. Immunol.* **2013**, *39*, 219–227. [CrossRef]
39. Schweitz, H.; Bruhn, T.; Guillemare, E.; Moinier, D.; Lancelin, J.; Lazdunski, M. Kaliclutines and Kaliseptine. Two different classes of sea anemone toxins for voltage-sensitive K⁺ channels. *J. Biol. Chem.* **1995**, *270*, 25121–25126. [CrossRef]
40. Stotz, S.C.; Spaetgens, R.L.; Zamponi, G.W. Block of voltage-dependent calcium channel by the green mamba toxin calcicludine. *J. Membr. Biol.* **2000**, *174*, 157–165. [CrossRef]
41. Mans, B.J.; Louw, A.I.; Neitz, A.W.H. Savignygrin, a platelet aggregation inhibitor from the soft tick *Ornithodoros savignyi*, presents the RGD integrin recognition motif on the Kunitz-BPTI fold. *J. Biol. Chem.* **2002**, *277*, 21371–21378. [CrossRef]
42. Peigneur, S.; Billen, B.; Derua, R.; Waelkens, E.; Debaveye, S.; Béress, L.; Tytgat, J. A bifunctional sea anemone peptide with Kunitz type protease and potassium channel inhibiting properties. *Biochem. Pharmacol.* **2011**, *82*, 81–90. [CrossRef] [PubMed]
43. Kvetkina, A.; Leychenko, E.; Chausova, V.; Zelepuga, E.; Chernysheva, N.; Guzev, K.; Pisyagin, E.; Yurchenko, E.; Menchinskaya, E.; Aminin, D.; et al. A new multigene HCIQ subfamily from the sea anemone *Heteractis crispa* encodes Kunitz-peptides exhibiting neuroprotective activity against 6-hydroxydopamine. *Sci. Rep.* **2020**, *10*, 1–14. [CrossRef] [PubMed]
44. Sintsova, O.; Gladkikh, I.; Monastyrnaya, M.; Tabakmakher, V.; Yurchenko, E.; Menchinskaya, E.; Pisyagin, E.; Andreev, Y.; Kozlov, S.; Peigneur, S.; et al. Sea anemone Kunitz-type peptides demonstrate neuroprotective activity in the 6-hydroxydopamine induced neurotoxicity model. *Biomedicines* **2021**, *9*, 283. [CrossRef] [PubMed]
45. Sokotun, I.N.; Il'ina, A.P.; Monastyrnaya, M.M.; Leychenko, E.V.; Es'kov, A.A.; Anastuk, S.D.; Kozlovskaya, E.P. Proteinase inhibitors from the tropical sea anemone *Radianthus macrodactylus*: Isolation and characteristic. *Biochemistry* **2007**, *72*, 301–306. [CrossRef] [PubMed]
46. Andreev, Y.A.; Kozlov, S.A.; Korolkova, Y.V.; Dyachenko, I.A.; Bondarenko, D.A.; Skobtsov, D.I.; Murashev, A.N.; Kotova, P.D.; Rogachevskaja, O.A.; Kabanova, N.V.; et al. Polypeptide modulators of TRPV1 produce analgesia without hyperthermia. *Mar. Drugs* **2013**, *11*, 5100–5115. [CrossRef] [PubMed]
47. Sintsova, O.V.; Monastyrnaya, M.M.; Pisyagin, E.A.; Menchinskaya, E.S.; Leychenko, E.V.; Aminin, D.L.; Kozlovskaya, E.P. Anti-inflammatory activity of a polypeptide from the *Heteractis crispa* sea anemone. *Russ. J. Bioorganic Chem.* **2015**, *41*, 657–663. [CrossRef] [PubMed]
48. Monastyrnaya, M.; Peigneur, S.; Zelepuga, E.; Sintsova, O.; Gladkikh, I.; Leychenko, E.; Isaeva, M.; Tytgat, J.; Kozlovskaya, E. Kunitz-Type peptide HCRG21 from the sea anemone *Heteractis crispa* is a full antagonist of the TRPV1 receptor. *Mar. Drugs* **2016**, *14*, 229. [CrossRef]
49. Sintsova, O.V.; Pisyagin, E.A.; Gladkikh, I.N.; Monastyrnaya, M.M.; Menchinskaya, E.S.; Leychenko, E.V.; Aminin, D.L.; Kozlovskaya, E.P. Kunitz-type peptides of the sea anemone *Heteractis crispa*: Potential anti-inflammatory compounds. *Russ. J. Bioorganic Chem.* **2017**, *43*, 91–97. [CrossRef]
50. Sintsova, O.V.; Palikov, V.A.; Palikova, Y.A.; Klimovich, A.A.; Gladkikh, I.N.; Andreev, Y.A.; Monastyrnaya, M.M.; Kozlovskaya, E.P.; Dyachenko, I.A.; Kozlov, S.A.; et al. Peptide blocker of ion channel TRPV1 exhibits a long analgesic effect in the heat stimulation model. *Dokl. Biochem. Biophys.* **2020**, *493*, 215–217. [CrossRef]
51. Kvetkina, A.N.; Leychenko, E.V.; Yurchenko, E.A.; Pisyagin, E.A.; Peigneur, S.; Tytgat, Y.; Isaeva, M.P.; Aminin, D.L.; Kozlovskaya, E.P. A New IQ-peptide of the Kunitz-type from the *Heteractis magnifica* sea anemone exhibits neuroprotective activity in a model of Alzheimer's Disease. *Russ. J. Bioorganic Chem.* **2018**, *44*, 416–423. [CrossRef]
52. Kumagai, P.S.; Araujo, A.P.U.; Lopes, J.L.S. Going deep into protein secondary structure with synchrotron radiation circular dichroism spectroscopy. *Biophys. Rev.* **2017**, *9*, 517–527. [CrossRef] [PubMed]

53. Delfin, J.; Martinez, I.; Antuch, W.; Morera, V.; Gonzalez, Y.; Rodriguez, R.; Marquez, M.; Larionova, N.; Diaz, J.; Chavez, M.; et al. Purification, characterization and of proteinase inhibitors from *Stichodactyla helianthus*. *Toxicon* **1996**, *34*, 1367–1376. [CrossRef]
54. Sreerama, N.; Woody, R.W. Estimation of protein secondary structure from circular dichroism spectra: Comparison of CONTIN, SELCON, and CDSSTR methods with an expanded reference set. *Anal. Biochem.* **2000**, *287*, 252–260. [CrossRef] [PubMed]
55. Grzesiak, A.; Helland, R.; Smalås, A.O.; Krowarsch, D.; Dadlez, M.; Otlewski, J. Substitutions at the P1' position BPTI strongly affect the association energy with serine proteinases. *J. Mol. Biol.* **2000**, *301*, 205–217. [CrossRef]
56. Garcia-Fernandez, R.; Pons, T.; Perbandt, M.; Valiente, P.A.; Talavera, A.; Gonzalez-Gonzalez, Y.; Rehders, D.; Chavez, M.A.; Betzel, C.; Redecke, L. Structural insights into serine protease inhibition by a marine invertebrate BPTI Kunitz-type inhibitor. *J. Struct. Biol.* **2012**, *180*, 271–279. [CrossRef]
57. Nelson, D.W.; Gregg, R.J.; Kort, M.E.; Perez-Medrano, A.; Voight, E.A.; Wang, Y.; Grayson, G.; Namovic, M.T.; Donnelly-Roberts, D.L.; Niforatos, W.; et al. Structure-activity relationship studies on a series of novel, substituted 1-benzyl-5-phenyltetrazole P2X7 antagonists. *J. Med. Chem.* **2006**, *49*, 3659–3666. [CrossRef]
58. Kvetkina, A.N.; Kaluzhskiy, L.A.; Leychenko, E.V.; Isaeva, M.P.; Ivanov, A.S.; Kozlovskaya, E.P. New targets of Kunitz-type peptide from sea anemone *Heteractis magnifica*. *Dokl. Biochem. Biophys.* **2019**, *487*, 260–263. [CrossRef]
59. Zhao, R.; Dai, H.; Qiu, S.; Li, T.; He, Y.; Ma, Y.; Chen, Z.; Wu, Y.; Li, W.; Cao, Z. SdPI, the first functionally characterized Kunitz-type trypsin inhibitor from scorpion venom. *PLoS ONE* **2011**, *6*, e27548. [CrossRef]
60. De Bomediano Camillo, L.M.; Ferreira, G.C.; Duran, A.F.A.; da Silva, F.R.S.; Garcia, W.; Scott, A.L.; Sasaki, S.D. Structural modelling and thermostability of a serine protease inhibitor belonging to the Kunitz-BPTI family from the *Rhipicephalus microplus* tick. *Biochimie* **2021**, *181*, 226–233. [CrossRef]
61. Zhang, X.; Guo, K.; Dong, Z.; Chen, Z.; Zhu, H.; Zhang, Y.; Xia, Q.; Zhao, P. Kunitz-type protease inhibitor BmSPI51 plays an antifungal role in the silkworm cocoon. *Insect Biochem. Mol. Biol.* **2019**, *116*, 103258. [CrossRef]
62. Chen, X.; Xue, B.; Wang, J.; Liu, H.; Shi, L.; Xie, J. Potassium channels: A potential therapeutic target for Parkinson's disease. *Neurosci. Bull.* **2018**, *34*, 341–348. [CrossRef] [PubMed]
63. Vaidya, B.; Sharma, S.S. Transient receptor potential channels as an emerging target for the treatment of Parkinson's disease: An insight into role of pharmacological interventions. *Front. Cell Dev. Biol.* **2020**, *8*, 584513. [CrossRef] [PubMed]
64. Oliveira-Giacomelli, A.; Albino, C.M.; de Souza, H.D.N.; Corrêa-Velloso, J.; de Jesus Santos, A.P.; Baranova, J.; Ulrich, H. P2Y6 and P2X7 receptor antagonism exerts neuroprotective/ neuroregenerative effects in an animal model of Parkinson's disease. *Front. Cell. Neurosci.* **2019**, *13*, 476. [CrossRef] [PubMed]
65. Cankurtaran-Sayar, S.; Sayar, K.; Ugur, M. P2X7 receptor activates multiple selective dye-permeation pathways in RAW 264.7 and human embryonic kidney 293 cells. *Mol. Pharmacol.* **2009**, *76*, 1323–1332. [CrossRef] [PubMed]
66. Kounnas, M.Z.; Moir, R.D.; Rebeck, G.W.; Bush, A.I.; Argraves, W.S.; Tanzi, R.E.; Hyman, B.T.; Strickland, D.K. LDL receptor-related protein, a multifunctional ApoE receptor, binds secreted β -amyloid precursor protein and mediates its degradation. *Cell* **1995**, *82*, 331–340. [CrossRef]
67. Demeule, M.; Regina, A.; Ché, C.; Poirier, J.; Nguyen, T.; Gabathuler, R.; Castaigne, J.P.; Béliveau, R. Identification and design of peptides as a new drug delivery system for the brain. *J. Pharmacol. Exp. Ther.* **2008**, *324*, 1064–1072. [CrossRef] [PubMed]
68. Laemmli, U.K. Cleavage of structural proteins during the assembly of the head of bacteriophage T4. *Nature* **1970**, *227*, 680–685. [CrossRef]
69. Andreev, Y.A.; Kozlov, S.A.; Vassilevski, A.A.; Grishin, E.V. Cyanogen bromide cleavage of proteins in salt and buffer solutions. *Anal. Biochem.* **2010**, *407*, 144–146. [CrossRef]
70. Gladkikh, I.; Monastyrnaya, M.; Leychenko, E.; Zelepuga, E.; Chausova, V.; Isaeva, M.; Anastuyuk, S.; Andreev, Y.; Peigneur, S.; Tytgat, J.; et al. Atypical reactive center Kunitz-type inhibitor from the sea anemone *Heteractis crispa*. *Mar. Drugs* **2012**, *10*, 1545–1565. [CrossRef]
71. Hwang, T.L.; Shaka, A.J. Water suppression that works. Excitation sculpting using arbitrary waveforms and pulsed field gradients. *J. Magn. Reson.* **1995**, *112*, 275–279. [CrossRef]
72. Provencher, S.W.; Glöckner, J. Estimation of globular protein secondary structure from circular dichroism. *Biochemistry* **1981**, *20*, 33–37. [CrossRef] [PubMed]
73. Dixon, M. The graphical determination of Km and Ki. *Biochem. J.* **1972**, *129*, 197–202. [CrossRef] [PubMed]
74. Huang, T.-T.; Hwang, J.-K.; Chen, C.-H.; Chu, C.-S.; Lee, C.-W.; Chen, C.-C. (PS) 2: Protein structure prediction server version 3.0. *Nucleic Acids Res.* **2015**, *43*, W338–W342. [CrossRef] [PubMed]
75. Zhang, J.; Liang, Y.; Zhang, Y. Atomic-level protein structure refinement using fragment-guided molecular dynamics conformation sampling. *Structure* **2011**, *19*, 1784–1795. [CrossRef] [PubMed]
76. Pettersen, E.F.; Goddard, T.D.; Huang, C.C.; Couch, G.S.; Greenblatt, D.M.; Meng, E.C.; Ferrin, T.E. UCSF Chimera—A visualization system for exploratory research and analysis. *J. Comput. Chem.* **2004**, *25*, 1605–1612. [CrossRef] [PubMed]
77. Waterhouse, A.; Bertoni, M.; Bienert, S.; Studer, G.; Tauriello, G.; Gumienny, R.; Heer, F.T.; De Beer, T.A.P.; Rempfer, C.; Bordoli, L.; et al. SWISS-MODEL: Homology modelling of protein structures and complexes. *Nucleic Acids Res.* **2018**, *46*, W296–W303. [CrossRef]
78. Krissinel, E.; Henrick, K. Inference of macromolecular assemblies from crystalline state. *J. Mol. Biol.* **2007**, *372*, 774–797. [CrossRef]
79. Chermak, E.; Petta, A.; Serra, L.; Vangone, A.; Scarano, V.; Cavallo, L.; Oliva, R. CONSRANK: A server for the analysis, comparison and ranking of docking models based on inter-residue contacts. *Bioinformatics* **2015**, *31*, 1481–1483. [CrossRef]

80. Mosmann, T. Rapid colorimetric assay for cellular growth and survival: Application to proliferation and cytotoxicity assays. *J. Immunol. Methods* **1983**, *65*, 55–63. [CrossRef]
81. Carmichael, J.; Degraff, W.G.; Gazdar, A.F.; Minna, J.D.; Mitchell, J.B. Evaluation of a tetrazolium-based semiautomated colorimetric assay: Assessment of chemosensitivity testing. *Am. Assoc. Cancer Res.* **1987**, *47*, 936–942.
82. Amazzal, L.; Lapôtre, A.; Quignon, F.; Bagrel, D. Mangiferin protects against 1-methyl-4-phenylpyridinium toxicity mediated by oxidative stress in N2A cells. *Neurosci. Lett.* **2007**, *418*, 159–164. [CrossRef] [PubMed]
83. Mello, P.D.A.; Filippi-Chiela, E.C.; Nascimento, J.; Beckenkamp, A.; Santana, D.B.; Kipper, F.; Casali, E.A.; Bruno, A.N.; Paccez, J.D.; Zerbini, L.F.; et al. Adenosine uptake is the major effector of extracellular ATP toxicity in human cervical cancer cells. *Mol. Biol. Cell* **2014**, *25*, 2905–2918. [CrossRef] [PubMed]
84. Yurchenko, E.A.; Menchinskaya, E.S.; Pislyagin, E.A.; Trinh, P.T.H.; Ivanets, E.V.; Smetanina, O.F.; Yurchenko, A.N. Neuroprotective activity of some marine fungal metabolites in the 6-hydroxydopamin- and paraquat-induced Parkinson's disease models. *Mar. Drugs* **2018**, *16*, 457. [CrossRef] [PubMed]
85. Leutou, A.S.; Yun, K.; Son, B.W. Induced production of 6,9-dibromoflavasperone, a new radical scavenging naphthopyranone in the marine-mudflat-derived fungus *Aspergillus niger*. *Arch. Pharmacol. Res.* **2016**, *39*, 806–810. [CrossRef] [PubMed]
86. Peigneur, S.; Cheneval, O.; Maiti, M.; Leipold, E.; Heinemann, S.H.; Lescrinier, E.; Herdewijn, P.; De Lima, M.E.; Craik, D.J.; Schroeder, C.I.; et al. Where cone snails and spiders meet: Design of small cyclic sodium-channel inhibitors. *FASEB J.* **2019**, *33*, 3693–3703. [CrossRef] [PubMed]
87. García-Fernández, R.; Peigneur, S.; Pons, T.; Alvarez, C.; González, L.; Chávez, M.A.; Tytgat, J. The Kunitz-type protein ShPI-1 inhibits serine proteases and voltage-gated potassium channels. *Toxins* **2016**, *8*, 110. [CrossRef]
88. Pislyagin, E.; Kozlovskiy, S.; Menchinskaya, E.; Chingizova, E.; Likhatskaya, G.; Gorpenchenko, T.; Sabutski, Y.; Polonik, S.; Aminin, D. Synthetic 1,4-naphthoquinones inhibit P2X7 receptors in murine neuroblastoma cells. *Bioorganic Med. Chem.* **2021**, *31*, 115975. [CrossRef]
89. Aminin, D.; Pislyagin, E.; Astashev, M.; Es'kov, A.; Kozhemyako, V.; Avilov, S.; Zelepuga, E.; Yurchenko, E.; Kaluzhskiy, L.; Kozlovskaya, E.; et al. Glycosides from edible sea cucumbers stimulate macrophages via purinergic receptors. *Sci. Rep.* **2016**, *6*, 39683. [CrossRef]



Article

QSAR, Docking, and Molecular Dynamics Simulation Studies of Sigmacidins as Antimicrobials against *Streptococci*

Jiqing Ye ¹, Xiao Yang ^{2,*} and Cong Ma ^{1,*}

¹ State Key Laboratory of Chemical Biology and Drug Discovery, and Department of Applied Biology and Chemical Technology, The Hong Kong Polytechnic University, Kowloon, Hong Kong, China; ji-qing.ye@polyu.edu.hk

² Department of Microbiology, Prince of Wales Hospital, The Chinese University of Hong Kong, Shatin, Hong Kong, China

* Correspondence: xiaoyang@cuhk.edu.hk (X.Y.); cong.ma@polyu.edu.hk (C.M.)

Abstract: *Streptococci* are a family of bacterial species significantly affecting human health. In addition, environmental *Streptococci* represent one of the major causes of diverse livestock diseases. Due to antimicrobial resistance, there is an urgent need for novel antimicrobial agent discovery against *Streptococci*. We discovered a class of benzoic acid derivatives named sigmacidins inhibiting the bacterial RNA polymerase- σ factor interaction and demonstrating excellent antimicrobial activity against *Streptococci*. In this work, a combinational computer approach was applied to gain insight into the structural basis and mechanism of action of sigmacidins as antimicrobials against *Streptococcus pneumoniae*. Both two- and three-dimensional quantitative structure-active relationships (2D and 3D QSAR) of sigmacidins displayed good predictive ability. Moreover, molecular docking and molecular dynamics simulation studies disclosed possible contacts between the inhibitors and the protein. The results obtained in this study provided understanding and new directions to the further optimizations of sigmacidins as novel antimicrobials.

Citation: Ye, J.; Yang, X.; Ma, C. QSAR, Docking, and Molecular Dynamics Simulation Studies of Sigmacidins as Antimicrobials against *Streptococci*. *Int. J. Mol. Sci.* **2022**, *23*, 4085. <https://doi.org/10.3390/ijms23084085>

Academic Editor: Dmitry Aminin

Received: 10 March 2022

Accepted: 5 April 2022

Published: 7 April 2022

Publisher's Note: MDPI stays neutral with regard to jurisdictional claims in published maps and institutional affiliations.



Copyright: © 2022 by the authors. Licensee MDPI, Basel, Switzerland. This article is an open access article distributed under the terms and conditions of the Creative Commons Attribution (CC BY) license (<https://creativecommons.org/licenses/by/4.0/>).

Keywords: *Streptococci*; antimicrobials; QSAR; MD simulation

1. Introduction

Streptococci are a large family of *Streptococcus* species widely present in the environment and as microbiota of mammals such as humans, wild animals and livestock. *Streptococcus pneumoniae*, belonging to the alpha-hemolytic streptococcal species, is one of the most common human pathogens leading to a range of pneumococcal diseases, including otitis media, sinusitis, pneumonia, septicemia, and meningitis [1]. The beta-hemolytic streptococcal species such as *Streptococcus pyogenes* (Group A *Streptococcus*, GAS) and *Streptococcus agalactiae* (Group B *Streptococcus*, GBS) represent the other two pathogens frequently triggering human diseases such as streptococcal pharyngitis (strep throat), impetigo, pneumonia, and meningitis [2,3]. In addition, more than one third of herd mastitis incidences are caused by “Environmental *Streptococci*” [4,5]. This name was coined after *Streptococci* which leads to animal diseases [6], such as *Streptococcus dysgalactiae*, *Streptococcus uberis* (Groups C and G *Streptococci*, GCS and GGS), and *Enterococcus* spp., which used to be classed in the genus *Streptococcus* (Group D *Streptococcus*) prior to 1984 [7]. The medical application to treat streptococcal infections by antibiotics is sometimes ineffective due to antimicrobial resistance [5,8]. As a result, *S. pneumoniae* has been listed in the World Health Organization Global Priority Pathogens List for which new antibiotics are urgently needed [9].

The emergence of multidrug resistance to current antibiotics among pathogens highlights the importance of the discovery of novel antimicrobials with minimized antimicrobial resistance. Protein-protein interactions (PPI) are appropriate targets for reducing antimicrobial resistance [10]. We focused on the specific and conserved bacterial PPIs for antimicrobial discovery [11]. Bacterial RNA polymerase (RNAP) comprises several subunits: 2α , β ,

β' , ω (Gram-positive bacteria include one more subunit ϵ) [12,13], and interacts with the bacteria-specific transcription factor σ to form a holoenzyme to recognize DNA promoters and initiate bacterial transcription. Therefore, this essential PPI represents an appropriate target for antimicrobial agent discovery [14]. Biochemistry studies have shown that the binding site between the region 2.2 of σ factor ($\sigma_{2.2}$) and the clamp helix region of the RNAP β' subunit (β' CH) is the major binding site for this PPI [15]. Based on the structural biological information [16,17] (Figure 1A), we designed a pharmacophore model and screened out three hit compounds (**C3**, **C4**, and **C5**) showing the specific inhibitory activity [18]. The optimization of compound **1** (**C3**) resulted in the discovery of a set of derivatives such as **3** (**C3-005**), **46** (ejmc **8e**), and **40** (jmc Cpd. **54**) with dramatically improved antibacterial activities, in particular against *Streptococci* including *S. pneumoniae*, *S. pyogenes*, *S. agalactiae*, and *Enterococcus faecalis* with minimum inhibitory concentrations (MIC) lowered to 1 $\mu\text{g}/\text{mL}$, comparable to current antibiotics in the market (Figure 1B) [19–21]. Considering the general structure of benzoic acid in this class of compounds and the protein σ factor on which these compounds mimic for binding, we named this class of antimicrobials as “sigmacidin”.

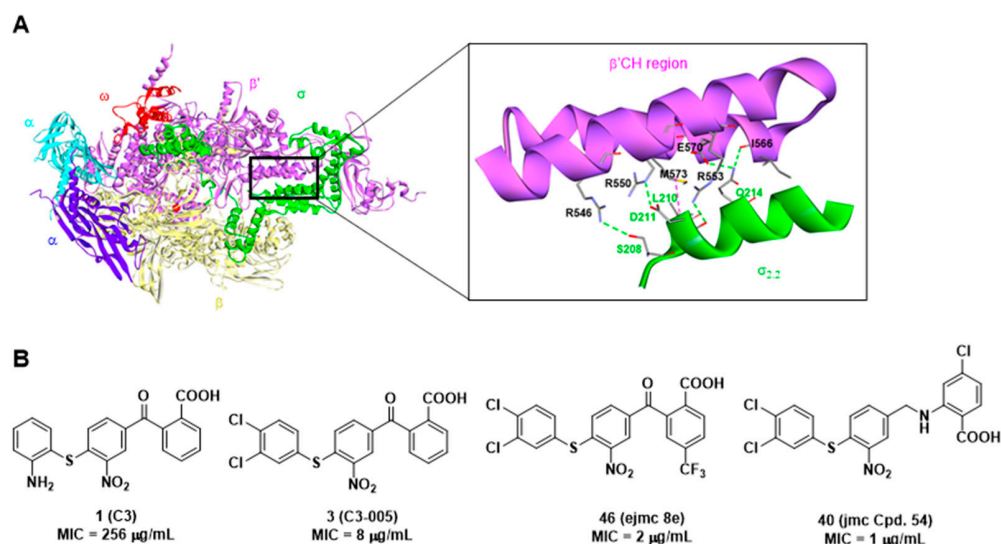


Figure 1. (A) *Escherichia coli* RNA polymerase holoenzyme ($\alpha_2\beta\beta'\omega\sigma$) (PDB: 1IW7, [17]) and the detailed interactions between β' CH and $\sigma_{2.2}$, hydrogen bonds: green, hydrophobic: magenta; (B) Chemical structures of reported sigmacidins derivatives targeting the RNAP- σ interaction and their activities against *S. pneumoniae*.

With a new class of antimicrobial agents in hand, we intend to make use of the quantitative structure-activity relationship (QSAR) analysis to explore the relationship between the observed antimicrobial activity and numerical descriptors in order to predict the biological properties of perspective compounds and guide future syntheses [22]. The 2D QSAR study considers physicochemical properties of signal atoms and functional groups and their contribution to biological activity, while 3D QSAR could foresee the potential three-dimensional structure of the ligand molecules [23]. In this study, statistical methods including multiple linear regression (MLR) and partial least square analysis (PLS) were applied to analyze the correlation between properties or descriptors of the molecules and molecular properties [24].

In an attempt to reveal the relationships between the chemical structures and their activity against the representative *S. pneumoniae*, we took fiftysix molecules reported previously [20,21] to generate a set of quantitative rules and construct both 2D and 3D QSAR models for the design of novel derivatives. Their structures are given in the supporting information (Table S1) and their activities against *S. pneumoniae* (MIC) are shown in Table 1. Moreover, molecular docking and molecular dynamics (MD) simulations were performed to gain insight into the structural basis and the inhibitory mechanism of the inhibitors.

Table 1. Compounds selected for modeling and their observed and predicted activity against *S. pneumoniae*.

Cpd.	MIC ($\mu\text{g/mL}$)	MW	MIC (M)	pMIC	2D QSAR		3D QSAR	
					Predicted pMIC	Δ^b	Predicted pMIC	Δ^b
1 ^a	256	394.40	6.49×10^{-4}	3.188	3.503	−0.315	3.616	−0.428
2 ^a	128	409.41	3.13×10^{-4}	3.505	3.579	−0.074	4.060	−0.555
3	8	448.28	1.78×10^{-5}	4.748	4.406	0.342	4.552	0.196
4	256	362.34	7.07×10^{-4}	3.151	3.295	−0.144	3.089	0.062
5	256	354.36	7.22×10^{-4}	3.141	2.899	0.242	2.994	0.148
6	128	409.42	3.13×10^{-4}	3.505	3.119	0.386	3.564	−0.059
7 ^a	64	395.43	1.62×10^{-4}	3.791	3.529	0.262	3.674	0.117
8	64	394.40	1.62×10^{-4}	3.790	3.508	0.282	3.642	0.148
9	128	394.40	3.25×10^{-4}	3.489	3.516	−0.027	3.692	−0.203
10	256	523.52	4.89×10^{-4}	3.311	3.942	−0.631	3.303	0.008
11	256	376.36	6.80×10^{-4}	3.167	3.224	−0.057	3.140	0.027
12	256	394.35	6.49×10^{-4}	3.188	3.328	−0.14	3.181	0.007
13	128	376.36	3.40×10^{-4}	3.468	3.575	−0.107	3.261	0.207
14	8	449.31	1.78×10^{-5}	4.749	4.541	0.208	4.437	0.313
15 ^a	256	463.29	5.53×10^{-4}	3.258	3.996	−0.738	4.507	−1.249
16	256	418.44	6.12×10^{-4}	3.213	4.095	−0.882	3.311	−0.098
17	128	397.38	3.22×10^{-4}	3.492	3.802	−0.31	4.072	−0.580
18 ^a	32	436.48	7.33×10^{-5}	4.135	4.154	−0.019	4.012	0.123
19	256	409.42	6.25×10^{-4}	3.204	3.069	0.135	3.467	−0.263
20	64	409.42	1.56×10^{-4}	3.806	3.229	0.577	3.827	−0.021
21	32	407.44	7.85×10^{-5}	4.105	4.247	−0.142	4.181	−0.076
22 ^a	256	383.38	6.68×10^{-4}	3.175	3.173	0.002	3.612	−0.437
23	32	448.28	7.14×10^{-5}	4.146	4.418	−0.272	4.426	−0.280
24	32	498.51	6.42×10^{-5}	4.193	4.182	0.011	3.936	0.256
25	64	428.85	1.49×10^{-4}	3.826	3.860	−0.034	3.894	−0.068
26	64	431.23	1.48×10^{-4}	3.829	4.013	−0.184	3.401	0.427
27	64	395.43	1.62×10^{-4}	3.791	3.660	0.131	3.462	0.329
28	256	395.43	6.47×10^{-4}	3.189	3.581	−0.392	3.366	−0.177
29	256	436.44	5.87×10^{-4}	3.232	3.228	0.004	3.632	−0.400
30	4	483.75	8.27×10^{-6}	5.083	4.915	0.168	4.469	0.614
31	16	479.33	3.34×10^{-5}	4.477	4.297	0.180	5.112	−0.635
32	16	534.41	2.99×10^{-5}	4.524	4.359	0.165	4.744	−0.221
33	64	484.38	1.32×10^{-4}	3.879	4.246	−0.367	3.787	0.092
34	16	463.33	3.45×10^{-5}	4.462	4.776	−0.314	4.466	−0.004
35	256	396.78	6.45×10^{-4}	3.190	3.656	−0.466	3.353	−0.163
36	4	528.20	7.57×10^{-6}	5.121	4.962	0.159	4.467	0.654
37	256	483.75	5.29×10^{-4}	3.276	4.912	−1.636	4.470	−1.194
38 ^a	4	449.31	8.90×10^{-6}	5.050	4.500	0.550	5.204	−0.154
39	16	403.28	3.97×10^{-5}	4.401	4.082	0.319	4.561	−0.160
40	1	483.75	2.07×10^{-6}	5.685	4.868	0.817	5.246	0.439
41 ^a	16	434.29	3.68×10^{-5}	4.434	4.798	−0.364	5.189	−0.755
42	32	418.29	7.65×10^{-5}	4.116	3.891	0.225	4.428	−0.311
43	32	446.35	7.17×10^{-5}	4.145	4.213	−0.068	4.449	−0.304
44 ^a	8	482.72	1.66×10^{-5}	4.781	4.773	0.008	4.648	0.133
45	8	482.72	1.66×10^{-5}	4.781	4.766	0.015	4.653	0.128
46	2	516.27	3.87×10^{-6}	5.412	4.925	0.487	4.725	0.687
47	4	468.74	8.53×10^{-6}	5.069	5.159	−0.090	5.289	−0.221
48	4	448.32	8.92×10^{-6}	5.050	5.073	−0.023	5.081	−0.031

Table 1. Cont.

Cpd.	MIC (µg/mL)	MW	MIC (M)	pMIC	2D QSAR		3D QSAR	
					Predicted pMIC	Δ ^b	Predicted pMIC	Δ ^b
49	8	478.30	1.67 × 10 ⁻⁵	4.777	4.278	0.499	4.681	0.096
50	8	466.27	1.72 × 10 ⁻⁵	4.766	4.512	0.254	4.592	0.174
51	4	516.27	7.75 × 10 ⁻⁶	5.111	4.914	0.197	4.737	0.374
52 ^a	2	502.29	3.98 × 10 ⁻⁶	5.400	5.271	0.129	5.273	0.126
53 ^a	8	464.32	1.72 × 10 ⁻⁵	4.764	4.611	0.153	5.126	-0.362
54	2	468.74	4.27 × 10 ⁻⁶	5.370	5.169	0.201	5.271	0.099
55	4	452.28	8.84 × 10 ⁻⁶	5.053	4.908	0.145	5.218	-0.164
56	2	502.29	3.98 × 10 ⁻⁶	5.400	5.251	0.149	5.243	0.157

^a Compounds taken for the test set; ^b Δ = Experimental pMIC—Predicted pMIC.

2. Results and Discussion

2.1. Two-Dimensional QSAR

2.1.1. Two-Dimensional QSAR Study

A 2D QSAR study for compounds against *S. pneumoniae* was performed to determine the factors/descriptors related to the antibacterial activities of compounds 1–56, and to disclose the structural features contributing towards the bacterial inhibitory activities. In this study, the molecular properties for the compounds in the training set were calculated using the “Calculate Molecular Properties” protocol in Discovery Studio 2016 (DS 2016).

Descriptors used for the building of the model were selected based on the results of the intercorrelation matrix between the calculated descriptors. In the present research, the selected descriptors have intercorrelation values lower than 0.5 (Table 2) to avoid model overfitting, and the result of the matrix analysis revealed the independence of these descriptors.

Table 2. Intercorrelation data of descriptors used to develop 2D QSAR Model.

Property	AlogP	HBA Count	LUMO Eigenvalue VAMP	Molecular Polar Surface Area
AlogP	1.000	-0.367	-0.264	-0.490
HBA Count		1.000	-0.114	0.405
LUMO Eigenvalue VAMP			1.000	-0.350
Molecular Polar Surface Area				1.000

A Multiple Linear Regression (MLR) analysis method was used to construct the model. The statistical quality of the MLR model was judged by the calculation of the squared correlation coefficient (r^2) for internal validation and the predictive squared correlation coefficient (r^2_{pred}) for external validation [25]. Moreover, the predictive power of the QSAR model was verified using LOO internal validation or cross validation (q^2). Usually, a value of $q^2 > 0.5$ is considered acceptable [26]. In this model, the r^2 was 0.732, r^2_{pred} was 0.613, and q^2 equaled 0.562, which indicated the true predictive ability of the model (Table 3)

Table 3. Regression statistics table.

R	r^2	r^2 (Adjusted)	r^2 (Prediction)	RMS Residual Error	q^2 (Cross-Validation)	RMS Residual Error (Cross-Validation)
0.856	0.732	0.705	0.613	0.399	0.562	0.526

2.1.2. Two-Dimensional QSAR Model Analysis

The predicted activities for the inhibitors versus their experimental activities and the residues between them are listed in Table 1. The correlation between the predicted activities

and the experimental activities are depicted in Figure 2. These results demonstrated that the predicted activities by the constructed MLR model were in good agreement with the experimental data, suggesting that the 2D QSAR model was reliable for structure-activity prediction.

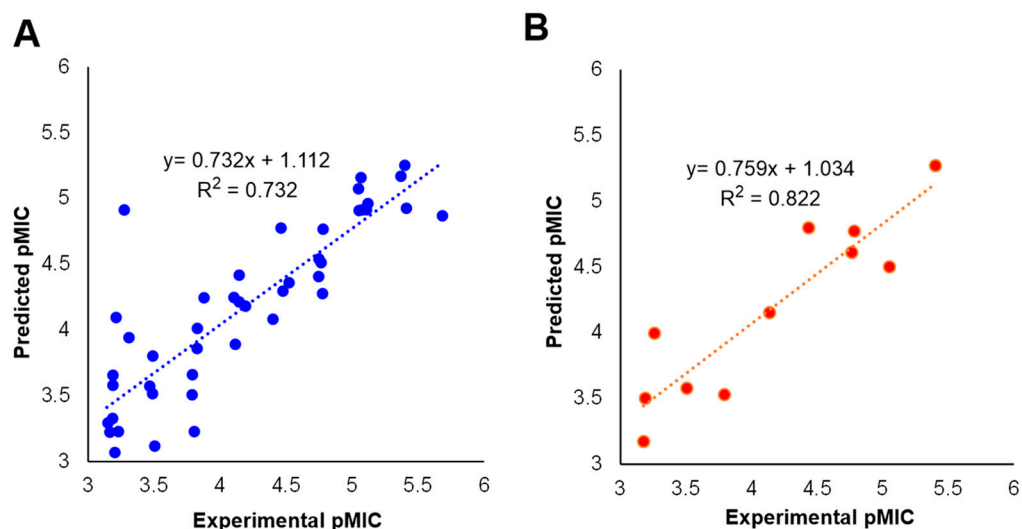


Figure 2. Predicted versus experimental pMIC of (A) the training set and (B) the test set.

Equation (1) represents the MLR model obtained by DS 2016. According to Equation (1), four descriptors, including (a) ALogP reflecting lipophilicity [27], (b) hydrogen bond acceptor (HBA) which is critical to potency, selectivity, permeability, and solubility [28], (c) molecular polar surface area, a guideline towards the improvement of oral absorption and permeability [29], and (d) LUMO eigenvalue that is related to electrostatic properties [30], were used to describe the relationship between chemical properties and the antimicrobial activity. Compared with the molecular polar surface area, AlogP, HBA count, and LUMO Eigenvalue showed higher correlations, and slight variations of these descriptors significantly affected the activity.

Equation (1) representing the 2D QSAR model:

$$\text{pMIC} = 0.5647 + 0.5705(\text{ALogP}) - 0.2073(\text{HBA Count}) + 0.0090 (\text{Molecular Polar Surface Area}) + 0.2049(\text{LUMO Eigenvalue VAMP}) \quad (1)$$

To further improve the predictive ability of the above model, an outlier analysis was conducted using the Find Outlier Molecules module of DS 2016 to identify the outliers in the dataset, and the acceptable level was set to 95 (95% confidence interval). Results showed that four compounds were returned as outliers, including compounds **10**, for which the Molecular PSA was too high, **33** for which the LUMO Eigenvalue VAMP was too low, and **39** and **43**, for which the Molecular PSA was too low. These four compounds were removed and a new 2D QSAR model was constructed. In the revised model, r^2 was 0.777, r^2_{pred} was 0.721, and q^2 equaled to 0.690, which indicated the improved predictive ability of the model (Table 4).

Table 4. Regression statistics table.

R	r^2	r^2 (Adjusted)	r^2 (Prediction)	RMS Residual Error	q^2 (Cross-Validation)	RMS Residual Error (Cross-Validation)
0.882	0.777	0.753	0.721	0.375	0.690	0.447

Equation (2) represents the revised MLR model. As shown in the equation, changes in the ALogP and LUMO Eigenvalue VAMP may affect the antimicrobial active significantly

as they have higher correlations in comparison with HBA count and molecular polar surface area.

Equation (2) representing the upgraded 2D QSAR model:

$$\text{pMIC} = 0.6578 + 0.5757(\text{ALogP}) - 0.07427(\text{HBA Count}) + 0.01056 (\text{Molecular Polar Surface Area}) - 0.2082(\text{LUMO Eigenvalue VAMP}) \quad (2)$$

2.2. Three-Dimensional QSAR

2.2.1. Molecular Alignment

Structural alignment of the molecules is critical to both the predictive accuracy of a 3D QSAR model and reliability of contour models. Therefore, we applied flexible alignment to align all the molecules in this study. The most active compound, **40**, was selected as the alignment template and the rest of the compounds were aligned to it by using the common substructure as displayed in Figure 3.

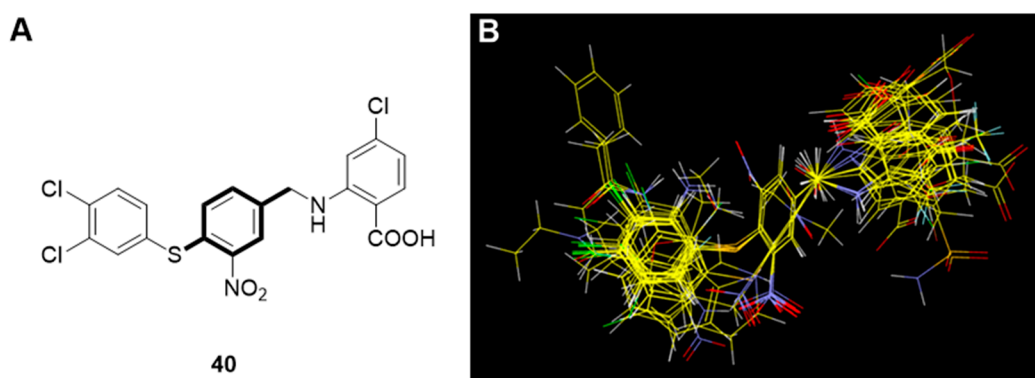


Figure 3. (A) Template used for molecular alignment of the PPI inhibitors (Compound **40** with the common motif bolded); (B) alignment of molecules on compound **40**.

2.2.2. Three-Dimensional QSAR Study

The 3D QSAR model in this study was built by the Field-Based model module in Maestro 10.2. The statistical parameters are presented in Table 5. Here, r^2 is the non-cross-validated value for the regression, r^2_{CV} is the LOO cross-validated correlation value, $r^2_{scramble}$ represents the average value of r^2 from a series of models built using scrambled activities, and “Stability” reflects the sensitivity of the model to omissions from the training set. Q^2 is directly analogous to r^2 , but is based on the test set predictions. When the r^2 value is larger than the stability value, this is an indication that the dataset is over-fit. As we set PLS factor to six considering the statistical results, the three-factor model was selected with r^2 and r^2_{CV} values of 0.805 and 0.568, respectively, and a stability value of 0.883 (Table 5).

Table 5. Statistical results of the 3D QSAR model.

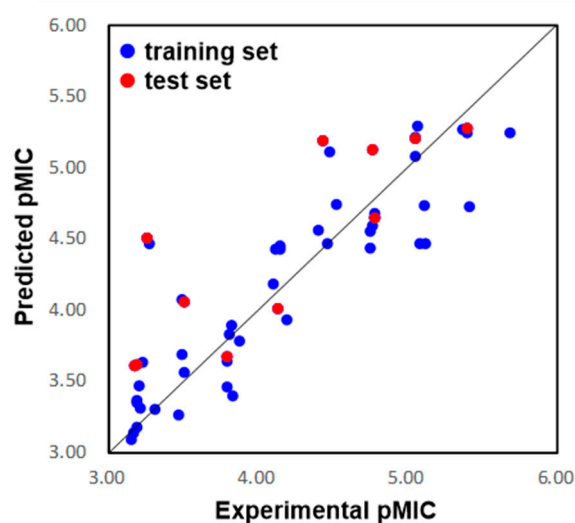
SD	r^2	r^2_{CV}	$r^2_{Scramble}$	Stability	F	P	RMSE	Q^2	Pearson-r
0.356	0.805	0.568	0.482	0.883	56.4	1.31×10^{-14}	0.52	0.528	0.835

The model was built using four fields, including steric, electrostatic, hydrogen bond (H-bond) donor, and H-bond acceptor. As shown in Table 6, the steric field and the hydrophobic field contributed significantly to the antibacterial activity with percentages of 36.1% and 29.8%, respectively.

Table 6. Field Distribution (%).

Steric	Electrostatic	Hydrophobic	H-Bond Acceptor	H-Bond Donor
36.1	9.4	29.8	9.8	14.9

The eleven compounds randomly selected by Maestro 10.2 were used as the test set to validate the predictive ability of the 3D QSAR model. As a result, the predicted pMIC values shown in Table 1 were in good alignment with the experimental data, with a Pearson-r (the correlation between the predicted and observed activity for the test set) value of 0.835 and a Q^2 value of 0.528. The correlation plots between the experimental and predicted pMIC values for both the training and test sets were shown in Figure 4. Though some outliers may possibly be generated, the results demonstrated the potential of the 3D QSAR model to be used for drug design with a good predictive power.

**Figure 4.** Plots of the predicted pMIC values by the 3D-QSAR model versus the observed pMIC values.

2.2.3. Interpretation of the 3D QSAR Contour Maps

To visualize the structure-activity relationship of these inhibitors, the steric, electrostatic, hydrophobic, H-bond donor, and H-bond acceptor contour maps of the models are displayed in Figure 5. The most active compound, **40**, was used for further analysis.

In the steric contour (Figure 5A), the green regions represented that the introduction of bulky substituents might increase activity, while steric hindrance should be avoided in the yellow regions. As shown in Figure 5A, a relatively large green contour was found around 3,4-diCl groups of compound **40**, indicating that bulky substituents might be preferred in this region, while at 5- and 6-positions of the right benzene ring, steric hindrance was unfavorable.

The electrostatic contour (Figure 5B) for compound **40** showed that a relatively large blue contour was located around the *para*-position to the -COOH group, suggesting that electron-deficient substituents may increase the activity. In addition, a small blue region was found to surround the -NO₂ group, this can explain why reduction or removal of -NO₂ resulted in reduction of the antimicrobial activity. In contrast, the red contour was mainly located around the linker, which meant electron-rich linkers may improve the activity.

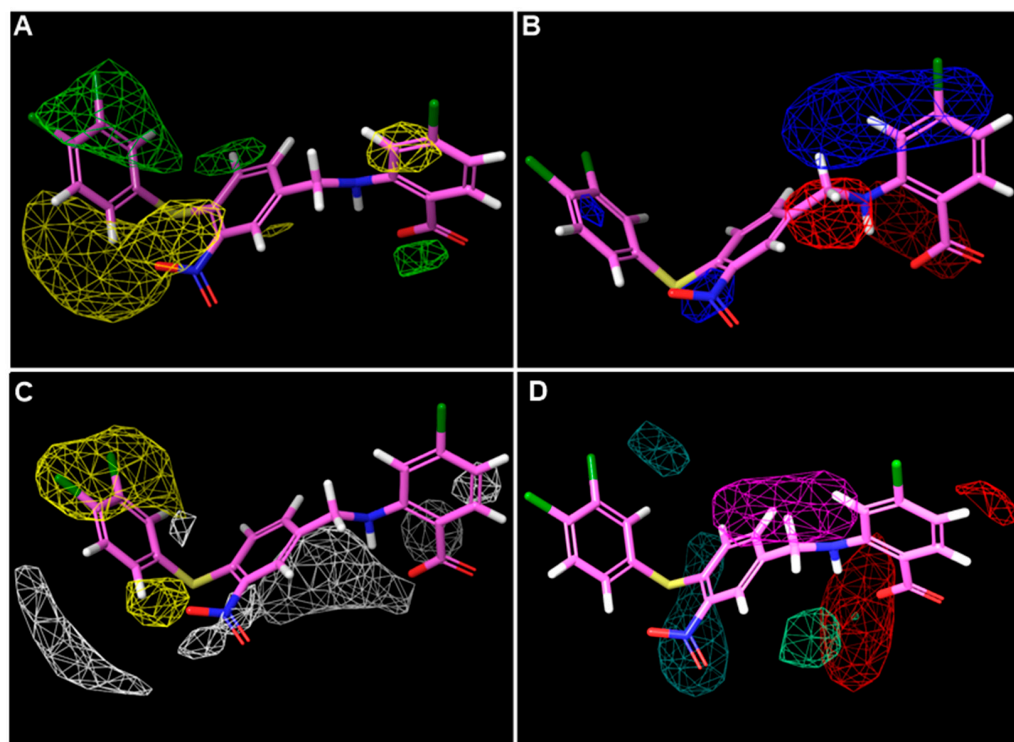


Figure 5. Three-dimensional QSAR StDev*Coeff contour maps using the most bioactive compound **40**. (A) Steric fields: favored (green) and disfavored (yellow); (B) electrostatic fields: electropositive (blue) and electronegative (red); (C) hydrophobic field: favored (yellow) and disfavored (white); (D) H-bond acceptor field: favored (Red) and disfavored (magenta); Hydrogen bond donor field: favored (blackish green) and disfavored (pale green).

On the hydrophobic contour map (Figure 5C), the yellow regions indicated that the hydrophobic groups were preferred, while the white regions favored hydrophilic groups. It was shown that a relatively large blue region appeared around the 3,4-diCl groups; together with the prediction of the steric contour, the models indicated that replacing the -Cl with bulky and hydrophobic substituents might be beneficial to the antibacterial activity. In the contrast, the white regions were adjacent to the molecule but did not wrap it up like the yellow regions.

H-bond acceptor and donor contour maps are displayed in Figure 5D. H-bond acceptors were favored as red regions and unfavored in the magenta regions. Moreover, H-bond donors were preferred as blackish green and pale green as the unfavorable regions. The magenta and blackish green contours covered the middle benzene ring, while the red and pale green regions encircled the -COOH group. Briefly, the H-bond acceptor and donor groups contributed less to the activity compared to the steric and hydrophobic groups.

2.3. Docking and MD Simulations Studies of Compound **1** and **40**

2.3.1. Docking Studies

To compare the differences between the most bioactive compound **40** and the hit compound **1** in the binding processes, their potential binding modes and key interactions were analyzed using the LibDock module of DS 2016. As shown in Figure 6A,B, the -NH₂ and -NO₂ groups of compound **1** formed hydrogen bonds with Asp542 (H...O 2.15 Å) and Arg550 (O...H 1.85 Å) of β'CH region, respectively. Additionally, some weak π-cation interactions existed between the aromatic ring of compound **1** and Arg553 and Arg546.

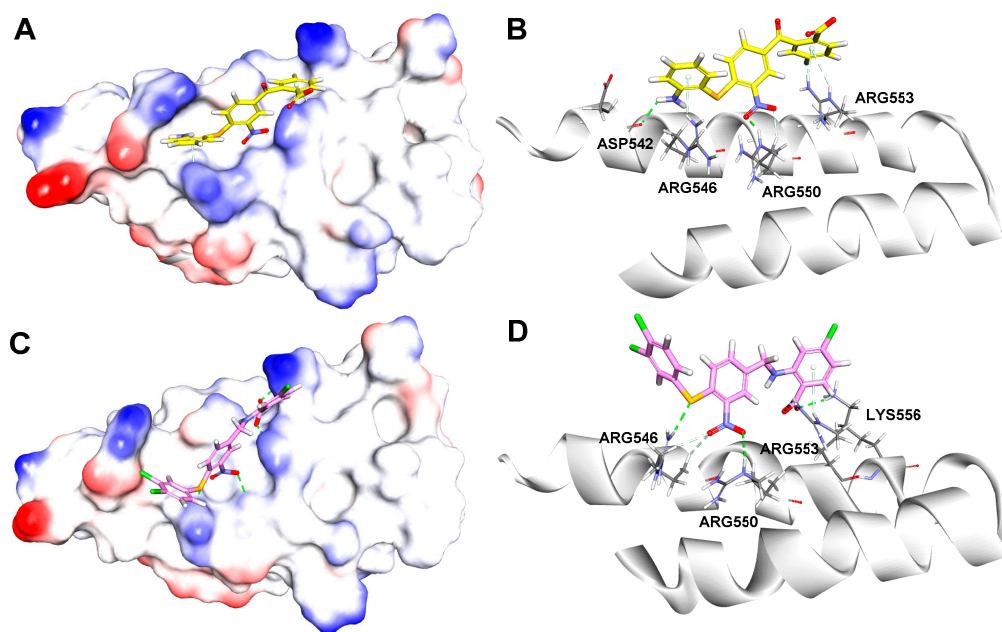


Figure 6. Binding modes and details of interaction of compound **1** (yellow, (A,B)) and compound **40** (magenta, (C,D)) in complex with β' CH extracted from RNAP holoenzyme (PDB: 1IW7, [17]).

In Figure 6C,D, it is suggested that compound **40** formed three classical hydrogen bonds with β' -CH region, including two H-bonds between the carboxylic group and Arg553 (O \cdots H 2.68 Å) and Lys556 (O \cdots H 2.32 Å), one H-bond between -NO₂ and Arg550 (O \cdots H 2.93 Å), while the S atom formed a nonclassical H-bond with Arg546 (S \cdots H 2.48 Å).

The docking results indicated both compounds made extensive contacts with β' CH. In comparison to the hit compound **1**, compound **40** made more interactions with the “hotspot” residues, including Arg546, Arg550, and Arg553 through hydrogen bonds.

2.3.2. MD Simulation Studies

To further understand the difference on the binding processes of hit compound **1** and compound **40**, 10 ns MD simulations based on the above-mentioned binding modes were performed. To study the dynamic stability of both systems, root-mean-square deviations (RMSD) from the starting structures were analyzed (Figure 7). The plots showed that both the two systems reached equilibrium within 6 ns, and the proteins and ligands in both systems were stable after equilibrium. Average RMSD values for the protein and ligand in **1**- β' CH bound system were 2.0 Å and 4.1 Å, respectively, while the corresponding values for the **40**- β' CH bound system were 2.3 Å and 4.0 Å, respectively. Moreover, it was observed that compound **40** fluctuated more violently which might be due to the distances of the connected bonds between **40** and β' CH in the docking model. They were slightly longer than the distances between compound **1** and β' CH. In addition, the protein in the **40**- β' CH system encountered more sizable rearrangement. This may be due to compound **40** having a more flexible structure. It could generate more conformations which require the protein to make more changes to adapt.

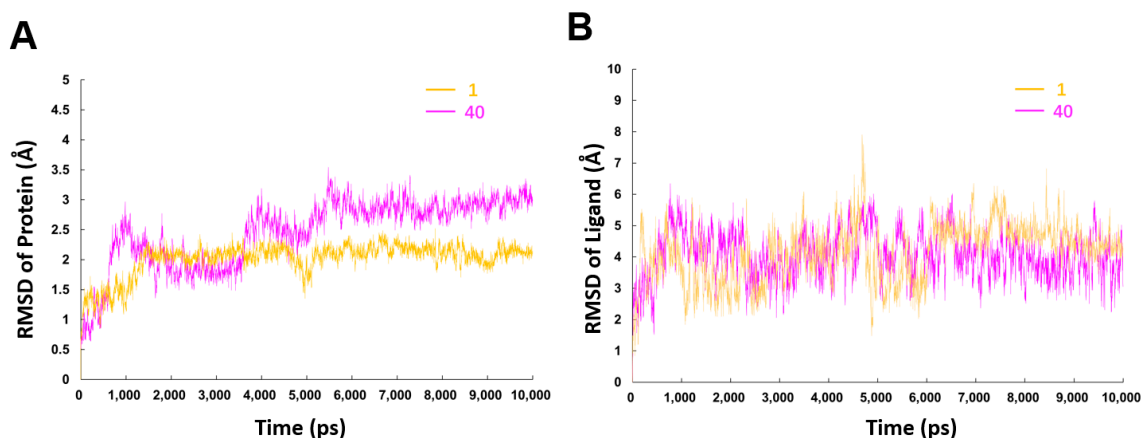


Figure 7. RMSD values of backbone atoms of the protein (A) and the heavy atoms in the ligands (B) for the compounds 1- and 40- β' CH systems as a function of the simulation time.

The energy of both complexes through MD simulation is shown in Figure 8. During the 10 ns production run, due to the existence of counter ions, the potential energy will often not decrease [31]. Results demonstrated that compound 40 in complex with the β' CH region had a much lower total energy compared to that of hit compound 1 (Figure 8A), especially the electrostatic energy (Figure 8B), while the *van der Waals* energies of the two systems were similar (Figure 8C). These results indicated that more attention should be given on the electrostatic energy when developing high-affinity inhibitors of the β' CH- σ interaction.

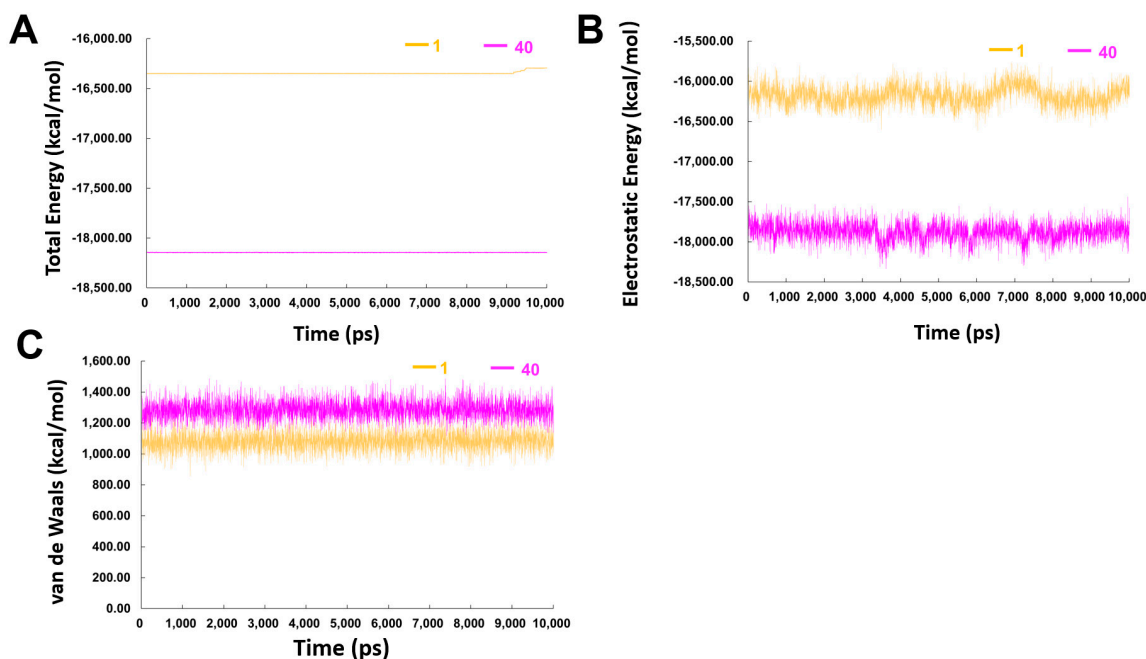


Figure 8. (A) Total energy (B) electrostatic energy and (C) van de Waals energy of the complexes of compounds 1– and 40– β' CH region in the 10 ns MD simulations.

The binding energy of both inhibitors with β' CH were calculated using the Calculate Binding Energy module of DS 2016. For each system, binding energy calculation was performed for snapshots extracted every 100 ps from the last 2 ns of the whole 10 ns MD trajectory. For each snapshot, the free energy was calculated for each molecular species (complex, protein, and ligand), and the binding free energy was defined as: $\Delta E_{\text{binding}} = \Delta E_{\text{Complex}} - \Delta E_{\text{Receptor}} - \Delta E_{\text{Ligand}}$ [32]. Results showed that the average binding energy for compounds 1 and 40 were -12.1359 kcal/mol and -9.8806 kcal/mol,

respectively. These results showed similar binding interactions of compounds, while compound **40** is a more flexible molecule, which may lead to higher binding energy as demonstrated.

To further understand the mechanic of action of the inhibitors, the final snapshots of the 10 ns trajectory were used to analyze the interactions between β' CH and compound **40** and **1**, respectively. For compound **1**, in comparison with the starting conformation, the most outstanding difference was that the benzoic acid moiety was turned over to form two hydrogen bonds between the carboxylic group and Arg549 and Arg553 (Figure 9A,B). Moreover, the nitro group not only retained the H-Bonding interaction with Arg550, but also formed a new hydrogen bond with Arg546.

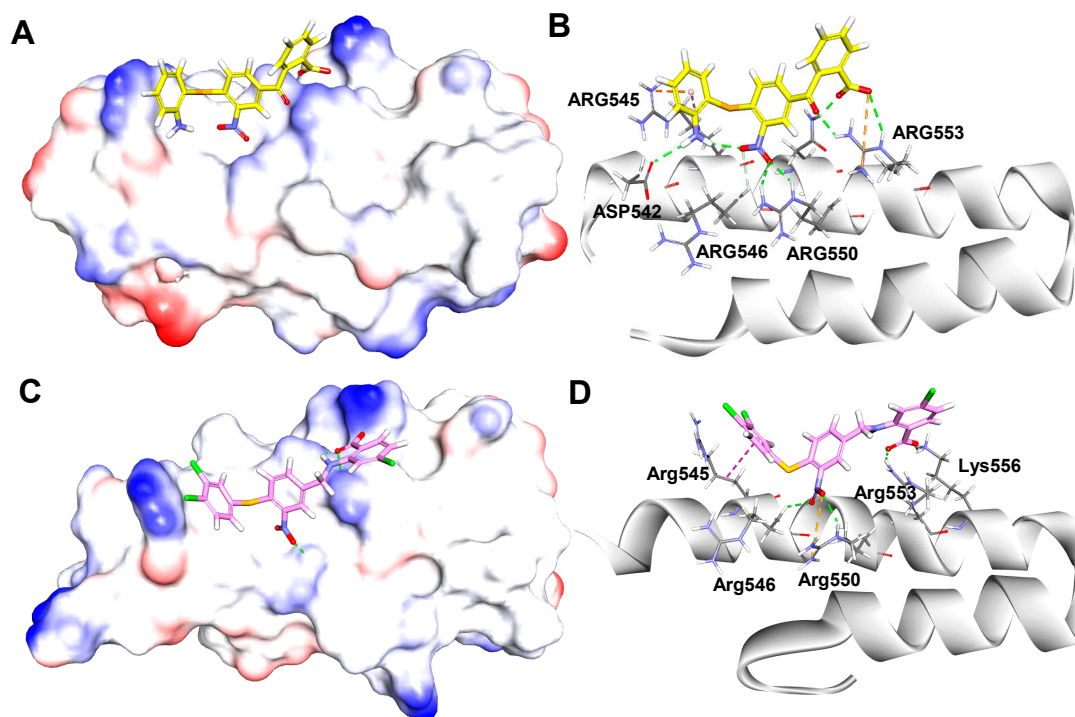


Figure 9. (A) Snapshot at 10 ns showed the binding mode of compound **1** in complex with β' CH region, and details of the interactions (B); (C) snapshot at 10 ns showed the binding mode of compound **40** in complex with β' CH region, and details of interactions (D). Hydrogen bonds (green), electrostatic interactions (yellow) and hydrophobic interactions (magenta).

For compound **40**, the three benzene rings of compound **40** positioned much closer to the surface of the helix. This led to the molecule that made more interactions with the key residues of β' CH region (Figure 9C). As shown in Figure 9D, the carboxylic acid group of **40** formed a hydrogen bond and a salt-bridge with residues Arg553 and Lys556, respectively. Moreover, the nitro group formed two hydrogen bonds with Arg546 and Arg550, while a salt bridge was also formed between the nitro group and Arg550. In addition, the 3,4-diCl group of the left benzene ring formed hydrophobic interactions with Arg545. Overall, these interactions may play key roles for the bioactivity of compound **40**.

3. Materials and Methods

3.1. Dataset

All small molecule RNAP- σ inhibitors and their antimicrobial activities (MIC, $\mu\text{g}/\text{mL}$) were adopted from previous studies [20,21]. The MIC values in units of microgram per milliliter ($\mu\text{g}/\text{mL}$) were transformed in molarity (M) and subsequently transformed to pMIC ($-\log\text{MIC}$). The dataset was divided into a training set for model generation and a

test set (Table 1) for model validation, containing 45 and 11 compounds, respectively. The test set was chosen randomly by Maestro 10.2.

3.2. Preparation of the Small Molecules

The 3D structures of compounds were generated using Maestro 10.2, geometrically minimized with MacroModel (Maestro 10.2) based on the OPLS-2005 force field and all other parameters were set to the default settings [33].

3.3. Two-Dimensional QSAR Model Construction

Two-dimensional molecular properties of the training set compounds were calculated by module "Calculate Molecular Properties" in DS 2016. Two-dimensional descriptors including PKa, AlogP, molecular weight, molecular property counts (Num_aromatic Rings, Num_H_Acceptors, Num_H_Donors, Num_Rings, Num_RotatableBonds), Molecular surface Area, Molecular Fractional Polar Surface Area, HOMO Eigenvalue VAMP, and LUMO Eigenvalue VAMP were adopted. The model was validated using the test set correlation and Leave-one-out (LOO) cross validation.

3.4. Three-Dimensional QSAR Model Construction

A 3D QSAR model was developed by Maestro 10.2. The alignment was achieved by using the Flexible Ligand Alignment module. The 3D QSAR model was generated by Field-based QSAR module with default parameters. The field style was set to Gaussian field, including steric, electrostatic, hydrophobic, H-bond acceptor, and donor field. The maximum PLS factor was set to six and in the PLS regression analysis, a leave-one-out (LOO) cross validation was performed to find the optimal number of components. The descriptors were generated in a 3D cubic lattice with grid spacing of 1 Å and extending to 3 Å units beyond the aligned molecules in all directions. In addition, the cutoff values for truncating steric force and electrostatic force fields were both set to 30 kcal/mol.

3.5. Docking and Molecular Dynamic Simulations

The crystal structure of the β' CH region was extracted from the crystal structure of bacterial RNAP (PDB: 1IW7, [17]) which was downloaded from Protein Data Bank. Structures of the compounds and the protein for docking were imported to DS 2016 and the conformations were generated with the protocol "Prepare Protein" and "Prepare Ligands", respectively. Molecular Docking was performed using the LibDock tool and the identified critical residues for the $\sigma_{2.2}$ - β' CH region PPI (including Arg546, Arg550, Arg553, Leu566) were defined as the binding sites. The docking process was conducted with the default parameters unless otherwise mentioned. MD simulation was conducted in a similar manner as described [34]. Binding free energy was calculated according to the literature [32].

4. Conclusions

Streptococci are an important bacterial family closely related to human wellbeing, while environmental *Streptococci* significantly affect herd health. Antimicrobial resistance to conventional antibiotics is emerging due to natural resistance mechanisms and antibiotic misuse. Therefore, novel antimicrobial agents are urgently required. We focused on bacterial transcription [35,36] and discovered a series of benzoic acid derivatives and named them sigmacidins. They were capable of mimicking bacterial transcription factor σ at the region 2.2 to disrupt its binding to RNAP and to exhibit excellent antimicrobial activity against *Streptococci* including *E. faecalis*.

In this study, a combined computational approach was applied to investigate the relationship of the structural basis and antimicrobial activities of sigmacidins. Both 2D and 3D QSAR models were constructed, and the binding poses of the inhibitors to the protein were obtained.

The 2D QSAR model constructed revealed close structure-activity correlation and contribution of various properties/descriptors in the activity. In the model identified

in this study, ALogP, hydrogen bond acceptor (HBA), molecular polar surface area, and LUMO eigenvalue were taken to describe the SAR. The 2D QSAR equation implied that the activity of the compounds was related to and can be improved by increasing AlogP, molecular polar surface area, and the LUMO eigenvalue. This equation will be useful to estimate antimicrobial activity of newly designed compounds. Two-dimensional QSAR for bioactivity prediction is simple and efficient; however, it was obtained based on limited structures of substituents and may have accurate correlations to a relatively small range of substitutions for further structural optimizations.

The 3D QSAR model gained further insight into the 3D structure information for the understanding of the SAR of these antimicrobials. The importance of the steric and hydrophobic properties of the 3,4-substitution of the left benzene ring was highlighted, while the substituents at *para*-position of the -COOH group could be further explored for novel derivative synthesis. Besides guiding the modifications of existing molecules, the constructed model can also be used directly for virtual screening to identified novel hits.

Finally, molecular docking indicated possible binding poses of the inhibitors in complex with β' CH and MD simulations used to rationalize the docked poses. In this study, the docking model of the **40**- β' CH system showed similar stability to **1**- β' CH and the binding free energy of **40**- β' CH was slightly higher than that of **1**- β' CH, probably due to its flexible structure. Fortunately, the surface of the protein fragment is enriched in arginine which is elastic and able to accommodate more conformational changes of compound **40**. In addition, compared to the starting docking models, after 10 ns simulation, both compounds formed more H-bonding contacts with β' CH region, especially with "hotspot" residues, including Arg546, Arg550, and Arg553. This indicated that the binding affinity might be increased by enhancing acidity of the inhibitors. For example, the nitro group can be replaced by acidic substituents. While compound **40** demonstrated significantly superior antibacterial activity to compound **1**, the possible reasons may include the greater bacterial cell membrane permeability of compound **40** which was optimized from hit compound **1**. Nevertheless, the docking and MD simulations showed some difference, probably due to the challenging PPI target with a relatively flat binding site. Here, we need to combine the two methods which put forward possible contacts between ligands and the β' CH region. This combination is useful for future structure-based drug design. The newly designed compounds that fulfill the requirement by these 3D features may be able to bind to the same target protein and possess significant antimicrobial activity, which remain to be experimentally evaluated.

Overall, the models established in this study provided useful indications for the design of novel sigmacidins derivatives against pathogenic *Streptococci*. Note that sigmacidins also demonstrated excellent antimicrobial activity against *Staphylococci* such as *Staphylococcus aureus*, *Staphylococcus epidermidis*, and *Staphylococcus Saprophyticus* [20,21]. We believe that the further development of sigmacidins via ligand-based and structure-based drug design will contribute to novel antimicrobial agent discovery in the post-antibiotic era.

Supplementary Materials: The following supporting information can be downloaded at: <https://www.mdpi.com/article/10.3390/ijms23084085/s1>.

Author Contributions: J.Y.: data curation; formal analysis; investigation; methodology; validation; visualization; writing—original draft. X.Y.: conceptualization; funding acquisition; investigation; methodology; project administration; resources; validation; visualization; writing—review and editing. C.M.: conceptualization; formal analysis; funding acquisition; investigation; methodology; project administration; resources; software; supervision; validation; writing—original draft; writing—review and editing. All authors have read and agreed to the published version of the manuscript.

Funding: The research was supported by Hong Kong Research Grants Council (PolyU C5008-19G and 15100021 to C.M.), Hong Kong Polytechnic University (1-ZE2E and State Key Laboratory of Chemical Biology and Drug Discovery to C.M.), Hong Kong RGC General Research Fund CUHK 14107919 (X.Y.), Hong Kong Food and Health Bureau HMRF 19180052 (X.Y.), and the Chinese University of Hong Kong (Faculty of Medicine Faculty Innovation Award FIA2018/A/03 to X.Y.).

Institutional Review Board Statement: Not applicable.

Informed Consent Statement: Not applicable.

Data Availability Statement: Supporting information for this article is available upon request from corresponding authors.

Acknowledgments: We thank Jinyi Xu of China Pharmaceutical University for the technical assistance.

Conflicts of Interest: The authors declare no competing financial interest.

References

1. Leonard, A.; Gierok, P.; Methling, K.; Gómez-Mejía, A.; Hammerschmidt, S.; Lalk, M. Metabolic inventory of *Streptococcus pneumoniae* growing in a chemical defined environment. *Int. J. Med. Microbiol.* **2018**, *308*, 705–712. [CrossRef] [PubMed]
2. Avire, N.J.; Whiley, H.; Ross, K. A review of *Streptococcus pyogenes*: Public health risk factors, prevention and control. *Pathogens* **2021**, *10*, 248. [CrossRef] [PubMed]
3. Raabe, V.N.; Shane, A.L. Group B *Streptococcus* (*Streptococcus agalactiae*). *Microbiol. Spectr.* **2019**, *7*. [CrossRef] [PubMed]
4. Rossitto, P.V.; Ruiz, L.; Kikuchi, Y.; Glenn, K.; Luiz, K.; Watts, J.L.; Cullor, J.S. Antibiotic susceptibility patterns for environmental *streptococci* isolated from bovine mastitis in central California dairies. *J. Dairy Sci.* **2002**, *85*, 132–138. [CrossRef]
5. Heelan, J.S.; Hasenbein, M.E.; McAdam, A.J. Resistance of Group B *Streptococcus* to Selected Antibiotics, Including Erythromycin and Clindamycin. *J. Clin. Microbiol.* **2004**, *42*, 1263–1264. [CrossRef] [PubMed]
6. Cameron, M.; Saab, M.; Heider, L.; McClure, J.T.; Rodriguez-Lecompte, J.C.; Sanchez, J. Antimicrobial susceptibility patterns of environmental *streptococci* recovered from bovine milk samples in the Maritime Provinces of Canada. *Front. Vet. Sci.* **2016**, *3*, 79. [CrossRef]
7. Facklam, R. What happened to the *streptococci*: Overview of taxonomic and nomenclature changes. *Clin. Microbiol. Rev.* **2002**, *15*, 613–630. [CrossRef]
8. Appelbaum, P.C. Resistance among *Streptococcus pneumoniae*: Implications for drug selection. *Clin. Infect. Dis.* **2002**, *34*, 1613–1620. [CrossRef]
9. WHO. Global Priority List of Antibiotic-Resistant Bacteria to Guide Research, Discovery, and Development of New Antibiotics. 2017. Available online: https://www.who.int/medicines/publications/WHO-PPL-Short_Summary_25Feb-ET_NM_WHO.pdf (accessed on 28 February 2022).
10. Kahan, R.; Worm, D.J.; De Castro, G.V.; Ng, S.; Barnard, A. Modulators of protein-protein interactions as antimicrobial agents. *RSC Chem. Biol.* **2021**, *2*, 387–409. [CrossRef]
11. Ma, C.; Yang, X.; Lewis, P.J. Bacterial transcription as a target for antibacterial drug development. *Microbiol. Mol. Biol. Rev.* **2016**, *80*, 139–160. [CrossRef]
12. Keller, A.N.; Yang, X.; Wiedermannová, J.; Delumeau, O.; Krásný, L.; Lewis, P.J. ϵ , a new subunit of RNA polymerase found in gram-positive bacteria. *J. Bacteriol.* **2014**, *196*, 3622–3632. [CrossRef] [PubMed]
13. Yang, X.; Lewis, P.J. Overproduction and purification of recombinant *Bacillus subtilis* RNA polymerase. *Protein Expr. Purif.* **2008**, *59*, 86–93. [CrossRef] [PubMed]
14. Tsang, T.F.; Qiu, Y.; Lin, L.; Ye, J.; Ma, C.; Yang, X. Simple method for studying in vitro protein-protein interactions based on protein complementation and its application in drug screening targeting bacterial transcription. *ACS Infect. Dis.* **2019**, *5*, 521–527. [CrossRef] [PubMed]
15. Burgess, R.R.; Anthony, L. How sigma docks to RNA polymerase and what sigma does. *Curr. Opin. Microbiol.* **2001**, *4*, 126–131. [CrossRef]
16. Murakami, K.S.; Darst, S.A. Bacterial RNA polymerases: The whole story. *Curr. Opin. Struct. Biol.* **2003**, *13*, 31–39. [CrossRef]
17. Vassylyev, D.G.; Sekine, S.I.; Yokoyama, S.; Yokoyama, S. Crystal structure of a bacterial RNA polymerase holoenzyme at 2.6 Å resolution. *Nature* **2002**, *417*, 712–719. [CrossRef]
18. Ma, C.; Yang, X.; Lewis, P.J. Bacterial Transcription Inhibitor of RNA Polymerase Holoenzyme Formation by Structure-Based Drug Design: From In Silico Screening to Validation. *ACS Infect. Dis.* **2016**, *2*, 39–46. [CrossRef]
19. Ye, J.; Chu, A.J.; Lin, L.; Yang, X.; Ma, C. First-in-class inhibitors targeting the interaction between bacterial RNA polymerase and sigma initiation factor affect the viability and toxin release of *Streptococcus pneumoniae*. *Molecules* **2019**, *24*, 2902. [CrossRef]
20. Ye, J.; Chu, A.J.; Harper, R.; Chan, S.T.; Shek, T.L.; Zhang, Y.; Ip, M.; Sambir, M.; Artsimovitch, I.; Zuo, Z.; et al. Discovery of Antibacterials That Inhibit Bacterial RNA Polymerase Interactions with Sigma Factors. *J. Med. Chem.* **2020**, *63*, 7695–7720. [CrossRef]
21. Ye, J.; Chu, A.J.; Lin, L.; Chan, S.T.; Harper, R.; Xiao, M.; Artsimovitch, I.; Zuo, Z.; Ma, C.; Yang, X. Benzyl and benzoyl benzoic acid inhibitors of bacterial RNA polymerase-sigma factor interaction. *Eur. J. Med. Chem.* **2020**, *208*, 112671. [CrossRef]
22. Lewis, R.A.; Wood, D. Modern 2D QSAR for drug discovery. *Wiley Interdiscip. Rev. Comput. Mol. Sci.* **2014**, *4*, 505–522. [CrossRef]
23. Lill, M.A. Multi-dimensional QSAR in drug discovery. *Drug Discov. Today* **2007**, *12*, 1013–1017. [CrossRef] [PubMed]
24. Verma, J.; Khedkar, V.M.; Coutinho, E.C. 3D-QSAR in drug design—A review. *Curr. Top. Med. Chem.* **2010**, *10*, 95–115. [CrossRef] [PubMed]

25. Shukla, A.; Sharma, P.; Prakash, O.; Singh, M.; Kalani, K.; Khan, F.; Bawankule, D.U.; Luqman, S.; Srivastava, S.K. QSAR and docking studies on capsazepine derivatives for immunomodulatory and anti-inflammatory activity. *PLoS ONE* **2014**, *9*, e100797. [CrossRef]
26. Datar, P.A. 2D-QSAR study of indolylpyrimidines derivative as antibacterial against *Pseudomonas aeruginosa* and *Staphylococcus aureus*: A comparative approach. *J. Comput. Med.* **2014**, *2014*, 765457. [CrossRef]
27. Caron, G.; Ermondi, G.; Scherrer, R.A. Lipophilicity, polarity, and hydrophobicity. In *Comprehensive Medicinal Chemistry II*; Elsevier: Amsterdam, The Netherlands, 2006; Volume 5, pp. 425–452.
28. Graton, J.; Le Questel, J.Y.; Maxwell, P.; Popelier, P. Hydrogen-Bond Accepting Properties of New Heteroaromatic Ring Chemical Motifs: A Theoretical Study. *J. Chem. Inf. Model.* **2016**, *56*, 322–334. [CrossRef]
29. Clark, D.E. What has polar surface area ever done for drug discovery? *Future Med. Chem.* **2011**, *3*, 469–484. [CrossRef]
30. Lohray, B.B.; Gandhi, N.; Srivastava, B.K.; Lohray, V.B. 3D QSAR studies of N-4-arylacryloylpiperazin-1-yl-phenyl-oxazolidinones: A novel class of antibacterial agents. *Bioorganic Med. Chem. Lett.* **2006**, *16*, 3817–3823. [CrossRef]
31. Shakil, S.; Danish Rizvi, S.M.; Greig, N.H. High throughput virtual screening and molecular dynamics simulation for identifying a putative inhibitor of bacterial CTX-M-15. *Antibiotics* **2021**, *10*, 474. [CrossRef]
32. Raharjo, S.J.; Mahdi, C.; Nurdiana, N.; Kikuchi, T.; Fatchiyah, F. Binding energy calculation of patchouli alcohol isomer cyclooxygenase complexes suggested as COX-1/COX-2 selective inhibitor. *Adv. Bioinform.* **2014**, *2014*, 850628. [CrossRef]
33. *MacroModel, Version 10.2*; Schrödinger, LLC: New York, NY, USA, 2013.
34. Meduru, H.; Wang, Y.T.; Tsai, J.J.P.; Chen, Y.C. Finding a potential dipeptidyl peptidase-4 (DPP-4) inhibitor for type-2 diabetes treatment based on molecular docking, pharmacophore generation, and molecular dynamics simulation. *Int. J. Mol. Sci.* **2016**, *17*, 920. [CrossRef] [PubMed]
35. Yang, X.; Ma, C.; Lewis, P. A vector system that allows simple generation of mutant *Escherichia coli* RNA polymerase. *Plasmid* **2014**, *75*, 37–41. [CrossRef] [PubMed]
36. Yang, X.; Ma, C.; Lewis, P.J. Identification of inhibitors of bacterial RNA polymerase. *Methods* **2015**, *86*, 45–50. [CrossRef] [PubMed]

MDPI
St. Alban-Anlage 66
4052 Basel
Switzerland
Tel. +41 61 683 77 34
Fax +41 61 302 89 18
www.mdpi.com

International Journal of Molecular Sciences Editorial Office

E-mail: ijms@mdpi.com
www.mdpi.com/journal/ijms





Academic Open
Access Publishing

www.mdpi.com

ISBN 978-3-0365-7682-4